

FINAL TECHNICAL REPORT

Asia Pacific Research Initiative for Sustainable Energy Systems

Office of Naval Research

Grant Award Number N00014-14-1-0054

November 1, 2013 to December 31, 2017



March 2018

Table of Contents

EXECUTIVE SUMMARY	3
TASK 1: PROGRAM MANAGEMENT AND OUTREACH	6
TASK 2: FUEL CELL SYSTEMS	6
2.1 Fuel Cell Development, Testing and Modeling	6
2.2 Contamination Mitigation and Field Testing.....	50
TASK 3: ALTERNATIVE FUELS	61
3.1 Methane Hydrates	61
3.2 Technology for Synthetic Fuels Production.....	95
3.3 Solar Fuels Production	151
TASK 4: OCEAN ENERGY	153
4.1 Ocean Thermal Energy Conversion (OTEC).....	154
4.2 Wave Energy Testing	185
4.3 Seawater Air Conditioning	197
TASK 5: GEOTHERMAL RESOURCE ASSESSMENT	198
TASK 6: MICROGRIDS/GRID INTEGRATION	198
6.1 Solar Monitoring	198
6.2 Secure Microgrids.....	209
TASK 7: ENERGY EFFICIENCY	263

Final Technical Report
Asia Pacific Research Initiative for Sustainable Energy Systems
Grant Award Number N00014-14-1-0054
November 1, 2013 to December 31, 2017

EXECUTIVE SUMMARY

This report summarizes work conducted under Grant Award Number N00014-14-1-0054, the Asia Pacific Research Initiative for Sustainable Energy Systems 2013 (APRISES13), funded by the Office of Naval Research (ONR) to the Hawaii Natural Energy Institute (HNEI) of the University of Hawaii at Manoa (UH). The overall objective of APRISES13 was to develop, test, and evaluate distributed energy systems, emerging technologies and power grid integration using Hawaii as a model for applicability throughout the Pacific Region. APRISES13 encompassed fuel cell research, evaluation and contaminant mitigation; battery cell testing; seabed methane hydrates extraction and stability; synthetic fuels processing and production to accelerate the use of liquid biofuels for Navy needs; alternative energy systems for electric power generation, and integration into secure-smart microgrids, and; energy efficient building technologies and platforms. Testing and evaluation of alternative energy systems includes Ocean Thermal Energy Conversion (OTEC), grid-scale battery energy storage, and development of several microgrid test projects.

Under Task 1, Program Management, HNEI provided overall program management and coordination, developed and monitored partner and subcontract agreements, and developed outreach materials for both technical and non-technical audiences. Additionally, HNEI continued to collaborate closely with ONR and NRL to identify high-priority areas requiring further detailed evaluation and analysis.

Under Task 2, Fuel Cell Systems, HNEI conducted testing and evaluation of single cells and balance of plant components to: support NRL efforts to develop fuel cell powered unmanned aerial vehicles (UAVs); continue the development of advanced diagnostics suitable for the design of low cost and high power density fuel cells, and; develop contaminant mitigation techniques by testing and evaluating filtration materials. Support to NRL included design and validation of a hydrogen gas management system. As well, work was done to minimize the cost of vanadium flow batteries by selecting salts of lower purity. HNEI also built a battery-testing laboratory and investigated key performance limiting aspects of battery modules.

Efforts under Task 3, Alternative Fuels, focused on the development, testing and evaluation of alternative fuels and technologies, and included activities in the areas of Methane Hydrates, Technology for Synthetic Fuels Production, and Low-cost Material for Solar Fuels Production. Methane hydrate destabilization was examined using non-toxic aqueous glycerol solutions, and

the Raman calorimeter facility was modified to study hydrate self-preservation phenomena. Several advanced technologies for synthetic fuels production were investigated. Fundamental properties of synthetic waste stream components were characterized and analyzed to predict fuel characteristics and reactivity of the composite heterogeneous waste. The properties and oxidation stabilities of biodiesel derived from catfish oil generated by processing plants in Vietnam was investigated. Biomass activity in a high-rate anaerobic digestion process was advanced through development of hybrid supports by further improving the design to eliminate gas hold up. To produce liquid fuels from synthesis gas, a solid phosphoric acid catalyst was investigated to derive hydrocarbon oils. The metabolic pathways associated with the degradation of fuels were further characterized to expand the database of genetic information to serve as the basis for rapid-detection, fuel-test capabilities and design of inhibitors. Corrosion inhibitors were investigated to attenuate corrosion in HRD fuel/seawater mixtures. A reproducibility study was conducted on the novel carbonization process along with exploration of the effects of heat-treatment to produce near-theoretical fixed-carbon yields. For solar fuels production, low-cost and environmentally friendly materials were investigated.

Task 4, Ocean Energy work included development of Ocean Thermal Energy Conversion (OTEC), Wave Energy Testing and Seawater Air Conditioning. Continued development and testing of new OTEC fabrication methods and designs focused on laser welded heat exchanger development, along with corrosion testing under a subaward to Makai Ocean Engineering. Wave energy testing research objectives and plans were further developed in collaboration with NAVFAC at the Navy's Wave Energy Test Site (WETS) off Marine Corps Base Hawaii (MCBH). In addition, numerical hydrodynamic modeling was also conducted on wave energy conversion devices and their performance. Seawater Air Conditioning (SWAC) pre-impact conditions were characterized with further deployments of long-term oceanographic mooring, water column profiling and sampling.

Funding for the Geothermal Resource Assessment planned for task 5 was reallocated to other areas of the program as approved by ONR.

Task 6, Microgrids/Grid Integration included a range of projects to develop, test and integrate secure microgrid technology including distributed energy resources. An analysis tool was developed to analyze PV performance as a function of environmental conditions. A low-cost real-time power monitor was developed with wireless communications for distribution system operations, controls, and analysis. Methods were developed to synthesize realistic PV inverter and distribution service transformer data by extrapolating results in a simulation environment using data collected in the field. The Hawaii Virtual Power Plant Demonstration Project with combined PV and battery energy storage systems (BESS) was initiated, with development of the project scope, partner roles and responsibilities identified, and utility approval secured. A series of problems with the Oahu BESS were analyzed and addressed, and testing initiated. Algorithms for the Molokai BESS were further modified to improve responses to grid conditions. For the Coconut Island DC microgrid, an electric boat and electric utility vehicle were procured, along with a

swappable battery system. Additionally, a request for proposals was developed to procure the PV, stationary battery, and integrator for the whole Coconut Island DC microgrid. Two projects were conducted for the Molokai electric grid, to address the impact of PV generation on voltage at the circuit level, and to compare two tools for system-level analysis. Development was continued on solar forecasting methods and systems, including deployment in an operational framework.

Projects completed under Task 7, Energy Efficiency included installation of PV systems on two Project FROG net zero energy platforms, expansion of the classroom comfort and energy utilization studies, as well as design of a desiccant dehumidification pilot and assessment of the applicability of ceiling fans to low energy, thermal comfort.

This report describes the work that has been accomplished under each of these tasks, along with summaries of task efforts that are detailed in journal and other publications, including reports, conference proceedings and presentations. Publications produced through these efforts are listed and available, or linked, on HNEI's website at <https://www.hnei.hawaii.edu/publications/project-reports#APRISES13>.

TASK 1: PROGRAM MANAGEMENT AND OUTREACH

This program-wide task provided management and coordination of all research, test, development and evaluation efforts under APRISES13. Partner and subcontract agreements were developed and monitored, and outreach materials for both technical and non-technical audiences were developed. In close collaboration with ONR, high-priority needs requiring further detailed evaluation and analysis were identified for application of emerging energy technologies, with a focus on Hawaii and the Asia-Pacific region. Task-specific information and more detail are provided below for partner, subcontract and outreach activities.

TASK 2: FUEL CELL SYSTEMS

Testing and evaluation was conducted on single cells and balance of plant components to: support NRL efforts to develop fuel cell powered unmanned aerial vehicles (UAVs); develop contaminant mitigation techniques by testing and evaluating filtration materials, and; continue the development of advanced diagnostics suitable for the design of low cost and high power density fuel cells. As well, work was done to minimize the cost of vanadium flow batteries by selecting salts of lower purity. Under this task, a battery-testing laboratory was build and key performance limiting aspects of battery modules were investigated.

2.1 Fuel Cell Development, Testing and Modeling

Under subtask 2.1, HNEI conducted testing and evaluation of single cells and balance of plant components to support NRL efforts to develop fuel cell powered UAVs; continued experiments and analysis to improve understanding of contamination mechanisms and develop recovery techniques for fuel cell contaminated with air or system contaminants; and continued the development of advanced diagnostics for use in the design of low cost and high power density fuel cells. Under this subtask, HNEI also initiated activities to characterize the impact of lower purity salts for use in vanadium flow batteries, a significant factor on system cost.

The key accomplishments were as follows: worked with NRL to identify and down select methodologies for high efficiency hydrogen recirculation and exhaust gas management applicable to the NRL 66 PRO system that would meet the stringent low weight and volume requirements while achieving hydrogen utilizations greater than 96 %; initiated performance testing of various vanadium salts purities to address fundamental cost issues of the technology; developed and tested

recovery techniques utilizing ozone treatment for fuel cells contaminated with acetonitrile, bromomethane and hydrogen chloride.

Details of the work conducted in each of these areas are described below, and in the publications and presentations referenced at the end of this section.

NRL Support

Under APRISES 2013 funding, HNEI engineers worked with NRL to identify and down select methodologies for high efficiency hydrogen recirculation and exhaust gas management applicable to the NRL 66 PRO system that would meet the stringent low weight and volume requirements while achieving hydrogen utilizations greater than 96 %. This work initially resulted in the selection of a dead-ended anode (DEA) operation mode with the hydrogen supplied to the anode at a constant pressure and periodically purged to remove water, nitrogen that has crossed over from the cathode through the membrane, and impurities contained in the hydrogen supply that build up in the down-stream section of the flow field.⁵⁻⁸ However, running fuel cells in DEA mode can result in uncontrolled volumes of gas being exhausted during purge operations. The purge valve must remain open for a sufficiently long time to flush water vapor, excess nitrogen, impurities and liquid water while minimizing the amount of unused hydrogen being simultaneously exhausted. The variability in the mixed gas density and composition and the mixed phase flow through the purge valve orifice is difficult to predict and thus conservative valve opening times are used resulting in excess hydrogen being expelled that lowers hydrogen utilization. In addition, to flush liquid water out of the gas channels, a minimum gas velocity must be reached and thus a relatively large purge valve orifice is needed, which also increases the purge volume uncertainty. HNEI suggested that this variability in gas composition and water phase is counteracted, while using a relatively large orifice to achieve high flows, by adding a ballast volume down-stream of the purge valve. The fuel cell is purged into a known volume termed a ‘flash ballast’. Subsequently, that volume is exhausted to the atmosphere. This modification enables control of the gas volume exhausted during each purge event, which is based on the operating pressure and the selected flash ballast volume. HNEI designed an optimized algorithm for initiating a purge event using a physical model of the fuel cell and the flash ballast subsystem developed in Matlab Simulink. The algorithm uses an accumulated load dependent timing such that for higher currents and product water amounts, the purge events happen more frequently. The ballast modification is also characterized by a theoretical hydrogen utilization greater than 98 %, the avoidance of sensors which would add weight, and the use of a single on/off purging valve. Under APRISES 2012, three prototype units will be built, tested, and shipped to NRL for incorporation into the NRL 66 PRO fuel cell system. This report provides a general review of the down-selection process, model and algorithm development efforts, and hardware prototypes. Detailed specifications for the hardware components, experiments, and algorithms will become available when the NRL 66 PRO development project has been completed. *Additional information can be obtained by contacting Karen Swider-Lyons at NRL in Washington D.C.*

Improvement and simplification of the Protonex ballast based pressure swing system and avoidance of intellectual property infringement were adopted as the first NRL 66 PRO system objectives for the design of the hydrogen gas management system. A hybrid version of a check

valve pressure swing based system designed for hydrogen/oxygen systems by the Japan Aerospace Exploration Agency¹¹ and the Protonex valve based system was developed by HNEI to accomplish these objectives, as shown in Figure 2.1.1c. This system reduced the number of active valves from four to two, equivalent to the number for a DEA system (Figure 2.1.1a), while providing the capability to run in a pressure swing configuration.

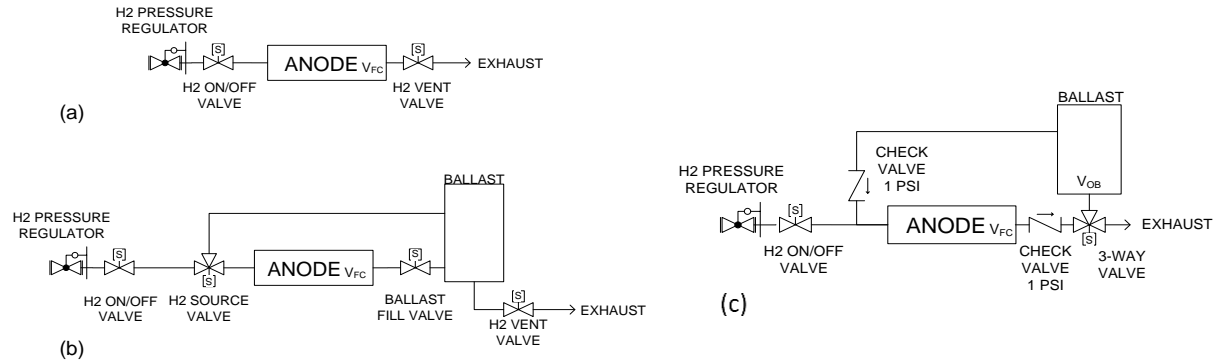


Figure 2.1.1. Fuel cell hydrogen recirculation and exhaust gas management schematics for lightweight UAVs.

For the NRL 66 PRO system, NRL engineers indicated that any ballast must be <1 L to fit inside the system chassis. Therefore, three key questions needed answers to design and size the system, avoid hydrogen starvation and provide sufficient flows to remove liquid water:

1. What is the acceptable level of nitrogen build-up in the ballast before a purge is initiated?
2. What is the optimal pressure swing range?
3. What is the maximum pressure decay rate when hydrogen is consumed in the ballast?

Essentially, the required combination of these parameters for safe operation represents the point where the diffusion rate of hydrogen to the electrode surface is still larger than the cumulative effect of convective flow away from the electrode due to gas expansion induced by the pressure decrease and the increasing flow of crossover nitrogen at the electrode surface promoted by the larger pressure difference between cathode and anode. If the pressure decay rate or nitrogen concentration is too high, hydrogen cannot diffuse at a sufficient rate to the electrode surface and support the operating current resulting in hydrogen starvation which can lead to electrode degradation by carbon corrosion.

These three parameters were obtained with single cell tests performed using an experimental apparatus that was developed to simulate the gas composition in a ballast by mixing and introducing hydrogen/nitrogen mixtures into a secondary ballast located at the fuel cell inlet. Subsequently, the gas from this secondary ballast is directed into the fuel cell thus simulating nitrogen accumulation while still exhausting into the fuel cell outlet ballast representative of the actual system, as shown in Figure 2.1.2. The sequence of valve operations controls gas flows and pressures into the various volumes and simulates the pressure swing behavior of the actual system. Additionally, conditions can be changed more rapidly than during actual operation thus broadening the range of accessible parameter values. Illustrative data are shown in Figure 2.1.2 with the cell

voltage plotted as a function of the gas pressure from the fuel cell inlet secondary ballast and nitrogen concentration simulating the accumulated nitrogen in the outlet ballast. For a 24 % nitrogen in hydrogen stream, the cell voltage rapidly begins to decay as the pressure decreases indicating a transition to hydrogen starvation. Analysis of all simulated experiments' results led to a maximum allowable nitrogen concentration of approximately 20 %, a pressure range of 210 to 170 kPa_g, and a maximum allowable pressure decay rate of 25 kPa/s to avoid hydrogen starvation and maintain a reasonable safety margin.

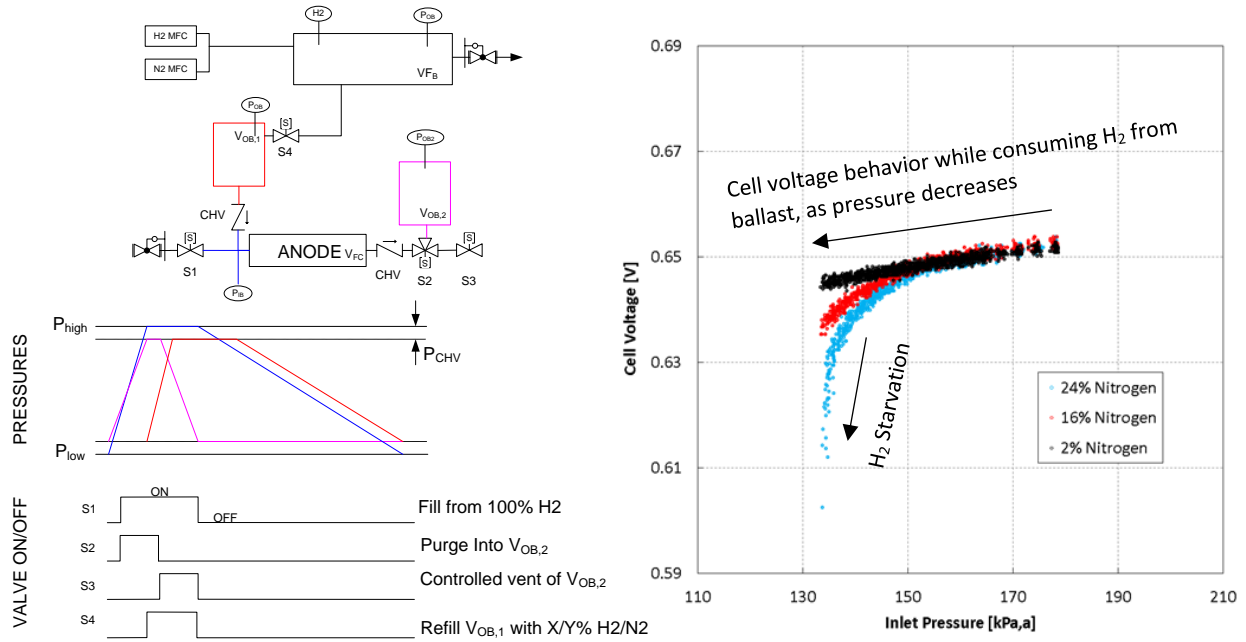


Figure 2.1.2. Experimental apparatus to study pressure swing hydrogen recirculation and example results.

Parameters values were used with a specifically developed ballast volume calculation, which yielded the required values as a function of stack power output (Figure 2.1.3). Required ballast volumes were unsurprisingly 2-3 L, which were larger than the hydrogen tank being used and the NRL specification of 1 L. It was concluded that an acceptable set of operating parameters preventing hydrogen starvation was not accessible to consider pressure swing recirculation for the NRL 66 PRO.

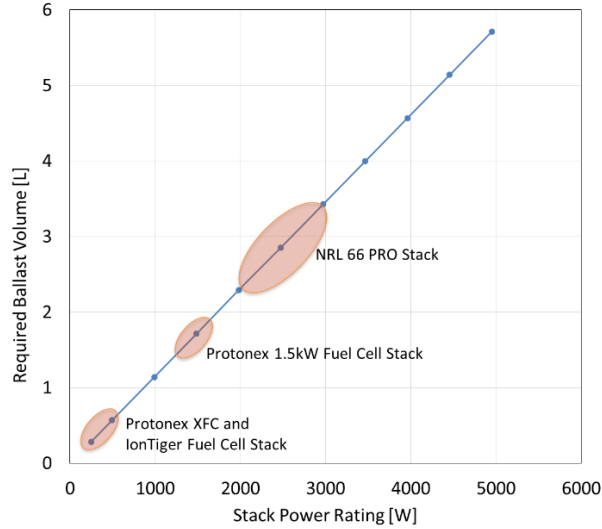


Figure 2.1.3. Pressure swing recirculation ballast size requirement versus stack power rating.

As a result of discussions between NRL and HNEI, a consensus was reached with a return to the DEA operating mode and an adaptation of the fuel cell outlet ballast approach to control the volume of gases exhausted during each purge. This flash ballast approach uses a constant pressure at the fuel cell inlet and for each purge event, a three-way valve first directs the gas from the fuel cell outlet into a small ballast (flash purges), which is followed by an exhaust of the ballast content to the vent through a check valve, as depicted in Figure 2.1.4. This method overcomes issues related to uncontrolled purging with a simple DEA approach without a ballast (Figure 2.1.1a), while minimizing the controls needed and meeting the low cost, mass, and volume requirements.

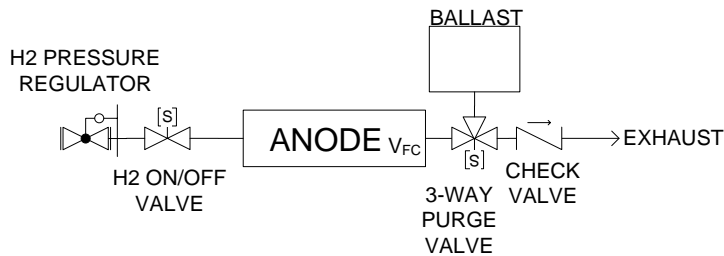


Figure 2.1.4. HNEI flash ballast DEA hydrogen management hardware layout.

After the hydrogen management methodology was selected, the focus shifted to the optimization of the hardware and control, including the optimal ballast size, purge valve flow, and purge valve timing algorithm. A finite volume physical model was developed in Matlab Simulink/Stateflow to complete this task. The finite volume model, illustrated in Figure 2.4.5, calculates changes in mole fractions of gas along the anode flow channel as hydrogen is consumed and nitrogen and water vapor diffuse from the cathode compartment through the membrane. Flash ballast purge events are simulated by opening valve V1, thus allowing the gas to flow from the anode into the ballast. Subsequently, valve V1 is closed and valve V2 is opened to exhaust the content of the ballast to a vent. The cycle is repeated for various time intervals. The cumulative flow of hydrogen exiting the vent is compared to the cumulative flow of fresh hydrogen into the fuel cell to estimate the hydrogen utilization. Power profiles from real UAV test flights are used to assess various hardware configurations and purge timing algorithms.

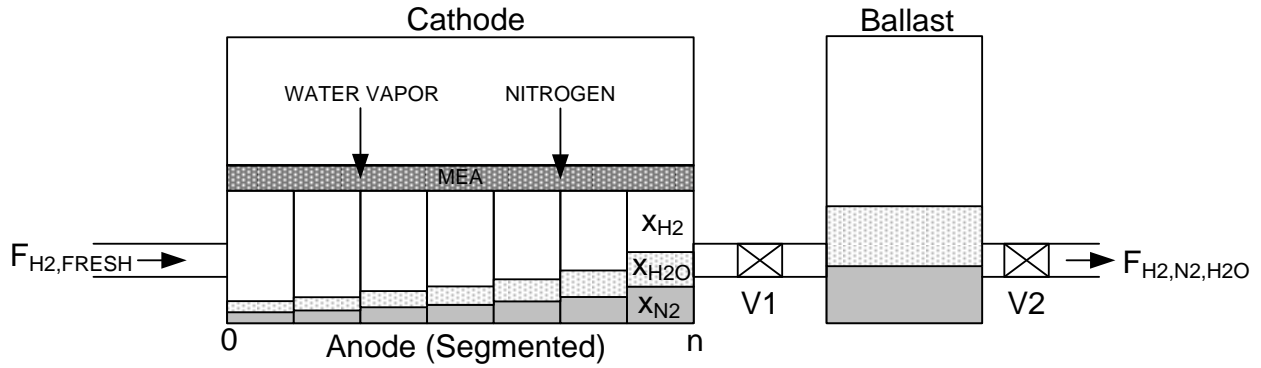


Figure 2.1.5. Finite volume model of a fuel cell anode with a segmented anode gas channel, flash ballast and, cathode water vapor and nitrogen diffusion processes.

An example of the model output used to evaluate the evolution of the gas mole fractions along the anode flow channel over time for a typical UAV power profile is shown in Figure 2.1.6. For this particular model run, the anode gas channel was discretized into 7 segments with segment 1 located at the inlet of the fuel cell.

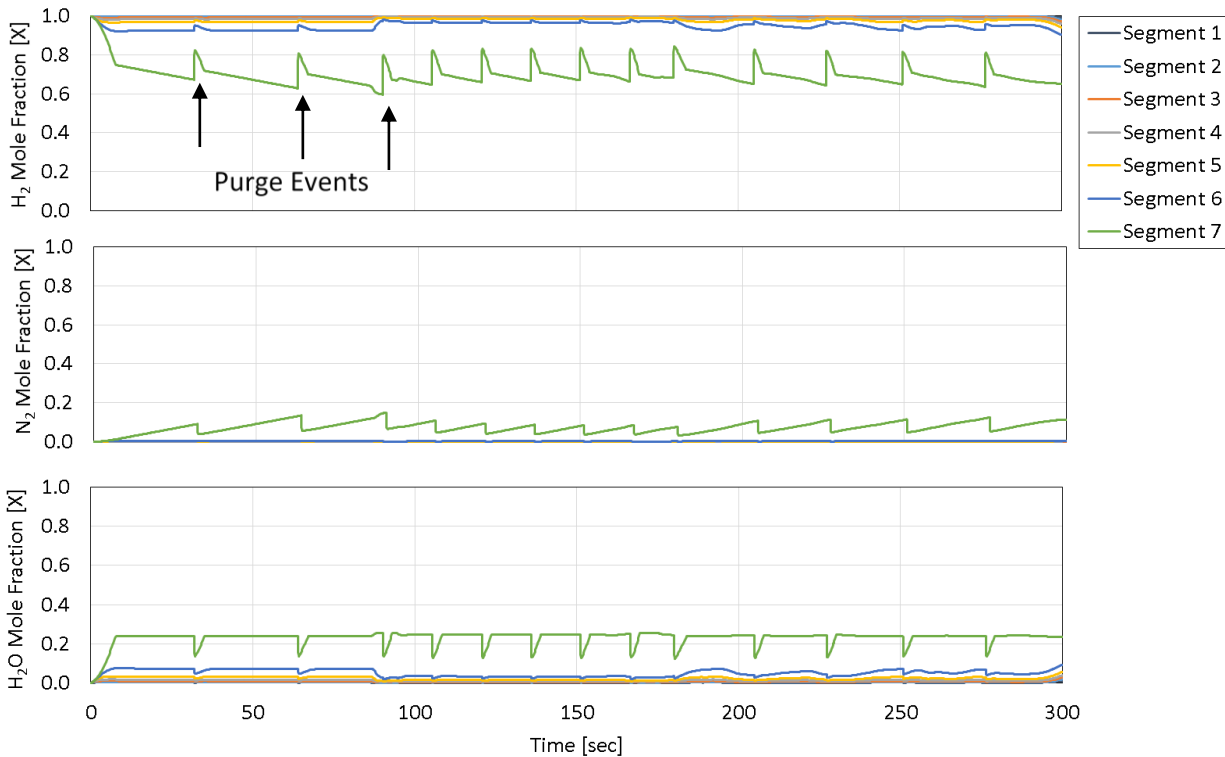


Figure 2.1.6. Example simulation results for the mole fraction of hydrogen, nitrogen and water vapor along the anode gas channel for a typical UAV power profile.

The majority of the accumulated nitrogen and water vapor for DEA operation is located at the outlet of the fuel cell (Figures 2.1.5 and 2.1.6). This situation highlights the goal of the simulation optimization routine with the concurrent minimization of the accumulation by purging and the

amount of excess hydrogen lost. Additionally, the simulation is also used to evaluate the adequacy of the purge valve and ballast sizes for the generation of flow pulses that are sufficiently large to flush out liquid water during each purge event (Figure 2.1.7).

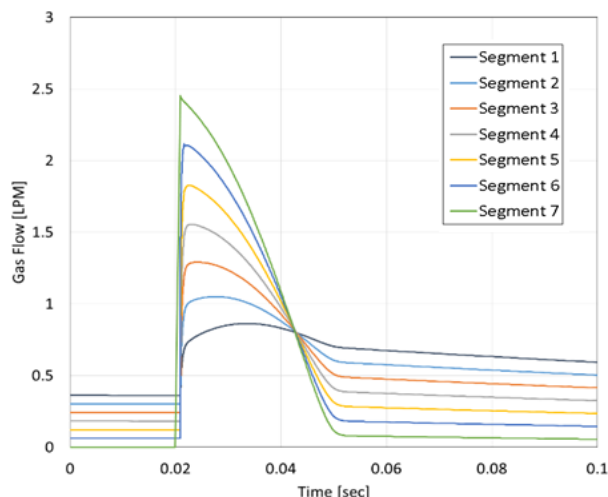


Figure 2.1.7. Example simulation results of the gas flow rate along the anode gas channel of a single cell within the fuel cell stack during a purge event.

The timing algorithm defines purge events. The simplest algorithm is based on a repeating cycle with constant time intervals, such as a combination of an 8 s constant pressure operation followed by 2 s purge into the ballast. Other algorithms that include current dependent time intervals were considered because nitrogen and water diffusion rates through the membrane are dependent on the power level. The optimized algorithm that was developed uses a load dependent purge strategy, which is analogous to the protocol used in ¹², with i) a purge event initiated after a certain number of load-hours has been reached or ii) a maximum amount of time has elapsed since the last purge. As a result, the elapsed time between purges and the purge duration are variable, with shorter time intervals between purges with a cell operated at high currents and, faster nitrogen and water vapor diffusion rates from the cathode. Figure 2.1.8 presents several examples of the variability in the hydrogen utilization as a function of the current level and algorithm type for parameters representing the developed prototype hardware design currently being evaluated after integration to the NRL PRO 66 system. A constant purge timing range of 5 to 30 s was selected on the basis of previous testing results for comparative purposes. Example model results for a hybrid load dependent strategy (a combination of constant time intervals at low current densities and load dependent time intervals at high current densities) are also shown in Figure 2.1.8. The power requirement to operate the valves is shown on the top right graph of Figure 2.1.8 as a percentage of the fuel cell rated power as a function of the current level. These power losses are not incorporated into the hydrogen utilization calculations. The average nitrogen concentration near the end of the flow field is also shown for the various strategies. However, cell voltages losses associated with the nitrogen buildup need to be evaluated in situ. These cell voltage losses were not included in the model to minimize complexity and avoid the need for model validation experiments. An evaluation of the purge approach and performance impact is currently ongoing (spring 2018) using a 49 cell NRL 66 PRO fuel cell stack.

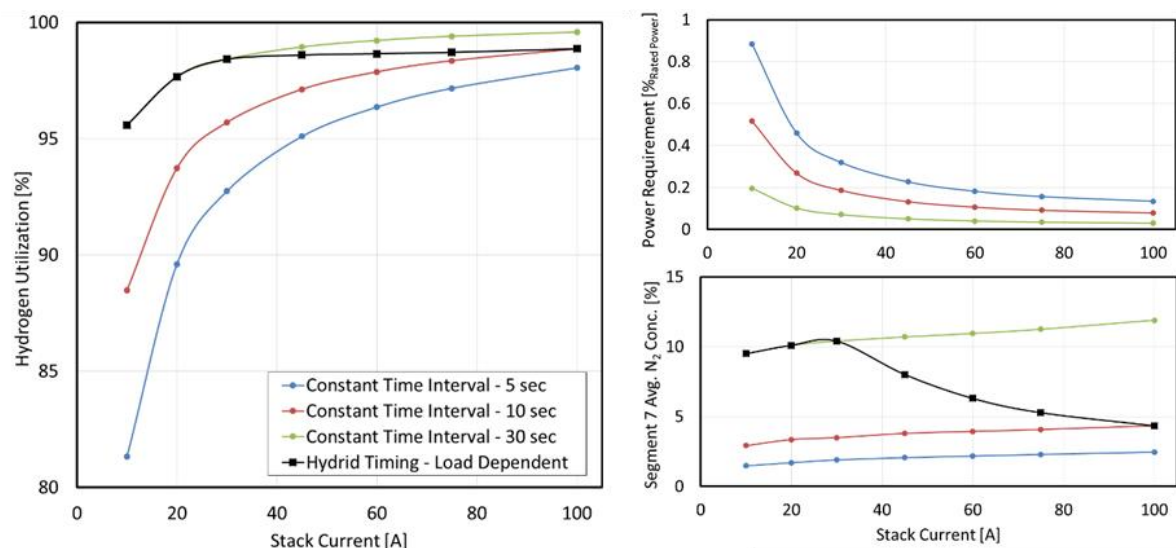


Figure 2.1.8. Example simulation results of purge algorithm effects on hydrogen utilization, nitrogen accumulation, and required valve power.

The flash ballast hardware is a three-way valve manifold with 3 ports (Figure 2.1.4). The three ports respectively connect to the hydrogen outlet of the fuel cell stack, to the ballast, and to the exhaust via a check valve. The manifold body was designed to overlap and attach to the existing port on the stack using the same screw holes, as shown in Figure 2.1.9a. The shape of the manifold and hardware was designed to fit into an available open space between the stack tubing (oxidant and coolant) and one of the stack end, as shown in the full 3D CAD layout in Figure 2.1.9b. As previously stated, high flow rates are desired to effectively flush out liquid water. However, light weight valves (<10 g) with large orifices are not commercially available. For the prototype design, four Parker 10xL_e solenoid valves were connected in parallel to achieve higher velocities during purge events. Future design upgrades will take into account a switch from solenoid valves to a servo-actuated plug valve with a power requirement that is independent of the orifice size. ULTEM 1000 was selected as the material for the prototype design. This material has an excellent chemical resistance and a wide operating temperature range in comparison to other options that were examined such as Nylon 66. ULTEM 1000 eliminated risks associated with material compatibility during the initial testing and evaluation phase of the system hardware layout and functionality. A lightweight, thin, aluminum bottle (50 or 125 mL volume) was selected for the ballast. A low cracking pressure check valve is used at the fuel cell exhaust to prevent back-diffusion of air into the ballast to reduce the risk of creating explosive gas mixtures. The fully assembled version of the flash ballast hardware, with a 125 mL ballast, is shown in Figure 2.1.9c. After completion of the hardware performance evaluation and purge algorithm tuning, three prototype flash ballast hardware systems will be shipped to NRL for integration into NRL PRO 66 fuel cell systems.

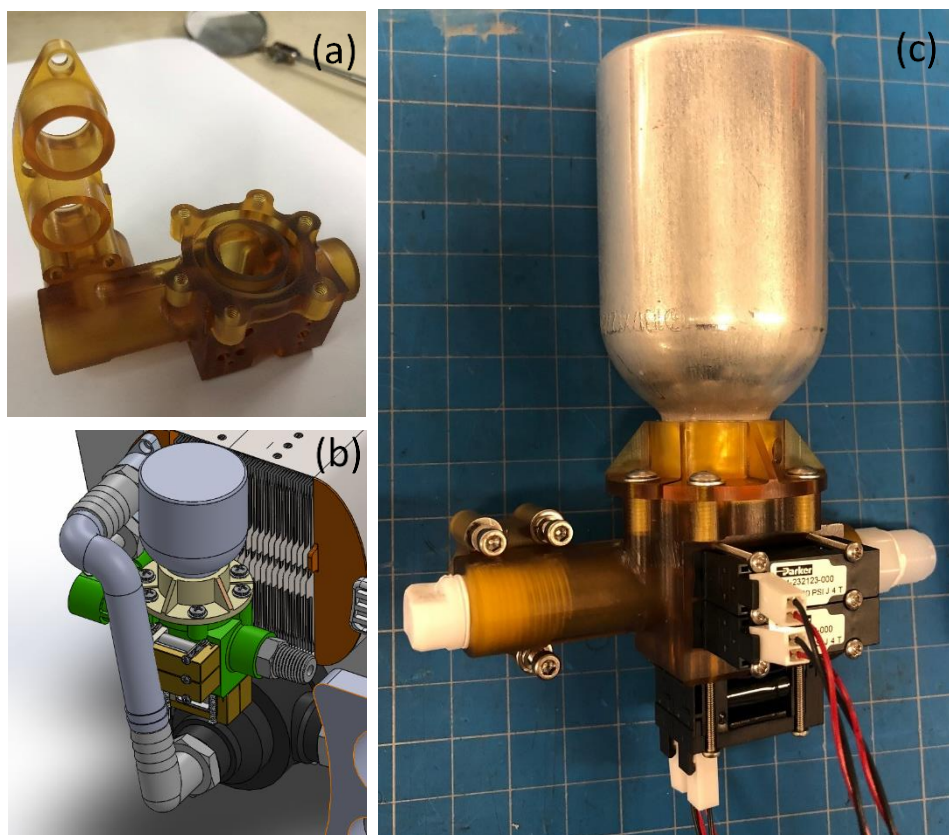
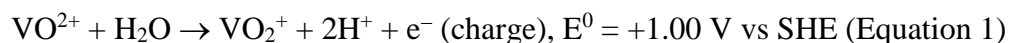


Figure 2.1.9. Flash ballast hardware. Stack end port manifold and flash ballast manifold body fit test (a), 3D CAD drawing of the flash ballast location in the fuel cell system (b), and first prototype of the flash ballast manifold (c).

Impact of Vanadium Salt Grades and Cost on Flow Battery Reactions

Under APRISES 2013, HNEI leveraged its contaminant expertise in Proton Exchange Membrane Fuel Cell (PEMFC) systems to initiate relevant activities in flow batteries. This required the acquisition and implementation of new capabilities to charge electrolytes (two compartments glass cell) in order to obtain electrolytes with one vanadium cation (among the 4 vanadium valences). As a first objective, which leverages HNEI expertise in contamination, focus was given to a better understanding of the cost minimization compromise using lower salt purity. It is anticipated that a lower purity and cost salt contains a larger amount of impurities, which are expected to have an adverse effect on voltage efficiency. As a secondary objective, the project was initiated to build expertise in flow batteries and be in a better position to evaluate the technology.

The following half-cell reactions take place in the vanadium redox flow battery (VRFB) (Figure 2.1.10). At the positive electrode, vanadium (IV) ions are transformed to vanadium (V) ions (the reverse reaction take place during the discharge):



At the negative electrode, vanadium (III) ions are transformed to vanadium (II) ions (the reverse reaction take place during the discharge):

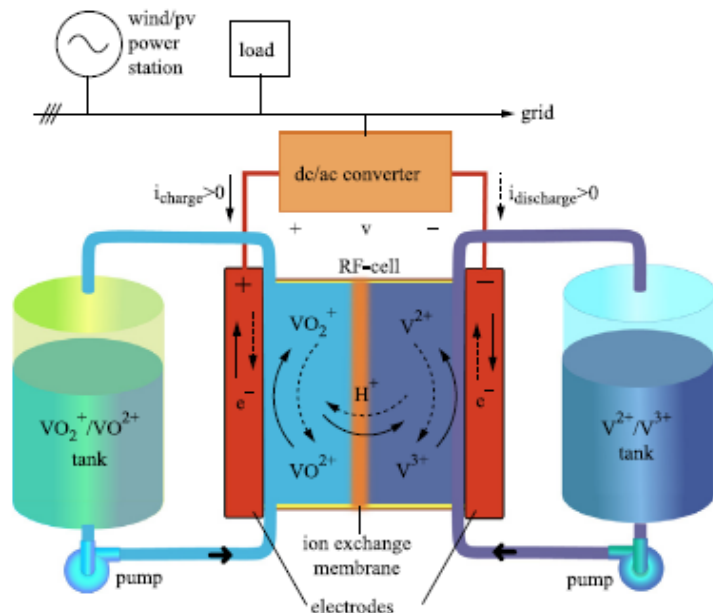
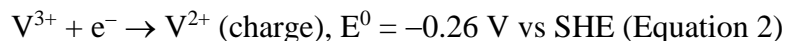


Figure 2.1.10. Schematic illustration of the redox reactions inside a VRFB.¹³

As a first step, various carbon electrodes, the incumbent catalyst material, were investigated to optimize the electrode potential, including glassy carbon, SGL 25BC gas diffusion layer, and, graphite powder, rod and plate. Among these electrode materials, graphite powder and rod both exhibited the best catalytic activity for $\text{VO}_2^+/\text{VO}^{2+}$ vanadium redox reactions. The purity impact of commercially available vanadium salts on $\text{VO}_2^+/\text{VO}^{2+}$ redox reactions was also evaluated. Five commercial vanadium salts (vanadium oxide sulfate, VOSO_4) with purities of 96, 97, 99.9 and 99.99 % on a metal basis were purchased. Figure 2.1.11 shows cyclic voltammetry (CV) curves for the different VOSO_4 salts dissolved in a H_2SO_4 supporting electrolyte, which demonstrates the charging and discharging performance of the VRFB positive electrode. Well defined anodic and cathodic peaks related to the $\text{VO}_2^+/\text{VO}^{2+}$ redox reactions were obtained in each case. Electrochemical data derived from CVs are given in Table 2.1.1. The potential of the coupled anodic (E_{pa}) and cathodic (E_{pc}) peaks are similar. However, for the VO^{2+} oxidation, the anodic peak current (I_{pa}) measured in the electrolyte with highest purity (99.99 %) is the largest whereas the electrolyte with least purity (96 %) shows the lowest cathodic peak current (I_{pc}). The reversibility of the $\text{VO}_2^+/\text{VO}^{2+}$ redox reactions is evaluated on the basis of the potential separation between peaks (ΔE_{p}) and the peak currents ratio ($I_{\text{pa}}/I_{\text{pc}}$). Values of 59 mV and 1 correspond to a reversible one-electron process.¹⁴ Table 2.1.1 results indicate that the reversibility of the $\text{VO}_2^+/\text{VO}^{2+}$ redox reactions in a V(IV) electrolyte is slightly poorer in the least pure electrolyte. These initial results need to be repeated and completed for the same reactions in a V(V) electrolyte and for $\text{V}^{3+}/\text{V}^{2+}$ redox reactions to complete the optimization of the quality/price ratio of vanadium salts and voltage efficiency of VRFBs.

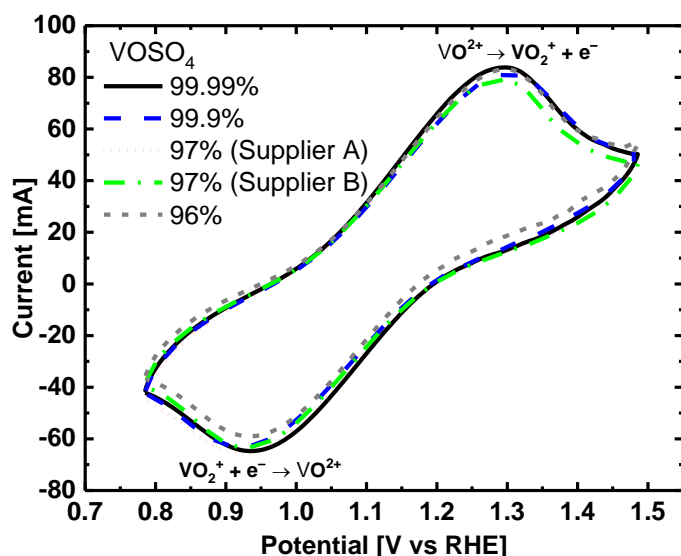


Figure 2.1.11. The $\text{VO}_2^+/\text{VO}^{2+}$ redox reactions on a graphite rod electrode recorded at 20 mV s^{-1} in N_2 saturated $3 \text{ M H}_2\text{SO}_4 + 1 \text{ M commercial VOSO}_4$ salts with different purities at 25°C .

Table 2.1.1. Electrochemical data obtained from the cyclic voltammograms recorded in Figure 2.1.11.

VOSO₄/purity (%)	E_{pa} (V)	E_{pc} (V)	I_{pa} (mA)	I_{pc} (mA)	ΔE_p (V)	I_{pa}/I_{pc}
99.99	1.296	0.933	83.822	64.729	0.363	1.295
99.9	1.299	0.919	81.112	63.042	0.380	1.287
97 (supplier A)	1.296	0.923	82.392	65.659	0.373	1.255
97 (supplier B)	1.289	0.929	79.002	63.330	0.360	1.247
96	1.296	0.934	83.349	59.115	0.362	1.410

Additional information was collected during this period to continue building expertise in this area. It was also realized that additional capabilities were needed to obtain solutions containing vanadium of other valences than (IV) because only the V(IV) sulfate salt compatible with the sulfuric acid based solution is available, confirm the vanadium concentration because a few of the salts are hydrates of unknown composition, and identify the impurities present in the commercial VOSO_4 salts by inductively coupled plasma (ICP) analysis for correlation with electrode performance data, which respectively required the acquisition of an electrolyte charging cell, a titrator, and a vanadium standard solution.

Figure 2.1.12 shows CV curves for various scan rates and rotation rates. As the potential scan rate increases (Figure 2.1.12a), the oxidation and reduction peak potentials of $\text{VO}_2^+/\text{VO}^{2+}$ redox reactions respectively shift toward positive and negative potentials. Similar information is important to quantitatively evaluate the reversibility of all vanadium reactions,¹⁴ which is related to the VRFB voltage efficiency. Figure 2.1.12b shows representative anodic polarization curves at 1600 and 2500 rpm rotation rates of the rotating disk electrode (RDE). The effect of rotation rate becomes significant at potentials above 1.2 V versus RHE. Results suggest that the redox behavior

of vanadium (IV) and (V) is governed by a diffusion controlled mechanism for large current densities. In practical terms, this information is tied to the maximum VRFB charge and discharging rates.

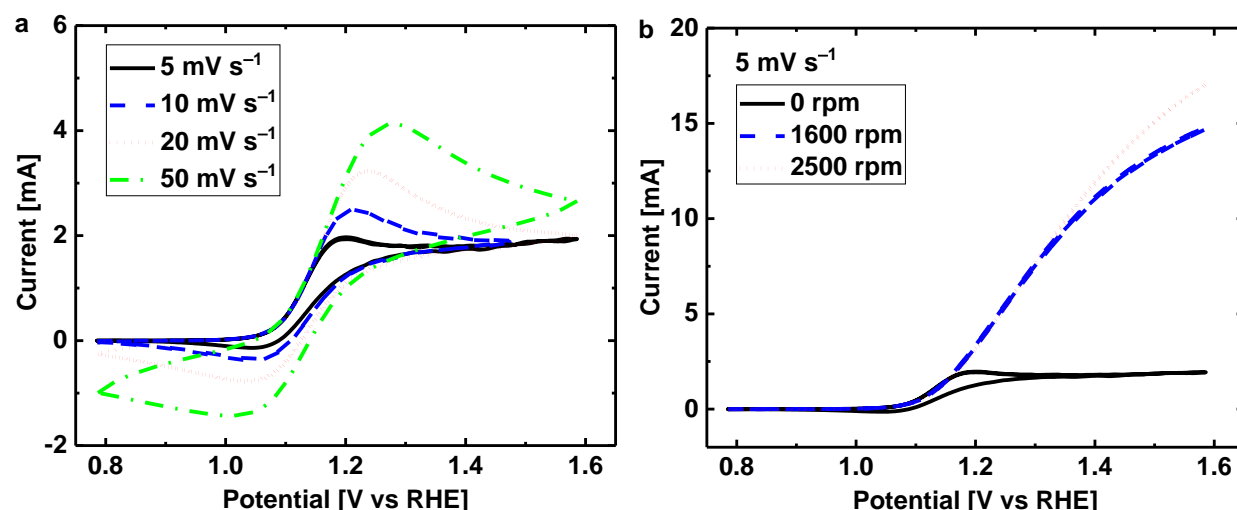


Figure 2.1.12. CV curves of $\text{VO}_2^+/\text{VO}^{2+}$ redox reactions on graphite powder coated on a rotating disc electrode in N_2 saturated 3 M H_2SO_4 + 1 M VOSO_4 at 25 °C.

It was also observed that the salt purity affects the stability of electrolytes, an important consideration for VRFBs to avoid flow blockages. Stability tests were carried out statically without any agitation. Each sample was monitored for the presence of a precipitate and for a solution color change. As shown in Figure 2.1.13, one sample with 0.5 M VOSO_4 in water was stable for more than 2 years (leftmost volumetric flask), whereas precipitates were found in all other solutions within just 2 or 3 days. The precipitates will be collected by filtration, rinsing and drying in air, for XRD analysis (phase and composition identification) to attempt an identification of the species causing this effect. Vanadium precipitation has already been recognized in a few reports focusing on finding additives that can stabilize solutions for a longer period of time.^{15,16}

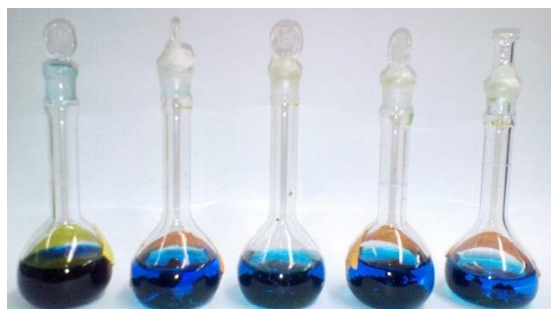


Figure 2.1.13. Stabilities of 0.5 M VOSO_4 aqueous solution prepared with different vanadium salt purities.

Initially, the vanadium (IV) electrolyte is prepared by dissolving VOSO_4 in a sulfuric acid solution (1 M VOSO_4 and 3 M H_2SO_4), a composition that is representative of VRFBs. Vanadium (II), (III), and (V) electrolytes are prepared by electrolytic oxidation and reduction of vanadium (IV) solutions. The experimental setup consists of several parts: a potentiostat, a two-compartment custom-made electrochemical cell separated by a membrane (Figure 2.1.14), a gas delivery system,

and a cooling/heating system. The potentiostat is used to control either the potential or current through electrodes. The vanadium (IV) electrolyte is added to both cell compartments (Figure 2.1.14, left). The gas delivery system is comprised of high purity inert gas (nitrogen) and a manifold to deliver the gas at ambient pressure to the electrochemical cell for electrolyte degassing (dissolved oxygen removal to prevent the oxidation of vanadium). The cell has an integrated water jacket that can be used to cool/heat the contents of both cell chambers. Two hose barbs provide access to the outer water jacket chamber. The cell is fully charged up to 1.6 V at a constant current density.¹⁷ The current density is determined by the maximum current output of the potentiostat and the active area of the electrodes. The blue vanadium (IV) in the positive compartment is converted into yellow vanadium (V) (Figure 2.1.14, right), whereas the vanadium (IV) in the negative compartment is converted into a dark cyan (Figure 2.1.14, right), an expected mixture of vanadium (III) and (IV) of undetermined composition (the titrator commissioning and use will confirm the composition). Both compartments are stirred to minimize vanadium mass transport especially near the end of the charging period. During electrolysis, Equation 1 takes place at the positive half-cell electrode. At the negative half-cell electrode, the reaction is:

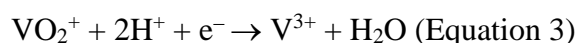


Figure 2.1.14. The electrolysis cell for vanadium (II), (III), and (V) electrolytes preparation.

Figure 2.1.15 shows CV curves for the negative and positive electrolytes after the electrolysis process. As shown in Figure 2.1.15a, the anodic/cathodic peaks associated with the oxidation of V^{2+} to V^{3+} and reduction of V^{3+} to V^{2+} appear at -0.1 and -0.5 V versus RHE, respectively. In addition, the anodic/cathodic peaks related to the $\text{VO}_2^+/\text{VO}^{2+}$ redox reactions also appear at 1.0 and 1.3 V versus RHE (Figure 2.1.15a). Therefore, these results confirm that the negative electrolyte is at least a mixture of vanadium (III) and (IV). The composition will be ascertained after the automatic potentiometric titrator is commissioned. As shown in Figure 2.1.15b, the $\text{VO}_2^+/\text{VO}^{2+}$ redox peaks confirm the presence of vanadium (IV) and (V) in the positive electrolyte. The titrator will equally be used to determine the concentration of electrochemically active species in the positive electrolyte. These measurements will determine if a second charging will be needed to prepare a V(II) electrolyte by charging a cell containing V(IV) and V(III) electrolytes.

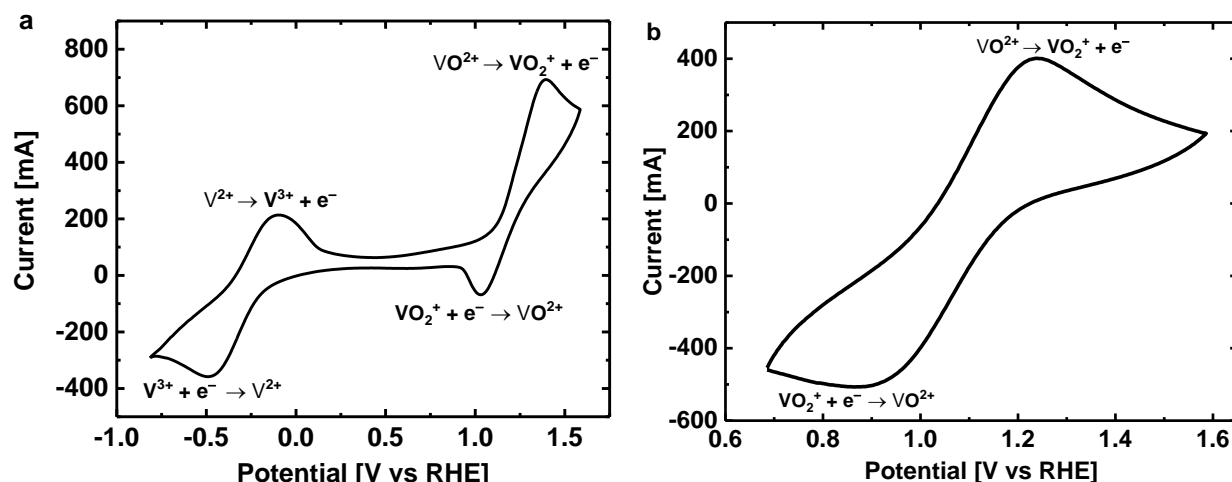


Figure 2.1.15. CVs recorded at 20 mV s^{-1} and 25°C for the V(IV) electrolytes after charging with graphite rod electrodes. Negative (a) and positive (b) electrolytes.

Future activities in 2018 may include the effect of selected impurities identified by ICP on all four vanadium reactions. In addition, the characterization of vanadium salt grades on vanadium reactions reversibility and the identification of the vanadium solution precipitates nature will be completed. The database is expected to illuminate the selection of the most appropriate vanadium salt purity to minimize cost and maximize voltage efficiency of a VRFB.

Effect of Contaminant Mixtures in Air on a Proton Exchange Membrane Fuel Cell (PEMFC)

Contaminant mixtures are of practical relevance for the operation of fuel cell devices in the field, (and support the filtration research under subtask 2.2). However, the effects of contaminant mixtures on PEMFCs have been investigated to a very limited extent, especially with advanced characterization techniques to identify mechanisms and facilitate the development of prevention and recovery procedures. The overwhelming majority of contamination reports only address the impact of a single species to isolate and facilitate data interpretation. The efforts described here supplement data initially acquired within a DOE funded project that included a baseline without contaminant and a ternary mixture of contaminants tests. Under APRISES 2013, the same contaminants were used to test single and binary contaminant mixtures. Model mixture contaminants were selected, propene- C_3H_6 , acetonitrile- CH_3CN , and bromomethane- CH_3Br , on the basis of previous studies with 21 mostly organic contaminants (with the exception of ozone).¹⁸ Propene was found to enhance the cell performance after contaminant injection was interrupted, which offered an opportunity to unravel information that could be used to maximize PEMFC efficiency. Acetonitrile was the only contaminant that led to ohmic losses (as described in a later sub-section of this report, “Effect of a long term PEMFC exposure to acetonitrile”). Bromomethane was chosen because like sulfur dioxide it leads to irrecoverable losses after the contamination period is stopped (warranting additional procedures to restore the initial cell voltage), an uncommon feature. The number of species was limited to three to minimize complexities associated with the number of tests required, injection hardware and data interpretation. The test plan focused on the identification of interactions between species at concentrations closer to those encountered in the atmosphere and with a commercially relevant catalyst loading of $0.1 \text{ mg of platinum per cm}^2$ on the cathode. Data are presented for almost all

selected characterization methods. It is emphasized that data analyses are still ongoing under other funding, and only preliminary conclusions are given in this report.

Figure 2.1.16 shows cell performance responses to individual, binary, or ternary contaminant mixtures. The cell voltage is relatively constant before the contaminant mixture is injected and varies in an acceptable range considering that an early design of Gore coated catalyst membranes was used, which was later improved to increase its stability. Generally, after contaminant injection, a short and rapid cell voltage drop is observed which is followed by a smaller and approximately constant voltage decay rate. A subsequent period of operation in excess of 100 h without contaminant (self-recovery) does not in all cases recover the cell voltage to a level corresponding to an extrapolation to 350 h on the basis of the 10 to 50 h operation period (effectively removing the baseline degradation). Only for C_3H_6 , CH_3CN and $CH_3CN + C_3H_6$ cases it is assumed that the cell performance approximately recovers to its initial value. The binary mixtures $CH_3CN + C_3H_6$ and $CH_3Br + CH_3CN$ interestingly lessen contamination effects in comparison to the single contaminant mixtures, whereas the mixture of $CH_3Br + C_3H_6$ results in a more severe effect on cell performance in comparison to individual contaminants. The ternary contaminant mixture $C_3H_6 + CH_3Br + CH_3CN$ is also beneficial and diminishes contamination effects in comparison to individual and binary mixtures of contaminants. Bromomethane is the only single contaminant leading to a large irrecoverable loss. Irrecoverable voltage losses were attributed to the formation of bromide Br^- anions by bromomethane hydrolysis which cannot be desorbed from the catalyst surface at the operating cathode potential.¹⁹ Figure 2.1.16 data justify these efforts because several results were unexpected. However, cell voltage values are insufficient to provide insight into contamination mechanisms including the existence of reactions or product/intermediates resulting from contaminant interactions.

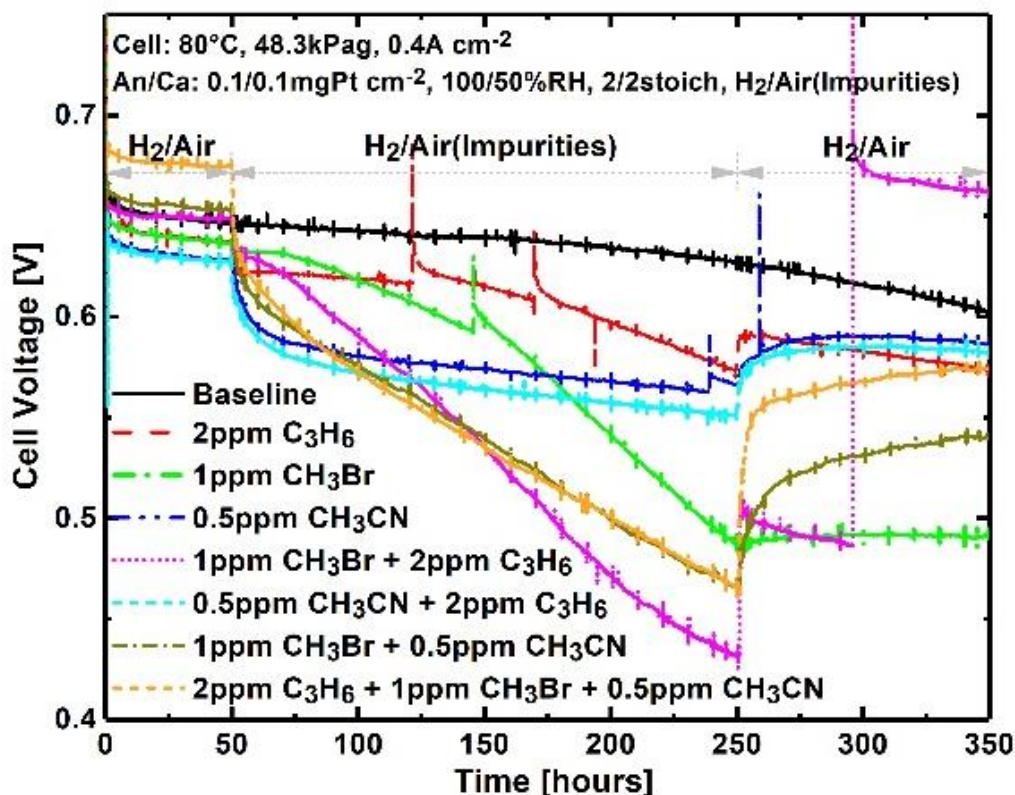


Figure 2.1.16. Cell voltage responses to individual or contaminants mixtures of propene-C₃H₆, acetonitrile-CH₃CN, and bromomethane-CH₃Br, at a constant current density of 0.4 A cm⁻².

Figure 2.1.17 illustrates electrochemical impedance spectra (EIS) collected before, during, and after contamination for all cases covered by figure 2.1.16 (imaginary impedance $\text{Im}(Z)$ as a function of the real impedance $\text{Re}(Z)$). All spectra show the expected features with two distinguishable and main depressed semicircles.²⁰ The high frequency intercept with the abscissa axis is indicative of the membrane resistance. The mid-frequency semicircle to the left is attributed to the slow oxygen reduction reaction whereas the low frequency loop to the right is ascribed to oxygen and water mass transport. A third semi-circle at high frequencies is barely visible as a faint shoulder and is due to the hydrogen oxidation reaction. After 200 or 180 h of exposure, both mid- and low-frequency semi-circles expand especially for cells exposed to the individual, binary and ternary contaminants containing CH₃Br. The semi-circle size increase denotes an increase in resistance that decreases the fuel cell voltage (Figure 2.1.16). Both semi-circles are subsequently and partially restored after self-recovery. After cyclic voltammetry scans and polarization curve diagnostic measurements, both semi-circles slightly shrunk or were unaffected in comparison to their original state. Figure 2.1.17 data indicate the absence of new semi-circles or other features for the binary and ternary mixtures, which suggest that synergistic reactions may not take place, have little impact or are masked by the two main loops.

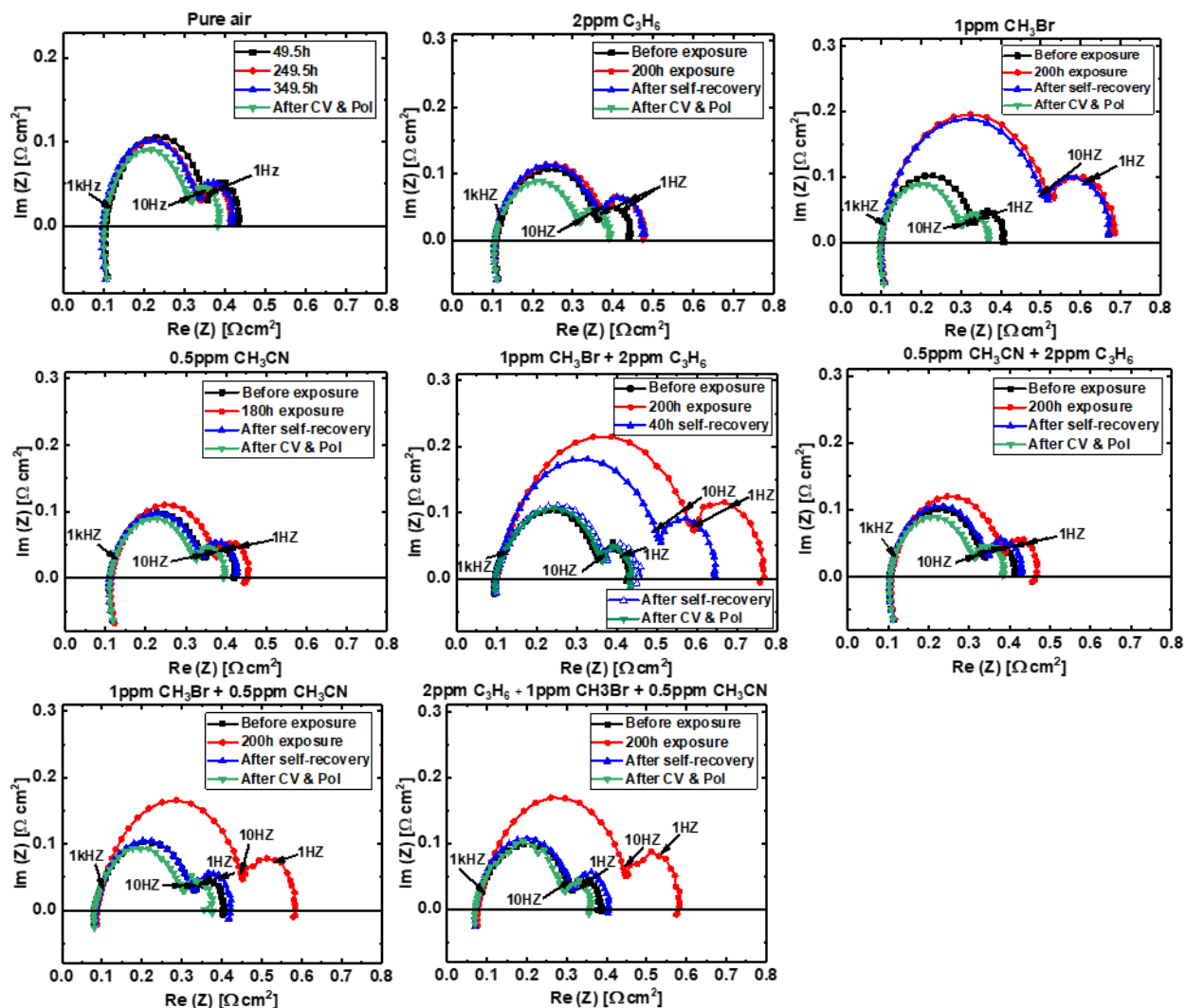


Figure 2.1.17. Electrochemical impedance spectra before, during and after contamination for cases depicted in Figure 2.1.16.

Figure 2.1.18 shows polarization curves with air obtained before contamination (BOT) and after self-recovery (EOT). Figure 2.1.19 derived from Figure 2.1.18 data shows the cell voltage loss for various current densities. All cells show a significant cell voltage loss peaking at 5 to 11 % at $\sim 0.6 \text{ A cm}^{-2}$ after the contaminant injection test with the exception of the cell exposed to 1 ppm CH_3Br + 2 ppm C_3H_6 due to the induced self-recovery at open circuit potential caused by a power failure. Otherwise and generally for other cases, cells are characterized at the end of the test by a larger kinetic loss at low current densities below 0.2 A cm^{-2} and a lower ohmic loss with a smaller polarization curve slope in the $0.5\text{-}1.5 \text{ A cm}^{-2}$ range. For a few cases, mass transport losses at high current densities above 1.5 A cm^{-2} have also decreased. This is most notable for the 1 ppm CH_3Br + 0.5 ppm CH_3CN case with an ohmic behavior that extends to 2 A cm^{-2} at the end of test and a departure from linearity occurring near 1.25 A cm^{-2} at the beginning of test. The significance of these results in relation to synergistic contaminant effects remains to be established.

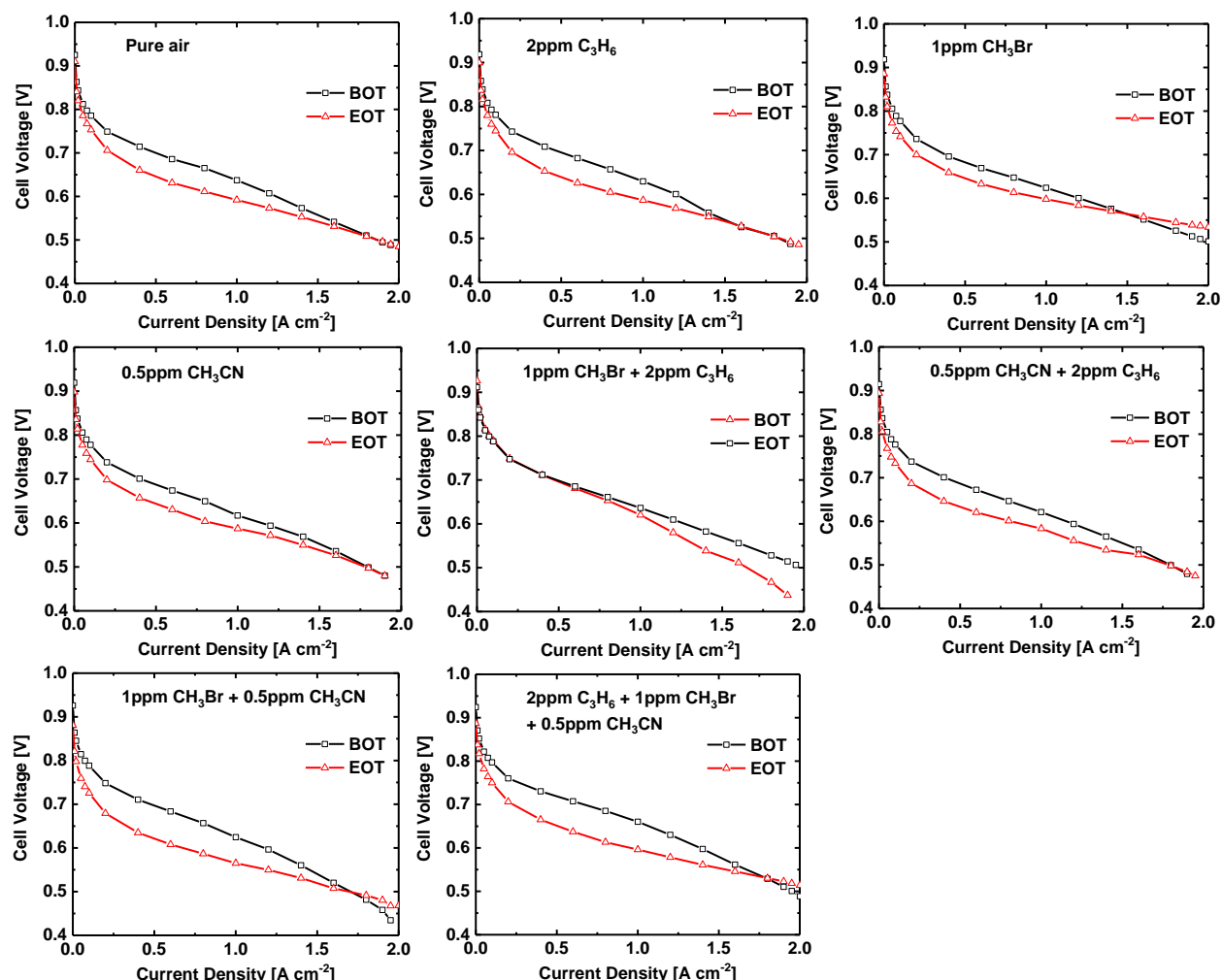


Figure 2.1.18. Polarization curves obtained with air before the cells were contaminated with contaminants and after the cells were subjected to recovery procedures.

Figure 2.1.20 shows cyclic voltammograms used to calculate the electrochemically active platinum catalyst areas at the beginning and end of the tests. Only representative curves (pure air and ternary contaminant mixture) are shown for simplification. All cyclic voltammograms at the beginning of test illustrate typical platinum supported on carbon features. The decreases in electrochemical surface areas for both cathode and anode are similar for cells exposed to pure air, 2ppm C_3H_6 , 0.5 ppm CH_3CN , and 0.5 ppm $CH_3CN + 2$ ppm C_3H_6 , contaminants that do not lead to significant cell voltage losses (Figure 2.1.16). The other four mixtures, which contain CH_3Br creating irreversible losses due to bromide accumulation on the catalyst surface, lead to large catalyst area losses for both cathode and anode with the exception of the anode for the binary mixture with propene. Again, a link between these results and synergistic effects remains to be explored.

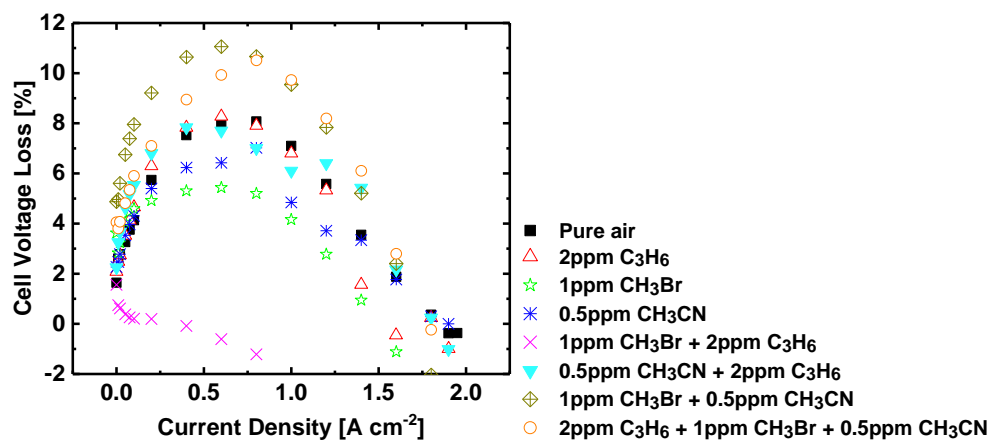


Figure 2.1.19. Cell voltage loss at various current densities derived from Figure 2.1.18.

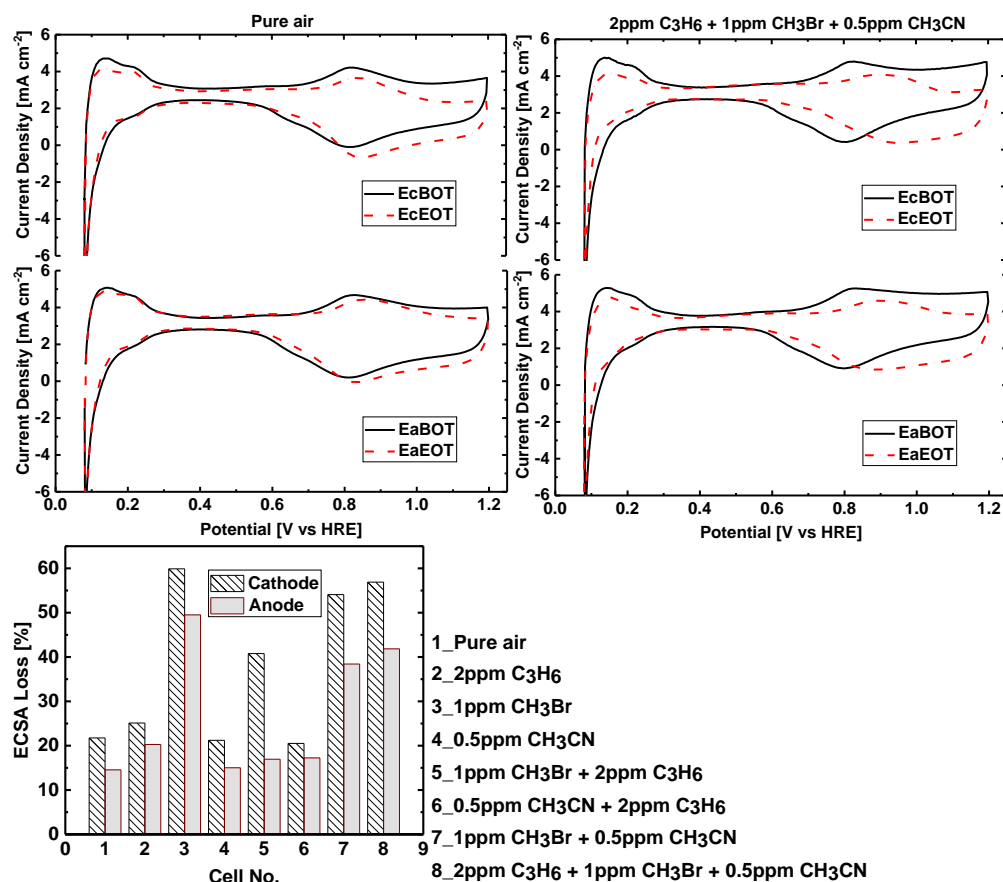


Figure 2.1.20. Cathode (Ec) and anode (Ea) cyclic voltammetry profiles and electrochemical surface area (ECSA) loss calculated at the beginning (BOT) and end (EOT) of test. 80 °C, 48.3 kPag, anode/cathode, 0.466/0.466 L min⁻¹, 100/50 % relative humidity, scan rate: 20 mV s⁻¹.

Figure 2.1.21 depicts the current responses for cells exposed to contaminants in nitrogen rather than air at the operating cathode potential of ~ 0.7 V versus HRE (~ 0.65 V cell voltage average at the beginning of the contamination period from Figure 2.1.16 + an ohmic compensation comprised

of a high frequency cell resistance from Figure 2.1.17 of $\sim 0.12 \Omega \text{ cm}^{-2} \times$ the operating current density of 0.4 A cm^{-2} from Figure 2.1.16 + a pseudo-reversible anode potential of $\sim 0 \text{ V}$ versus RHE). For simplification, these tests were designed to obtain contaminant interactions information without the interfering presence of oxygen. Before contaminant exposure at 5 h, current densities for all cells range from 2.8 to 3.2 mA cm^{-2} . During contaminant exposure, there is an initial sharp increase or decrease in the current density due to gas switching dynamics (time scales of approximately a few min are too short in comparison to the time scales of generally 10 h or more associated with contamination in Figure 2.1.16, and, calculated currents for complete oxidation or reduction of the contaminants are too small to affect the overall current). Subsequently, the current density returns to its pre-contamination value. Cyclic voltammetry was employed to identify residues on the cathode catalyst surface. As revealed in Figure 2.1.22, cyclic voltammograms were initiated at the applied potential of 0.7 V versus HRE with a scan directed toward negative potential values. Cyclic voltammograms for contaminant exposure cases are compared to a blank with only pure N_2 exposure. Beginning (BOT) and end (EOT) of test data have a similar trend as the electrochemically active platinum catalyst area (ECSA) data in Figure 2.1.20. Individual, binary and ternary contaminant mixtures containing CH_3Br lead to an observable decrease in peak currents for platinum oxidation and reduction (peaks centered at $\sim 0.8 \text{ V}$ versus HRE), and, hydrogen adsorption and desorption/oxidation (peaks centered at $\sim 0.1 \text{ V}$ versus HRE). More importantly, new species resulting from interactions between contaminants were not detected. Fuel cell outlet water analyses (not shown) are ongoing and may reveal additional clues. Outlet gases were not analyzed to either avoid damage to instruments by bromomethane or streams were too dilute for mass spectrometry analyses.

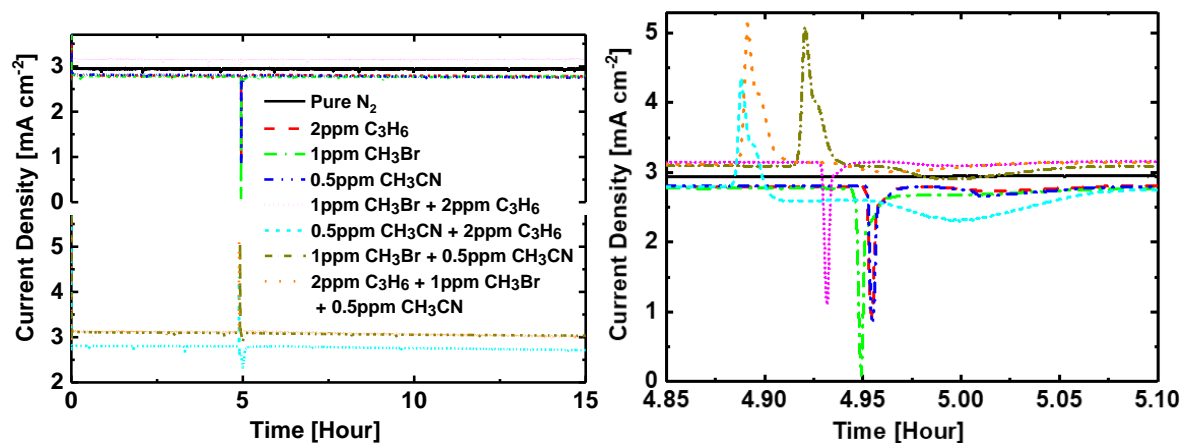


Figure 2.1.21. Cell current density response to contaminants injected at 5 h. Anode/cathode, 100/50 % relative humidity, H_2/N_2 at the operating cathode potential of $\sim 0.7 \text{ V}$ versus HRE.

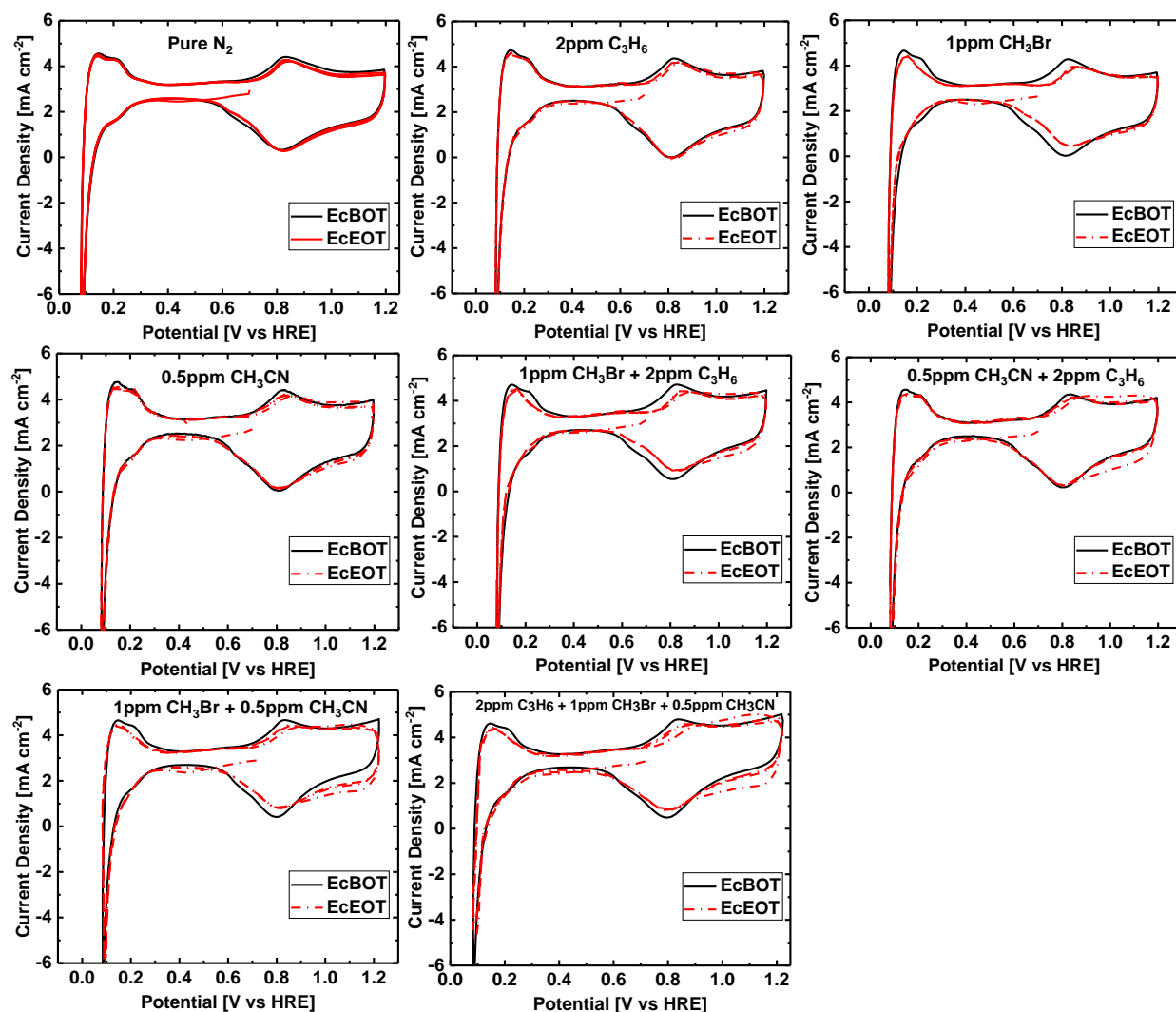


Figure 2.1.22. Cathode (Ec) cyclic voltammetry profiles before (BOT) and after (EOT) exposure to contaminants in anode/cathode, 100/50 % relative humidity, H_2/N_2 at the operating cathode potential of ~ 0.7 V versus HRE.

Measurement and Separation of Reactant Mass Transfer Coefficients in Fuel Cells

The cost of fuel cells is still relatively too high to effectively compete with internal combustion engine technology. Fuel cell operation at high current densities and a decrease in expensive platinum catalyst loading are approaches that are currently being investigated to directly (platinum catalyst) and indirectly (higher current densities increase power density which in turn reduce application volume and material needs) decrease cost. However, such operating conditions and membrane/electrode assembly design promote reactant mass transfer limitations.²¹ Under an Army Research Office grant, HNEI is currently developing a measurement method based on the use of current distributions obtained with a low oxygen concentration and gas diluents of different molecular weights to separate reactant mass transfer coefficient into fundamental contributions to identify processes limiting oxygen and hydrogen transport in electrodes and facilitate membrane/electrode assembly design optimization. In most cases, the measurement of the mass transfer coefficient is performed at operating conditions that are significantly different than

nominal fuel cell operation, under mass transfer control at the limiting current. HNEI has recently expanded its measurement method to current densities lower than the limiting current.²² However, a validation cannot be completed because other approaches do not currently exist to verify the validity of the measured mass transfer coefficients at relatively low current densities.

HNEI initiated under APRISES 2011 activities to cross-validate its mass transfer coefficient measurement method by developing models based on a physical representation of the processes occurring in membrane/electrode assemblies to interpret impedance spectroscopy data. In contrast, equivalent electrical circuit models are not preferred because they are not based on the desired physico-chemical parameters including mass transfer related ones. Generally, impedance models can be derived from transient cell performance descriptions but they require computationally intensive and slow numerical solutions. Under APRISES 2013 and in collaboration with the Institute of Energy and Climate Research, Jülich, Germany, analytical models that were previously derived using the restrictive constraint of a low current density were used to fit impedance spectra obtained for a low practically relevant air stoichiometry with a segmented cell at HNEI. These models include a one dimensional through the membrane/assembly plane (1D) and quasi-two dimensional (quasi-2D to take account of low air stoichiometries creating significant oxygen concentration gradients along the flow field channel) versions. For larger current densities, a third model was also used to analyze segmented cell impedance data. For this case, an analytical solution was not found. However, the model was restricted to a 1D version to minimize computations and find a numerical solution. These activities, which support the Army Research Office grant, extend APRISES 2011 results which were obtained with impractical operating conditions, oxygen, a high stoichiometry and a low current density, that minimize but do not eliminate mass transfer limitations.

Figure 2.1.23, left shows the impedance spectra for all ten segments of the fuel cell. The graphs are laid out to mimic the serpentine flow channel layout with the air inlet corresponding to the upper right graph and the arrows between the graphs indicating the air flow direction. Impedance spectra are characterized by two main semi-circular loops in this imaginary ($\text{Im}(Z)$) versus real ($\text{Re}(Z)$) impedance Nyquist representation. The mid-frequency loop to the left and the low frequency loop to the right were previously ascribed to oxygen reduction and oxygen/water transport processes, respectively. Model fits indicate that the 1D model is only applicable to the mid-frequency loop and above a specific frequency (boundary frequency) located near the intersection of both loops. In contrast the quasi-2D model is applicable to both loops.

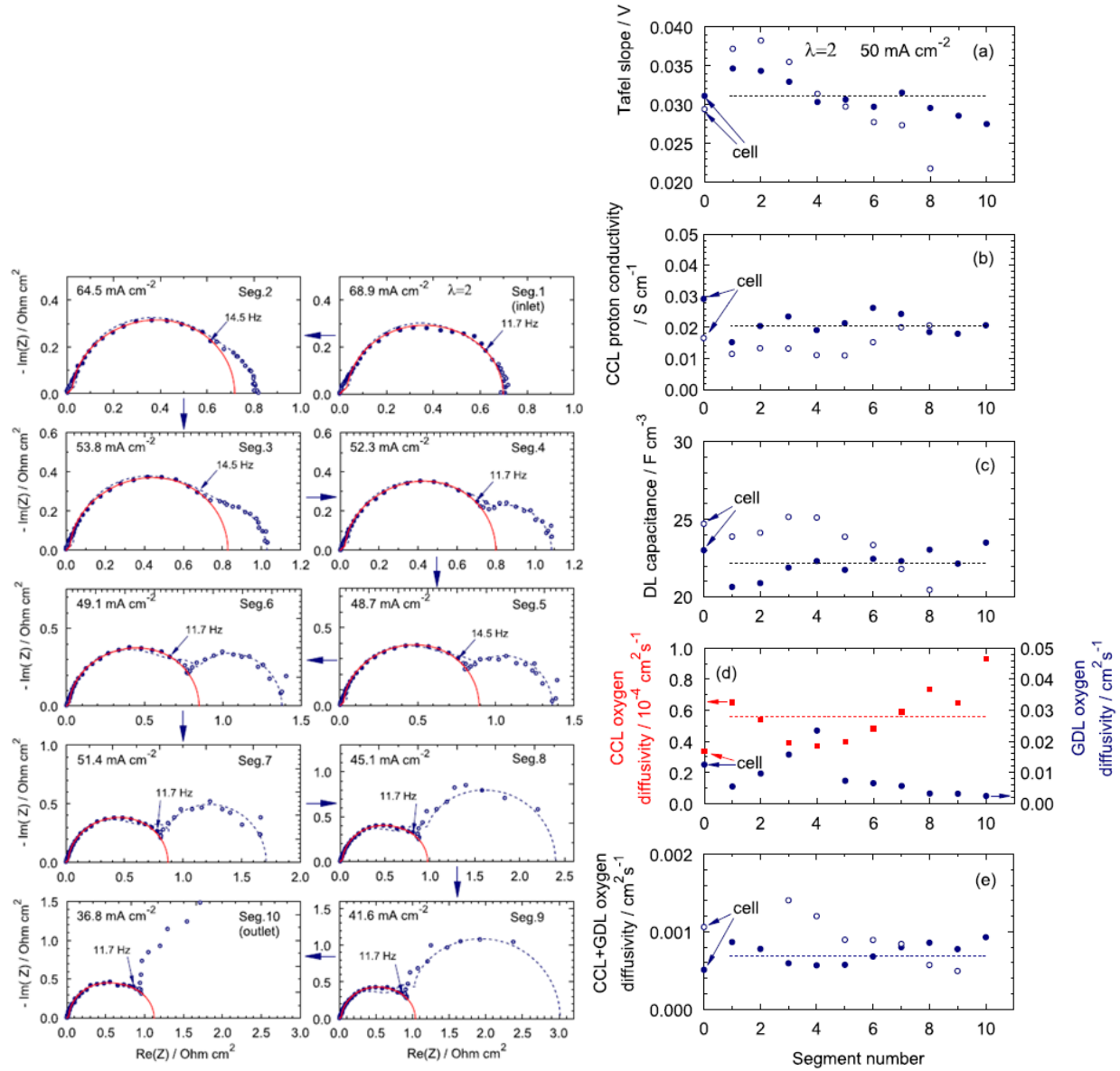


Figure 2.1.23. Experimental impedance spectra (symbols) and fitted mathematical models (lines) for an air stoichiometry of 2 and 0.05 A cm⁻² (left). The solid lines correspond to the 1D model whereas dash lines relate to the quasi-2D model. Fitted parameters for segments 1-10 (right). Filled circles data points were obtained with the 1D model whereas open circles data points were derived with the quasi-2D model. Dash lines refer to average 1D model parameters. Parameters obtained by fitting impedance spectra for the entire cell are indicated by data points for the zero segment number.

Figure 2.1.23, right illustrates local (segments 1-10 data points), average (dash line) and overall (segment 0 data points) parameters determined by both 1D and quasi-2D models including oxygen diffusivities. Generally, all values are in reasonably good agreement. This observation indicates that the simpler and lower dimensional order 1D model is sufficient to interpret impedance spectra as long as only data points above the boundary frequency are used.

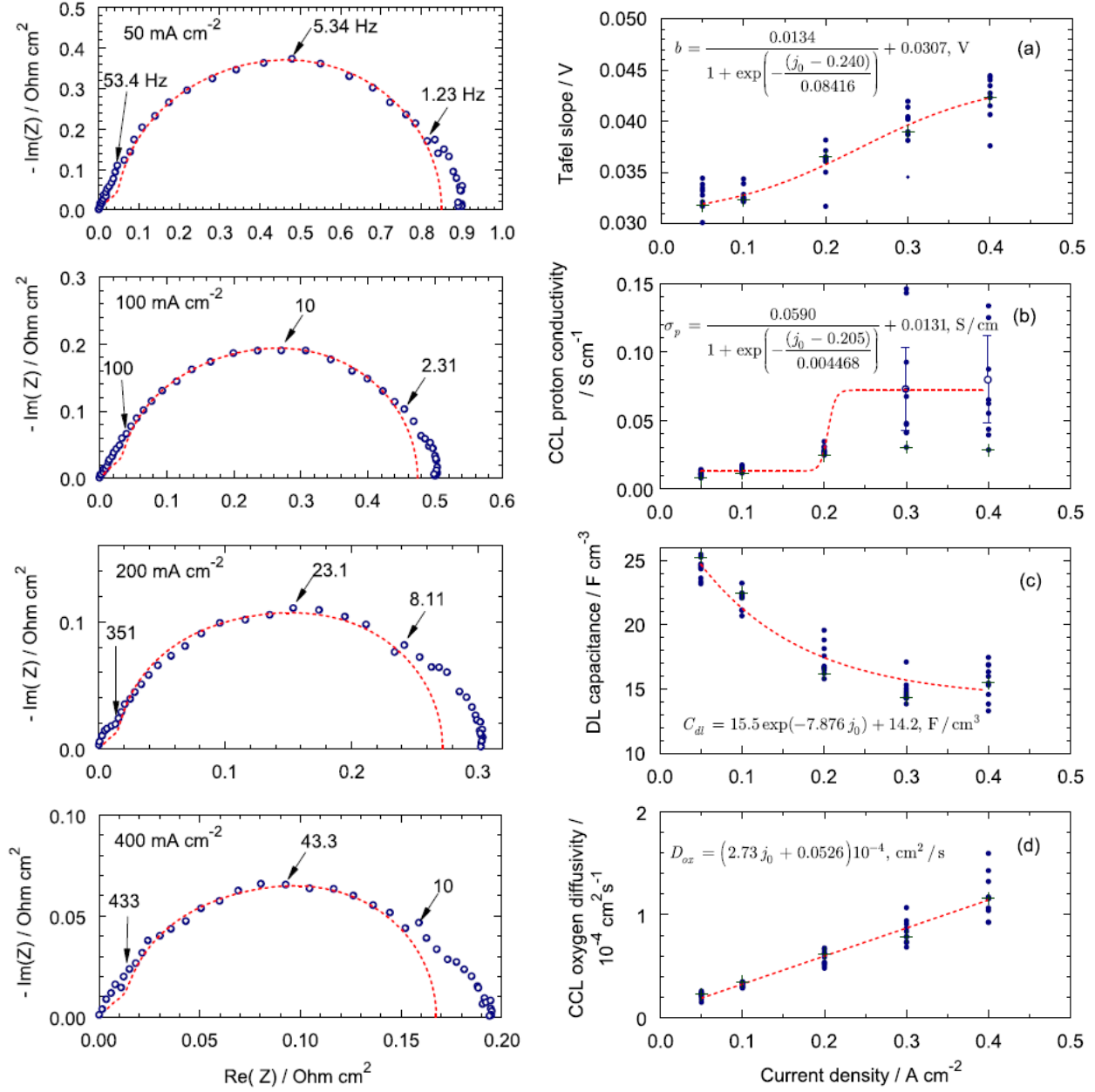


Figure 2.1.24. Experimental impedance spectra for the entire cell (symbols) and fitted mathematical model (lines) as a function of current density (left). Numbers correspond to frequencies in Hz. The effect of current density on fitted model parameters (right). Filled circles correspond to individual segment parameters whereas filled circles with crosses indicate values obtained from fitting the entire cell spectra. Empirical correlations (dash lines) were used to correlate data.

Figure 2.1.24, left depicts impedance spectra for the entire segmented cell for different current densities. The numerical 1D model correctly reproduces the mid-frequency loop. The resulting model parameters are illustrated in figure 2.1.24, right. Parameter values at 0.05 A cm⁻² are consistent with those from figure 2.1.23. All parameters are affected by the current density including a remarkable six-fold increase in oxygen diffusivity. Oxygen diffusivities remain to be

correlated with the oxygen mass transfer coefficient and complete the measurement method validation. More details are provided in the Publications and Presentations Resulting from these Efforts section (items 2 and 3).

Effect of a Long Term PEMFC Exposure to Acetonitrile

The durability of PEMFCs is still below the expected target due to processes such as carbon corrosion of the catalyst support, platinum catalyst nano-particle agglomeration and membrane structure decomposition. Additionally, most contaminants introduced in the air and hydrogen streams also negatively affect cell performance. More specifically, at the cathode, tests completed at room temperature with a rotating ring/disc electrode show that most contaminants increase the yield of the hydrogen peroxide side reaction.²³ The peroxide is subsequently decomposed into oxygenated radicals by the action of leftover species in the ionomer or membrane such as iron.²⁴ In turn, the peroxide and radicals slowly attack and decompose the ionomer and membrane. However, it was recently unknown whether or not exposure to a contaminant for a long period of time would affect ionomer and membrane durability because such tests were not previously completed. This is an important consideration because hydrogen peroxide is susceptible to decomposition at temperatures higher than room temperature but below the specified PEMFC operating temperature of approximately 80 °C. Therefore, it was unclear if a contaminant could affect ionomer or membrane durability. The initial work reported here, including data acquisition, was completed with DOE funds. Under APRISES 2013, data analysis was completed.

Acetonitrile was selected as an initial model contaminant because it is relatively concentrated in air (~3 ppm) in comparison to other species.¹⁸ Acetonitrile adsorbs on the platinum catalyst surface affecting the oxygen reduction reaction and it is subject to hydrolysis decomposing to acetaldehyde and ammonia. In turn, ammonia reacts with water producing ammonium ions that ion exchange with protons in the ionomer and membrane affecting its ionic conductivity (among other things).²⁵⁻²⁷ Therefore, acetonitrile offers an additional and secondary opportunity to verify the long term accumulation of foreign cations in the ionomer and membrane because organic contaminants acting in such a manner, affecting the ionomer membrane, are uncommon. In contrast, inorganic cations such as sodium, potassium, calcium and magnesium that are present in seawater require a liquid water path to reach the ionomer. This is usually prevented by the hydrophobic gas diffusion layer²⁸ and as a result contamination by these species is less likely. For these long duration tests requiring significant testing resources, a comprehensive set of analytical methods was selected to characterize as many degradation aspects as possible and extract the maximum amount of information: electrochemical impedance spectroscopy (EIS, electrochemical reactions), cyclic voltammetry (CV, electrochemically active Pt catalyst area), transmission electron microscopy (TEM, Pt particle agglomeration and Pt deposition in the electrolyte membrane), ion chromatography (IC, F⁻ emission rate in fuel cell exhaust water, an ionomer degradation product, and the formation of NH₄⁺ and other ions), scanning electron microscopy (SEM, catalyst layer and membrane thickness).

Figure 2.1.25 displays the cell voltage and high frequency resistance for a blank test and a test that included a 1000 h period of contamination with 5 ppm acetonitrile. A large loss in cell voltage of ~0.13 V and increase in cell resistance of ~20 % is noted at the beginning of the contamination period revealing the high sensitivity of these low catalyst loading and commercially relevant

materials ($0.1 \text{ mg Pt per cm}^2$). The cell resistance continuously increases during the contamination period owing to the accumulation of ammonium ions in the ionomer and membrane. These results do not provide direct information about the ionomer and membrane chemical degradation in part because the cell resistance and cell voltage changes include several cumulative contributions.

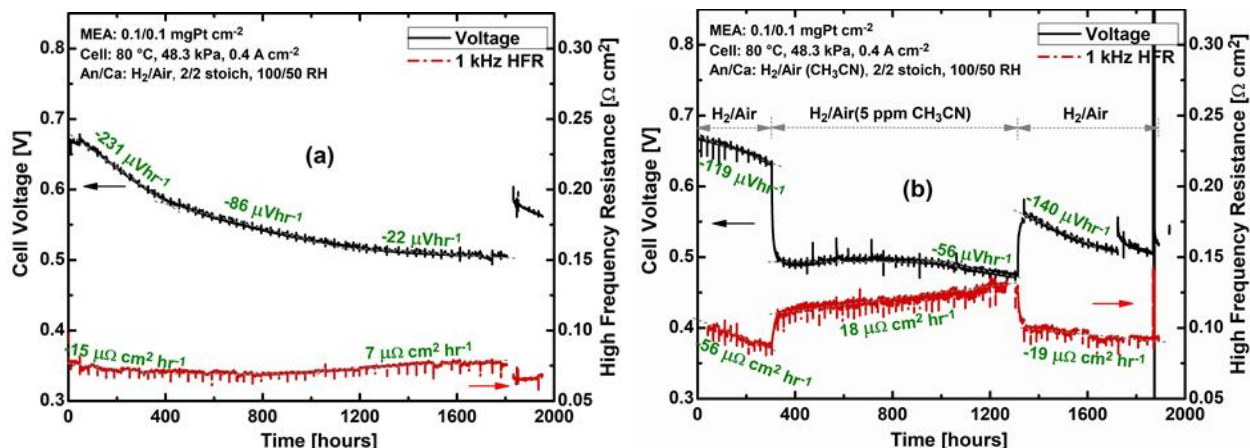


Figure 2.1.25. Cell voltage and high-frequency (1 kHz) resistance variation during long term (approximately 1900 hours) PEMFC operation with neat air in the cathode (a), referred to as a blank test and 5 ppm acetonitrile (for 1000 hours) in the air stream (b), referred to as a contamination test.

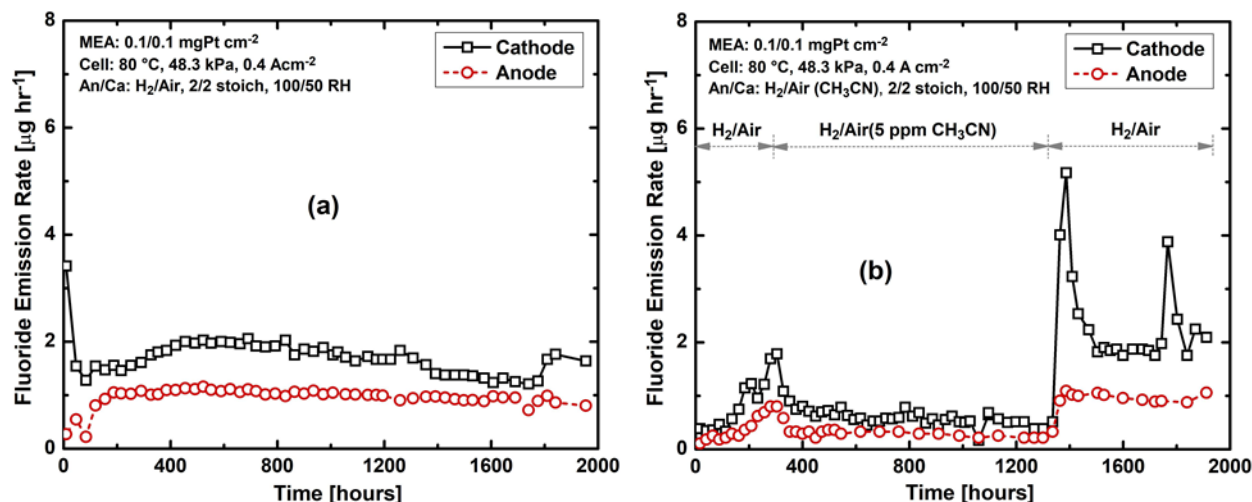


Figure 2.1.26. Fluoride emission rate during the long term blank test (a) and 5 ppm acetonitrile (for 1000 hours) contamination test (b).

Figure 2.1.26. data are more specific to ionomer and membrane degradation because these materials contain fluorine that is lost as fluoride as a result of the hydrogen peroxide and oxygenated radicals attack. Figure 2.1.26 reveals that the fluoride emission rate is consistently less in the anode compartment for both blank and contamination tests. This observation is attributed to the relatively larger production or presence of hydrogen peroxide and radicals near the cathode. More importantly, a decrease in the fluoride emission rate occurs during the entire contamination period, which is ascribed to a reaction between acetonitrile or its hydrolysis products and either

hydrogen peroxide or radicals. In other words, acetonitrile acts as an imperfect scavenger that slows degradation.

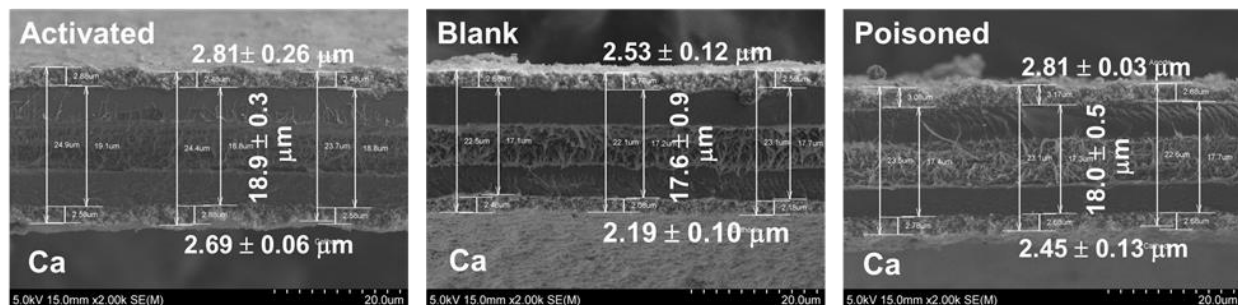


Figure 2.1.27. Cross-section SEM images of the membrane/electrode assemblies before and after the long term blank test and contamination tests. Three measurements for each point, 6 to 9 points for each sample, 5 samples for each MEA (\pm standard deviation).

Figure 2.1.27 presents evidence for the scavenging effect of acetonitrile with membrane/electrode assembly cross-section measurements of both catalyst layers and membrane thickness. For the blank test, the membrane thickness decreased by 1.3 microns in comparison to an activated membrane/electrode assembly from a cell that was operated only for the activation period (~ 1 day). Cathode and anode catalyst layers, which contain ionomer, decreased in thickness by 0.5 and 0.28 microns, respectively. In contrast, for the contamination test, the membrane thickness only decreased by 0.9 micron, the cathode catalyst layer was thinned by 0.24 micron and the anode was unaffected.

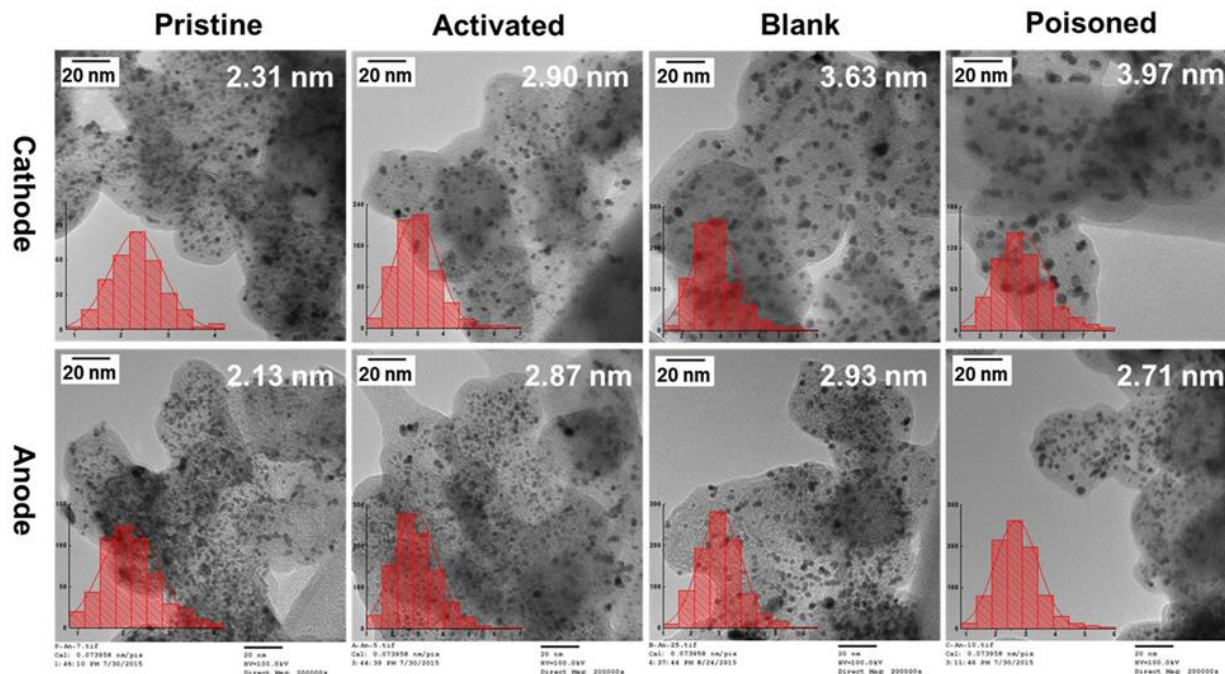


Figure 2.1.28. TEM images of the pristine membrane/electrode assembly, and the membrane/electrode assemblies before and after the long term blank test and contamination test. Average platinum particle sizes are based on statistics of 5-7 Pt/C powder samples collected from the inlet, center, and outlet locations.

The long term tests also revealed that catalyst degradation was accelerated by acetonitrile (Figure 2.1.28). The analysis of a series of TEM images revealed that both activation and operation without a contaminant increases the platinum particle size in comparison to a pristine, as received cathode catalyst (as part of the membrane/electrode assembly). Cell operation with acetonitrile led to an additional increase in platinum particle size. Platinum dissolution is not expected to be responsible for particle growth because the cathode potential is estimated at less than 0.7 V vs HRE, a value below the potential needed for platinum dissolution. Therefore, it is hypothesized that platinum particle growth occurs by particle migration on the catalyst carbon support surface, which is modified by acetonitrile adsorption. The anode catalyst was minimally influenced by cell operation and contamination (Figure 2.1.28). More details are provided in the Publications and Presentations Resulting from these Efforts section (items 1, 4-6).

Recovery of Fuel Cell Performance Losses Caused by Contamination

Sulfur and halogen based compounds are important airborne contaminants that reach significant concentrations near volcanoes (SO₂, HCl) and marine environments (CH₃Br, chloride salts) such as in Hawaii, which have a severe impact on PEMFCs even at ppm levels. The contamination mechanism for these species eventually lead to sulfur or halogen anion adsorption on the cathode catalyst surface. Neat air operation is insufficient to restore cell voltage losses. Also, adsorbed sulfur and halogen anions cannot be fully oxidized or reduced within the PEMFC environment under nominal operating conditions. Single cell procedures were developed to modify the cathode electrode potential and alternate it between low and high values.^{29,30} However, the desorbed anion is restricted to the platinum/ionomer interface due to Donnan exclusion; the high concentrations of positively charged protons in the ionomer restrict the penetration and movement of negatively charged anions. More importantly, such recovery methods are not easily applicable to stacks because control of every cathode potential is required multiplying electrical connections and equipment needs.

Ozone was proposed as an oxidant to recover cell performance losses in a stack with a platinum catalyst loading of 0.4 or 0.5 mg Pt cm⁻².³¹⁻³³ The introduction of ozone to a PEMFC at open circuit simultaneously elevates the cathode potential of all cells to a value up to 1.6 V versus HRE, which is sufficient to fully oxidize sulfur compounds. Under APRISES 2011, HNEI attempted to develop a similar method using nitrous oxide (N₂O), another potent oxidant gas with a reduction potential of 1.77 V versus HRE.³⁴ Unfortunately, these attempts were unsuccessful due to the low open circuit voltage. This was attributed to the rich nitrogen electrochemistry and multiple reactions, which lowers the effective cathode potential with the presence of multiple mixed potentials.

Under APRISES 2013, ozone was used to mitigate the effect of halogen compounds (bromomethane and hydrogen chloride) contamination in PEMFCs because such an approach has not yet been demonstrated for this contaminant class. A low commercially relevant platinum catalyst loading (0.1 mg cm⁻²) was employed. The expected main cathode and anode reactions for the induced electrochemical corrosion cell for a PEMFC at open circuit are:

Cathode: $O_3 + 2H^+ + 2e^- \rightarrow O_2 + H_2O$, $E^0=2.076$ V vs SHE (Equation 4)

Anode: $2Br^- \rightarrow Br_2(aq) + 2e^-$, $E^0=1.09$ V vs SHE (Equation 5) or

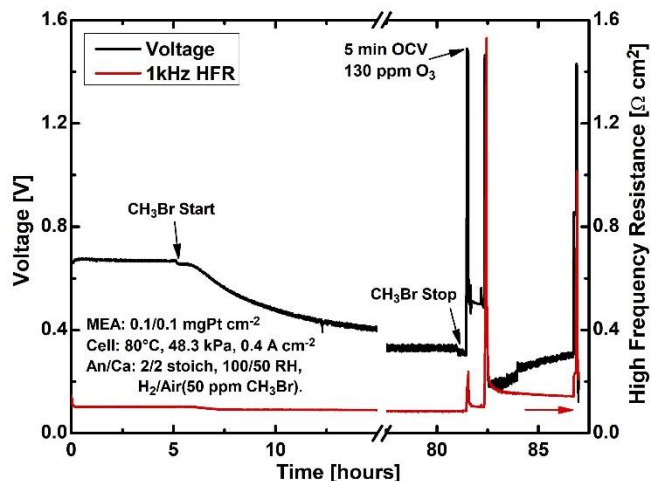
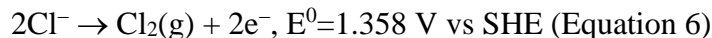


Figure 2.1.29. The cell voltage and high frequency resistance transient responses to bromomethane contamination and ozone exposures.

Figure 2.1.29 shows that the 50 ppm bromomethane exposure caused a significant cell performance loss of ~350 mV. After the bromomethane injection was interrupted, the performance essentially remained the same. Subsequently, the current was interrupted and the ozone was introduced to the cathode. The cell displayed a high open circuit voltage (OCV) of 1.49 V and a higher cell high frequency resistance (HFR) during the 5 min ozone exposure. After ozone exposure, the cell voltage was restored to 0.511 V corresponding to a 53 % recovery of the cell performance loss. The cell was subjected to a second ozone exposure to improve cell recovery. Unfortunately, the second ozone exposure decreased the cell voltage and increased the cell HFR. The effects of the third ozone exposure were similar to those of the second exposure. Figure 2.1.29 demonstrated that the recovery concept is sound with a high OCV but is only partly effective. Also, the ozone procedure also caused cumulative damage to the low catalyst loading membrane/electrode assembly. Diagnostic tests were completed to determine the incomplete cell voltage recovery and cell degradation cause.

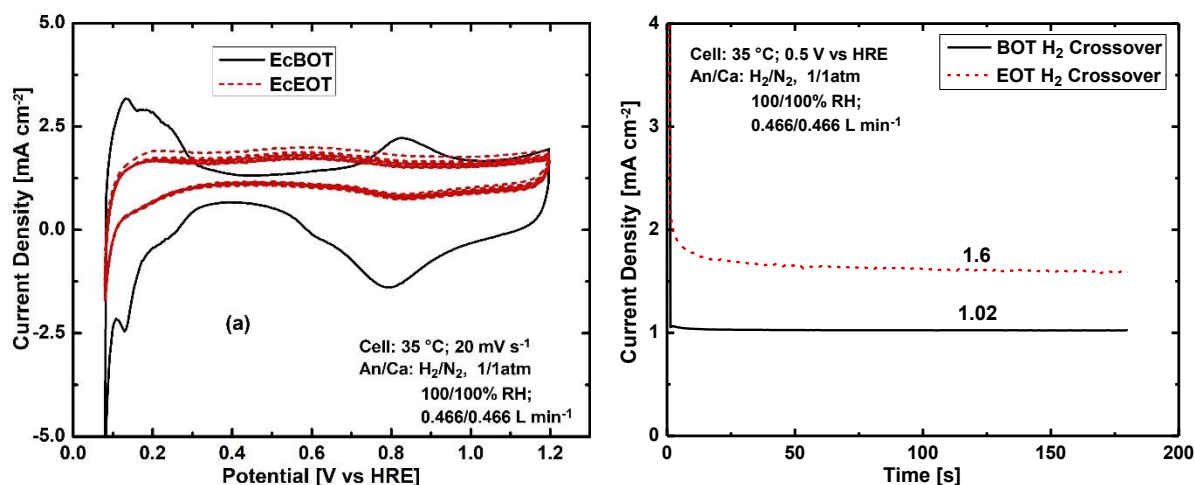


Figure 2.1.30. Cathode cyclic voltammetry profiles (a) and hydrogen crossover before and after bromomethane contamination and ozone exposures (b).

Figure 2.1.30a shows that cyclic voltammograms were significantly affected by successive ozone treatments with a large decrease in platinum oxidation and reduction peaks (centered around 0.8 V versus HRE) and hydrogen adsorption and desorption/oxidation peaks (from 0.1 to 0.4 V versus HRE). Therefore, almost all of the platinum has disappeared, which is tentatively ascribed to corrosion of the carbon support and collapse of the electrode structure. The hydrogen crossover rate also significantly increased (Figure 2.1.30b), which suggests ionomer and membrane decomposition, an additional factor contributing to the electrode structure collapse.

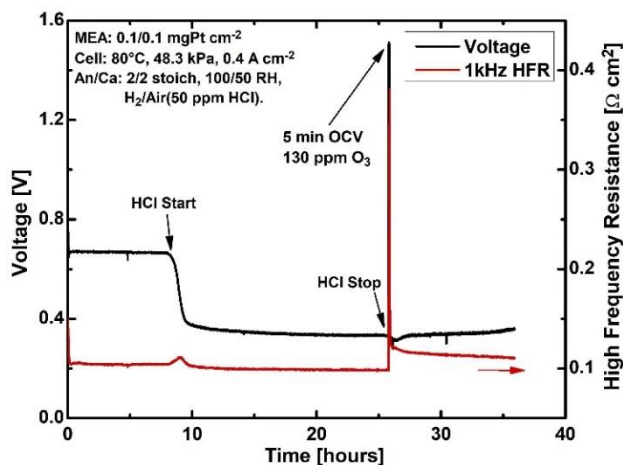


Figure 2.1.31. The cell voltage and high frequency resistance transient responses to hydrogen chloride contamination and ozone exposures.

Figure 2.1.31 illustrates the cell voltage responses to hydrogen chloride contamination and ozone exposure. The 50 ppm hydrogen chloride caused an approximate 330 mV cell voltage loss, a value that is similar to the effect of bromomethane (Figure 2.1.29). The introduction of ozone into the cathode again created a high OCV at 1.51 V. During the 5 min ozone exposure, the cell HFR significantly increased during this period. However, the cell voltage did not recover after the ozone exposure.

Figure 2.1.32a depicts a decrease in cyclic voltammogram peak heights that is similar but is not as extensive as for bromomethane (Figure 2.1.30) after hydrogen chloride contamination and ozone exposure. The hydrogen crossover rate also increased by ~20 % (Figure 2.1.32b). The catalyst activity loss is assigned to chloride adsorption on the platinum surface (no recovery, Figure 2.1.31), carbon corrosion and ionomer decomposition (Figure 2.1.32b).

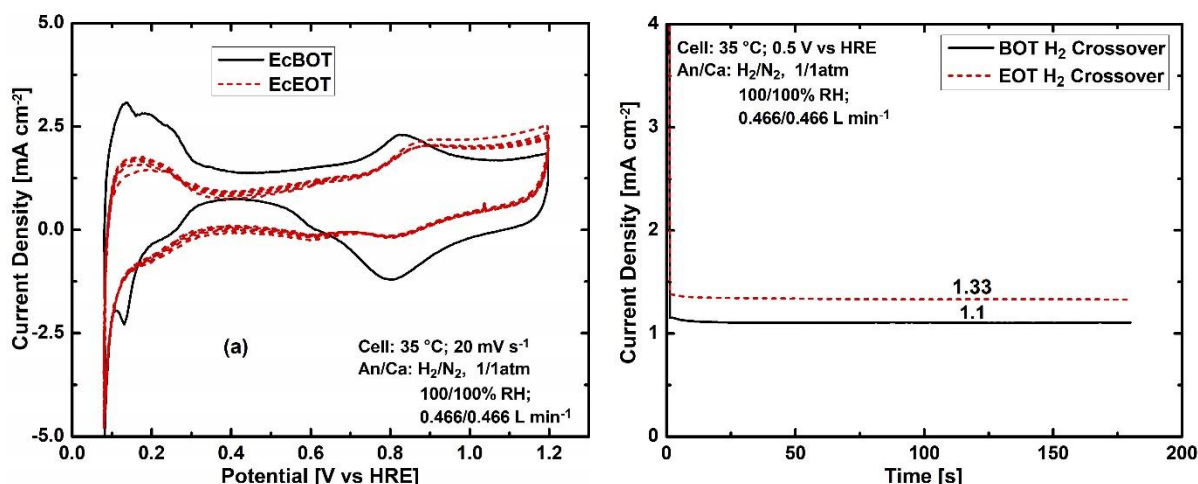


Figure 2.1.32. Cathode cyclic voltammetry profiles (a) and hydrogen crossover before and after hydrogen chloride contamination and ozone exposure (b).

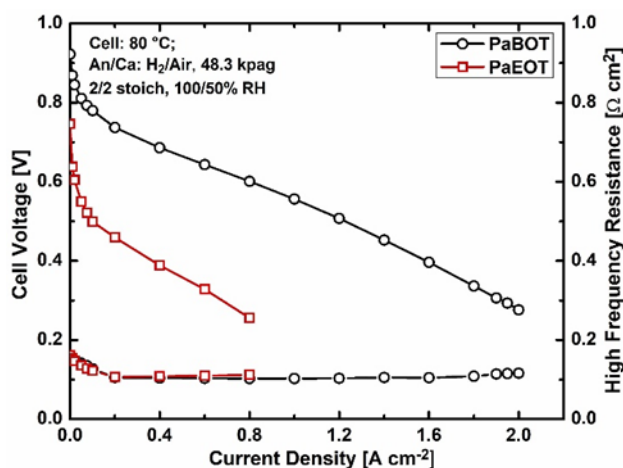


Figure 2.1.33. Polarization curve before and after hydrogen chloride contamination and ozone exposure.

The cell polarization curve was obtained after ozone exposure for comparison to the cell state before the contamination exposure (Figure 2.1.33). The cell is characterized by a low OCV and a largely reduced cell voltage that is symptomatic of a kinetic loss (translation of the entire polarization curve to lower current densities). These results agree with the conclusions extracted from cyclic voltammetry and hydrogen crossover analyses (Figure 2.1.32).

The unexpected bromomethane and hydrogen chloride results contrast with sulfur compounds reports,³¹⁻³³ claiming a complete PEMFC performance recovery by ozone. This observation incited an additional test to repeat these results under similar operating conditions with a higher cathode catalyst loading (0.4 mg Pt cm⁻²) and a lower room temperature. Results are shown in Figure 2.1.34. The 10 ppm sulfur dioxide contamination period decreased the cell voltage by 290 mV. The neat air operation restored ~45% of the cell voltage loss. However, the cell voltage was slightly improved by 50 mV with a 10 min exposure to 1000 ppm ozone (Figure 2.1.34a). Figure 2.1.34b polarization curves confirm the relatively small and incomplete recovery after ozone exposure.

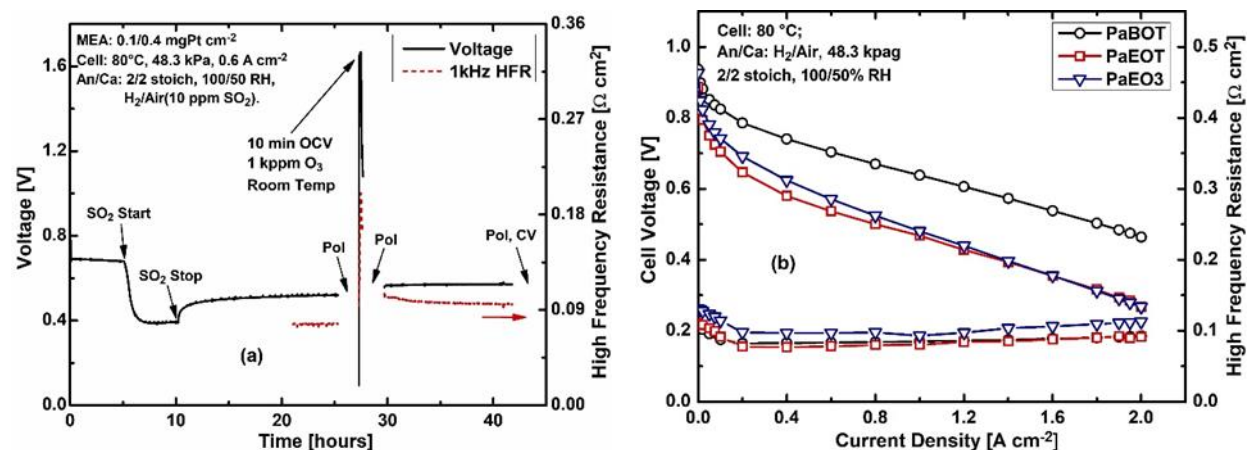


Figure 2.1.34. The cell voltage and high frequency resistance transient responses to the sulfur dioxide contamination and the ozone exposure (a). Polarization curves before (PaBOT) and after (PaEOT) sulfur dioxide contamination, and after ozone exposure (PaEO3) (b).

Additional tests are planned to ascertain the accuracy of the results and ensure the fuel cell community is not misled with the previously proposed ozone treatment to recover cell voltage losses induced by contamination. This is particularly important considering that a few reports highlights the contamination effect of ozone itself including irreversible damage to the membrane/electrode assembly catalyst by dissolution and ionomer.^{18,35} Additional tests will focus on differences with previously reported conditions including cell temperature, ozone concentration and exposure duration, and catalyst loading. The latter commercially relevant parameter is important because low platinum catalyst loading membrane/electrode assemblies are more sensitive to contamination.³⁶

Publications and Presentations Resulting from these Efforts

Journal Publications

1. Y. Zhai, J. Ge, J. Qi, J. St-Pierre, 'Effect of Acetonitrile Contamination on Long-Term Degradation of Proton Exchange Membrane Fuel Cells', *J. Electrochem. Soc.*, 165 (2018) in press.
2. T. Reshetenko, A. Kulikovskiy, 'Variation of PEM Fuel Cell Physical Parameters with Current: Impedance Spectroscopy Study', *J. Electrochem. Soc.*, 163 (2016) F1100.
3. T. Reshetenko, A. Kulikovskiy, 'Comparison of Two Physical Models for Fitting PEM Fuel Cell Impedance Spectra Measured at a Low Air Flow Stoichiometry', *J. Electrochem. Soc.*, 163 (2016) F238.

Conference Presentations

4. Y. Zhai, J. Ge, J. St-Pierre, 'Long Term Effects of Airborne Contaminants in PEMFC Cathode', in *Meeting Abstracts*, Electrochemical Society volume 2015-2, The Electrochemical Society, Pennington, NJ, 2015, abstract 1508.
5. Y. Zhai, J. Ge, J. Qi, K. More, J. St-Pierre, 'Long Term Effects of an Airborne Contaminant on a Proton Exchange Membrane Fuel Cell', 3rd International Workshop on Degradation Issues of Fuel Cells and Electrolysers, 2015.
6. Y. Zhai, J. Ge, J. St-Pierre, 'Long Term Effects of an Airborne Contaminant on a Proton Exchange Membrane Fuel Cell', 15th International Symposium on Electroanalytical Chemistry, 2015, abstract K-4.

References

1. P. Cohn, A. Green, M. Langstaff, M. Roller, *Commercial drones are here: The future of unmanned aerial systems*, December 2017, retrieved from <https://www.mckinsey.com/>.
2. Protonex Technology, *Unmanned Systems*, retrieved from <https://protonex.com/solutions/unmanned-systems/>.
3. Intelligent Energy, *Fuel Cell Power for Drones*, retrieved from <http://www.intelligent-energy.com/our-products/drones/overview/>.
4. HUS Energy Systems, *HYCOPTER hydrogen fuel cell UAV*, retrieved from <https://www.hus.sg/hydrogen-multi-rotor/>.
5. S. Kocha, J. D. Yang, J. Yi, *AIChE J.*, 52 (2006) 1916.
6. Y. Matsuda, Y. Hashimasa, D. Imamura, M. Akai, *Rev. Automot. Eng.*, 30 (2009) 167.
7. K. D. Baik, M. S. Kim, *Int. J. Hydrogen Energy*, 36 (2011) 732.
8. H. Karimäki, L. C. Pérez, K. Nikiforow, T. M. Keränen, J. Viitakangas, J. Ihonon, *Int. J. Hydrogen Energy*, 36 (2011) 10179.
9. J. P. Owejan, United States Patent 7,960,062, June 14, 2011.
10. K. A. Fennimore, United States Patent Application 2008/0160360, July 3, 2008.
11. M. Uno, T. Shimada, K. Tanaka, *J. Power Sources*, 196 (2011) 2558.
12. F. Al-Saleh, V. Buday, O. Klein, T. von Unwerth, S. Scholl, *J. Fuel Cell Sci. Technol.*, 11 (2014) 011001.
13. P. Alotto, M. Guarnieri, F. Moro, *Renew. Sustain. Energy Rev.*, 29 (2014) 325.
14. A. J. Bard, L. R. Faulkner, *Electrochemical Methods - Fundamentals and Applications*, 2nd edition, Wiley, New York, 2011.
15. M. Bon, T. Laino, A. Curioni, M. Parrinello, *J. Phys. Chem. C*, 120 (2016) 10791.
16. N. Kausar, A. Mousa, M. Skyllas-Kazacos, *ChemElectroChem*, 3 (2016) 276-282.
17. H. J. Lee, N. H. Choi, H. Kim, *J. Electrochem. Soc.*, 161 (2014) A1291.
18. J. St-Pierre, Y. Zhai, M. S. Angelo, *J. Electrochem. Soc.*, 161 (2014) F280 and *J. Electrochem. Soc.*, 162 (2015) X7.
19. Y. Zhai, O. Baturina, D. Ramaker, E. Farquhar, J. St-Pierre, K. Swider-Lyons, *Electrochim. Acta*, 213 (2016) 482.
20. Y. Zhai, K. Bethune, G. Bender, R. Rocheleau, *J. Electrochem. Soc.*, 159 (2012) B524.
21. A. Z. Weber and A. Kusoglu, *J. Mater. Chem. A*, 2 (2014) 17207.

22. J. St-Pierre, T. V. Reshetenko, *Electrochem. Soc. Trans.*, 75 (14) (2016) 63.
23. J. St-Pierre, M. Angelo, K. Bethune, J. Ge, S. Higgins, T. Reshetenko, M. Virji, Y. Zhai, *Electrochem. Soc. Trans.*, 61 (23) (2014) 1.
24. M. Zatoń, J. Rozière, D. Jones, *Sustain. Energy Fuels*, 1 (2017) 409.
25. J. St-Pierre, *J. Power Sources*, 196 (2011) 6274.
26. J. St-Pierre, *Int. J. Hydrogen Energy*, 36 (2011) 5527.
27. Y. Zhai, J. Ge, J. St-Pierre, *Electrochem. Commun.*, 66 (2016) 49.
28. M. A. Uddin, J. Park, L. Bonville, U. Pasaogullari, *Int. J. Hydrogen Energy*, 41 (2016) 14909.
29. B. D. Gould, G. Bender, K. Bethune, S. Dorn, O. A. Baturina, R. Rocheleau, K. E. Swider-Lyons, *J. Electrochem. Soc.*, 157 (2010) B1569.
30. Y. Zhai, O. Baturina, D. Ramaker, E. Farquhar, J. St-Pierre, K. Swider-Lyons, *Electrochim. Acta*, 213 (2016) 482.
31. B. K. Kakati, A. R. J. Kucernak, K. F. Fahy, *Electrochim. Acta*, 222 (2016) 888.
32. B. Kakati, A. Unnikrishnan, N. Rajalakshmi, R. Jafri, K. Dhathathreyan, A. Kucernak, *Int. J. Hydrogen Energy*, 41 (2016) 5598.
33. B. K. Kakati, A. R. J. Kucernak, *J. Power Sources*, 252 (2014) 317.
34. K. Kanazawa, H. Yamamura, M. Nakayama, K. Ogura, *J. Electroanal. Chem.*, 521 (2002) 127.
35. L. Franck-Lacaze, C. Bonnet, S. Besse, F. Lapique, *Fuel Cells*, 9 (2009) 562.
36. J. St-Pierre, Y. Zhai, J. Ge, T. Reshetenko, M. Angelo, T. Molter, L. Bonville, U. Pasaogullari, X. Wang, J. Qi, O. Ozdemir, A. Uddin, N. Khajeh-Hosseini-Dalasm, J. Park, S. Ganesan, W. Collins, S. Wessel, T. Cheng, 'The Effect of Airborne Contaminants on Fuel Cell Performance and Durability', in DOE Hydrogen and Fuel Cells Program - 2014 Annual Progress Report, United States Department of Energy, DOE/GO-102014-4504, November 2014, pp. V-133-V-139.

Battery Testing

APRISSES13 funding was used to build a battery-testing laboratory within HiSERF and to study the impact of several pack-related issues on commercial Li-ion batteries. The objective of the new battery laboratory is to test single cells (SCs) and modules used in battery energy storage systems (BESS) and other applications. In addition to building the laboratory, some key performance limiting aspects of battery modules were investigated: paralleling, imbalance, and overdischarge (Overcharge was investigated under HEET10). Results have been published in scientific literature [1-3].

HiSERF battery testing laboratory

The latest generation battery testing equipment powerful enough to test grid-size BESS single cells and modules was selected. Three ARBIN LBT battery testers were procured with different characteristics to provide a total of 62 individual testing channels, including 40x5V/25A channels to test small size batteries, 20x5V/100A to test large Li-ion cells found in BESS systems, and 2x25V/100A channels to test small modules.

The laboratory was designed with the highest safety standards in mind. To do so, we decided to retrofit an industrial refrigerator with its own air conditioning and ventilation system to provide complete isolation from the rest of the facility. All batteries are tested inside one of the six temperature chambers also purchased under APRISES13, all equipped with smoke, CO₂ and H₂ sensors. This is to detect any gassing and send a signal to automatically shut down all testing, purge the chamber with nitrogen, sound an alarm, as well as notify authorized personnel. The facility became operational in April 2015 and the first set of experiments were conducted and reported under HEET10.



Figure 2.1.35 (Left) Entrance to the laboratory, a self-contained converted refrigeration unit. (Center) 20 channel Arbin battery tester and climate chamber by its side. (Right) large format battery energy storage cells in the climate chamber.

Overdischarge

Various degrees of overdischarge events may occur in a battery pack where the intrinsic cell variability, extrinsically induced imbalance, and variations in the operating conditions may be present. For this study, we chose to focus on a commercial battery with a composite positive electrode, i.e. a mix of two different electrochemically active phases, LiNi_xAl_yCo_{1-x-y}O₂ (NCA) and LiMn₂O₄ (LMO). This is because the interaction between the two phases could introduce some unusual electrochemical behavior at low voltages.

The overall performance of the cells at room temperature was comparable to other cells from the same batch that were investigated previously [4-6]. Figure .1.36(a) shows that the most distinct feature on the discharge curves is in the highlighted region towards the end of discharge (EOD), where an excess capacity was exhibited below 2.4 V, in overdischarge conditions, for rates higher than C/5 (discharge in 5 hours). The associated incremental capacity (dQ/dV) curves, as shown in

Figure .1.36(b), clearly show an additional reaction in the low voltage region below 2.4 V in the discharge regime. Interestingly, no clearly identifiable complementary dQ/dV peak appears in the subsequent C/2 charge regime as indicated in Figure .1.36(c). Additionally, no anomaly was detected in the rest cell voltage measurements at the EOD or end-of-charge (EOC) in the tests either. This phenomenon is reproducible with other cells of the same batch, which eliminates the possibility of involving incidents caused by cell variability, defects or artifacts from equipment or specific measurements. This additional capacity is peculiar since it only appears at rates higher than C/5 (i.e. discharge in less than 5 hours); the dQ/dV peak position is also rate-dependent. Both suggest a kinetic origin. Furthermore, the capacity associated with this low-voltage reaction is higher with higher rates (e.g. from just 26 mAh at C/2 to 140 mAh at 5C).

Additional testing was performed to understand more about the phenomenon; low temperature experiments showed that there was even more additional capacity at low voltage and that it was appearing even for the lowest rates. Moreover, it was shown to be electrochemical and reversible with a 0.8V potential hysteresis. The presence of this additional electrochemical process is not a random event as it happened reproducibly under various circumstances. Based on electrochemical considerations, this reaction was identified to be the over-lithiation of LMO from LiMn_2O_4 to $\text{Li}_2\text{Mn}_2\text{O}_4$. The absence of commensurate dQ/dV peaks in the low voltage range (< 2.5 V) from either constituents of the positive electrode versus a graphite electrode suggests that this additional dQ/dV peak is related to the composite nature of the positive electrode.

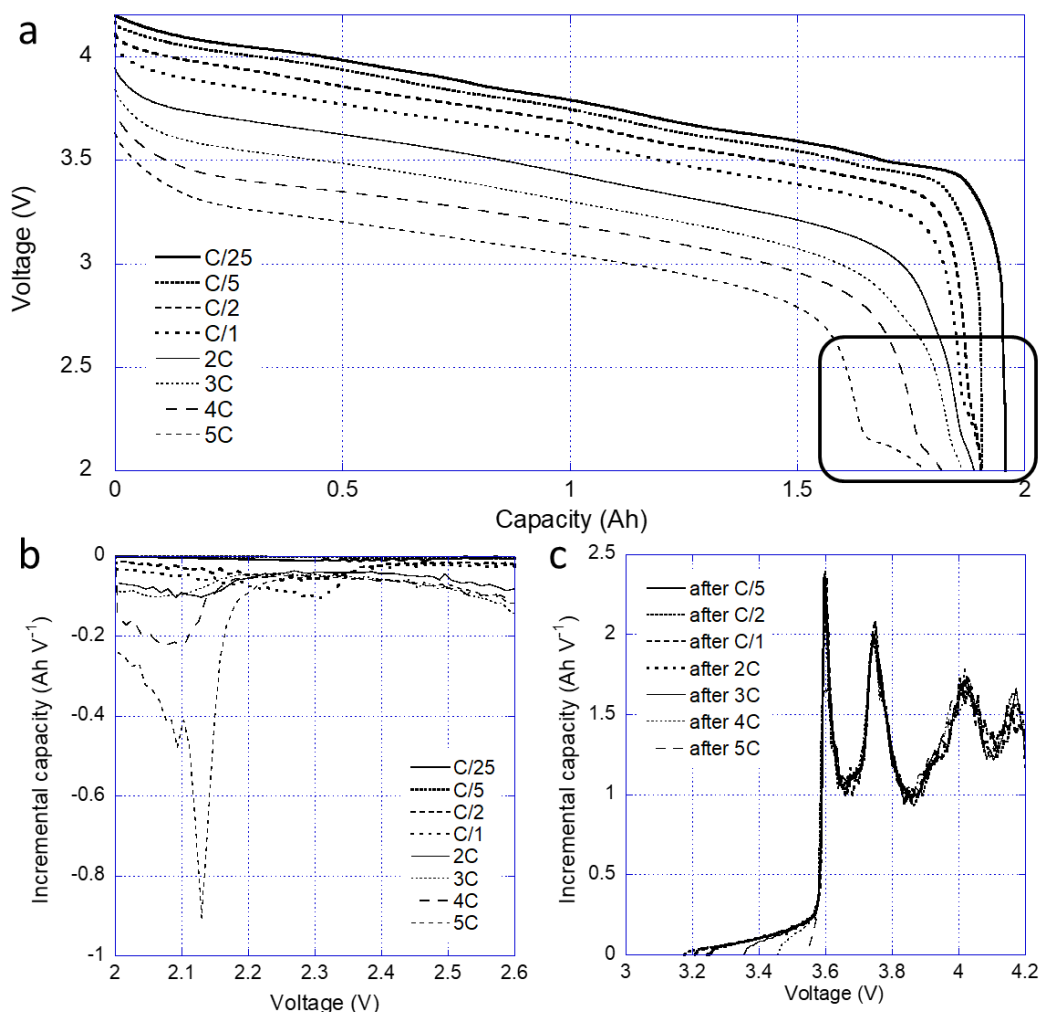


Figure 2.1.36: (a) Voltage versus capacity discharge curves for the G || {NMC+LMO} cell from C/25 to 5C, (b) the associated incremental capacity (dQ/dV) curves in the low voltage region, and (c) the dQ/dV curves of the subsequent C/2 charge regime showing no evident trace of additional capacity.

Although this LMO to $\text{Li}_2\text{Mn}_2\text{O}_4$ reaction has been reported in half-cell experiments for composite electrodes versus Li electrodes, where there is a significant excess of lithium ions; it should not occur in a commercial cell that uses a graphite electrode as a negative electrode (NE). This is because, in the latter the accessible Li content is constrained by what was initially in the positive electrode (PE) and therefore no excess lithium is available for reaction. As previously determined, the overdischarge process seems to be induced by certain kinetic limitations; we therefore investigated further the kinetics of each constituents of the PE. LMO was found to exhibit a higher rate capability than NCA. Since LMO was kinetically more favorable, we hypothesized that it could end up with an “over-lithiated” state, while NMC suffers “under-lithiation.”

To validate this hypothesis, we used the HNEI 'alawa model and toolbox to provide a mechanistic explanation of how NMC and LMO work in the composite PE during discharge. In Figure 7(a), three schematic discharge curves at C/20, C/2, and 1C, are illustrated for (a) NMC and (b) LMO, respectively, against a Li counter electrode in half-cell experiments. It should be noted that the capacity in the figures is scaled in proportion to the composition of the composite PE (2/3rd NCA/ 1/3rd LMO). As shown, the NMC exhibits a constant voltage decrease (solid solution) at high voltage and a voltage plateau (phase transformation) near 3.70–3.80 V which is less marked for higher rates. Since the NMC does not exhibit good rate capability, there is a significant capacity difference between the low and high rates. LMO has a better rate capability with three distinct potential plateaus, including the LMO-to-Li₂Mn₂O₄ one at about 2.80 V. Our simulations show that with an infinite amount of lithium ions, Figure 7(c), the additional capacity was visible even at low rates but that with a set amount of lithium ions, Figure 7(d), the additional capacity is only visible for higher rates. The model was therefore successful in validating our hypothesis and explained, for the first time in the field, all the features of this particular behavior of LMO based composite electrodes throughout an overdischarge scenario. More detail can be found in the peer reviewed publication [2].

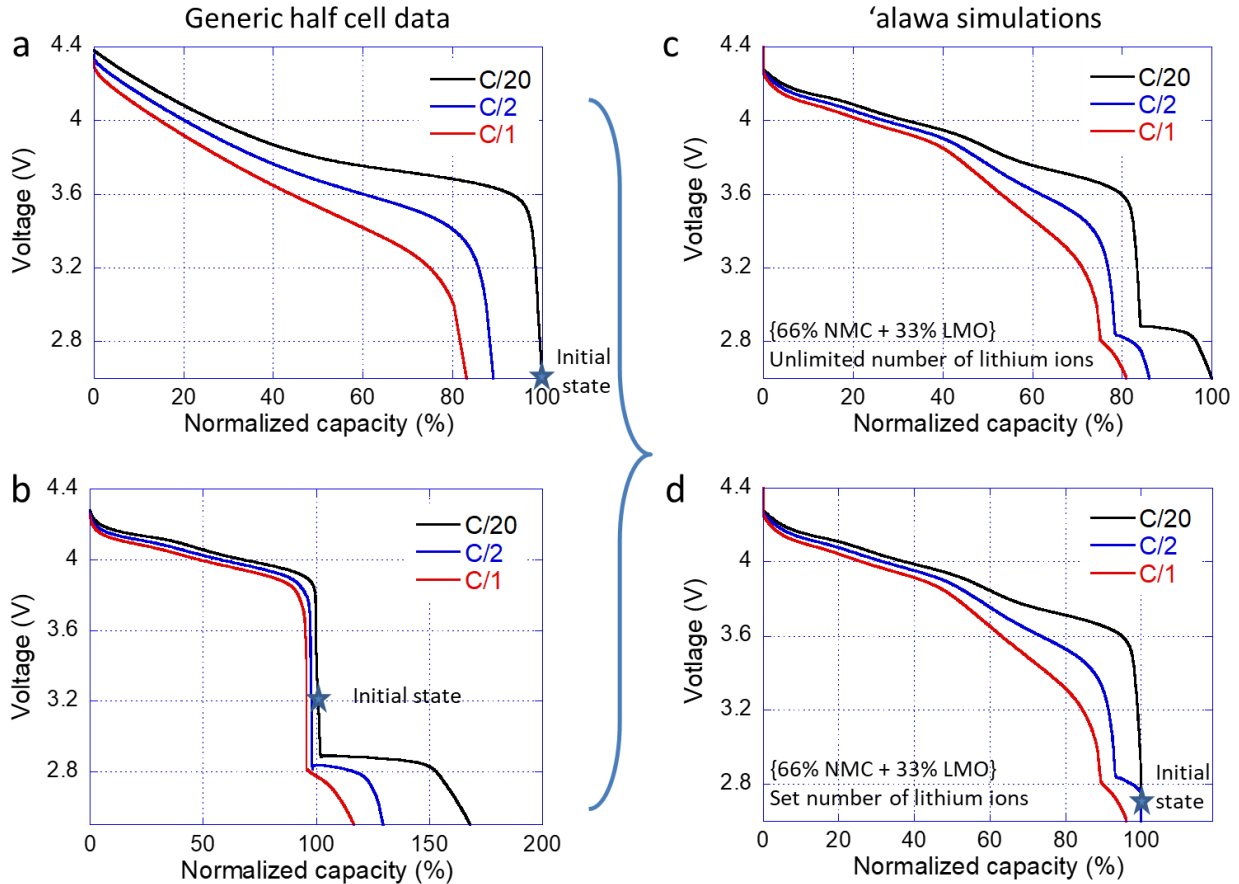


Figure 2.1.37: Schematic of the discharge curves synthesized from (a) the NMC and (b) LMO discharge curves with half-cell potential versus Li/Li⁺ to (b) the resulting c-PE of a {2/3 NMC + 1/3 LMO} composition with an unlimited source of Li-ion supply, and (c) the c-PE of the same composition but with limited supply of Li-ions from the NE.

Paralleling

Most battery-pack modules contain cells in parallel. For example, the COASTAL BESS modules are composed of 7 cells in parallel. It was therefore essential for us to investigate the behavior of cells in parallel and to model them. To do so, we developed the *kaulike* model [1] that uses a simple equivalent circuit model (ECM) as a core. The concept of this model is to determine the intersection of voltage versus rate curves for each single cell in a pack based on their current, state of charge (SOC), and to derive the transient balancing current and the voltage. Figure 2.1.38 illustrates the *kaulike* approach with an example of two cells in parallel, one with a low SOC and one with a high SOC. Based on the ECM, it is possible to calculate the voltage as a function of the rate for the entire SOC range, Figure 2.1.38(a). Knowing the SOC of the two cells in parallel, their voltages can thus be estimated for all possible rates (red and blue bar on Figure 2.1.38(a)), Figure 2.1.38(b & c). Figure 2.1.38(d) represents these two SOC's (red and blue), on the same voltage scale (left, y axis) with the corresponding rate of both cells (the top and bottom x axis). The rate of the pack (assembly) is shown on the second (right) y axis, corresponding to the sum of the rates of the single cells. Knowing the rate of the pack, the balancing current and voltage for a time step can then be deciphered by looking for corresponding SC rates and voltage on Figure 2.1.38(d). The same calculation is repeated for each model iteration with an updated SOC. For a pack comprising strings of cells in series, the voltage versus rate curves are calculated for the entire strings. More detail and validation can be found in [1].

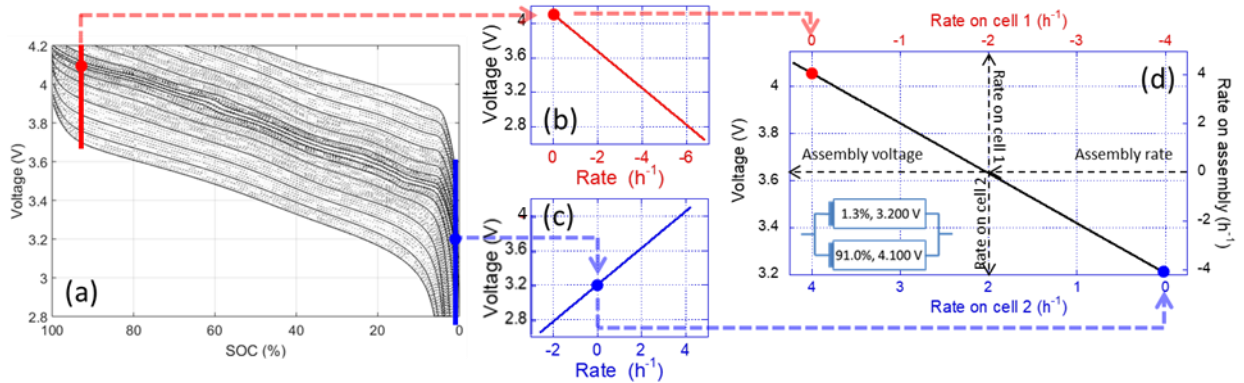


Figure 2.1.38. Schematic representation of the *kaulike* model [1]. (a) Highlights the result of the simulation of all the different rates using the ECM. (b) and (c) illustrate the relationship between voltage and rate at a given SOC. (d) showcases how the two voltage versus rate curves can be plotted on the same scale. The top x axis represents the rate of cell 1, the bottom x axis the rate of cell 2. The left y axis is the voltage on both SCs and the right y axis the rate on the assembly (the sum of the rates of the SCs).

To validate the precision and accuracy of the ECM simulations, three multi-cell assemblies were used in experiments with increasing complexity: 1S2P (1 in series, 2 in parallel), 1S3P and 2S2P. To validate extremes in the design of experiments and to achieve the maximum contrast in the magnitudes and variations of the balancing current, one of the strings was set to an almost fully discharged state intentionally, and another more than half charged. To ensure safety, in the 2S2P

experiment, the strings were assembled with cells of similar SOC (i.e. with minimal cell variability in SOC within a string).

Figure presents a series of results of the experimental testing on (a) 1S2P, (b) 1S3P, and (c) 2S2P configurations, each with a comparison between the experimental data (in gray) and the simulations (in black). For the 1S2P experiment, one cell was set to 5.0% SOC and the other to 65.0% SOC. For the 1S3P experiment, a third cell at 35.0% SOC was added. The solid lines are the string voltage profiles (with the scale on the left), and the dotted lines are the current evolutions (with the scale on the right). Overall, the simulation results for the voltage and current evolutions are in good agreement with the experimental data. In Figure 2.1.39(a), the voltage dropped to 3.705 V first within 6 minutes, bounced to about 3.712 V in 15 m, then decayed to 3.691 V about one and a half hours later. The simulation results appear accurate for the second and third stage but a few mV off in the first stage. The evolutions of the current profiles in the strings between the experiment and the simulations also show great precision. In both strings, the current quickly fell below 1C and took about three hours to reach a stabilized state. The third string in the 1S3P assembly was initially at a potential close to the final equilibrium potential. Thus, the string did not involve much balancing with current fluctuations ranging from $-0.03C$ to $0.03C$ throughout the experiment. The inset in Figure 2.1.39(b) shows an enlarged view of this current evolution in comparison with the simulation. The accuracy issue was still there for the first six minutes, but the simulation was sufficiently accurate for the rest of the experiment. Aside from the small initial discrepancy in current estimation, overall the model simulated the essential parts well: the evolution of the cell balancing voltage and the alternating charge and discharge periods.

Figure(c) shows a 2S2P experiment with the comparison between the experimental and simulated voltage and current profiles. Figure(d) shows the evolution of the individual SOC simulated by the model. In the design of experiments, one of the strings comprises cells of 65.0% and 35.0% SOC and the other string at 5.0% and around 10% (9.3%) SOC. The voltage and current variations follow the trends as observed in the previous studies: the profiles from the simulation are sufficiently precise and accurate with small discrepancies in the first five minutes. The final SOC determined from the model were consistent with the SOC derived from the open circuit voltage (OCV) of the four cells in the assembly, as shown in Figure(d). At equilibrium, the cells exhibited 21.0% SOC departure from their initial SOC. The final SOC value is also consistent with half of the difference of the initial SOC between the two strings, i.e. each string showed 21.2% in SOC variation, for a total of 42.5%.

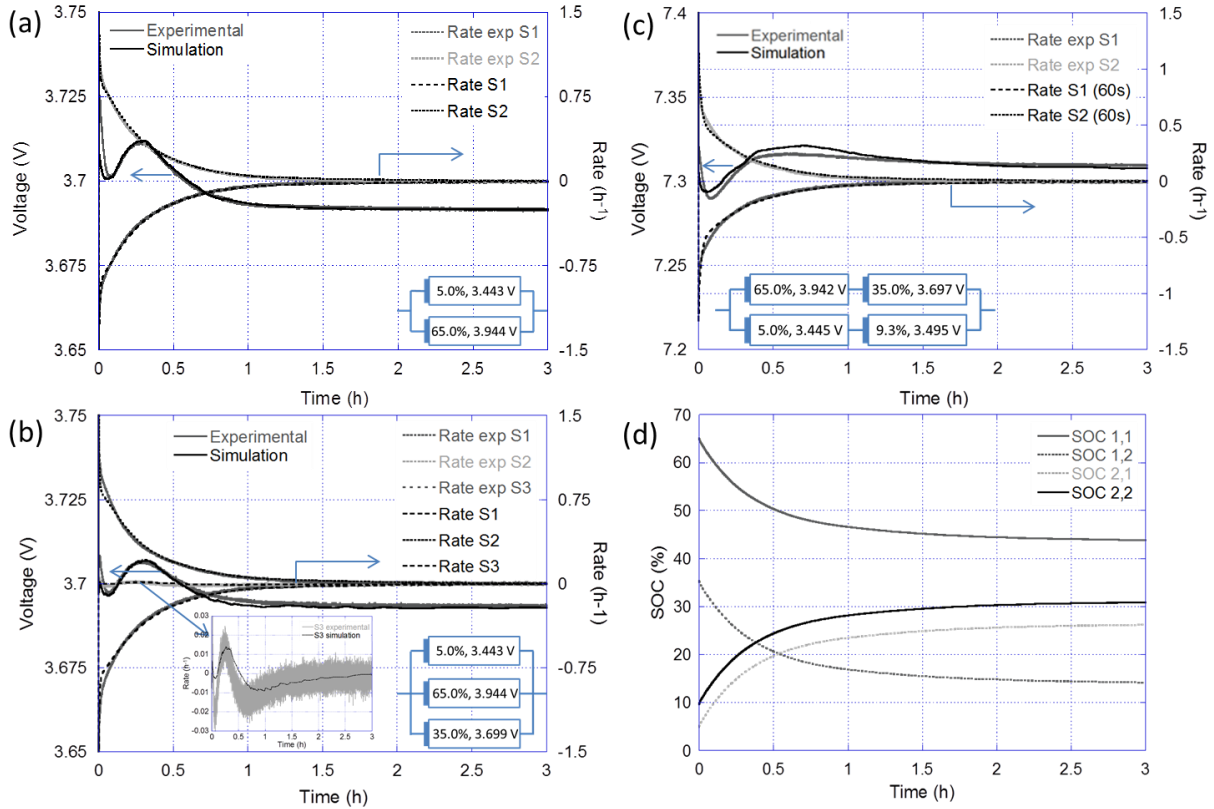


Figure 2.1.39: (a) Comparison of simulated and experimental cell voltage versus time profiles generated from a 1S2P, (b) a similar comparison with cell voltage versus time profiles from a 1S3P configuration; (c) A 2S2P simulation versus experimental voltage and current profiles, and (d) temporal SOC variations among the cells.

The *kaulike* approach offers a precise and accurate methodology to simulate the electrochemical behavior of cells or strings in parallel configurations. It was further proved that this approach is useful to assess the impacts of cell failures in open or short circuit conditions with a variety of different assembly configurations and to simulate the impacts of string swapping in aged assemblies [1]. This *kaulike* approach may be very useful for prognosis of large BESS with a large number of cells or modules in parallel configurations that are prone to cell or module failures, asymmetric degradation among cells, modules and strings, and replacement of cells, modules or strings in maintenance or repair. This approach could be a key diagnostic and prognostic method to address system level durability, reliability and safety issues.

Imbalance

In battery assemblies, SOC determination is more complicated than in single cells. This is because all single cells are slightly different and might not act perfectly in sync. Each battery pack, therefore, has a characteristic open pack voltage ($OPV=f(packSOC)$) function and, subsequently, no universal function can be used to describe it. As the pack ages, this complexity increases tremendously because of the likelihood of worsening in the cell balancing due to disparities in aging among the cells.

These issues increase the difficulty in performing accurate SOC determination in battery packs, since the $OPV=f(packSOC)$ function needs periodic calibration via additional characterization. This is the stumbling block for battery manufacturers or pack integrators to provide reliable operation of the battery system. Several methods were proposed in the literature to access the SOC and the state-of-health (SOH) of battery packs, but they are all beyond the capability of Battery Management Systems (BMSs) to date. To overcome this difficulty, we proposed a novel approach, named *anaku* [3], that offers a simple solution for BMS implementation while retaining sufficient accuracy for SOC and determination. This approach requires two separate measurements of steady cell voltage for all cells in a pack after a sufficient rest period, as well as accurate accounting of capacity change between these two measurements. In addition, the two measurements need to be at different SOC levels with negligible aging in-between.

This method allows monitoring and tracking the SOC of the pack, as well as the SOC of each single cell in the pack. The following benefits could be obtained from this simple process:

- (1) Individual cell SOC can be monitored accurately in the course of pack operation,
- (2) The cell imbalance in the pack can be tracked and quantified,
- (3) Cell-level control and monitoring can be enhanced for better reliability and safety,
- (4) Logistic requirements and accumulated errors can be minimized.

When coupled with our mechanistic modeling tools, the diagnosis (e.g. SOH, imbalance) and prognosis of pack performance (e.g. remaining useful life, or RUL) would become feasible. This method also makes estimation techniques such as those based on noise filtering (e.g. Kalman filters) or machine-learning for SOC and SOH estimations functional, since many empirical errors could be minimized. The *anaku* model [3] characterizes imbalance by deciphering two parameters for each SC the scaling factor and the translation factor. Based on these factors, the signature of the battery pack can be calculated from the SCs using a simple set of equations [3]. The OPV can then be expressed as a function of the OCV of all the SC comprising the pack. To account for imbalance, the OCVs of the different SCs need to be scaled or against each other. This is done with scaling and translation factors. More details on the equations and their validation can be found in [3]. The principles of the *anaku* model are graphically represented on Figure for a 3S1P configuration. Assuming that two rest cell voltages are available and that the capacity exchanged between them is known, the signature of the pack can be calculated by vertically aligning the blue boxes that represents each SC ΔSOC . On the left of Figure 2.1.40 it can be seen that the 3 cells have different capacity ratios (Q_r) as, for the same exchanged capacity, the ΔSOC (the size of the blue box) is different. By applying a scaling and a translation, the blue area under all three curves can be aligned (Figure 2.1.40 right). Once aligned, the voltage curves can be summed vertically to calculate the battery pack signature despite differences in Q_r , OCV curves, SOH, and initial SOC.

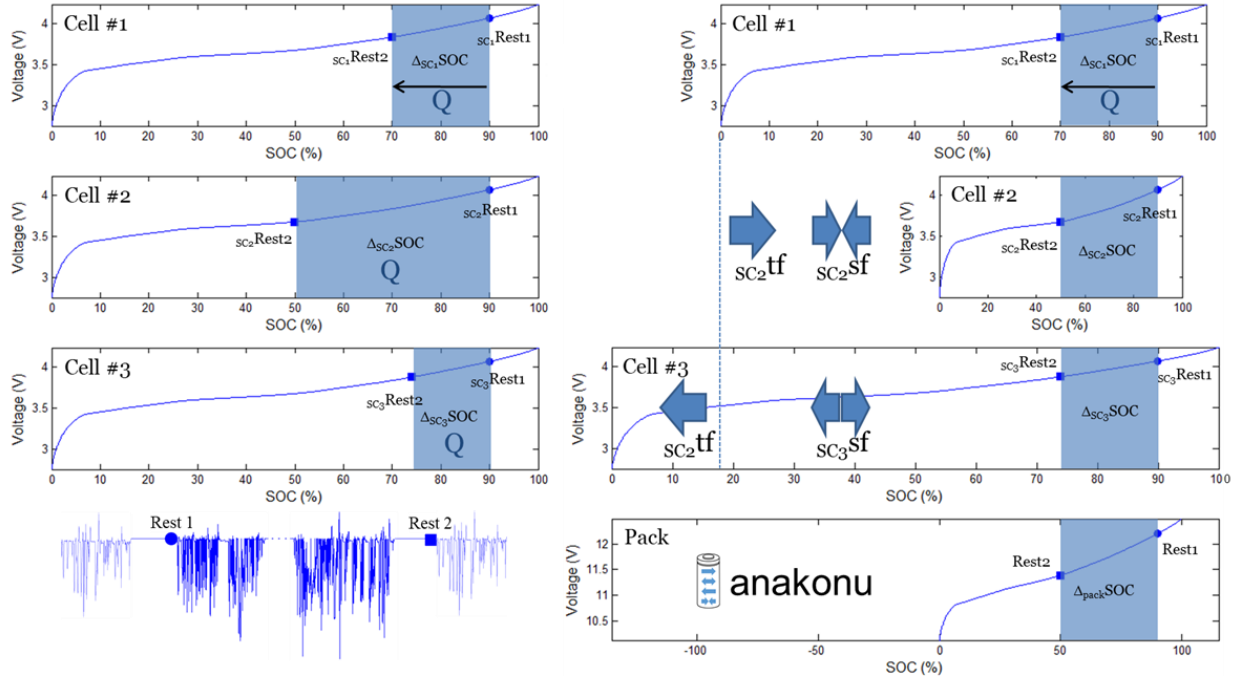


Figure 2.1.40. Schematic representation of the *anakonu* model [3].

In a previous work, [7], a 3S1P G||NMC pack was extensively tested at different rates (C/5, C/2, C/1, 2C and 2.5C) to explain which method is the most effective to determine the SOC of the pack experimentally. In that investigation, the $OPV=f(\text{packSOC})$ and packQr were determined experimentally. Using the RPVs at the beginning and end of any of the discharge or charge regimes, the simulated $OPV=f(\text{packSOC})$ curve could be derived by the *anakonu* method and used for validation. The curve of the initial state is shown in Figure 2.1.41, in which the circles represent the experimental data obtained in the prior work and the solid line the reconstructed function using the *anakonu* method. The mean error in the voltage between the two $OPV=f(\text{packSOC})$ curves is 3.5 mV, which is about the same as the tester's voltage resolution, ± 3 mV. The maximum error is 8.5 mV, near 45% SOC. The error in estimation between the SOC inferred from the *anakonu* method and that reported in [7] is on average $\pm 0.2\%$ and the most 0.55%. This is comparable to the error inherent in the tester's voltage resolution. In contrast, deriving the $OPV=f(\text{packSOC})$ function by using typical techniques [7] would have led to errors of 3% on average (c.f. [7], with an upper and lower bound from +7% to -3%); an order of magnitude larger.

In short, the *anakonu* method is very effective in deriving the $OPV=f(\text{packSOC})$ function for a battery pack. The method comprises a one-time determination of the $OCV=f(\text{scSOC})$ function on a sample cell and only requires two measurements of the RPVs of all the cells in the pack during operation. This verification indicates that this *anakonu* method provides an accurate account of SOC imbalance in the cells introduced in this case study before cycle aging. It can produce $OPV=f(\text{packSOC})$ function and packQr for a battery pack accurately and reliably even for cells significantly out of sync. It can be used as a pack design tool to assess the capacity influenced by degree of imbalance. As cells age, while the cell imbalance in the pack could increase, it can be used as a diagnostic and prognostic tool to analyze the SOC variations with aging conditions.

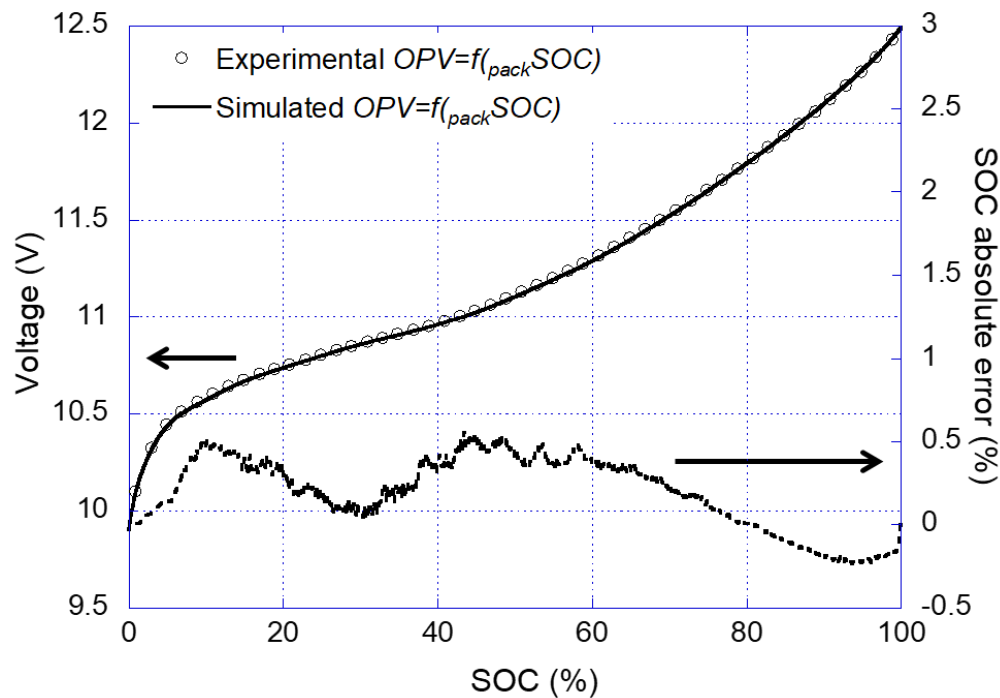


Figure 2.1.41: Comparison of experimental and simulated $OPV=f(packSOC)$ function for a 3S1P G||NMC string with 10% SOC imbalance.

In summary, much was accomplished under APRISES13 battery efforts. Not only was a battery facility built but significant progress was made in the understanding of how different key aspects of battery packs affect the single cells. These studies pave the way to develop a complete BESS model under APRISES15 and APRISES16 funding.

Publications Resulting from these Efforts

1. Dubarry, M.; Devie, A.; Liaw, B. Y., Cell-balancing currents in parallel strings of a battery system. *J. Power Sources* **2016**, 321, 36-46, 10.1016/j.jpowsour.2016.04.125
2. Dubarry, M.; Truchot, C.; Devie, A.; Liaw, B. Y.; Gering, K.; Sazhin, S.; Jamison, D.; Michelbacher, C., Evaluation of Commercial Lithium-Ion Cells Based on Composite Positive Electrode for Plug-In Hybrid Electric Vehicle (PHEV) Applications: IV. Over-Discharge Phenomena. *J. Electrochem. Soc.* **2015**, 162, (9), A1787-A1792, 10.1149/2.0481509jes
3. Dubarry, M.; Truchot, C.; Devie, A.; Liaw, B. Y., State-of-Charge Determination in Lithium-Ion Battery Packs Based on Two-Point Measurements in Life. *J. Electrochem. Soc.* **2015**, 162, (6), A877-A884, 10.1149/2.0201506jes

References

4. Dubarry, M.; Truchot, C.; Cugnet, M.; Liaw, B. Y.; Gering, K.; Sazhin, S.; Jamison, D.; Michelbacher, C., Evaluation of commercial lithium-ion cells based on composite

positive electrode for plug-in hybrid electric vehicle applications. Part I: Initial characterizations. *J. Power Sources* **2011**, 196, (23), 10328-10335, 10.1016/j.jpowsour.2011.08.077

5. Dubarry, M.; Truchot, C.; Liaw, B. Y.; Gering, K.; Sazhin, S.; Jamison, D.; Michelbacher, C., Evaluation of commercial lithium-ion cells based on composite positive electrode for plug-in hybrid electric vehicle applications. Part II. Degradation mechanism under 2C cycle aging. *J. Power Sources* **2011**, 196, (23), 10336-10343, 10.1016/j.jpowsour.2011.08.078
6. Gering, K. L.; Sazhin, S. V.; Jamison, D. K.; Michelbacher, C. J.; Liaw, B. Y.; Dubarry, M.; Cugnet, M., Investigation of path dependence in commercial lithium-ion cells chosen for plug-in hybrid vehicle duty cycle protocols. *J. Power Sources* **2011**, 196, (7), 3395-3403, 10.1016/j.jpowsour.2010.05.058
7. Truchot, C.; Dubarry, M.; Liaw, B. Y., State-of-charge estimation and uncertainty for lithium-ion battery strings. *Appl. Energy* **2014**, 119, 218-227, DOI 10.1016/j.apenergy.2013.12.046

2.2 Contamination Mitigation and Field Testing

Under subtask 2.2, HNEI developed advanced fuel cell air purification materials and novel sensor devices to allow the use of fuel cells to be expanded into harsh environmental conditions. These novel materials and devices were tested in controlled laboratory conditions under this effort.

The key accomplishments of this subtask were as follows; the development of novel air filtration materials which outperform commercially available state of the art materials; the development and installation of a novel sensor system and operational protocols which are designed to allow fuel cell vehicles to sense and react to dangerous air contaminants in the atmosphere to protect the fuel cell from damage while allowing the vehicle to operate consistently.

In support of the materials characterization for both novel air filtration materials and the Environmental Sensor System (ESS) design, an air filtration test bed was designed and fabricated at HNEI's Hawaii Sustainable Energy Research Facility (HiSERF). Experiments were performed to allow estimates of adsorption capacity of contaminants with both commercial and novel air filter materials. Under other APRISES funding, field testing is planned onboard a fuel cell electric bus at Hawaii Volcanoes National Park (HAVO), where the environment contains detrimental volcanic gas contaminants such as the acidic gases SO₂, NO₂ and H₂S, similar to battlefield conditions with exploded ordinance.

Proton Exchange Membrane (PEM) fuel cells produce electricity by combining oxygen and hydrogen in the presence of a platinum catalyst [1] and have been demonstrated as a reliable power source for stationary [2] and mobile applications [3]. To fuel PEM fuel cells, hydrogen is typically sourced from a high pressure, onboard tank and oxygen is sourced from the surrounding air. Air contaminants contained within the air delivered to the fuel cell could be poisonous to the fuel cell and cause fuel cell performance degradation. Environmental air quality, from which the oxygen

is sourced, varies based on location and can be highly contaminated depending on the area of operation [4, 5]. Air contamination can be comprised of both atmospheric particulates and poisonous gases from natural, industrial sources or exploded ordinance on a battlefield [6-8]. For example, PEM fuel cells used to power vehicles could be exposed to internal combustion engine exhaust [9] from vehicles on the roadway. PEM fuel cells used in stationary industrial applications could be exposed to industrial exhaust gases such as flue gas exhaust [8]. Air contamination has the potential to cause temporary or permanent performance loss when the contaminant gas molecule forms a chemical or physical bond with the platinum catalyst on the surface of the electrode and hinders the active catalyst site [10] in addition to other contamination mechanisms which can disable a fuel cell [11].

The PEM fuel cell industry has addressed this problem by applying increasingly complex air filtration technologies to the cathode air inlet over the past 25 years, starting with large particulate filtration and later incorporating chemical filtration [12]. More complex air filtration such as fast cycle pressure swing adsorption exists but is not utilized because of the difficulty to integrate [13]. Furthermore, the state of art fuel cell chemical filtration technologies for gas contaminants removal utilize non-regenerable absorbents. However, the widespread commercialization of fuel cells in the future would lead to the generation of significant volumes of hazardous sorbent waste. Hence the need for alternate materials with the potential for high gas contaminant sorption performance (break through times, selectivity, kinetics and sorption capacity) and regeneration, especially under harsh operational environments with elevated levels of the gas contaminants. Ionic liquids, permanent porosity liquids, and inorganic solid bimetallic compounds incorporated into nanoporous materials offer the most promising pathway. Tolerance limits for several contaminants are available [14] to help assess the need for a filter, and stack compatible recovery procedures have recently appeared in the literature [15-17].

Field Testing and Commercial Filter Testing

A system was developed to allow fuel cell vehicles to operate in highly contaminated environments which previously would have rendered the fuel cell damaged and inoperable. The system is comprised of a novel sensor device to understand the environmental conditions the fuel cell is operating in, laboratory testing to understand the performance of the commercial air filtration material used to purify the air, and a series of protocols to shut down the fuel cell and operate on stored battery power when the fuel cell encounters extremely high air contamination.

Under Task 2.2, the next advancement in fuel cell air filtration technology has been developed as a novel sensor device called the Environmental Sensor System (ESS), Figure 2.2.1. The ESS detects air contamination in the environment in which the fuel cell is operating and transmits that data to the fuel cell control system in real time. Through the ESS, the control software can respond to changing air contaminant conditions by adjusting operation of the fuel cell electric vehicle through calling for shutdown of the fuel cell when air contaminants are above damaging levels. When the fuel cell is operating in an environment with low levels of air contamination where the onboard air filter is capable of purifying the air to safe levels, the cumulative exposure of air

contaminants to the air filter can be calculated. This integration allows the air filter lifetime to be estimated. This will allow the air filter to be exchanged at the appropriate time. The ESS can also be used to detect air contaminants that break through the air filter by monitoring the air flowing directly into the cathode after it has passed through the air filter. Air contaminant breakthrough is considered an emergency situation and if detected by the ESS, the control software is programmed to shut down the fuel cell, protecting it from contaminant exposure and permanent impairment. This use of the ESS has the potential to significantly extend fuel cell lifetime and reduce O&M costs and operational breakdowns. The ESS is capable of sensing multiple air contaminants using a customizable array of air contaminant sensors. The ESS has beneficial applications in mobile and stationary fuel cell or hybrid fuel cell systems which incorporate batteries or stored oxygen. As a demonstration of the technology, the ESS is currently being installed on two fuel cell electric buses that will be operated at HAVO) under other APRISES funding.

HAVO experiences intermittent volcanic eruptions causing intermittent air contamination levels of up to 5 ppm SO₂ and 1 ppm H₂S. The fuel cell manufacturer (Hydrogenics™) specifications state that an exposure above 4 ppb in the anode or cathode fuel will void the warranty and negatively impact the fuel cell performance. This is an ideal environment to demonstrate the ESS technology on a fuel cell vehicle. A fuel cell operating in this environment without an ESS would experience a detrimental performance loss due to SO₂ and H₂S poisoning [10, 18, 19]. The ESS will be equipped with SO₂, NO, NO₂ H₂S electrochemical sensors and a photoionization detector (PID) to detect volatile organic compounds (VOC) from other traditional internal combustion engine (ICE) vehicles. The SO₂, H₂S, NO, and NO₂ sensors are 3-electrode electrochemical devices in standard 4 series packages, sourced from Enmet LLC, with a resolution of 0.1 ppm and a range of 0 – 30 ppm. The VOC sensor is a PID, sourced from Enmet LLC, with a resolution of 0.01 ppm and a range of 0–20 ppm. The ESS has a temperature and humidity sensor with a range of -40 to 140 degrees Fahrenheit, and 0 – 100% RH. The resolution is 1 degree Fahrenheit and 1% RH. It also has an atmospheric pressure sensor with a range of 0 – 30 PSIA with a resolution of 1 PSI. The ESS is comprised of two Environmental Sensor Arrays. The ESS boxes were installed above the driver as shown in Figure 2.2.2.

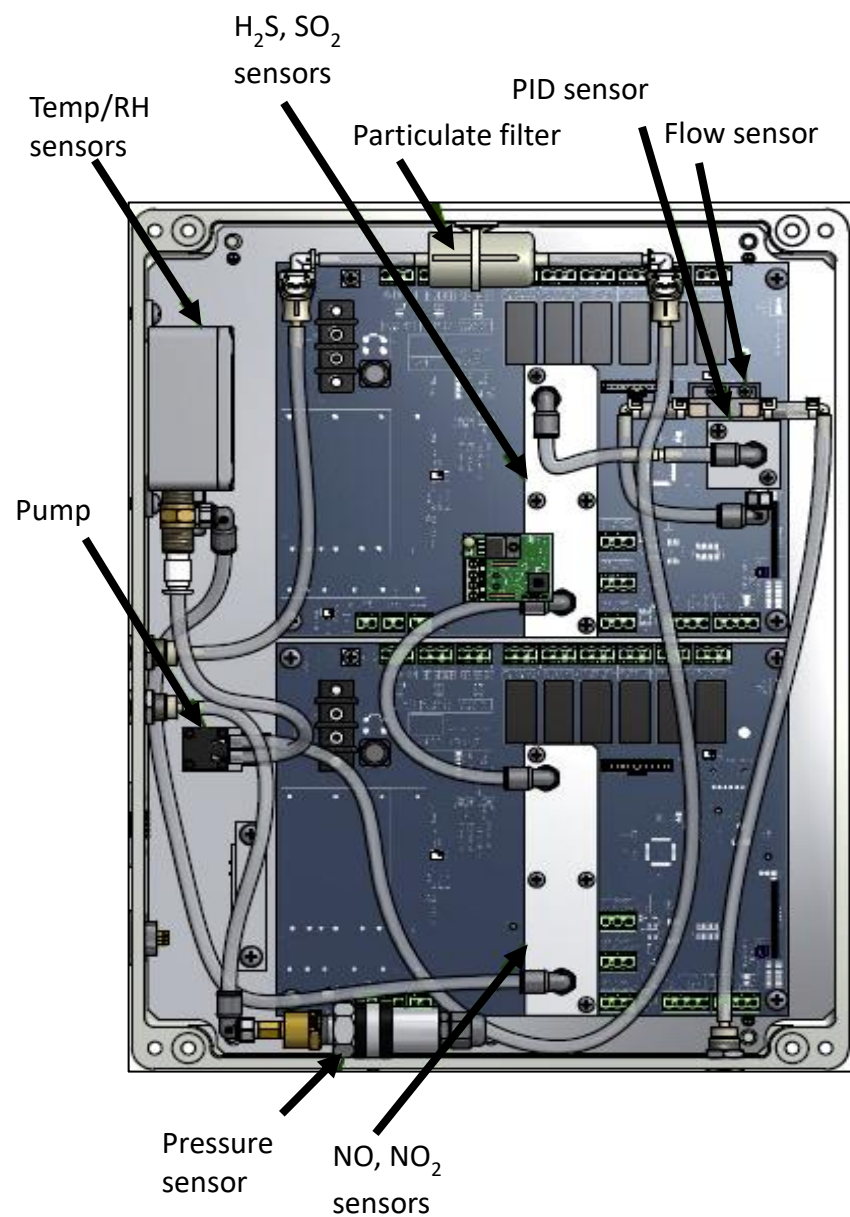


Figure 2.2.1: Diagram of the Environmental Sensor System (ESS) internal components (Enmet LLC).

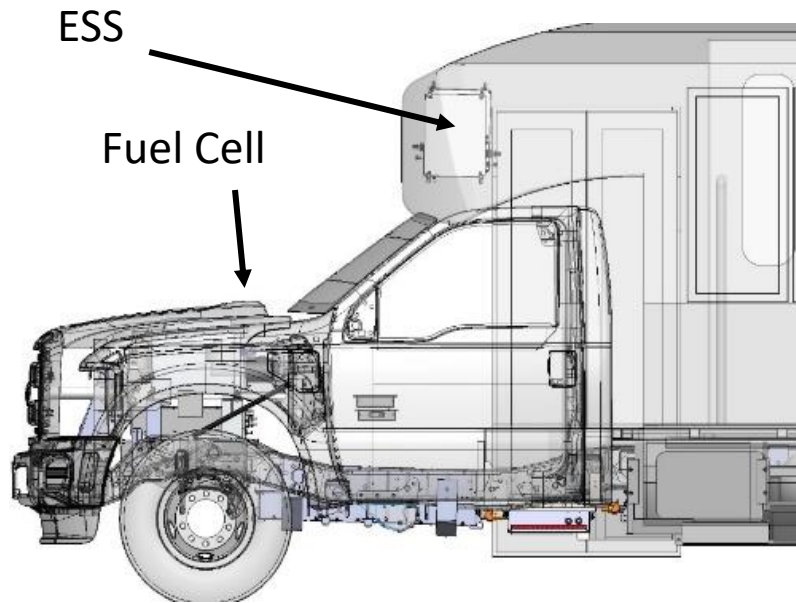


Figure 2.2.2: Drawing of the Fuel Cell Electric Bus with placement of the ESS.

After communication between the ESS and the bus CAN system was confirmed, the bus protection protocol was programmed and tested using the bus control software. The system is designed such that the bus control software will shut down the fuel cell and operate on the power stored in the onboard 28 KWhr lithium ion battery when the ESS (Box A or Box B) signals a contaminant concentration has been sensed above the customizable threshold which is set in the bus control software. As an initial proof of functionality, the ESS Box A, which senses the environmental conditions in which the bus is operating, was set to shut the fuel cell off when contaminant concentration is detected above 0.5 ppm for SO₂, H₂S, NO₂, NO, and 5 ppm for VOC. After the bus control software was programmed and communication between the bus software and ESS was established, contaminant gases were introduced directly into the ESS Box A inlet. This simulated a high air contaminant environment to allow the functionality of the control system, the communications and the ESS Box A to be tested. In figure 2.2.3, the fuel cell can be seen operating at full current when there are no air contaminants sensed by the ESS Box A and the current drops to zero when the ESS Box A senses the air contaminants are above the customizable setpoints.

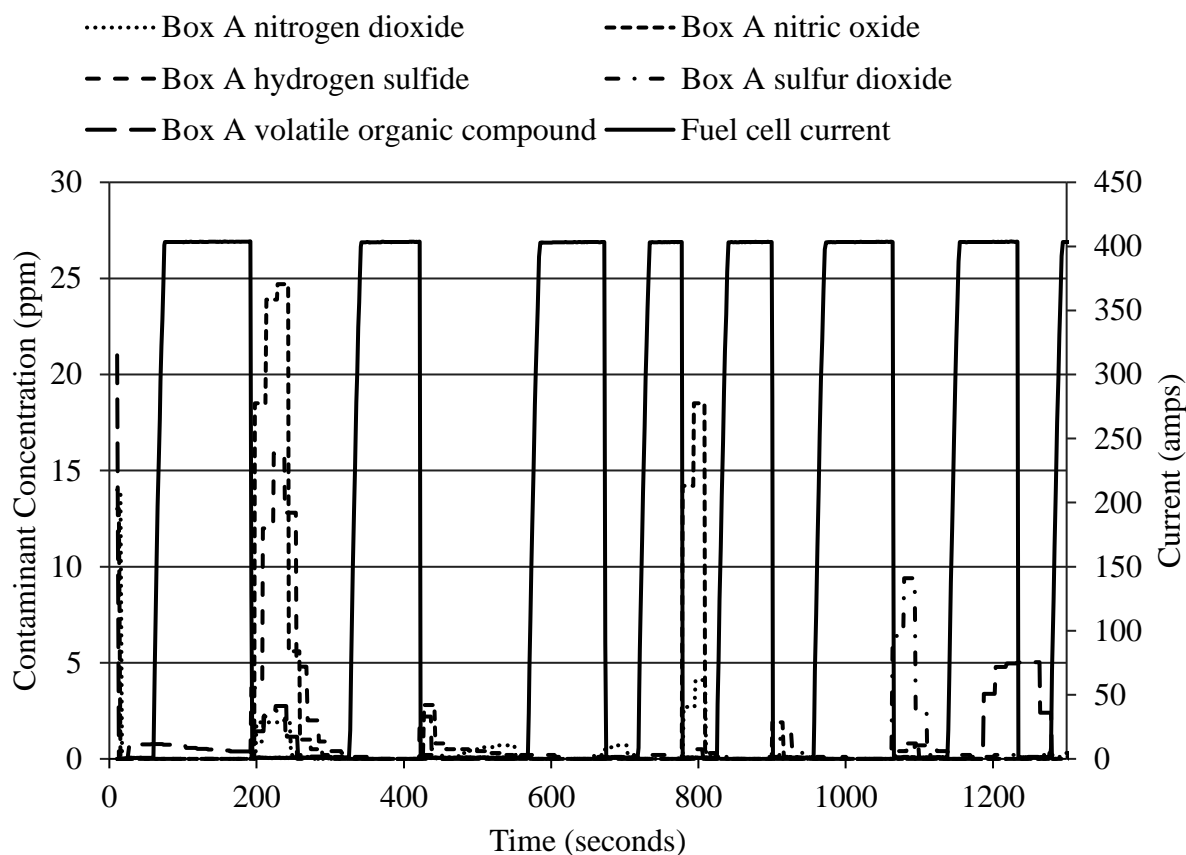


Figure 2.2.3: Fuel cell current response during simulated high air contaminant environment for ESS Box A,

Complete details can be found upon publication of the paper resulting from this effort (listed at the end of this subtask).

Air Filtration Materials Development

Under APRISES13 research on the development of advanced air filtration materials was performed to improve gas contaminant mitigation performance and enable efficient fuel cell operation under harsh environments. SO_2 is one of the most detrimental gas contaminants for PEM fuel cells, as it binds irreversibly to the Pt catalyst. In APRISES13, our research effort was geared towards the investigation of supported ionic liquid materials as advanced high performance sorbent materials for SO_2 mitigation from air. We explored ionic liquids due to their potential for high sorption capacities, high kinetics and reversibility [20-24]. Ionic liquids are a class of “green compounds” which have recently received considerable attention in numerous applications due to their negligible volatility, large liquidus range, and tunable chemical properties [25-31]. These liquids have recently been shown to be capable to partially regeneratively absorb a variety of

contaminants through physisorption and chemisorption processes [32]. However, the practical use of ionic liquids in gas separation is limited by their high viscosity and the small gas-liquid interface which reduces gas diffusion rates through the ionic liquids [33, 34].

In order to mitigate the effects of high viscosity of the ionic liquids, we synthesized activated carbon sorbents loaded with ionic liquid. This was achieved by impregnating a variety of thin films of ionic liquids onto a coconut based granulated activated carbon, and evaluating the sorption performance at relatively high concentration (15 ppm) of SO₂ in simulated air. Amongst the ionic liquid sorbents studied, the 1-ethyl-3-methylimidazolium acetate loaded activated carbon ([C₂mim][Ac] sorbent) exhibited the highest SO₂ sorption capacity performance. The sorption results clearly indicated that some ionic liquids such as 1-hexyl-3-methylimidazolium bis(trifluoromethylsulfonyl)imide with high absorptivity in pure SO₂ perform poorly under practical conditions. As a result of the superior performance of the [C₂mim][Ac] sorbent under practical conditions, further analysis were performed on the sorbent. Figure 2.2.4 shows the activated carbon before and after ionic liquid impregnation indicating effective incorporation of the 1-ethyl-3-methylimidazolium acetate.

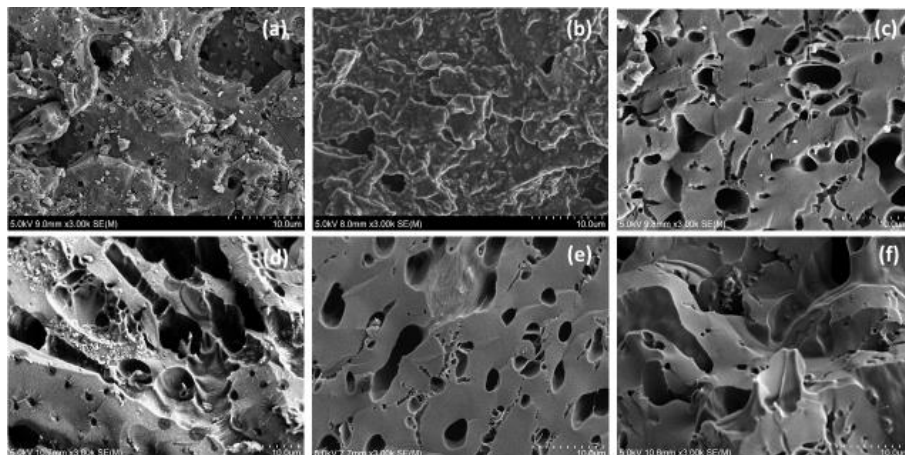


Figure 2.2.4 The SEM images showing the external surfaces prior to SO₂ sorption of; (a) activated carbon and (b) 1-ethyl-3-methylimidazolium acetate loaded activated carbon ([C₂mim][Ac] sorbent). The internal surface prior to SO₂ sorption of; (c) activated carbon and, (d) [C₂mim][Ac] sorbent. The internal surfaces after SO₂ sorption of; (d) activated carbon and (e) [C₂mim][Ac] sorbent.

The performance of the [C₂mim][Ac] sorbent increased along with ionic liquid loading onto the activated carbon. The SO₂ breakthrough time of [C₂mim][Ac] sorbent was greater than pure activated carbon and KOH loaded activated carbon standard (KOH sorbent) confirming the potential of the sorbent in practical SO₂ sorption from air, Figure 2.2.5.

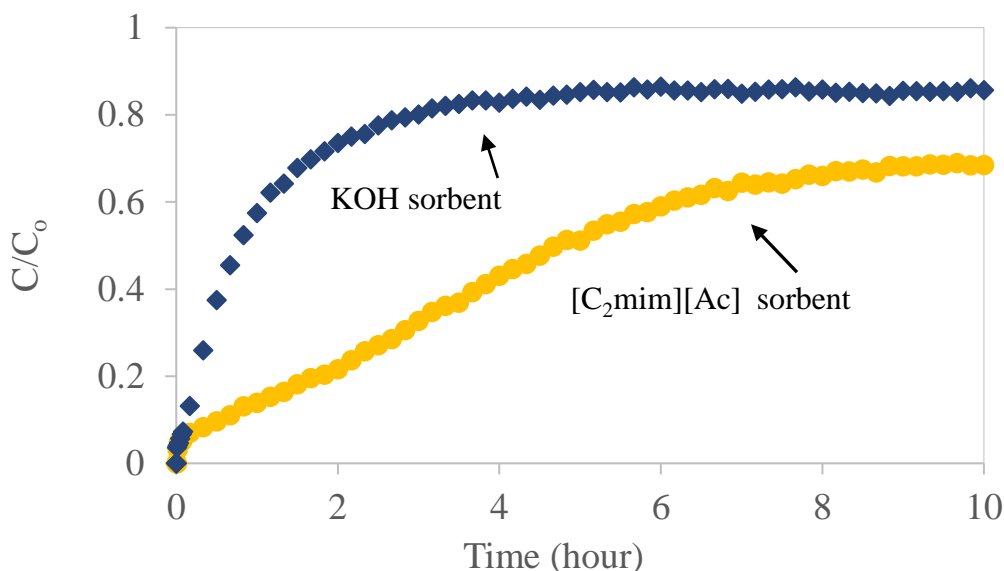


Figure 2.2.5 The SO₂ breakthrough curve of the [C₂mim][Ac] sorbent and potassium hydroxide loaded activated carbon standard (KOH sorbent) at 15LPM simulated air containing 15 ppm SO₂ and 50 % relative humidity.

The mechanism of SO₂ sorption by [C₂mim][Ac] sorbent was elucidated by a combination of techniques including FTATR, Solution NMR and thermal analysis (TGA and DSC) of SO₂ sorbed [C₂mim][Ac] sorbent, Figure 2.2.6. The FTATR analyses indicated the presence of both physisorbed and chemisorbed SO₂.

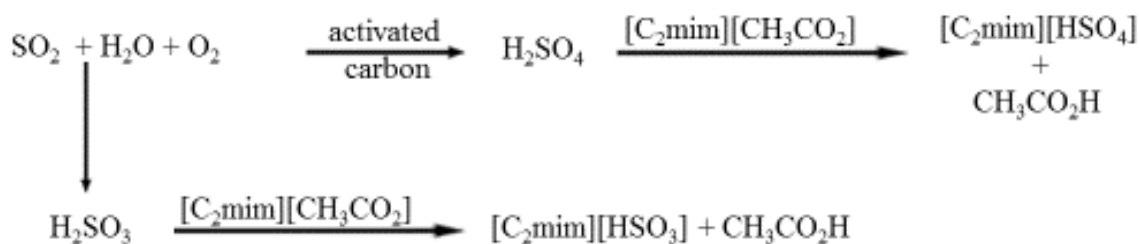


Figure 2.2.6. Proposed chemisorption mechanism of SO₂ by the [C₂mim][Ac] sorbent.

The effect of humidity, temperature, activated carbon support and ionic liquid loading on SO₂ sorption performance of [C₂mim][Ac] sorbent was also evaluated under APRISES 13. For detailed information on Methods, Results and Discussion of work performed under the air filtration materials development effort, see *Severa, G.; Bethune, K.; Rocheleau, R.; Higgins, S. (2015). SO₂ sorption by activated carbon supported ionic liquids under simulated atmospheric conditions., Chemical Engineering Journal, 265, 249-258.*

Using other funding, a materials chemistry laboratory for use in novel purification materials development was successfully designed and renovated, including the installation of new epoxy laboratory work surfaces, chemical storage cabinet, new cabinetry, and a sink.. Under APRISES13 funding, laboratory equipment including a glovebox and TGA-DSC for use in synthesis and

characterization of purification materials was purchased and successfully installed in the renovated lab.

Under APRISES12 we are performing experiments focused on simultaneous acidic gas (SO₂ and NO₂) contaminant sorption. Furthermore theoretical modeling of gas contaminant sorbent binding interactions will be done to gain understanding of the chemistries occurring during gas contaminant sorption. Regeneration methods of the various sorbents will also be explored.

Publications Resulting from these Efforts

1. Severa, G.; Bethune, K.; Rocheleau, R.; Higgins, S. (2015). SO₂ sorption by activated carbon supported ionic liquids under simulated atmospheric conditions, *Chemical Engineering Journal*, 265, 249-258.
2. Higgins, S.R., Ewan, J., St-Pierre, J., Severa, G, Davies, K., Bethune, K., Goodarzi, A, Rocheleau, R., *Environmental Sensor System for Expanded Capability of PEM Fuel Cell Use in High Air Contaminant Conditions*, Submitted to Journal of Renewable and Sustainable Energy, currently under review.

References

- [1] C. Berger, Handbook of fuel cell technology, Prentice-Hall, Englewood Cliffs, N.J., 1968.
- [2] A.J.L. Verhage, J.F. Coolegem, M.J.J. Mulder, M.H. Yildirim, F.A. de Bruijn, 30,000 h operation of a 70 kW stationary PEM fuel cell system using hydrogen from a chlorine factory, *International Journal of Hydrogen Energy* 38(11) (2013) 4714-4724.
- [3] T. Fletcher, R. Thring, M. Watkinson, An Energy Management Strategy to concurrently optimise fuel consumption & PEM fuel cell lifetime in a hybrid vehicle, *International Journal of Hydrogen Energy* 41(46) (2016) 21503-21515.
- [4] M. Masiol, S. Squizzato, G. Formenton, R.M. Harrison, C. Agostinelli, Air quality across a European hotspot: Spatial gradients, seasonality, diurnal cycles and trends in the Veneto region, NE Italy, *Science of The Total Environment* 576 (2017) 210-224.
- [5] L. Huang, J. Hu, M. Chen, H. Zhang, Impacts of power generation on air quality in China—part I: An overview, *Resources, Conservation and Recycling* 121 (2017) 103-114.
- [6] J.M. Moore, P.L. Adcock, J.B. Lakeman, G.O. Mepsted, The effects of battlefield contaminants on PEMFC performance, *Journal of Power Sources* 85(2) (2000) 254-260.
- [7] P.A. Nadeau, C.A. Werner, G.P. Waite, S.A. Carn, I.D. Brewer, T. Elias, A.J. Sutton, C. Kern, Using SO₂ camera imagery and seismicity to examine degassing and gas accumulation at Kīlauea Volcano, May 2010, *Journal of Volcanology and Geothermal Research* 300 (2015) 70-80.

- [8] K. AlRafea, A. Elkamel, S.A. Abdul-Wahab, Cost-analysis of health impacts associated with emissions from combined cycle power plant, *Journal of Cleaner Production* 139 (2016) 1408-1424.
- [9] J. Gallus, U. Kirchner, R. Vogt, T. Benter, Impact of driving style and road grade on gaseous exhaust emissions of passenger vehicles measured by a Portable Emission Measurement System (PEMS), *Transportation Research Part D: Transport and Environment* 52, Part A (2017) 215-226.
- [10] J. St-Pierre, Proton exchange membrane fuel cell contamination model: Competitive adsorption followed by a surface segregated electrochemical reaction leading to an irreversibly adsorbed product, *Journal of Power Sources* 195(19) (2010) 6379-6388.
- [11] J. St-Pierre, M. Angelo, K. Bethune, J. Ge, S. Higgins, T.V. Reshetenko, M.B.V. Virji, Y. Zhai, PEMFC Contamination - Fundamentals and Outlook, *ECS Transactions* 61(23) (2014) 1-14.
- [12] D.M. Kennedy, D.R. Cahela, W.H. Zhu, K.C. Westrom, R.M. Nelms, B.J. Tatarchuk, Fuel cell cathode air filters: Methodologies for design and optimization, *Journal of Power Sources* 168(2) (2007) 391-399.
- [13] J. St-Pierre, D.P. Wilkinson, Fuel cells: A new, efficient and cleaner power source, *AIChE Journal* 47(7) (2001) 1482-1486.
- [14] Y.Z. J. St-Pierre, J. Ge, M. Angelo, T. Reshetenko, T. Molter, L. Bonville, U. Pasaogullari, W. Collins, S. Wessel, The Effect of Airborne Contaminants on Fuel Cell Performance and Durability, DOE Hydrogen and Fuel Cells Program - 2013 Annual Progress Report, United States Department of Energy, DOE/GO-102013-4260 V-1-V-6
- [15] B.K. Kakati, A.R.J. Kucernak, K.F. Fahy, Using corrosion-like processes to remove poisons from electrocatalysts: a viable strategy to chemically regenerate irreversibly poisoned polymer electrolyte fuel cells, *Electrochimica Acta* 222 (2016) 888-897.
- [16] B.K. Kakati, A. Unnikrishnan, N. Rajalakshmi, R.I. Jafri, K.S. Dhathathreyan, A.R.J. Kucernak, Recovery of Polymer Electrolyte Fuel Cell exposed to sulphur dioxide, *International Journal of Hydrogen Energy* 41(12) (2016) 5598-5604.
- [17] R. Baron, J. Saffell, Amperometric Gas Sensors as a Low Cost Emerging Technology Platform for Air Quality Monitoring Applications: A Review, *ACS Sensors* 2(11) (2017) 1553-1566.
- [18] J. St-Pierre, Y. Zhai, M. Angelo, Quantitative ranking criteria for PEMFC contaminants, *International Journal of Hydrogen Energy* 37(8) (2012) 6784-6789.
- [19] B.D. Gould, O.A. Baturina, K.E. Swider-Lyons, Deactivation of Pt/VC proton exchange membrane fuel cell cathodes by SO₂, H₂S and COS, *Journal of Power Sources* 188(1) (2009) 89-95.
- [20] G. Yu, X. Chen, SO₂ Capture by Guanidinium-Based Ionic Liquids: A Theoretical Study, *The Journal of Physical Chemistry B* 115(13) (2011) 3466-3477.

- [21] J.L. Anderson, J.K. Dixon, E.J. Maginn, J.F. Brennecke, Measurement of SO₂ Solubility in Ionic Liquids, *The Journal of Physical Chemistry B* 110(31) (2006) 15059-15062.
- [22] J. Huang, A. Riisager, R.W. Berg, R. Fehrmann, Tuning ionic liquids for high gas solubility and reversible gas sorption, *Journal of Molecular Catalysis A: Chemical* 279(2) (2008) 170-176.
- [23] C. Froschauer, H.K. Weber, T. Röder, H. Sixta, G. Laus, B. Lendl, H. Schottenberger, No Matter of Course: Ionic Liquids as SO₂-Selective Gas Absorbers, *Lenzinger Berichte* 91 (2013) 30-43.
- [24] L. Zhang, Z. Zhang, Y. Sun, B. Jiang, X. Li, X. Ge, J. Wang, Ether-Functionalized Ionic Liquids with Low Viscosity for Efficient SO₂ Capture, *Industrial & Engineering Chemistry Research* 52(46) (2013) 16335-16340.
- [25] D.R. MacFarlane, N. Tachikawa, M. Forsyth, J.M. Pringle, P.C. Howlett, G.D. Elliott, J.H. Davis, M. Watanabe, P. Simon, C.A. Angell, Energy applications of ionic liquids, *Energy & Environmental Science* 7(1) (2014) 232-250.
- [26] B. Kirchner, Topics in current chemistry, in: B. Kirchner (Ed.) *Ionic liquids*, Springer-Verlag new york, 2009, p. 40.
- [27] P. Wasserscheid, T. Welton, *Ionic liquids in synthesis*, Wiley-VCH Verlag, Weinheim, 2003.
- [28] J. Palomar, J. Lemus, M.A. Gilarranz, J.J. Rodriguez, Adsorption of ionic liquids from aqueous effluents by activated carbon, *Carbon* 47(7) (2009) 1846-1856.
- [29] G. Severa, G. Kumar, M. Troung, G. Young, M.J. Cooney, Simultaneous extraction and separation of phorbol esters and bio-oil from *Jatropha* biomass using ionic liquid-methanol co-solvents, *Separation and Purification Technology* 116(0) (2013) 265-270.
- [30] J.L. Anderson, J.K. Dixon, J.F. Brennecke, Solubility of CO₂, CH₄, C₂H₆, C₂H₄, O₂, and N₂ in 1-Hexyl-3-methylpyridinium Bis(trifluoromethylsulfonyl)imide: Comparison to Other Ionic Liquids, *Accounts of Chemical Research* 40(11) (2007) 1208-1216.
- [31] Y. Shang, H. Li, S. Zhang, H. Xu, Z. Wang, L. Zhang, J. Zhang, Guanidinium-based ionic liquids for sulfur dioxide sorption, *Chemical Engineering Journal* 175(0) (2011) 324-329.
- [32] W. Wu, B. Han, H. Gao, Z. Liu, T. Jiang, J. Huang, Desulfurization of Flue Gas: SO₂ Absorption by an Ionic Liquid, *Angewandte Chemie International Edition* 43(18) (2004) 2415-2417.
- [33] J. Lemus, J. Palomar, M. Gilarranz, J. Rodriguez, Characterization of Supported Ionic Liquid Phase (SILP) materials prepared from different supports, *Adsorption* 17(3) (2011) 561-571.
- [34] Z. Zhang, L. Wu, J. Dong, B.-G. Li, S. Zhu, Preparation and SO₂ Sorption/Desorption Behavior of an Ionic Liquid Supported on Porous Silica Particles, *Industrial & Engineering Chemistry Research* 48(4) (2009) 2142-2148.

TASK 3: ALTERNATIVE FUELS

This effort focused on the development, testing and evaluation of alternative fuels and technologies, and included activities in the areas of: Methane Hydrates; several areas of Technology for Synthetic Fuels Production including waste stream characterization, properties and oxidation stabilities of biodiesel, high-rate anaerobic digestion, liquid fuels from synthesis gas, metabolic pathways associated with the degradation of fuels, corrosion inhibitors for HRD fuel/seawater mixtures, novel carbonization, and; Low-cost Material for Solar Fuels Production.

3.1 Methane Hydrates

The APRISES 2013 Methane Hydrates activities comprised three subtasks: Hydrate Energy, Environmental Impacts of Methane Release from Hydrates, and International Collaborative R&D.

Objectives

National R&D programs on methane hydrates were initiated in Japan and India in the mid-1990's with the goal of commercial gas production within a 20 year time horizon. The U.S. established its own program in May 2000. The Methane Hydrate Research and Development Act of 2000 (Public Law 106-193) included seven technical areas of focus: (1) identification, exploration, assessment, and development of methane hydrate as a source of energy; (2) technology development for efficient and environmentally sound recovery of methane from hydrates; (3) transport and storage of methane produced from methane hydrates; (4) education and training related to methane hydrate resource R&D; (5) assessment and mitigation of environmental impacts of natural and purposeful hydrate degassing; (6) development of technologies to reduce the risks of drilling through methane hydrates; and (7) support of exploratory drilling projects. The objectives of the Methane Hydrates Task of the APRISES initiative reflect most of the priorities of P.L. 106-193, but emphasize those areas of particular relevance to the ONR and which are consistent with the overall goals of APRISES. Specifically, the development of hydrates and related sources of seafloor methane as logistical fuels for Naval applications, and related marine environmental issues, have been the principal areas of interest; exploratory drilling projects and seafloor stability/safety have received limited attention. Work also was performed to explore engineering applications of hydrates such as hydrogen fuel storage. Task objectives were devised to leverage fully the hydrate R&D expertise and infrastructure that had been developed at HNEI during previous research programs on CO₂ ocean sequestration and deep oil spills.

During the present reporting period, the goals of the APRISES Methane Hydrates Task were to:

- Pursue development of methods to recover methane gas from hydrates.
- Investigate environmental impacts of methane hydrates on the marine environment.
- Promote international collaborative research on methane hydrates.

Specific technical initiatives that were pursued to attain the above goals included:

- Continue laboratory experiments on hydrate destabilization using chemical inhibitors.
- Initiate studies to investigate the hydrate self-preservation phenomena.
- Investigate the mechanisms of microbial methane metabolism in ocean sediment.
- Develop and test facilities to assess the behavior of methane gas leakage from seafloor hydrates in the deep ocean.
- Organize the 9th International Workshop of Methane Hydrate R&D.

Scope of Work and Approach

Work on the Methane Hydrates Task focused on the three primary areas and is described below.

Hydrate Energy

Practicable and environmentally acceptable methods to destabilize hydrate reservoirs in seafloor sediments and arctic permafrost must be developed in order to release and collect the methane gas for energy applications. Hydrate destabilization strategies also are of critical importance to the operation of natural gas transport pipelines, which are vulnerable to blockage by solid hydrate plugs. Under prior ONR awards, significant progress was made by HNEI in elucidating the mechanisms by which various chemical reagents destabilize pure methane hydrate. Technical articles detailing these results have been published in the archival literature, and topics that warrant additional study have been identified.

For APRISES FY13, the priorities of this subtask focused on two critical areas of practical importance to fuel gas production from hydrate reservoirs and flow assurance: 1) the hydrate self-preservation phenomenon that has been observed during pore pressure reduction in sediment reservoirs; and 2) chemical decomposition of hydrates.

Methane hydrates have been observed to exist in a metastable state at significantly higher temperatures and lower pressures than expected based on their thermodynamic stability curves. This “self-preservation” phenomenon has both positive and negative practical implications. Production of methane gas from hydrate deposits by pore pressure reduction or application of thermal energy or chemicals will obviously be hindered, while methane transport as solid hydrate pellets will benefit. Self-preservation also may reduce the rate of release of methane from deposits in the deep ocean sediment and permafrost due to global warming or drilling events. To date, there are almost no reports of calorimetric studies of the self-preservation effect. Toward this end, we have developed a strategy that leverages our novel Raman calorimeter facility to study the energetics of this important phenomenon.

We previously have conducted experimental investigations of the effects of various chemical reagents, including ethanol, methanol, 2-propanol, ethylene glycol (Kinoshita, 2008), and a number of transition metal salts found in seawater (Sylva *et al.* 2016), on methane hydrate stability.

Under the APRISES FY13 grant, we extended these investigations to examine aqueous solutions of glycerol. Glycerol is non-toxic and environmentally benign. It is a triol and has three hydroxyl groups which we have posited is a primary factor in promoting hydrate destabilization by tying up free water at the surface of the solid hydrate phase and disrupting the dynamic equilibrium between hydrate formation and decomposition (Kinoshita, 2008; Nihous *et al.* 2009). The aforementioned alcohols and ethylene glycol have one and two hydroxyl groups, respectively.

Environmental Impacts of Methane Release from Hydrates

The primary goal of this activity is to elucidate the mechanisms by which microbes control free methane gas levels in, and methane leakage from, the seafloor sediment and arctic permafrost; and to better understand the generation of methane in the water column. While this goal is directly relevant to methane fuel production from naturally-occurring accumulations of hydrates, the results are also important to assessments of the environmental impacts of deep ocean oil spills--like the 2010 Deepwater Horizon incident--and marine and terrestrial waste disposal (e.g., near-shore organic runoff and deposition; dumping of dredged material; landfills).

A secondary goal of the proposed activity is to explore the effect of hydrate formation on mass transfer from natural gas bubbles in the deep ocean. Hydrate formation on the surface of natural gas or methane bubbles released from the seafloor, either naturally or as a result of a spill or disposal event, may affect the dissolution and distribution of this contaminant in the water column.

In cooperation with the marine biogeochemistry group at NRL, we have collected sediment, pore water, and water column samples during research cruises in the Gulf of Mexico, off the North Slope of Alaska, and off New Zealand. Conventional incubation and culturing of the benthic microbes found in these samples has proven to be very difficult. As part of Task 3.1, HNEI collected and successfully cultured marine microbes found in surface waters around Hawaii that have the potential to metabolize various hydrocarbons. As an alternative to testing benthic microbes, we instead decided to employ these surface microbes as a proxy and investigated their population dynamics in aqueous media enriched with CH₄.

Pressure chambers and the Raman spectrograph developed under previous ONR awards can be utilized to study the effects of hydrate films on the dissolution of bubbles of methane or natural gas mixtures at deep ocean conditions. In order to observe dissolution processes that occur as these buoyant bubbles slowly rise hundreds of meters through the water column from the seafloor, the bubbles can be stabilized in space by a downward flow of chilled seawater within a recirculating vertical water tunnel enclosed in the pressure chambers. Here, the downward drag forces exerted on the bubbles by the flowing water balance the upward buoyancy forces. Shrinkage (dissolution) of the bubbles over time can be monitored through windows in the chambers with an existing close-up digital video system and image analysis software. Raman spectroscopy will be employed in the future to detect hydrate film formation at the gas-water interface.

International Collaborative Research and Development

Pursuant to the goal of promoting international R&D cooperation on methane hydrates, HNEI will provide support for and served as a member of the International Organizing Committee of the International Fiery Ice Workshop on methane hydrates

Technical Accomplishments

The principal technical accomplishments of the APRISES Methane Hydrates Task for each of the components identified above are described in the following sections.

Hydrate Energy

The primary accomplishments of this subtask were: (1) modified and validated the HNEI Raman calorimeter facility and developed a strategy to employ this facility to study hydrate self-preservation phenomena; and (2) continued and extended our experimental investigation of the decomposition of methane hydrates using thermodynamic inhibitors.

Methane Hydrate Self-Preservation

Destabilized (i.e., melting) methane hydrates have been observed to persist for periods of time in a metastable state at significantly higher temperatures and lower pressures than expected based on their thermodynamic stability curves. This “self-preservation” phenomenon usually occurs at conditions below the freezing point of water. It has been proposed that the endothermicity of hydrate decomposition may result in freezing of the produced water which inhibits guest molecule (e.g., methane) transport (Stern *et al.* 2003; Takeya *et al.* 2005; Bai *et al.* 2015).

Hydrate self-preservation is expected to hinder production of fuel methane gas from hydrate deposits by pore pressure reduction or application of thermal energy or chemicals. Although most natural methane hydrate marine reservoirs exist at temperatures above the ice point, local temperature depression can occur during rapid destabilization; permafrost hydrate deposits generally exist at temperatures below the water ice point.

In consideration of the practical importance of the self-preservation phenomenon to hydrate energy systems, we modified our Raman calorimeter in order to simulate conditions that can result in hydrate self-preservation during pore pressure reduction. The modified instrument can now be employed to investigate the energetics of hydrate self-preservation. Pore pressure reduction is the method of choice to destabilize hydrates for industrial-scale production of methane from seafloor reservoirs. This method entails drilling down into the free gas lens that exist below the hydrate stability zone due to the geothermal temperature gradient, and removing the gas. Pressure in the overlying porous matrix that contains the solid hydrate consequently drops, causing the hydrates to decompose.

Conventional differential scanning calorimeters (DSC) allow the user carefully to control sample temperature by means of heating and cooling systems. Provisions generally are not available actively to control pressure in the sample cell. The gas supply/exhaust system of the Setaram BT2.15 DSC that we have been using in our hydrate investigations previously was equipped with two buffer tanks that significantly increase total system (gas) volume to minimize changes in sample pressure due to temperature changes or hydrate formation and decomposition.

To simulate hydrate destabilization by depressurization, gas will be vented from the modified DSC system shown in the schematic diagram in Figure 3.1.1. The rate of depressurization is controlled with a programmable mass flow controller (Omega Engineering model FMA5514A-ST; 0-1 slpm) installed in the sample cell vent line downstream of a pressure regulator. The regulator steps down the high pressure in the cell and maintains a relatively stable inlet pressure to the mass flow controller to ensure proper operation. Sample pressure is monitored and recorded continuously with an inline pressure transducer. By isolating the buffer tank with a shut-off valve (not shown in the Figure), the minimum time to reduce pressure in the sample cell by venting from a maximum safe operating value of about 10 MPa to ambient is slightly in excess of 10 minutes. A wide range of pressure reduction profiles can be achieved with the new programmable system.

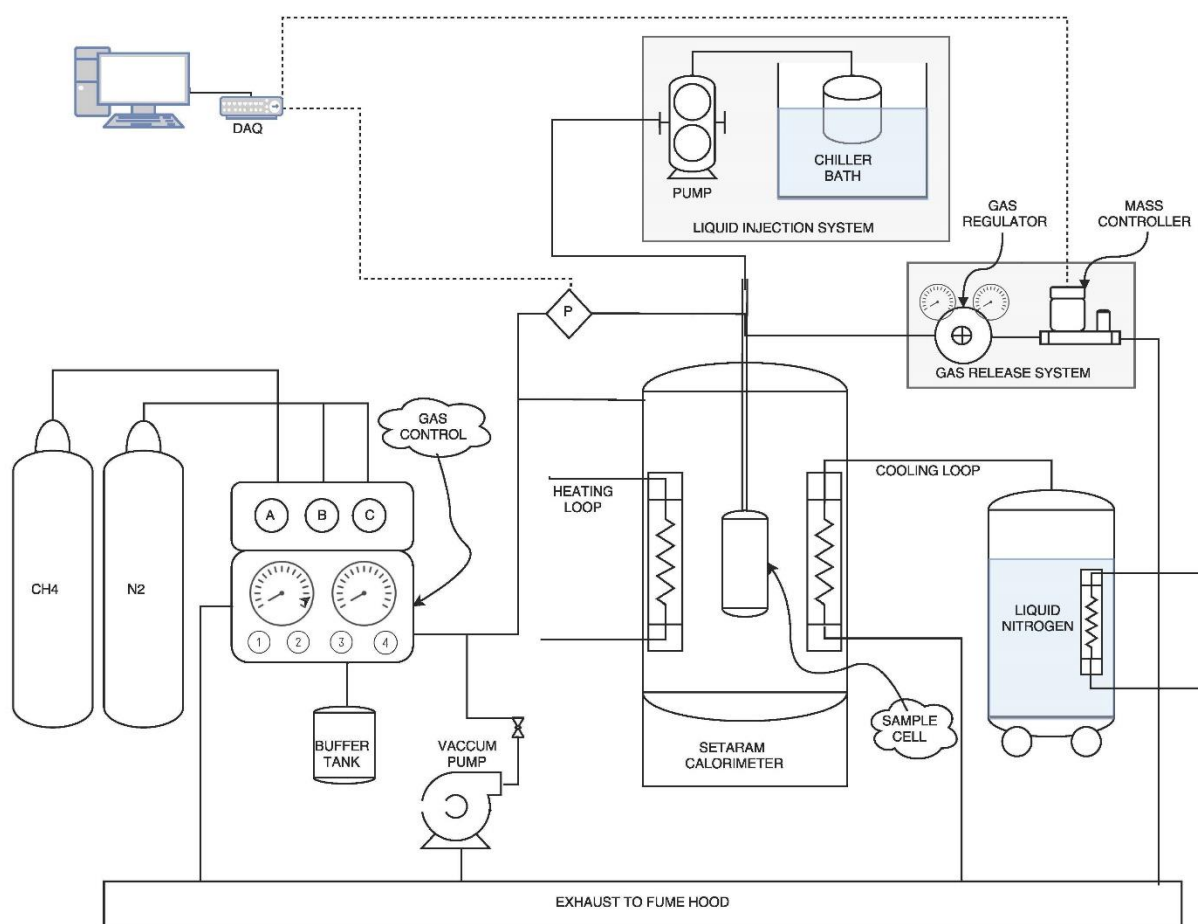


Figure 3.1.1 Schematic diagram of the Setaram BT2.15 DSC after modification of the gas control system to simulate hydrate destabilization by pressure reduction.

During depressurization, the DSC temperature control system could be disabled to avoid heat addition or removal from the sample as it decomposes, to avoid interfering with the freezing of

water produced by hydrate decomposition (which has been proposed as the mechanism of self-preservation). This strategy, however, is not viable, since DSC operation is predicated on monitoring the difference in heat flows between the instrument's heating and cooling systems and the sample and reference cells. Consequently, experiments will be conducted at lower pressures where the hydrate melting temperature is less than the freezing point of water. Hydrate will initially be formed at elevated pressure at temperatures above 0°C. The temperature of the hydrate sample will then be lowered to below 0°C. Pressure will be reduced to a value that corresponds to a selected hydrate melting point between, say, -5°C and -1°C, and the system will be allowed to equilibrate. Thereafter, temperature will be slowly ramped up to slightly below the hydrate melting point at the system pressure and held at that value. Controlled de-pressurization will then occur, causing the hydrate to decompose at constant temperature. Raman spectroscopy will be employed to confirm the presence of residual hydrate at various points during de-pressurization.

Figure 3.1.2 shows an example of a thermogram recorded during a shakedown test of the de-pressurization system. The calorimeter sample cell contained dry N₂ gas at 10 MPa. The calorimeter was set to maintain a constant temperature of about 5°C. Gas was vented using the mass flow controller at a rate of 1 slpm. The purpose of this test was to confirm proper operation of the calorimeter during controlled de-pressurization. The added energy (yellow area in the figure) is needed to compensate for cooling in the cell as the gas expands.

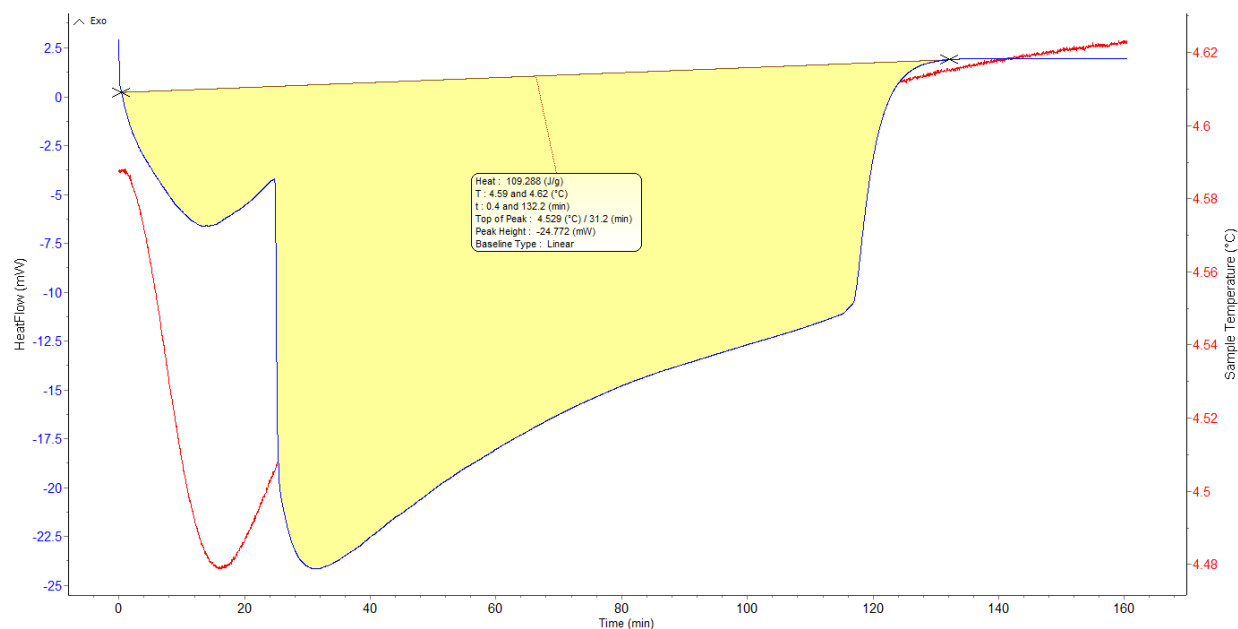


Figure 3.1.2 Calorimeter thermogram during controlled venting (de-pressurization) of the sample cell from 10 MPa to 0.1 MPa at 5°C.

The modified facility has been tested and validated and hydrate self-preservation experiments currently are ongoing.

Reagent Destabilization of Methane Hydrates

Clathrate hydrates can be induced to dissociate (melt) or prevented from forming by application of thermodynamic inhibitors such as alcohols and salts. These inhibitors shift the equilibrium between the three phases, hydrate (H), liquid water (Lw), and guest molecular vapor (V) to lower temperature or higher pressure (Sloan & Koh, 2008). It has been posited that dissolved inhibitors tie up water molecules needed for hydrate formation via hydrogen bonding, as in the case of alcohols and glycols (Nihous *et al.*, 2009), or via Coulombic forces, as in the case of salt ions (Sloan & Koh, 2008).

Alcohols are frequently employed by the oil industry to avoid hydrate blockages in natural gas pipelines since the potential for undesirable side reactions (such as corrosion) is low relative to salts; however, amounts needed may reach 50 wt% (aq), leading to high costs and disposal problems (Kelland, 1994; Dholabhai *et al.*, 1997). Moreover, the fundamental mechanism of action of alcohols on hydrate stability remains unclear (Kinoshita, 2008; Nihous *et al.*, 2009).

In an earlier investigation conducted by HNEI (Kinoshita, 2008), laboratory experiments were performed to quantify the effectiveness of four common thermodynamic hydrate inhibitors that included three alcohols and one diol: 1) methanol (CH_3OH); 2) ethanol ($\text{C}_2\text{H}_5\text{OH}$); 3) 2-propanol (isopropyl alcohol, $\text{C}_3\text{H}_7\text{OH}$); and 4) ethylene glycol ($\text{C}_2\text{H}_4(\text{OH})_2$). The alcohols are characterized by a single hydroxyl (OH) group, while the diol has two.

Methane hydrate samples in a modified high-pressure gas circulation cell in a Calvet-Tien calorimeter were decomposed by injection of a fixed amount of an inhibitor at constant temperature and pressure. The amount of hydrate that decomposed per mole of inhibitor was inferred from the calorimeter thermograms by comparing the amount of heat absorbed with the heat of formation of the hydrate. Differences in the molecular structure of the inhibitors were then considered to explain the results.

Results of experiments conducted at -5°C and 6.89 MPa indicated that, on a per mole basis, ethylene glycol disassociates the most hydrate, followed in order by methanol, ethanol, and then 2-propanol. Based on these experimental data and mobile order thermodynamics calculations, it was posited that thermodynamic inhibitors work by tying up liquid water at the hydrate surface and hence, by disrupting the dynamic equilibrium between hydrate decomposition and formation. The effectiveness of a reagent is believed to depend on the number of hydrogen bonding sites (e.g., hydroxyl groups) and the other structural characteristics such as the size of its alkyl group.

According to the above hypothesis, compounds with additional hydroxyl groups such as triols, tetraols, etc. should be more effective hydrate inhibitors than the simple alcohols and diol tested to date. Unlike simple alcohols and diols, however, polyhydric alcohols with four or more hydroxyl groups exist as solids at room temperature and below. In consideration of this, glycerol ($\text{C}_3\text{H}_5(\text{OH})_3$), a triol, was selected for additional testing to extend the previous results. The melting point of glycerol is approximately 17.8°C . High concentration aqueous solutions of glycerol can be injected to decompose methane hydrate in the calorimeter sample cell. The primary challenge is to account for the effect of the water component of the glycerol solution.

Methods and Materials

Figure 3.1.3 presents a schematic diagram of the setup employed in the experiment. Hydrate samples are formed in a Setaram model BT2.15 II Calvet-Tien calorimeter. Custom top closures for the high pressure calorimeter sample cells were fabricated with a penetration connected to a 6.35 mm (0.25 inch) o.d., 5.0 mm (0.194 inch) i.d. stainless steel tube. This tube encloses a 3.18 mm (0.125 inch) o.d. fiberoptic probe to obtain Raman spectra of the samples. A 0.79 mm (0.03125 inch) o.d. PEEK tube also is enclosed within the 6.35 mm tube and is employed to inject the glycerol solution into the cell.

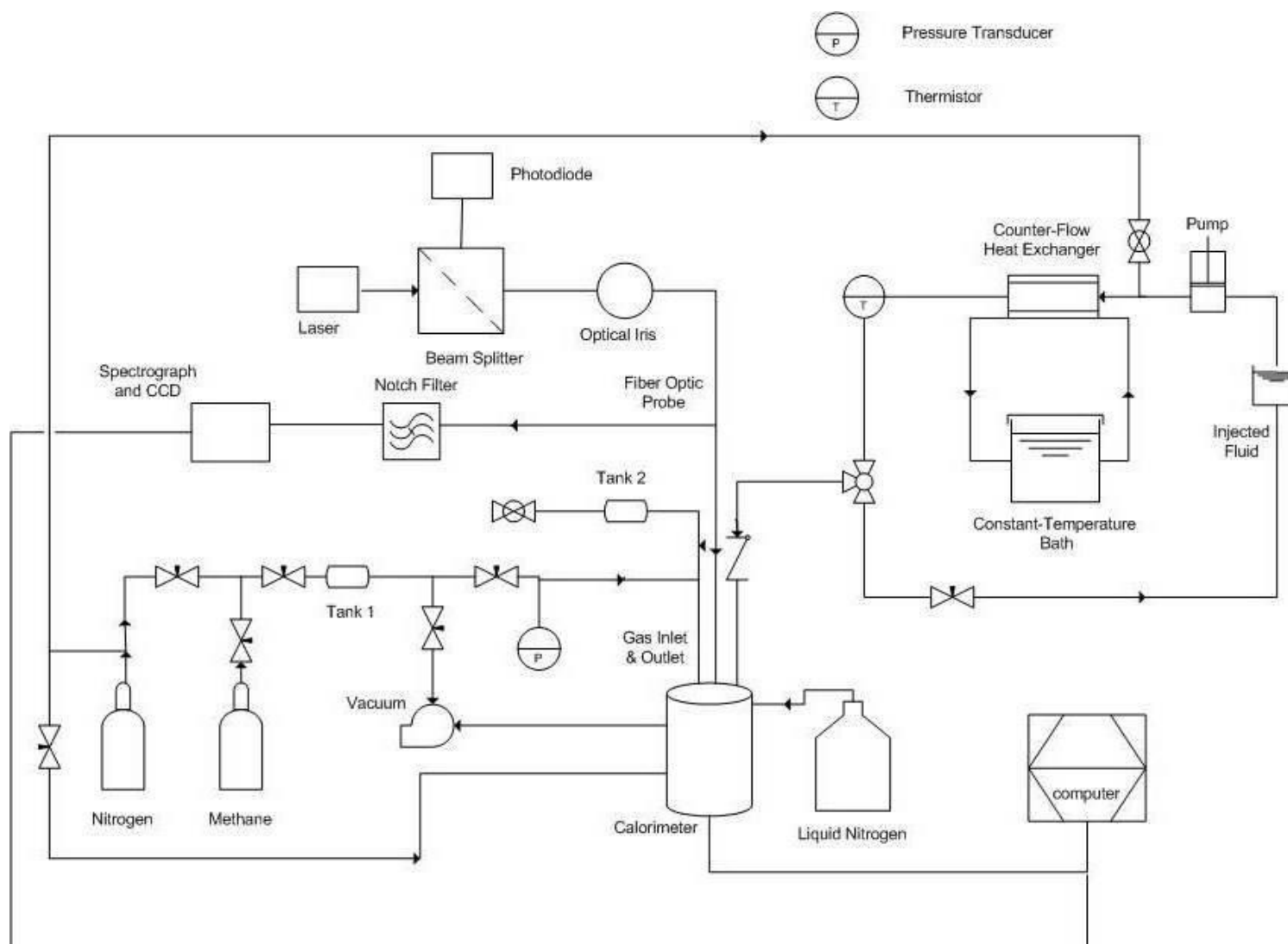


Figure 3.1.3. Schematic diagram of experimental setup to investigate hydrate destabilization using thermodynamic inhibitors.

Glycerol is a solid at temperatures below 17.8°C. Since the pressure required for stable methane hydrate at 17.8°C exceeds the 1500 psig operating limit of the Setaram calorimeter, it was necessary to inject aqueous solutions of glycerol rather than pure reagent. (In our previous investigation, pure liquid, methanol, ethanol, 2-propanol, and ethylene glycol were injected to induce hydrate destabilization.) As seen in Figure 3.1.4, the freezing points of glycerol-water solutions can be much lower than pure glycerol.

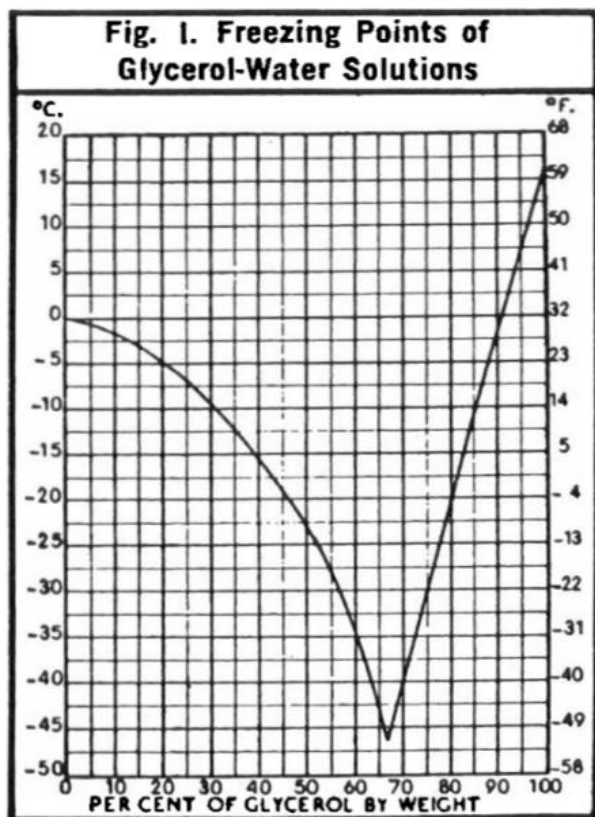


Figure 3.1.4 Freezing point of glycerol-water solution at 1 atm. as a function of w% glycerol (from http://www.aciscience.org/docs/physical_properties_of_glycerine_and_its_solutions.pdf “Physical Properties of Glycerine and its Solutions”).

The glycerol solution is stored in a closed flask in a water bath and circulated through a heat exchanger using an Eldex high pressure liquid metering pump before being routed into the sample cell. The heat exchanger was employed to try to match the temperature of the inhibitor to that of the hydrate sample in order to avoid hydrate decomposition driven by thermal effects.

Hydrate samples in the calorimeter cells are maintained under an atmosphere comprising high pressure methane gas (99.99% purity). Injection of the liquid inhibitor displaces and compresses the gas. In order to prevent any significant changes in pressure which may affect hydrate stability, the calorimeter gas supply system was equipped with two buffer tanks that increase total system volume to the extent that the small amount of liquid inhibitor added results in minimal

compression. A transducer interfaced to our data acquisition system continuously monitors pressure in the sample cell. Maximum pressure perturbations were $< 1\%$. The N_2 cylinder (99.99%) and vacuum pump in the schematic are used to purge the system between experiments.

During experiments, the calorimeter is purged of atmospheric air using a vacuum pump and dry nitrogen gas. After purging, it is cooled using liquid N_2 . Following a protocol for methane hydrate synthesis similar to one developed previously by Kinoshita (2008), distilled deionized water was sprayed into a liquid N_2 bath to generate fine ice crystals. Crystals smaller than about $200\ \mu m$ were collected, weighed, and loaded into a sample cell. The assembled cell was then inserted into the cold calorimeter test well, purged with N_2 , and pressurized slowly with methane.

When the pressure in the cell reached 10.4 MPa (1500 psig), the temperature of the calorimeter was held at $-5^\circ C$ and allowed to equilibrate. Once the calorimeter reached steady-state, the sample temperature was increased from $-5^\circ C$ to $-1^\circ C$ at a rate of $0.1^\circ C/min$. The temperature ramp rate was then decreased to $0.01^\circ C/min$ and the sample temperature rose slowly to $5^\circ C$ over a period of about 10 hours. During this time, the ice phase melted and methane hydrate formed. The glycerol solution was subsequently injected with the sample temperature held constant at $5^\circ C$.

Results and Discussion

Figure 3.1.5 presents a thermogram of the first 20 hours of the experiment. The measured sample temperature history is shown in red. The blue curve is the heat flow into or out of the cell. The portions of the heat flow curve corresponding to ice melting and hydrate formation are indicated in the Figure. Since, at 10.4 MPa, methane hydrate is stable at temperatures below about $15^\circ C$, hydrate formation occurs concurrently while the ice phase is melting. The point in the thermogram when heat flow becomes positive (i.e., exothermic from the sample) simply indicates that energy released by hydrate formation has begun to exceed the amount of energy absorbed by the melting ice in the cell.

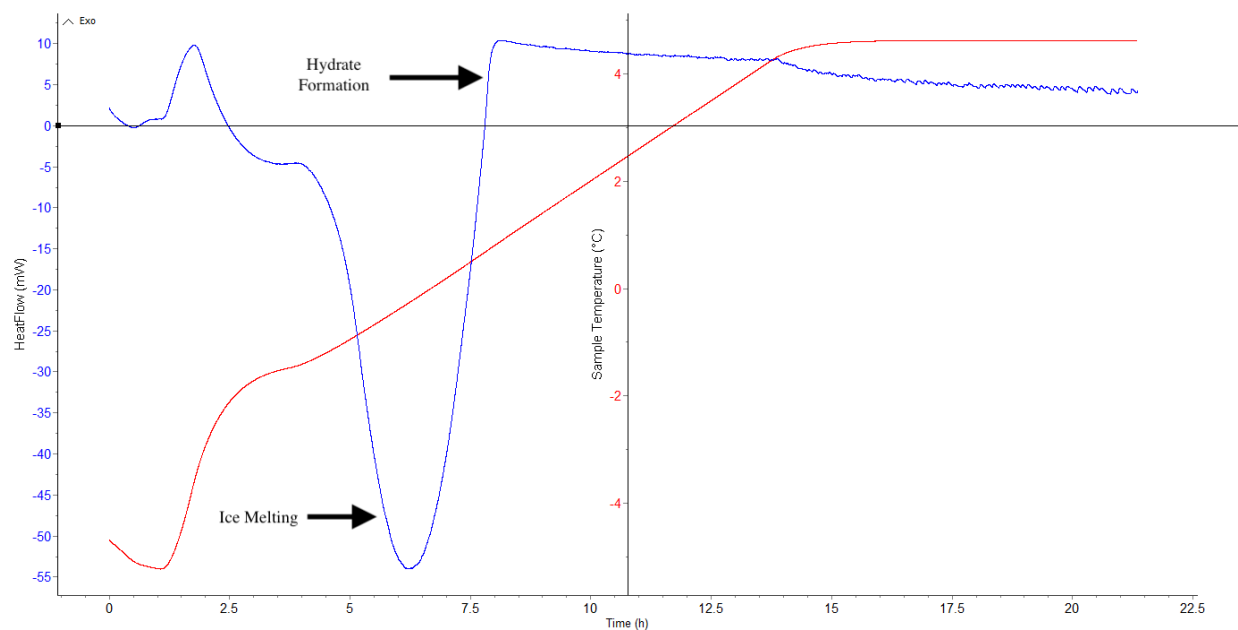


Figure 3.1.5 Calorimeter thermogram of methane hydrate synthesis at 10.4 MPa.

Figure 3.1.6 presents a representative thermogram of the glycerol injection. The results correspond to a case where equal masses of glycerol and distilled water were mixed to form a 50 w% solution, which corresponds to a glycerol mole fraction of 0.1636. This concentration was selected to facilitate pumping of the solution through the small PEEK tubing. The viscosity of the mixture increases rapidly with glycerol concentration.

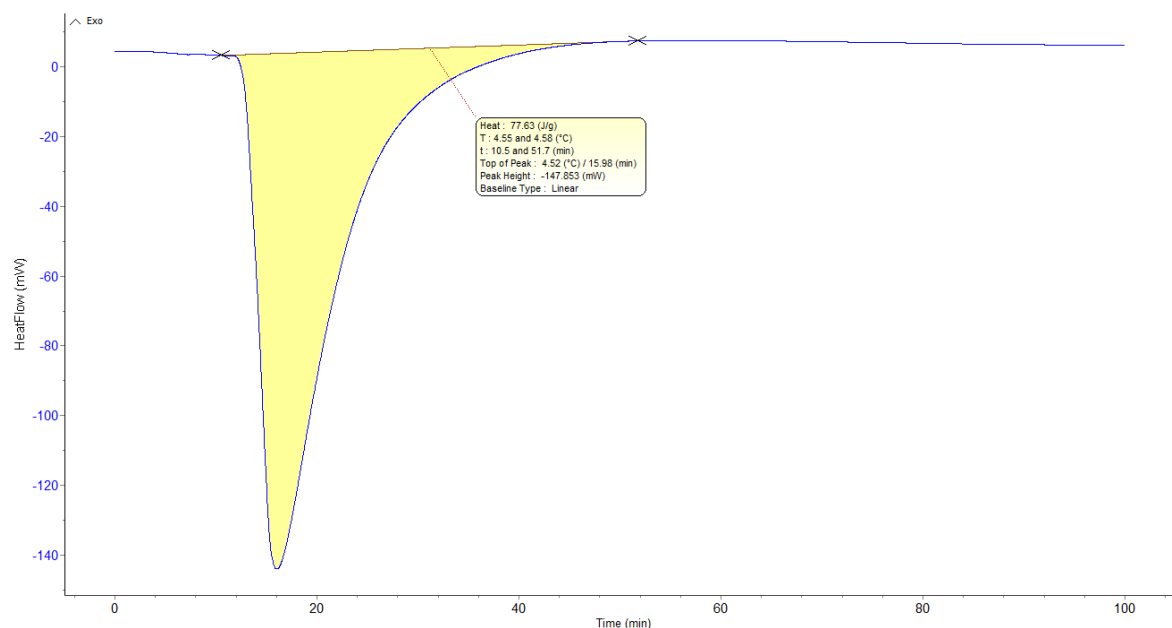


Figure 3.1.6 Calorimeter thermogram of injection of 50 w% glycerol-water solution onto methane hydrates at 10.4 MPa and 5°C.

The solution was injected at the 10 minute point in the Figure and the sample was monitored for approximately one hour post injection. The total mass of the injected glycerol solution was 1.15 g, which corresponds to 0.00624 moles of glycerol. The negative value of heat flow indicates that the processes occurring in the sample cell were endothermic overall, indicating melting of the hydrate phase.

The overall heat flow measured by the calorimeter is expected to comprise three primary components: 1) heat absorbed by the hydrate as it dissociates; 2) the enthalpy of solution due mixing of the glycerol solution with produced water from the melting hydrates; and 3) sensible heat associated with any difference in the temperature of the injected glycerol solution and calorimeter setpoint temperature (5°C). The enthalpy of solution and sensible heat components were estimated using data from the literature shown in Figures 3.1.7 and 3.1.8. Due to the small amount of produced water relative to the amount present in the 50 w% glycerol solution, the enthalpy of solution component was not significant in this test. It was determined, however, that the sensible heat contribution was not negligible. Although the glycerol solution was cooled to about -5°C in the bath and heat exchanger, substantial warming apparently occurred in the injection lines upstream of the sample cell. Solutions to this problem are being explored.

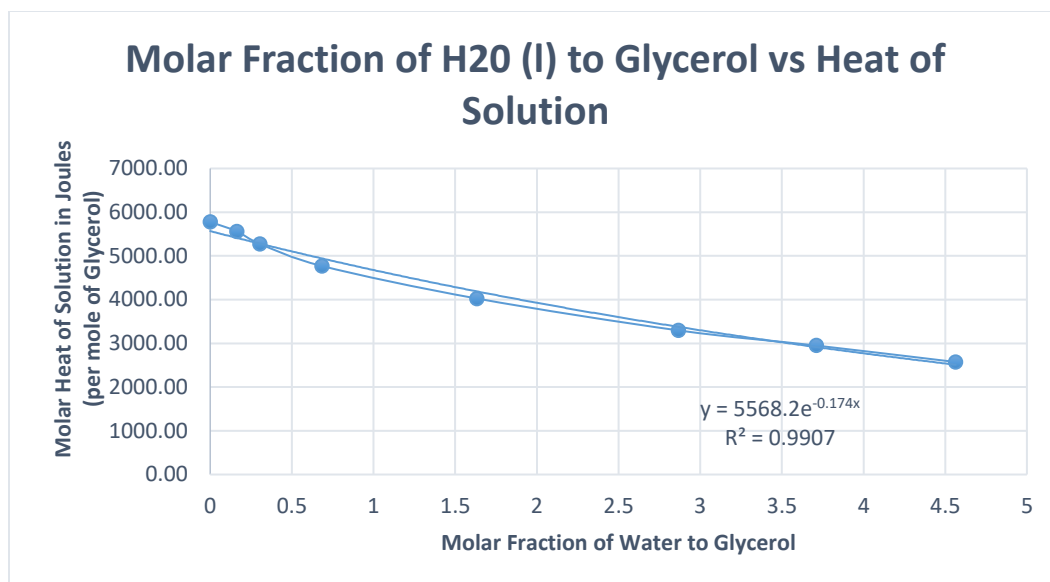


Figure 3.1.7 Heat of solution of glycerol and water at 1 atmosphere pressure (data from http://www.aciscience.org/docs/physical_properties_of_glycerine_and_its_solutions.pdf “Physical Properties of Glycerine and its Solutions”).

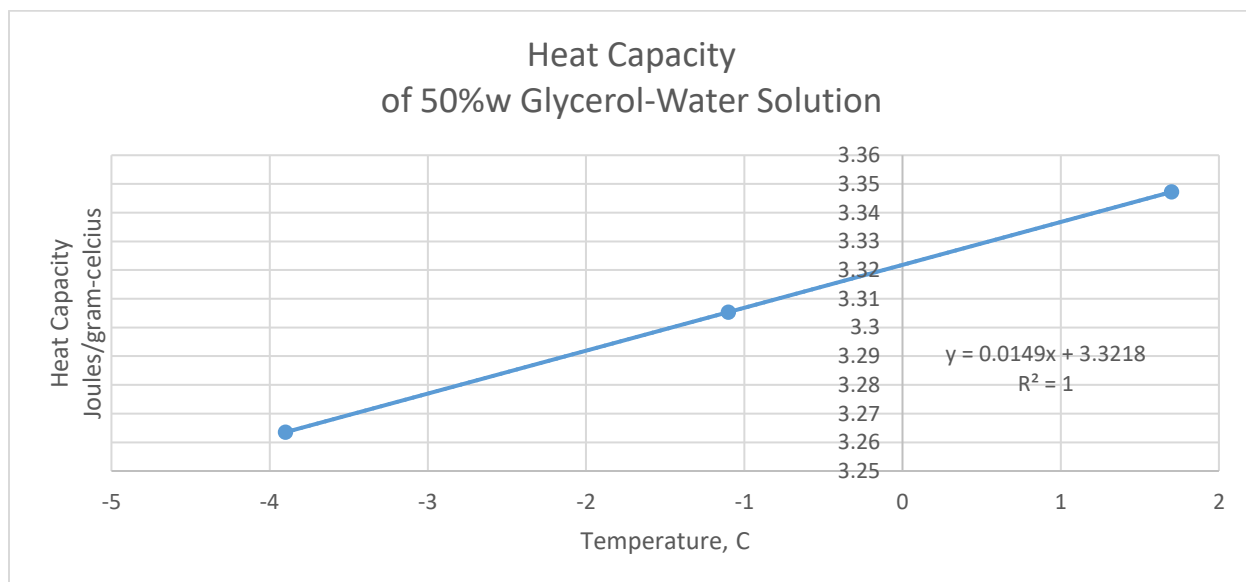


Figure 3.1.8 Heat capacity of glycerol-water solutions at 1 atmosphere pressure (data from http://www.aciscience.org/docs/physical_properties_of_glycerine_and_its_solutions.pdf “Physical Properties of Glycerine and its Solutions”).

After accounting for the heat of solution and sensible heat addition portions of the total energy transferred to the sample obtained by integrating the thermogram (i.e., the yellow area in Figure 3.1.6), it was possible to estimate the number of moles of methane hydrate dissociated by the

injected glycerol. This calculation requires a value for the molar heat of dissociation of hydrate. Reported values in the technical literature vary widely, between around 15 kJ/mol to 55 kJ/mol (Rueff *et al.* 1988; Ota *et al.* 2005; Avlonitis, 2005; Li *et al.* 2007). Table 3.1.1 presents the results for the data presented in Figure 3.1.6. The number of moles and corresponding mass of hydrate dissolved by the glycerol solution are provided for four different values of molar heat of dissociation. Even when employing the lowest value of molar heat of dissociation from the literature (which yields the largest number of moles of hydrate dissolved), the effectiveness of the glycerol solution, in terms of moles of hydrate dissolved per mole of glycerol is low relative to the previously tested alcohols and diol (Kinoshita 2008). In that study, effectiveness ranged from about 0.1 to 0.9 based on a hydrate heat of dissociation, of 54.5 kJ/mol. 2-propanol was the least effective and ethylene glycol dissociated the most hydrate per mole.

Table 3.1.1. Hydrate dissociation by 50 w% solution of glycerol.

Heat of Dissociation (Joules/mole)	Moles of hydrates	Mass of hydrates (g)	Effectiveness (mol hydrate/mol glycerol)
14,500 (Rueff)	0.0029	0.3411	0.46
17,530 (Avlonitis)	0.0024	0.2865	0.38
28,800 (Li)	0.0015	0.1786	0.24
54,490 (Ota)	0.0008	0.0955	0.13

A possible explanation for the relatively poor performance of glycerol as a hydrate inhibitor may be that, while the three alcohols and diol were injected as pure substances in our earlier study, glycerol was injected as a relatively dilute aqueous solution due to its high freezing point. Kinoshita (2008) posited that alcohols and related compounds are effective inhibitors since their hydroxyl groups tie up water produced when the hydrate phase is destabilized and thereby disrupt the dynamic equilibrium between hydrate dissociation and formation. The presence of additional free water in the 50 w% glycerol solution (which corresponds to approximately five molecules of H₂O for each molecule of glycerol) may significantly reduce its capacity to tie up produced water. Additional experiments are being planned to test this assertion by injecting different glycerol-water solutions and solutions of ethanol and glycerol.

Environmental Impacts of Methane Release from Seafloor Hydrates

Technical accomplishments of this subtask included: (1) collected and cultured microbial communities from shallow sediments rich in organic matter (where methanotrophic and methanogenic activity is expected to occur) and investigated the response of these communities to

elevated levels of methane gas; and (2) completed fabrication and validation testing of a novel laboratory facility to study the effects of hydrate formation on rising buoyant methane and natural gas bubbles in the deep ocean.

Effects of Elevated Methane Levels on Mixed Communities of Methanogens and Methanotrophs

An *in situ* exploratory investigation of the effects of elevated methane levels on microbial communities in both sediment and overlying water was completed. The results from this study are relevant to understanding impacts of methane leakage from hydrate reservoirs on the population dynamics of these communities, particularly in the water column.

Sediment and water samples were collected from a brackish water environment having a mostly seawater composition as a result of semi-diurnal tidal flushing. The location is impacted by terrestrial run-off and exists adjacent to a major roadway. An area within this waterway with a sediment deposition thickness of approximately 25 cm was targeted for sampling, since a preliminary examination of the sediment suggested significant methanogenic activity. The presence of methanogenic archaea subsequently was determined using a short fragment length PCR analysis (ARCH349F and bacteria 519R Primers) described by Turner *et al.* (1999) and Takai & Hirikoshi (2000).

Nearly 2.5 kg of sediment was collected along with 4 L of the overlying water. The sediment and water samples were then transferred into a 9.5 L Pyrex bottle (18.7 cm X 47.0 cm) shown in Figure 3.1.9 and allowed to equilibrate for 72 hours before the addition of methane. Approximately 3×10^3 cells/mL were estimated in the initial water sample through direct heterotrophic cell counts using marine agar. The biological communities were then enriched with methane gas that was bubbled into the bottom of the sediment at an rate of about 16.5 cm³/hr. The Pyrex bottle was loosely covered to permit atmospheric gas exchange. DNA was extracted from both the sediment and water samples after 3, 6, 10, and 14 days of incubation. Sampling points in the sediment were located 0 cm, 6 cm, and 13 cm below the sediment-water interface. Collected DNA was verified before sequencing by PCR using 16S and Archaea primers designed for metagenomic sequencing as shown in Figure 3.1.10 (Klindworth *et al.*, 2012). The collected DNA samples were then sent out for Illumina sequencing by the University of Hawaii's Advanced Studies in Genomics, Proteomics and Bioinformatics group (<http://www.hawaii.edu/microbiology/asgpb/>). Biome analysis was performed using Geneious 10.2.3 software (<https://www.geneious.com/>).



Figure 3.1.9 Pyrex bottle used to incubate samples. Sediment depth was 13.1 cm; 4 liters of water.

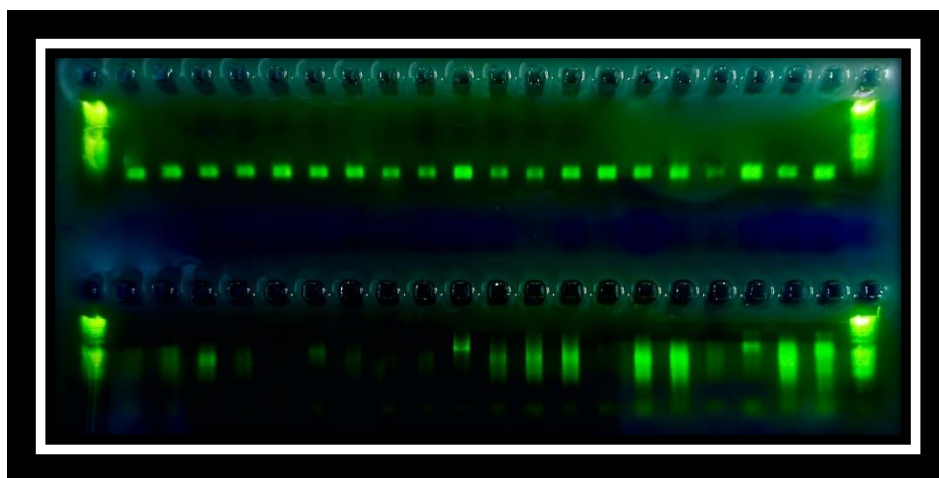


Figure 3.1.10 Rows 1 and 22 1kb DNA ladder. Top and bottom rows are 16S and *Archaea* amplification, respectively.

The individual Illumina sequenced DNA samples generated between 260,000 and 700,000 reads for both the bacterial 16S (20 samples) and archaea (20 samples) amplifications. The sequencing utilized primers having short reads (<300bp) that targeted conserved regions. With these primers, the next-generation sequencing data can be used to predict general distributions, and benefit from greater total coverage, but are limited in specificity. From the generated read data, 50,000 were selected and analyzed. Population estimates were determined based on numeric changes in methanogenic archaea and methanotrophic bacteria sequenced reads shown in Figure 3.1.11 and Figure 3.1.12.

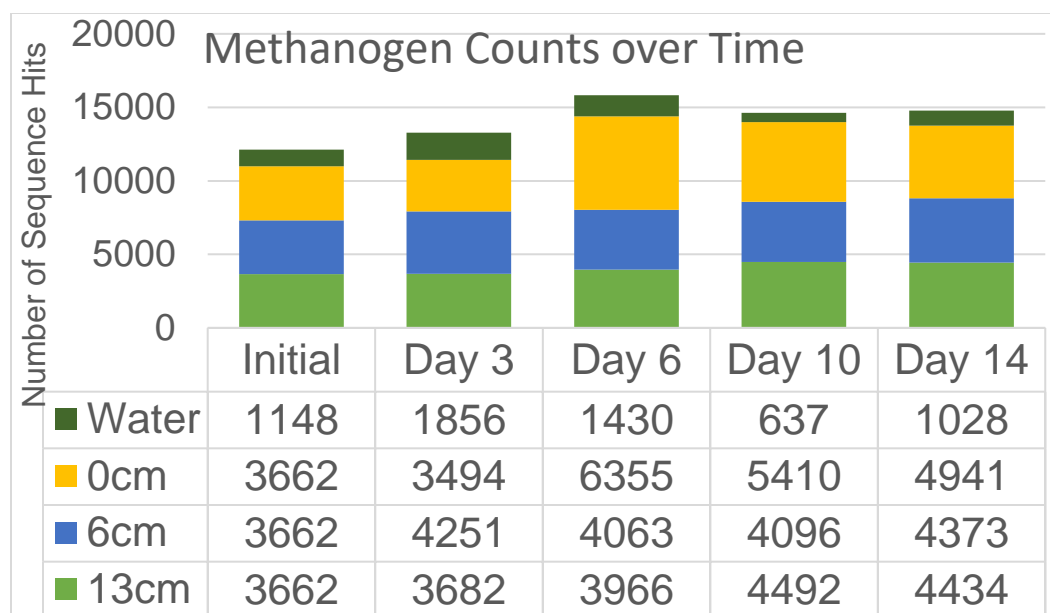


Figure 3.1.11 Counts of methanogens in sediment and water over a 14 day period. Control *Archaea* counts for presence of methanogens in sediment and in water were 4434 and 3670, respectively.

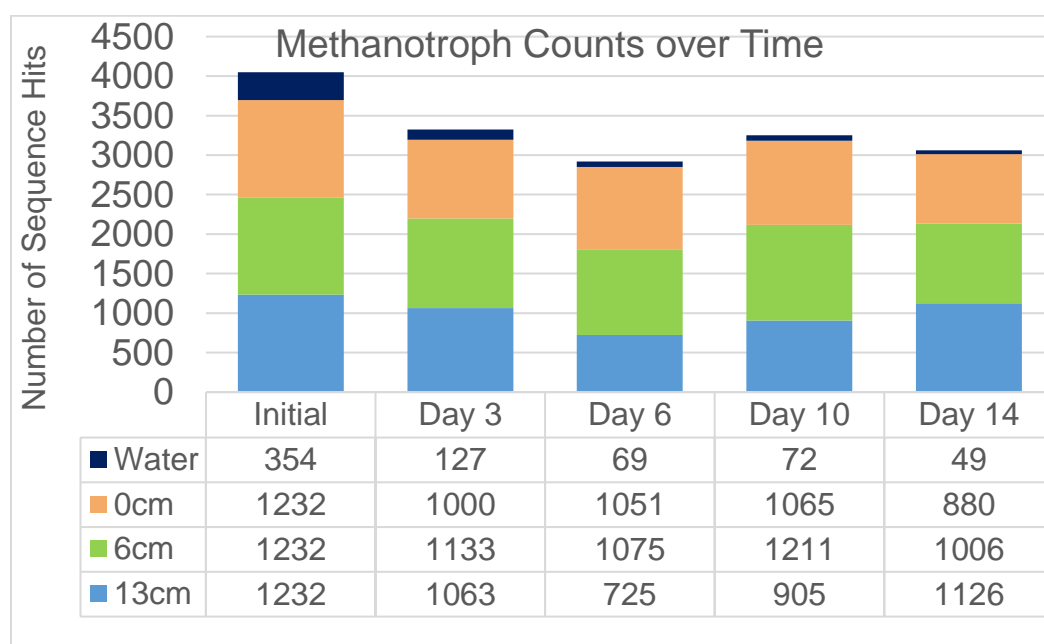


Figure 3.1.12 Counts of methanotrophs in sediment and water over a 14 day period. Control bacterial 16S counts for presence of methanotrophs in sediment and in water were 163 and 848, respectively.

Addition of methane appeared to elicit a small increase in the total number of methanogens and a decrease in the number of methanotrophic bacteria. This behavior was not expected. We posit that this might be due to anoxia. The introduction of methane at relatively high rate into the partially closed incubator would tend to favor anaerobic metabolisms. Anoxic conditions promote sulfate reduction and anaerobic oxidation of the available organic carbon sources, which generates CO₂. CO₂, in turn, supports methanogenic metabolism. The population of methanogenic organisms was observed to increase in the sediment phase and decreased slightly in the water. As seen in Figure 3.1.13, pH measured in both the sediment and water increased over time. These data suggest that the generation of CO₂ may not have been the dominant metabolic mechanism, or that CO₂ was being stripped by the bubbled methane gas.

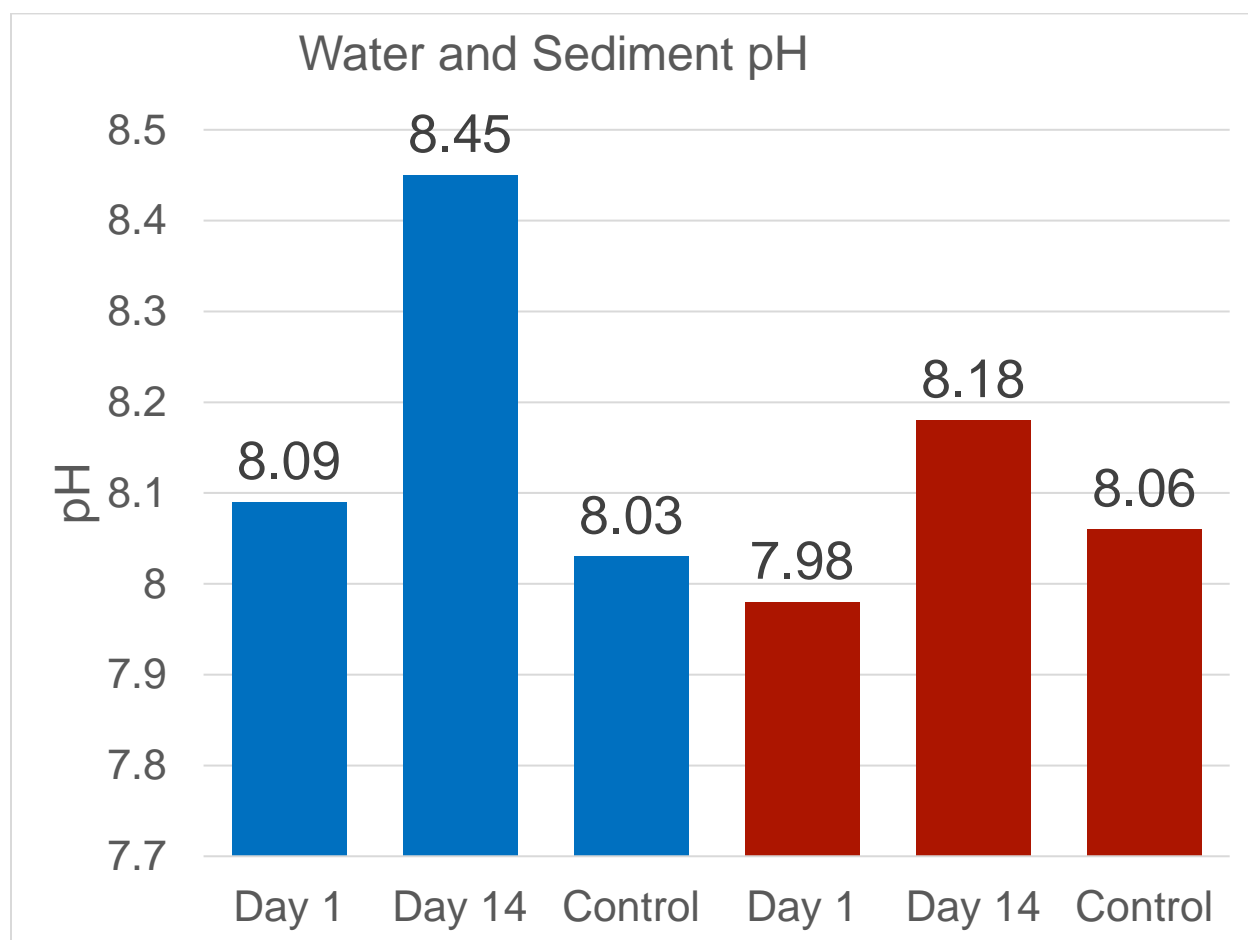
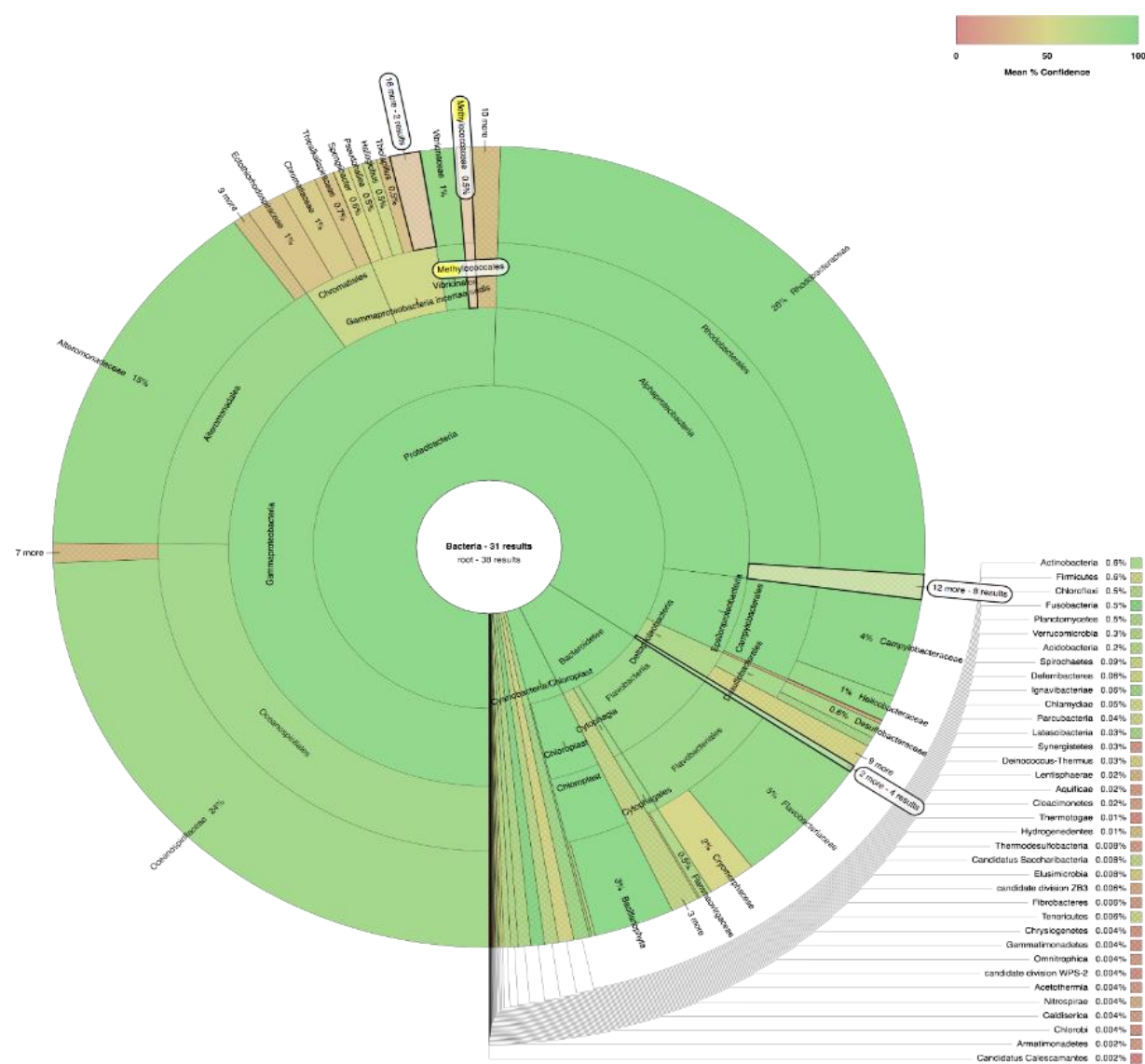


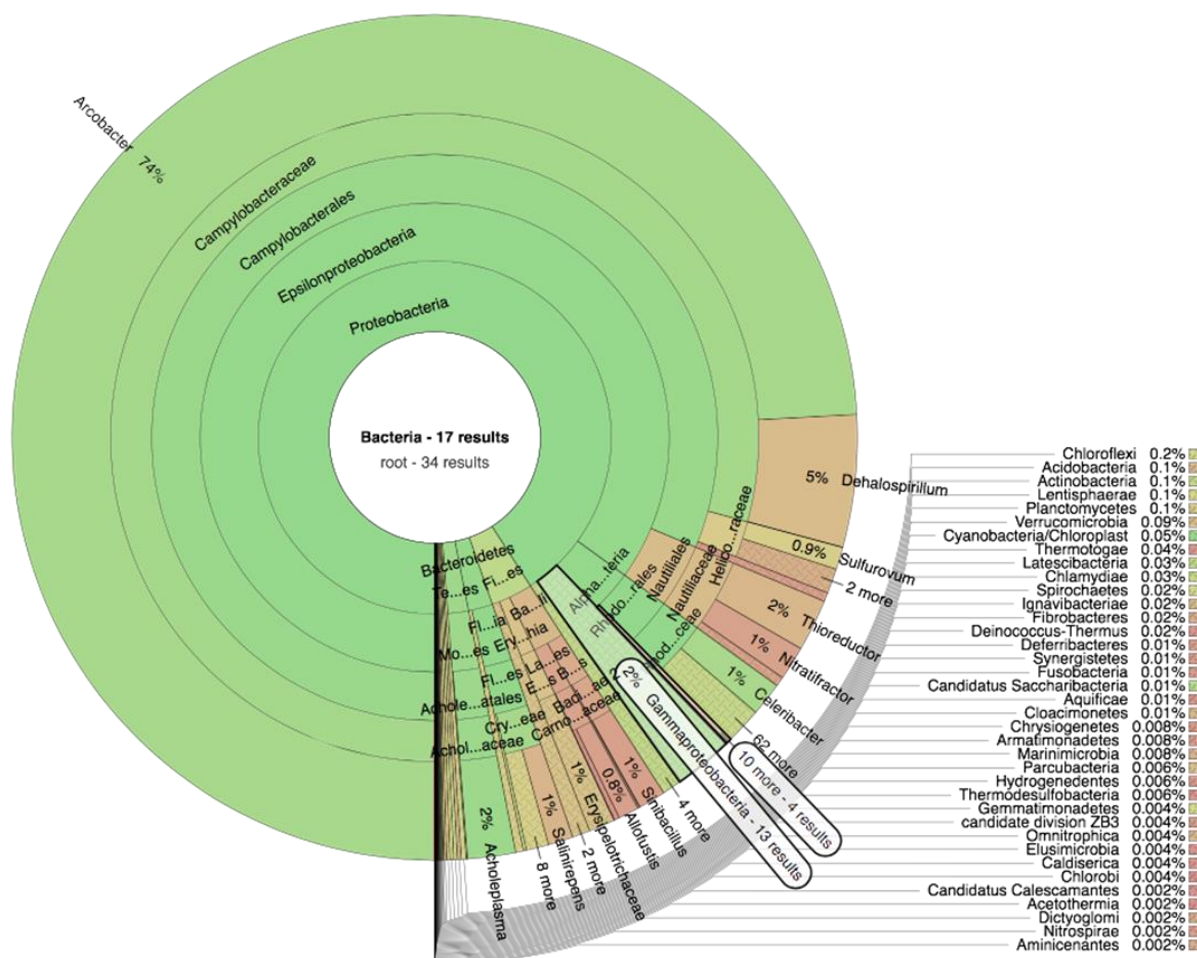
Figure 3.1.13 pH measured in the sediment (red) and overlying water (blue) on Days 1 and 14. pH of the corresponding controls are also included in this figure.

In the water phase, the present results suggest that the addition of methane appears to decrease bacterial diversity at the family and genus levels compared to controls. *Arcobacter* was determined to be dominant and represented 74% of the total population as seen in Fig. 3.1.14. This genus was

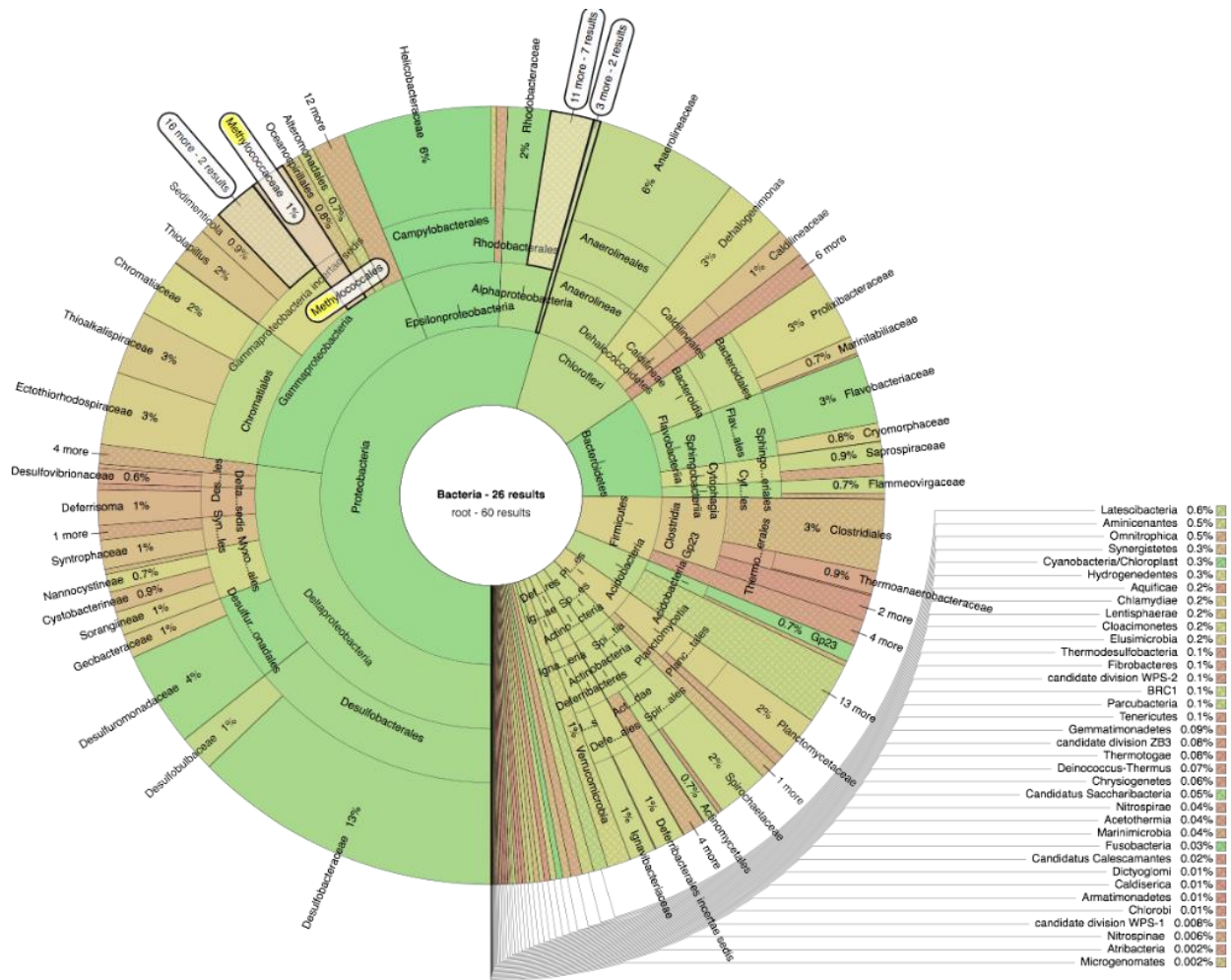
not observed in the original sediment. The composition of Archaea did not exhibit a noticeable change in its distribution shown in Fig. 3.1.15.



(A)

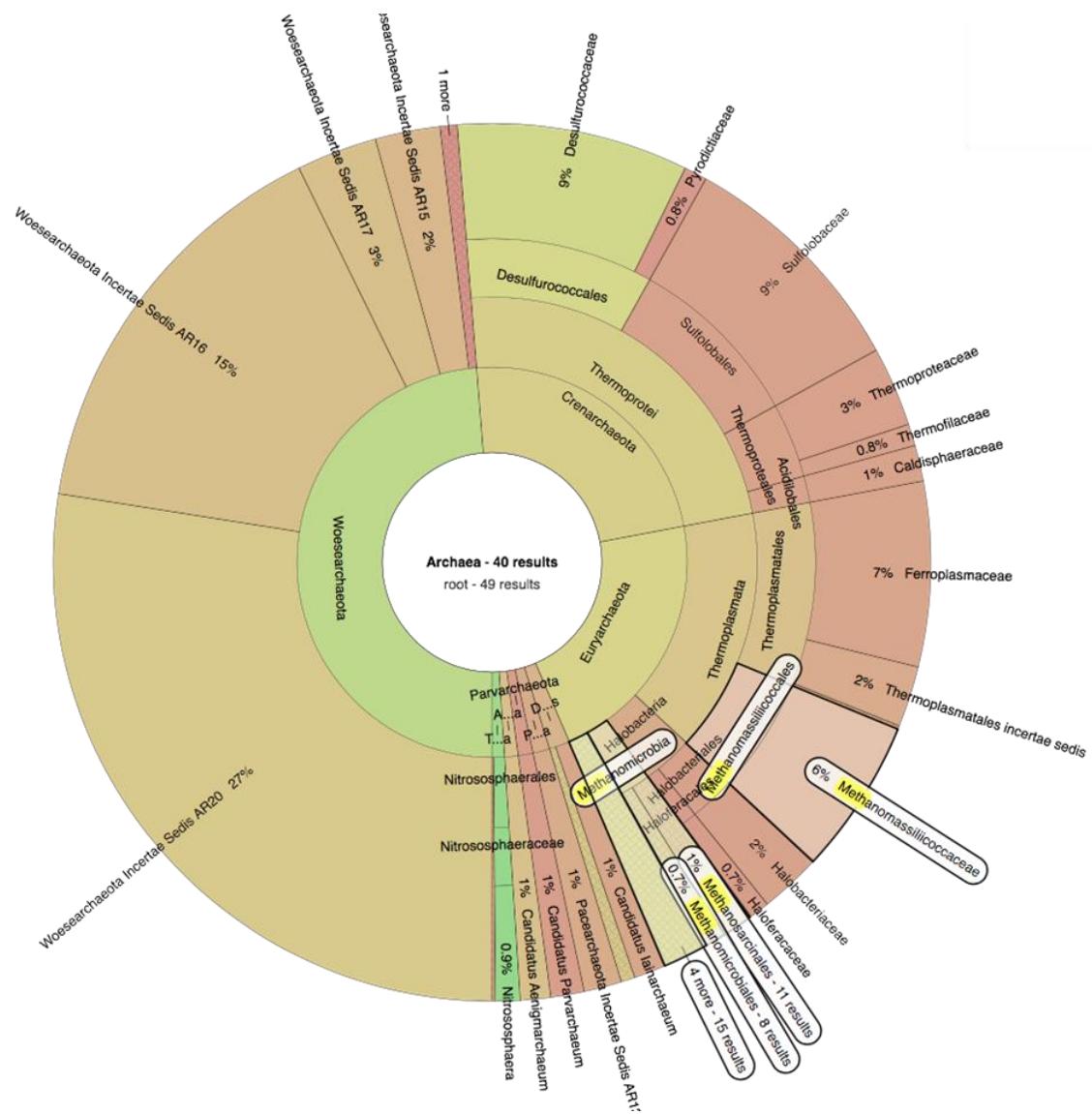


(B)



(C)

Figure 3.1.14 Bacterial 16S and *Archaea* diversity of water samples to the family or genus level. (A) Bacterial 16S, Initial; (B) Bacterial 16S, Final; (C) Bacterial 16S Control, Final.



(B)



While the data from this study are undergoing additional analysis, they appear to have good potential to provide useful insight that can be applied to assess impacts of strong methane flux occurring in marine and estuarine environments. Specifically, the results suggest that, depending on the strength of the flux into the water column, generation of anoxic conditions may elicit a localized reduction of methanotrophic bacteria communities.

As noted in the preceding section, methane gas bubbles released in the deep ocean from natural seafloor seeps or from oil and gas production activities can affect the microbial communities that constitute the foundation of the ocean food web. The extent of local impacts on the marine environment depend on dissolution and transport of the buoyant bubbles; e.g., bubbles that dissolve slowly relative to their vertical rise speed will distribute methane over a wider area in the vertically-stratified deep ocean, resulting in lower concentrations.

In large regions in the ocean, pressures and temperatures fall within the hydrate stability zone and this solid phase can form on methane bubbles at the gas-water interface (Teng *et al.* 1995; Masutani & Adams, 2000). These hydrates films represent a barrier to mass transfer that impedes methane dissolution and also may affect the hydrodynamics of the ascending bubbles (Masutani & Adams, 2000).

Following the approach employed by Maini & Bishnoi (1981) and Masutani & Adams (2000), the ascent of buoyant bubbles over great distances in the oceanic water column can be simulated in a relatively small laboratory facility by stabilizing the bubbles in space with a downward flow of seawater in a water tunnel. The seawater velocity can be adjusted so that the associated drag force on the bubble balances the buoyancy force. The (relatively) stationary bubble experiences similar hydrodynamic forces that would act on a freely rising bubble.

Previously in our laboratory Nagamine (2014) utilized the aforementioned technique in an experimental study to investigate the break-up and dissolution of buoyant droplets of crude oil treated with dispersants. This study was part of a program funded by the Gulf of Mexico Research Initiative in response to the 2010 Deepwater Horizon oil spill. An atmospheric pressure water tunnel was employed, since pressure has only a modest effect on the dissolution of oil in seawater.

Since the flow characteristics of the water tunnel developed by Nagamine (2014) have been well characterized, it was decided to employ that design with minimal modifications in the present Task. The transparent plastic (acrylic and polycarbonate) water tunnel was installed inside available pressure chambers in order to simulate conditions in the ocean down to depths of approximately 1000 m.

A photograph of the main components of the plastic water tunnel is shown in Figure 3.1.16. Figures 3.1.17 and 3.1.18 provide a schematic diagram of the Deep Ocean Simulator (DOS) facility and a photograph of the assembled pressure chamber, respectively.



Figure 3.1.16 Photograph of the water tunnel.

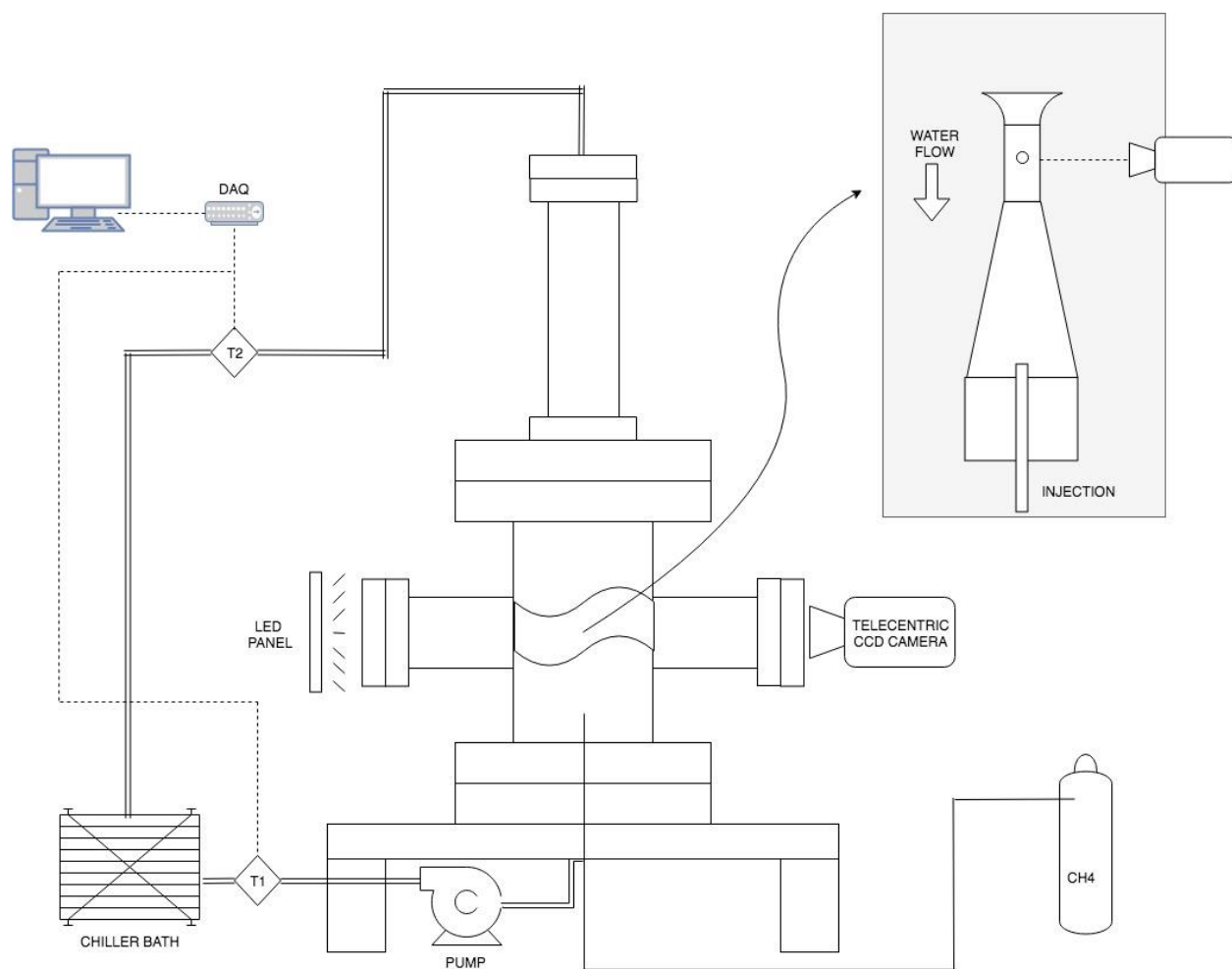


Figure 3.1.17 Schematic diagram of the Deep Ocean Simulator facility.



Figure 3.1.18 Photograph of the pressure chamber.

Synthetic seawater chilled to temperatures representative of the deep ocean is circulated through the pressure chamber via tubing connectors installed in the upper and lower closures (flanges) with a digitally speed-controlled, magnetically coupled gear pump (Micropump model 223/56C; Leeson Micro Series AC Inverter). The insulated stainless steel pressure chamber is completely filled with pressurized synthetic seawater. The transparent water tunnel mounted inside on the centerline of the lower section of the two-part pressure chamber comprises an inlet contraction followed by a cylindrical, 102 mm long, constant area (25.4 mm i.d.) viewing section. A conical diffuser is attached to the exit of the viewing section. The diffuser has a half angle of less than 7.5°, which is small enough to avoid flow separation (Sparrow *et al.* 2009). Streamwise velocity in the diffuser decreases rapidly, by a factor of about 20, as the flow proceeds downward from inlet to outlet. This wide range of velocities allows various sizes of bubbles to remain trapped in the water tunnel (and not be swept away and lost), so that the pump speed can be adjusted periodically to reduce seawater flow velocity as the bubbles dissolve over time.

The cylindrical pressure chamber comprises two sections, each approximately 1 m in length. The 146 mm i.d. upper section serves as a low-velocity, run-in plenum that supplies the water tunnel. The plastic water tunnel is mounted in the 298 mm i.d. lower section that is equipped with a pair of high pressure viewports (J.M. Canty Fuseview Sightglass; approx. 100 mm clear aperture; 10 MPa operating pressure) positioned opposite to one another to allow observation of the bubble dissolution process. Both sections are fabricated from 316 stainless steel in compliance with all applicable ASME pressure vessel codes and are certified for operation at pressures up to 1500 psig (10.44 MPa) between -4°F and 130°F (-20°C and 54°F). Inner surfaces of the chamber are coated with PTFE. As seen in Figure 3.1.18, numerous threadolet penetrations in the walls of the pressure chamber allow for the insertion of measuring probes, including the fiberoptic probe employed in the Setaram DSC to conduct Raman measurements. An injection tube extends vertically into the pressure chamber from a tubing connector installed in the bottom flange. The injector is used to generate gas bubbles by means of a system of pressure concentrators and valves supplied by compressed gas cylinders.

The clear constant area viewing section of the water tunnel is aligned with the two large viewports. Gas bubbles stabilized with the downward flow of seawater are illuminated with an LED panel (Metaphase Technologies model FR-BL) mounted in front of one viewport and are monitored with a telecentric CCD camera (Prosilica GT1920 with Thorlabs 0.128 Bi-telecentric lens) through the opposite viewport. The telecentric camera lens provides constant magnification across the span of the 25.4 mm i.d. viewing section, to avoid errors in estimating changes in size over time of the dissolving bubbles as they transit toward and away from the camera.

Under funding from APRISES FY13, the DOS facility was assembled and tested. Given the relatively high ambient temperatures in the laboratory (typically ~26°C) and the large surface area of the pressure chambers and lines where heat transfer can occur, there was concern regarding the ability to maintain low, stable seawater temperatures that fall within the hydrate stability regime and are representative of deep ocean conditions. Tests confirmed, however, that we are able to maintain water temperature in the pressure chamber at below 7°C for at least one full day.

Figures 3.1.19 and 3.1.20 provide representative images obtained during operation of the DOS facility with the telecentric CCD camera. In this test, bubbles of N_2 gas were captured in the constant area viewing section of the water tunnel. Gas bubbles with diameters between 1 mm and 8 mm have been successfully stabilized and observed for periods of up to 5 hours. The spatial resolution of the imaging system is estimated to be $<50\ \mu\text{m}$. The confirmed range of operating conditions of the facility are:

- pressure: up to 1500 psig (10.4 MPa);
- temperature: 6°C to over 35°C with fresh water (the lower limit reflects practical limitations on subcooling the recirculating water in the chiller bath due to freezing in the lines); est. 3°C to over 35°C with seawater (which freezes at a lower temperature than fresh water);
- bubble size: 1mm to 8mm; smaller or larger bubbles have been difficult to stabilize for extended periods of time.

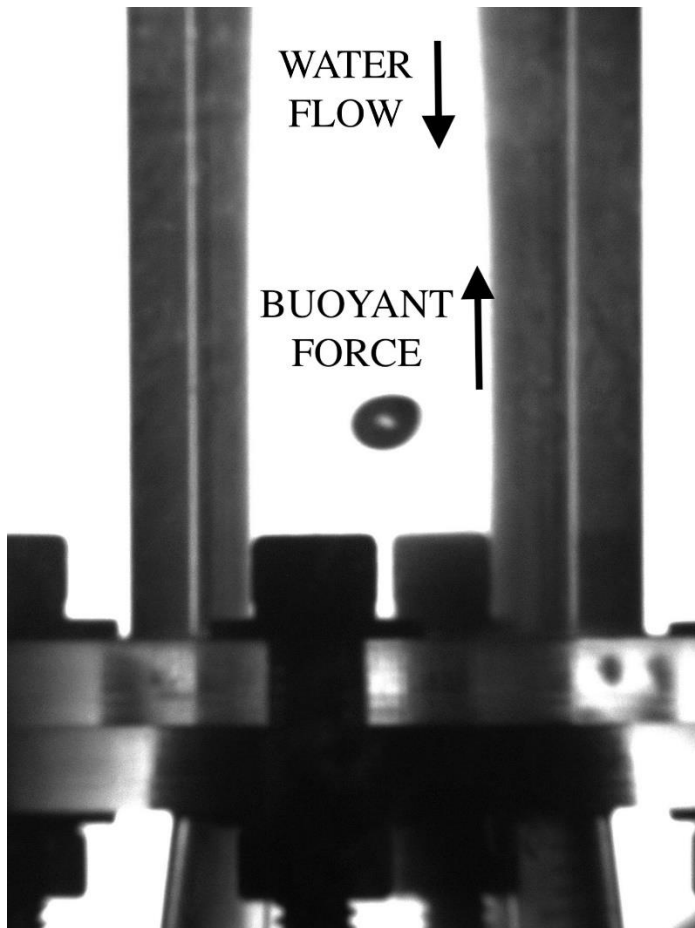


Figure 3.1.19 Image of a 6 mm gas bubble stabilized in the DOS water tunnel.

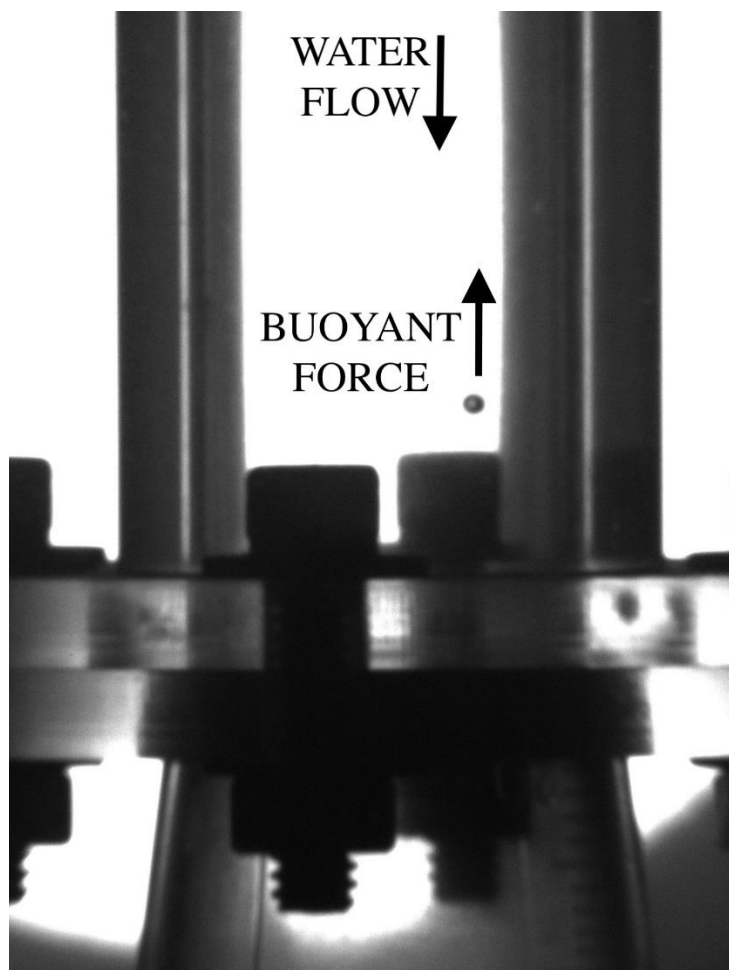


Figure 3.1.20 Image of a 1.3 mm gas bubble stabilized in the DOS water tunnel.

To summarize, fabrication and testing of the DOS facility have been completed. The facility is ready for operation and experimental investigations of the dissolution behavior of buoyant methane droplets under deep ocean conditions have been initiated.

International Collaborative Research and Development

The 9th International Workshop on Methane Hydrate R&D was held in Hyderabad, India on 9-12 November 2014. HNEI served on the organizing committee and as a sponsor for this 9th (and previous) workshops. The 9th Workshop was attended by 106 scientists, engineers, and other stakeholders. The workshop comprised two keynote lectures, 10 national reports, six breakout sessions and 46 individual research presentations consisting of 16 oral and 30 poster presentations. The Final Workshop Report is available online at <http://www.igu.in/19-3/12report.pdf>.

References

1. Avlonitis, D. 2005. An investigation of gas hydrates formation energetics. *AIChE J.*, **51**(4),1258-1273. doi:10.1002/aic.10374.
2. Bai, S., Zhang, D., Zhang, X., and Chen, G. 2015. Origin of self-preservation effect for hydrate decomposition: coupling of mass and heat transfer resistances. *Sci. Rep.*, **5**, article no. 14599. doi:10.1038/srep14599.
3. Dholabhai, P.D., Parent, J.S., Bishnoi, P.R. 1997. Equilibrium conditions for hydrate formation from binary mixtures of methane and carbon dioxide in the presence of electrolytes, methanol and ethylene glycol, *Fluid Phase Equilibria*, **141**, 235-246.
4. Glycerine Producers Association. 1963. Physical properties of glycerine and its solutions. New York, N.Y.
5. Kelland, K., 1994. Natural gas hydrates: Energy for the future. *Marine Pollut. Bull.* **29**: 307–311.
6. Kinoshita, C.K. 2008. An experimental investigation employing combined calorimetry and raman spectroscopy of thermodynamic inhibitors used to decompose methane hydrates. M.S. thesis. University of Hawaii, Honolulu, Hawaii.
7. Klindworth, A., Pruesse, E., Schweer, T., Peplies, J., Quaste, C., Horn, M., and Glockner, F.O. 2013. Evaluation of general 16S ribosomal RNA gene PCR primers for classical and next-generation sequencing-based diversity studies. *Nucleic Acids Res.* **41**(1). doi:10.1093/nar/gks808.
8. Li, X.-S., Xu, C.-G., Zhang, Y., Ruan, X.-K., Li, G., and Wang, Y. 2016. Investigation into gas production from natural gas hydrate: a review. *Appl. Energ.*, **172**, 286-322.
9. Li, Z.Z.; Guo, X.Q.; Chen, G.J.; Wang, J.B.; Yang, L.Y.; Wang, T. 2007. Experimental and kinetic studies on methane replacement from methane hydrate formed in SDS system by using pressurized CO₂. *J. Chem. Ind. Eng.*, **58**, 1197–1203.
10. Maini, B.B., and Bishnoi, P.R. 1981. Experimental investigation of hydrate formation behaviour of a natural gas bubble in a simulated deep sea environment. *Chem. Eng. Sci.*, **36**(1), 183-189.
11. Masutani, S.M., and Adams, E.E. 2000. Experimental study of multi-phase plumes with application to deep ocean spills. Final report to the U.S. Department of the Interior, Minerals Management Service. Contract No. 1435-01-98-CT-30946.
12. Nagamine, S.I. 2014. The effects of chemical dispersants on buoyant oil droplets. M.S. thesis. University of Hawaii, Honolulu, Hawaii. 122 pp.
13. Nihous, G.C., C.K. Kinoshita, and S.M. Masutani. 2009. A determination of the activity of water-alcohol mixtures using mobile order thermodynamics. *Chem. Eng. Sci.* **64**(11), 2767-2771.
14. Ota, M., Abe, Y., Watanabe, M., Smith, R.L., and Inomata, H. 2005. Methane recovery from methane hydrate using pressurized CO₂. *Fluid Phase Equilibr.* **228**, 553–559.

15. Rueff, R.M., Sloan, E.D., and Yesavage, V.F. 1988. Heat-capacity and heat of dissociation of methane hydrates. *AIChE J.*, 34, 1468–1476.
16. Sloan, E.D., Koh, C.A., 2008. Clathrate hydrates of natural gases, 3rd edition, Taylor & Francis, CRC Press, Boca Raton, FL.
17. Sparrow, E.M., Abraham, J.P., and Minkowycz, W.J. 2009. Flow separation in a diverging conical duct: Effect of Reynolds number and divergence angle. *Int. J. Heat Mass Tran.*, **52**(13), 3079-3083.
18. Stern, L.A., Circone, S., Kirby, S.H., and Durham, W.B. 2003. Temperature, pressure, and compositional effects on anomalous or “self: preservation of gas hydrates. *Can. J. Phys.* **81**(1-2), 271-283. doi:[10.1139/p03-018](https://doi.org/10.1139/p03-018).
19. Sylva, T.Y., Kinoshita, C.K., and Masutani, S.M. 2016. Inhibiting effects of transition metal salts on methane hydrate stability. *Chem. Eng. Sci.* **155** doi: 10.1016/j.ces.2016.06.028
20. Takai, K. and Horikoshi, K. 2000. Rapid detection and quantification of members of the archaeal community by quantitative PCR using fluorogenic probes. *Appl. Environ. Microbiol.*, **66**, 5066–5007.
21. Takeya, S., Uchida, T., Nagao, J., Ohmura, R., Shimada, W., Kamata, Y., Ebinuma, T., and Narita, H. 2005. Particle size effect of CH₄ hydrate for self-preservation. *Chem. Eng. Sci.*, 60(5), 1383-1387. doi: 10.1016/j.ces.2004.10.011.
22. Teng, H., Kinoshita, C.M., and Masutani, S.M. 1995. Hydrate formation on the surface of a CO₂ droplet in high-pressure, low-temperature water, *Chem. Eng. Sci.*, **50**(4), 559-564. doi: 10.1016/0009-2509(94)00438-W.
23. Turner, S., Pryer, K.M., Miao, V.P.W., and Palmer, J.D. 1999. Investigating deep phylogenetic relationships among cyanobacteria and plastids by small subunit rRNA sequence analysis. *J. Eukaryot. Microbiol.*, **46**, 327–338.

3.2 Technology for Synthetic Fuels Production

3.2a Hydrogen Production for Fuel Cell Applications

Military contingency bases (CBs) generate large amounts of solid waste which have been identified as one of their most costly logistic and sustainment burdens (Ruppert et al., 2004). For security reasons, consolidating and removing the waste is not always practical. Alternative methods are preferred that would process the waste on site with low environmental impact. The zero footprint camp (ZFC) concept considers the use of waste materials at force provider or CBs as resources to meet the base's energy needs (Ruppert et al., 2004). Efforts to identify the components and their relative contributions in waste streams from different bases have provided the basis for the design of waste handling systems that include energy conversion as the central component. Test and evaluation of waste to energy (WTE) systems with the potential application at CBs has been conducted (Margolin et al., 2015). Test methods developed for CB WTE systems include recipes for synthetic or composite waste streams that can be used to evaluate system performance and enable direct comparison between candidate WTE systems. Characterization of the material components of the synthetic waste stream is a first step in informing design of WTE systems for CB applications. Toward that end, this task focused on acquiring samples of components of the synthetic waste streams and analyzing their fundamental properties. In addition to informing design of WTE systems, these analyses can also play a role in the redesign of goods and packaging knowing that they will be used as fuel at the end of their useful life.

Gasification is a WTE approach that converts the solid waste organic matter to a combustible gas that can be used to produce heat and electricity. The goal of a gasification process is to convert the chemical enthalpy of the solid waste into chemical enthalpy stored in the product gas species. Unlike solar and wind energy generation, gasification systems can provide baseload power and this can be particularly valuable for applications in isolated places, such as military CBs.

Information on the composition and reactive properties of fuels is important in guiding the design and operation of gasifier systems and improving performance. The waste stream is a heterogeneous mixture consisting of food waste, glass, metals, paper products, plastics, rubber, leather, textiles, wood, etc. Compared with a typical US municipal solid waste (MSW), CB waste normally has more food and wood and less glass and yard waste. The majority of the waste source is military supply packaging materials including cardboard, glass, metal, plastic, wax paper, and MRE (Meals Ready to Eat) packing (Margolin et al., 2015; Ruppert et al., 2004). The wastes from the CBs usually exhibit unique composition varied with collecting location, military activity and mission, consumption patterns, eating habits, and social structure (Ludwig et al., 2003). The assortment of materials creates challenges in characterizing the fuel properties of the waste stream. To simulate wastes with varied composition, Margolin et al (Margolin et al., 2015) proposed recipes of readily available commercial products to prepare synthetic CB waste (SCBW). SCBW recipes provide base case conditions for testing and comparison of WTE systems.

Synthetic/composite waste samples or multi-component mixtures can be studied by using a simple mathematical approach, the weighted sum of the corresponding components, under the assumption of negligible interactions between the components in the reaction (Cozzani et al., 1995; Heikkinen

et al., 2004). Cozzani (Cozzani et al., 1995) studied pyrolysis of “paper and cardboard”, plastics, and wood-like materials, the key components and representative for refuse derived fuels (RDF). The reaction behavior of the RDF samples can be predicted by the weighted sum of the reaction rates of tested components. Similarly, Heikkinen (Heikkinen et al., 2004) investigated pyrolysis of waste components and their mixtures in a thermogravimetric analyzer (TGA). Based on the TGA characteristics of both individual components and the simulated mixtures, the composition of an unknown waste mixture was identified. It appears that the method is applicable for pyrolysis, however, it has not been widely recognized for use in gas-solid applications and reactions such as those relevant to steam gasification.

In this paper, the fuel characteristics (ultimate analysis, heating values, proximate analysis, and reactivity with steam) of individual components were measured and used to predict the behavior of the composite SCBW. The apparent kinetic parameters were determined assuming Arrhenius kinetics. In addition, equilibrium syngas composition resulting from steam gasification was predicted from ultimate analysis results. These efforts provide a simple methodology for characterizing multi-component solid waste mixtures that can inform the design of WTE systems.

Materials and Method

The following sections detail the materials and methods used in the investigation of CB waste stream components.

Solid Waste Recipes and Individual Components

Table 3.2a.1 summarizes eight recipes for SCBW classified into seven categories of combustible materials: #1 Cardboard, #2 Mixed paper, #3 Food waste, #4 Plastics, #5 Wood, #6 Rubber & neoprene, and #7 Textile. Each category contains one or multiple representative component(s), for example, #2 is represented by white paper (#2-1) and food trays (#2-2); and #3 by dog food (#3-1), canola oil (#3-2) and water (#3-3). Seven types of plastics are aggregated under #4 in Table 3.2a.1. Table 3.2a.2 details the plastics composition in each of the SCBW recipes in Table 3.2a.1 with individual components that include PET (#4-1, polyethylene terephthalate), HDPE (#4-2, high density polyethylene), PVC (#4-3, polyvinyl chloride), LDPE (#4-4, low density polyethylene), PP (#4-5, polypropylene), PS (#4-6, polystyrene), and others (#4-7). As specified by Margolin et al. (Margolin et al., 2015), all of the above materials are readily available commercial products that can be purchased, as detailed in Table 3.2a.3.

Notice that the categories of “#8 Metals” and “#9 Glass” are incombustible and intentionally excluded from the experiments. These components may be sorted for recycling prior to energy conversion. The category of “#10 miscellaneous wastes/other” was also excluded, due to their uncertain composition as well as its relatively small amount (2-3%). Thus, the non-combustible portion ranged from 6-10% across all of the recipes and was assumed to be included in the ash component when fuel properties are reported on the basis of whole waste materials.

Table 3.2a.1. Recommended “standard” and “challenge” recipes by weight percent, wt/% (adapted from Margolin et al., 2015).

Recipe	Standard Recipe	Challenge Recipes with primary category			
		Mixed Paper	Food waste	Plastic	Wood
Waste Category	R1	R2	R3	R4, R5, R6, R7	R8
#1 Cardboard	15	19	11	10	10
#2 Mixed paper	10	38	7	6	6
#2-1 White paper	1	3.8	0.7	0.6	0.6
#2-2 Food tray	9	34.2	6.3	5.4	5.4
#3 Food waste	32	18	51	21	21
#3-1 Dogfood	6.7	3.8	10.7	4.4	4.4
# 3-2 Canola oil	1.9	1.1	3.1	1.2	1.2
# 3-3 Water	23.4	13.1	37.2	15.4	15.4
#4 Plastic (total) ¹	15	8	11	44	10
#5 Wood	14	8	10	9	43
#6 Rubber	1	1	1	1	1
#7 Textile	3	2	2	2	2
#8 Metals	6	3	4	4	4
#9 Glass	1	1	1	1	1
#10 Miscellaneous Waste/Other	3	2	2	2	2
Total	100	100	100	100	100
Non-combustible portion ²	10	6	7	7	7

Note:

1. Including 7 types of plastic materials. See the detail in Table 3.2a.2.

2. Including Metals, Glass, and Miscellaneous waste/other.

Table 3.2a.2. Contents of plastic materials in the recipes, wt/% (adapted from Margolin et al., 2015).

Plastic Type ¹	Standard recipe	Challenge Recipes						
		Cardboard /Paper	Food	Total plastic	#1 PET ²	#3 PVC ³	#6 PS ⁴	Wood
Recipe #	R1	R2	R3	R4	R5	R6	R7	R8
#4 Plastic (total)	15	8	11	44	44	44	44	10
#4-1 PET	6	3.2	4.4	17.7	27.8	12.9	11.1	4
#4-2 HDPE	2.7	1.4	2.0	7.8	4.8	5.7	4.9	1.8
#4-3 PVC	0.9	0.5	0.7	2.6	1.6	13.7	1.6	0.6
#4-4 LDPE	2.7	1.4	2.0	7.8	4.8	5.7	4.9	1.8
#4-5 PP	0.3	0.2	0.2	0.8	0.5	0.6	0.5	0.2
#4-6 PS	1.8	1.0	1.3	5.4	3.3	4	19.6	1.2
#4-7 Other	0.6	0.3	0.4	1.6	1	1.2	1	0.4

Note:

1. PET = polyethylene terephthalate, HDPE = high density polyethylene, PVC = polyvinyl chloride, LDPE = low density polyethylene, PP = polypropylene, PS = polystyrene, Other = Other plastics that may include polycarbonate, acrylic, nylon, bioplastics, composites, etc.

2, 3, and 4. The numbers in bold represent the plastic type that is being challenged: PET because of its relatively high amount due to surges in water bottle usage; PVC because of the presence of chlorine, and PS because of the aromatic rings in its molecular structure.

Table 3.2a.3. Simulated waste components used in experiments (adapted from Margolin et al., 2015).

Waste category	Id #	Represented material
Cardboard	#1	300Uline 11x17", 1/8" inch thick, corrugated pads model no. S3585
Mixed paper	#2-1 #2-2	Costco Copy Paper, Letter, 20lb, 92-Bright Chinet® Beige 5-Compartment Molded Fiber Cafeteria Tray - 8.5" x 10.5"
Food waste	#3-1 #3-2 #3-3	Gravy Train® Beef Dry Dog Food Crisco Pure Canola Oil, 128 Ounce Water
Plastics	#4-1 PET #4-2 HDPE #4-3 PVC #4-4 LDPE #4-5 PP #4-6-1 PS #4-6-2 PS #4-7 other	12 oz. Vinegar bottle by Aloha Bottling Co. (no lids) 128 oz. 1- Gallon Bottle Clear by Aloha Bottling Co. (no lids) 1-1/2 in. x 10 ft. PVC Sch. 40 DWV Plain End Pipe Fortune Plastics DuraRoll LDPE 30 Gallon Waste Can Liner, Star Seal, Clear, 0.19 Mil, 36" x 30" Choice-Pac 3D-1429T Polypropylene Bowl, White, Medium, 24-Ounce White Heavy Weight PolySty Plastic Fork Dart Container 95HT3 Carryout Food Container, Foam Hinged 3-Compartment, 9-1/2 x 9-1/4 x 3 Verbatim 700 MB 52x 80 Minute Branded Recordable Disc CD-R - 100-Disc Spindle, FFP 97458
Wood	#5	2 in. x 4 in. x 96 in. Prime Kiln Dried Heat-Treated Untreated SPF Stud
Rubber	#6	International Mulch #rm16bk-mw 16lb Black Rubberific Mulch
Textile	#7	#7: All Rags Cotton blend t-shirt material, light to medium weight, no color

The eight recipes adapted from the literature (Margolin et al., 2015) to simulate the composition of the waste in the study, included a standard recipe (R1) and seven “challenge” recipes (R2-R8). The challenge recipes include elevated quantities of a single component, either mixed paper (R2), food waste (R3), plastic (R4-R7), or wood (R8). Four plastic challenge recipes are included based on elevated contents of total plastics (44%) and in particular plastic components as well. Details of the types of plastics included in each recipe are provided in Table 3.2a.2. Recipe R4 has an elevated (44%) content of mixed plastics; R5 has elevated content of polyethylene terephthalate (PET) typically present as water bottles; R6 has a high content of polyvinyl chloride (PVC) and therefore chlorine; and R7 has a high content of polystyrene (PS) and therefore elevated concentrations of aromatic ring molecules.

Samples listed in Table 3.2a.3 were analyzed using a LECO CHN628 analyzer for the elements C, H, and N, and a Parr 6200 Calorimeter for higher heating value (HHV). The exceptions were samples #3-2 canola oil and #4-3 PVC, where analytical data were cited from the literature (Bhimani, 2011, May; Zevenhoven et al., 1997). Proximate analysis and steam reactivity tests were conducted in a TGA described above using 100-200 mg of sample as a single piece or as divided pieces.

Composite CB samples were prepared according to the selected recipes (Table 3.2a.1 or Table 3.2a.4). Materials were milled into 2 mm particles using a Fritsch Cutting Mill and then further reduced to 0.2 mm using a Retsch Ultra Centrifugal Mill (ZM200) under liquid nitrogen. The materials were mixed in a blender and then assembled into composite pellets (Parr 2811 Pellet Press) of ~200 mg or 100 mg with a common diameter of 13mm and heights of ~2 mm or 1 mm, respectively. The smaller pellets were made with the 0.2 mm material. Pellets were subjected to proximate analysis and steam reactivity tests in the TGA test unit.

Table 3.2a.4. Recipes of composite waste pellet samples used for method evaluation (steam reactivity), wt%.

Id #	Components	F1 (standard)	F3 (food)	F8 (wood)
#1	Cardboard	29.6	26.9	15.4
#2-1	White paper	2.1	1.9	0.9
#2-2	Food tray	18.1	12.0	0
#3-1	Dog food	13.4	26.8	6.6
#4-1	PET	0	0	0
#4-3	PVC	1.8	1.7	0
#4-6	PS-1	1.1	0.9	0.6
#5	Wood	27.7	24.9	68.7
#6	Rubber	0	0	0
#7	Textile	6.3	5.0	7.7
Sum		100.0	100.0	100.0

TGA tests for proximate analysis and reactivity in steam

Methods used for the TGA tests are presented in the following sections.

TGA facility

A TGA was designed and assembled to characterize the reactivity of the SCBW components and mixtures prescribed in Tables 1 and 2. Commercially available thermogravimetric analyzers accommodate sample masses on the order of 1 to 10 mg and this was deemed to be too small to evaluate the multi-component, inhomogeneous waste streams. A schematic of the TGA system capable of accommodating sample masses of 200 mg is shown in Figure 3.2a.1. The system employs a platinum, 80 mesh, sample basket with a capacity of ~0.5 ml, suspended from a precision balance (Mettler Toledo, Model AG 204) in a vertically-oriented, 25 mm diameter, quartz tube. A tube furnace (Barnstead Thermolyne) is used to control the heating rate and

temperature of the sample and the reactive environment in the tube can be selected from metered flows of air, nitrogen, and/or steam. The latter is fed to the process as water using a peristaltic pump (Masterflex L/S). Reactants gases and water are introduced to the reactor through concentric tubes with water in the inner, 3 mm tube and nitrogen or an air/nitrogen mixture in the annulus between the 3 mm inner tube and the 6 mm outer tube. Valve V3 is used to direct air or nitrogen to the lower gas inlet. Nitrogen introduced at the upper gas inlet provides shroud gas to prevent air intrusion through the passage for the basket suspension wire. The sample mass is monitored by the balance and the temperature near the sample is determined by type K thermocouples. Signals from both are output through data acquisition systems and recorded. Products of the sample decomposition are swept from the quartz tube volume by the reactant gas streams and pass through a condenser and a sample pump before exhausting. The sampling pump is used to adjust the outlet flow and balance it with the incoming reactant flows.

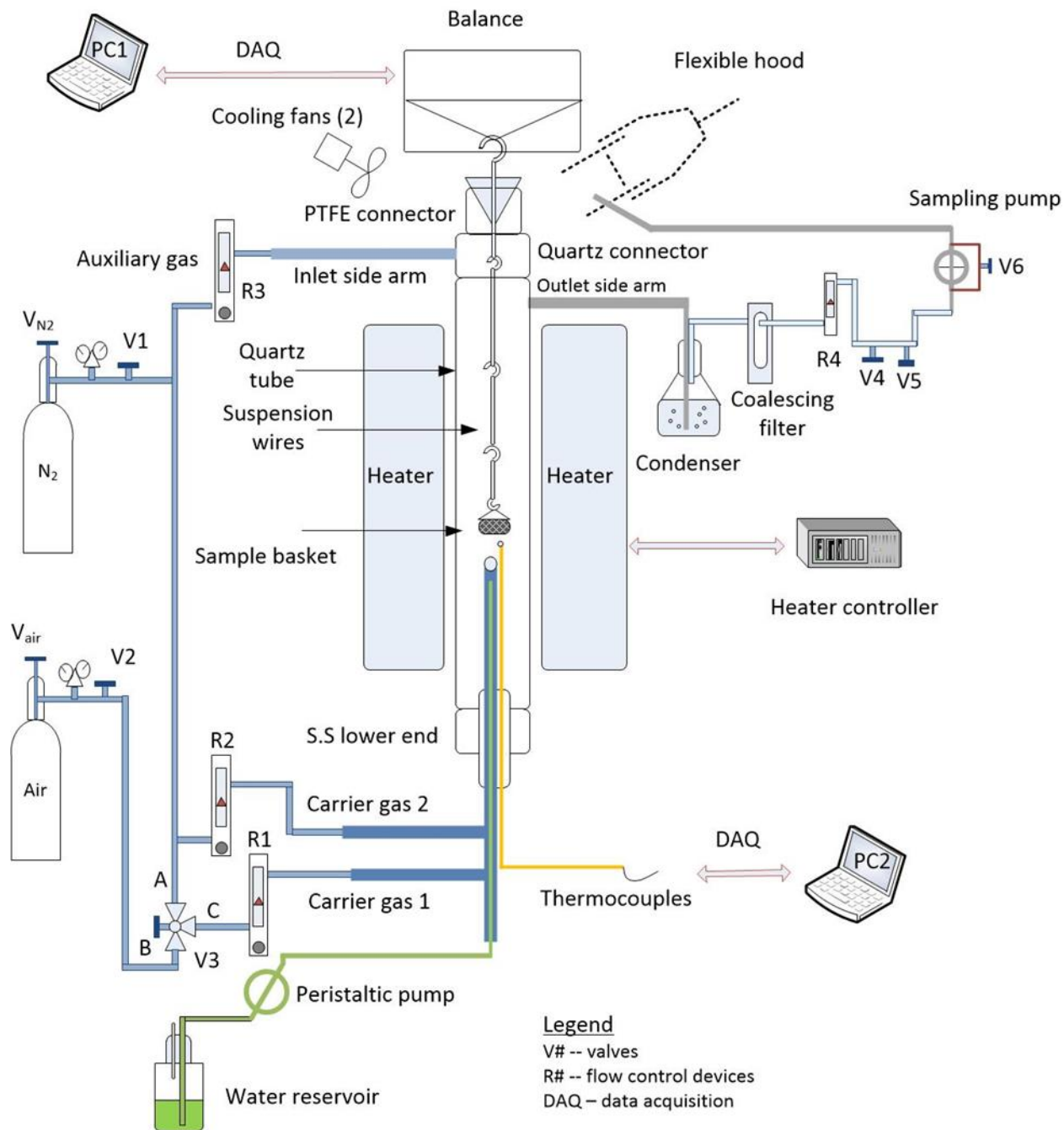


Figure 3.2a.1 Schematic of the thermogravimetric analyzer (TGA) system for composition analysis and reactivity evaluation.

TGA tests

Proximate analysis identifies four fuel fractions: moisture content (MC), volatile matter (VM), fixed carbon (FC), and ash. Cantrell et al. (Cantrell et al., 2010) compared results of ASTM

methods for volatile matter and ash content with TGA methods and found them to be directly comparable for analyzing livestock manure samples over a wide range of composition.

Proximate analyses were begun by placing a sample (~100 mg) in the platinum sample basket at ambient temperature and lowering it into position in the quartz tube suspended from the balance. To initiate the test, a total nitrogen flow of 500 mL/min was introduced into the TGA and the temperature was ramped at a rate of 20 °C/min to 600 °C. Devolatilization was complete after a 20 minute hold time at 600 °C. Carrier gas 1 flow in Figure 3.2a.1 was switched from nitrogen flow (200 mL/min) to air to oxidize the residual char. Figure 3.2a.2 depicts a typical TGA profile of #5 wood illustrating the three stages of mass loss normally observed. The first stage of mass loss is due to moisture removal by drying, the second stage is devolatilization, and the third is attributed to the fixed carbon oxidation. Ash content, VM, and FC are directly obtained from the weight measurement of samples. MC is calculated by difference therein the summary of these four fractions is 100.

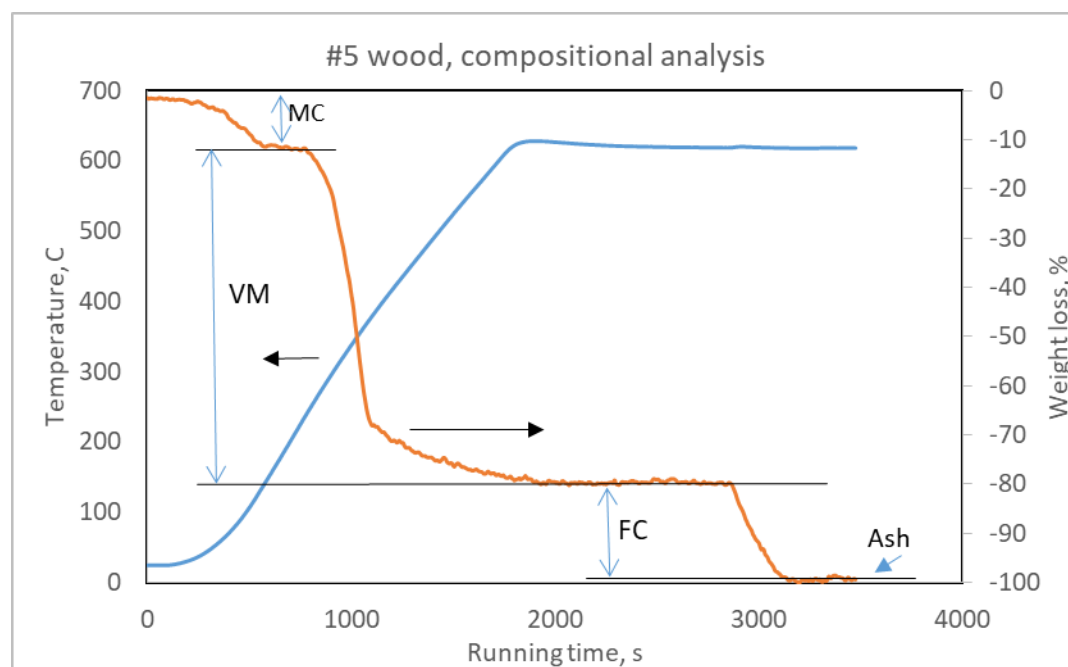


Figure 3.2a.2 Typical TGA graph showing proximate analysis for a wood sample at a heating rate of 20 °C min⁻¹ under a nitrogen atmosphere: MC (moisture content), VM (volatile matter), FC (fixed carbon), and ash.

Fuel reactivity was determined by reacting the sample and steam in the TGA and is expressed as a conversion rate or instantaneous reaction rate as a function of time or conversion (Umeki et al., 2012). Under a steam environment, moisture and VM mass losses typically result from vaporization and thermal decomposition, respectively. The remaining char reacts heterogeneously with steam at a rate estimated (for cellulose at 800°C) to be ~10⁴ times slower than occurs under

an oxygen environment (DeGroot and Richards, 1991). Two reaction stages evident in a TGA profile, show weight losses due to devolatilization (pyrolysis) and the following reaction of char with steam. The latter is obviously much slower than the devolatilization rate, and largely defines the characteristic time of the overall reaction. Char reactivity is therefore important in WTE system design.

Char reactivity is affected by its morphological structure, which is especially influenced by the initial devolatilization or pyrolysis conditions, and the amount and composition of inorganic matter (Raveendran and Ganesh, 1998). The devolatilization conditions have been investigated in several parametric studies (Cetin et al., 2005; Chen et al., 1997; Kumar and Gupta, 1994; Moilanen and Muehlen, 1996) that included heating rate, temperature, residence time and pressure. In order to eliminate the effects of devolatilization conditions on char formation and maintain similar reaction condition, measurements were performed on an “in-situ” char that was generated under the same reactive atmosphere and reaction temperature. The test procedures are described below.

The initial sample (~200 mg) was placed in the platinum basket, lowered into the TGA reaction tube, and heated at 100 °C/min in the presence of nitrogen flow at 500 mL/min. When the temperature approached 300 °C, after ~3 minutes of heating, 0.05 g/min of deionized (DI) water was introduced into the reactor with 200 mL/min nitrogen. The temperature ramp continued to the desired test temperature, 825, 875, or 925 °C (values of interest in gasification) and was held at this final temperature for 50 minutes or until the sample weight attained a final stable value. The Carrier Gas 1 (Figure 3.2a.1) nitrogen flow (300 mL/min) was then switched to air to oxidize the remaining char residue. A typical TGA profile for sample #5 wood is shown in Figure 3.2a.3 illustrating the rapid devolatilization, slow char-steam reaction and residual char burn-off stages of the test.

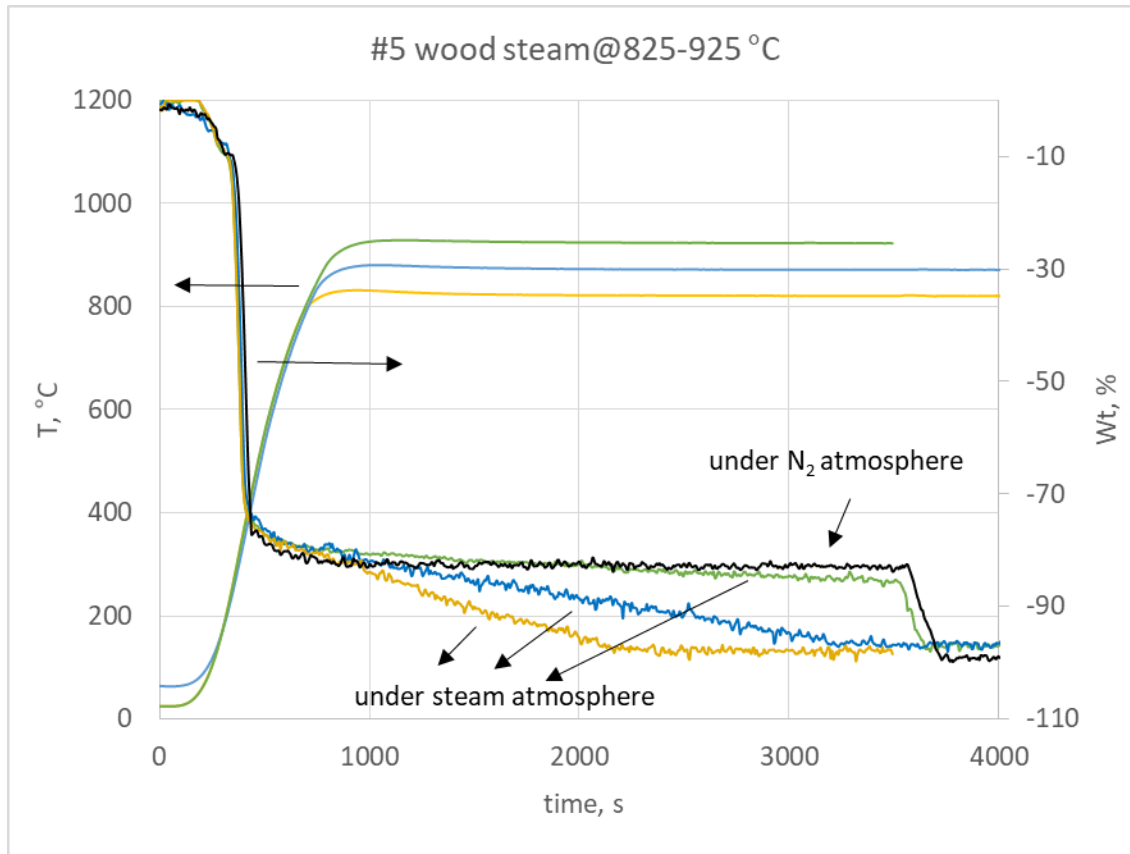


Figure 3.2a.3 Typical TGA graph showing reactivity in steam for a wood sample heated at $100\text{ }^{\circ}\text{C min}^{-1}$ to a final temperature of 825, 875, and 925°C as indicated in the graph (yellow, blue and green curves respectively). Black curve is wood sample under N_2 (no steam), heated at $100\text{ }^{\circ}\text{C min}^{-1}$ to a final temperature 925°C .

Fuel reactivity is evaluated by reaction rate or the rate of sample mass loss under specified conditions of reaction temperature, heating rate, pressure, and reaction atmosphere. As shown in Figure 3.2a.4, the reaction rate, k , at temperature (T) can be calculated by using Eq.1.

$$k(T) = \frac{\Delta M}{\Delta t} \quad (1)$$

where,

$$\Delta M = \frac{M_1 - M_2}{M_0 - M_f} \quad (2)$$

$$\Delta t = t_2 - t_1 \quad (3)$$

and M_o is dry sample mass after moisture removal; M_1 is sample mass at time t_1 and temperature T_1 ; M_2 is sample mass at time t_2 and temperature T_2 ; and M_f is the sample mass after residual carbon removal with oxygen. The reaction temperature (T) is the average temperature value between the reaction time t_1 and t_2 in Eq.4:

$$T = \frac{1}{n} \sum_{j=1}^n T_j \quad (4)$$

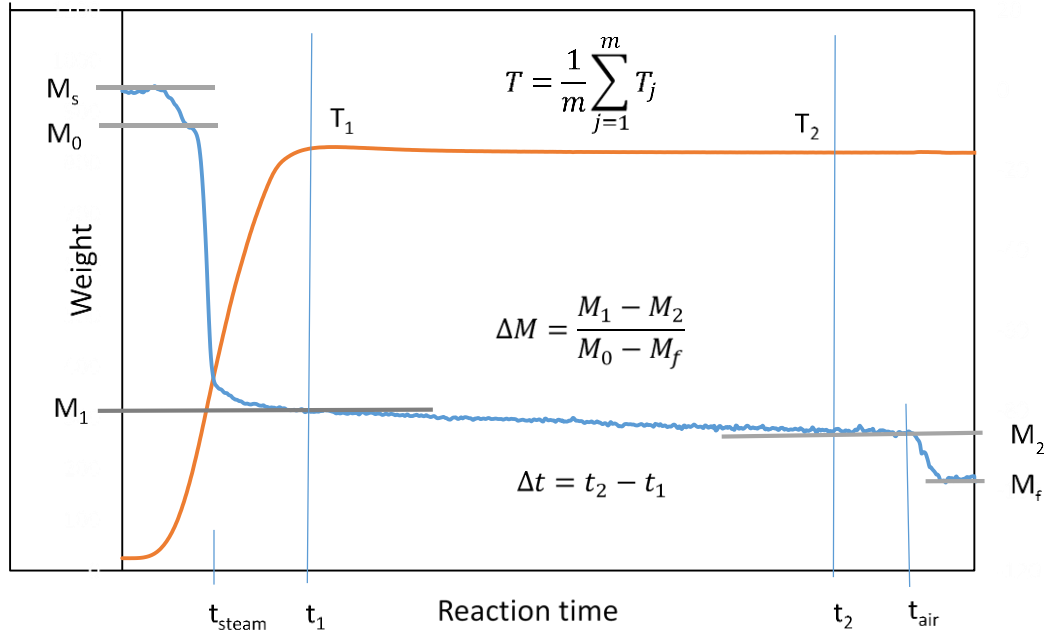


Figure 3.2a.4 Illustrative sketch of reaction rate determination. (M_s : sample initial mass; M_o : sample mass after moisture off; M_1 : sample mass at time t_1 and temperature T_1 ; M_2 : sample mass at time t_2 and temperature T_2 ; M_f : sample mass after char burnt off; t_{steam} : starting time for steam introducing; t_{air} : starting time for air introducing).

Weighted Sum Method for Fuel Properties

With the assumption that there are negligible interactions between the fuel components, the composite fuel properties were predicted using a weighted sum method, shown in Eq.5.

$$X_{cf} = \sum_{i=1}^n x_i y_i \quad (5)$$

where X_{cf} is the calculated property of a composite fuel; x_i is the property value of each individual component (i); and y_i is the mass fraction of each individual component in the composite fuel. Mass fraction values are derived from the composite recipes listed in Tables 1 and 2. The method was applied to ultimate analysis (C, H, N), HHV, and proximate analysis (MC, VM, FC, and ash), although the last group is the only one potentially affected by the validity of the assumption of negligible interactions between the fuel components.

In addition, fuel reactivity of a composite fuel was assembled from the individual components' TGA curves and their mass fractions. It was assumed that the reaction is the sum of independent reactions from each component, occurring in parallel and with negligible, component-to-component interaction.

The method was evaluated by subjecting selected samples to proximate analysis and reactivity tests in steam. Proximate analysis experimental results for a composite pellet were compared with a calculated value from individual components using Eq. 5. Similarly, steam reactivity results from composite samples were compared to values calculated from individual components.

Apparent Kinetics Studies

Kinetic studies of fuel pyrolysis and gasification are important in the design and operation of thermochemical conversion processes. Based on the reactivity measurements for the waste components, the apparent kinetic parameters can be simply determined using the Arrhenius Equation:

$$k(T) = Ae^{-\frac{E_a}{RT}} \quad (6)$$

or

$$\ln k(T) = -\frac{E_a}{RT} + \ln A \quad (7)$$

where, k is the reaction rate (s^{-1}); A is a pre-exponential factor (s^{-1}); E_a is activation energy ($kJ\ mol^{-1}$); R is the universal gas constant ($8.314\ J\ mol^{-1}\ K^{-1}$); and T is temperature (K). Using experimentally derived values of $k(T)$ and T and Eq. 7, values of E_a and A were derived using linear regression.

Syngas Composition Prediction

FactSage (Bale et al., July, 1996) software was used to calculate chemical equilibrium products using the elemental composition of the synthetic waste fuels and conditions typical of steam gasification: a temperature of 850 °C, 1 bar pressure, and a steam to dry fuel weight ratio of 2:1. The ultimate analysis results were used as inputs to the FactSage calculation.

Results and Discussion

The following sections present results and discussion of the CB waste investigations.

Individual Components

The following sections present results of measurements made on individual components.

Fuel properties

Table 3.2a.5 lists the ultimate, HHV, and proximate analysis results for the 16 individual components (15 solids and 1 liquid). These components comprise ~90% weight fraction of the recipes in Tables 1 and 2.

Table 3.2a.5 Proximate analysis, ultimate analysis and higher heating value (HHV) of individual waste component.

Components	Proximate analysis, %				Ultimate analysis, %			High heating value, MJ/kg
	MC _w	VM _d	FC _d	Ash _d	C _d	H _d	N _d	HHV _d
#1 Cardboard	8.2	79.3	16.0	4.7	46.3	6.4	0.2	16.8
#2 Mixed paper								
# 2-1 White paper	4.5	75.1	13.9	11.0	38.9	5.7	0.1	12.5
# 2-2 Food tray	7.0	84.2	12.1	3.7	44.0	6.6	0.2	16.3
#3 Food waste								
# 3-1 Dog food	6.0	71.4	21.4	7.2	47.6	7.0	3.5	17.6
# 3-2 Canola oil*	0	100	0	0	80.2	10.9	0.1	40.2
#4 Plastics								
#4-1 PET	0	83.9	16.0	0.1	61.3	4.2	0.1	23.1
#4-2 HDPE	0	99.1	0.0	0.9	84.7	13.8	0.1	46.4
#4-3 PVC	0	78.8	12.5	8.7	37.8	4.9	0.1	21.2**
#4-4 LDPE	0	86.6	0.0	13.4	73.5	12.2	0.2	37.6
#4-5 PP	0	100	0.0	0.0	83.7	13.9	0.1	45.8
#4-6-1 PS	0	78.3	21.4	0.3	74.0	5.5	0.1	30.8
#4-6-2 PS	0	100	0.0	0.0	90.0	7.7	0.1	41.2
#4-7 Other	0	100	0.0	0.0	91.0	7.4	0.5	40.1
#5 Wood	11.9	77.2	22.5	0.3	51.1	6.9	0.4	18.3
#6 Rubber	0	64.5	30.0	5.5	79.3	7.4	0.4	38.4
#7 Textile	6.1	89.3	8.5	2.2	43.9	6.8	0.2	16.1
Note:								
Abbreviations: MC: moisture content, VM: volatile matter, FC: fixed carbon, Ash: ash content; C: carbon, H, hydrogen, N, nitrogen, w: wet basis, d: dry basis.								
*: Data from (Bhimani, 2011)								
**: Data from (Zevenhoven, 1997)								

Proximate analysis results show that components in the categories #1, #2, #3, #5 and #7 contain moisture in a range of 4.5% to 11.9% in equilibrium with the ambient conditions. No inherent moisture was detected for plastics and rubber (#4 and #6), which are petroleum-derived materials.

VM contents ranged from 65-100% dry basis across all samples. Plastics had high VM content from 78% to 100%. The latter was measured for three plastics (#4-5 PP, #4-6-2 PS and #4-7 Other) and canola oil, indicating that these materials can be completely volatilized in a thermochemical process at temperatures above 600 °C. Rubber had the lowest VM content at 64.5%.

As expected, FC contents were largely inversely related to VM content. Rubber had the largest FC content, 30%, with wood following at 22.5%. The three plastics with 100% VM had no FC content detected. Textile had the lowest measured FC content, 8.5%. Ash is the incombustible fraction of the CB waste components. LDPE and white paper have high ash contents of 13.4% and 11.0%, respectively. Canola oil and some plastics have little or no ash detected, including PET, PP, PS2 and polystyrene foam in the “other” category. Wood had very low ash content at 0.3%.

Elemental compositions from the ultimate analyses of the test samples are also included in Table 3.2a.5. Results show that element contents vary across samples, even within the same category. For example, C contents of plastics range from 37.8% for PVC to 91% for PS. Similarly, H contents of plastics vary between 4.2% for PET and 13.9% for PP. Rubber has higher contents of C (79.3%) and H (7.4%) than that of the other non-plastic solid samples. Liquid canola oil has relatively high contents of C (80.2%) and H (10.9%). In addition, the highest N content is found for the sample dogfood, 3.5%, owing to its protein content. In comparison, other component N contents range from 0.1-0.5%.

HHV of samples are related with the contents of carbon, hydrogen, and ash. The plastic samples typically have HHV's greater than 30 MJ/kg, with the exception of PET and PVC, with HHV values slightly higher than 20 MJ/kg. Rubber and canola oil have elevated HHV, 38.4 and 40.2MJ/kg, respectively. The remaining samples have lower HHV's ranging from 12.5 to 23.1 MJ/kg. With consideration of the waste sources, replacing glass and metal with plastic (e.g. in the packaging materials) could provide the greatest potential for improving the heat of combustion of the waste.

The HHV of a material can be estimated from the ultimate elemental analysis. A number of models including empirical formulas have been developed (Channiwala and Parikh, 2002; Kieseler et al., 2013; Mott and Spooner, 1940). These models can be tuned for categories of fuels, such as coal or biomass, by adjusting the coefficients in the equations. In this study, the HHV predicted by two formulas using the measured ultimate analyses were compared with the measured HHV. The selected formulas (Channiwala and Parikh, 2002; Mott and Spooner, 1940) are:

1. Channiwala and Parikh– formula, HHV1, based on 225 data points from the entire spectrum of fuels including gaseous, liquid, and solids. The formula was selected due to its general validity. The equation is:

$$\text{HHV1} = 0.3491 \text{ C} + 1.1783 \text{ H} + 0.1005 \text{ S} - 0.1034 \text{ O} - 0.0151 \text{ N} - 0.0211 \text{ ash} \quad (8)$$

2. Dulong-formula, HHV2, one of the first ultimate analysis correlation developed for HHV of fuels. The equation is:

$$\text{HHV2} = 0.3383 \text{ C} + 1.443 (\text{H} - \text{O}/8) \quad (9)$$

The calculated results are compared with the measurements, as shown in Figure 3.2a.5. The average bias error (ABE) and the average absolute error (AAE) are calculated using the equations (10) and (11), respectively, and their values for the Channiwalla and Dulong HHV correlations are also shown in Figure 3.2a.5.

$$ABE(\%) = \frac{1}{n} \sum_{i=1}^n \frac{HHV_{i,calculated} - HHV_{i,measured}}{HHV_{i,measured}} \times 100 \quad (10)$$

$$AAE(\%) = \frac{1}{n} \sum_{i=1}^n \left| \frac{HHV_{i,calculated} - HHV_{i,measured}}{HHV_{i,measured}} \right| \times 100 \quad (11)$$

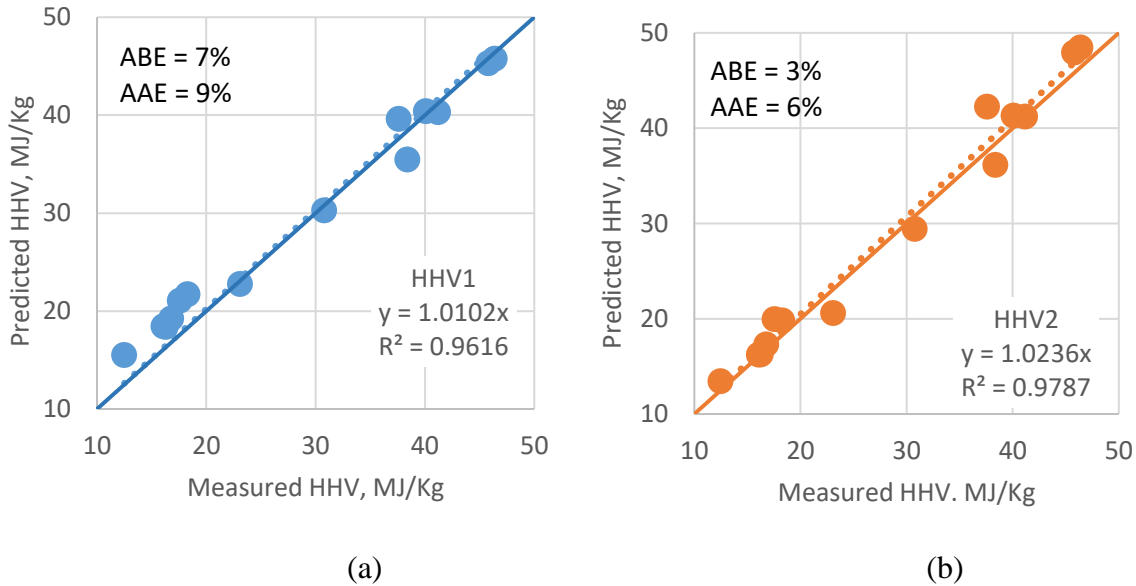


Figure 3.2a.5 Comparison of measured and calculated higher heating value (HHV) using correlation Eqs. 8 and 9 in a), on left and b) on right, respectively.

Figure 3.2a.5 shows the correlation between the predicted and the measured HHV of 13 CB waste components with an average absolute error (ABE) of 7%, and an average bias error (AAE) of 9% using the Channiwalla and Parikh formula (Eq. 8). The errors are reduced when using Dulong formula (Eq. 9), with ABE of 3% and AAE of 6%. As the correlations offer a low cost alternative, the results predicted by both equations are acceptable and applicable to the solid waste materials.

The above measurements demonstrate the range of fuel characteristics of individual components of the composite CB waste materials. Variability may also result from materials acquired from different sources or manufacturers. For example, a proximate analysis for cardboard in the

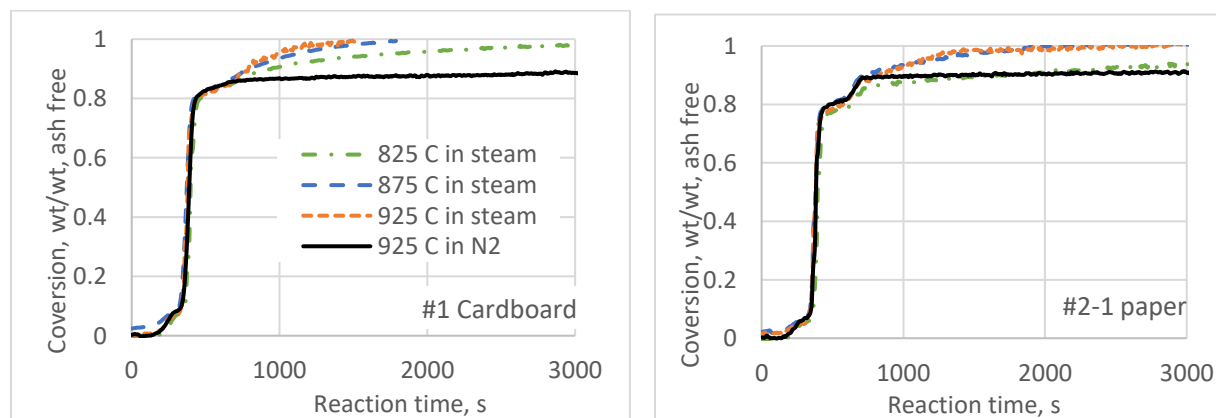
literature (Vounatsos; et al., 2012) reported 7.16% ash, 86.42% VM, and 6.34% FC, which is not in complete agreement with the measurements reported in Table 3.2a.5, 4.7% ash, 79.3% VM and 16% FC. Some types of waste material exhibit significant variation in fuel characteristics as reported (Zhou et al., 2014) for components that were collected from different locations in China.

Fuel Reactivity in Steam

Ten of the materials in the CB waste had measurable contents of fixed carbon (FC) and were subjected to steam reactivity tests. Based on the data in Table 5, the test samples included #1 Cardboard, #2 Mixed paper (# 2-1 white paper, # 2-2 food tray), #3 food waste (# 3-1 dogfood), #4 plastic (#4-1 PET, #4-3 PVC, #4-6-1 PS), #5 wood, #6 rubber and #7 textile.

Results show that all test samples have similar reaction patterns as shown in Figure 3.2a.3 (above), where #5 wood was tested in a steam atmosphere at final temperatures of 825, 875 and 925 °C. A reaction at 925 °C under nitrogen atmosphere (w/o steam) was also tested as reference.

Figure 3.2a.3 shows that when the sample was heated, moisture and volatile matter were promptly released resulting in sharp reductions of sample mass corresponding to drying and devolatilization. A subsequent slower mass loss is attributed to the heterogeneous reaction of the solid residue (char) with steam. The rapid devolatilization stage approaches completion before the final test temperature is reached, and the reaction of char with steam begins as the final temperature is reached (~850 s). Sample weight loss continues due to the heterogeneous steam-carbon reaction, albeit at reduced rates, until the sample mass approaches a final constant value. At test temperatures of 875 and 925 °C, the mass loss curves approach a common final value of ~97%. The TGA curve for the wood sample at 925 °C under nitrogen shows no significant weight loss after devolatilization is complete at ~750 s. Similar behavior was observed for all 10 samples tested. The conversion curves of the test samples heated at 100 °C min⁻¹ to reaction temperatures of 825, 875, and 925 °C in steam atmospheres and the reference tests at 925 °C in nitrogen are shown in Figure 3.2a.6 (below).



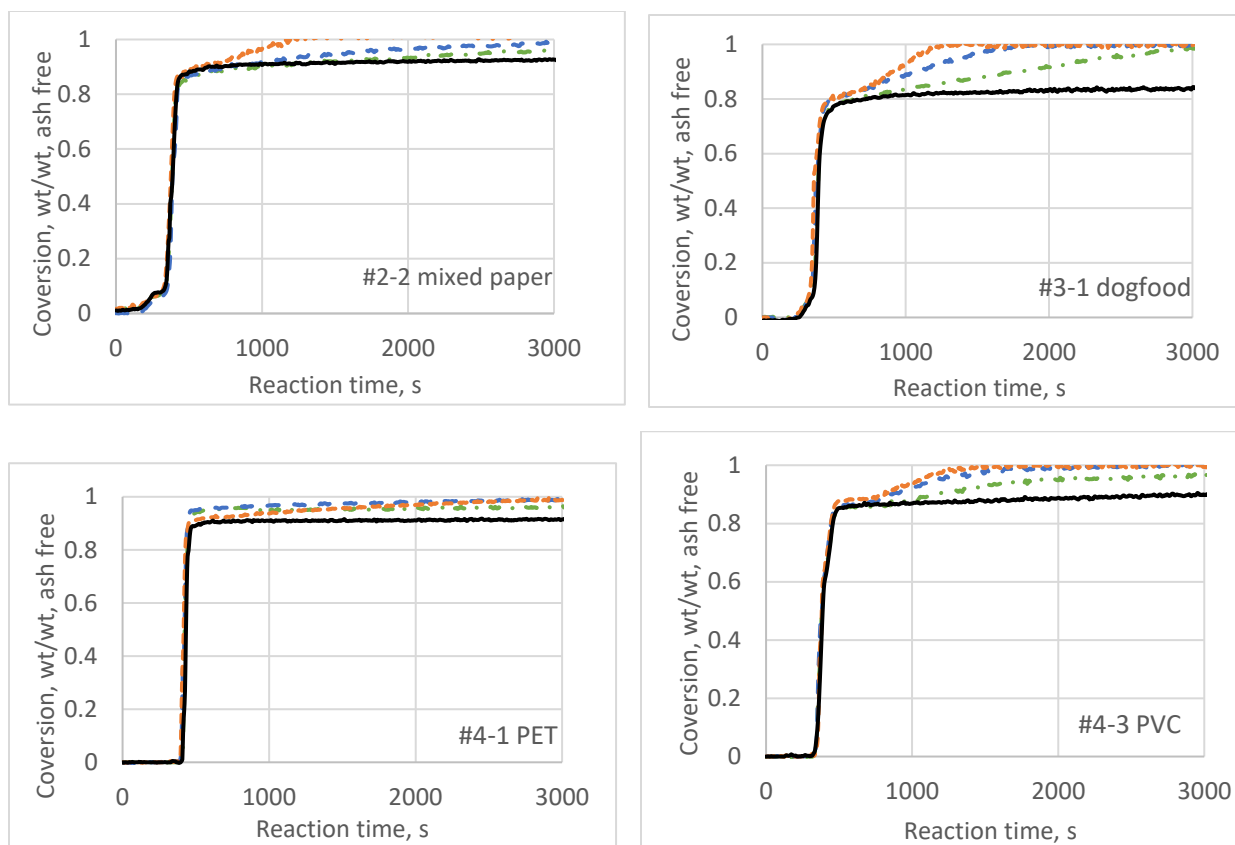
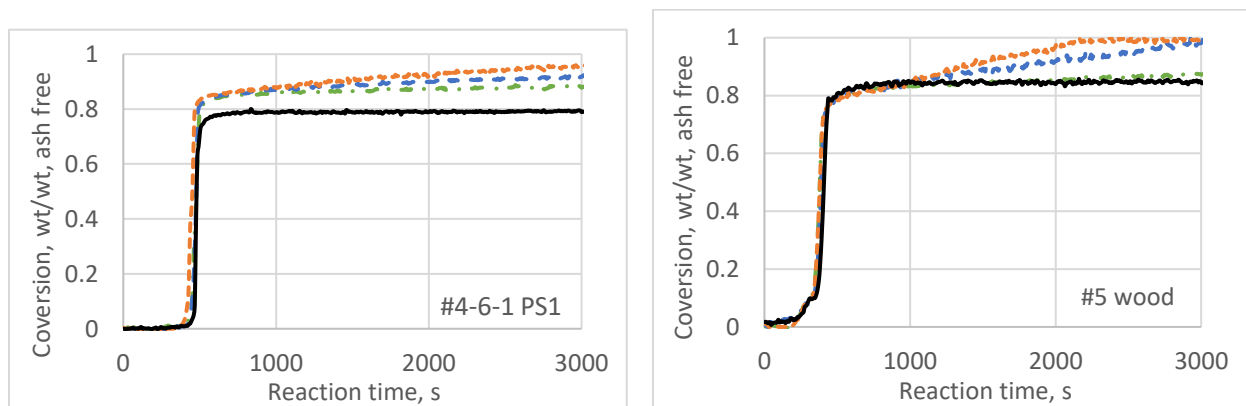


Figure 3.2a.6 Conversion curves of individual contingency base (CB) waste components in steam atmosphere under $100\text{ }^{\circ}\text{C min}^{-1}$ heating rate to final temperatures of $825\text{ }^{\circ}\text{C}$ (green), $875\text{ }^{\circ}\text{C}$ (blue), $925\text{ }^{\circ}\text{C}$ (orange), and in N_2 atmosphere (black) at $925\text{ }^{\circ}\text{C}$. (All figures have the same legend as shown for #1 cardboard.)



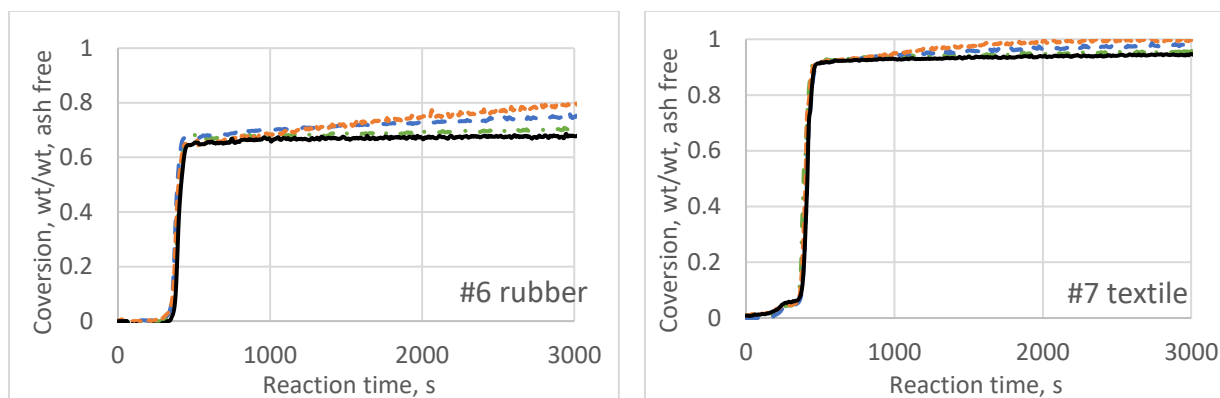


Figure 3.2a.6 (continued) Conversion curves of individual CB waste components in steam atmosphere under $100\text{ }^{\circ}\text{C min}^{-1}$ heating rate to final temperatures of $825\text{ }^{\circ}\text{C}$ (green), $875\text{ }^{\circ}\text{C}$ (blue), $925\text{ }^{\circ}\text{C}$ (orange), and in N_2 atmosphere (black) at $925\text{ }^{\circ}\text{C}$. (All figures have the same legend as shown for #1 cardboard).

The reaction rates for the devolatilization and char-steam reaction stages in Figure 3.2a.6, are summarized in Table 3.2a.6. The devolatilization rates in nitrogen at $925\text{ }^{\circ}\text{C}$ ranged from 7.2 (#4-PVC) to $18.7\text{ mg g}^{-1}\text{ s}^{-1}$ (#4-1 PET), whereas steam devolatilization at the same temperature produced rates of 8.1 (#6 Rubber) to $850\text{ mg g}^{-1}\text{ s}^{-1}$ (#4-3 PVC). Steam char reaction rates at $825\text{ }^{\circ}\text{C}$ ranged from 2.2 (#4 PET) to $79.4\text{ }\mu\text{g g}^{-1}\text{ s}^{-1}$ (#3-1 dogfood). Raising the TGA temperature from 825 to $875\text{ }^{\circ}\text{C}$ increased the steam reaction rates by a factor of 1.5 (#4-6-1 PS) to 6.1 (#4-1 PET). Further increasing the temperature from 875 to $925\text{ }^{\circ}\text{C}$ produced a more moderate response, with reaction rates increasing by factors ranging from 1.1 (#4-3 PVC) to 2.1 (#3-1 Dog food and #4-1 PET).

Table 3.2a.6 Reaction rates of devolatilization and char in steam for individual CB waste components.

Sample	Temperature ($^{\circ}\text{C}$)	Atmosphere	Devolatilization (mg/g/s , ash free)	Char Reaction ($\mu\text{g/g/s}$, ash free)
#1 Cardboard	825	steam	9.31	55.0
	875	steam	9.30	143.0
	925	steam	10.0	271.0
	925	N_2	8.86	12.4
#2-1 White paper	825	steam	10.1	37.9
	875	steam	10.5	99.9
	925	steam	10.6	160.0

	925	N ₂	9.28	8.54
#2-2 Café tray	825	steam	10.5	31.6
	875	steam	10.6	108.0
	925	steam	11.0	189.0
	925	N ₂	10.2	9.49
#3-1 Dog food	825	steam	9.63	79.4
	875	steam	9.46	158.0
	925	steam	9.62	325.0
	925	N ₂	9.91	13.6
#4-1 PET	825	steam	21.6	2.16
	875	steam	22.1	13.1
	925	steam	24.2	27.0
	925	N ₂	18.7	1.71
#4-3 PVC	825	steam	7.23	50.6
	875	steam	780.0	181.0
	925	steam	847.0	200.0
	925	N ₂	7.24	15.3
#4-6-1 PS	825	steam	11.3	18.6
	875	steam	13.7	28.6
	925	steam	13.6	43.4
	925	N ₂	11.1	2.53
#5 Wood	825	steam	9.73	26.1
	875	steam	9.70	66.7
	925	steam	9.07	115.0
	925	N ₂	8.21	2.23
#6 Rubber	825	steam	8.85	12.4
	875	steam	9.29	29.9
	925	steam	8.06	53.4
	925	N ₂	8.21	6.82
#7 Textile	825	steam	10.0	10.8
	875	steam	10.8	28.6
	925	steam	11.1	50.7
	925	N ₂	10.9	8.81

The relationship between reaction temperatures and reaction rates of char with steam is described using the Arrhenius equation, as shown in Figure 3.2a.7(a). The kinetic parameters (E_a and A) and the correlation coefficients (R^2) of $\ln k$ vs $1/T$ calculated using Eq. 7 are presented in Table 3.2a.7. Comparing the reaction rates of char with steam, a reactivity ranking can be derived from Table 3.2a.6 or Figure 7(A):

Dog food (#3-1) > Cardboard (#1) \approx PVC (#4-3) > Write paper (#2-1) \approx Café tray (#2-2)
 > Wood (#5) > PS (#4-6-1) \approx Rubber (#6) \approx Textile (#7) > PET (#4-1).

The samples' activation energies (E_a) range from 90-274 kJ mol⁻¹, with PET (#4-1) having the highest value, 274.3 kJ mol⁻¹ and PS (#4-6-1) displaying the lowest value, 91.1 kJ mol⁻¹. The remaining materials lie in a tighter range from 152.1 to 199.5 kJ mol⁻¹. Similar activation energies, 167 to 238 kJ mol⁻¹, were reported in the literature (Fermoso et al., 2008) for char samples prepared from bituminous coal, pet coke, chestnut residues and olive stones and subjected to steam gasification at 725-1050 °C.

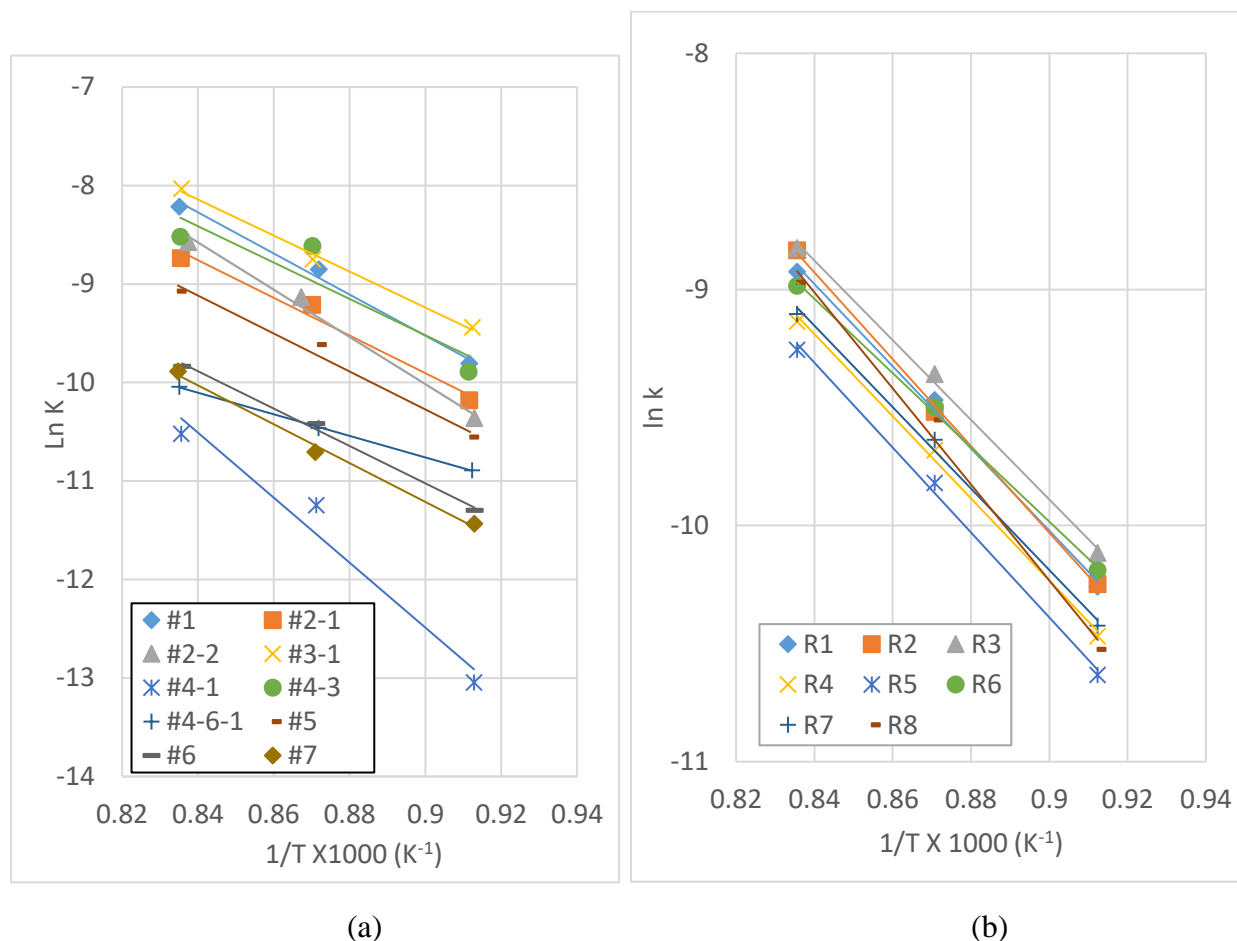


Figure 3.2a.7 Arrhenius plot for the char-steam reaction of the waste components (a) and synthetic fuels (b).

Table 3.2a.7 Summary of kinetic parameters for CB waste components reactions with steam over the temperature range from 825-925 °C.

Waste component	Pre-exponential factor (A)	Activation energy, kJ/mol (E_a)	Correlation coefficient (R^2)
#1 Cardboard	1.1E+04	173.6	0.9912
#2-1 White paper	1.5E+03	159.0	0.9794
#2-2 Café tray	1.1E+05	199.5	0.9918
#3-1 Dog food	1.4E+03	152.1	0.9953
#4-1 PET	3.0E+07	274.3	0.9617
#4-3 PVC	1.2E+03	153.5	0.8393
#4-6-1 PS	4.1E-01	91.1	0.9995

#5 Wood	1.2E+03	160.4	0.9836
#6 Rubber mulch	4.3E+02	157.8	0.9952
#7 Textile	6.9E+02	164.0	0.9942

Method Evaluation

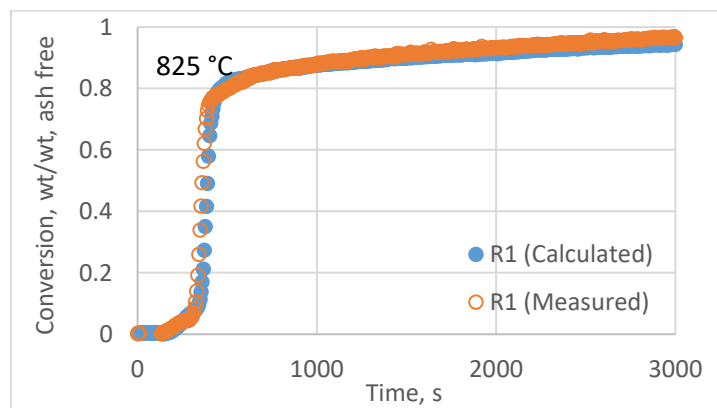
Table 3.2a.8 presents results of proximate analysis of the composite pellet samples from recipes R1, R2, R3, R4 and R8, and the values calculated from proximate analysis results of the individual components. Results are comparable with maximum absolute differences of 1.2% for VM, 0.9% for FC, and 0.4% of ash.

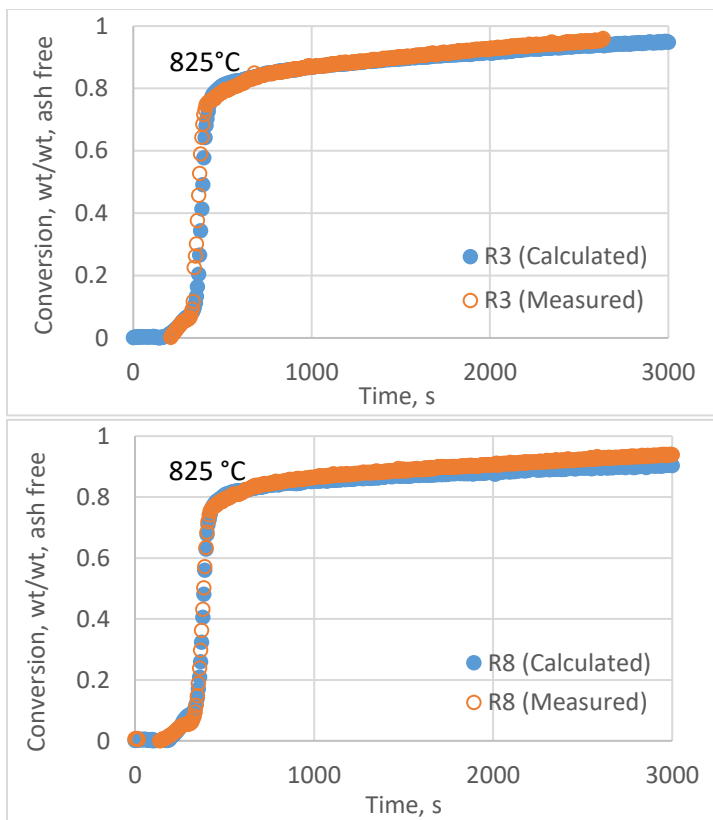
Figure 3.2a.8 shows the conversion curves that were measured in a steam atmosphere for composite pellet samples, and the curves that were calculated using the recipes and reactivity data of individual components. The curves show close agreement across all fuels and reaction temperatures.

Table 3.2a.8 Comparison of the result from proximate analysis measurements of CB composite pellets and the values calculated using measurements of individual CB waste components included in Table 3.2a.5 but excluding metals, glass, and miscellaneous waste/other fractions shown in Table 3.2a.1 (values are normalized and reported on a dry basis).

Recipe No.	R1		R2		R3		R4		R8	
	Meas	Calc	Meas	Calc	Meas	Calc	Meas	Calc	Meas	Calc
VM	81.8	82.3	83.9	82.7	81.5	81.7	81.5	81.7	80.1	80.0
FC	15.3	14.8	13.2	14.1	15.9	15.1	15.9	15.1	18.5	18.1
Ash	2.9	2.9	2.9	3.1	2.7	3.1	2.7	3.1	1.4	1.8

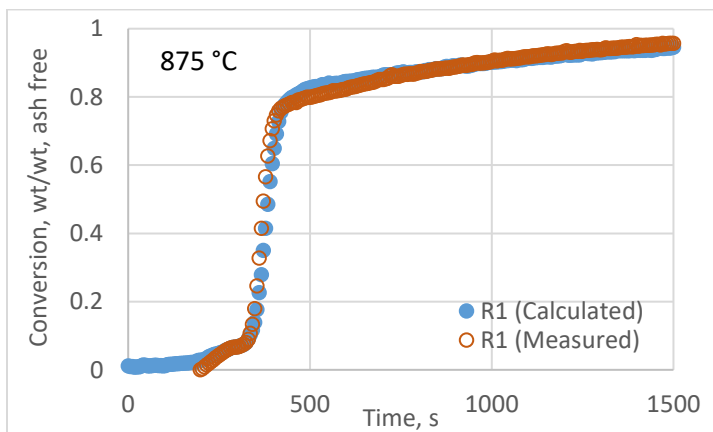
Meas = Measured
Calc = Calculated

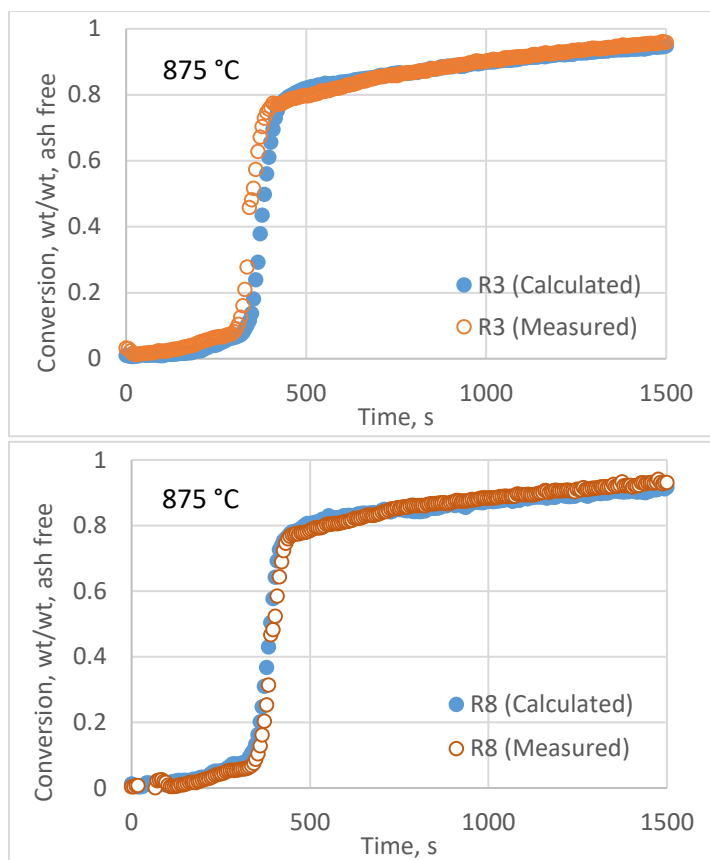




(a)

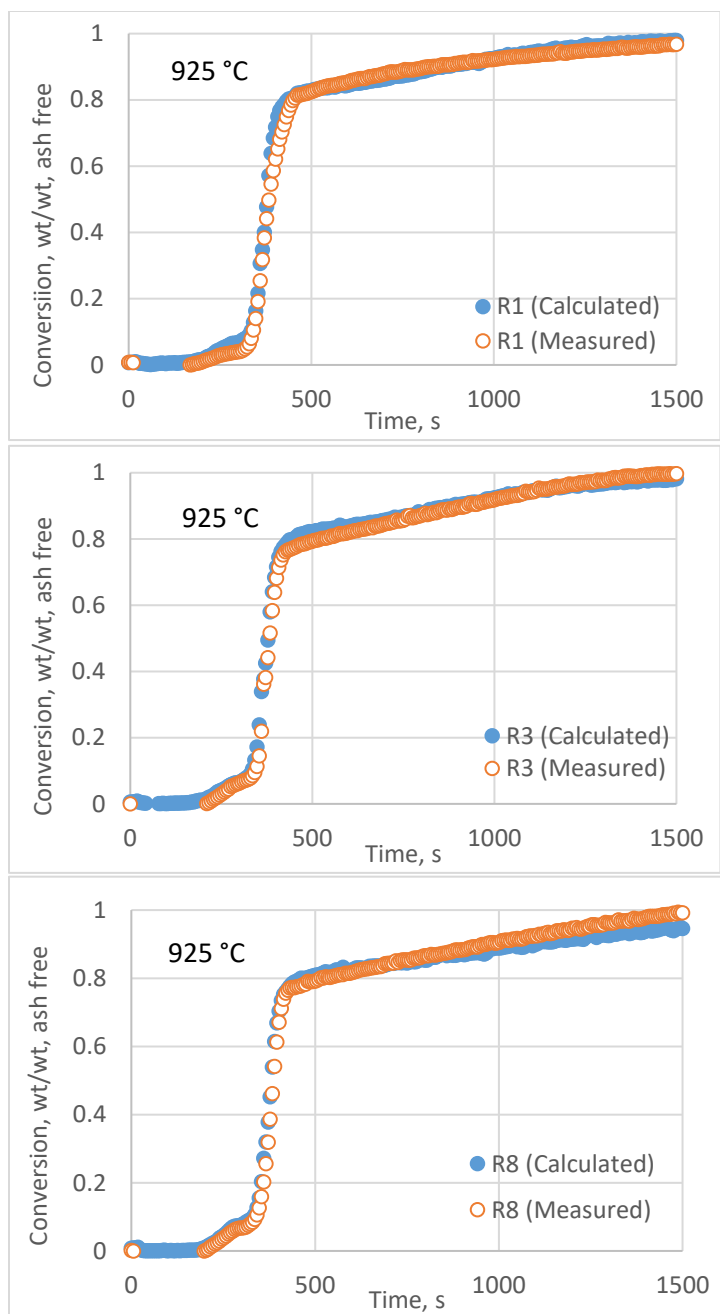
Figure 3.2a.8 Comparison of TGA curves at 825 °C (a), 875 °C (b, below), and 925 °C (c, below) measured in a steam atmosphere for CB composite waste pellets and calculated from recipes and individual CB waste component kinetic data (Table 3.2a.4).





(b)

Figure 3.2a.8 (continued) Comparison of TGA curves at 825 °C (a), 875 °C (b), and 925 °C (c) measured in a steam atmosphere for CB composite waste pellets and calculated from recipes and individual CB waste component kinetic data (Table 3.2a.4).



(c)

Figure 3.2a.8 (continued) Comparison of TGA curves at 825 °C (a), 875 °C (b), and 925 °C (c) measured in a steam atmosphere for CB composite waste pellets and calculated from recipes and individual CB waste component kinetic data (Table 3.2a.4).

Synthetic Fuels

The following sections present results of measurements made on synthetic fuel blend mixtures.

Fuel Properties

The analytic results of the individual CB waste components (Table 3.2a.5) and the compositional recipes (Tables 1 and 2) were used to calculate fuel properties using Eq. 5. Results of this effort are presented in Table 3.2a.9. Note that in Table 3.2a.9 ultimate analysis and HHV results are reported on a dry basis, and proximate analysis on an “as received” basis. The components in the categories of “Glass and Metals” and “Miscellaneous waste/others” were included when composite values were calculated but were assumed to be inert components that contributed to the ash fraction.

Table 3.2a.9 Fuel properties of CB composite waste fuels based on Table 3.2a.1 and Table 3.2a.2 recipes and including metals, glass, and miscellaneous water/other fractions shown in Table 3.2a.1.

Recipes	Proximate analysis, %				Ultimate analysis, %			High heating value, MJ/kg
	MC _w	VM _d	FC _d	Ash* _d	C _d	H _d	N _d	HHV _w
R1. Standard	27.5	70.9	12.7	16.3	46.8	6.2	0.5	14.9
R2. challenge (Card board/paper)	18.6	76.6	13.1	10.3	45.4	6.3	0.3	15.4
R3. challenge (Food)	40.6	72.1	13.3	14.5	48.2	6.4	0.7	12.6
R4. challenge (Plastic, total)	18.0	77.6	10.7	11.7	56.4	6.9	0.3	20.8
R5. challenge (Plastic, PET)	18.0	76.7	12.4	10.9	54.6	6.1	0.3	19.3
R6. challenge (Plastic, PVC)	18.0	76.3	11.4	12.4	51.8	6.4	0.3	19.5
R7. challenge (Plastic, PS)	18.0	78.5	10.3	11.2	59.3	6.7	0.3	21.7
R8. challenge (Wood)	22.1	72.9	16.5	10.7	48.4	6.4	0.4	16.9
Notes:								
Abbreviations: see Table 3.2a.5.								
*Ash content includes Metal, Glass and Miscellaneous waste and others (see Table 3.2a.1)								

Fuel properties of the synthetic fuels are totally determined by their composition and the property of the waste components. According to the standard recipe, **Fuel (R1)** is 27.5% MC (wet basis), 70.9% VM (dry), 12.7% FC (dry), and 16.3% ash (dry). **Fuels (R2-R8)**, based on the challenge recipes (R2-R8), are strongly impacted by their primary components. For example, when food

waste is the primary component (R3), MC is higher than 40% due to the water included in the recipe and the inherent moisture present in the other recipe components. **Fuels (R4-R7)** (Plastics as primary), **Fuel (R2)** (Card board/paper as primary), and **Fuel (R8)** (Wood as primary) have lower MC values of 18-22.1%.

Fuel (R1) has the lowest VM content, 70.9% and the highest ash content, 16.3% among these CB waste fuel recipes. Compared with the others, the fuels with plastics as primary components, **Fuels (R4-R7)**, have higher VM contents, 76-78%. Excluding **Fuel (R1)**, the ash contents of the other CB composite fuel recipes range from 10.3%-14.5%. Values in Table 3.2a.9 are comparable with literature data, for example, Margolin et al. (Margolin et al., 2015) estimated moisture contents for the recipe fuels, R1, R2, R3, R4-7, and R8 of 29.7%, 19.5%, 42.1%, 19.5%, and 22.9%, respectively.

Ultimate analysis results are also listed in Table 3.2a.9. Synthetic fuels with plastics as primary components, **Fuels (R4-R7)**, have higher C contents, from 51.8% to 59.3%, than the other CB recipes, **Fuels (R1-R3)** and **Fuel (R8)**, each with less than 50%. The contents of H and N in all the samples are varied from 6.1 to 6.7%, and 0.3 to 0.7%, respectively. The addition of plastics increased HHV (wet basis), with **Fuels (R4-R7)** HHV $\sim 20 \text{ MJ kg}^{-1}$, compared with the other recipe fuels that range from 12.6 to 16.9 MJ kg^{-1} (wet basis). The reduced HHV results from their higher MC and ash contents.

Fuel Reactivity

Recall that only individual component that generated significant char were selected for fuel reactivity tests, i.e. #1 Cardboard, #2-1 Paper, #2-2 Mixed Paper, #3-1 Dog food, #4-1 PET, #4-3 PVC, #4-6-1 PS1, #5 Wood, #6 Rubber, and #7 Textile. The normalized fractional contributions of each of these components to the char produced from the eight CB waste recipes are presented in Table 3.2a.10. The reaction rates for the composite chars (from the eight recipes) with steam were obtained using Eq. 1 and are presented in Table 3.2a.11.

Figure 3.2a.9 shows simulated conversion curves for the eight CB waste recipe fuels. The y-axis starts at 0.7 showing the end of the devolatilization portion of the curve and highlighting the period from ~ 500 to 3000 s that is dominated by char-steam reactions. Mass losses during this period were calculated from the reactivity data of individual components (Figure 3.2a.6) and the char composition (Table 3.2a.10). The reaction rate curves show a strong dependence on reaction temperature (Figure 3.2a.7(B)) that can be described using the Arrhenius equation.

Table 3.2a.10 Composition ¹ of the CB composite waste fuels (char) that were used to simulate fuel reactivity in steam.

Test components ²	Fuel 1	Fuel 2	Fuel 3	Fuel 4	Fuel 5	Fuel 6	Fuel 7	Fuel 8
#1 Cardboard	0.263	0.251	0.233	0.185	0.159	0.166	0.198	0.140
#2-1 White paper	0.018	0.050	0.015	0.011	0.010	0.010	0.012	0.008
#2-2 Food tray	0.158	0.452	0.134	0.100	0.086	0.090	0.107	0.076
#3-1 Dog food	0.118	0.050	0.227	0.081	0.070	0.073	0.087	0.062
#4-1 PET	0.105	0.042	0.093	0.325	0.443	0.215	0.220	0.056
#4-3 PVC	0.016	0.006	0.014	0.049	0.026	0.228	0.032	0.008
#4-6-2 PS	0.009	0.004	0.008	0.027	0.015	0.018	0.108	0.005
#5 Wood	0.245	0.106	0.212	0.166	0.143	0.150	0.178	0.603
#6 Rubber	0.018	0.013	0.021	0.018	0.016	0.017	0.020	0.014
#7 Textile	0.053	0.026	0.042	0.037	0.032	0.033	0.040	0.028

Note:

1. The composition is calculated by using the selected test components and their normalized contents in the recipes as listed in Table 3.2a.1 and Table 3.2a.2;
2. The test components were selected based on the individual components that have significant amount of FC in proximate analysis and observed char-steam reaction in reactivity tests.

Table 3.2a.11 Simulated reaction rate ($\mu\text{g g}^{-1} \text{s}^{-1}$, ash free) of CB composite waste fuel (char) in steam atmosphere at isothermal temperature of 825, 875, and 925°C.

CB composite Wastes	R1	R2	R3	R4	R5	R6	R7	R8
825 °C	35.1	35.5	40.4	28.4	24.1	37.6	29.7	26.9
875 °C	77.3	73.5	86.3	62.4	54.4	75.0	65.4	71.0
925 °C	133	146	147	108	95.6	125	111	127

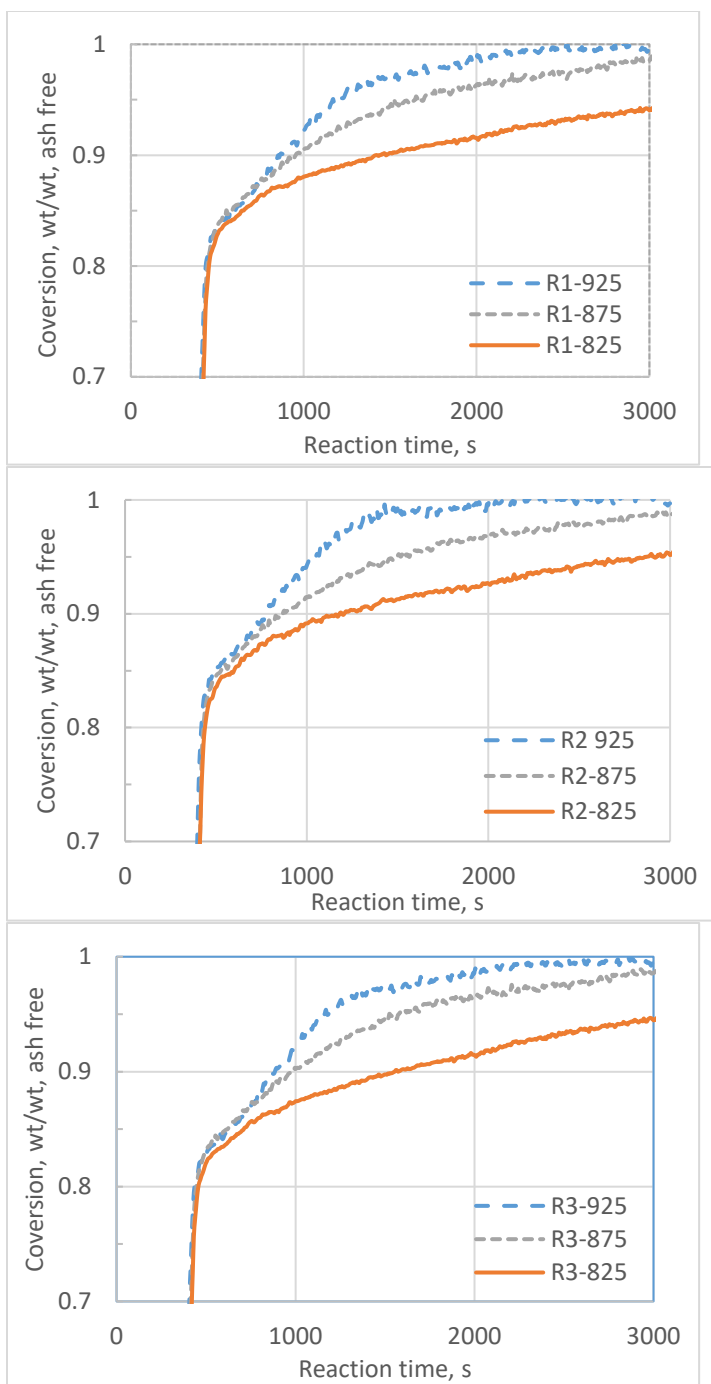


Figure 3.2a.9 Conversion curves of synthetic fuels in steam atmosphere at temperatures of 825, 875, and 925 °C.

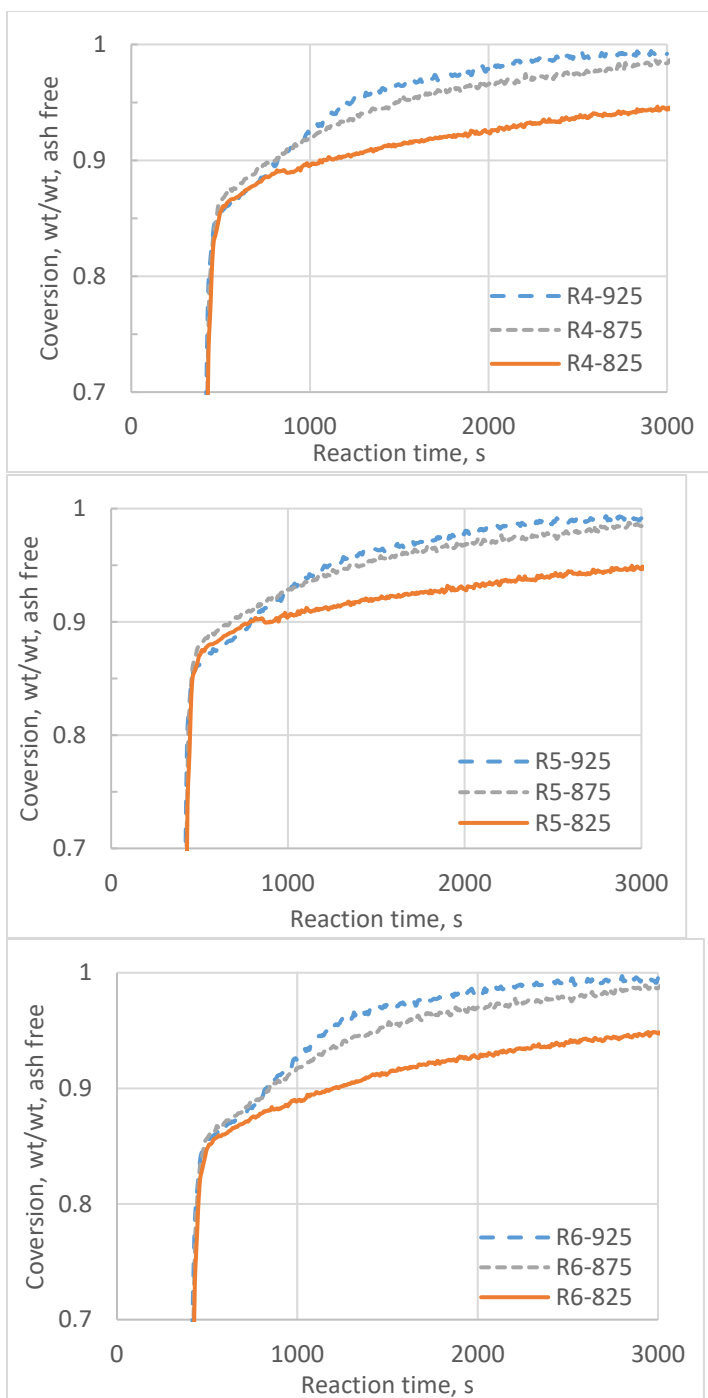


Figure 3.2a.9 (continued) Conversion curves of synthetic fuels in steam atmosphere at temperatures of 825, 875, and 925 °C.

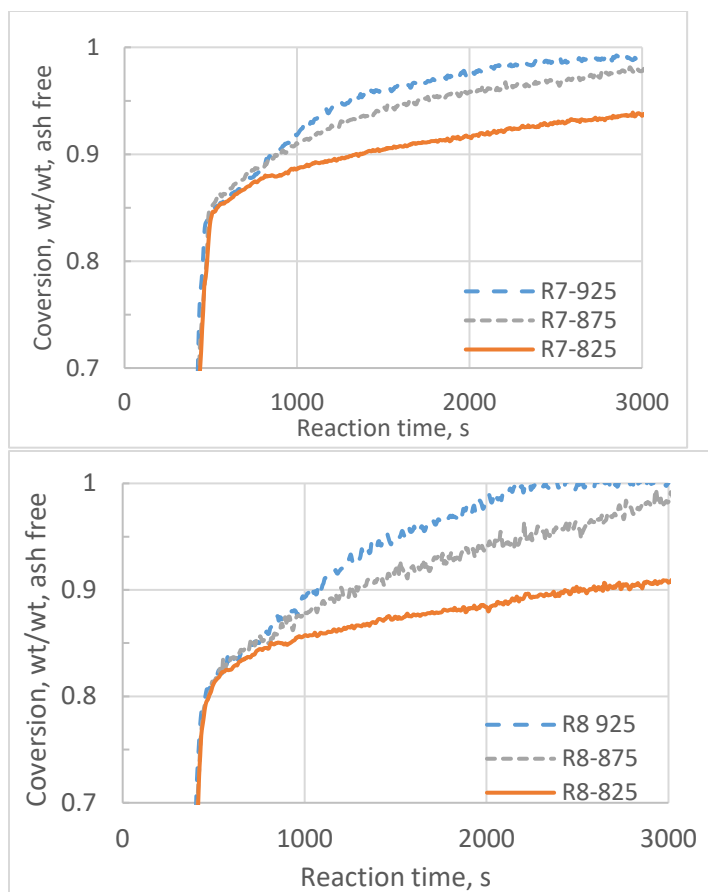


Figure 3.2a.9 (continued) Conversion curves of synthetic fuels in steam atmosphere at temperatures of 825, 875, and 925 °C.

Based on the results in Figure 3.2a.7(b) and Table 3.2a.11, the ranking (high to low) of CB waste recipes for reaction rate of char with steam over the temperature range from 825-925 °C is:

R3 (food) > R2 (cardboard/paper) \approx R1 (standard) \approx R6 (PVC)

> R8 (wood) > R7 (PS) \approx R4 (plastic) > R5 (PET).

The kinetic parameters (E_a and A) and the correlation coefficients (R^2) of $\ln k$ vs $1/T$ calculated using Eq. 7 are presented in Table 3.2a.12. The activation energy (E_a) ranges from 130 to 169 kJ mol⁻¹, with R6 (PVC as primary component) and R8 (wood as primary component) having the lowest and highest values, respectively.

Table 3.2a.11 Simulated reaction rate ($\mu\text{g g}^{-1} \text{s}^{-1}$, ash free) of CB composite waste fuel (char) in steam atmosphere at isothermal temperature of 825, 875, and 925°C.

CB composite Wastes	R1	R2	R3	R4	R5	R6	R7	R8
825 °C	35.1	35.5	40.4	28.4	24.1	37.6	29.7	26.9
875 °C	77.3	73.5	86.3	62.4	54.4	75.0	65.4	71.0
925 °C	133	146	147	108	95.6	125	111	127

Table 3.2a.12. Kinetic parameters of CB composite waste fuel recipe (char) in steam derived from data at temperatures of 825, 875, and 925 °C.

CB composite Wastes/recipes	Pre-exponential factor, s^{-1} (A)	Activation energy, kJ mol^{-1} (E_a)	Correlation coefficient, (R^2)
R1. Standard recipe	2.8E+02	144.7	0.9966
R2. challenge (Card board/paper)	6.7E+02	152.8	0.9991
R3. challenge (Food)	2.0E+02	140.2	0.9974
R4. challenge (Plastic, total)	2.8E+02	144.7	0.9966
R5. challenge (Plastic, PET)	3.3E+02	149.5	0.9969
R6. challenge (Plastic, PVC)	6.5E+01	130.8	0.9987
R7. challenge (Plastic, PS)	2.8E+02	144.7	0.9966
R8. challenge (Wood)	3.2E+03	169.1	0.9911

Fuel Gasification and Product Gas Composition Prediction

Table 3.2a.13 lists the inputs to and outputs from chemical equilibrium calculations for composite CB waste fuels R1-R8 under steam gasification conditions at 850 °C. Results indicate that primary gas products are H_2 , CO_2 , and CO. Results were compared to explore the effects of the fuel composition on gas production and composition as shown in Figure 3.2a.10 and Figure 3.2a.11.

In Figure 3.2a.10, **Fuel (R7)** has the greatest total dry gas production per unit of dry fuel, 0.139 mol g^{-1} , and **Fuel (R4)** follows at 0.134 mol g^{-1} . Fuel (R2) has the lowest gas production, 0.106 mol . The remaining fuels' values range from 0.112 to 0.126 mol g^{-1} . **Fuels (R4-R7)** with plastics as primary components have greater gas production than the others. Gas composition varies with fuel types, 63.8-64.9% for H_2 , 15.7-21.2% for CO_2 , and 14.5-19.6 % for CO. The difference is caused by the elemental composition, as shown in Figure 3.2a.11, where the total gas, H_2 and CO production are plotted against fuel carbon content. CO_2 production is also included but shows no correlation with fuel carbon content. The equilibrium calculations indicate that differences between fuels will affect equilibrium product gas composition and that fuel carbon content is a useful predictor of gas productivity.

Table 3.2a.13. Chemical equilibrium calculation of product composition from steam gasification of CB composite waste fuels.

CB composite wastes	R1	R2	R3	R4	R5	R6	R7	R8
Input (mol)								
C	1	1	1	1	1	1	1	1
H	1.5786	1.6535	1.5822	1.4578	1.3312	1.4722	1.3463	1.5756
N	0.0092	0.0057	0.0125	0.0046	0.0047	0.005	0.0043	0.0071
O	0.4844	0.6234	0.4704	0.3288	0.3864	0.4217	0.2848	0.5289
H ₂ O	2.85	2.94	2.77	2.36	2.44	2.57	2.25	2.76
Output (mol)								
H ₂	1.858	1.793	1.862	1.855	1.769	1.824	1.818	1.812
H ₂ O	1.778	1.972	1.696	1.227	1.331	1.477	1.097	1.732
CO ₂	0.558	0.593	0.546	0.466	0.498	0.517	0.442	0.558
CO	0.440	0.406	0.452	0.531	0.499	0.481	0.553	0.440
CH ₄	0.002	0.001	0.002	0.004	0.003	0.002	0.004	0.000
Others	0.005	0.003	0.006	0.002	0.002	0.003	0.002	0.005
Total gas	4.641	4.767	4.564	4.084	4.103	4.304	3.917	4.548
Total gas (dry)	2.863	2.796	2.868	2.857	2.772	2.827	2.820	2.816
Output (dry gases, % in mol)								
H ₂	64.9	64.1	64.9	64.9	63.8	64.5	64.5	64.4
CO ₂	19.5	21.2	19.0	16.3	18.0	18.3	15.7	19.8
CO	15.4	14.5	15.8	18.6	18.0	17.0	19.6	15.6

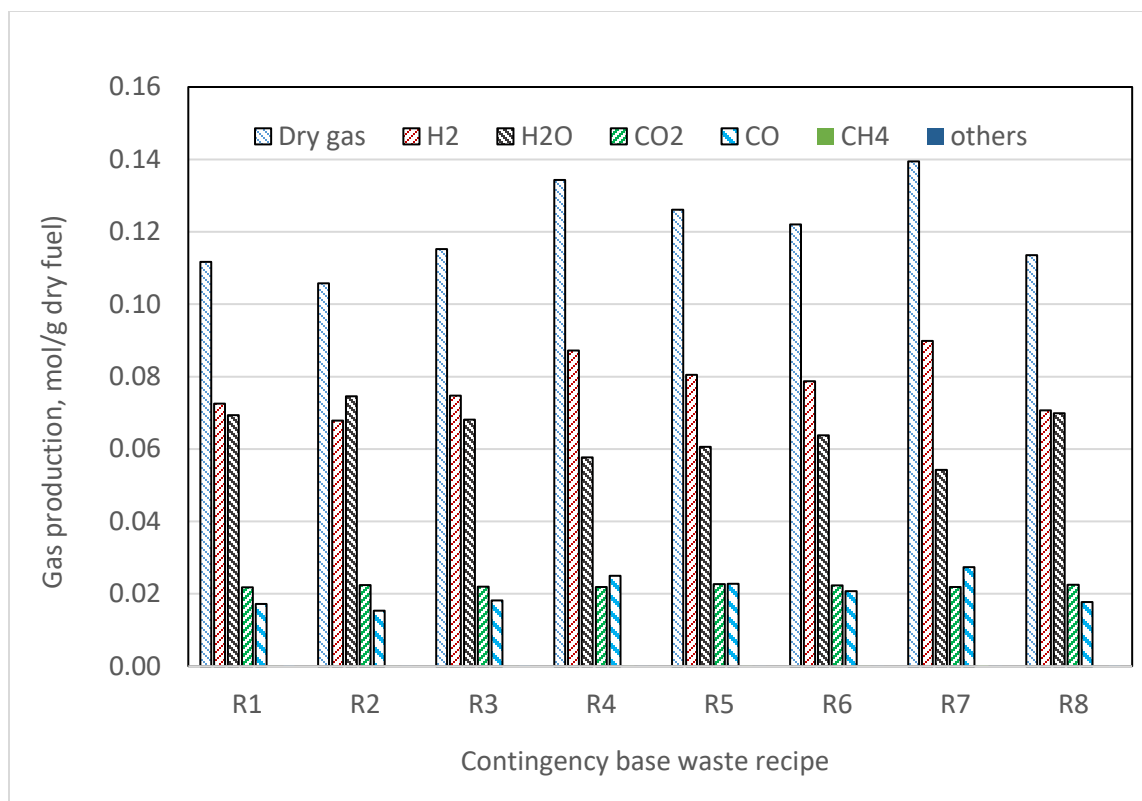


Figure 3.2a.10 Gas production and composition of synthetic waste fuels from Table 3.2a.9 under steam-gasification (850°C). Note: denominators of y-axis values include ash.

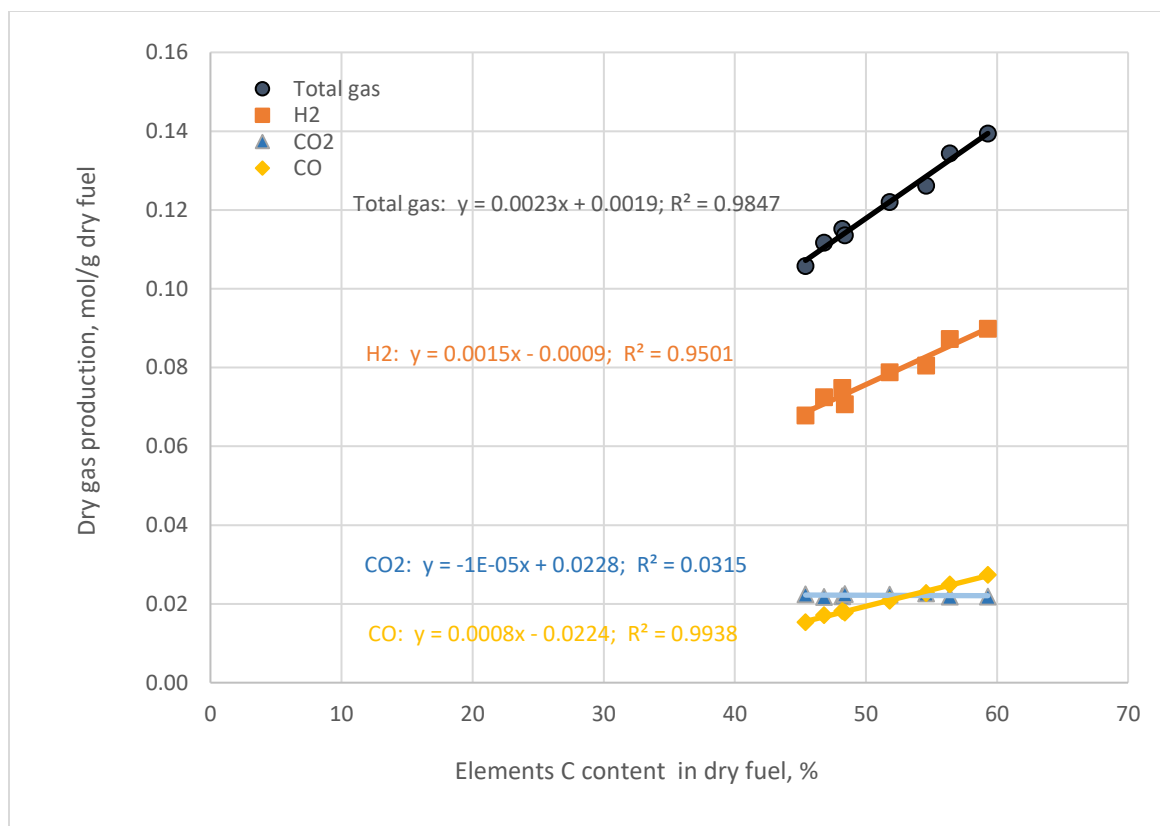


Figure 3.2a.11 Relationship between fuel-carbon content and the gas production including H₂, CO₂, and CO.

Conclusions

Contingency base (CB) waste composition is an important factor in the design of WTE systems that can reduce waste management impacts and contribute to zero footprint camp goals. Individual components of CB waste recipes were subjected to proximate, ultimate and higher heating value analyses. Steam reactivity of chars generated from individual waste components was characterized over a range from 825 to 925 °C and kinetic parameters derived. Data for individual waste components and CB waste recipes were used with a weighted sum approach to predict fuel characteristics and reactivity of the composite heterogeneous waste. Predictions were compared with experimental results for pelleted, composite samples. Syngas production and composition at conditions typical of steam-gasification processes (850 °C) were determined assuming chemical equilibrium. In specific, the current results support the following conclusions:

1. Fuel properties of CB composite waste recipes depend on composition as reflected in differences in ultimate analysis, HHV, and proximate analysis. The plastic components increase carbon content and HHV of the synthetic fuels. Correlations of ultimate analysis and HHV reported in the literature adequately described the relationships for individual CB waste components.

2. The assumption of no significant interactions between individual components of the composite fuels appears valid since the proximate analysis results from individual components successfully predicted the behavior of the composite.
3. Devolatilization and char oxidation defined two stages present in all of the steam reactivity tests. Devolatilization was faster than char-steam reactions, irrespective of devolatilization atmosphere (nitrogen or steam). Steam reactivity of chars derived from the composite waste fuels varied with composition, yielding (under the assumption of Arrhenius kinetics) activation energy values ranging from 130 to 170 kJ mol⁻¹ and pre-exponential factors from 65 to 3200 s⁻¹.
4. Chemical equilibrium calculations indicated that H₂, CO₂, and CO were primary gas products for steam gasification at 850 °C, 1 bar pressure, and a steam to dry fuel ratio of 2:1 by weight. Gas production and composition are affected by sample composition, especially the content of carbon.

References

- Bale, C.W., Pelton, A.D., W.T., T., July, 1996. F*A*C*T 2.1-User's Manual. Ecole Polytechnique de Montreal/Royal Military College, Canada.
- Bhimani, S.M., 2011, May. Experimental characterization of canola oil emulsion combustion in a modified furnace. Thesis of Master of Science. Texas A&M University.
- Cantrell, K.B., Martin, J.H., II, Ro, K.S., 2010. Application of thermogravimetric analysis for the proximate analysis of livestock wastes. J. ASTM Int. 7, No pp. given.
- Cetin, E., Gupta, R., Moghtaderi, B., 2005. Effect of pyrolysis pressure and heating rate on radiata pine char structure and apparent gasification reactivity. Fuel 84, 1328-1334.
- Channiwala, S.A., Parikh, P.P., 2002. A unified correlation for estimating HHV of solid, liquid and gaseous fuels. Fuel 81, 1051-1063.
- Chen, G., Yu, Q., Sjoestroem, K., 1997. Reactivity of char from pyrolysis of birch wood. J. Anal. Appl. Pyrolysis 40,41, 491-499.
- Cozzani, V., Petarca, L., Tognotti, L., 1995. Devolatilization and pyrolysis of refuse derived fuels: characterization and kinetic modeling by a thermogravimetric and calorimetric approach. Fuel 74, 903-912.
- DeGroot, W.F., Richards, G.N., 1991. Gasification of cellulosic chars in oxygen and in nitrogen oxides. Carbon 29, 179-183.
- Fermoso, J., Arias, B., Pevida, C., Plaza, M.G., Rubiera, F., Pis, J.J., 2008. Kinetic models comparison for steam gasification of different nature fuel chars. Journal of Thermal Analysis & Calorimetry 91, 779-786.
- Heikkinen, J.M., Hordijk, J.C., de Jong, W., Spliethoff, H., 2004. Thermogravimetry as a tool to classify waste components to be used for energy generation. J. Anal. Appl. Pyrolysis 71, 883-900.

Kieseler, S., Neubauer, Y., Zobel, N., 2013. Ultimate and Proximate Correlations for Estimating the Higher Heating Value of Hydrothermal Solids. *Energy & Fuels* 27, 908-918.

Kumar, M., Gupta, R.C., 1994. Influence of carbonization conditions and wood species on carbon dioxide reactivity of resultant wood charcoal powder. *Fuel Process. Technol.* 38, 223-233.

Ludwig, C., Hellweg, S., Stucki, S., 2003. *Municipal solid waste management : strategies and technologies for sustainable solutions*. Berlin, New York : Springer.

Margolin, J.A., Marrone, P.A., Randel, M.A., Allmon, W.R., McLean, R.B., Bozoian, P.M., 2015. *Test Standards for CB Waste-to-Energy Technologies*. US Army Research Laboratory

Moilanen, A., Muehlen, H.-J., 1996. Characterization of gasification reactivity of peat char in pressurized conditions. Effect of product gas inhibition and inorganic material. *Fuel* 75, 1279-1285.

Mott, R.A., Spooner, C.E., 1940. The calorific value of carbon in coal: the Dulong relation. *Fuel* 19, 226-231, 242-251.

Raveendran, K., Ganesh, A., 1998. Adsorption characteristics and pore-development of biomass-pyrolysis char. *Fuel* 77, 769-781.

Ruppert, W.H., Bush, T.A., Verdonik, D.P., Geiman, J.A., Harrison, M.A., 2004. *Force provider solid waste characterization study*, U.S. Army Research, Development and Engineering Command Natick Soldier Center.

Umeki, K., Moilanen, A., Gomez-Barea, A., Konttinen, J., 2012. A model of biomass char gasification describing the change in catalytic activity of ash. *Chem. Eng. J. (Amsterdam, Neth.)* 207-208, 616-624.

Valkenburt C., Walton CW., Thompson BL., Gerber MA., Jones SB., DJ, S., 2008. *Municipal Solid Waste (MSW) to Liquid Fuels Synthesis, Volume 1: Availability of Feedstock and Technology*, PNNL-18144, Pacific Northwest National Laboratory, Richland, WA. .

Vounatsos;, P., Atsonios;, K., Agraniotis;, M., Panopoulos;, K., Grammelis, P., 2012. *Report on RDF/SRF gasification properties*.

Zevenhoven, R., Karlsson, M., Hupa, M., Frankenhaeuser, M., 1997. Combustion and Gasification Properties of Plastics Particles. *Journal of the Air & Waste Management Association* 47, 861-870.

Zhou, H., Meng, A., Long, Y., Li, Q., Zhang, Y., 2014. An overview of characteristics of municipal solid waste fuel in China: Physical, chemical composition and heating value. *Renewable and Sustainable Energy Reviews* 36, 107-122.

3.2b Biomass Energy Systems for Remote Applications

The present work investigates the properties and oxidation stabilities of biodiesel derived from catfish oil (B100 CFO) generated by the fish processing plants in Vietnam. The composition and physicochemical properties of the B100 CFO were measured, including oxygen content (~11 wt%), viscosity ($4.5306 \text{ mm}^2 \text{ s}^{-1}$), density (0.8772 g cm^{-3}), peroxide value (28.13 mg kg^{-1}), heat of combustion (39.18 MJ kg^{-1}), and acid number ($0.12 \text{ mg KOH g}^{-1}$). Methyl oleate (46.44 wt%) was the dominant fatty acid methyl ester. B100 CFO was found to have poorer low-temperature quality than most vegetable oil derived biodiesels as determined by fusion and crystallization properties. Novel modified ASTM D5304 and D2274 tests were employed to study the oxidation process of B100 CFO and the impact of oxidation time on its stability. Under ASTM 5304 test conditions, rapid O_2 consumption by B100 CFO occurred after 8 h, behavior similar to commercial biodiesel stabilized with antioxidant additives. The influence of oxidation condition and time on the B100 CFO physicochemical properties and low-temperature qualities was also investigated according to ASTM methods. Three oxidation stages were identified in B100 CFO based on the peroxide value change during the modified ASTM D5304 and D2274 tests. B100 CFO was also found have superior oxidation stability in comparison with B100 derived from waste cooking oil. This is the first report on oxidation stability of B100 derived from catfish oil. Complete details can be found in the publication listed below.

Publications Resulting from these Efforts

Oxidation stability of biodiesel derived from waste catfish oil, Jinxia Fu, Bui Thi Buu Hue, Scott Q.Turn, Science Direct, August 2017, Vol 202, pp 455-463, <http://dx.doi.org/10.1016/j.fuel.2017.04.067>

3.2c High-Rate Anaerobic Digestion

Under previous funding, HNEI conducted research to understand how surface coatings affect biofilm thickness, microbial composition, and biomass activity in a high-rate anaerobic digestion process. Our goal has been to develop the understanding required to produce next generation biofilm carriers that limit growth of biofilms to thin-films possessing highly efficient populations of active methanogenic microbial communities. Based upon results from prior ONR-funded research (soon to be reported under APRISES 12), hybrid chitosan-biochar media supports were shown effective over bulk biochar in terms of *specific* biological oxygen demand (BOD_5) and total suspended solids (TSS) reduction rates, almost by a factor of 5, with all other operating parameters being equal. The hybrid supports, however, tended to swell and promote gas hold up. Under this funding, we focused on further improving the design to eliminate gas hold up and deploying the technology at a demonstration scale.

Under APRISES 12 visual and microscopic inspection of the hybrid support media after six months operation further verified differentiated growth of biofilms, with thick bioactive films observed on the biochar and thinner sparser films on the chitosan surfaces. Although successfully demonstrating the efficacy of the creation of hybrid supports possessing surfaces of biofilm inhibiting and stimulating materials, the chitosan component of the material exhibited significant swelling after six months of operation. The swelling ultimately imposed resistance to fluid flow

through the reactor which, although not an issue at lab scale, would not be acceptable at demonstration or industrial scale as it would ultimately impose too great a pressure head. To address this issue, in APRISES13 we modified the hybrid support material to comprise biochar islands attached to thin strips of polyvinyl chloride which possess low surface energy and to which biofilms bond poorly. As such, it was hypothesized that the internal recycle applied to the bioreactors would provide internal fluid currents that would be sufficient to dislodge biofilms and, in the process, repeat the results of the chitosan-biochar hybrid supports yet without the swelling of the chitosan films.

To test these results, the modified hybrid supports were suspended in the same reactor configuration as used to test the chitosan-hybrid materials. Reactor conditions were similar across all operating parameters except the feed stream to be treated was a simulated wastewater composition as opposed to grease trap wastewater. More specifically, the feed provided to the reactor was comprised of sodium acetate trihydrate (for carbon) at 3067 mg/l, peptone, meat extract, and urea (for nitrogen) at 614 and 1406 and 383 mg/l, respectively, and a range of minerals and salts. After six months of operation (OLR of 3.31 kg COD/m³/d) BOD₅ and COD reduction rates of 94.04 and 93.03 % were achieved. Total suspended solids were largely removed (digested) and volatile organic acids were not in detectable concentrations.

Visual inspection of the packing materials show good integrity of the biochar, no swelling effects, and thick films coating the biochar with thin and sparse films covering the PVC surfaces between them. To date we have completed lab scale fabrication and evaluation of several methods to produce biochar based filamentous biofilm supports – including PVC filamentous ribbons coated with biochar powder. In future funding we look to test these hybrid supports under which wastewater containing contaminants of emerging concern as well as pathogens relevant to wastewater treatment are examined.

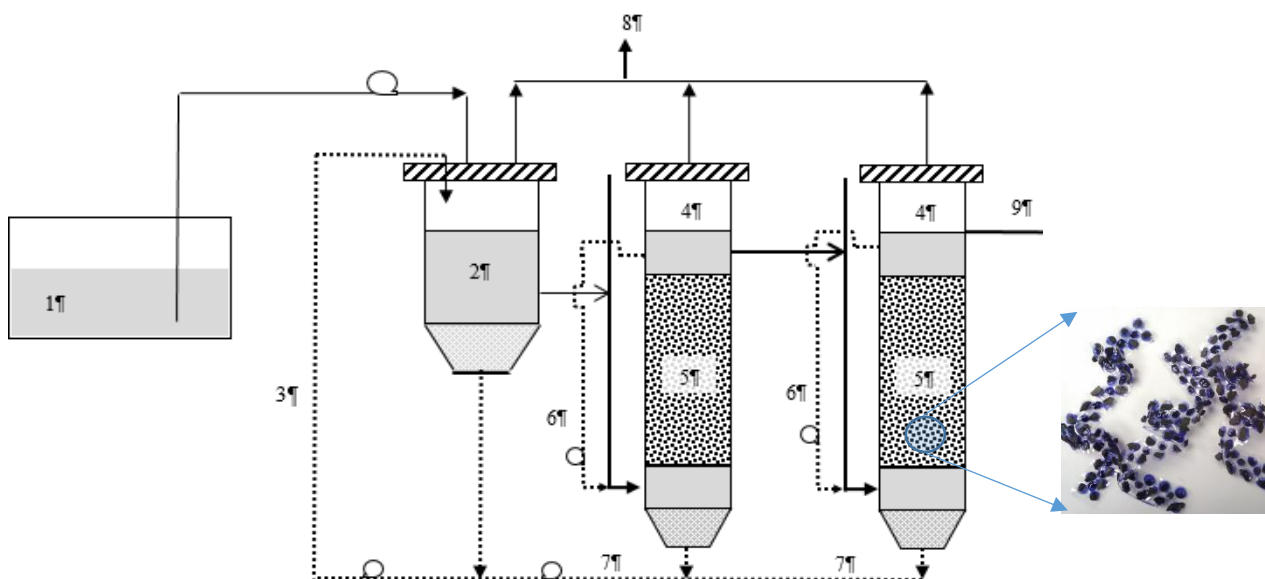


Figure 3.2c.1. Legend: (1) Wastewater Feed; (2) Hydrolysis Reactor; (3,7), Solids Recycle; (4) Anaerobic Reactors; (5) Hybrid PVC-Biochar Packing Material (see insert); (6) Internal Recycle Loops; (7) Aerobic Recycle; (8) Biogas; (9) Effluent.

3.2d Liquid fuels from Synthesis Gas

This task aims to develop a new technology to produce liquid fuels from syngas (H_2 , CO , and CO_2). In a novel bioreactor developed at HNEI, a hydrogen-oxidizing bacterium can produce a large amount of polyhydroxybutyrate (PHB, $C_4H_6O_2$) from CO_2 . Under controlled conditions, the PHB content accounts for 60 wt% of the dry cell mass. In previous work, the biopolyester was liquefied via a conventional thermal liquefaction reaction, generating a liquid of low heating value because of a high residual oxygen content. Deoxygenation of PHB is therefore a key operation in producing hydrocarbon oil for high grade liquid fuels. In this work, a solid phosphoric acid (SPA) catalyst was investigated to reform PHB into hydrocarbon oils [1]. The catalyst has been used in oil refineries for propylene oligomerization and alkene alkylation.

Method and Results

Solid phosphoric acid (SPA) catalyst. The SPA catalysts were prepared by following a published protocol [2]. Specifically, the catalyst was activated in air at temperatures of 420 °C, 560 °C and 720 °C, and labeled as SPA420, SPA560, and SPA720, respectively [3]. The solid acid contains active phosphoric acid species (i.e. H_3PO_4 , $H_4P_2O_7$ and $H_5P_3O_{10}$) covalently bonded with silicon, and the acid content can be controlled for desired performance. The catalyst was ground into powder and mixed with PHB powder at predetermined mass ratios for reactions. The acid content of a fresh or used catalyst was determined by titration with a base solution, and the total acid was

determined by boiling the SPA solids in water for 60 min to hydrolyze the silicon ortho- and pyro-phosphates, thereby releasing the fixed phosphoric acid from silica.

Reaction temperature measured with Differential Scanning Calorimetry (DSC).

The solids of PHB, SPA, and their mixture were heated in a differential scanning thermal analyzer under a N₂ stream [1]. PHB is a polyester with high crystallinity (60-70%) and it melted around 170 °C, resulting in an endothermic peak in the DSC thermogram (not shown here). The solid-to-liquid phase change absorbed 62.8 J per g PHB. The DSC thermogram of catalyst SPA420 on its own has a stable base line without substantial heat release and absorption, indicating little phase change, reaction or mass loss during the heating. In contrast, the DSC thermogram of PHB and SPA420 mixture exhibits a huge sharp endothermic peak at 212.5 °C as shown in Figure 1, followed by five small endothermic peaks between 215 and 230 °C. It indicates that the catalytic PHB reforming is an endothermic reaction, absorbing 360 J per g PHB. The major reaction occurs at 212.5 °C in a very short period of time. The following small endothermic peaks might reflect the continuing reactions of major intermediates that occurred at higher temperatures. A reaction temperature of 240 °C is therefore sufficient for complete PHB conversion. It should be pointed out that this reaction temperature is quite low in comparison with the high temperatures (500 – 650 °C) of conventional biomass liquefaction. The mild reaction conditions could provide some advantages in reactor cost, energy consumption, and operation expenses.

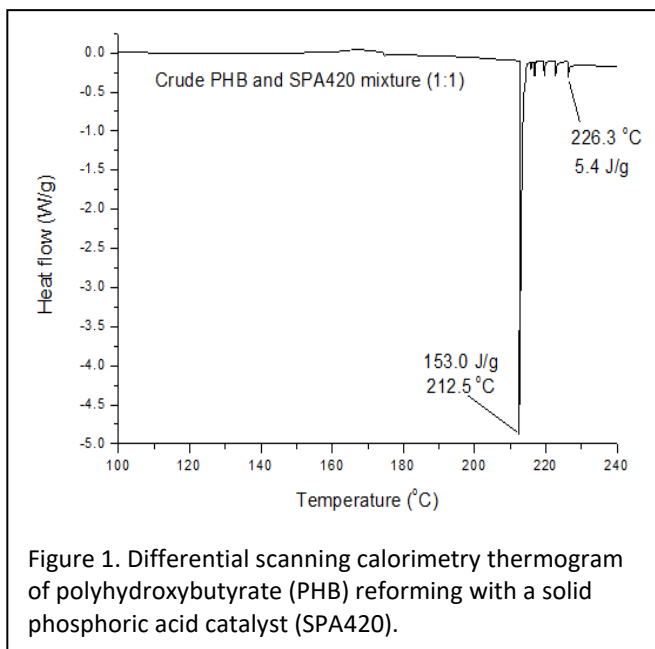


Figure 1. Differential scanning calorimetry thermogram of polyhydroxybutyrate (PHB) reforming with a solid phosphoric acid catalyst (SPA420).

Hydrocarbon oils from catalytic PHB reforming.

Pre-determined amounts of PHB and catalyst were heated in a thermal reactor (Parr Instrument Co. USA) under nitrogen to 240 °C and maintained for 6 hours. After the reactor was cooled down to 40 °C, the gas products were measured with a gas chromatograph. The reactor was then connected to a cooling and condensing system as shown in Figure 2. Under slow visible bubbles of N₂ in the collector, the reactor was heated slowly and the reaction products were evaporated and condensed in the collectors. The liquid products were collected in two temperature ranges: a light oil from 40 °C to 240 °C and a heavy oil from 240 °C to 310 °C. Aqueous solutions formed in the reaction were also collected and separated from the oils in a separating funnel. The SPA catalyst in the reactor was finally collected as a dry solid. Some char-like byproducts were deposited on SPA and their mass was determined based on weight increase of the SPA solid.

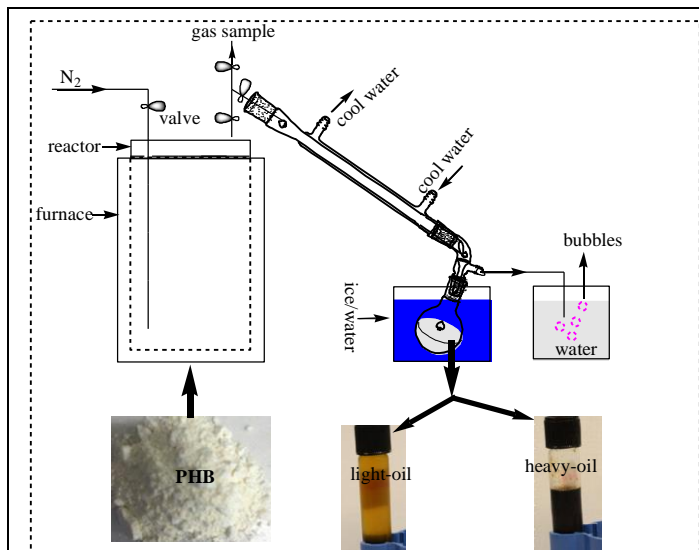


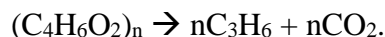
Figure 2. Schematic diagram of a laboratory facility for oil production and separation.

The reaction products were distributed among three phases: a gas phase (CO₂, propylene and CO), a liquid phase (hydrocarbon oils and an aqueous solution), and a solid phase (char-like deposit on SPA). Table 1 gives the mass yields of major products and the overall mass recovery (89 – 98 wt%) based on the initial mass of PHB feedstock. Interestingly, the gas products accounted for 48 – 53 wt% of the raw PHB. FT-IR spectra of gas samples reveal that CO₂ and propylene were the main products while CO was a minor one. It was further confirmed that CO was primarily formed from the residual cell mass in the PHB feedstock.

Table 1. Mass recovery and product yields of PHB reforming on SPA420 catalyst

PHB (wt%)	PHB: SPA (g : g)	CO ₂ (wt%)	C ₃ H ₆ (wt%)	CO (wt%)	Light-oil (wt%)	Heavy-oil (wt%)	Water (wt%)	Solid residue (wt%)	Mass recovery (wt%)
98	1:1	41	9	0	23	7	7	7	94
87	2:1	29	17	2	13	6	6	16	89
87	1:1	35	16	2	19	5	7	12	96
87	1:2	39	9	2	22	6	8	12	98

Formation of a large amount of CO₂ and C₃H₆ reflected a main reaction of PHB deoxygenation:



Under SPA catalysis, propylene was further oligomerized into hydrocarbon oil. The theoretical yield for this process is 48.8 wt%. Under these experimental conditions, the yields of light oil and heavy oil were 23 wt% and 7 wt%, respectively, and the total oil yield was 30 wt%, or 61% of the theoretical yield. The high yield of propylene (9 wt%) indicates that propylene oligomerization was not completed, resulting in a reduced oil yield. If propylene can be completely converted into oil, the yield could reach 80% of the theoretical value. The mass ratio of PHB to SPA was a determining factor on the yields of oil and propylene. With a crude PHB feedstock (87% PHB), the total oil yield was 28 wt% with 9 wt% of propylene yield at a high SPA dosage (crude PHB: SPA420 = 1:2), but the oil yield dropped to 19 wt% with the propylene yield being increased to 17 wt% at a low SPA dosage (crude PHB: SPA420 = 2:1).

A small amount of aqueous solution (7 wt%) and char-like solid (7 wt%) were also formed from PHB, which might reflect a minor reaction of PHB deoxygenation:



The aqueous solution contained some water soluble compounds, accounting for about 6 wt% of organic carbon. Under typical reaction conditions, less than 20% of oxygen in PHB was removed as water. The high bacterial residue of crude PHB generated more solid byproducts (12 – 16 wt%). Indeed, no liquid oil was formed from the residual cell mass in a control experiment.

Characterization of PHB oils. The light oil derived from PHB is a yellowish transparent liquid with a boiling point range between 40 °C and 240 °C, and the heavy oil is a dark brownish liquid with a boiling point range between 240 °C and 310 °C. Their FT-IR spectra (Figure 3) are quite similar, exhibiting the methyl and methylene groups (3080 cm⁻¹ – 2820 cm⁻¹), carbonyl groups (1700 cm⁻¹) and aromatic groups (1450 cm⁻¹ to 1650 cm⁻¹). Chemical analysis of the oils further confirmed the presence of alkanes, alkenes, aromatics, and oxygen-containing ketones [1]. By comparing the FT-IR spectra, one can find that the relative content of carbonyl groups (C=O) of heavy oil was higher than that of light oil. This is confirmed with the elemental analysis of the oils as shown in Table 2.

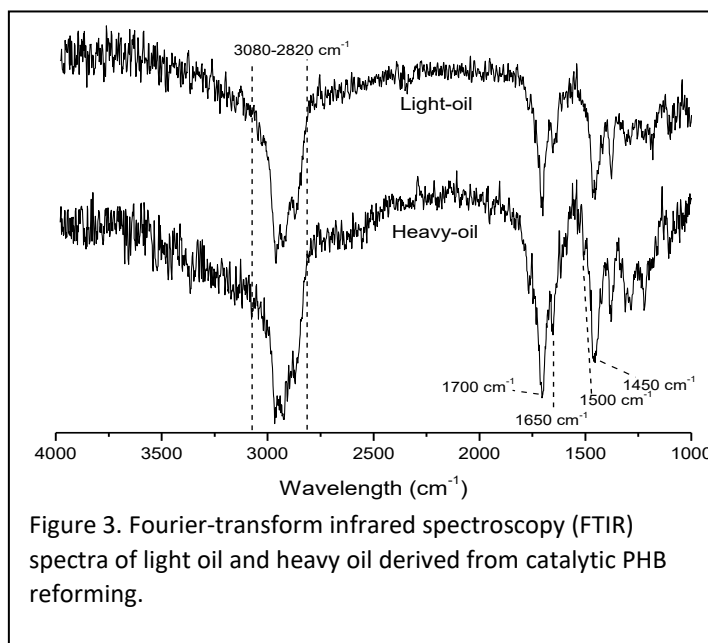


Figure 3. Fourier-transform infrared spectroscopy (FTIR) spectra of light oil and heavy oil derived from catalytic PHB reforming.

Table 2. Comparison of the oils derived from PHB with commercial gasoline and biodiesel^a.

	Gasoline	Light oil	Heavy oil	Biodiesel ^b
BP (°C)	40-200	40-240	240-310	182-338
C (wt%)	80.40	81.37	79.38	76.96

H (wt%)	12.30	11.30	9.67	11.85
N (wt%)	0.15	0.14	0.23	-
O (wt%)	7.15	7.19	10.72	11.19
HHV (MJ/kg) ^c	41.8	41.4	38.4	39.7

- The commercial gasoline, light oil and heavy oil were blind samples analyzed by Hazen Research Inc.
- The properties of commercial biodiesel are cited from reference [4].
- High heating value (HHV) of liquid fuels

The oxygen content of the fuels is calculated by rounding the major elements (C, H, O and N) up to 100 wt%, not including the minor elements (S, P, etc.). The light oil contains less oxygen (7.19%) than the heavy oil (10.72%). Correspondingly, the high heating value (HHV) of light oil (41.4 MJ/kg) is higher than that of heavy oil, (38.4 MJ/kg). Importantly, the HHVs of two PHB oils are very close to those of commercial gasoline (41.8 MJ/kg) and biodiesel (39.7 MJ/kg), respectively. According to the boiling point range, HHV and elemental composition, the light oil is a gasoline-grade fuel and the heavy oil a biodiesel-grade fuel.

Chemical composition of PHB oil. The major chemicals of hydrocarbon oil were identified by using a gas chromatograph equipped with a mass spectrometer detector (GCMS) and the relative composition was determined based on the peak areas of the compounds [1]. The hydrocarbons can be divided into five groups: alkenes, alkanes, benzenes, naphthalenes and oxygen-containing compounds as shown in Table 3. Alkenes and benzenes are the predominant chemicals and their relative compositions varied, depending on the activation temperature and repeated uses of the catalyst. A SPA activated at 720 °C (SPA720) generates more alkenes and less aromatics than a SPA activated at 420 °C (SPA420). This might be related to the type and content of active phosphoric acid species in the catalysts. Interestingly, the repeated use of the same batch catalyst (SPA420) also affects the oil composition, alkenes and aromatics in particular. Since aromatics have a high octane number (> 100) and high energy content, PHB oil could be a good source of bio-based aromatics that can improve the energy content and performance of conventional fuels in modern gasoline engines. Alkenes, on the other hand, are a major group of jet fuel for modern turbine engines. In Table 4, the major hydrocarbons are divided into groups according to their carbon numbers. Smaller (<C6) and larger (>C18) hydrocarbons were not detected in the oils. On a fresh catalyst, hydrocarbons with C9, C10 and C13 were the main products under the typical reaction conditions, primarily alkenes (C9) and alkyl benzenes (C10 and C13). The influence of catalyst reuse can also be found on the molecular mass of hydrocarbons.

Table 3. The major chemical groups and their distribution in PHB oils^a

Catalyst ^b	Alkenes (%)	Alkanes (%)	Benzenes (%)	Naphthalenes (%)	Oxygenated ^c (%)	Total aromatics (%)
SPA420 (fresh)	2.6	0.9	65.8	11.2	19.6	77.0
SPA560 (fresh)	6.2	2.4	63.1	9.1	19.2	72.2

SPA720 (fresh)	22.5	3.1	50.9	3.8	19.6	54.7
SPA420 (used 4 th)	49.4	0	39.7	0.8	10.2	40.5
SPA420 (used 7 th)	57.0	0	31.1	2.0	9.9	33.1

a. Based on peak area percentage of GCMS chromatograms

b. SPA: PHB (98 wt%) = 1:1 mass ratio

c. Oxygen-containing compounds

Table 4. Carbon numbers of major hydrocarbons in PHB oil^a

Catalyst ^b	C ₆ (%)	C ₇ (%)	C ₈ (%)	C ₉ (%)	C ₁₀ (%)	C ₁₁ (%)	C ₁₂ (%)	C ₁₃ (%)	C ₁₄ (%)	C ₁₅ (%)	C ₁₆₋₁₈ (%)
SPA420 (fresh)	0.1	0.4	1.0	9.0	25.8	6.6	8.1	34.9	9.3	3.0	1.8
SPA560 (fresh)	0.2	1.8	2.6	12.8	30.0	4.1	6.3	33.1	5.5	3.5	0
SPA720 (fresh)	0.2	1.1	3.4	28.5	24.2	1.9	3.6	32.3	4.1	0.6	0
SPA420 (used 4 th)	0.9	2.7	3.7	46.3	19.7	2.4	3.8	19.6	0.9	0	0
SPA420 (used 7 th)	3.1	2.2	3.7	55.7	11.7	1.1	3.2	17.0	2.2	0.1	0

a. Based on the peak area percentage of GCMS chromatograms

b. SPA catalyst : PHB (98 wt%) = 1:1 mass ratio

Influences of catalyst activation temperature and dosage. As shown above, the oil composition was affected by SPA catalyst, including its activation temperature, dosage and reuse. As shown in Table 3, the total aromatics, based on the GCMS peak areas, declined from 77.0% on fresh SPA420 (activated at 420 °C) to 54.7% on fresh SPA720 (activated at 720 °C). This is attributed to the decrease of total solid acid with activation temperature. The total acid content of SPA420 is 79 wt% (as H₃PO₄ wt% in SPA), declined to 71 wt% of SPA560, and further to 37 wt% of SPA720.

The catalyst dosage affects the oil composition, too, as shown in Table 5. A high mass ratio of PHB to catalyst (4:1) generated a large amount of oxygen-containing compounds (82 wt%), indicating a low extent of polyester deoxygenation. The oxygenated compounds, however, can be reduced to a very low level (<9 wt%) with a high catalyst dosage (PHB:SPA=1:3). Interestingly, the aromatics content also reached a very high level (88.6%), composed of 73% benzenes and 15% naphthalenes with the high catalyst dosage. This observation indicates that the oil composition can be controlled in quite a broad range by adjusting the catalyst dosage.

Table 5. Effect of SPA420 dosage on oil composition ^a

PHB:SPA (wt : wt) ^b	Alkenes (%)	Alkanes (%)	Benzenes (%)	Naphthalenes (%)	Oxygenated (%)	Total aromatics (%)
-----------------------------------	----------------	----------------	-----------------	---------------------	-------------------	------------------------

4 : 1	0.0	1.4	16.6	0	82.0	16.6
2 : 1	8.6	3.6	46.6	0.5	40.6	47.1
1 : 1	22.1	0.4	53.1	3.0	21.4	56.1
1 : 2	1.5	0.6	73.0	13.2	11.6	86.2
1 : 3	0.8	1.9	73.5	15.1	8.7	88.6

- a. Based on peak area percentage of GCMS chromatogram
- b. Mass ratio of PHB (98 wt%) to fresh SPA420

Catalyst reuse. Catalyst reuse and life time is important when considering economic factors and oil costs. After the reaction in this experiment, some char-like byproducts were deposited on the catalyst, causing catalyst deactivation. In comparison with a fresh SPA (Figure 4A), the surface image of a used SPA catalyst is shown in Figure 4B. The elemental contents of catalyst surface were determined with energy dispersive spectroscopy (EDS). The deposit covered the catalyst surface and the active phosphoric acid species, resulting in a decrease of phosphorous (P) content from 22.8 wt% to 17.49 wt% while an increase of carbon content from 7.57 wt% to 25.54 wt%. The char-like deposit could be partially removed by re-calcination at 420 °C (Figure 4C) or by washing with methylene chloride (Figure 4D). A substantial amount of byproducts could be dissolved in methylene chloride and the washed catalyst surface had a similar P and C content of the fresh SPA. The recovered SPA catalyst after solvent wash was reused for PHB reforming. In the repeated use of a SPA420, it was found that the oil composition changed with the reuse time. As shown in Table 3, the relative content of aromatics decreased while the relative content of alkenes increased with catalyst reuse. This is attributed to a change in type and content of the solid acid of the catalyst. After four repeated reuses, for example, the total solid acid content of the catalyst declined from 79% for a fresh SPA420 down to 60 wt%, and after seven repeated reuses to 49%. Correspondingly, the free acid of total acid was increased significantly. The so called free acid is the acid that can be quickly released into water because of their weak association with silicon matrix. The decrease of total acid with increase in free acid might be attributed to water hydrolysis by the water formed in the reaction. Under the reaction conditions (240 °C for 6 hours), the product water could hydrolyze and dissociate the solid phosphoric acid from the silicon matrix and may even destroy the catalyst's solid matrix, generating a soft mud-like solid. This problem may be solved by removing the product water once it was generated.

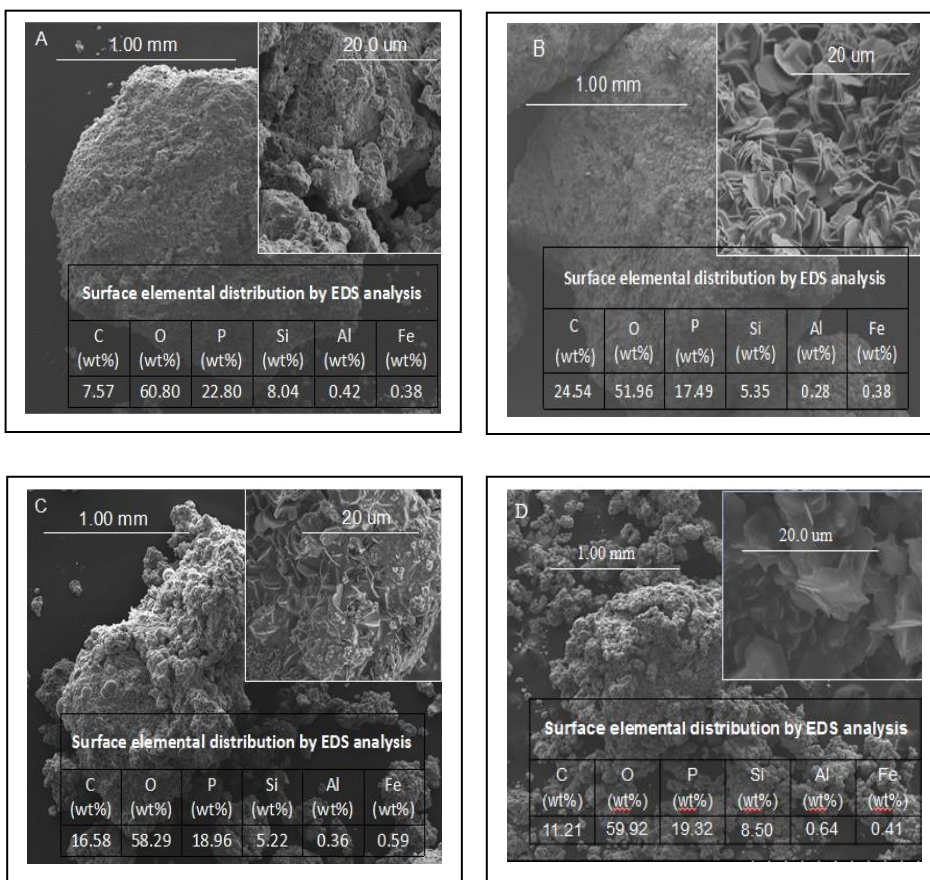


Figure 4. Scanning electronic microscopy (SEM) images and energy dispersive spectroscopy (EDS) analysis of SPA420 catalysts: (A) a fresh catalyst; (B) a used catalyst without treatment; (C) a used catalyst after re-calcination at 420 °C; and (D) a used catalyst after methylene chloride wash.

References

- [1] Kang S, Yu J. A gasoline-grade biofuel formed from renewable polyhydroxybutyrate on solid phosphoric acid, *Fuel* 2015; 160:282-290.
- [2] Prinsloo NM. Preparation of a solid phosphoric acid catalyst from low-quality kieselguhr parameters controlling catalyst quality and performance. *Ind Eng Chem Res* 2007; 46: 7838-43.
- [3] Ohtsuka H, Aomura K. Activation of solid phosphoric acid by heat treatment. *Bull Jpn Petrol Inst* 1962; 4: 3-14.
- [4] Tyson KS. Biodiesel handling and use guidelines. DIANE Publishing 2009.

3.2 e) Bio-contamination of Fuels

Evidence suggests that all fuels are susceptible to bio-contamination resulting in microbial induced corrosion of fuel system components and fuel degradation. These problems are often associated with the presence of water. Furthermore, tactical fuels often have specific purity requirements, subjecting them to higher standards. For this reason, comparisons of tactical fuels with other blends of fuels are not universally applicable. Also, the recent trend toward blending of fuels from renewable resources has the potential to introduce contamination issues not previously seen, ranging from biological contamination to chemical stability. In this task, we will conduct research to inform the development of capabilities to (1) rapidly detect the presence of microbial populations in fuels, specifically those associated with fuel degradation, and (2) design inhibitors to combat the microbial degradation of fuel. Characterization of the eukaryotic degradation pathways were used to expand the database of genetic information that will serve as the basis for rapid-detection, fuel-test capabilities and design of inhibitors that can be added to fuels to prevent microbial degradation.

To further our understanding of the metabolic pathways associated with the degradation of fuels we have previously isolated a biological fuel contaminant, *Moniliella wahieum*. To determine this metabolic pathway, we are seeking to obtain a relatively comprehensive genome analysis for *M. wahieum* and also its gene annotation. This analysis has encountered many problems associated with difficulty in getting high-quality DNA and its subsequent analysis. While previously generated sequenced data from both the University of Hawaii, Advanced Studies in Genomics, Proteomics and Bioinformatics (ASGPB) and the University of Washington, PacBio Sequencing Services center (GS-PACBIO) facility resulted in useful data, the investigation was incomplete. The continued generation of genome sequence data was performed at the Duke Center for Genomic and Computational Biology (DUGSIM), using newer 3rd generation sequencing protocols (SMRT), as a paid service. Analysis of the data is performed at HNEI. Comparatively, 3rd generation techniques can overcome short sequence reads that are problematic for eukaryotic genomes which have many repeats. Furthermore, an enhanced method for extracting DNA is being utilized that is resulting in the production of higher quality DNA extracts. DNA extraction first involved the removal of produced polysaccharides followed by the enzymatic digestion of the glucan and chitin components of the cell wall.

Initial results from DUGSIM generated almost 4 Gbp of polymerase read data. A preliminary assembly using the Falcon assembler suggests that nearly 50% genome coverage was achieved (Figure 1). The 50% coverage is based upon the *Moniliella sp.* MCA 3643 v1.0 genome analysis described within the JGI mycocosm database (<https://genome.jgi.doe.gov/Monili2/Monili2.info.html>).

Extracted DNA samples were again sent to Duke to increase the genome sequence coverage, this time utilizing 2 SMRT cells. Results from this analysis generated over 10 Gbp of polymerase read data, but are still requiring assembly. Repository of the genome project data has been initiated with the National Center for Biotechnology Information (NCBI) and can be found under accession number PRJNA433019 (<https://www.ncbi.nlm.nih.gov/bioproject/433019>).

Extensive annotation and assembly are also still required. However, an example for metabolic pathway elucidation is provided using the initial results showing the genome presence of enzymes associated with catabolic beta-oxidation (Figure 2).

Under APRISES13, it was determined that the degradation of diesel was enhanced through a cometabolic process in the presence of biodiesel fuel. In this study, a statistical analysis was performed using previous results with *Moniliella wahieum*, was able to show a higher than 30% increase in the rate that diesel fuel was biologically oxidized (Ye *et al.* 2017). Alkanes first undergo omega-oxidation and are subsequently processed for beta-oxidation. Biodiesel influenced upregulation of a metabolic intermediary, pathway or specific enzyme produced also have impacts on the diesel alkanes. The upregulated metabolism has strong implication for considerations involving the blending of fuels.

Again utilizing *M. wahieum* as a model organism, it was also determined that nanoparticles could be used to inhibit biological growth. Two different compounds were investigated to assess its impacts on *M. wahieum* growth. It was decided that AgO, which is commonly used for biological sterilization, was able to inhibit growth at a concentration of only 12 ppm (Zhang *et al.* 2018). From these results, the potential use of nanoparticle silver has the potential for biological inhibition of water contaminated biofuels or blended fuels. Examination in a blended fuel environment however, requires further examination.

Publications Resulting from these Efforts

Ye C., Ching T.H., Yoza B.A., Masutani S.M., Li Q.X. 2017. Cometabolic degradation of blended biodiesel by *Moniliella wahieum* and *Byssochlamys nivea* M1. *Intern. Biodeter. Biodegrad.* 125; 166-169

Zhang L., Li Q.X., Zhou L., Liang H., Qin H., Masutani S. Yoza B. 2018. Toxicity of lanthanum oxide nanoparticle to the fungus *Moniliella wahieum* Y12 isolated from biodiesel. *Chemosphere.* 199; 495-501

3.2f Biofuel Corrosion Control

The substitution of biofuels for conventional fuels such as F-76 can result in unexpected issues and forms of corrosion, which may affect normal operational procedures. Under APRISES11, we showed that corrosion rates of 1018 plain-carbon steel (UNS G10180) in the seawater-fuel mixtures were driven by oxygen reduction and were highest in HRD-76, followed by the F-76/HRD-76 blend, and then F-76. This ordering corresponded to that of the dissolved-oxygen diffusion coefficients which were also ordered (from highest to lowest) as HRD-76, blend, and F-76. White precipitate (i.e., carbonates and hydroxides) formation in the fuel layer was found primarily only on the steel samples exposed to the HRD-76/seawater mixtures. The precipitate formation was likely induced by a high amount of oxygen reduction (in the fuel layer) that

generated OH^- , which precipitated the carbonates and hydroxides. Under APRISES13, corrosion inhibitors were investigated to attenuate corrosion in the HRD fuel/seawater mixtures. An oxygen scavenger (i.e., sodium sulfite, Na_2SO_3) and various cathodic corrosion inhibitors (i.e., zinc chloride, ZnCl_2 ; and sodium phosphate, NaPO_4) were evaluated to determine if the corrosion rates could be attenuated in HRD-76/ASTM seawater mixtures. Experiments were conducted in the aerobic and anaerobic conditions at room temperature. The HRD-76 fuel was unfiltered. The corrosion of the steel samples was characterized visually, and by measuring weight loss.

To attenuate corrosion, an oxygen scavenger (i.e., sodium sulfite, Na_2SO_3) and various cathodic corrosion inhibitors (i.e., zinc chloride, ZnCl_2 ; sodium phosphate, NaPO_4) were evaluated. Experiments were conducted in the HRD-76/ASTM seawater mixture in the aerobic and anaerobic conditions at room temperature ($\approx 25^\circ\text{C}$). The HRD-76 fuel was unfiltered. The corrosion of the steel samples was characterized visually, and by measuring weight loss. The Na_2SO_3 oxygen scavenger and ZnCl_2 and NaPO_4 cathodic inhibitors were initially used in concentrations of 10 mg/L, 10 mg/L, and 20 mg/L, respectively, either individually or mixed together (i.e., ZnCl_2 and NaPO_4), but did not have any significant effect on the corrosion rate, which is likely due to the very high chloride concentration in the ASTM seawater. The oxygen scavenger and inhibitor concentrations were then increased by an order of magnitude to 100 mg/L, 100 mg/L, and 200 mg/L for Na_2SO_3 , ZnCl_2 and NaPO_4 , respectively, when used individually or mixed (i.e., ZnCl_2 and NaPO_4). The average corrosion rates decreased by 12%, 10%, 13%, and 26%, respectively, for Na_2SO_3 , ZnCl_2 , NaPO_4 , and mixture of ZnCl_2 and NaPO_4 . The compounds are salts and need a polar water-based solvent to dissolve. Hence, these inhibitors are likely only concentrated in the water phase and not the fuel. Corrosion on the coupons was only significant in the water layer.

Materials

ASTM Seawater

The synthetic, artificial seawater specified in ASTM D1141-98 was used in these experiments.

1018 Steel

Plain carbon 1018 steel (Unified Numbering System for Metals and Alloys specification UNS G10180) was chosen for investigation based on its similar chemical composition to that of ASTM A36 steel and API Spec 5L X60, which are often used for fuel storage tanks and pipelines. Chemical composition of 1018 steel reported by the UNS specification was 0.15-0.20% carbon, 0.60-0.90% manganese, 0.04% max. phosphorus, 0.05% max. sulfur, with the balance percent as iron.

Corrosion Inhibitors

An oxygen scavenger and corrosion inhibitors were investigated for the attenuation of corrosion for the 1018 steel in the HRD F-76 fuel/ASTM seawater mixture. The oxygen scavenger and corrosion inhibitors were added to the ASTM seawater in the following concentrations: 10 mg/L Na_2SO_3 oxygen scavenger; 10 mg/L ZnCl_2 cathodic inhibitor; 20 mg/L NaPO_4 cathodic inhibitor;

mixed 10 mg/L ZnCl + 20 mg/L NaPO₄; 100 mg/L Na₂SO₃ oxygen scavenger; 100 mg/L ZnCl cathodic inhibitor; 200 mg/L NaPO₄ cathodic inhibitor; and mixed 100 mg/L ZnCl + 200 mg/L NaPO₄.

Procedure

Corrosion Cells

Ground bars of 1018 steel were cut into coupons (5.715 x 2.54 x 0.3175 cm). A BenchMark 320 dot-peen marking system was used to pin stamped each coupon with a unique identification number. Coupons were then acetone-washed to remove oil residue and stored in a dry box (<1% relative humidity) to prevent corrosion. The initial mass of each coupon was determined to the fourth decimal place. All 100 ml Pyrex sample bottles were pre-cleaned with a 1% Liquinox solution, rinsed with deionized water and dried. Coupons were placed in the sample bottles and sterilized by autoclaving at 132°C for 15 min, with their loosely placed solid orange caps tightened after the bottles cooled.

The unfiltered HRD-76 fuel was considered to contain representative, naturally occurring microbial communities. Coupons were positioned in each bottle at a 45° angle to expose the bottom half of the coupon to the water phase and the top half to the fuel phase (Figure 1c-e).

Triplicate fuel-seawater mixtures (40 mL fuel + 40 mL seawater) were prepared and exposed under two different environmental conditions: V – “Vented”, aerobic, air-filtered through 0.22 µm membrane (grey cap, Figure 1 a and c); T – “Tightened (cf. non-vented)” anaerobic (solid orange cap, Figure 1 b and d).

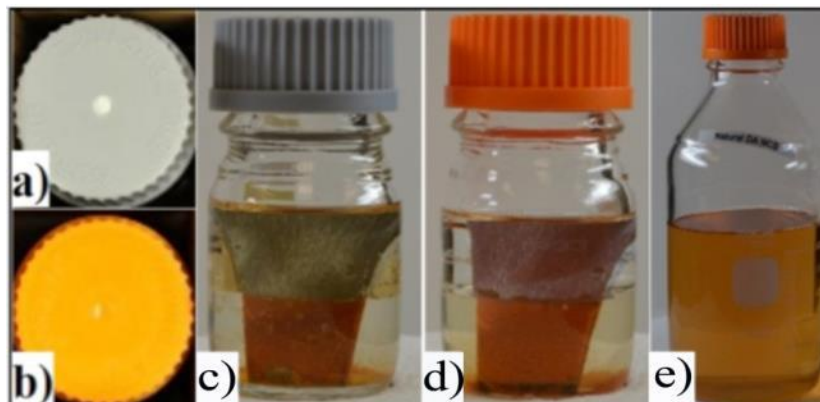


Figure 1. Sample bottle design a) Grey cap with filter (vented); b) Solid orange cap (non-vented); c) Vented grey cap on sample bottle with fuel/seawater; d) Tightened orange cap on sample bottle with fuel/seawater; e) HRD-76 fuel.

Mass loss / corrosion rate

Loose corrosion products were removed from each coupon prior to chemical cleaning per ISO 8407¹ C.3.5. The cleaned coupons were stored at 1% RH in a dry cabinet for at least 1 hour before weighing to determine mass loss. The total mass loss from each coupon was determined by subtracting the final weight of each cleaned coupon from the initial weight. Corrosion rates (CR) were calculated (Eq 1) for each coupon.

Corrosion rate in mm/year by ASTM G1:1999 (ASTM International, 1999):

$$(Eq\ 1) \quad \text{Corrosion Rate (mm/yr)} = \frac{K \times W}{A \times T \times D}$$

K = constant (8.76×10^4 = conversion factor of $\frac{\text{cm}}{\text{hr}}$ to $\frac{\text{mm}}{\text{yr}}$ via ASTM G1.8.1.2)

T = time of exposure

A = Surface area in cm^2 based on average coupon size
 $(2 \times [5.715 \times 0.3175 + 5.715 \times 2.54 + 0.3175 \times 2.54]) = 34.27 \text{ cm}^2$

W = mass lost in grams

D = density of steel in g/cm^3 (7.86 g/cm^3 chosen from ASTM G1 Appendix X1.1)

Results

Mass loss/Corrosion rate

Corrosion rates for 1018 steel exposed to the HRD-76 fuel/ASTM seawater in aerobic and anaerobic conditions were determined. (Table 1).

¹ ISO 8407:1991 International Organization for Standardization “Corrosion of Metal and Alloys - Removal of Corrosion Products from Corrosion Test Specimens”

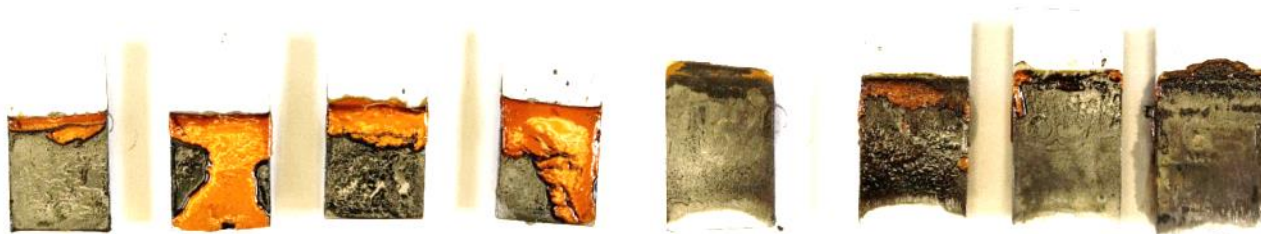
Table 1: Corrosion of 1018 Steel in HRD-76/ASTM Seawater

Condition	Cap Type	Inhibitor	Corrosion Rate (mm/y)	Std. Dev.	% Change Based on Aerobic Control
Control	Aerobic	No Inhibitor	0.049	0.004	0
Control	Anaerobic	No Inhibitor	0.037	0.010	-24
Oxygen Scavenger	Anaerobic	10 mg/L Na ₂ SO ₃	0.034	0.003	-31
	Anaerobic	100 mg/L Na ₂ SO ₃	0.036	0.009	-26
Average					-27
Standard Deviation					3
Oxygen Scavenger	Aerobic	10 mg/L NaSO ₃	0.049	0.002	0
Cathodic Inhibitor	Aerobic	10 mg/L ZnCl	0.050	0.002	4
	Aerobic	20 mg/L NaPO ₄	0.047	0.006	-3
Mixed Cathodic Inhibitor	Aerobic	Mixed 10 mg/L ZnCl + 20 mg/L NaPO ₄	0.047	0.002	-4
Average					-1
Standard Deviation					3
Oxygen Scavenger	Aerobic	100 mg/L NaSO ₃	0.043	0.006	-12
Cathodic Inhibitor	Aerobic	100 mg/L ZnCl	0.044	0.004	-10
	Aerobic	200 mg/L NaPO ₄	0.042	0.001	-13
Mixed Cathodic Inhibitor	Aerobic	Mixed 100 mg/L ZnCl + 200 mg/L NaPO ₄	0.036	0.004	-26
Average					-15
Standard Deviation					7

Corrosion Product Characterization

Visual Observations

Many of the samples hosted a fragile exterior orange rust layer over a black rust that was more adherent to the metal surface (Figures 2 – 4).



Aerobic Control Front (a)

Aerobic Control Back (b)

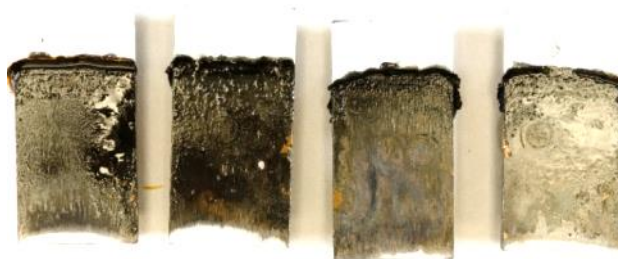


Anaerobic Front (c)

Anaerobic Back (d)



Anaerobic 10 mg/L Na_2SO_3 Front (e)



Anaerobic 10 mg/L Na_2SO_3 Back (f)



Anaerobic 100 mg/L Na_2SO_3 Front (g)

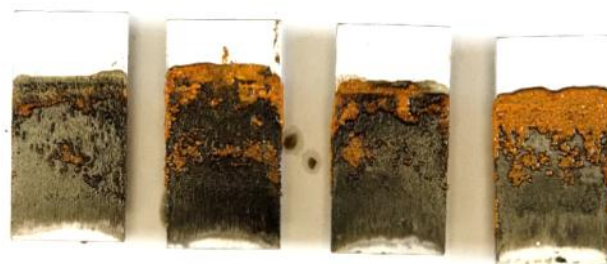


Anaerobic 100 mg/L Na_2SO_3 Back (h)

Figure 2: Photos of samples after 1 month exposure in HRD-76/ASTM seawater at room temperature. Aerobic front (a), aerobic back (b), anaerobic front (c), aerobic back (d), anaerobic 10 mg/L Na_2SO_3 front (e), anaerobic 10 mg/L Na_2SO_3 back (f), anaerobic 100 mg/L Na_2SO_3 front (g), and anaerobic 100 mg/L Na_2SO_3 back (h)



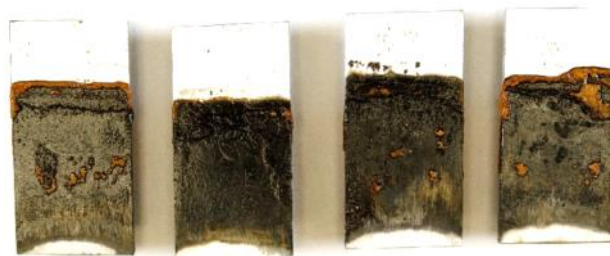
Aerobic 10 mg/L Na_2SO_3 Front (a)



Aerobic 10 mg/L Na_2SO_3 Back (b)



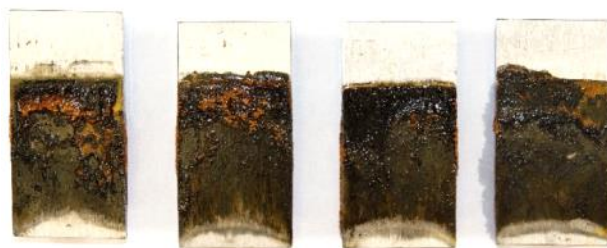
Aerobic 10 mg/L ZnCl Front (c)



Aerobic 10 mg/L ZnCl Back (d)



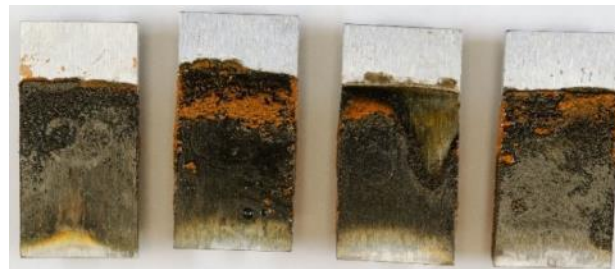
Aerobic 20 mg/L NaPO_4 Front (e)



Aerobic 20 mg/L NaPO_4 Back (f)



Aerobic Mixed 10 mg/L ZnCl + 20 mg/L NaPO_4 Front (g)



Aerobic Mixed 10 mg/L ZnCl + 20 mg/L NaPO_4 Back (h)

Figure 3: Photos of samples after 1 month exposure in HRD-76/ASTM seawater at room temperature. Aerobic 10 mg/L Na_2SO_3 front (a), aerobic 10 mg/L Na_2SO_3 back (b), aerobic 10 mg/L ZnCl front (c), aerobic 10 mg/L ZnCl back (d), aerobic 20 mg/L NaPO_4 front (e), aerobic 20 mg/L NaPO_4 back (f), aerobic mixed 10 mg/L ZnCl + 20 mg/L NaPO_4 front (g), and aerobic mixed 10 mg/L ZnCl + 20 mg/L NaPO_4 back (h).



Aerobic 100 mg/L Na_2SO_3 Front (a)



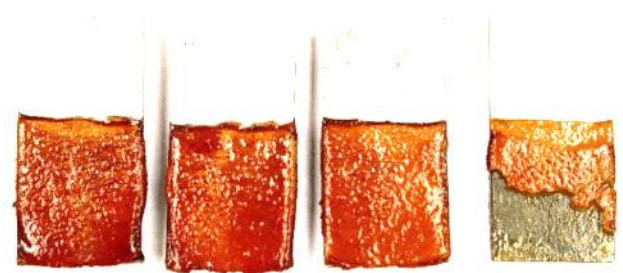
Aerobic 100 mg/L Na_2SO_3 Back (b)



Aerobic 100 mg/L ZnCl Front (c)



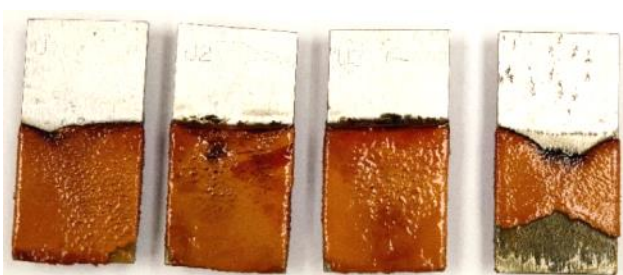
Aerobic 100 mg/L ZnCl Back (d)



Aerobic 200 mg/L NaPO_4 Front (e)



Aerobic 200 mg/L NaPO_4 Back (f)



Aerobic Mixed 100 mg/L ZnCl + 200 mg/L NaPO_4 Front (g)



Aerobic Mixed 100 mg/L ZnCl + 200 mg/L NaPO_4 Back (h)

Figure 4: Photos of samples after 1 month exposure in HRD-76/ASTM seawater at room temperature. Aerobic 100 mg/L Na_2SO_3 front (a), aerobic 100 mg/L Na_2SO_3 back (b), aerobic 100 mg/L ZnCl front (c), aerobic 100 mg/L ZnCl back (d), aerobic 200 mg/L NaPO_4 front (e), aerobic 200 mg/L NaPO_4 back (f), aerobic mixed 100 mg/L ZnCl + 200 mg/L NaPO_4 front (g), and aerobic mixed 100 mg/L ZnCl + 200 mg/L NaPO_4 back (h).

Discussion

In the previous findings, oxygen reduction was a major driving force for corrosion in the seawater mixtures with HRD-76, HRD-76/F-76 blend, or the F-76. In this study, the average corrosion rate of the 1018 steel exposed to the HRD-76/ASTM seawater mixture decreased by 24% in the tight-sealed cell (anaerobic condition) compared to the vented cell with a cap having a hole and 0.22 μm filter (aerated condition). Since the cells were sealed in air, some of the corrosion could be possibly attributed to residual oxygen. Therefore, an oxygen scavenger Na_2SO_3 was added in concentrations of 10 and 100 mg/L to the anaerobic cells. The average corrosion rates were reduced by 31% and 26%, respectively, compared to the aerated condition. However, taking into consideration the standard deviation (Table 1), the oxygen scavenger Na_2SO_3 did not have a significant effect in reducing corrosion in the anaerobic cells. Corrosion is also possible via hydrogen evolution.

The Na_2SO_3 oxygen scavenger and ZnCl and NaPO_4 cathodic inhibitors were initially used in concentrations of 10 mg/L, 10 mg/L, and 20 mg/L, respectively, either individually or mixed together (i.e., ZnCl and NaPO_4). These low concentrations are typical for inhibitor applications. In the HRD-76/ASTM seawater mixture (aerobic condition), the inhibitors used individually or mixed (i.e., ZnCl and NaPO_4) at these typical concentrations, did not have any significant effect on the corrosion rate (Table 1), which is likely due to the very high chloride concentration in the ASTM seawater. The oxygen scavenger and inhibitor concentrations were then increased by an order of magnitude to 100 mg/L, 100 mg/L, and 200 mg/L for Na_2SO_3 , ZnCl and NaPO_4 , respectively, when used individually or mixed (i.e., ZnCl and NaPO_4). The average corrosion rates decreased by 12%, 10%, 13%, and 26%, respectively, for Na_2SO_3 , ZnCl , NaPO_4 , and mixture of ZnCl and NaPO_4 . These reductions in corrosion rates are modest and it may not be practical to use these corrosion inhibiting compounds at these or higher levels. The compounds are salts and need a polar water-based solvent to dissolve. Hence, these inhibitors are likely only concentrated in the water phase and not the fuel. Corrosion on the coupons was only significant in the water layer (Figures 2, 3, and 4).

Conclusions

At normal inhibitor concentration levels, the Na_2SO_3 (10 mg/L) oxygen scavenger and ZnCl (10 mg/L) and NaPO_4 (20 mg/L) cathodic inhibitors used either individually or mixed together (i.e., ZnCl and NaPO_4) did not have any significant effect on reducing the average corrosion rate of the 1018 steel in the HRD-76/ASTM seawater mixture (aerated condition) at room temperature. When the oxygen scavenger and inhibitor concentrations were then increased by an order of magnitude, the average corrosion rates decreased by 12%, 10%, 13%, and 26%, respectively, for Na_2SO_3 (100 mg/L), ZnCl (100 mg/L), NaPO_4 (200 mg/L), and mixture of ZnCl and NaPO_4 . The compounds are salts and need a polar water-based solvent to dissolve. Hence, these inhibitors are likely only concentrated in the water phase and not the fuel. Corrosion on the coupons was only significant in the water layer.

3.2g Waste Management Using the Flash-Carbonization

A novel carbonization process that realizes near-theoretical fixed-carbon yields in ~3 h is presented. Fuels were carbonized in a hermetically sealed reactor at an initial nitrogen pressure of 0.1 MPa. During a carbonization test, the reactor vessel retained all pyrolytic products inside the hot reaction zone invoking high pressures as the temperature was raised. Given the elevated partial pressures of volatiles and their extended residence times, secondary, heterogeneous, char-forming reactions between the hot solid and the tarry vapors appeared to be promoted. This resulted in charcoals with a remarkably high fixed-carbon yield, noncondensable gases mainly composed of CO₂, and negligible amount of free tars. This work presents a reproducibility study on the experimental method and explores the effects of heat-treatment temperature, particle size, mass loading, and immersion time on product distributions and charcoal properties. Proximate and elemental analyses, heating values, and scanning electron microscopy images of charcoal are presented. Higher heat treatment temperatures (from 300 °C to 400 °C), smaller grains (from <2 mm to <0.2 mm), longer immersion times (from 30 minutes to 190 minutes), and greater mass loadings (from 130 g of biomass per liter of reactor to 165 g of biomass per liter of reactor) intensified wood devolatilization without losing charcoal fixed-carbon yields. Final charcoal products had lower volatile matter contents and improved fixed-carbon contents. Temperature produced the strongest effect, transforming the virgin spruce with a fixed-carbon content of 15% to charcoals with fixed carbon contents of 52% at 300 °C and 73% at 400 °C. The increase in temperature resulted in a transient plastic phase that changed the char appearance from loose, particulate matter to a smooth, shiny solid product with the appearance of coke. Complete details can be found in the publication listed below.

Publications Resulting from these Efforts

Carbonization of Biomass in Constant-Volume Reactors, Maider Legarra, Trevor Morgan, Scott Turn, Liang Wang, Øyvind Skreiberg, and Michael Jerry Antal Jr., Energy & Fuels, American Chemical Society, 2018, Vol. 32 (1), pp 475–489, <http://dx.doi.org/10.1021/acs.energyfuels.7b02982>

3.3 Solar Fuels Production

The overarching goal of this project continues previous ONR-funded efforts to develop novel thin film materials (primarily Cu₂ZnSn(S,Se)₄, or CZTSSe) for solar energy conversion. The main objective is to replace costly vacuum-based fabrication techniques with cheap liquid-based processes. In our approach, we are developing inks which can be easily coated on various substrates using high-throughput techniques, including spin coating and inkjet printing. Under past ONR funding, our group developed a technology to form CZTS (sulfide) thin films using nano-crystalline “inks” made of CZTS (sulfide) nanoparticles with controlled composition, size and

morphology. In this process, inks are simply printed onto substrates and heated under controlled atmosphere to create a dense and crystalline thin film materials, comparable to those obtained with conventional vacuum-based techniques. The resulting CZTS (sulfide) solar absorbers were successfully integrated into functional solar cells, with PCE of approx. 2.3%. Although promising, this approach had two major pitfalls. First, the optical bandgap of the CZTS (sulfide) solar absorber (1.5 eV) allowed for absorption only in the UV (250 nm) to near infrared (830 nm) portion of the solar spectrum, which limits the cells photocurrent density output to 20 mA/cm². Second, nanoparticles tend to agglomerate quickly in our inks after initial dispersion, making the printing step difficult. Capping the particles with organic ligands (e.g. dodecanethiol) could prevent agglomeration, however the amount of residual carbon left from the ligands after the heating step can contaminate the absorber and deteriorate its electronic properties.

Under APRISE13, our team revisited the printing process to address both aforementioned pitfalls. First, we replaced nanoparticle-based inks with ones containing only molecular complexes of copper, zinc and tin. First attempts using acetates as chemical reagents and methanol as solvent led to unstable inks that would precipitate almost instantly (brown ink labeled “V1” in Figure 3.1). Replacing acetates with chlorides (SnCl₂, CuCl and ZnCl₂) tuned out to be the key to achieve stable inks (V2). The resulting solutions were very easy to process, leading to highly uniform coatings (see center picture in Figure 3.1). The coated inks were then dried at 250°C in air to remove the solvent and finally heated under sulfur atmosphere at 550°C, leading to a dense and crystalline CZTS (sulfide) absorber. In a second experiment, sulfur was replaced with selenium during the heating stage to reduce the absorber bandgap and extend its light absorption from near infrared (830 nm) to infrared (1,200 nm). The resulting CZTSe (selenide) thin films possessed excellent crystallographic and microstructural characteristics (no voids), with an optical bandgap of 1.0 eV, allowing solar photon absorption up to 1,240 nm. During the next APRISES effort, our team will integrate these CZTSe (selenide) absorbers into solar cells and test their PCE performances.

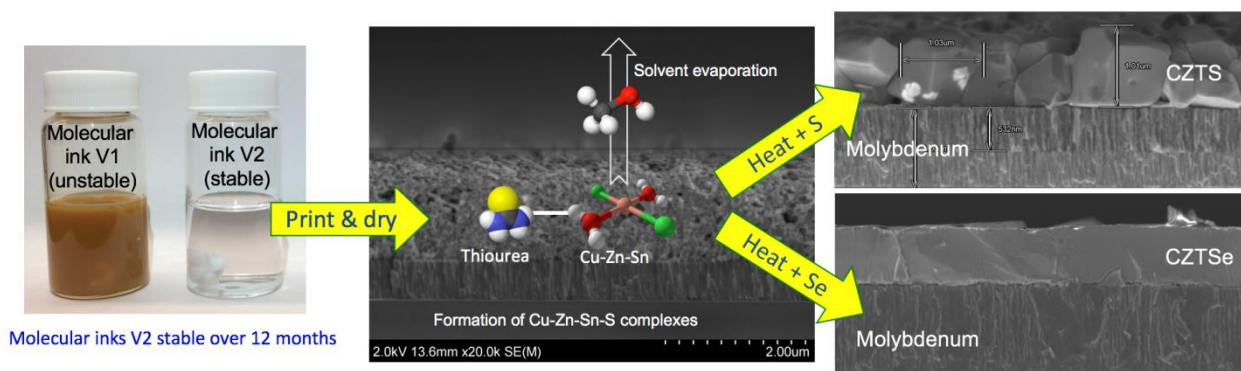


Figure 3.3.1. (Left) picture of molecular inks, V1 (unstable) and V2 (stable). (Center) Cross sectional scanning electron micrograph of a printed ink onto a molybdenum substrate. (Right) Cross sectional scanning electron micrographs of a CZTS (top) and a CZTSe (bottom) solar absorbers.

Also under this APRISES13 effort, our team investigated innovative “n-type” layers, a key component in photovoltaic operation. When combined with the “p-type” CZTSe absorber, the n-type layer forms an asymmetric electronic structure, or diode, that pulls the photo-generated electrons out of the solar cell. Without this diode, no current could flow out of the device. Conventional chalcopyrite devices use toxic cadmium sulfide (CdS, 2.4 eV) as n-type layer. Here we propose to evaluate Zn(O,S), an environmentally friendly material with optical properties that can be adjusted by controlling the oxygen to sulfur ratio (an attribute that CdS does not have). This way, the optical and energetic properties of Zn(O,S) could in theory be matched to those of the p-type absorber, yielding higher conversion efficiencies. In this work, 100nm thick Zn(O,S) layers were synthesized via reactive sputtering in a vacuum chamber using a ZnS target, under various flow rates of oxygen (O₂) gas. The optical bandgap (or color) of the Zn(O,S) films was successfully tuned from 2.7 eV to 3.3 eV by varying the O₂ flow from 5 standard cubic centimeters per minute (sccm) to 0 sccm, respectively (Figure 3.2, left). A 2.7 eV ZnOS buffer layer was then integrated over a CuInGaSe₂ baseline absorber system. When compared to CdS, ZnOS allows for more light to be transmitted to the undelaying absorber, resulting in a higher photocurrent density (approx. +1-2 mA/cm², Figure 3.2, right). In the next APRISES effort, we will test ZnOS on CZTSe-based solar cells and report on their conversion efficiency.

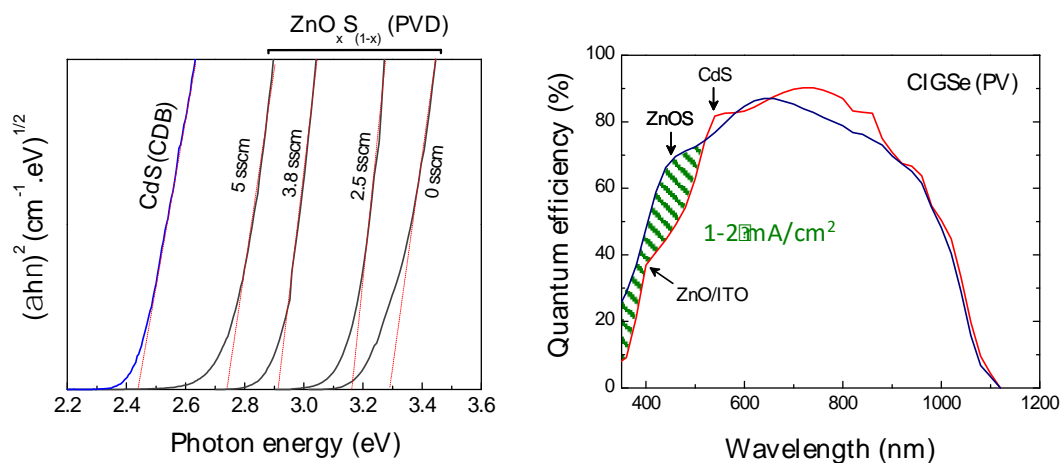


Figure 3.3.2. (Left) Tauc plot of bandgap tunable ZnOS buffer layers. (Right) Quantum efficiency measured on CuInGaSe₂ (CIGSe) solar cells integrated with 2.4 eV CdS compared with 2.7 eV ZnOS buffer layers.

TASK 4: OCEAN ENERGY

Ocean Energy work included development of Ocean Thermal Energy Conversion (OTEC), Wave Energy Testing and Seawater Air Conditioning. Under a subaward to Makai Ocean Engineering, new OTEC fabrication methods and designs continued to be developed and tested, focusing on

laser welded heat exchanger development, along with corrosion testing. Wave energy testing research objectives and plans were further developed in collaboration with NAVFAC at the Navy's Wave Energy Test Site (WETS), and numerical hydrodynamic modeling was also conducted on wave energy conversion devices and their performance. SWAC pre-impact conditions were characterized with further deployments of long-term oceanographic mooring, water column profiling and sampling.

4.1 Ocean Thermal Energy Conversion (OTEC)

HNEI subcontracted with Makai Ocean Engineering Inc. to advance the long term goal of developing an economically viable (Ocean Thermal Energy Conversion) OTEC power plant. Building on previous ONR-funded work, APRISES13 focused on new OTEC heat exchanger fabrication methods and designs, and corrosion testing. OTEC research and demonstration work is conducted at the Ocean Energy Research Center (OERC), located within the Natural Energy Lab of Hawaii Authority (NELHA) in Kailua Kona, Hawaii. This report summarizes the work performed between January 2015 and November 2017 specifically pertaining to:

- Laser lab equipment and installation
- Laser welded heat exchanger development
- Corrosion testing

Under previous APRISES funding, Makai developed the Foil Fin Heat Exchanger (FFHX), which uses epoxy to join titanium foil to aluminum fins. Incompatibility of the epoxy with ammonia limited the working fluid to Propane, an inferior refrigerant to ammonia in OTEC applications. Makai investigated other techniques of joining the foil to the fins and concluded that laser welding was the best alternative. Initial trials yielded positive results: at small sample sizes, Makai was able to successfully weld the titanium foil to the fins and hold high pressure without leaks. Throughout development of scaling up the heat exchanger size, defects were observed periodically, exposing aluminum to the surface. Corrosion tests confirmed the catastrophic nature of the defects, and thus the design required a zero-tolerance for defects. Makai then developed a new design, the Titanium Foil Heat Exchanger (TFHX), which eliminated the aluminum fins. Through thermal simulations and analysis, it was realized that the performance would improve due to its compactness, and thus it was a better heat exchanger for OTEC applications. The TFHX uses two sheets of titanium foil which are formed through a proprietary process, creating the working fluid passages. Makai repeated the development steps and based on the results, Makai decided to move forward with the TFHX design to construct and qualify a full-size plate under this APRISE13 effort.

Makai also continued long term corrosion testing, building on previous ONR-funded efforts. Aluminum plate samples remained in the warm and cold multi-column imaging racks (MCIR) with continued acid and hypochlorite treatments. FFHX and TFHX samples have also been tested in the cold seawater MCIR. Aluminum box beam samples also remained in warm and cold seawater; as of December 1, 2017, the box beam samples have been tested for over 8 years.

Laser Welded Heat Exchanger Development

Under previous APRISES efforts, Makai built and tested six configurations of Epoxy-Bonded Heat Exchangers (EBHX); however, because epoxy is incompatible with ammonia as mentioned earlier, a new manufacturing method was required to make heat exchangers for OTEC applications. Makai identified laser welding as the most suitable method for fabricating FFHXs, as laser welding produces a strong, ammonia-compatible weld that is also seawater corrosion resistant.

Unable to find industry standards or best practices to perform laser welding of titanium foil to aluminum fins as proposed for FFHXs, Makai established rigorous development and qualification steps to learn the intricacies of the laser welding process and to characterize the foil-fin welds. In addition to developing a welding protocol, Makai also developed the FFHX design and fabrication method. Makai's development plan entailed:

- 1) demonstrate proof-of-concept of the foil-fin weld process and characterize the foil-fin weld strength with small samples,
- 2) demonstrate the foil-fin weld process for prototype sized samples and verify welds meet requirements for use in an OTEC HX,
- 3) fabricate a sealed and manifolded prototype plate (includes all components and weld types - foil-fin, foil-manifold, and foil-midplate) and verify plate meets requirements for use in an OTEC HX, and
- 4) fabricate a full-sized plate and verify plate meets requirements for use in an OTEC HX.

Makai provided proof-of-concept of the foil-fin laser weld using 2"x2" samples. Initial laser weld development was performed with a scanhead on a stationary stage. Since fabrication of a full-sized plate would require a precision motorized stage with either a scanhead or a weld head and associated auxiliary equipment, Makai decided it was advantageous to incorporate the stage (including stage software, fixturing, and auxiliary systems) earlier rather than later in the development process. Makai developed custom software that coordinated stage motion, weld location, timing of laser firing, and safety controls.

Prototype-sized (12"x12") samples of foil-fin welds were initially fabricated using the scanhead but development shifted to the motorized stage because argon delivery was readily available on the motorized stage. Welds were evaluated for strength by pressure testing and samples were sent out for energy dispersive spectroscopy (EDS) evaluation to learn more about weld composition. Although the fabricated foil-fin weld samples were not able to achieve a pressure rating > 250 psi, Makai believed the issue could be resolved with more development in weld techniques and Makai moved forward with developing software and designing and procuring fixturing used to fabricate and test a prototype plate, which is a prototype-sized sealed and manifolded plate.

Makai was nearly successful at fabricating a fully sealed prototype plate. Weld defects were present on all fabricated plates and had to be patched with epoxy. When pressure tested, the plates

were unable to attain the required 250 psi pressure rating. Acceleration welds, which were used at the start of the weld lines, were suspected to be weak.

Although Makai investigated different methods to eliminate acceleration welds to improve the FFHX pressure rating, Makai still had reservations about being able to reliably produce defect-free foil-fin welds at the lengths needed for OTEC heat exchangers.

Laser Lab

All laser welding work is performed in Makai's Laser Lab located within the Water Quality Laboratory building at NELHA. A 19' X 16' Class 10,000 cleanroom was built inside the Water Quality Laboratory building to provide a clean environment for part assembly and welding operations and to restrict access to the work area for safety concerns. The laser, optics, laser support systems, motorized stage, auxiliary equipment, and safety system are located within the cleanroom. Components of each system are listed in Figure 4.1.1. Non-essential and potentially contaminating equipment (air compressor, argon tanks, chiller, and water supply) are housed outside the cleanroom.

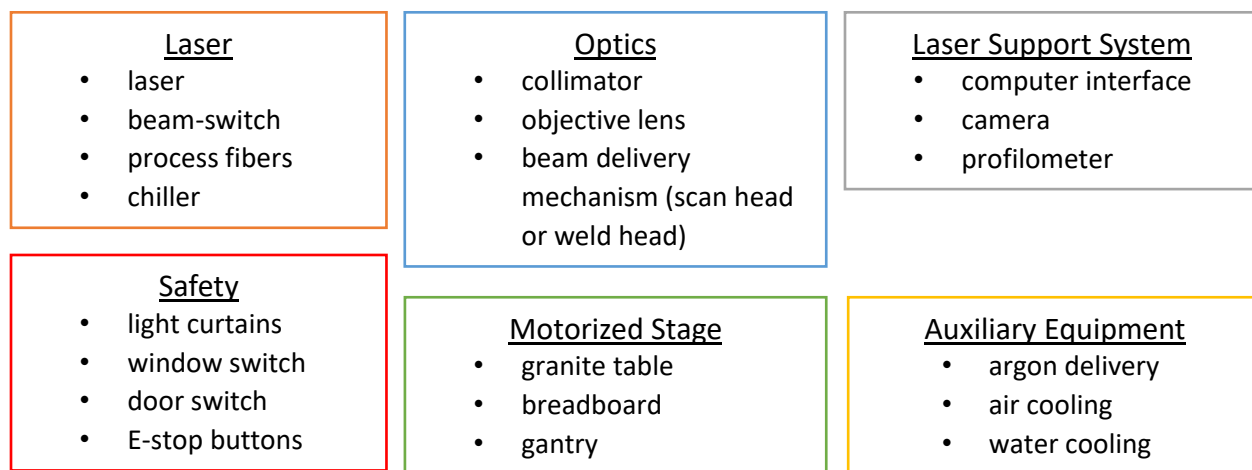


Figure 4.1.1. List of components in each system.

Laser, Optics, and Laser Support System

In January 2015, Makai visited three laser welding manufacturers: Miyachi America, Rofin Inc., and IPG Photonics and developed a set of specifications for a laser system that would meet Makai's requirements for creating foil-fin welds (Table 4.1.1). Makai planned to construct a fin indexing machine and perform initial foil-fin trials at a manufacturer's facility, but decided it was more efficient to purchase a laser system and perform trials on-site in Makai's own facilities. Makai purchased the fiber laser system from IPG Photonics.

Table 4.1.1. Laser specifications

Power	100-1000 W
Type	Diode Pumped Ytterbium Fiber Laser
Fiber diameter	100 μm
Chiller – cooling capacity	5.9 kW @ 60 Hz
Chiller – refrigerant	R407C
Chiller – water flow rate	6.2 gpm @ 62.2 psia

Makai has two stations for weld development – a scanner station with a scan head and a motorized stage with a weld head. By incorporating a beam switch, both the scanner station and the motorized stage and weld head can use the same laser, albeit not simultaneously (Figure 4.1.2). A four-port beam switch was purchased from IPG Phototonics. The beam switch accepts the 100 μm fiber input from the laser while the process fibers to the scan head and weld head are 150 μm .

A ScanLabs IntelliSCANde 20 scan head was selected for the scanner station. The scanner station can be used for samples at the prototype scale (12”x12”) and smaller. The scanner station uses a primary optic to collimate the beam exiting the process fiber, a secondary optic (objective lens) to focus the beam (and determine the laser spot size), and the scan head, which houses precise, moving mirrors to direct the beam along the required weld path. The field of view of the scan head limits the size of the sample.

Table 4.1.2. Scan Head Specifications

Aperture	20 mm
Typical scan angle	± 0.35 rad
Repeatability (RMS)	< 0.4 μrad
Dither (position noise, RMS)	< 1.6 μrad
Typical marking speed	1 m/s
Typical positioning speed	11 m/s

A Haas Laser Technologies weld head was selected for the motorized stage. Samples up to the full-size FFHX can be produced on the motorized stage. On the motorized stage, the weld head houses the primary and secondary optics to focus the beam. The beam is directed by moving the weld head along the required weld path. A key advantage of the weld head is that it incorporates a manifold for shield gas delivery directly at the weld spot.

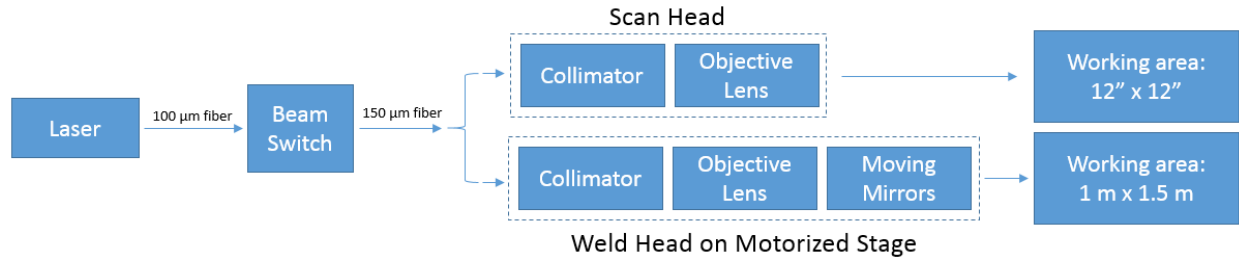


Figure 4.1.2. Comparison of scanner station vs. weld head on motorized stage.

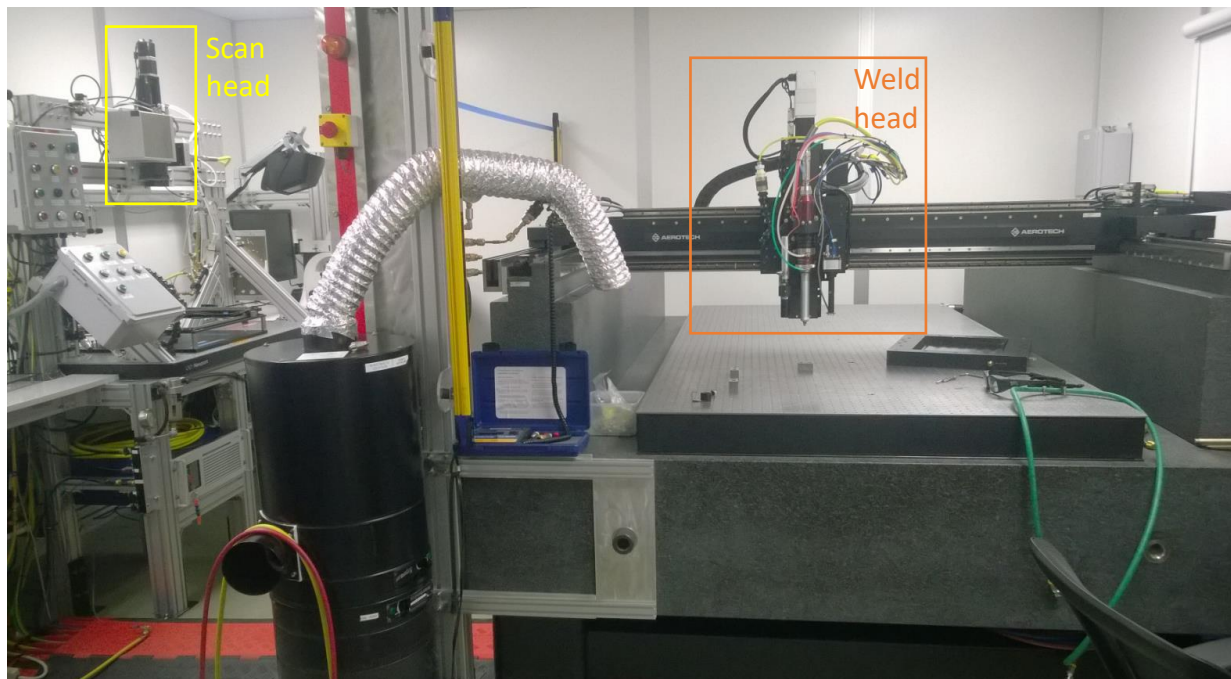


Figure 4.1.3. Scan head station and weld head station on motorized stage.

Communications to control the scan head were performed with a LaserDESK software via a RTC5 PCIe control board. A Nd:YAG camera adapter was also purchased from Scan Labs to image the field of view of the scan head. The scan head, camera adapter, and collimator are mounted together and attached to a moveable z-stage to allow adjustment for the different focal length objective lenses. The profilometer is mounted separately on an independent x-y stage.

Custom LabVIEW programs were written to control the movement of the motorized stage synchronized with the laser power and firing signals. A custom mount was designed for the weld head, a profilometer, and a camera (Figure 4.1.3).

Safety system

Makai's laser is classified as a Class 4 laser. The safety practices relevant to laser operations are listed in OSHA Regulation 21 CFR 1040 which is based on recommendations found in ANSI 136.1. Safety features must protect personnel during welding operations and against inadvertent exposure to the laser beam. When laser welding operations were relocated to the Water Quality Laboratory Building in Fall 2015, Makai found it impractical to shield all windows in the building and restrict access to a NELHA building; instead, Makai constructed a 19' x 16' cleanroom and confined all laser operations to within the cleanroom. The cleanroom serves as the primary safety barrier for welding operations.

In case hazardous conditions are present, Makai's safety system has two main responses: 1) stop stage motion (protects equipment and operators) via the E-stop circuit and/or 2) disable/discontinue laser emission via the laser interlock circuit. The circuits are fail-safe in that any hazardous condition will activate its circuit. The E-Stop circuit is automatically reset when the hazardous condition is cleared but the Laser Interlock Circuit requires a manual reset. This extra step ensures the laser will not unexpectedly turn on when a trip condition is cleared.

The E-Stop Circuit can be activated by five components:

- Emergency-stop buttons – there are two emergency-stop buttons which are manually operated. One is located immediately next to the stage, and a second outside the cleanroom next to the stage drives. The emergency-stop buttons are wired in series, so either button will trigger an emergency-stop on the stage motors and the laser interlock circuit.
- Light curtain sensors – there are two light curtains on the front and left planes of the motorized stage (the easily accessible sides) which trigger the E-Stop circuit if the vertical plane is breached. Light curtains are arrays of infrared beams that surround the stage. The position of the curtains is determined by the nominal speed of a falling person and the stage's maximum deceleration time. Light curtain signals are wired to a safety relay which also verifies that the light curtains are functioning (no errors to prevent a triggered condition from sending the trip signal) and there is no active trip signal.
- Magnetic breakaway/crash detection – if the weld head impacts an object (fixture, sample, stage component), the E-Stop circuit is triggered.
- Stage faults such as over-current and tracking/alignment errors.

The Laser Interlock Circuit can be activated by four components:

- Stage-triggered – if the E-Stop circuit is triggered, the laser emission is disabled. Emergency buttons, light curtains, breakaway/crash detection, and stage faults will trigger the E-Stop circuit which automatically triggers the Laser Interlock Circuit. This protects personnel from inadvertent exposure to the laser and prevents the laser from burning through a surface if the stage is stopped.
- Door switch – the door must be closed before the laser can be powered on. There are also indicator lights which indicate the status of the door. If the door is opened while the laser is on, the laser interlock circuit is triggered.

- Window switches – curtains covering the windows must be fully lowered before the laser can be powered on. There are also indicator lights which indicate the status of the curtains. If the curtains are raised while the laser is on, the laser interlock circuit is triggered.
- Scan head error – if an error is detected the laser interlock circuit is triggered. This is only relevant during scan head operations.

Clean Room

In addition to being the primary safety barrier, Makai's Class 10,000 cleanroom provides a clean environment for part assembly and welding operations. Dust contamination is detrimental to weld quality, particularly for foil-fin welds. In keeping with the main purpose as a research and development space where frequent re-entry is expected and new components are constantly brought in, Makai's cleanroom was selected to provide adequate cleanliness control without being overly cumbersome. The Class 10,000 rating restricts the number of particles per cubic meter that are greater than 0.5 μm . Only basic protective gear (smocks, shoe cover, and head covers) are required inside the cleanroom.

Air flow within the cleanroom is designed to be laminar; turbulent flow patterns can stir up particles. Two sets of air filters are used; a washable pre-filter is used to extend the life of the HEPA filters because the building in which the cleanroom is housed in has significant dust. Air within the cleanroom is changed between 60-90 times each hour. The cleanroom is also maintained under positive pressure to prevent contaminants from being drawn in.

Auxiliary systems

Auxiliary systems include the water cooling system, air cooling system, and argon shield gas delivery system. The auxiliary systems are manually controlled from the Auxiliary Control Panel (Figure 4.1.4).

Water Cooling System

The laser, laser fiber couplers, scan head and weld head collimators, scan head electronics and beam switch are water cooled. Water cooling is provided by the laser chiller and is routed to each component. The scan head and weld head collimators, fiber couplers and weld head are cooled in series because the scan head and weld head are not operated simultaneously. This also eliminates the risk of cooling the wrong component. Cooling water flow is initiated by turning on the chiller, which is located in the sound-proof enclosure outside the clean room.

Cooling water for welding fixtures is also available and provided by city water. City water is not temperature controlled but has a nominal temperature of 20°C.



Figure 4.1.4. Auxiliary Control Panel (top), argon flow is regulated by flow rate (bottom left), and cooling air flow is pressure regulated.

Air Cooling System

The scan head internal space (which houses the mirror galvanometers) and the weld head objective lens are air cooled. The stage motors can also be air cooled although cooling has not been necessary with the current usage pattern. Filtered, dry compressed air is used for air cooling. The cooling air flow rate is pressure regulated (Figure 4.1.4). The compressor and oil and humidity filters are located outside the cleanroom in the sound-proof enclosure.

Argon Shield Gas System

Argon is used as a shield gas for weld operations to prevent oxidation during welding. Argon can be directed to the weld point via a coaxial nozzle on the weld head or other locations through auxiliary flexible nozzles. Argon flows are controlled by flow meters on the control box (Figure

4.1.3). Argon flow to the fixtures is pressure rather than flow regulated. Argon shielding can be provided to the scan head station through the use of an argon box; however, the sample must be fit entirely inside the box.

Laser Hardware synchronization

Laser welded heat exchanger fabrication requires setting the weld path, welding, and continuous safety monitoring any time the stage or laser is active. Makai has developed custom software that synchronizes stage motion, data acquisition, laser firing, and safety systems. Each system was purchased individually but is integrated into one main control system. It was crucial to carefully consider the time latencies between stage positioning, profilometer data collection, and laser firing.

Welding on the motorized stage is performed by moving the weld head along the desired weld path. A successful weld requires that the weld head is positioned precisely over the desired weld location and the laser is fired at exactly the correct time and for the correct duration. Each independent system must be synchronized to maintain the positioning precision ($\pm 5 \mu\text{m}$) of the stage during welding.

One of the benefits of the Aerotech stage is its precise communication timing using its Position Synchronized Output (PSO) feature. The stage can output a digital signal precisely timed with its position. This digital output signal is triggered on a hardware level to avoid longer, inconsistent delays that would occur if the commands were issued by software ($>100 \text{ ms}$). The stage's Y-axis NDrive HPe servo drive is the 'master timer' of the system; it is used to trigger data collection and laser firing. The total delay between the PSO output signal and data sampling is $5.3 \mu\text{s}$ ($10.6 \mu\text{m}$ at maximum stage velocity). This latency does not affect stage accuracy because the measurement is synchronized to the stage's actual position at the time the measurement is recorded except for profilometer measurements. The profilometer is limited by its photodetector readout time; the fastest the profilometer can sample is 2000 Hz. Stage velocity must be limited to 5 mm/s to ensure positioning error are less than $10 \mu\text{m}$ while taking profilometer measurements.

Once the weld locations have been determined from profilometer scans we can precisely position the stage and time the laser firing. The PSO output signal is used to fire the laser by sending a digital signal to the laser's hardware input. Due to signal latency, laser firing can lag by as much as $40 \mu\text{m}$ at maximum stage velocity. Additionally, for added precision, software can manipulate the coordinates such that the PSO output signal is sent at an earlier stage position.

Finally, although the profilometer and weld head are securely mounted on the Z-stage, their relative position can change if either (or both) component is remounted. The offsets can also drift as thermal changes are made in the optics of the weld head. For this purpose, the weld head optics are always cooled during welding operations. The profilometer and weld head positions are calibrated relative to the stage encoders (and thus, to each other) before any operation that requires high positioning accuracy.

Laser Welding Software

Makai's custom-developed software suite consists of programs that are essential to laser welded heat exchanger fabrication. Programs are modified for specific applications but in general, the software suite consists of 1) stage motion control, 2) 2-D and 3-D profilometer scans, 3) stage calibration, 4) fin indexing and welding, and 4) custom weld path/pattern programs.

Stage Motion Control

The stage can be positioned with explicit positioning commands or with the use of a joystick. Positioning commands can be in the form of absolute coordinates or incremental moved. The motion control program automatically retracts the weld head and profilometer prior to initiating horizontal motion to prevent accidental collisions.

The motion control program constantly monitors the status of the E-Stop circuit and automatically resets the stage drives for common (light curtains, door and window switches, emergency stop buttons and laser interlock) faults. Once the unsafe condition is removed, the program automatically sends the reset command to the stage drives which is required for the drives to resume normal operation. Automatic reset is desirable because the common faults are frequently intentionally tripped; without the automatic software reset, fault resetting would require manual commands each time, unnecessarily adding time to fabrication process. Infrequent stage faults (over-currents, incorrect motion, or velocity tracking) stop the stage drives via the E-Stop Circuit but are not automatically cleared; they require manual acknowledgement and clearing of the fault cause.

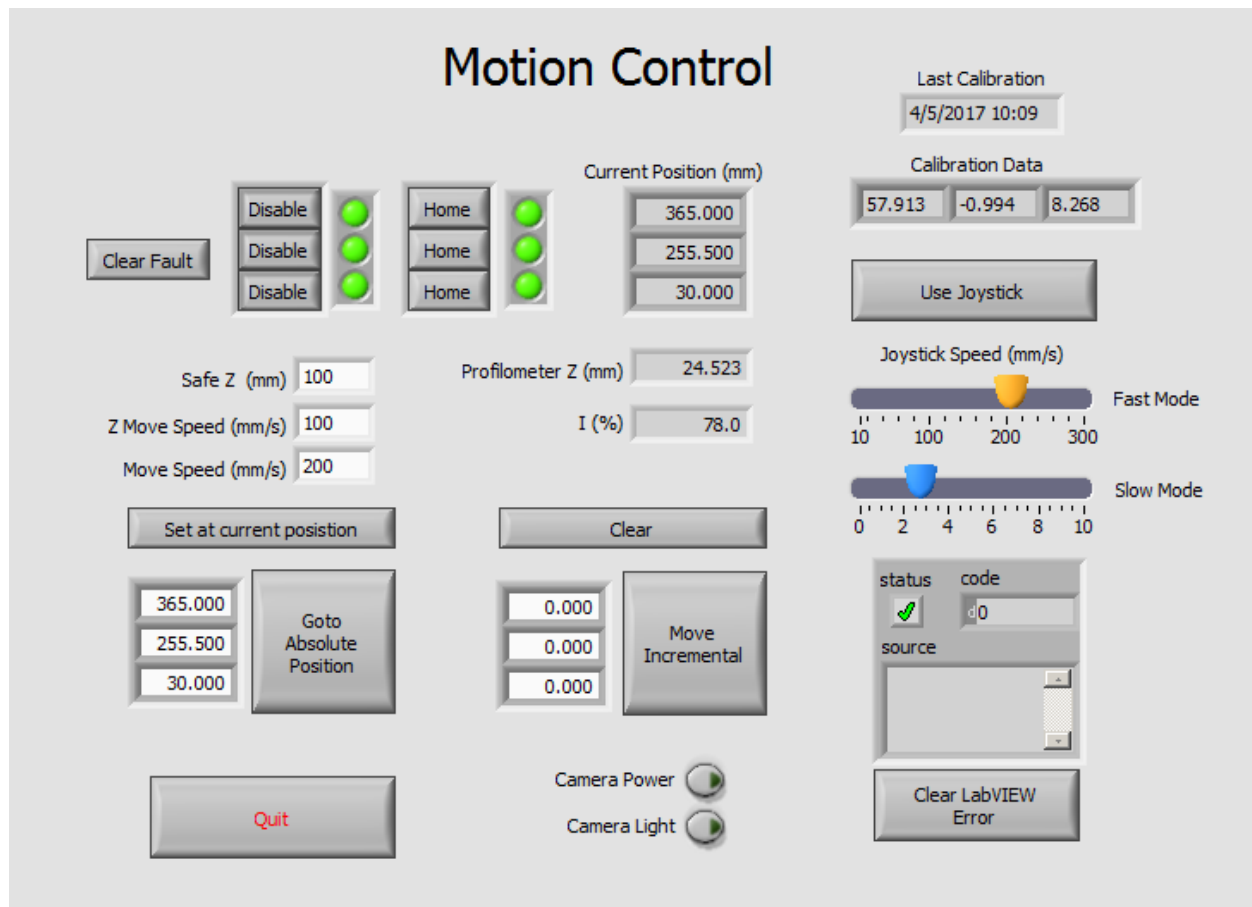


Figure 4.1.4. Stage motion control program. Stage position can be set by entering coordinates, specifying incremental movement, or using the joystick controller.

Profilometer Scans

Profilometer scans are typically used to establish weld locations. The Profilometer Scan program can generate 2-D or 3-D surface plots.

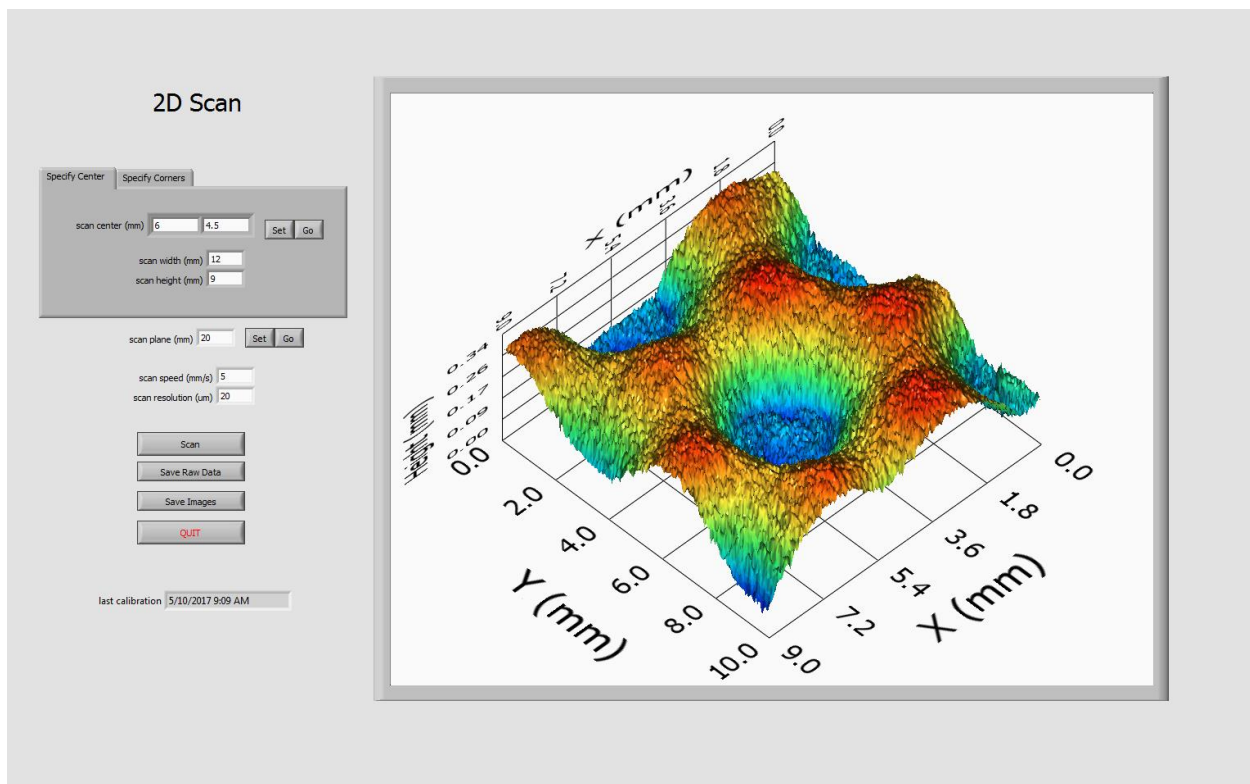
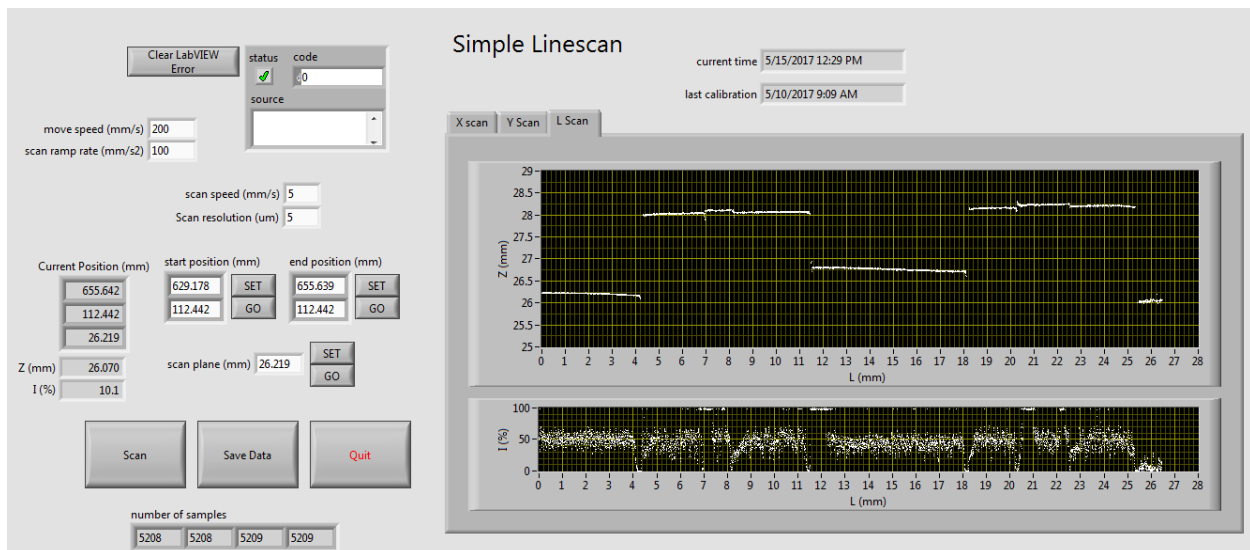


Figure 4.1.5. 2-D and 3-D profilometer scans.

Stage Calibration

The Stage Calibration program determines the relative positional offset of the profilometer and laser spot focus to ensure that welding is performed precisely at the intended location. Precision calibration is critical to match the weld locations established with the profilometer to the actual

position of the laser weld spot. Without calibration, the repeatability of weld positioning would be poor and unacceptable for heat exchanger laser welding applications.

To calibrate the system, a short pulse from the laser is fired onto a reference plate. This mark is scanned by the profilometer. The laser mark is near circular and the program uses a LabVIEW machine vision module to fit a circle to the spot based on the image intensity gradient. Once the center of this circle is determined, the horizontal offsets between the weld head and profilometer is known. Next the profilometer is moved to a point on the stage surface and measures the distance to the stage. This establishes the Z-offset between the profilometer and the stage surface. The calibration offsets are written to a file, which is referenced by all other laser welding related programs.

A repeatability study determined that the system can be calibrated to better than 20 μm using the Stage Calibration program.

Fin Indexing

The Fin Indexing program is used to weld titanium foil to aluminum fins. This entails identifying the center of contact between the fins and titanium foil and welding within 50 μm of the center of contact. If the fins were perfectly rounded, the highest point of each crest would be the center of contact. In practice, fins are not symmetrical and the highest point in the crest is not necessarily the center of contact. In many of our fin styles the highest point is near the edge of the fin instead of the center.

The Fin Indexing program performs three profilometer linescans and applies a peak finding algorithm to coarsely determine the weld locations. Since welds must be located at the center of contact instead of the fin peaks, two secondary processes are performed. One analysis looks at the gradient of the fin profiles and determines the locations of the steepest slopes of the corrugation. The center point between the upslope and downslope is assumed to be the center of contact. A second analysis uses the height of the initially found peak and surrounding points on the profile that are within a pre-set value (value changes depending on fin pitch) of the peak height. From these data points an average location is found and is assumed to be the center of contact. The value of the center of contact of these two methods is averaged to produce our best determination of the weld location. This location can be shifted by as much as 300 μm from the peak found from the initial three linescans. Once the weld locations are determined, the Fin Indexing program coordinates stage motion and laser firing to make the welds.

Custom Weld Path/Pattern

The underlying principles and logic behind integrating profilometer scans to determine weld paths are replicated in multiple programs written to produce a specific weld path or pattern. After the profilometer scans are performed, the user interactively chooses weld locations based on features identified in the scan. The software computes the geometry of the weld path based on the user-selected points and performs the welds. Laser firing parameters are also user-specified.

Laser Welded Heat Exchanger Development

Makai's laser welded heat exchanger development required an iterative design and fabrication process. Makai's approach was to first determine if a laser welded heat exchanger could be designed at the OTEC-scale. This initial step was crucial in assessing the suitability of the heat exchanger in the context of an OTEC power plant; the ability to construct and integrate the heat exchanger (e.g., manifold-to-piping connections) had to be considered. Using the preliminary design as a guide, the next steps were to conduct the detail design, fabrication, and testing of each component of the laser welded heat exchanger.

Weld strength and manufacturing repeatability are critical to the viability of a laser welded heat exchanger. Laser welding of titanium foil to aluminum fins or titanium foil to titanium foil for use in heat exchangers is a novel concept. Without industry standards and best practices, Makai has had to develop all aspects of the production process, from cleaning protocols to the fixtures and welding parameters required to produce the foil-fin or foil-foil weld. Makai established rigorous development and qualification steps to learn the intricacies of the laser welding process and to characterize the laser welded heat exchanger plates.

Production Process and Techniques

Variables that can affect weld strength and success rate are separated into six categories:

Cleaning methods

Makai has found it effective to use a different cleaning method for each component. Titanium manifold/frame parts are cleaned in accordance with "ASTM B600-11: Standard Guide for Descaling and Cleaning Titanium and Titanium Alloys". Aluminum fin sheets are cleaned for 30 minutes in an indirect ultrasonic bath using a degreaser solution heated to 35°C and rinsed with de-ionized water. All parts are blown dry with ionizing air gun or compressed air.

Surface contact

Surface contact is crucial to obtaining a good weld. If surface contact is lost, the laser could burn through the foil. Makai learned that it is important that the entire foil surface is kept flat and free of tension. When changes were made to component thicknesses, the fixtures holding the components had to be redesigned so that the foil would lie flush against the component it was being welded to. Finally, inadvertent wrinkling or tenting could result in loss of contact. In one step of the fabrication process, foil has to be removed by carefully cutting and tearing the unwanted portion. This step was initially performed unaided, but Makai has since developed cutting and tearing tools to protect the remaining foil from wrinkling.

Argon gas delivery

Welds can be made with or without argon as a shielding gas. If argon is used, the delivery rate, stand-off distance, use of a nozzle, and use of leading or trailing edge cups can be varied. When argon is used, some of the laser energy is consumed by argon ionization; i.e., at the same laser power, less energy is transferred to the titanium foil when argon is used. Argon flow rates that are

too high can also cause turbulence and unintended mixing of argon and air at the weld zone. Argon is also delivered through fixtures to prevent oxidation on the back side of a weld.

Argon Parameters	Range
Nozzle Size (mm)	2.5 or 4.5 (no nozzle)
Standoff Distance (mm)	1-8
Flow Rate (SCFH)	1-5

Weld parameters

Weld parameters include laser power, welding speed, and weld type. Parameter selection depends on the components that are welded together.

Weld Parameter	Range
Power	10-100%
Speed (mm/s)	10 – 750
Type	Constant velocity, acceleration, accelerated start, dual accelerated start, split accelerated start, split truncated acceleration, spot, pulsed, moving dots

Weld type is defined by timing of the laser firing and laser power in relation to stage motion.

Weld Type	Description
Constant Velocity	Stage accelerates up to speed and laser is turned on at the required position and remains on at constant velocity and power until the weld path is complete. Laser is turned off once the weld is completed. Requires the availability of an acceleration distance before and deceleration distance after weld.
Acceleration	This weld uses the stage's analog velocity tracking to set the laser power proportional to the actual velocity.

Accelerated Start	This is an 'acceleration weld' that starts with laser power ramp up with velocity but then turns off the laser while the stage is still at constant velocity. Requires sufficient deceleration distance.
Dual Accelerated Start	Uses two 'accelerated start welds' to weld a line. One weld starts on the left edge and turns off the laser half way, the other weld starts on the right edge and welds back to the middle. The separation between the two weld lines in the middle is set with 'weld middle separation' parameter.
Split Accelerated Start	This is the 'dual accelerated start weld' but splits the fin line into two separate line segments. This helps keep the weld line in the middle of the crest.
Split Truncated Acceleration	Basically an 'acceleration weld' that turns off the laser firing before the stage's motion reaches zero velocity. The 'split' weld splits the fin line into two separate line segments. Programmatically these two segments are joined with a slight radius curve ('corner rounding') so the stage motion stays continuous at the transition between the two line segments. During this move the stage is at constant speed throughout the entire weld, even in the 'corner rounded' section.
Spot	Laser is fired at a specified power and for a specified time with the stage at rest.
Pulsed	Constant velocity weld where laser power is pulsed between a specified range at a specified frequency.
Moving Dot	A spot weld where the stage is moving at a constant velocity. This weld can be used to achieve a weld spot that is slightly larger than the spot size (set by optics).

Design configuration

Foil thickness, weld pattern, weld spacing, and fin density are all categorized as design variables that distinguish one heat exchanger design from another. For FFHXs, higher fin densities are expected to be more advantageous for heat transfer and strength (pressure rating) but also increases the total weld length. Surface contact may also be difficult to achieve at the higher fin densities, as the peaks and troughs are less pronounced. For TFHXs, weld pattern and spacing affect the pressure rating, heat transfer area, and passage heights.

Fixture Design

An improperly designed fixture, e.g. one that placed too much tension in the foil when holding it in place, affected the ability to produce high quality, reliable welds. Design changes and changes in fabrication methods also required re-design of fixtures. Because there were no guidelines for

the type of laser welding Makai is developing, when troubleshooting weld failures, Makai has had to carefully consider each variable, including fixture design, to determine and correct the underlying cause of the failure.

Weld Characterization

A successful laser welded heat exchanger must exceed a pressure rating of 250 psi and be reliably produced.

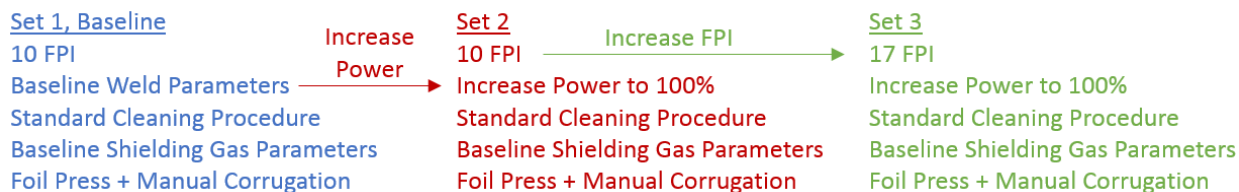
Foil Fin Heat Exchanger (FFHX)

Although sections of successful foil-fin welds have been performed, foil-fin weld failures are still common. Weld failures appear as burn-throughs, aluminum craters, scalloped weld beads, and edge failures (Figure 4.1.6). Any aluminum that is present on the titanium surface will result in galvanic corrosion in seawater and is considered a failure. Additionally, any path for seawater to reach the aluminum fins is also considered a failure. Weld failures can arise from lack of surface cleanliness, inadequate fin-to-foil contact, availability of shielding gas, and localized variations in foil or fin manufacturing (such as thickness) that render the weld parameters ineffective. Makai sent out several foil-fin weld samples for energy dispersive spectroscopy analysis and confirmed that good welds did not have aluminum on the surface whereas in weld failures, aluminum was present on the surface (Figure 4.1.7).

Weld strength can be affected by the quality of the weld bead, changes in fin density, use of shielding gas, and weld parameters. The factors resulting in a highly reproducible, consistent weld may conflict with the factors that produce the strongest weld.

Makai designed a Fin Foil Weld Certification (WC-FF) fixture (Figure 4.1.8) to fabricate and pressure test foil-fin welds independently of the rest of the heat exchanger fabrication process. The WC-FF was designed to securely hold the fin-foil assembly during handling and welding, seal (and hold) the fin-foil chamber and under pressure, and pressure test samples up to 500 psi.

Makai fabricated 13 samples, separated into three sets, on the WC-FF fixture. The three sets were:



The weld success rate (number of weld lines with defects / total number of weld lines) and pressure at failure was recorded for each sample (

Figure 4.1.9). Defects were patched with epoxy prior to pressure testing. Increasing laser power from 90% to 100% on the 10 FPI samples did not improve the pressure rating or weld success rate. Increasing fin density to 17 FPI improved the pressure rating by over 100 psi (not including the

samples that failed at the epoxy patch) but there was ~10% decrease in weld success rate compared to the 10 FPI samples.

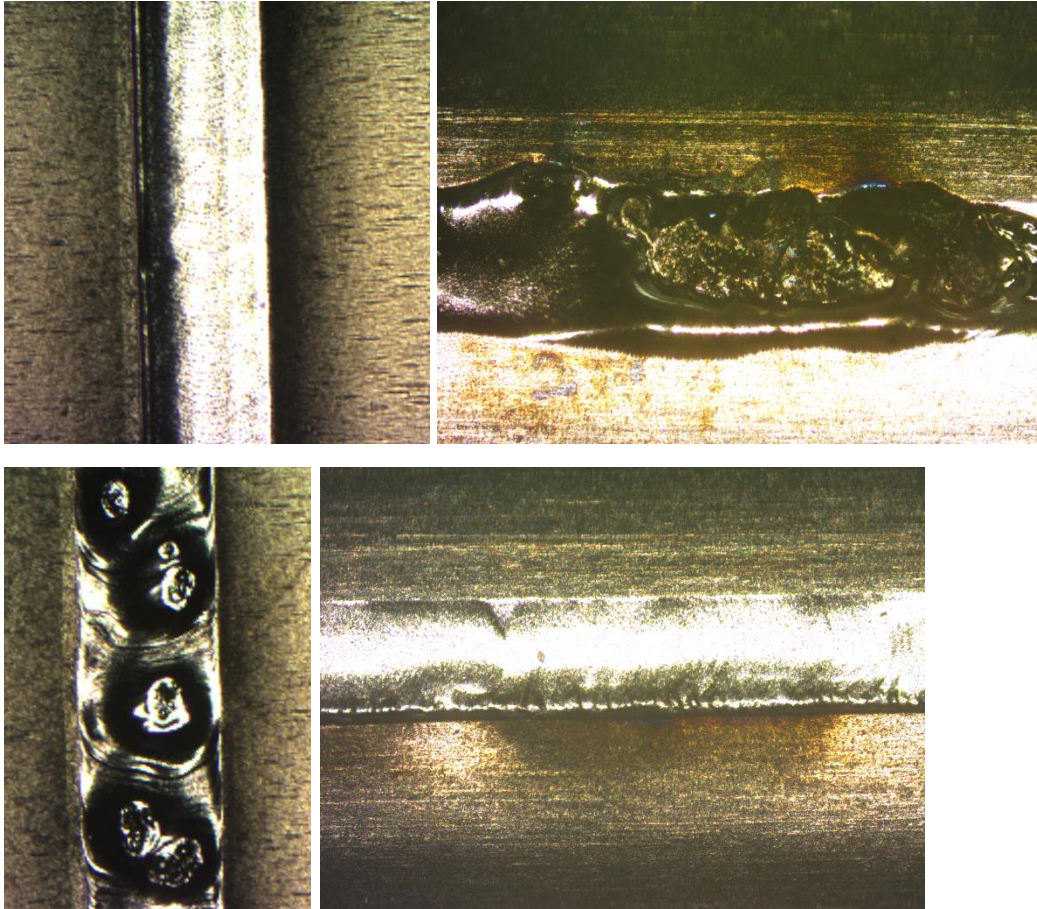


Figure 4.1.6. Top row, left to right: good weld – consistent weld bead width, burn through. Bottom row, left to right: craters, edge failure (torn along the bottom edge).

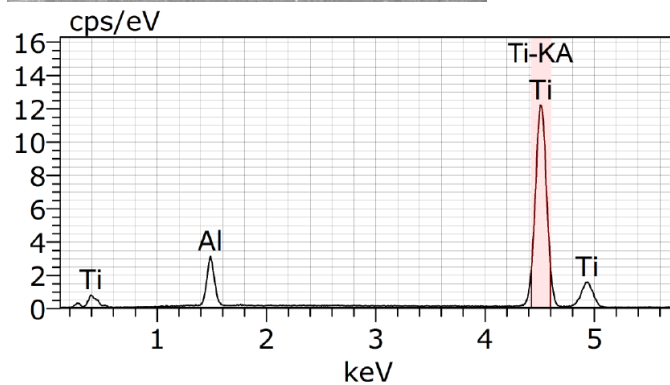
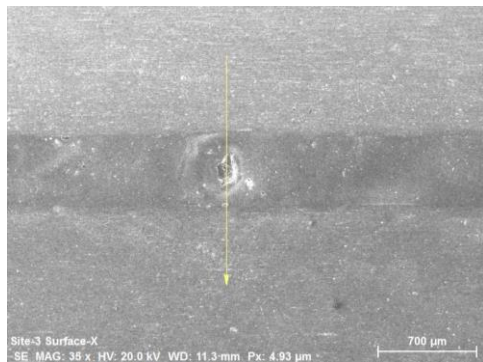
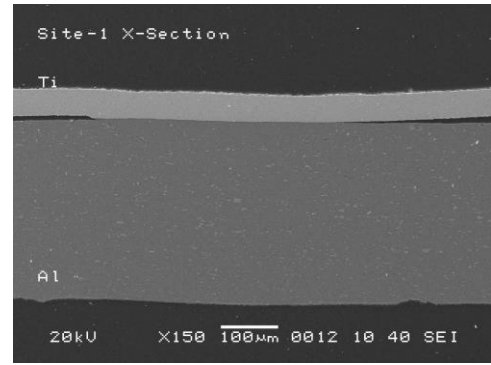
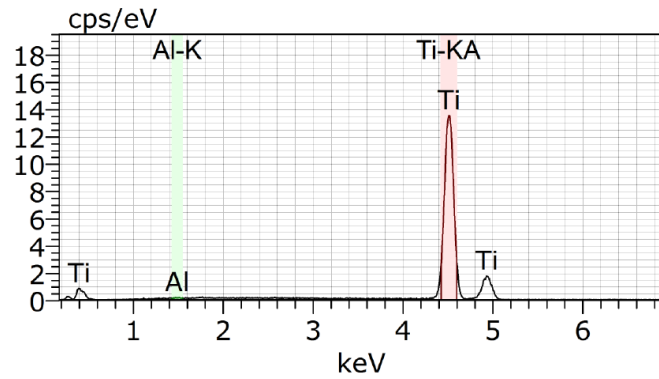
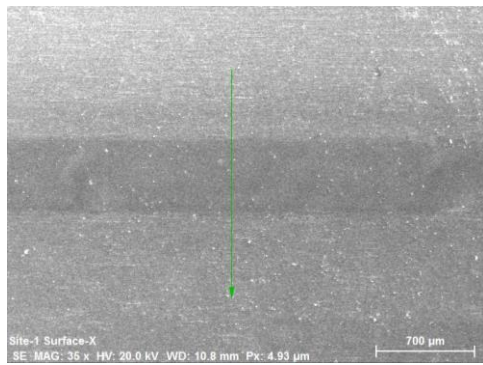


Figure 4.1.7. Energy dispersion spectroscopy (EDS) of a good weld and a burn-through. No aluminum is on the surface in the good weld. In the burn-through, there is a gap in the titanium which exposes the underlying aluminum. An aluminum peak is present on the x-ray spectra of the

burn-through at ~ 1.5 keV whereas no aluminum peak is present on the x-ray spectra of the good weld.

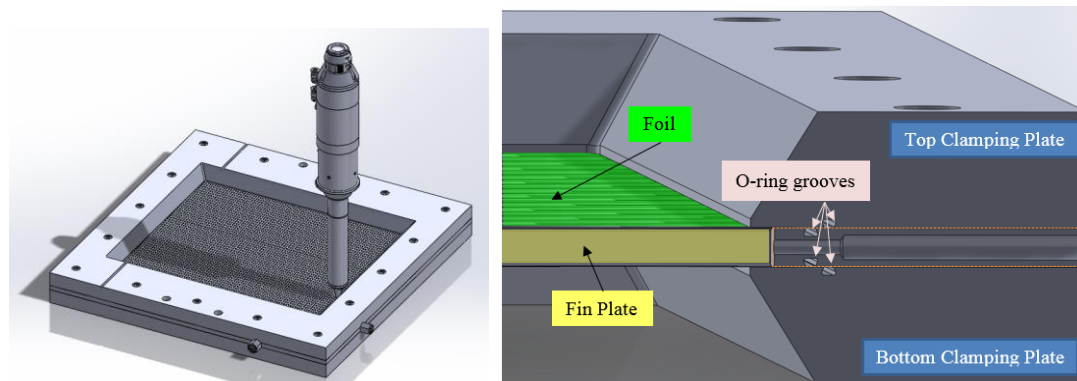
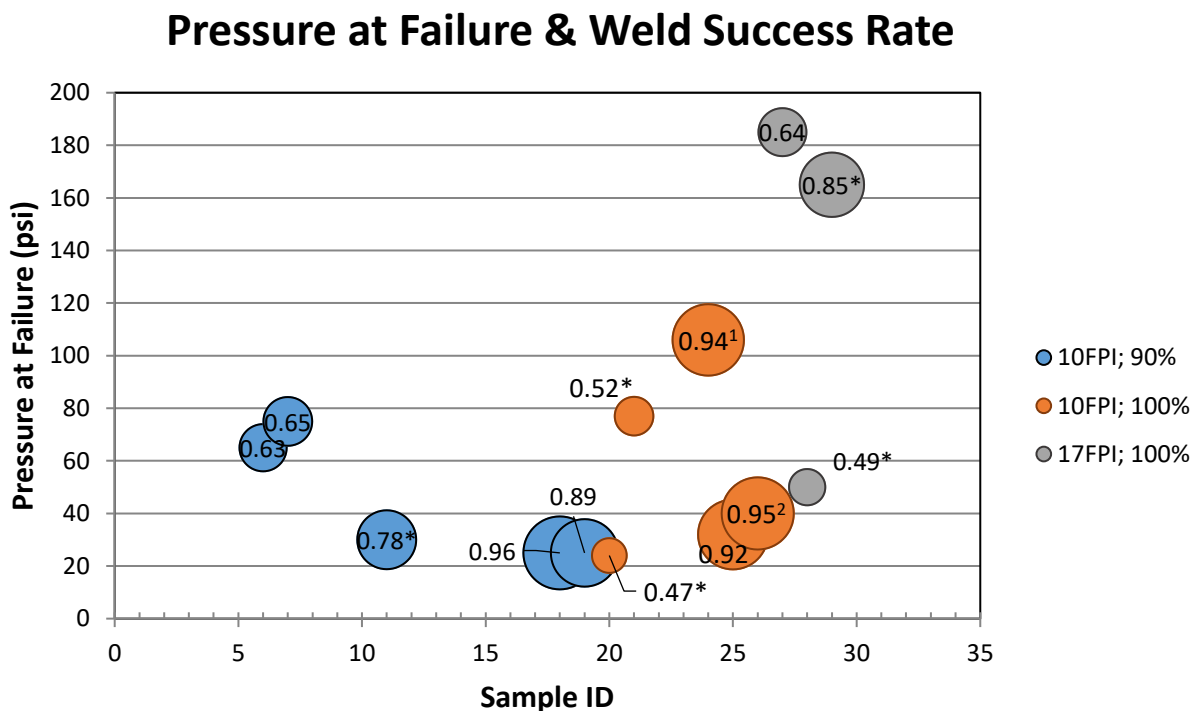


Figure 4.1.8. Fin-Foil Weld Certification Fixture (WC-FF) utilizes clamping plates to hold a sheet of aluminum fins sandwiched between two pieces of titanium foil in place. A pressure port in the fixture is used to pressurize the sample and test the weld strength.



Notes: Samples with * failed at epoxy patch. ¹Foil ruptured without weld delamination.

²Two welds began to delaminate at 40 psi. Pressure tested up to 72 psi when foil ruptured.

Figure 4.1.9. Pressure rating and weld success rate. Circle size and data label indicate the proportion of good weld lines to total number of weld lines.

Titanium Foil Heat Exchanger (TFHX)

Due to difficulties in obtaining a high weld success rate at the fin densities required to meet the required pressure ratings, Makai began an alternate development path for laser welded heat exchangers, the TFHX. In the TFHX, aluminum fins have been eliminated and the working fluid passages are formed using a proprietary process. The contours of the working fluid passages also provide surface ripples to enhance seawater convection.

Foil-foil welds have had high success rates. The pressure rating of the TFHX depends mostly on the titanium foil thickness, weld spacing, and weld diameter (Figure 4.1.10). Foil-foil weld samples were tested in a fixture similar to the WC-FF fixture.

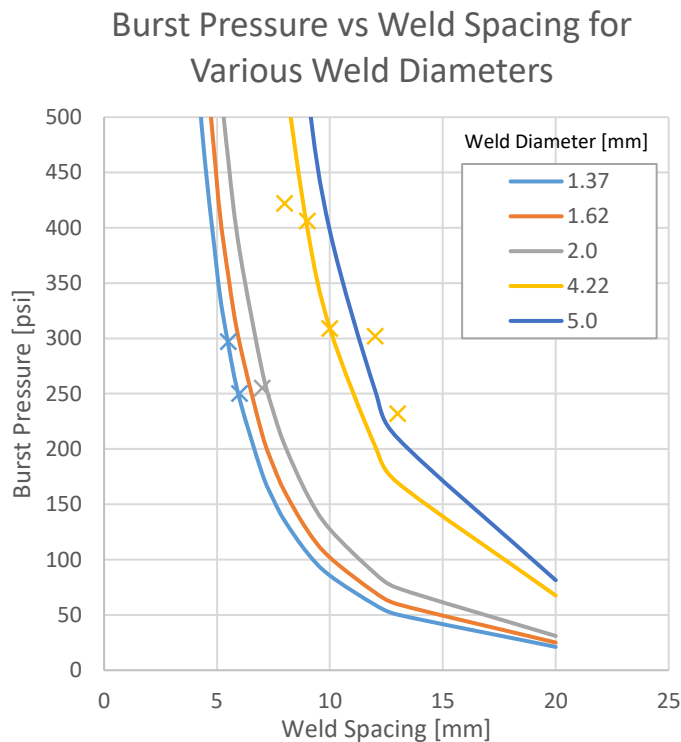


Figure 4.1.10. Burst pressure using 0.0025" thick titanium foil depends on weld spacing and weld diameter. The solid lines are predicted values and "x" marks represent test data.



Figure 4.1.11. A TFHX weld certification sample. Weld certification samples were used to demonstrate the success of foil-foil welds and establish patterns that would meet the required pressure rating.

Sealed and Manifolded Prototype

Successful foil-foil welds encouraged Makai to continue with TFHX development with fabrication of a sealed and manifolded prototype-sized plate. A TFHX plate consists of two pieces of foil, with two manifolds welded to each piece of foil. The manifolds direct working fluid into the working fluid passages and provide an internal seal that separates the working fluid passages from the seawater passages. A foil-foil perimeter weld forms the external seal.

Custom-designed fixtures were used to position and secure components during the TFHX prototype-sized plate fabrication process. Fabrication at the prototype-scale allowed Makai to test out the fixturing and fabrication process and make improvements prior to full-sized plate fabrication.

Once the foil-foil welds are complete, the TFHX plate can be pressure tested with dry compressed air (Figure 4.1.12).

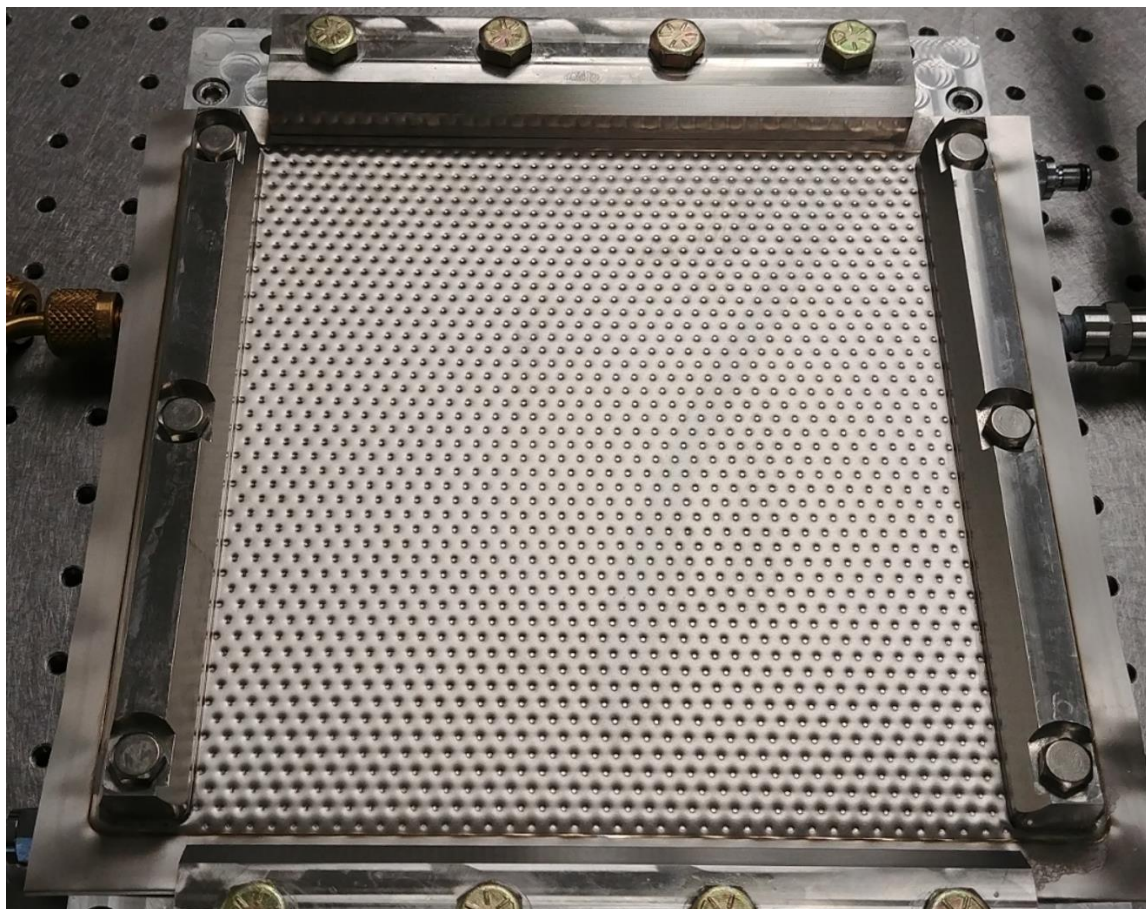


Figure 4.1.12. TFHX prototype plate being pressure tested.

Full-Scale TFHX Plate

Makai scaled up the fixtures designed for the prototype-sized TFHX to create fixtures for the full-scale, 1.2-m long TFHX plate.

A few modifications were required to scale the fixtures to accommodate 1.2-m plate production. Locating pins and threaded inserts were added to ensure all parts were correctly aligned over entire the 1.2-m length. Additionally, in the full-scale TFHX plates, the manifold thicknesses are slightly different to accommodate o-rings, which are used to isolate the seawater from the working fluid passages when multiple plates are stacked together in a heat exchanger. Different templates are required for each manifold thickness to ensure the foil lies flush with the manifolds during welding.

The first 1.2-m TFHX plate (TFHX3B-01, Figure 4.1.13) was successfully constructed on the first attempt on November 9, 2017. The plate took 7.33 man-hours (2 engineers, about 4.67 hours) to construct. Improvements to the fabrication time can be attained by following and assembly line method to construct similar parts in sequence rather the one plate to finish.

TFHX3B-01 has 2.3-mm weld diameters spaced 7.5 mm apart in a triangular grid. The effective heat transfer area is 0.268 m² which is 91.5% of the total foil surface area (0.29 m²). The effective heat transfer area is reduced because the area occupied by the foil-foil welds do not allow working fluid to pass through and cannot be included in the overall heat transfer area.

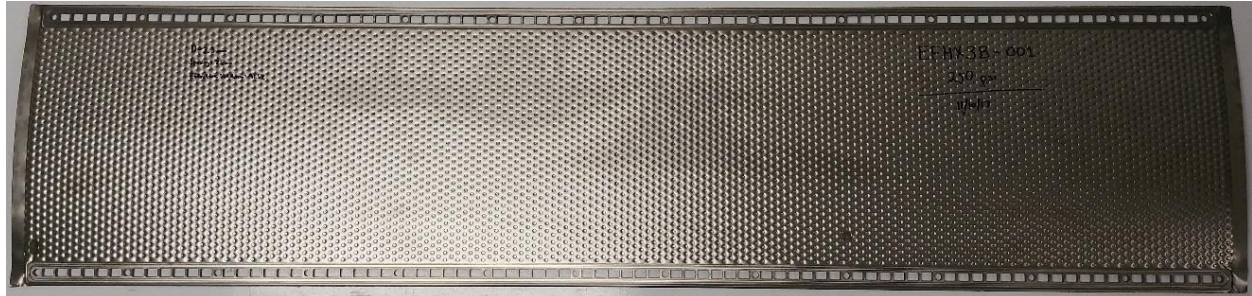


Figure 4.1.13. First full-scale TFHX plate (TFHX3B-01).

The weld pattern was chosen to have a predicted burst pressure of 325 psi. TFHX3B-01 was tested to a pressure of 250 psi, which was determined by applying a 1.3X safety factor to the expected burst pressure of 325 psi.

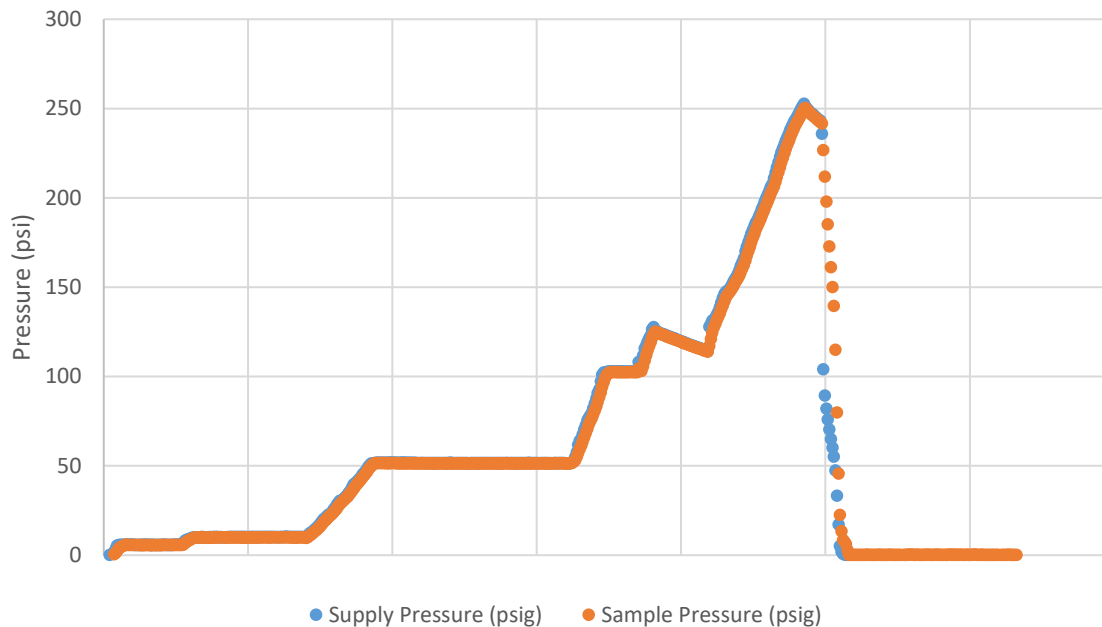


Figure 4.1.14. Supply pressure and sample pressure recorded while pressure testing TFHXB3-001.

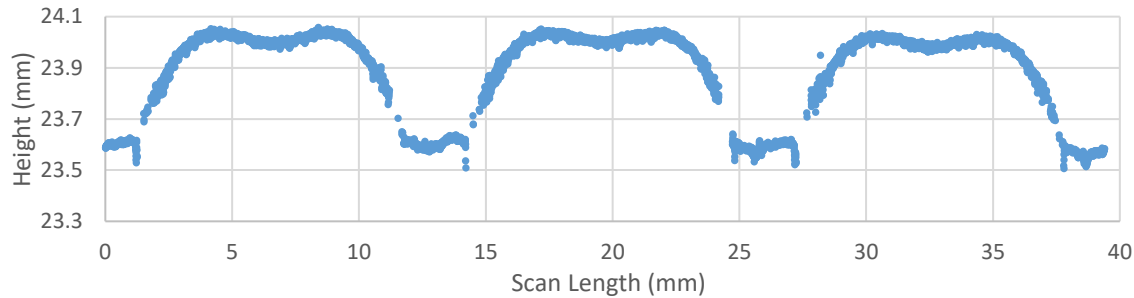


Figure 4.1.15. Line scan of TFHX3B-001 surface while pressurized to 125 psi.

Makai has developed a TFHX Performance Model which predicts heat exchanger performance based on heat exchanger physical dimensions and working fluid and coolant temperatures. Makai plans on testing different configurations of TFHX (under other funding) to determine the best configuration for OTEC and to verify the empirical data correlate with theoretical and previously derived empirical models. New empirical equations relating weld spacing and weld diameter to convective coefficients and pressure drop may be derived from our testing/data collection.

Comparison to EBHX Plates

Previously, Makai constructed and tested EBHXs which utilized epoxy to bond aluminum fin sets to titanium foil sheets. Two 1.5-m EBHX plates required 8.25 man-hours to fabricate. The limitations of the EBHX plates compared to the TFHX plates are:

- Pressure rating - The maximum burst pressure of an EBHX was ~800 PSI, while the highest pressure observed on a fabricated TFHX sample was 503 PSI. With appropriate design parameters, the TFHX is predicted to be able to hold 2100 PSI while maintaining a 93% effective heat transfer area.
- Heat transfer - Foil-foil welds reduce the effective heat transfer area because there is no working fluid channel in the area occupied by the weld. Although there is no reduction in heat transfer area in the EBHX, epoxy acts as an additional layer in parallel to the foil. Epoxy has a thermal conductivity ~ ten times less than that of foil. Both the additional thickness and low thermal conductivity increases the resistance to heat transfer and reduces heat transfer performance.
- Compactness - By eliminating the aluminum fins, two or more TFHX plates can be placed in the same space as one EBHX plate. Having nearly double the heat transfer area more than compensates for any improvement in performance gained through the addition of fins.
- Ammonia compatibility - Epoxy is not ammonia (R717) compatible. EBHX performance testing was limited to using propane (R290) as the working fluid. Propane has low heat of vaporization, making it unfavorable for OTEC applications. The TFHX is compatible with multiple working fluids, including R717, R290, and R134A.
- Epoxy Creep - Over time, the epoxy will stretch and deform when pressurized; some epoxies will significantly deform for 150 days when under load. This epoxy characteristic required that a long term-term qualification test be performed to ensure a plate that initially

held 250 PSI would not fail after one day due to creep issues. The TFHX will not continually deform under static pressure, pressure testing is a quick, reliable process.

- Epoxy Absorption - Certain epoxies can absorb up to 3.4% of R290, and 2.9% of seawater compared to their initial mass, leading to a significant weight increase in a large EBHX unit.
- Sealing Issues - At working pressures, the EBHXs were prone to leaking because the corrugated sealing surface caused inconsistent o-ring compression. The TFHX uses standardized o-ring groove dimensions for a reliable seal.
- Fabrication Timeline - EBHXs had to be construction on a precise schedule due to the pot life of epoxy and BoeGel. TFHX components can be cleaned, prepped and stored indefinitely without sacrificing weld quality.

2MW Heat Exchanger

In designing a 2 MW-sized laser-welded heat exchanger (including headers and interfaces) for installation on the HX Testing Facility, Makai established that the laser-welded heat exchanger concept can be scaled-up for an OTEC-sized heat exchanger. Currently, Makai is focused on constructing and testing smaller TFHXs to fully understand and model the effects of weld spacing, foil thickness, cross-flow versus counter-flow configuration, etc. as well as improving the fabrication process and exploring new heat exchanger designs.

Laser-welded heat exchanger development is an iterative process. As seen in the shift from FFHX to TFHX, in some instances, the proposed design cannot be reasonably fabricated and fabrication challenges have driven design changes that result in a better heat exchanger. With each change to improve the fabrication process or performance, fixtures have to be re-designed, the production steps have to be re-evaluated, and the final component has to be re-tested.

Corrosion Testing

Corrosion testing is on-going and this section summarizes Makai's corrosion-related findings from October 2014 to January 2016 only.

As of January 2016, corrosion samples included box samples, representative heat exchanger samples, and plate, ultrasonic and mini-FFHX samples in the Multi-Column Imaging Rack (MCIR).

Box Coupons

Box coupons have been tested since 2009. 5-year samples of WSW, CSW, and DSW were removed in November 2014. One column of 4.5-year DSW samples was also removed in November 2014. Poorly performing CSW samples were removed in March 2015 (exposed 4.78 years) during repurposing of testing facilities. The remaining CSW and Rack 5 (box samples in CSW that received 45-day WSW pre-treatment) samples were consolidated into one rack (separate seawater flow for Rack 5 samples) and moved into the newer CSW testing room. The remaining WSW rack was also moved into the newer WSW testing room.

In WSW, the 5-year samples had a few pits on both samples of Alloy 1100, Alloy 3003, and Alloy 5052; a few pits on one of the two samples of Alloy LA83I and Alloy LA83P; and no pits on either of the two samples of Alloy 6063. The maximum pit depth observed on the 5-year samples was less than 0.1 mm for all alloys and the average percent pitted area was less than 0.01%. The overall maximum pit depth observed in WSW was 0.45 mm on an Alloy 3003 sample after 2 years, which was most likely due to a manufacturing defect or a bias testing condition. All alloys continued to perform well in WSW.

In CSW, the 4.33-year samples were removed as part of recovery from unexpected NELHA CSW operations; severely corroded samples were preferentially removed and processed but not analyzed. The 4.78-year samples were removed as part of consolidation of Makai's corrosion testing; again, the worst samples were preferentially removed. The 5-year samples were removed as part of planned corrosion testing.

Both 4.78- and 5-year samples were processed and analyzed. The data were biased for the 4.78-year samples, because the worst of the samples were removed from the rack. The overall maximum pit depth observed in CSW was over 2 mm on an Alloy 6063 4.78-year sample. On the 5-year samples, maximum pit depths were around 0.7 mm and the average pitted areas were under 0.1%.

Alloys continue to perform unpredictably in CSW. Alloys 1100 and 3003 have the least scatter. Although some Alloy 3003 samples have had pits > 0.5 mm, most have performed well. Alloys 1100, LA83I, and LA83P had a few very poorly performing outlier samples, but in general, the weight loss results and pitting statistics follow a trend of increasing pits and pit depths with exposure time. Alloys 5052 and 6063 had highly variable performance; it is possible these alloys are subject to more manufacturing variability that affects performance.

In DSW, all 4.5- and 5-year samples had pits. Alloys 6063 and LA83I had severe pitting, with pit coverage across most of the sample surface. Alloys 1100 and LA83P had several large pits, but pit coverage was generally limited to a few locations. Alloys 3003 and 5052 had several significant pits, but the pits were in discrete locations; pit coverage was minimal. The overall maximum pit depth in DSW was observed on an Alloy 6063 sample after 5 years. In addition to pitting corrosion, crevice corrosion was also severe. Alloys 6063 and LA83I had over 10% pitted area after 5 years. Alloy 3003 had the lowest pitted area at ~ 0.2%. In addition to pitting, crevice corrosion was also severe for the DSW samples. All alloys performed poorly in DSW.

No new WSW pre-treatment samples were removed for analysis. Based on previous analysis of the 4-year samples, except for Alloy 6063, the WSW pre-treatment samples performed better than the CSW samples.

Flat Coupons

All flat coupons were decommissioned in March 2015 in favor of MCIR testing. The intent of the small flat samples was to test duplicates of manufacturing methods (brazing, friction stir welding (FSW), electropolishing). Unfortunately, the small sample area lead to results that were heavily influenced by crevice corrosion at/around the gasket/PEM mount and flow induced anomalies.

For the brazed samples in WSW, small pits were observed on the leading edges of most samples. There was also some corrosion on the unexposed side of each sample, around the PEM mount, suggesting some crevice corrosion at the gasket interface. For the FSW samples in WSW, small pits were observed on the leading edges of most samples. Several samples also had small pits on the surface of the sample. There was no corrosion around the PEM mount, as a different gasket sealing method was used for this rack. For the electropolished/plain samples, only a few samples had very small pits on the leading edges and on the surface. Brazed, FSW, and welding are all acceptable joining methods in WSW; however, brazed surfaces must be machined smooth, unfinished brazed surfaces preferentially pitted.

All CSW flat coupons had pits. Brazed joints do not perform well in CSW. FSW samples were adversely affected by cold work introduced to the sample during PEM mounting.

The CHART coupon in 3P2 was decommissioned in March 2015 after 2.8 years in WSW. A few pits were identified under the microscope: one on the weld bead, one near the gasket, and several clustered in a few areas on the surface. Although pits were present, pitting was considered minor.

Representative Heat Exchanger Samples

Old representative heat exchanger CSW samples had severe gasket corrosion and were decommissioned in April 2015 to make room for new samples. Of the new samples, one sample was directly exposed to CSW while the other received the WSW pre-treatment. All samples remain free of corrosion. The WSW pre-treated sample and WSW samples have black flecks on the surface and within the tubes that appear to be biofouling. Heat exchanger designs must carefully consider interior low-flow areas when using materials susceptible to corrosion.

FFHX coupons

FFHX corrosion samples testing began in June 2015. The first three samples were removed after 2 months due to corrosion at weld defects and at the gasket interface. The last two samples were tested starting in September 2015. Corrosion product was observed at weld defects and in several locations where no obvious weld defects were identified. It is most likely that the defects were small and overlooked during inspections by eye. The FFHX corrosion testing emphasized the importance of reliable welds – defects most likely exposed the aluminum fins to seawater and began to corrode preferentially. For an OTEC heat exchanger, any breach from seawater to working fluid is considered a failure of the heat exchanger and must be avoided.

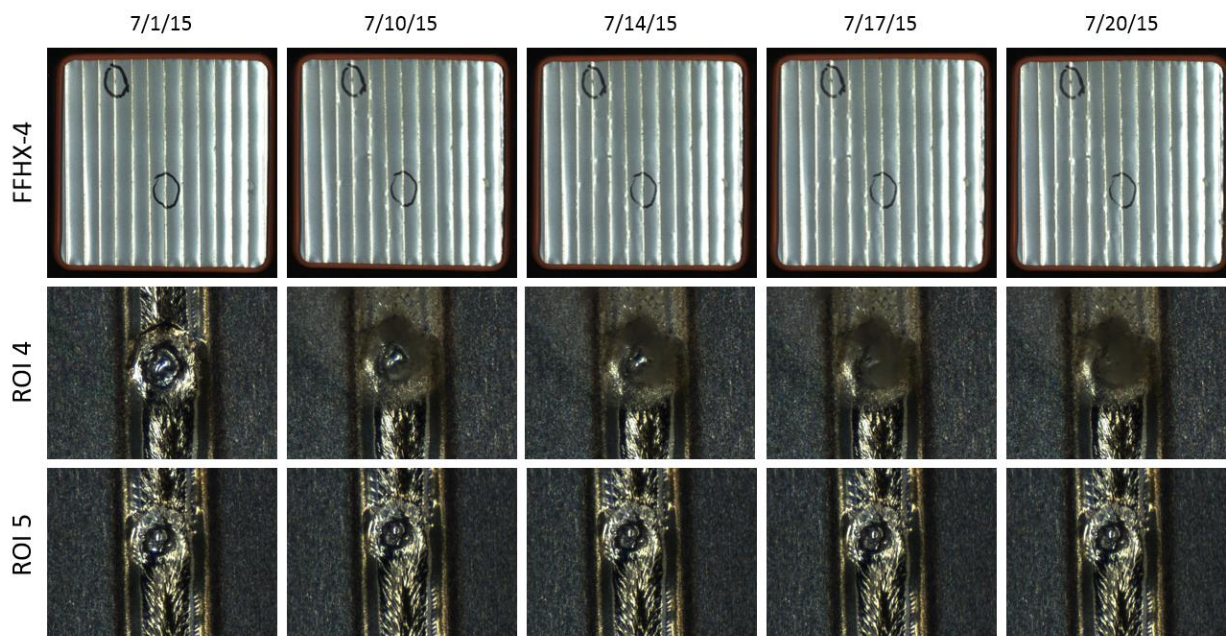


Figure 4.1.16. Development of corrosion product on previously identified weld defect. Regions of interest (ROI) at burn-through locations are marked on FFHX-4. ROI 4 is the top circle, ROI 5 is the lower circle. After 20 days, corrosion developed around ROI 4 but not ROI 5.

Pit Mitigation Treatments

Makai has continued investigations into pit mitigation treatments in CSW in the MCIR. Acid treatments performed based on OCP-based intervals delayed the onset of pitting by over a year compared to the control sample. Pits appeared on the acid-treated sample only after a dry-out vice acid treatment was performed. Acid treatments performed on a 2-month interval were ineffective. WSW pre-treatment delayed the onset of pitting by ~ 2 years. Ozone treatment was tested but increased pitting in CSW samples.

Hypochlorite treatments (provided to ultrasonic samples) in CSW have maintained shiny, like-new sample surfaces. WSW pre-treated ultrasonic samples have also performed well, although testing has only been underway for 8 months.

Acid treatments were tested in WSW but results have been inconclusive as neither the control nor any of the treated samples had pits.

Biofouling

Makai tested ozone, iodine, and chlorine dioxide treatments in addition to daily hypochlorite treatments for biofoulant control. Hypochlorite treatments are the most effective. As long as hypochlorite treatment is consistent, it is effective at preventing biofilm/biofouling; however, once biofilm begins to form (e.g., due to failure in the bleach delivery system), hypochlorination is does not remove the film and additional material can accumulate on the film. Although manual cleaning

is effective at removing biofilm, it is time consuming and impractical for heat exchangers. Acid treatments and flow reversals remove most of the biofilm and can be implemented for a heat exchanger.

Conclusions and Next Steps

Makai's work has focused on new OTEC heat exchanger designs and fabrication methods and corrosion testing.

Makai continues to conduct corrosion testing of aluminum alloys in 915-m cold seawater (DSW), 674-m cold seawater (CSW), and surface seawater (WSW). 5-year box beam samples were removed from DSW, CSW, and WSW. DSW and CSW samples had pits on nearly all samples. Pitting was most severe in DSW. Although some samples in CSW had few pits, alloy performance has been unpredictable; Makai does not recommend the use of untreated aluminum alloys for use in condensers. WSW samples had little to no pitting.

Aluminum plate samples remain in the warm and cold multi-column imaging racks (MCIR) with continued pit mitigation treatments. Treatments performed when open-circuit potentials indicate have been successful, although new pits have been observed if treatments have been delayed by as little as a 48 hours.

Biofouling has become a problem for warm seawater samples. Any missed or reduced hypochlorite dosages lead to formation of a biofilm. Once the biofilm is formed, hypochlorination becomes less effective. Biofouling may be particularly severe at the OERC due to the age and condition of the warm seawater supply pipelines. Makai has previously found light penetration through PVC pipe walls is sufficient for algal growth. Much of the warm seawater distribution utilizes unshielded, above-ground, white, PVC pipes. Acid cleaning, flow reversals, or mechanical cleaning is required to remove the biofilm. Biofouling can cause microbially induced corrosion (MIC) and reduce heat transfer performance. Previous studies on ozone and iodine treatment were unsuccessful at preventing biofouling; consistent, reliable hypochlorination treatment with dosages based on the oxidation reduction potential (ORP) has been most effective at preventing biofouling.

FFHX and TFHX samples have also been tested in the cold seawater MCIR. As expected, FFHX samples have failed at burn-throughs where aluminum is in contact with seawater. TFHX samples are being tested (under other funding) in order to observe biofouling growth and fatigue response due to fluctuations in flow.

Makai's TFHX is fabricated almost entirely from titanium foil using Makai-developed laser welding methods. The TFHX offers several advantages over Makai's previous heat exchanger concepts, the EBHX and FFHX (Table 4.1.3). Primarily, the manufacturing reliability made FFHX unfavorable while ammonia incompatibility and issues with epoxy creep and absorption eliminated the EBHX.

Makai's cleaning protocol, laser welding parameters, and fabrication fixtures and process have resulted in an over 90% weld success rate for the TFHX welds. Makai fabricated and successfully pressure-tested the first 1.2-m long TFHX plate in November 2017.

Table 4.1.3. Comparison of TFHX, FFHX, and EBHX

	Working Fluid Compatibility	Manufacturing Reliability	Time to Fabricate	Pressure Rating	Compactness
TFHX	No restrictions	High success rate	1 st single plate, 5.5 man-hours*	Max tested pressure = 503 psi but pressure rating depends on weld pattern, >2100 psi possible	>1000 m ² of heat transfer area per m ³
FFHX	No restrictions	~ 60% of weld lines had defects	N/A	Max tested pressure = 185 psi	< 300 m ² of heat transfer area per m ³
EBHX	Incompatible with ammonia	High success rate	2 plates, 8.25 man-hours	Max tested pressure = 800 psi	< 300 m ² of heat transfer area per m ³

* Fabrication time for the first plate from start to finish. Future plates will utilize assemblyline style process and is expected to significantly reduce average fabrication time per plate.

Makai's immediate goal is to build more plates and performance test multiple TFHX configurations under other funding. Test results will be used to validate the TFHX Performance Model and, if necessary, to develop new empirical correlations to predict how design parameters affect performance. In addition to the current cross-flow design, a conceptual design has been developed for a counter-flow heat exchanger using new manifolding methods. A long-term test of the TFHX at the 100 kW Testing Station is also planned to collect data about the effects of biofouling and mitigation methods. Eventually, Makai will investigate methods to fully automate the fabrication process which will make TFHXs economically competitive with existing commercially available heat exchangers.

4.2 Wave Energy Testing

Wave energy testing research objectives and plans were developed under APRISES13 to be conducted in collaboration with NAVFAC and the US Department of Energy (USDOE) at the Wave Energy Test Site (WETS) on Oahu. In addition, oversight was provided to investigate the effectiveness of a light work-class remotely operated vehicle (ROV) for use in support of wave energy testing at WETS. Also under this task, numerical hydrodynamic modeling of wave energy conversion (WEC) devices and their performance in realistic seas were conducted, resulting in a well-developed capability that now directly supports the Navy WETS program.

APRISES13 funds related to wave energy marked the beginning of HNEI's major ramp-up of research effort related to this form of renewable power generation. Building on ONR and NAVFAC efforts to test a wave energy converter from Ocean Power Technologies (OPT) in the early 2000's, the Navy undertook, in 2011, a push to expand WETS from one test berth to three. HNEI funding from USDOE, which created the Hawaii National Marine Renewable Energy Center, initiated HNEI's involvement in this Navy expansion of WETS, in the form of supporting the necessary environmental assessment through site characterization and analysis, including wave regime studies, bottom surveys, and bathymetric data collection. This HNEI support was key to the ultimate finding of no significant impact (FONSI) in February 2014, which allowed the construction of the two deeper berths to proceed beginning in September 2014. Previous year ONR funds contributed to these efforts, which resulted in the establishment, in the spring of 2015, of the full 3-berth test site, fully cabled to shore and ready to support testing of point absorber and floating oscillating water column (OWC) WEC devices of up to 1 MW power production.

HNEI's involvement with NAVFAC through these efforts resulted in an opportunity in 2013/14 to pursue additional NAVFAC congressional funds to greatly enhance and extend support to WETS testing. APRISES13 funds were utilized to support a research program manager (a former Navy oceanographer), who fleshed out research objectives in support of wave energy testing at WETS, and ultimately assumed the role of Project Manager for HNEI WETS support. Research objectives include environmental data collection and analysis (WEC acoustic signatures, electromagnetic fields, and protected marine species monitoring), power performance and durability analysis for each deployed WEC (including wave measurement, wave forecasting and hindcasting, regular inspections and tracking and analysis of maintenance issues, power matrix development, and numerical hydrodynamic modeling), and substantial logistical support, with emphasis on developing a site-dedicated research vessel designed to perform most routine functions envisioned at WETS. These research objectives and plans were developed in consultation with NAVFAC under APRISES13 funding.

Now in its fourth year, this NAVFAC/USDOE research program has produced several notable highlights, including:

- 1) Completion of EA and buildout of deep test berths (60 and 80m water depths)
- 2) Deployment of Northwest Energy Innovations Azura WEC from June 2015 to December 2016, at the WETS 30m berth (Figure 4.2.1)
- 3) Deployment of Fred. Olsen, Ltd. (Norway) Lifesaver WEC from March 2016 to April 2017, at the WETS 60m berth (Figure 4.2.2)

- 4) Modification (larger float with larger moment arm, addition of new heave plate) and redeployment of Azura at the 30m berth
- 5) Preparation of Lifesaver for a second deployment, planned for spring 2018, incorporating lessons learned from the first deployment and integrating an environmental sensing and subsea data/power transfer capability directly powered by electricity generated by the WEC
- 6) Extensive underwater acoustic measurements and analysis during each WEC deployment, employing both drifting and fixed sensor packages, resulting in important findings of very low-level acoustic signatures of both devices
- 7) Hull modification, launch, and near completion of WETS site-dedicated vessel Kupa'a, by Sea Engineering, Inc. (Figure 4.2.3).

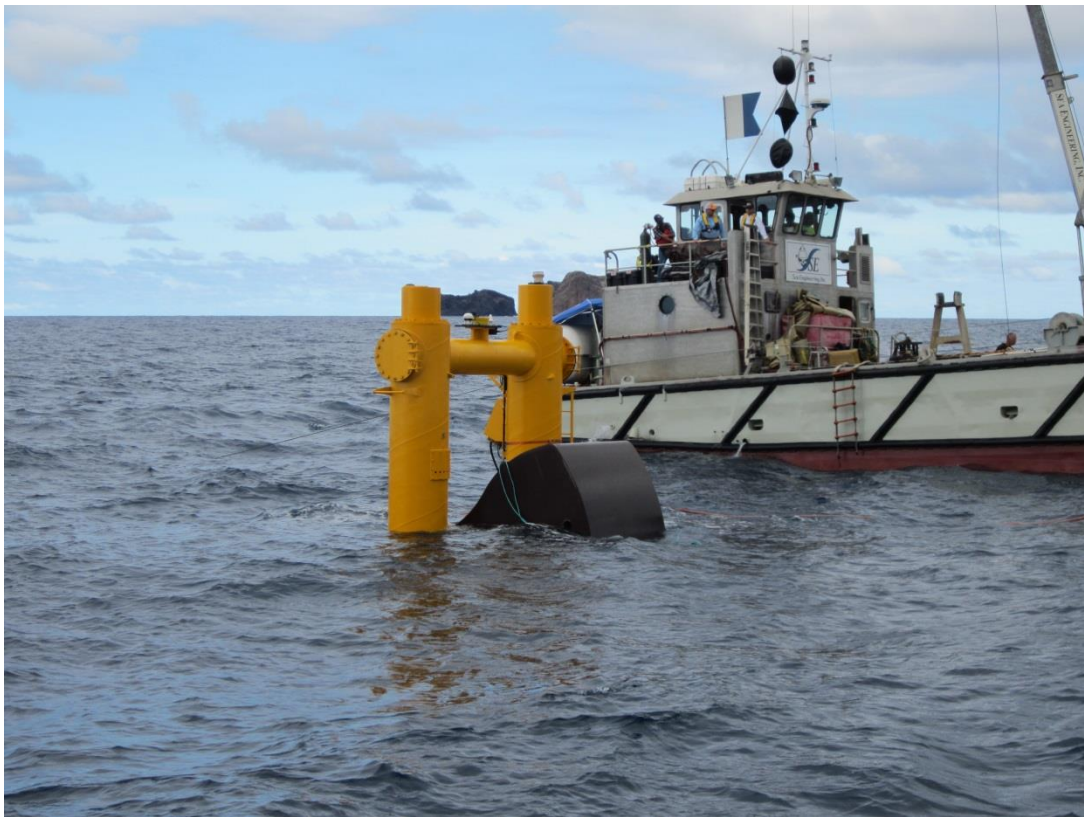


Figure 4.2.1. Northwest Energy Innovations Azura wave energy converter, during deployment in late May 2015 at the Wave Energy Test Site (WETS) 30m test berth.



Figure 4.2.2. Fred. Olsen, Ltd. Lifesaver wave energy converter during deployment in March 2016 at the WETS 60m test berth.



Figure 4.2.3. WETS site-dedicated support vessel Kupa'a, just prior to launch in May 2017. Vessel is nearing readiness for full support at WETS.

Several additional WEC deployments, with associated device and mooring inspections, hydrodynamic modeling, wave measurement and forecasting, power matrix development, and durability assessments, are planned in the coming years, beginning with Irish company Ocean

Energy in the fall of 2018 at the WETS 60m berth. NAVFAC funding will be used to conduct this work.

Once the new NAVFAC funds were in hand in mid-2014, salary support for project management transitioned to those new funds. However, APRISES13 funds supported the oversight of a research effort to examine the effectiveness of a light work-class ROV for use in support of wave energy testing at WETS. Under separate ONR funds, this ROV was purchased after extensive market and requirements studies, and is now being integrated into the site-dedicated vessel mentioned previously. It is shown in Figure 4, onboard the Sea Engineering, Inc. vessel Huki Pau during initial trials, with its control van also visible in the photo. It is anticipated that this ROV will provide a critically important capability for carrying out wave energy related research, including environmental sensing deployments, mooring and WEC inspections, and many minor subsea repairs. HNEI management/oversight of this project has ensured that the ROV integration directly addresses Navy requirements.



Figure 4.2.4. Super Mohawk ROV and control van aboard Sea Engineering, Inc. vessel Huki Pau in Honolulu Harbor, during initial sea trials.

Numerical Modeling

A major emphasis under APRISES13 in support of wave energy research at HNEI and wave energy objectives on the part of NAVFAC EXWC has been placed on numerical hydrodynamic modeling of WECs and their performance in realistic seas. This has been undertaken both in direct

support of WEC developers and independently to add robustness and understanding to the power performance data collected during each WEC deployment. During 2016, numerical modeling was conducted, including linear potential theory and computational fluid dynamics, to support wave energy developers, conduct independent numerical modeling research, and conduct other operational analyses as dictated by events and requirements at WETS. This established the groundwork for what has become a robust support capability, including a range of numerical tools and expertise, in support of Navy wave energy research and operational systems, with recent emphasis on WEC mooring systems. An outline of achievements in this area under APRISES follows.

Numerical modeling of WEC devices was conducted to more thoroughly predict and understand the performance results obtained during in-ocean testing. This is a key aspect of HNEI's independent assessment of WEC performance during WETS testing. Modeling efforts began in 2016 with the setup of numerical methodologies based on state of the art software (e.g. WAMIT, FLOW3D, WEC-Sim) so that performance of WEC devices could be estimated. Since the Azura WEC was the first to undergo trials at WETS, this device formed the basis for initial application of these methodologies. The skill set developed through the numerical modeling of Azura is now allowing HNEI to provide similar design developmental support to upcoming WEC developers expecting to deploy at WETS (under separate funding).

A widely used method for modeling WEC device response in waves is estimation of added mass and wave damping coefficients from Boundary Element Method software (e.g. WAMIT), which are then used to solve the equations of motion of the device in the time domain subject to wave loads, power take off (PTO) forces, and mooring forces. In this method, nonlinearities arising from PTO forces or viscous drag can be easily incorporated. WEC-Sim (open source code developed collaboratively between the National Renewable Energy Lab and Sandia National Lab) follows this methodology and was used extensively for estimation of the power characteristics of Azura. An in-house code was also developed, in order to confirm/verify some of the results from WEC-Sim, while viscous drag coefficients were obtained from Computational Fluid Dynamics code or from the literature.

Power Performance of Northwest Energy Innovations (NWEI) Azura Device

Azura is a two-body WEC that consists of a heavy spar and a light float. The two bodies are connected through a hinge that also includes a PTO. Trials at WETS during 2015/2016 (under other funding) and subsequent APRISES13 numerical modeling indicated that modifications to the float and spar should improve power production. This finding formed the basis of a new project to complete these modifications and redeploy the device at WETS under other funding. (Supported by NAVFAC, the second deployment has now taken place, beginning in February 2018.) The baseline and modified devices are shown in Figure 4.2.5.

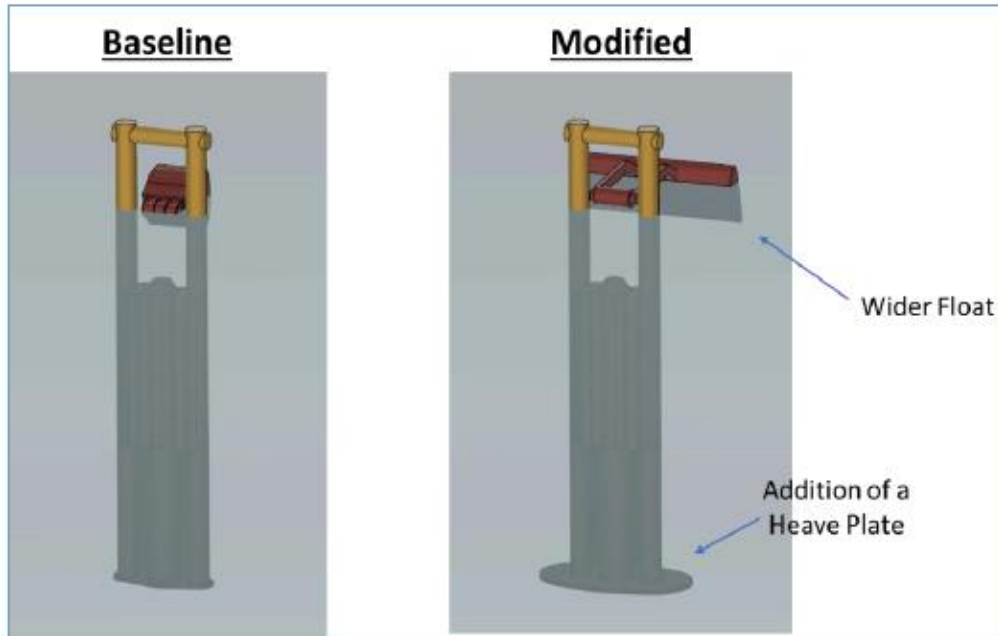


Figure 4.2.5. Azura device. Left panel shows the Baseline device (Version1). The modified device (Version 2) is shown in right panel.

(a) Baseline Azura

Hydrodynamic coefficients of the device were calculated with WAMIT. These coefficients were compared with those obtained from NEMOH (another open-source BEM tool), as generated by NWEI. The coefficients agreed well. Added mass and damping coefficients for the Spar, from these codes (WAMIT {generated by UH} and NEMOH {generated by NWEI}) are shown in Figure 4.2.6.

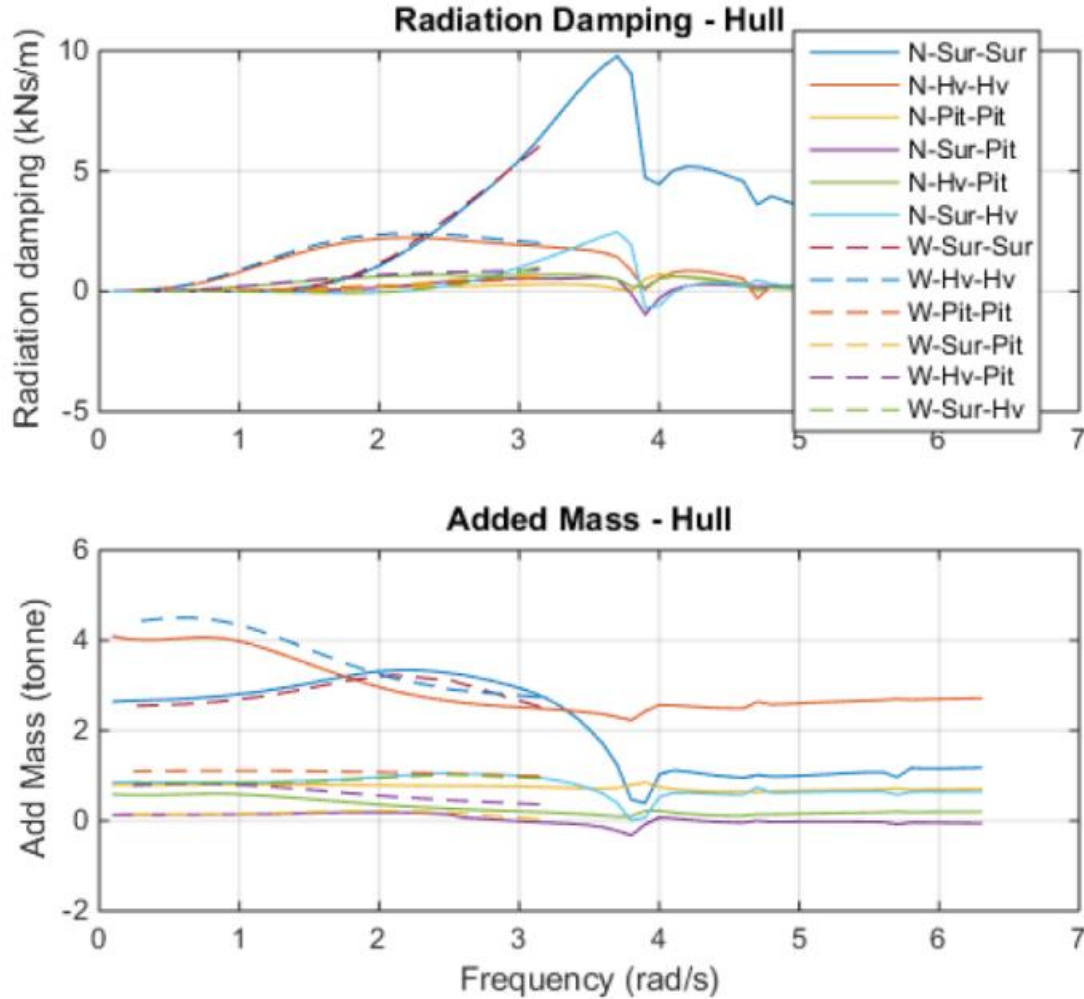


Figure 4.2.6. Radiation damping and added mass coefficients for the Azura spar (Baseline). In the legend, N denotes NEMOH, W denotes WAMIT. Sur, Hv & Pit denote the surge, heave and pitch motions.

The numerical model of the Azura device was set up using WEC-Sim. The Simulink/Simmechanics model that represents the two bodies (body (1) is spar, body (2) is float), connected through a rotational PTO, is shown in Figure 4.2.7. The drag coefficients were calculated using the OpenFOAM CFD solver and taken from the literature. Unlike floating bodies such as ships, which are wall sided, the geometry of the float changes substantially near the still waterline. For this reason, it was found that calculating the wave excitation and hydrostatic forces based on the wetted surface area improved the model results.

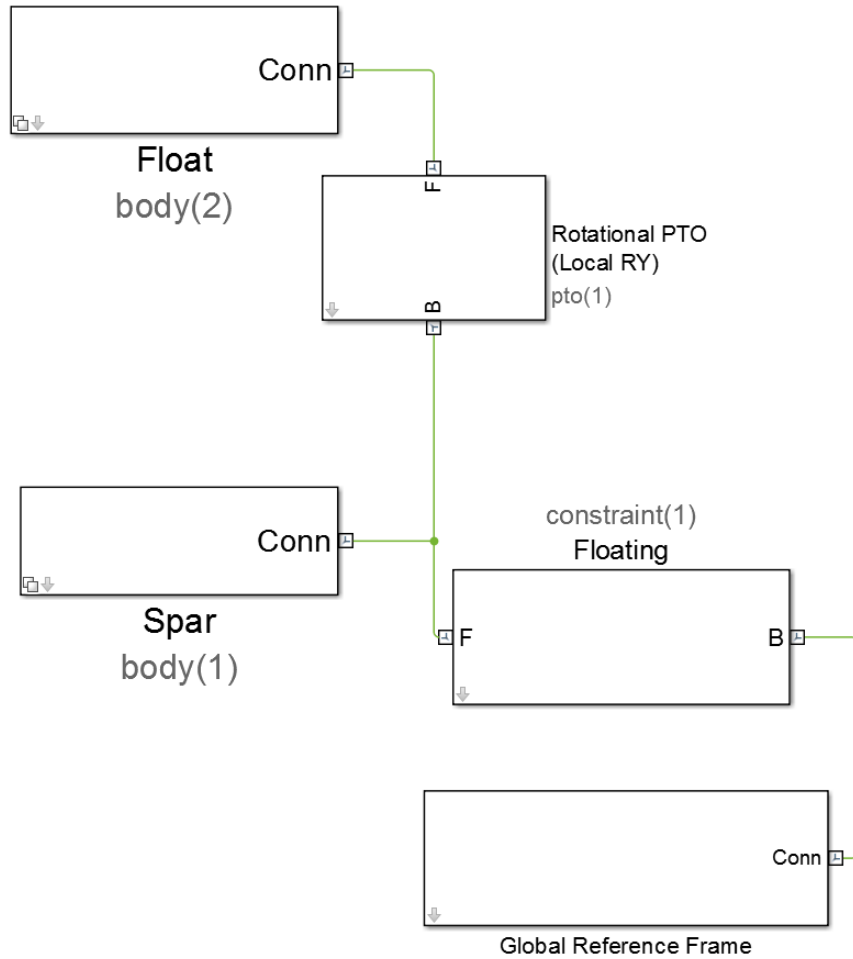


Figure 4.2.7. WEC-Sim Model of Azura Device.

The WEC-Sim model was tuned extensively based on trial data of the baseline device obtained at WETS during the fall of 2015. The trial data provided valuable results of the Response Amplitude Operators (RAO) for the spar and float. The dissipation in the WEC-Sim model was adjusted until the response in the numerical model matched that of trial data. Model runs in selected irregular seas – represented by significant wave height, H_s and energy period, T_e – were then carried out. As these results agreed well with the NWEI predictions, the complete power matrix for the Baseline Azura was generated. This is shown in Figure 4.2.8.

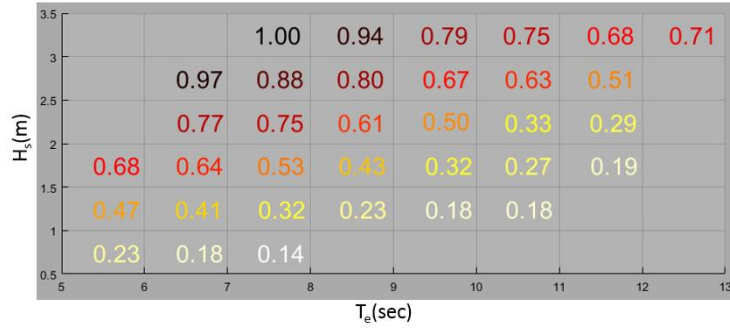


Figure 4.2.8. Azura Baseline Normalized Electric Power Matrix. Power is normalized by maximum power generated by Baseline Azura, during this deployment period.

(b) Modified Azura

The most frequent energy period occurring at WETS is 7.5 sec. It is seen from Figure 8 that the generated power begins to fall off at these wave periods, relative to shorter period waves on the left side of the plot. In an attempt to push the device to better performance at these more frequently observed wave periods, based on APRISES13 modeling results, a plan was developed (under NAVFAC funding) to modify the device. Since the working principle of the device is the relative rotation between the spar and float, it was expected that reducing the vertical motions of the spar, through the addition of a heave plate at its base, would result in larger relative rotations at the hinge, and thus better performance. Additionally, a float, with a larger underwater volume, would increase the power output simply by absorbing more energy from the incident waves. These options were explored in the Modified Version (shown in Figure 4.2.5), which was completed in 2017 and deployed at WETS in early 2018.

(i) Estimation of viscous coefficients with FLOW3D

The Flow3D CFD solver was used for estimation of the drag coefficients of the *full size* float and spar of the Modified Azura device. Since the geometry used in FLOW3D was actual size, scale effects in the CFD results are expected to be small. To estimate the heave coefficients for the spar, the Flow3D code solves the turbulent Navier Stokes equations using a user-specified turbulence model, which in this case is the Renormalized Group (RNG) model. A numerical flume is set up in FLOW3D and the spar is subjected to oscillatory motion in the heave direction with a velocity, $U = U_m \sin(2\pi ft)$, where U is the heave velocity of the spar, U_m is the maximum heave velocity, f is the frequency of oscillation and t is time. The hydrodynamic forces, F_h , acting on the spar are acquired from Flow3D with its post processor (FlowSight). Morison's equations are used to approximate F_h ,

$$F_h = C_a \rho \nabla \frac{dU}{dt} + \frac{1}{2} \rho C_d S |U| U. \quad (1)$$

In Eq. 1, C_a is the added mass coefficient and C_d is the drag coefficient, ∇ is the volume of the spar and S is the area of the heave plate connected to the spar. The full size spar, undergoing heave

oscillation tests in the numerical flume, is shown in Figure 4.2.9. The drag coefficient, C_d , estimated above in Eq. 1, was used as input for the WEC-Sim and in-house codes.

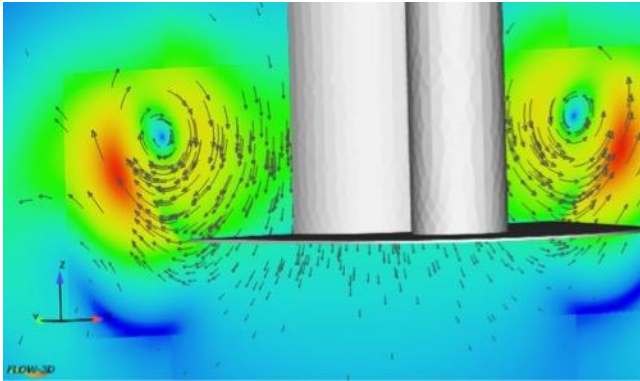


Figure 4.2.9. Snap shot of full size spar of Azura undergoing heave oscillation tests in numerical tank. The central vertical plane in the fore-aft direction is colored by velocity magnitude. Also shown are velocity vectors.

(ii) WEC-Sim model: The WEC-Sim model was set up for the Modified Azura, using the FLOW3D viscous drag coefficients. The model was then used to generate the power matrix. The comparison between the power matrices for the Baseline and Modified versions of Azura is shown in Figure 4.2.10.

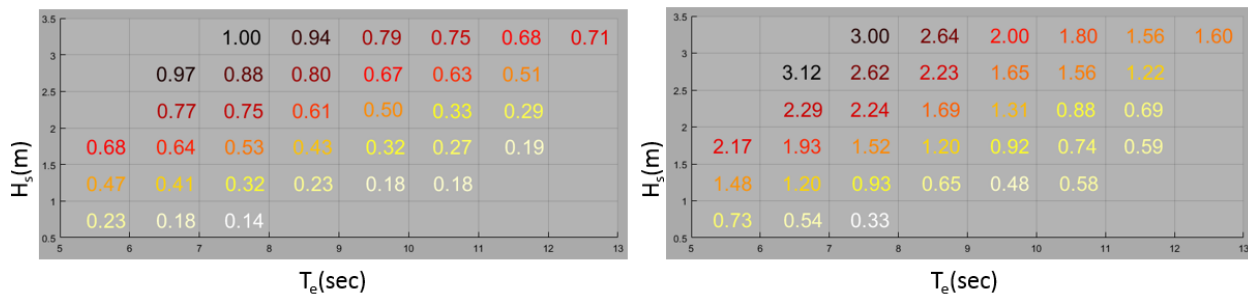


Figure 4.2.10. Power Prediction for Baseline (left) and Modified (right) Azura. Power data for both versions is normalized by maximum power of Baseline Azura.

From Figure 4.2.10, it is clear that the Modified Azura (with the heave plate and new float) can generate 2 to 3 times the power of the Baseline version.

(iii) In-house model: we also developed an in-house code to allow for select test configurations to be comparatively run as a check on our WEC-Sim results. Consistent predictions between the two codes will increase confidence in our numerical modeling predictions. The in-house code also uses the diffraction/radiation solution, like WEC-Sim. Where the WEC-Sim and the In-house code differ is in the implementation of the hinge that connects the float and the spars. In WEC-Sim,

this connection (the hinge) is modeled using Simulink/Simmechanics MATLAB toolbox. In the in-house code, it is modeled by suitably modifying the equations of motion of the two bodies, using constraints imposed by the hinge. Linear motion constraints for small motions were incorporated in the equations of motion. We also derived nonlinear and exact motion constraints suitable for relatively large wave heights. The study showed that WEC-Sim follows the nonlinear constraints exactly. It was also found that the in-house linear and non-linear versions of the code show good agreement with WEC-Sim at smaller wave heights, but only the nonlinear solver compares well with WEC-Sim at relatively large wave heights. A poster based on the in-house model was presented at the Marine Energy Technology Symposium in Washington, DC in May, 2017.

Resource Specific Wave Energy Converter

The trend in Figure 4, which shows electric power generation decreasing with energy period for a given wave height led us to begin research on resource specific WECs. When the natural period of the WEC matches the wave period, resonance or large device motions occur, which can in turn enhance power generation. The natural period of the device is a function of its hydrostatic stiffness. In the case of heave, the hydrostatic stiffness is simply a function of the water-plane area. By varying this area, the natural period of the device may be shifted upwards or downwards. Our initial concept of a resource-specific WEC is shown in Figure 4.2.11. It consists of a disk (a good wave maker) surrounded by cylinders. When some or all of these cylinders are flooded or submerged, the hydrostatic stiffness and natural period of the device changes. This concept was initially developed under APRISES13 funding and later formed the basis for a proposed task within FY16 NAVFAC funding. However, following extensive study (under other funding), it was found that in addition to resonance, the wave making property of the device is also important. Modification of device geometry to change resonance may produce counter-productive effects in terms of wave making, and thus negatively impact performance. While this concept will thus not be directly pursued, the exercise produced an important research result, in that it elucidated this tradeoff between resonance and wave making. Under other funding, a follow-on concept, involving a submerged disc not dependent on resonance, is now being explored and has recently been proposed for development.

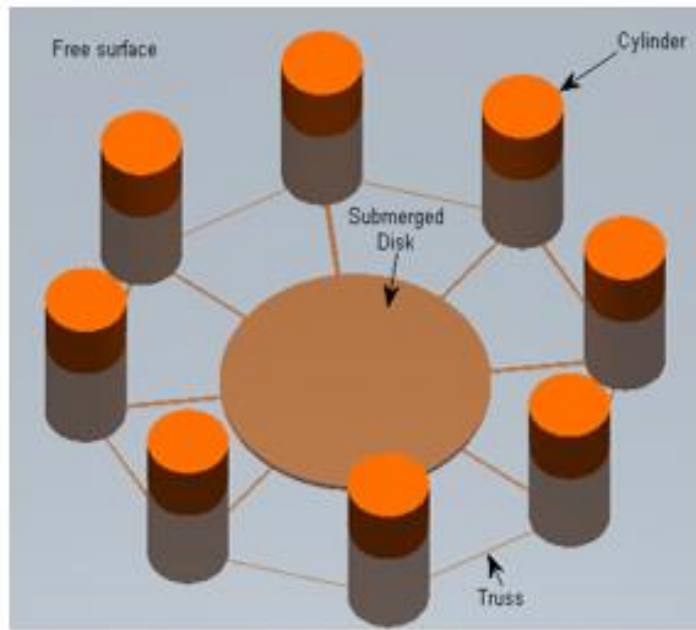


Figure 4.2.11: Resource Specific Wave Energy Converter.

International Energy Association, Ocean Energy Systems Task 10 WEC Modeling

The Ocean Energy Systems organization under the International Energy Association recently initiated its “Task 10”, which offers participating organizations, of which HNEI is one (based on our involvement in WETS and established numerical modeling capability), an opportunity to validate their WEC modeling software. Through a number of web seminars, the participants had an opportunity to compare, discuss their results, and learn potential methods for improving their modeling techniques. For this effort, we used WEC-Sim to model the conceptual WEC, which is a heaving sphere. Decay, regular and irregular wave tests were carried out. This task has further increased our confidence in the WEC-Sim solver and served as a useful interaction with other WEC modelers around the world.

Summary

In conclusion, APRISES13 wave energy funds have allowed HNEI to establish important wave energy research capabilities and to create a solid research program in support of NAVFAC objectives at their Wave Energy Test Site in Hawaii.

Publications Resulting from These Efforts

Numerical Modeling of a Multibody WEC Using Constraint Equations, K. Rajagopalan, G. Nihous, L. Vega, P. Cross, Marine Energy Technology Symposium, Washington, DC, May, 2017.

U.S. Navy Wave Energy Test Site – Early Findings, P. Cross, L. Vega, K. Rajagopalan, G. Nihous, N. Li, A. Rocheleau, P. Anderson, European Wave and Tidal Energy Conference, Cork, Ireland, September, 2017.

4.3 Seawater Air Conditioning

To understand ecosystem response and the overall environmental impact of seawater air conditioning (SWAC), a new marine renewable energy technology, a comprehensive and long term oceanographic monitoring program is needed. Oceanographic monitoring allows the exploration of novel scientific questions related to renewable energy effects on marine ecosystems while providing important, trustworthy, and practical information on the necessary monitoring protocols to ensure the safe, reliable, and economically feasible growth of SWAC nation-wide. APRISES 13 funding supported an oceanographic research program at the site proposed for SWAC development off the coast of Oahu, consisting of 1) long term oceanographic mooring deployments and 2) water column profiling and bottle sampling cruises.

The oceanographic mooring was deployed near-continuously at the proposed SWAC site, and instruments recorded time-series measurements of temperature, salinity, pressure, dissolved oxygen, currents, backscatter, turbidity, chlorophyll, and nitrate. The water column profiles and bottle samples for oxygen, dissolved gases, pH, chlorophyll, nutrients, and flow cytometry were taken at approximately quarterly intervals at both the proposed intake and effluent sites for the SWAC system.

Data collection has allowed for a characterization of the physical and biological properties of the receiving waters of the SWAC system. We have determined that SWAC-driven artificial upwelling will expel a diffused plume of warmed deep seawater into the 100-140 m zone of the Oahu, Hawaii slope. The plume will have higher nutrient levels and lower oxygen levels than ambient conditions. The 100-140 m range is slightly below the chlorophyll maximum, but irradiance levels at the effluent depth are sufficient to support net photosynthesis, and the effluent's high nutrient concentration and location in the pycnocline could lead to rapid horizontal advection of the plume and expansion of the spatial scale of impacts. Analysis of backscatter data revealed that the mesopelagic boundary community will be subjected to impacts from SWAC at both their daytime and nighttime depth habitats. In their daytime habitat, entrainment of organisms in the SWAC intake pipe is a risk; in the nighttime habitat, the community's depth range overlaps with the effluent plume, and the introduced physical gradients may cause attraction to or avoidance of the affected region.

Overall, these baseline data provide an understanding of pre-impact conditions at the future SWAC site. More detail can be found in the publications listed below. The deployments of the long-term oceanographic mooring, water column profiling, and bottle sampling were also partially supported

by APRISES 12 funding. Water column profiling and bottle sampling efforts were partially supported by other funding (NSF, Gordon and Betty Moore Foundation).

Publications resulting from these efforts

Comfort, C. M., McManus, M. A., Clark, S. J., Karl, D. M., & Ostrander, C. E. (2015). Environmental properties of coastal waters in Mamala bay, Oahu, Hawaii, at the future site of a seawater air conditioning outfall. *Oceanography*, 28(2), 230-239.

Comfort, C. M., Smith, K. A., McManus, M. A., Neuheimer, A. B., Sevadjan, J. C., & Ostrander, C. E. (2017). Observations of the Hawaiian Mesopelagic Boundary Community in Daytime and Nighttime Habitats Using Estimated Backscatter.

TASK 5: GEOTHERMAL RESOURCE ASSESSMENT

Funding for this task 5 was reallocated to other areas of the program as approved by ONR, as a result of the unforeseen loss of key geothermal faculty.

TASK 6: MICROGRIDS/GRID INTEGRATION

6.1 Solar Monitoring

Under subtask 6.1, HNEI conducted testing, evaluation and maintenance of ten types of photovoltaic (PV) technologies and developed an analysis tool to characterize the impact of irradiation, ambient temperature, and soiling on PV performance.

The key accomplishments were as follows: developed an understanding of fundamental performance drivers of PV technology; developed a relationship between the performance of each PV technology and a variety of environmental conditions to down select the optimal technology for each environmental condition; developed and installed novel devices to monitor soiling and shading impacts on PV performance.

This work builds on and expands the PV performance testing and analysis conducted under APRISES11 funding. Existing HNEI PV test beds were used, primarily the test bed at Maui Economic Development Board (MEDB), commissioned in February 2016 in Kihei, Maui (under previous funding). This test platform consists of 15 grid-connected PV systems using 10 types of PV modules and 3 system architectures (microinverters, string inverters, optimizers). To separate

module performance from system performance, a module of each PV technology is tested with an IV tracer. The tested PV technologies include 4 standard p-type crystalline (1 mono and 3 polycrystalline), 3 high efficiency n-type monocrystalline (1 with a heterojunction intrinsic thin layer, 1 with rear contacts, and 1 bifacial), and 3 thin-films (2 Copper Indium Gallium Selenide (CIGS), and 1 Cadmium Telluride (CdTe)). All modules are mounted on a carport with 20° tilt and 197°N azimuth.

Numerous sensors were installed on the MEDB test platform to monitor environmental parameters potentially affecting the PV performance including a reference (secondary standard) thermopile pyranometer, a masked thermopile pyranometer device for diffuse and direct irradiance, and a weather station collecting ambient temperature (AT) and rainfall along with other parameters. Testing and hardware were described under previous reports (including final technical reports for APRISES11, as well as for USDOE Hawaii Distributed Energy Resource Technologies for Energy Security (DE-FC26-06NT42847, DE-EE0003507)).

Method

Daily performance is commonly evaluated using the performance ratio (PR), defined by the International Electrotechnical Commission (IEC) 61724 [1], (Equation 1). PR is the operating performance of a PV system or module corresponding to the daily average efficiency relative to the datasheet specifications defined at standard test conditions (STC). In our analysis approach inspired from the loss factor model [2], PR is separated (Equation 2) into current performance (IP, Equation 3), and normalized voltage (VN, Equation 4), also referred to as voltage performance. IP and VN provide additional criteria to understand the performance differences between PV technologies and manufacturers.

Equation 1

$$PR = \frac{\int_{\Delta t} P_{PV} \cdot dt}{P_{MP,STC}} \times \frac{G_{STC}}{\int_{\Delta t} G \cdot dt},$$

Equation 2

$$PR \approx IP \times VN,$$

Equation 3

$$IP = \frac{\int_{\Delta t} I_{PV} \cdot dt}{I_{MP,STC}} \times \frac{G_{STC}}{\int_{\Delta t} G \cdot dt},$$

Equation 4

$$VN = \frac{\overline{V_{PV}}}{V_{MP,STC}}$$

where P_{PV} is the power of the PV module [W]; G_{STC} is the STC irradiance [=1 kWm⁻²]; Δt is the period of analysis [hour]; I_{PV} and V_{PV} are the operating current [A] and voltage [V] of the PV module; $P_{MP,STC}$, $I_{MP,STC}$ and $V_{MP,STC}$ are the power [W], current [A], and voltage [V] of the maximum power point at STC.

During the first year of operation at MEDB from April 2016 to March 2017, the daily performance of the PV modules tested with the IV tracer were observed to vary mainly due to irradiation, AT, and soiling. Shading became relevant only at the end of the first year of operation in February 2017 due to new structures built on the neighboring property. The shading effect is visualized on 2 PV systems during 22 months of operation later in this section.

The performance criteria, PR, VN, and IP, are simulated as a function of the main parameters using empirical models (Equation 5) determined with least-square linear regression. First, the impact of soiling is evaluated with the linear correlation of the performance decrease with the duration of dry periods (DDP) i.e. consecutive days without rain. Next, AT is correlated with the performance criteria that are corrected to remove the soiling impact. Then, the performance criteria, corrected for soiling and AT, are studied versus irradiation. This last step requires 2 linear fits for low and high solar conditions as presented under previous reporting [3]. The irradiation breakpoint is defined by identifying the linear relationship between direct and global solar energy. The breakpoint is estimated at 2.2 kWhm⁻², cut-off point when irradiation is diffuse or when direct light is also collected. The impact of the parameters on PV performance are: $(k_{SS} \times DDP)$ for soiling, $(k_{AO} + k_{AS} \times AT)$ for AT, and $(k_{IO} + k_{IS} \times IRR)$ for irradiation.

Equation 5

$$Perf = k_{SO} + k_{SS} \times DDP + k_{AO} + k_{AS} \times AT + k_{IO} + k_{IS} \times IRR$$

where $Perf$ is defined in equation (1, 3-4); k_{SO} , k_{SS} are the offset and slope of the performance versus DDP; k_{AO} , k_{AS} are the offset and slope of the performance corrected for soiling versus AT; k_{IO} , k_{IS} are the offset and slope of the performance corrected for soiling and AT versus irradiation.

Results

Figure 6.1.1 shows the daily values of the main drivers of PR including the irradiation, AT, and DDP. The daily irradiation averaged 5.5±1.3 kWhm⁻². Daytime temperature averaged 28.0±1.8°C with highs in September and lows in January-February. Dry periods are usually less than 30 days long except from September to December with a 77-day dry period. Correlation between irradiation and AT at MEDB is weak with a correlation coefficient (CC) estimated at 42%. This supports the assumption of uncorrelated parameters for the selected model (Equation 5).

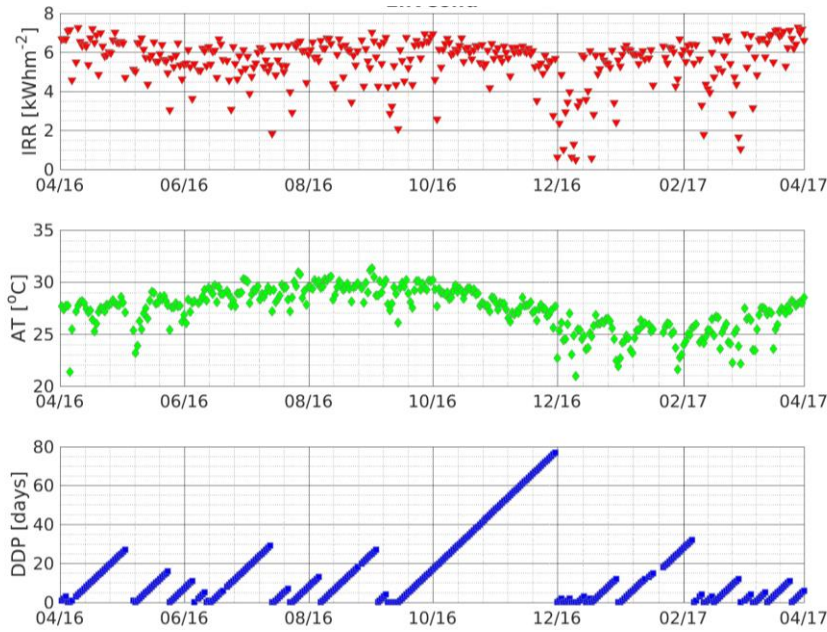


Figure 6.1.1. Daily average values of the main PV parameters from April 2016 to March 2017 at MEDB: irradiation (IRR), ambient temperature (AT), and duration of dry periods (DDP).

Figure 6.1.1 shows the daily performance criteria (PR, VN, and IP) for a polycrystalline PV module (S3) taken as an example and the contribution of the main drivers obtained with the empirical model. The parameter DDP is replaced by the more explicit term “soiling”. Irradiation impact is separated into low (LIRR) and high (HIRR) irradiation for when below and above the 2.2 kWhm^{-2} breakpoint. VN shows low variability, with a range of 9% over the year, mostly affected by AT (with lows in September, highs in January) and the irradiation. IP shows a range of 24%, although it stays almost constant yearlong except for periodic incremental decreases related to the dry periods due to soiling, and high IP values observed in overcast conditions. AT also affects IP, with lower IP values in winter than in summer. The variation of PR with a range of 24% combined the variation observed on VN and IP.

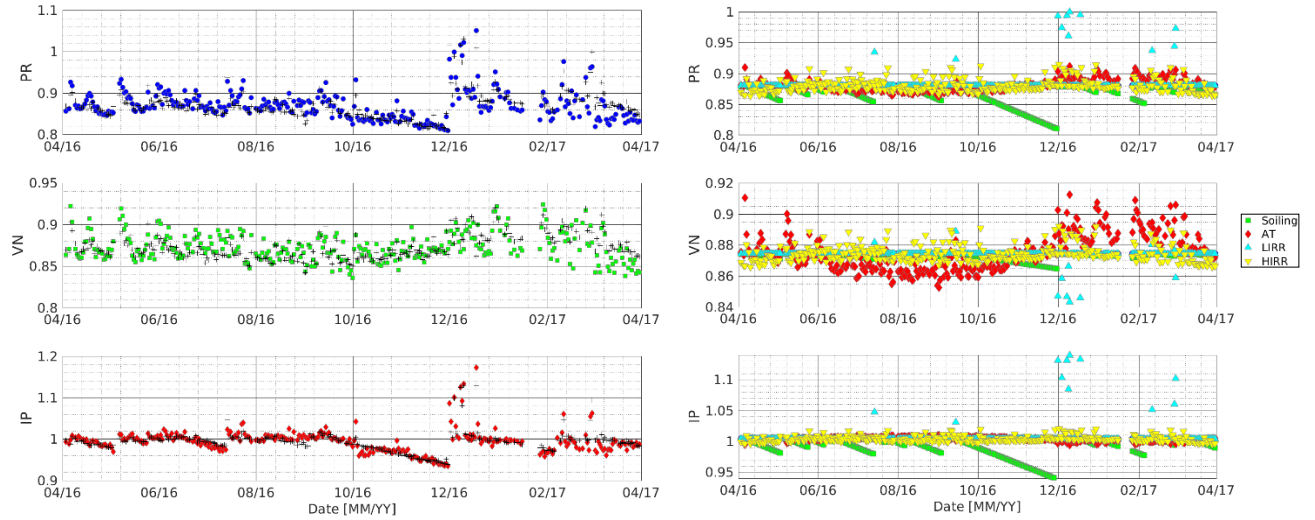


Figure 6.1.2. Daily average performance (PR, VN, IP) of a polycrystalline PV module (S3) tested at MEDB from April 2016 to March 2017. Left: Data and model results (black crosses); Right: Contribution of the main drivers (soiling, AT, irradiation) on each performance criteria.

Graphs on the left in Figure 6.1.2 include data collected from the test beds and values produced by the model (black crosses). The correlation between PV performance and the empirical model is at 71-85% for PR, 71-76% for VN, and 85-91% for IP. The mean relative error (MRE) is below 1.0% for IP and VN and between 1.0% and 1.4% for PR. In comparison, the few previous models for daily energy [4], [5] obtained MRE below 5%. Therefore, this HNEI modelling approach provides a better approximation of PR than the models in the literature.

Table 6.1.1 presents the yearly average PV performance and the impact of the main drivers estimated as a percent of the yearly energy production for each PV module. The acronym of the PV modules starts with a letter indicating the PV technology (C for the CIGS thin-film, D for the CdTe thin-film, H for the high-efficiency crystalline, S for standard crystalline) followed by a digit to differentiate the manufacturers. Performance criteria include PR, the daily yield (PV energy production per installed Watt), and the operating efficiency (η_{op} , PV energy production per area). PR is about 88-89% for most modules, 91% for H1, and ~96% for the CdTe. Daily yield is proportional to PR varying between 4.8 and 5.3 Wh per installed W. However, the operating efficiency takes into account the STC efficiency of the modules leading to higher values for the H modules, followed by the S modules, and finally the thin films.

The impact of the main drivers on PR is summarized below:

- The main driver of PR is soiling which decreases the yearly energy production by 1.2% to 1.7%. This corresponds to 0.07% to 0.1% per day during the dry period. As the pyranometer is also affected by soiling, correction using the correlation between soiling on a flat PV module compared to a dome-shape thermopile pyranometer provided in [6] leads to a soiling impact between 0.09% to 0.13% per day.
- Low irradiation has a significant impact on daily PR (high values) but not on the yearly energy production (<0.1%) because of the mostly sunny test location.

- The impact of AT is estimated between $\pm 0.2\%$ and $\pm 0.4\%$. AT has almost no impact on the CdTe module as previously reported [7].
- Irradiation impact is evaluated at $\pm 0.3\text{--}0.4\%$ for most modules except 2 H modules at $\pm 0.2\text{--}0.3\%$ and the reported CIGS. The latter exhibits no sensitivity to the irradiation and was diagnosed with low optical performance (IP) and reduced performance in low light conditions [8], [9]. This module should not be considered representative of the CIGS technologies. Another CIGS is in test at MEDB however its testing with the IV tracer was not successful during the first year of operation. Results on this second CIGS will be reported for the second year available in future publication.

Table 6.1.1. Yearly PV performance and impact of the main drivers as a percent of the yearly PV energy production.

PV	Yearly average performance			Impact of main drivers (% of yearly PV production)			
	Daily Yield [Wh/W]	η_{op} [%]	PR [%]	Soiling [%]	AT [$\pm\%$]	LIRR [%]	HIRR [$\pm\%$]
C1	4.8	11.7	87.7	-1.2%	0.23%	0.00%	0.01%
D1	5.3	10.3	95.7	-1.7%	0.04%	0.07%	0.34%
H1	5.0	17.3	91.0	-1.2%	0.18%	0.03%	0.17%
H2	4.9	17.5	88.9	-1.2%	0.36%	0.04%	0.26%
H3	4.9	16.1	88.3	-1.6%	0.16%	0.03%	0.34%
S1	4.9	13.7	89.2	-1.4%	0.32%	0.04%	0.33%
S2	4.9	13.5	89.0	-1.5%	0.20%	0.05%	0.34%
S3	4.8	13.4	86.4	-1.5%	0.35%	0.05%	0.37%
S4	4.9	14.6	88.5	-1.5%	0.25%	0.05%	0.36%

Figure 6.1.3 compares the performance of the different PV modules as a function of irradiation at different ambient temperatures using the model presented in equation (5). For both graphs, soiling is considered null. The analysis results are as follow:

- The CdTe module outperforms all other PV at all irradiation and temperature levels.
- At low irradiation, the S modules perform slightly better than the H modules especially H3.
- At low AT, all crystalline PV modules have similar performance within 6%.
- At high AT and high irradiation (above 2.2 kWhm^{-2}), most crystalline have similar PR except H1 with higher performance and S3 the worst performer.
- C1 performance is almost constant at all irradiation and AT levels competing with the crystalline modules only in warm and highly sunny conditions.

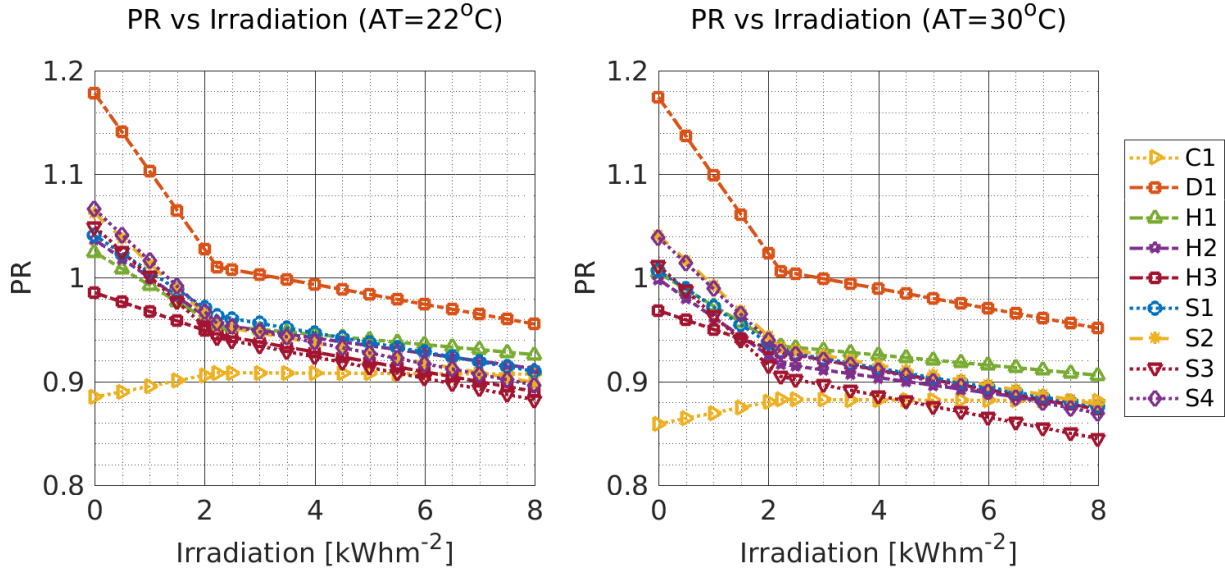


Figure 6.1.3. Performance ratio (PR) as a function of irradiation for all PV modules tested at MEDB for 2 ambient temperature (22°C and 30°C). Empirical model presented in equation (5) fitted to first year results and considering no soiling.

Shading can also be an important driver of the PV performance. Figure 6.1.4 shows the daily AC PR of 2 PV systems made of the same H modules differing in terms of system architectures. Grid-connected systems were turned off from mid-June 2018 to September 2018. The system using microinverters (blue dots) exhibits a drop of performance from 85% down to 75% in December 2017. The system using a string inverter (green squares) suffers a significant performance degradation with a drop down to 45%, almost half of the initial performance (85%). This difference between the 2 systems started to be significant in February 2017 when the neighboring property installed new structures which caused shading. Impact of shading degrades the PV performance for about 4 months of the year which would lead to a decrease of the yearly PV production by 2% for the microinverter system and 7% for the string inverter system.

Before comparing system configurations under shaded conditions, it is necessary to characterize the shadow that can differ between PV systems. More information will be provided in further publication once the shadow detection system described below provides data to correlate the performance drop with the shaded area.

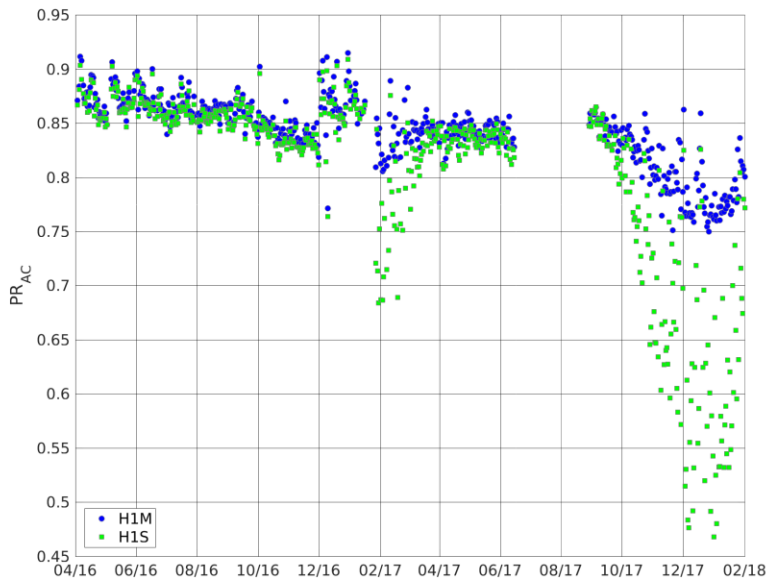


Figure 6.1.4. AC performance ratio of 2 systems differing in terms of system architectures: microinverter (H1M) and string inverter (H1S) for 22 months of operation. Shading consequently affecting the PV systems during winter months from February 2017.

Conclusions

- An empirical model was developed to predict the daily PV energy production (by modelling PR) with an error below 2%. The model accounts for the effect of soiling, AT, and irradiation.
- From the data collected at MEDB during the first year of operation, the main driver of the yearly average PR is soiling reducing the PV production by less than 2%.
- Comparing the PV module performance in different environmental conditions, we recommend based on PR results (when performance per area is not the primary criteria only the performance per installed W) to use the S modules instead of the H ones in overcast conditions. In sunny conditions, all crystalline perform similarly. However, at high AT (30°C), crystalline modules exhibit higher performance variability with one H module to prefer and one S to avoid. The CdTe module outperforms all other PV. CIGS technology will need additional data to conclude on the performance of this technology in Maui.
- Next, the model will be improved by adding the effect of shading and aging, the latter requiring longer testing and monitoring. Shading at MEDB would reduce the yearly PV production by up to 7% depending on the system configuration and shadow shape.

Development of existing PV test platforms

To evaluate the impact of shading at the MEDB test platform, a system is required to characterize the shadow shape on the different PV systems. Two main approaches were considered for shadow detection: a photosensor-based design and an image-based design.

The photosensor design would consist of a large array of photocells spread across the PV array. The intensity of light of each photocell would be recorded using microcontrollers. This approach has a high resolution for light intensity, but the spatial resolution depends on the number of sensors and therefore cost. If the distance between sensors is too large, the system wouldn't be able to detect shadows on individual PV cells within a single module.

The image-based design uses cameras to view the reflected light coming from the PV array. Multiple cameras can be used to overcome the limited field-of-view of a single camera. The images can show a difference between shaded areas and non-shaded areas, but it cannot accurately measure the intensity of light unless a calibrated point on the image is known by another type of light sensor. The spatial resolution depends on the resolution of the camera and its distance from the array. A general comparison of the two approaches is shown in Table 6.1.2.

Table 6.1.2. Comparison between photosensor-based and image-based design for shadow detection

	Photosensor-based Design	Image-based Design
Light intensity resolution	High	Low
Spatial resolution	Low	High (depending on camera resolution and location)
Hardware cost	\$500+ (depending on spatial resolution)	~ \$400
Development time	3-4 months	1-2 months

Image-based shadow detection was chosen because of spatial resolution, cost, and development time. To get the best views, it was negotiated with MEDB's neighboring company to place 3 wireless cameras on the structures casting shadows on our PV platform. The camera mounting was expected to be completed in September 2017. However, the neighboring company was rebuilding part of their infrastructure which led to delays. Camera installation was completed on February 20th, 2018. Figure 6.1.5 shows the picture collected by one the newly installed cameras while shading is affecting the bottom of the PV test platform.



Figure 6.1.5. Picture collected by one of the newly installed camera for shadow detection.

From these collected pictures, shadow detection algorithms need to evaluate the percentage area of shadow on a given PV module, the number of cells covered, and the shape of the shadow. This shadow coverage will be correlated with the power of the PV systems monitored by the HNEI DAS. It is therefore essential to have both the wireless cameras and DAS synchronized with the same NIST time-servers.

Shadow detection algorithms were studied under this subtask. Selected software is Matlab also used for the PV performance analysis.

The first step for shadow detection is the calibration of the cameras. The intrinsic (focal length, optical center, and skew coefficient), extrinsic (location of the camera in 3-D world space), and lens distortion properties are estimated using test images of known patterns such as a checkerboard using the Matlab function “Camera Calibrator”.

Once the cameras have been calibrated, distances and sizes can be calculated using the known size of objects in the image. Another way to get distances and size is to transform the image to correct for perspective using the Matlab function “fitgeotrans”. This latter technique should be selected because it facilitates the calculation of the percentage of area based on pixel count.

The final step is to separate the shaded area from the rest of the PV module. The first investigated technique is color thresholding using the red-green-blue (RGB) color space. Shadows are visibly darker than lit areas (Figure 6.1.5). A threshold number for the intensity of light, for example the blue channel, can be used to mask the image to reveal and approximate the shaded area. Another approach proposed in [10] is to convert the image to the hue-saturation-value (HSV) color space, threshold the image to find large shadows and use fuzzy logic to classify these regions as shadow or non-shadow. The final solution for shadow detection algorithms will be reported in further publication.

In addition to the shadow detection system, an additional solar sensor was installed at MEDB on February 20th, 2018. The goal is to establish the correlation of irradiance measurement between a flat amorphous solar cell pyranometer (commonly used on residential PV installations) and a thermopile pyranometer. Amorphous solar cells are spectrally sensitive which can lead to important error in irradiance measurement in our tropical environment. The expected correlation

will improve the analysis of existing HNEI PV test platforms, the Hawaii Project FROG (Flexible Response to Ongoing Growth) classrooms located in Oahu and Kauai [11], equipped with such solar cell sensor.

Finally, the HNEI test bed located at UH Manoa campus was partially maintained under previous funding with the calibration of the pyranometers [3]. Under this subtask, the electrical sensors were calibrated, a rain gauge was installed, and the 2 arrays of PV modules were washed. Collected data will allow for soiling evaluation at the site.

Publications Resulting from these Efforts

S. Busquet, J. Kobayashi, D. Matthews, R. E. Rocheleau, “Test protocols and monitoring system to assess grid-connected PV systems.”, to be submitted to a peer-review journal (Measurements, Elsevier).

S. Busquet, D. Matthews, J. Kobayashi, R. E. Rocheleau, “Daily performance and main drivers of PV modules operating in Maui.”, to be submitted to a peer-review journal (Energy, Elsevier).

References

- [1] “IEC 61724-1 - Photovoltaic system performance – Part 1: Monitoring IEC,” *IEC Stand.*, no. 1.0, 2017.
- [2] S. Sellner, J. Sutterluti, L. Schreier, and S. Ransome, “Advanced PV module performance characterization and validation using the novel Loss Factors Model,” in *38th IEEE Photovoltaic Specialists Conference*, 2012, pp. 2938–2943.
- [3] HNEI Report, “Final Technical Report of the Office of Naval Research Asia Pacific Research Initiative for Sustainable Energy Systems (N00014-12-1-0496), Subtask 6.1. Solar Hydrogen at Marine Corps Base Hawai‘i,” 2017.
- [4] E. L. Meyer and E. Ernest van Dyk, “The effect of reduced shunt resistance and shading on photovoltaic module performance,” *Conf. Rec. Thirty-first IEEE Photovolt. Spec. Conf. 2005.*, pp. 1331–1334.
- [5] C. Cañete, J. Carretero, and M. Sidrach-de-Cardona, “Energy performance of different photovoltaic module technologies under outdoor conditions,” *Energy*, vol. 65, pp. 295–302, 2014.
- [6] M. Waters, T. Tirumalai, M. Gostein, B. Stueve, and S. Francisco, “Soiling Rates of PV Modules vs . Thermopile Pyranometers,” pp. 2–4.
- [7] J. A. del Cueto, “Comparison of energy production and performance from flat-plate photovoltaic module technologies deployed at fixed tilt,” *29th IEEE Photovolt. Spec. Conf.*, pp. 1523–1526, 2002.

- [8] S. Busquet, J. Kobayashi, and R. E. Rocheleau, “Operation and performance assessment of grid-connected PV systems in operation in Maui, Hawaii,” in *44th IEEE Photovoltaic Specialist Conference and Exhibition*, 2017.
- [9] S. Busquet, J. Kobayashi, and R. E. Rocheleau, “Daily Performance Comparison of PV modules Operating in Maui,” in *33rd European Photovoltaic Solar Energy Conference and Exhibition*, 2017, pp. 2311–2315.
- [10] M. Karakose and K. Firildak, “A shadow detection approach based on fuzzy logic using images obtained from PV array,” in *2015 6th International Conference on Modeling, Simulation, and Applied Optimization (ICMSAO)*, 2015, pp. 1–5.
- [11] HNEI Report, “Task 4. Alternative Energy Systems, Subtask 4.3. PV Deployment and Testing, for Office of Naval Research Hawai`i Energy and Environmental Technologies (HEET) Initiative (N0014-10-1-0310),” 2016.

6.2 Secure Microgrids

Power Grid Monitoring Project

The objective of this project was to develop a low-cost real-time power monitor with wireless communications for distribution system operations, controls, and analysis. Our approach leveraged advances in RF communications, smart meter integrated circuits, and open source software to create a fully integrated device for this application. The device is intended to support HNEI's research and field demonstrations on the distribution grid as well as provide a solution that could be commercialized to help solve grid operational issues with high penetrations of distributed energy resources (DER) such as photovoltaic (PV).

In order to improve the resiliency of the electric grid and allow high penetrations of distributed PV, there is a need for better real-time situational awareness of the distribution circuit. On circuits with very high penetration of PV, power backfeeds from residential customers to the grid. This can introduce issues such as overvoltage and violations of thermal limits on the electrical lines. High penetrations of PV also has an effect at the system level and may require additional operational reserves to protect against transient cloud coverage. Better power grid monitoring can help the utility identify and address these issues and ultimately operate the grid more reliably with large amounts of distributed PV.

HNEI has previously deployed 60 distribution-level power monitoring devices under the DOE-funded Maui Smart Grid Infrastructure project. This work showed that commercial power monitors are currently inadequate for system-wide deployment on the distribution grid. Some do not accurately measure reactive power under bi-directional active power flow, which is essential

for advanced methods of voltage regulation. Others provide advanced measurement of reactive power, harmonics, and numerous other metrics, but are very expensive (~\$3000/unit) and still require communications equipment with a commercial data plan (up to \$100/mo), a power supply, and a weather resistant enclosure. These are designed primarily to record power quality data for post-processing and event detection rather than to stream basic data such as RMS voltage, RMS current, active and reactive power, and frequency in real time for controls and grid operation.

A low-cost, integrated solution was developed in this project for circuit- or system-wide monitoring to address the specific needs of utility operations under high penetrations of PV. The essential features and requirements of the device are:

- Measurement of root mean square (RMS) current, RMS voltage, active and reactive power, and frequency
- Sampling every 1 s or faster
- Up to 3 electrical phases
- Weatherized for exposure to UV light, thermal extremes, and precipitation
- Small package with simple and secure mounting options
- Self-powered from service lines
- Built-in communications for real-time data retrieval

The power monitor is primarily intended for installation at service transformers. HNEI believes that the service transformer is a key nodal point on the grid because it aggregates the load of several utility customers yet is close to the edge of the grid where it can provide or support high fidelity controls via demand response. Due to the aggregation, it can potentially cover the utility's service area at a lower cost than smart meters, yet it can complement smart meters by providing a communication gateway and receiving data from those meters at the very edge of the grid. The service transformer offers relatively easy access and low voltages that can be monitored with low-cost electronics. Service transformers are typically mounted on utility poles which provide good elevation for RF transmission. The transformer itself is a key piece of utility equipment that is prone to failure, and in fact other commercial products have focused on detecting transformer anomalies without providing the full capabilities required for distribution system operations, controls, and analysis with high penetrations of DER.

Design

In order to reduce the cost of the device, it is important to consider (1) the cost of parts and manufacturing, (2) the installation of the device onto the utility pole, and (3) the monthly commercial data charges. In order to reduce the cost of parts and manufacturing, the design is based on printed circuit boards (PCBs) that integrate commercial electrical components: an application-specific integrated circuit (ASIC) for smart meters, a microcontroller, a wireless mesh transceiver, a Global Positioning System (GPS) receiver, power supplies, and an optional single board computer (SBC) and Long Term Evolution (LTE) modem.

In order to reduce the cost of installation, the device is fully integrated in a small weather resistant package (NEMA 4X / IP65) and has simple bayonet connectors and built-in mounting flanges with optional magnets. In order to avoid the need for reinstallation, the device's microcontroller allows run-time self-programming with the potential for over-the-air configuration and firmware updates.

The monthly data charges are reduced by using a wireless mesh network to aggregate data onto a gateway device with a single commercial data plan, as shown in Figure 6.2.1. Each device's data is transmitted over the open 900 MHz industrial, scientific and medical (ISM) band to other power monitors in the mesh and finally to the gateway, which has a modem with a commercial LTE wireless data plan. The gateway gathers data from devices on the wireless mesh as well as its own power monitor. It streams the data using an open-source message queue software to a server, which stores the data in a MySQL database and provides it to clients via a web plotting interface (Figure 6.2.2) and JSON-based queries. With proper credentials, external devices can also access the raw data stream for low-latency controls.

HNEI has developed several prototypes of the power monitor. The first version, shown in Figure 6.2.3a, was the initial proof of concept of the remote (non-gateway) device with single split phase measurement. The second version, shown in Figure 6.2.3b, added full three-phase measurement, the capability of accepting Rogowski coil-based current transducers (CTs) as well as traditional CTs, full galvanic isolation for safety, and a GPS receiver for accurate global time synchronization. It is DIN-rail mounted and has the option to include a SBC to serve as the gateway. The third and current version, shown in Figure 6.2.3c, adds a small LTE modem, an enhanced microcontroller with digital signal processing (DSP) capabilities, a supercapacitor-based backup power supply, and flash memory for data retention and logging of power failures. It has modular input, wireless, and gateway boards and is packaged inside a NEMA 4X / IP65 enclosure with NEMA 6P / IP67 connectors.

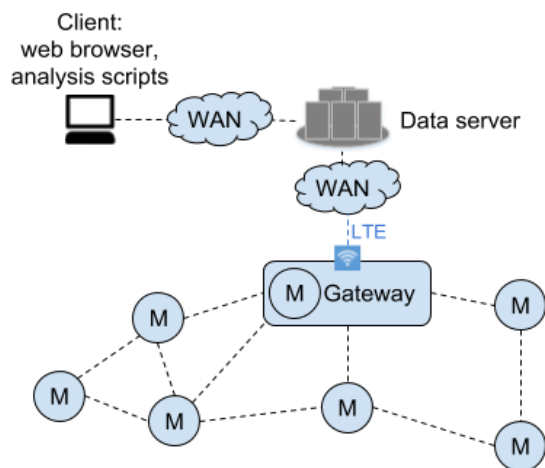


Figure 6.2.1: Mesh network topology with gateway to data server



Figure 6.2.2: Plot of frequency from web interface

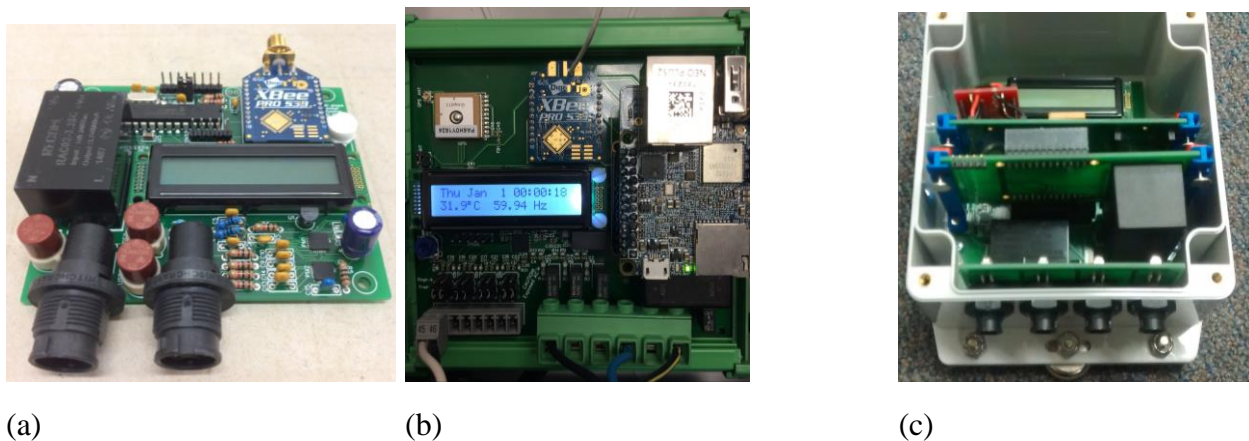


Figure 6.2.3: Design progression of the power monitor

Education and Outreach

HNEI involved students in the development of the power monitor, beginning with a semester-long electrical engineering project course for eight juniors at the University of Hawaii at Manoa. The course included lectures and hands-on experience covering the fundamentals of AC power, lab safety, circuit board design and fabrication, microcontroller programming in C, SBC programming in Python, and RF communications. The course received excellent reviews, and a Senior Capstone Design course was later offered to four of the students, focusing on aspects of software development: over the air programming, serial communications and error checking, data analysis in Python, DSP, and wireless mesh drivers. This work culminated with a poster presentation at an undergraduate research symposium. The poster is available on the HNEI website along with a video produced by the students. One of the students has been hired as a student employee for further work outside of APRISES 13 funds.

In order to support the students and the power monitor development, we established a Power Monitoring Lab within existing lab space. The lab has appropriate equipment, safety protocols, and training to assemble, solder, and test these devices.



Figure 6.2.4: Students assembling printed circuit boards with a postdoc

Results

Version 2 of the device was compared against PQube 3, a high-end power quality meter. As shown in Figure 6.2.5a, the frequency compares favorably ($\pm 0.05\%$). The RMS voltage (Figure 6.2.5b) is also reasonably accurate ($\pm 0.25\%$), but there was some erroneous data due to communications issues that have since been resolved. These results were compiled before calibration; under other funding, calibration and further evaluation is currently being conducted on Version 3. The RMS current (Figure 6.2.5c) shows a systematic scaling error, which was identified as an issue with a signal reference that caused clipping. The hardware fix has been implemented for Version 3.

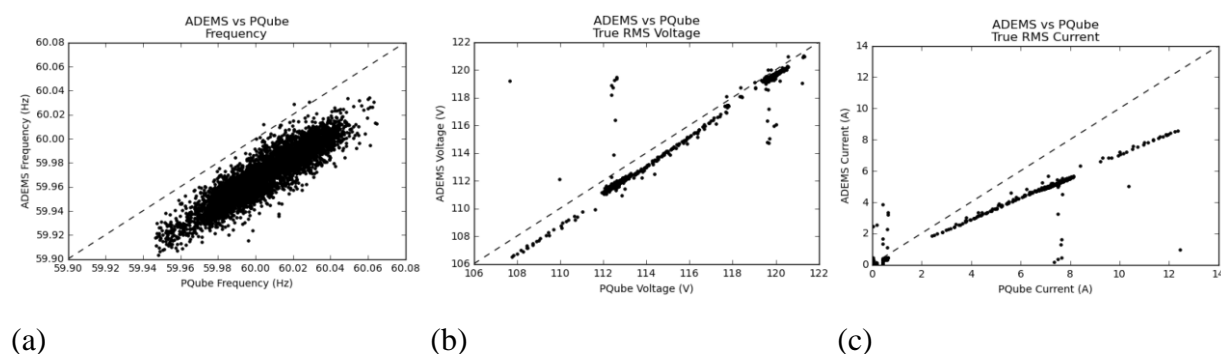


Figure 6.2.5: Results from Version 2 of the power monitor

The device meets or exceeds the basic requirements identified in the project objectives. Power monitoring has been demonstrated, with the results available on the device's LCD, in an interactive web-based plotting tool, and in analysis code or spreadsheets using a JSON API. It records total and fundamental RMS voltage, total and fundamental RMS current, total and fundamental active power, and fundamental reactive power on all three phases, as well as line frequency. The sampling period is adjustable down to 0.1 s, or it can be based on line frequency down to a single cycle. The device is compact ($6'' \times 5'' \times 4''$) and rated up to IP65 (dust tight and protected against

water projected from a nozzle). It has built-in power supplies and communications so that it only requires connection to the phases, neutral, ground, and current transducers. The wireless mesh is secured with 128 bit AES encryption and is self-configuring and self-healing for ease of use and robustness.

The platform provides the opportunity for many advanced features to be added in the future. Power measurements are based on an integrated circuit with advanced power quality metrics and event triggering available based on fast internal sampling (32 kHz). The gateway is capable of 5Mbps upload, which could provide high-resolution data streaming (128 samples per line cycle) on demand with additional software development. The device contains a microcontroller with the capability for DSP and low-latency controls; the gateway also contains a high-performance single board computer (quad-core 64-bit ARM) that could host many additional functions including modeling and controls. Each device contains a GPS module with the potential to enable precisely synchronized system-wide measurement (down to 20 ns) and Phase Measurement Unit (PMU) features. The on-board flash memory (128 MB, 4 days of data) and backup power supply (20 s) could be used for data retention and logging during grid dropout.

The total cost of the remote device, including power supplies, CTs, enclosure, and mounting hardware, is an order of magnitude cheaper than existing options. Volume production and additional engineering could reduce the cost further.

The system has been designed to allow 10 to 20 power monitors per gateway. This will reduce the ongoing cost of the commercial data plan by at least an order of magnitude. Based on current AT&T rates, the monthly cost is \$4/device or lower.

Conclusion and Future Applications

HNEI has developed a power monitor system that meets the initial requirements. A device was deployed for long-term testing (under other funding) on the UH Manoa campus and on the Camp Foster Marine Corps Base in Okinawa. Also under other funding, components have been acquired to build 20 units for deployment in Hawaii. Thermal, weather, impact, and further wireless testing will be performed prior to deployment. Additional software development will also be completed to allow over-the-air configuration and firmware updates.

This project has established a platform for future technology development projects. Based on this technology, HNEI currently has a pending ARPA-E OPEN 2018 concept paper and a subawardee role in a pending ONR DURA proposal. Using funding outside of APRISES 13, HNEI has hired two part-time student employees and a summer intern to assist with the testing, deployment, and ongoing software development. HNEI currently has a provisional patent on the system and is considering a patent application.

Load and PV Inverter Data Synthesis Project

Initially funded under APRISES 11, this Maui Advanced Solar Initiative project, demonstrated that Photovoltaic (PV) inverters can be controlled to effectively manage voltage at the local distribution level by directly affecting the secondary voltage of service transformers. Therefore PV inverters can directly impact the voltage at the customer service points. Inverters can be controlled simultaneously such that in aggregate it provides more capacity to shift load and manage voltage at the secondary side of service transformers. Due to the limited number of controllable PV inverter systems in the field, voltage impact at the feeder level was not demonstrated. The primary objective of our research under APRISES 13 was to develop methods to synthesize realistic PV inverter and distribution service transformer data. This was done by extrapolating results in a simulation environment using data collected in the field.

The first step to synthesizing data is to understand the field collected measurements that were available from the Maui Advanced Solar Initiative project. The power meter used in the data collection system of that project is the E51 from Veris Industries. It was determined that this meter computes and provides non active power as its reactive power reading. Reactive power plays an important role in the voltage stability of the grid. Injection or absorption of reactive power provides an opportunity for voltage control on the distribution grid. Accurate power measurements are necessary for voltage control application and model simulations. Unlike the Veris E51, the PQube3 utilizes IEEE standards in the computation of real and reactive power which we used as a baseline for this test. As such, a field deployment of a PQube3 and Veris E51 monitoring the same distribution service transformer was conducted to collect data to compare the differences between the devices, and to determine if the rest of the field collected data needed to be post-processed prior to its use in synthesizing simulated data sets. E51

For a single-phase nonsinusoidal system, IEEE 1459 standard recommends the use of the following formula to calculate active power:

$$P = \frac{1}{kT} \int_{\tau}^{\tau + kT} v(t)i(t)dt,$$

where $v(t)$ and $i(t)$ are instantaneous voltage and current measurements, respectively. PQube3 utilizes this formula to calculate the active power. The Veris meter E51 utilizes the Teridian 71M6513 3-phase energy meter integrated circuit (IC) as their measurement microchip. According to the documentation of the microchip, it uses the above formula to calculate the active power. Since both meters use the same formula, we expected the active power measurements collected by the two meters to be reasonably similar as illustrated in Figure 6.2.6 below.

E51The method in which the Veris E51 computes reactive power does not comply with the IEEE 1469-2010 standard. To calculate reactive power, the Veris E51 uses the triangle formula $Q^2 = S^2 - P^2$, where $S = V_{rms} I_{rms}$ is the apparent power and P is the real power. However, in a nonsinusoidal system, the triangle formula $Q^2 = S^2 - P^2$ measures

$$Q = Q_1 + Q_2 + \dots + Q_n,$$

where $Q_h = V_h I_h \sin \theta_h$ can be positive or negative (See IEEE 1459 Standard, Annex A.2). Then $Q \leq \sum |Q_h|$ is not a reliable indicator of reactive power.

IEEE 1459-2010 standard recommends measuring *fundamental* reactive power using the formula:

$$Q_1 = \frac{\omega}{kT} \int_{\tau}^{\tau+kT} i_1 [\int v_1 dt] dt = V_1 I_1 \sin \theta_1.$$

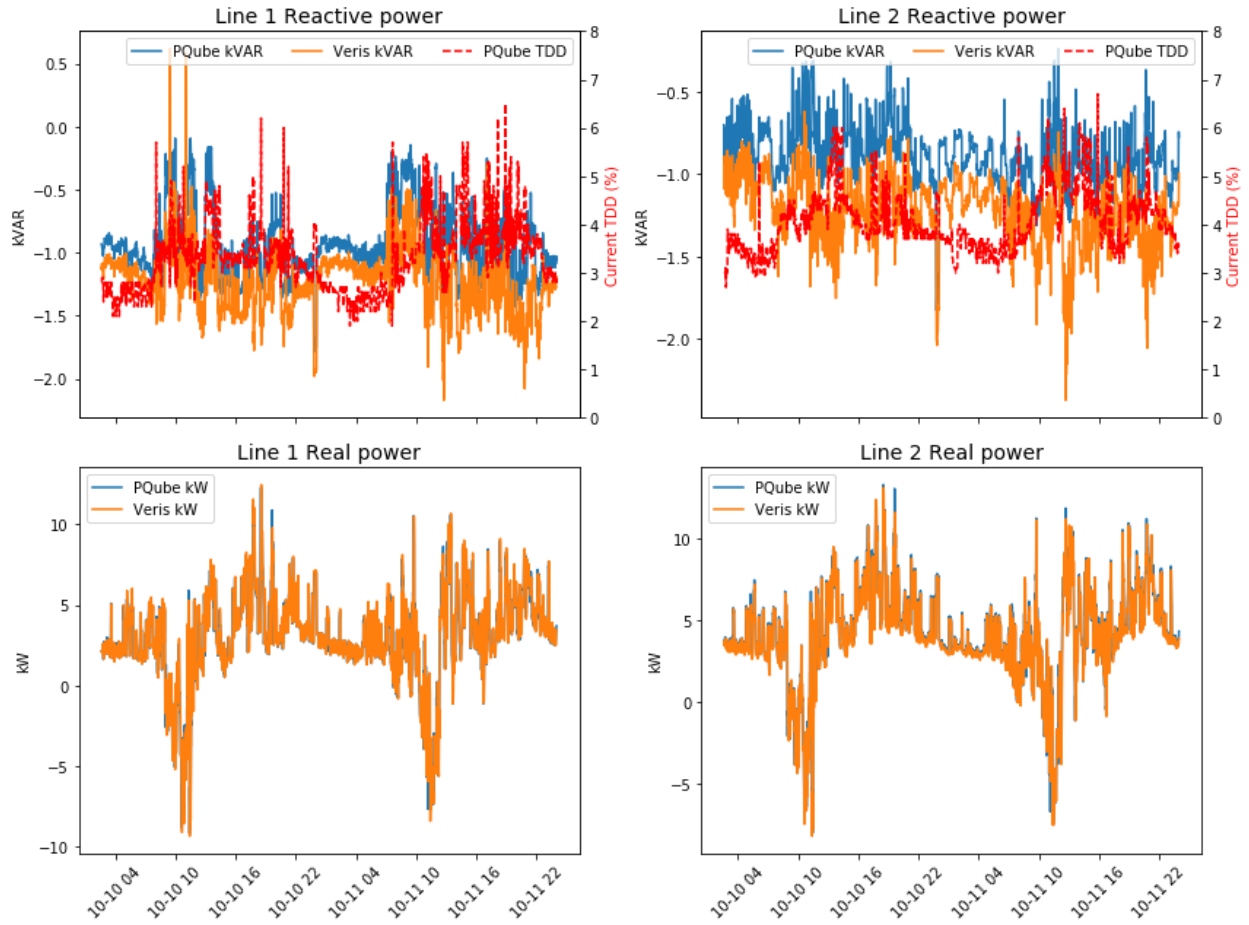
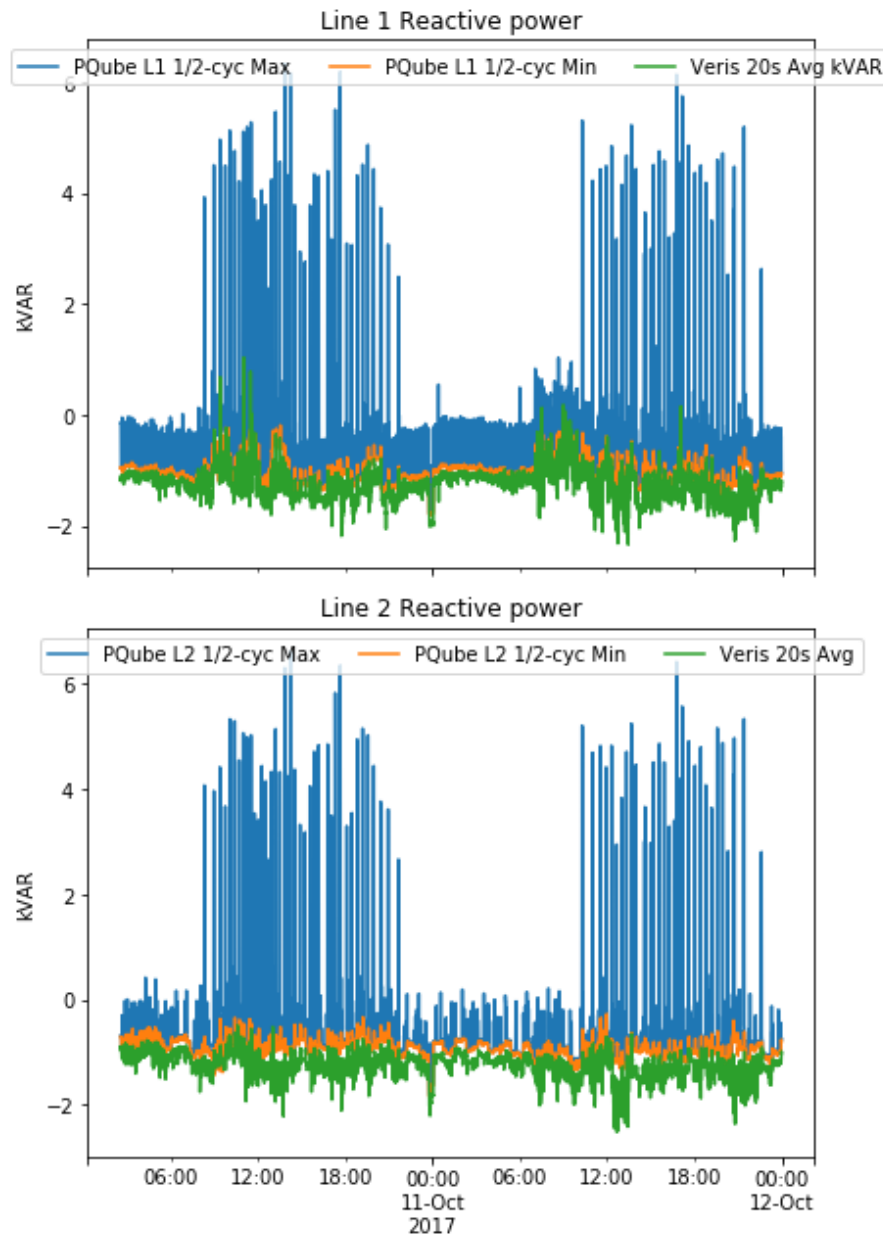


Figure 6.2.6: Comparison of real and reactive power measurements from Veris and PQube meters.

Therefore the Veris E51 meter cannot be configured to calculate the fundamental reactive power. The Veris meter was set up to collect 1 second resolution data for the Maui Advanced Solar Initiative project. To compare with the PQube readings, we resampled the Veris data by averaging over a minute. In Figure 6.2.6, we observe that the real power measurements from the Veris and PQube3 meters are similar, as expected. The small differences can be explained by the differences in the sampling frequencies of the two meters. The reactive power measurements, on the other

hand, vary significantly between the two meters. There are significant harmonic distortions present in the system as verified by the current TDD measured by the PQube3 meter. Therefore, the different methods used by the two meters yield different values.

Figure 6.2.7: Comparison of PQube3 1/2 cycle minimum and maximum readings



versus 20 second average Veris readings.

To further check the integrity of the Veris reactive power readings, we took the average of the one second resolution reactive power readings from the Veris meters over 5, 10, 20, and 60 seconds. Then we compared these average readings with the 1/2-cycle minimum and maximum reactive

power (kVAR) readings from the PQube3 meter. We observed that the Veris readings often fall outside this minimum/maximum range. Figure 6.2.7 shows the PQube3 1/2-cycle minimum and maximum readings versus 20 second average Veris readings. Further analysis on the comparison will be done to develop a method for post processing the reactive power readings from the Veris E51 meter.

PV Inverter Data Synthesis

In order to extrapolate the field demonstrated results of utilizing distributed PV inverters to control voltage in a modeling environment, it is necessary to generate simulated data where field data is not available. One of the primary objectives of our research under APRISES 13 is to develop a method to simulate unknown residential PV power generation using the field collected PV data. The following section details our methodology and an initial evaluation of the effectiveness of our method.

The method consists of the following steps:

- Preprocess data
- Determine the nearest known PV system
- Simulate unknown PV system power generation

The preprocess data step removes duplicate data entries and data dropouts due to data transmission errors which is likely caused by communication errors that occur from cellular signal dropouts.

The function and data structure to delete duplicate timestamps is expressed as follows.

$$f_{duplicate}(T_i, KW_i, D_a) \rightarrow \{T_n, KW_n\}$$

- $T_i = \text{timestamp } (i = 1, m) (m = \text{the maximum number of input rows})$
- $KW_i = \text{electric power expressed as kilowatt(kW) generated by known PV}$
- $D_a = \text{function ID to delete duplicate rows } (a = 1, b)$
- $(b = \text{the maximum number of function})$
- $T_n = \text{timestamp } (n = 1, p) (p = \text{the number of rows after delete duplicates})$
- $KW_n = \text{electric power expressed as kilowatt(kW) generated by known PV}$

The function and data structure to fill missing timestamps is expressed as follows:

$$f_{missing}(T_n, KW_n, F_r) \rightarrow \{T_q, KW'_q\}$$

- F_r = function ID to fill missing rows ($r = 1, s$)
- (s = the maximum number of functions)
- T_q = timestamp ($q = 1, 86400$) (86400 = the number of timestamps for 1 day)
- KW'_q =
filled electric power expressed as kilowatt(kW) generated by known PV

In addition to communication based data errors, it was determined that the field collected data contained large spikes introduced by the Veris meter. Thus, we applied a function to detect and adjust the data accordingly. An example applying the Hampel filter is shown in following figure. The blue line is the raw data containing spikes and the red line is filtered data.

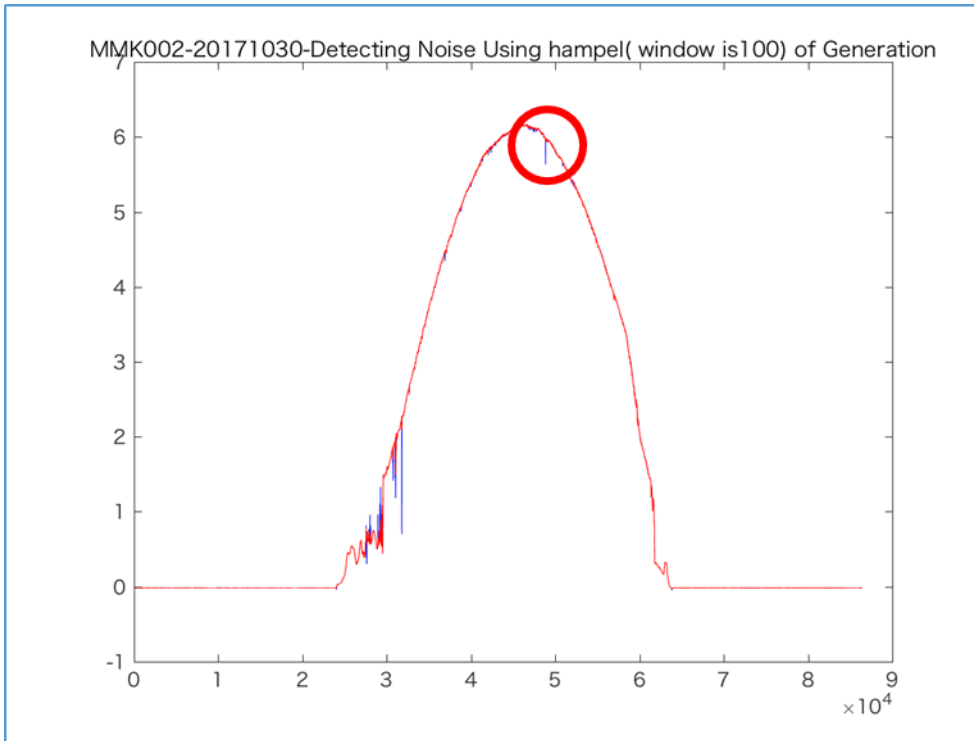


Figure 6.2.8: PV Inverter Power Output Noise Filter.

To simulate the unknown PV power, the physical distance between all the unknown PV systems to the PV systems where field data is available is determined. The field data of the closest known PV generation is then rescaled to the PV system size to produce the synthetic PV power generation data.

Results

To evaluate the effectiveness of this method, two days were selected: clear sky and high variable cloud cover as shown in Figure 6.2.9 below.

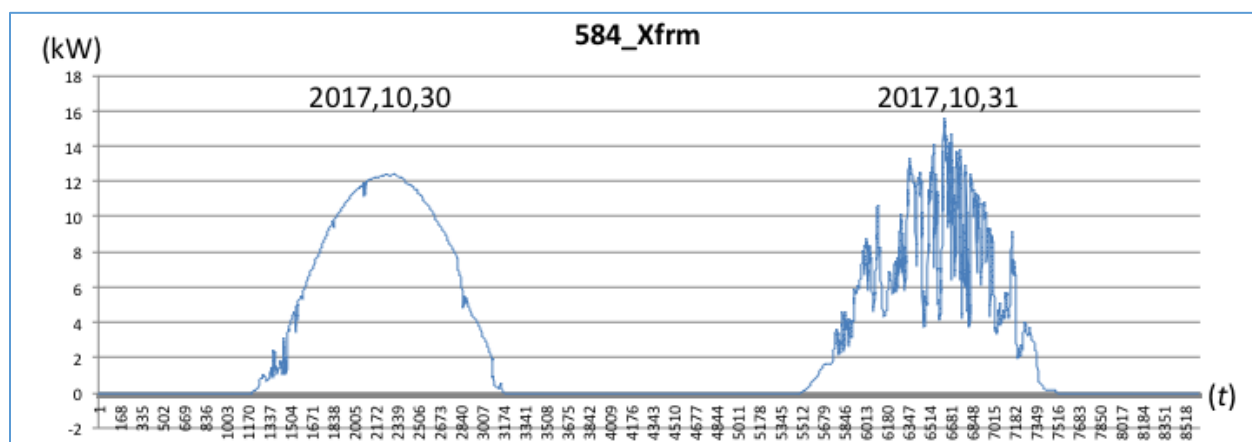


Figure 6.2.9: Clear Sky and Highly Variable Days.

These two representative days provide an initial understanding of the error range of this data simulation method. The error analysis is performed by withholding the data from a single PV system and utilizing the other known PV systems to generate synthetic data. A correlation represented in percent between the generated synthetic data and the actual field collected data is computed to determine the similarities over the course of a day as shown in Figure 6.2.10.

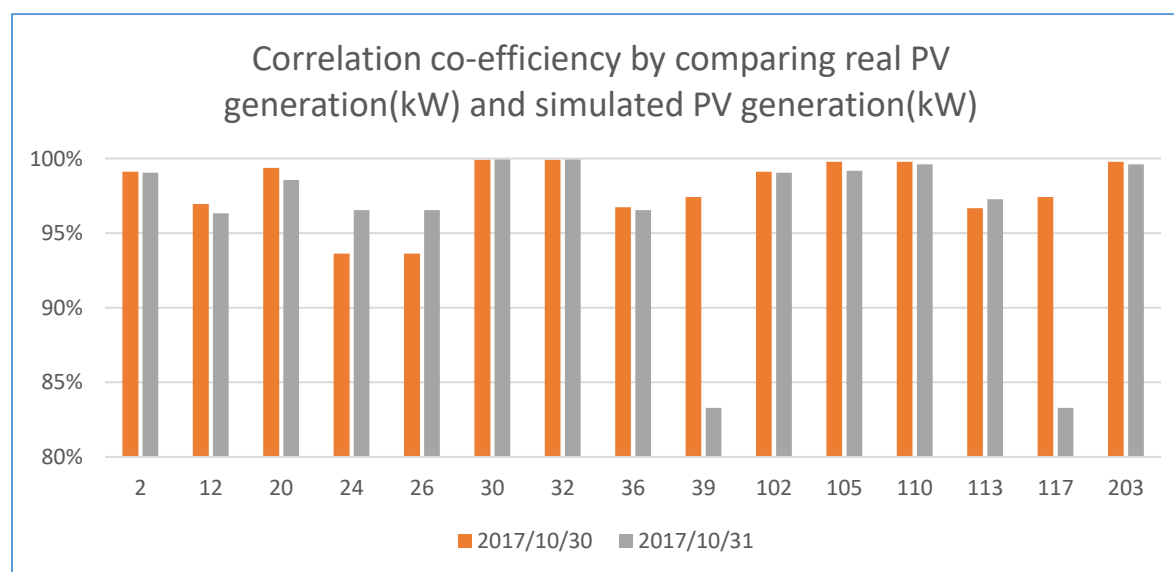


Figure 6.2.10: Correlation coefficient of simulated and field collected data.

In approximately 26 cases (out of 30 cases) the correlation is 96% indicating that the simulated PV data has similar characteristics as the field collected data. As previously stated, the correlation represents the similarities in the peaks and valleys over the course of an entire day. The timeseries plot comparing the actual field data and synthesized data is shown in Figures 6.2.11 and 7 for the two selected days. On a clear sky day, as illustrated in Figure 6.2.11, the profiles are similar but the peak generation does not occur at the same time. On a highly variable day, as illustrated in Figure 6.2.12, the profiles are similar for portions of the day. There is a period of time where the synthesized data is significantly lower in magnitude due to the use of the data from the closest neighbor.

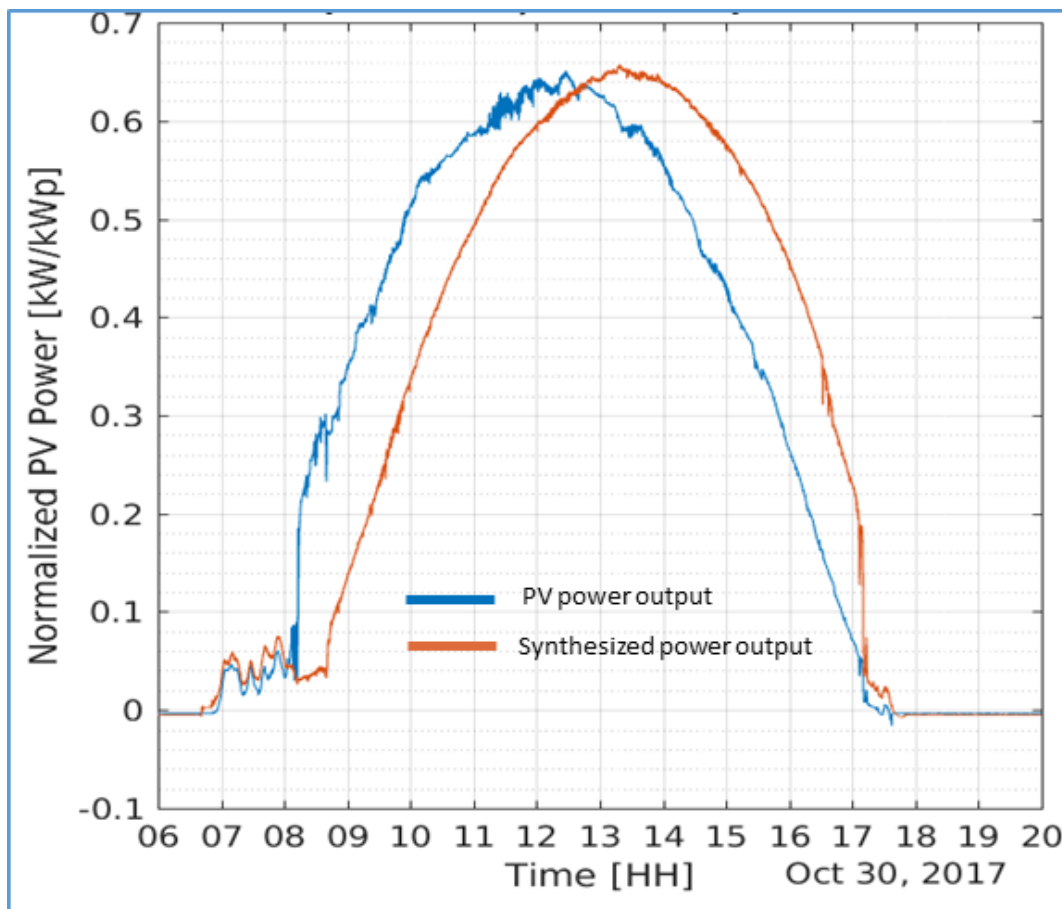


Figure 6.2.11: PV active power (actual and synthetic) for clear sky day.

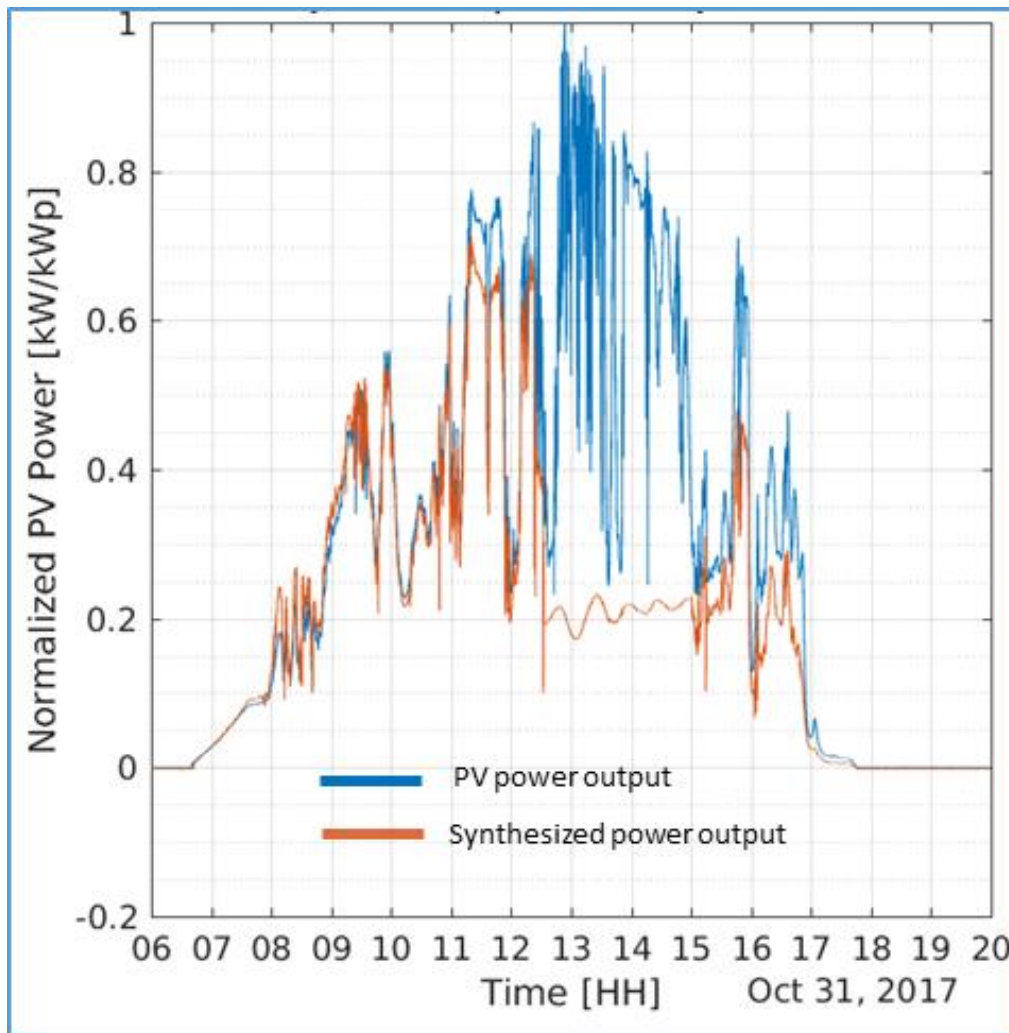


Figure 6.2.12: PV active power (actual and synthetic) for high variable day.

Under other funding, further analysis and performance metrics are being developed. We are also exploring methods that will take into account cloud movements over the course of a day so that the physical distance is not the only determining factor in the data selection of a known PV system.

Synthetic Load Generation

In addition to distributed PV generation, the load data representing residential power usage is required to perform power flow simulations. The Maui Meadows neighborhood is supplied by 103 single-phase service transformers. We installed Veris E51 meters on 29 service transformers to collect distribution transformer load data. However, to successfully test different algorithms, the simulation environment must have data from all 103 transformers. Therefore we must generate synthetic load data for the remaining 75 service transformers in a way such that the total load sums to the SCADA measurements collected at the substation.

The transformers serving the Maui Meadows neighborhood have diverse characteristics in terms of kVA ratings, numbers of loads connected, types of loads (residential homes, vacation rentals etc.), distributed PV connected, loading, etc. Therefore it is difficult to predict the load behaviors at the unobserved transformers. The customer billing information could potentially provide some insight into the loading of different transformers. So in our first approach for generating synthetic load data at the unobserved transformers, we utilize the customer electric bills.

For synthetic load data generation, we collected customer billing information from Maui Electric Company for May-June 2017. The goal of this data generation approach is to obtain average daily load profiles of the unobserved transformers using the billing information and SCADA data collected at the substation transformer. The average load profile generation method is described below:

- Calculate the per phase load at the substation transformer based on the phase current measurements.
- Match the billing addresses to the houses modeled in the DEW Maui Meadows model.
- For each service transformer, find the average monthly loading factor using the following formula:

$$\text{loading factor} = \frac{\text{Total billed energy to houses connected to transformer}}{\text{Total billed energy to all the houses connected to that phase}}$$

- Multiply the SCADA phase power by the loading factor to obtain the average daily profile of the service transformer

To analyze the performance of this approach, we compare the generated average load profiles with measured average load profiles at the transformers with meters. During the synthetic data generation process, we encountered several problems with the data. We observed that the SCADA phase current readings are 0 whenever the reactive power readings are negative. This is a shortcoming of the meter located at the substation. We also found inconsistencies in the number of houses modeled in DEW and the billing addresses. These inconsistencies were resolved by locating the physical location on Google Maps and estimating the transformer serving the particular addresses.

Figure 6.2.13 to Figure 6.2.16 show the comparison of some estimated load profiles and actual measured load profiles.

659_Xfrm: Comparison of actual and estimated average daily profile

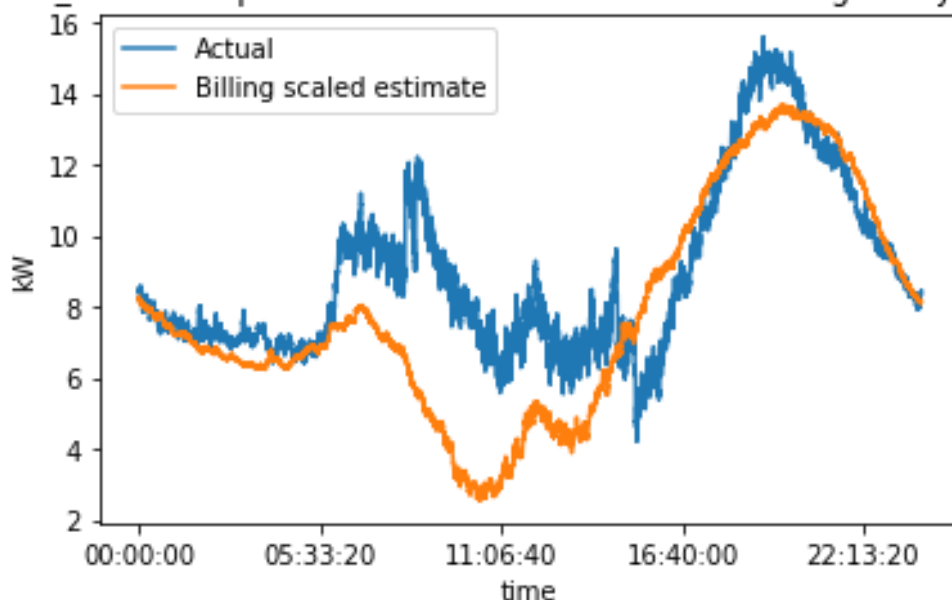


Figure 6.2.13: Comparison of actual (based on measured data) and estimated (based on billing data) average daily profiles of transformer 659_xfrm (MMK049).

694_Xfrm: Comparison of actual and estimated average daily profile

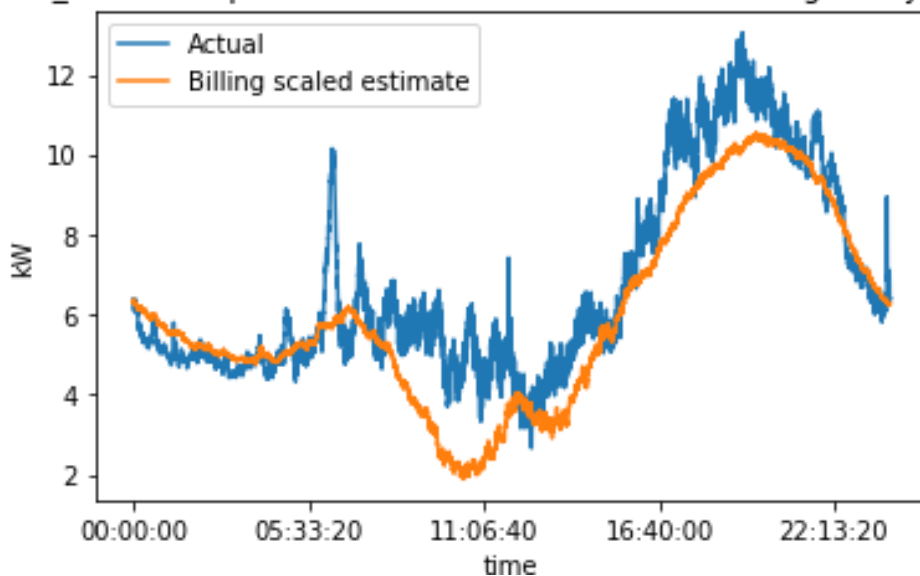


Figure 6.2.14: Comparison of actual (based on measured data) and estimated (based on billing data) average daily profiles of transformer 694_xfrm (MMK028).

627_Xfrm: Comparison of actual and estimated average daily profile

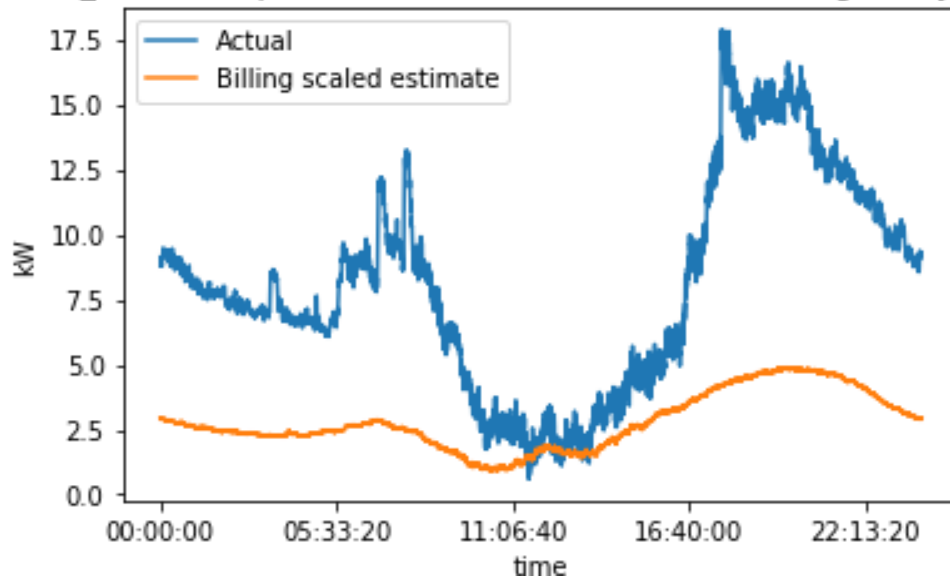


Figure 6.2.15: Comparison of actual (based on measured data) and estimated (based on billing data) average daily profiles of transformer 627_xfrm (MMK001).

640_Xfrm: Comparison of actual and estimated average daily profile

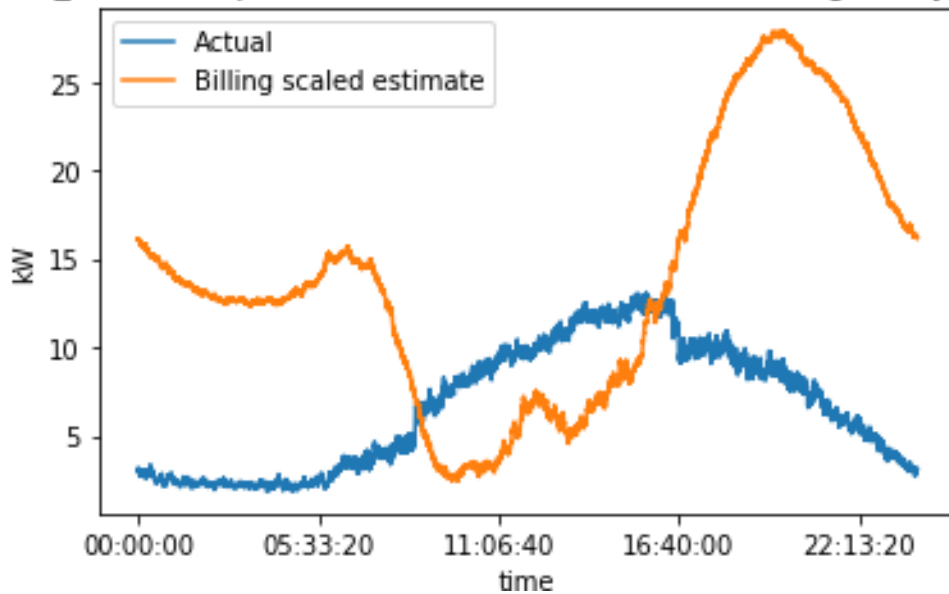


Figure 6.2.16: Comparison of actual (based on measured data) and estimated (based on billing data) average daily profiles of transformer 640_xfrm (MMK109).

As shown in the figures, for some transformers, the billing information represents the loading reasonably well. But this method performs poorly for other transformers. Also note that the load

profiles are very smooth and closely follow the SCADA profile. Thus the profiles generated this way are rather deterministic (lack random behaviors expected from loads). To overcome these shortcomings, a probabilistic method for synthetic data generation is analyzed.

Probabilistic Approach

We begin by generating load data for night time hours. Since there is no back-feed at night, the active power readings are all positive. Thus the SCADA readings at night are the sum of all transformer loads, i.e.,

$$P_{SCADA} = \sum |P_i| = \sum P_i,$$

where P_i are the transformer loads. To generate the synthetic load data we propose to use the Dirichlet distribution, which is a multivariate generalization of the Beta distribution. Dirichlet distribution is often used in statistics to model proportions.

Properties of Dirichlet Distribution

Parameters: $\alpha_1, \dots, \alpha_k$ concentration parameters, where $\alpha_i > 0$.

Support: x_1, x_2, \dots, x_k where $x_k \in (0, 1)$ and $\sum_{i=1}^k x_i = 1$.

PDF: Let $\underline{X} = [X_1, X_2, \dots, X_k]$ and $\underline{\alpha} = [\alpha_1, \alpha_2, \dots, \alpha_k]$. Then

$$f_{\underline{X}}(\underline{x}; \underline{\alpha}) = \frac{1}{B(\underline{\alpha})} \prod_{i=1}^k x_i^{\alpha_i-1}.$$

The normalizing constant is a multivariate Beta function.

Mean:

$$\mu_i = \frac{\alpha_i}{\sum_{i=1}^k \alpha_i}$$

Variance:

$$\sigma_i^2 = \frac{\alpha_i(\alpha_0 - \alpha_i)}{\alpha_0^2 (\alpha_0 + 1)},$$

where $\alpha_0 = \sum_{i=1}^k \alpha_i$.

Using the definitions of mean and variance, we can calculate the parameters α_i as

$$\alpha_i = \mu_i \left(\frac{\mu_i(1 - \mu_i)}{\sigma_i^2} - 1 \right)$$

Then the proposed probabilistic data generation method can be summarized as follows:

- Find the average per kVA load profile from the measured transformers. Assume that the unobserved transformers follow the same per kVA load profile.

- For each unobserved transformer, multiply by the kVA ratings to get the average kW profile.
- Find the parameters $\alpha_1, \dots, \alpha_k$ from the average load at that particular time step.
- Generate the load data at unobserved transformers using a Dirichlet distribution with parameters $\alpha_1, \dots, \alpha_k$.

Future Work

Under other funding, methods to improve PV and load data simulation will continue to be investigated. Currently, a method to determine cloud movement is being developed and will be incorporated into the PV data simulation system. Ultimately, the simulated “realistic” data sets will provide the ability to develop and test control algorithms for distributed energy resources on an entire feeder with high penetration of distributed PV systems.

Hawaii Battery Energy Storage System Virtual Power Plant Demonstration Project

As reported under previous funding awards, at the completion of the JUMPSmart Maui smart grid project HNEI’s Grid System Technologies Advanced Research Team (“Grid**START**”) negotiated and executed an Equipment Transfer Agreement with the New Energy and Industrial Technology Development organization of Japan (NEDO) that resulted in HNEI acquiring a majority of the grid assets implemented in the project. These assets were worth well in excess of \$1 million. The equipment included Sunverge Solar Integration System (“SIS”) distributed battery energy storage system (BESS) units, micro-Distribution Management System (DMS) control units, medium voltage section switches and the computer server platform that was used to host the Electric Vehicle (EV) Energy Control System and Distribution Management System.

HNEI is leveraging the acquisition of the SIS BESS units to conduct the Hawaii BESS+PV Virtual Power Plant Demonstration Project (Hi-VPP). APRISES 13 funding was used to develop the project scope, identify the roles and responsibilities of the project partners, and secure the acquired approval from the utility to move forward with the proposed Hi-VPP project.

The Hi-VPP project will be completed under other funding to demonstrate and assess the technology and the prioritization of alternative use cases based on stakeholder interests and functional/economic trade-offs, e.g., customer versus utility grid benefits. The project will quantify the business value proposition of combined BESS+PV resources deployed at two locations owned by project partners Maui Electric Company and Haleakala Solar Company in the town of Kahului on the island of Maui, Hawaii.

During the JUMPSmart Maui smart grid project, six (6) Sunverge SIS BESS units were installed at the Haleakala Solar business office and three (3) were installed by Maui Electric at their Kahului

base yard. Under the future funding, these distributed resources will be collectively operated as a VPP utilizing the Sunverge Software Platform (“SSP”). Sunverge is also a partner in this planned demonstration project.

Future funding awards will be used for the implementation of the project including the installation of the service connection to the SIS BESS units at the Haleakala Solar location and testing the use cases summarized below.

1. Consumer Value

Providing consumer value is the goal of an individual SIS unit when it is not providing VPP services to the distribution or bulk power system. To achieve this goal, the SSP includes functional tools to ensure that consumer needs can be served while also providing grid services. These tools include the ability to reserve battery capacity for specific functions and a program prioritization model to stack or layer activities. These key pieces of functionality ensure that a single SIS can provide multiple services, both to the consumer and as part of the VPP, simultaneously, or at least on a prioritized basis. These tools will be investigated as part of the planned future demonstration.

Use cases in the consumer value category of VPP capabilities to be evaluated in the planned demonstration include consumer bill savings; and backup power.

2. Distribution System Benefit

VPPs have the flexibility to provide a variety of services to the electricity grid. As needs change, either seasonally or over time, the VPP can easily be reprogrammed to offer other services. The VPP can also be used to address geographically-specific issues. Because of their distributed nature, DER can provide locationally specific support, and can do so in a more efficient manner than many other devices.

The use cases in this category focus on services offered by the VPP that provide value to the distribution network. This can include distribution grid support and deferral, voltage support, and renewables integration or firming. To provide these services, the fleet of SIS units are aggregated and dispatched as a VPP according to the specific requirements of the use case.

Use cases in the distribution system benefits category of VPP capabilities to be evaluated in the planned future demonstration include distribution grid deferral through peak reduction, and

PV time shifting for current backflow prevention.

3. Bulk Power System Benefit

The VPP can also be used to provide energy, capacity, and ancillary services to the bulk power system. VPP energy can be dispatched during times of system peak demand (which may not necessarily be coincident with distribution circuit peak demand) where energy production costs from traditional generation can rise significantly. Energy delivered through the VPP (if lower in cost than traditional generation) would provide energy savings to customers. Similarly, during periods of high renewable energy output resulting in a system aggregate excess of available energy, the VPP could be dispatched to increase demand and reduce curtailment of renewables. VPP

capacity can also be supplied to system operators to meet peak demand when available capacity is limited or to supply other ancillary services such as operating reserves and frequency responsive resources. The market opportunities in Hawaii for providing these services to the bulk power system are currently under development by the utility and the Public Utilities Commission, this planned future project will test the technical capabilities of Sunverge's system to provide a range of grid services.

Use cases recommended for consideration in the planned demonstration include:

- i. Dispatchable firm capacity
- ii. Load shifting
- iii. Renewables (PV) firming through end of day ramping control
- iv. Replacement reserves

Molokai Project

Under APRISES 13 funding, two projects were conducted for the Molokai electric grid. The first, PV Hosting Capacity Analysis, addressed the impact of PV generation on voltage at the circuit level. The second, Production Cost Benchmark Study, compared two tools for system-level analysis.

PV Hosting Capacity Analysis

Following the model development and preliminary analysis completed under APRISES 11, HNEI conducted a PV hosting capacity analysis for all of the circuits that comprise the electrical power distribution system on the island of Molokai to determine the impact of PV generation on voltage at the circuit level. A distribution model was used (Figure 6.2.17) with Distribution Engineering Workstation (DEW) modeling software. The power distribution system of Molokai was modeled previously under APRISES11. In this system, circuit 1 was modeled from the substation transformer to each customer service. Other circuits were modeled from the substation transformer to each distribution transformer. All distributed PV sites for the island were modeled separately. Under APRISES13, a range of PV penetration levels and locations on the grid were analyzed to determine the PV hosting capacity for each circuit on the island. The Supervisory Control and Data Acquisition (SCADA) data for the month of July 2017 (the most recently available power flow data for the island of Molokai at the time of analysis) was used for this report. For confidentiality purposes, all circuit labels in this report are genericized.

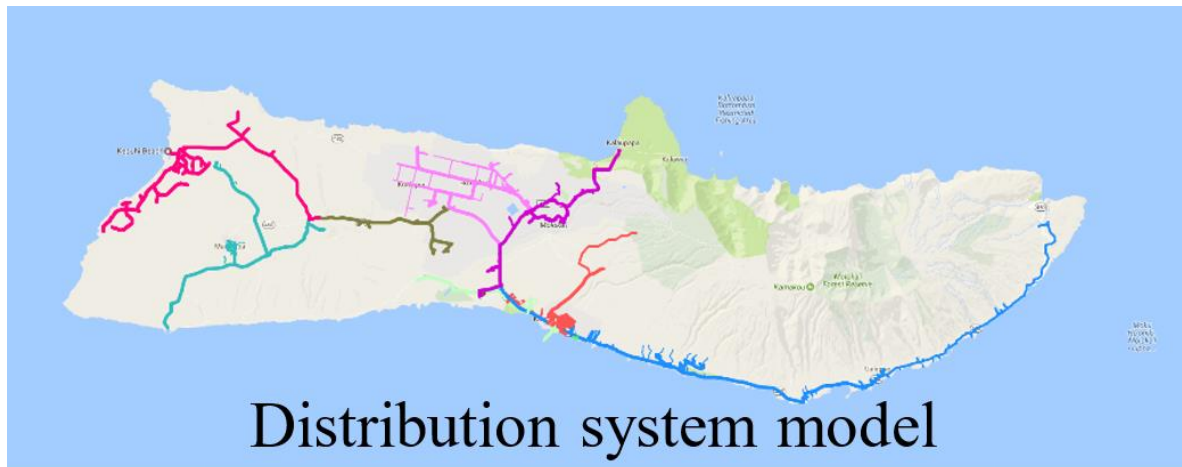


Figure 6.2.17: Distribution System Model for Molokai.

Load generation:

The only load data available for the island of Molokai was the SCADA data at the beginning of every circuit. To perform the PV hosting capacity analysis, load data must be generated for all the load buses in the system. In this project, load data was generated to each customer service for circuit 1 and to each distribution transformer for the other circuits. The procedures to generate load data for DEW PV hosting capacity analysis using the available circuit data (customer billing, transformer kVA rating, SCADA) are as follows:

1. Energy data was created for every load bus (customer services for circuit 1, distribution transformers for others) using the billing data for circuit 1 and distribution transformers' kVA ratings for the other circuits. Due to incomplete billing data, HNEI manually assigned billing to some of the load buses on circuit 1.
2. A baseline load for each load bus was then created using the energy data and the load profile from the class load study for Molokai.
3. SCADA data for Molokai only contains the net power flow across all phases and the current on each phase. To get the estimated net power flow on each phase, the net power flow on three phases was divided by a ratio calculated from the per phase current data with the assumption of uniform voltage across all phases.
4. The net power flow per phase was then injected at the beginning of each circuit.
5. PV generation for each PV site was calculated from the name plate (kW rating) value and National Renewable Energy Laboratory's (NREL) clear sky solar data for Hawaii.
6. Using the net power flow per phase and the PV generation from the clear sky data, DEW automatically calculated the gross load for each load bus by scaling the baseline load to match flow at the beginning of each circuit.

The gross load generated by DEW was then saved as a data set to be use with the PV hosting capacity application.

PV Hosting Capacity Methodology:

DEW software comes with a built-in PV hosting capacity application. This application was used by HNEI to determine the hosting capacity for every circuit on Molokai. The methodology for the PV hosting capacity analysis using DEW's built in application is as follows:

1. The times of analysis were selected as the time of maximum PV generation to daytime load and the time of maximum daytime load in the month of July 2017.
2. The impact of PV generation on each circuit was analyzed in 5% increments in PV penetration (the percent of total PV kW rating for each circuit over the minimum daytime load for each circuit for the month of July 2017) starting from the current level of penetration up to 600%. The 600% penetration level was chosen to ensure there is enough range to properly analyze overvoltage and flicker violations.
3. For each PV penetration step, DEW performed 10 random placements of PV systems in 10kW size such that the total kW rating of all PVs in the circuit matched the specified penetration level.
4. Power flow analysis was performed at every placement to determine the effect of PV generation on the system. The criteria for power flow violations are: voltage on a load bus or PV site of more than $\pm 5\%$ the nominal voltage, current flow that is greater than the specs for a component in the circuit.
5. Flicker analysis was also performed at every PV penetration level. The flicker analysis was done by ramping the power generated by PV sites at each penetration level from 20% - 100% of rated kW. The flicker noticeability and flicker irritability criteria were defined as a voltage fluctuation of more than $\pm 0.84\text{V}$ and $\pm 1.99\text{V}$ at a PV site.

Results and Discussion

The PV hosting capacity analysis results are shown below. For the sake of readability, only detailed results for circuit 1 are presented. The overall results for PV hosting capacity analysis are summarized in Table 2.

PV Hosting Analysis Result for Circuit 1

Circuit 1 serves the Kaunakakai area of Molokai. It contains 111 distribution transformers with peak daytime load of 1.89MW and minimum daytime load of 0.64MW for the month of July 2017. As of July, 2017, circuit 1 has 85 installed PV sites giving it a baseline penetration level of 100.5% minimum daytime load (648kW). The topology of circuit 1 is shown in Figure 6.2.18.



Figure 6.2.18: Circuit 1 Topology.

The analysis results for circuit 1 are shown in Figure 6.2.19. Each point on the plot represents the highest voltage recorded on the circuit for a PV placement scenario. The first blue vertical bar shows the penetration level at which the voltages of a PV placement scenario start to cross the overvoltage violation threshold. The second bar shows the penetration level at which all PV placement scenarios resulted in voltages that exceeded the overvoltage violation threshold. For circuit 1, overvoltage violations were not present at the base penetration level (100.5% of minimum daytime load). From the 340% to 350% penetration level, some of the random placements showed overvoltage violations. After the 350% penetration level, all random placements of PV resulted in over voltage violations. Flicker noticeability and irritability were present at the base penetration level (100.5%). This means for circuit 1, although new PV sites can be added without causing overvoltage violations, it is not possible to add new PV sites to this circuit because it would increase the flicker irritability violation.

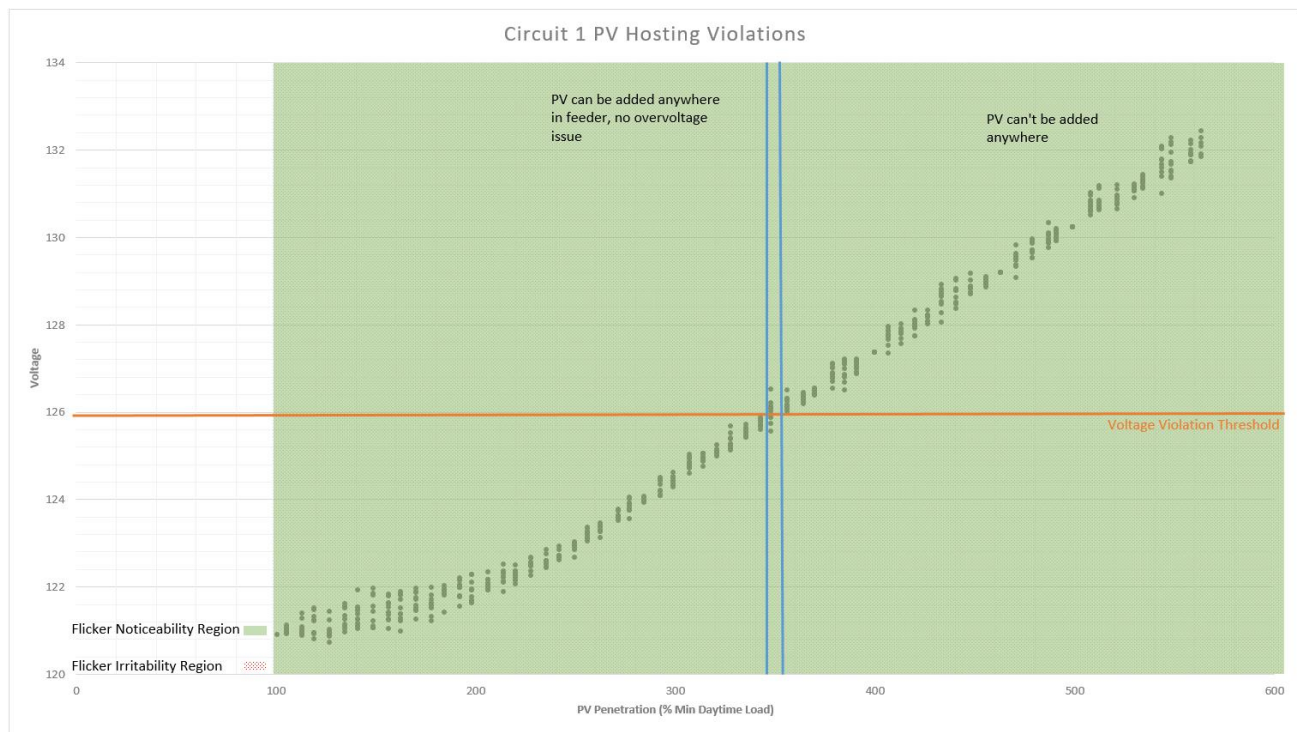


Figure 6.2.19: PV Hosting Capacity Analysis Results for Circuit 1.

HNEI PV Hosting Capacity Analysis Results:

The daytime maximum/minimum load and PV penetration level for all circuits in Molokai are shown in Table 6.2.1. Circuit 1, 2 and 5 have a much higher level of PV penetration compared to the other circuits.

Circuit	Maximum Daytime Load (MW)	Minimum Daytime Load (MW)	Total Installation rating)	PV (kW)	PV Penetration Level
1	1.89	0.64	648		100.50%
2	0.48	0.17	220.6		129%
3	0.62	0.24	70.9		29.04%
4	1.38	0.33	89.1		26.96%
5	1.33	0.52	573		111.26%
6	0.7	0.42	186.4		44.70%

Table 6.2.1: Daytime Maximum/Minimum Load and PV Penetration Level for Molokai's Circuits.

The PV hosting capacity analysis results are summarized in Table 6.2.2. Circuits with a high level of PV penetration have less available hosting capacity. Flicker problems are the limiting factors for increasing PV hosting capacity.

Circuit	Current PV Penetration Level	Overvoltage (PV penetration level)	Flicker Noticeability (PV penetration level)	Flicker Irritability (PV penetration level)	Available Hosting Capacity
1	100.50%	340%	100.50%	100.50%	Less than 5%
2	129%	445%	129%	210%	30-50%
3	29.04%	No Violation	160%	370%	More than 50%
4	26.96%	360%	55%	160%	More than 50%
5	111.26%	215%	111.26%	111.26%	Less than 5%
6	44.70%	410%	44.70%	110%	More than 50%

Table 6.2.2: PV Hosting Capacity Analysis Results.

Production Cost Benchmark Study

Previous work under APRISES11 (Subtask 6.2 Secure Micro-grids – Molokai Project) included production cost modeling using the HOMER Pro software. HNEI found significant limitations with the use of HOMER, particularly with respect to representing real-world commitment and dispatch constraints. To address these limitations and allow analyses to be conducted on much larger grids (such as Oahu), under APRISES13 HNEI licensed PLEXOS Integrated Energy Model software from Energy Exemplar and conducted an initial benchmark study to compare HOMER and PLEXOS production cost modeling of the Molokai grid. HNEI also evaluated a lightweight capacity/expansion planning feature of PLEXOS.

Features Comparison:

The following table compares the benefits of HOMER and PLEXOS:

HOMER

- Inexpensive
- Easy to run full-factorial of expansion options
- Simple to set up and change model

PLEXOS

- Detailed models with extensive options
- Extensive reporting features
- Method to manage multiple versions of models

- Detailed fuel curves (nonlinear)

Production Cost Case Study:

Figure 6.2.20 shows selected results from the benchmark study. Neither HOMER nor PLEXOS closely represents the actual operation of the grid (SCADA). This is likely due to the fact that HOMER and PLEXOS do optimal dispatch, whereas Molokai does not currently have an energy management system (EMS). Operation is manual based on isochronous generation of two diesel generators at once. HNEI's PLEXOS model did not yet incorporate this constraint, which is otherwise non-optimal. It is generally more efficient to run one generator at its highest allowable setpoint (75%) for maximum efficiency and another generator much lower to provide operating reserves.

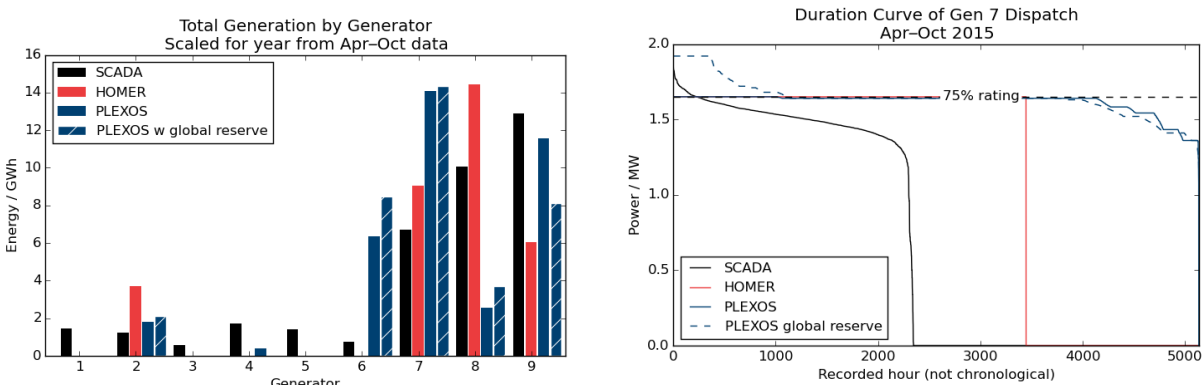
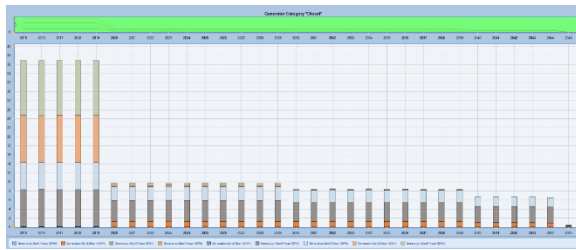


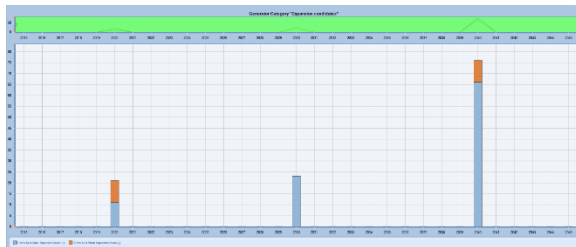
Figure 6.2.20: Comparison of diesel generator commitment and dispatch on Molokai among HOMER, PLEXOS, and actual grid operation (SCADA).

Evaluation of PLEXOS Capacity Planning:

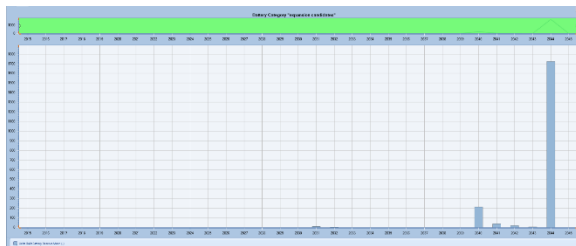
In addition to the HOMER versus PLEXOS comparison, HNEI also evaluated a feature of PLEXOS that performs a lightweight version of capacity/expansion planning. The results of the buildout optimization to meet Hawaii's Renewable Portfolio Standards (RPS) targets is shown in Figure 6.2.21. Due to the interplay between the RPS constraints and economics, PLEXOS introduces additional solar, wind and later batteries to meet the increases in Hawaii's RPS targets in 2020, 2030, 2040 and 2045.



(a)



(b)



(c)

Figure 6.2.21: Molokai optimal build-out plans from PLEXOS to meet Hawaii Renewable Portfolio Standards (RPS) targets, from 2015 to 2045: (a) diesel generator dispatch, (b) renewable installation (blue solar, orange wind), and (c) battery installation.

Conclusions

HNEI's benchmark study indicated that PLEXOS has significant additional features and capabilities over HOMER. However, HOMER remains a useful tool for small microgrids and very small island grids. PLEXOS will allow HNEI to evaluate larger grids such as Oahu's, but will require a larger engineering investment to set up the model for Oahu's power system.

Coconut Island DC Microgrid Project

Following the planning, data gathering, and energy modeling and component sizing work done under APRISES 11, HNEI started the procurement and implementation phase of the project

under APRISES 13. APRISES 13 supported the purchase and development of an electric boat (E-Boat), the procurement of an electric utility vehicle (E-car), the procurement of the swappable battery system used to power the E-Boat and E-Car and the development of a request for proposals to procure the PV, Stationary Battery, and integrator for the whole DC microgrid. Other funding awards will be used to procure and install the balance of the equipment of the DC microgrid project and the subsequent research, testing, demonstration and evaluation of the DC microgrid system.

Coconut Island is a 28-acre (113,000 m²) island in Kaneohe Bay off the island of Oahu that is home to the Hawaii Institute of Marine Biology of the University of Hawaii. One of the goals for the island is to become a model for sustainable living systems, which makes Coconut Island the ideal place to host the Coconut Island DC Microgrid project. The project site is shown in Figure 6.2.22. It is an ideal site for a technology-based test bed since it is representative of a tropical marine environment in an isolated location with critical power needs to be supported. It is directly exposed to persistent trade winds resulting in a highly corrosive environment for material and technology testing in a micro-climate representative of those that are typically encountered by coastal installations.

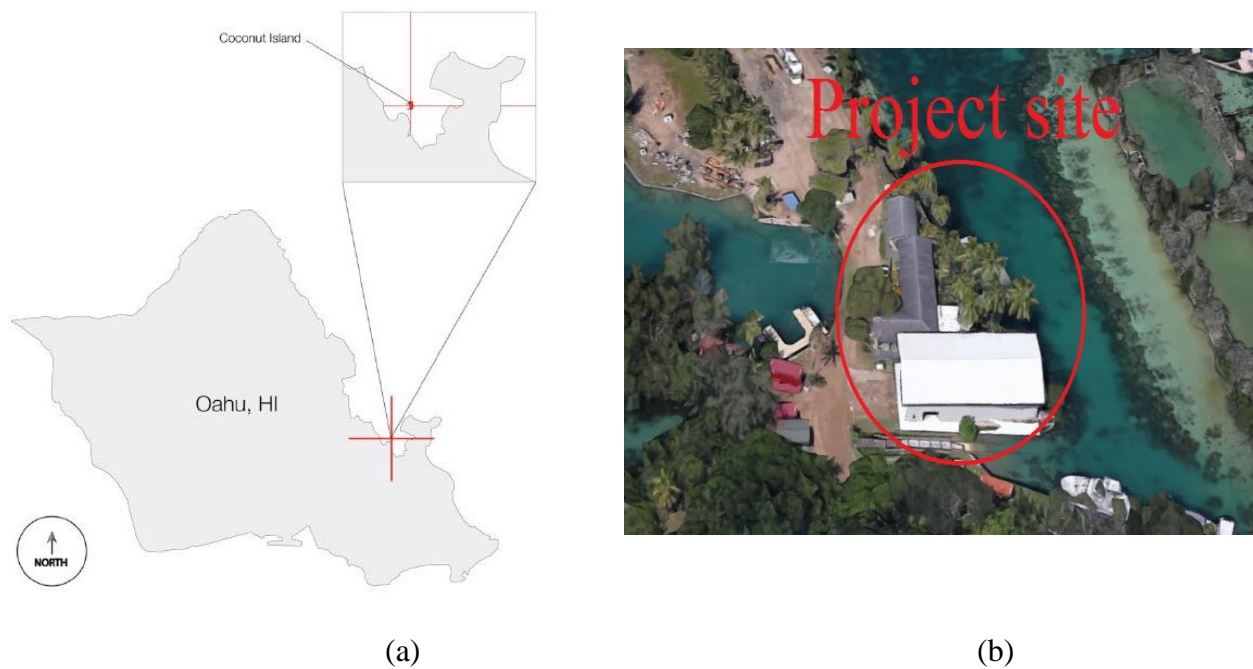


Figure 6.2.22: a) Coconut Island location b) DC microgrid project buildings.

The Coconut Island DC Microgrid Project will integrate a DC distribution system into two existing buildings on the island that are currently served by standard AC power, namely the Marine Mammal Research Project building and the Boat House. The DC microgrid will incorporate PV panels and a stationary battery energy storage system (BESS) as the primary energy sources to a

380V DC bus. A grid connected rectifier will supplement the PV and BESS when energy from the PV system and BESS is insufficient to serve the buildings' loads. Figure 6.2.23 below shows the conceptual schematic for the microgrid.

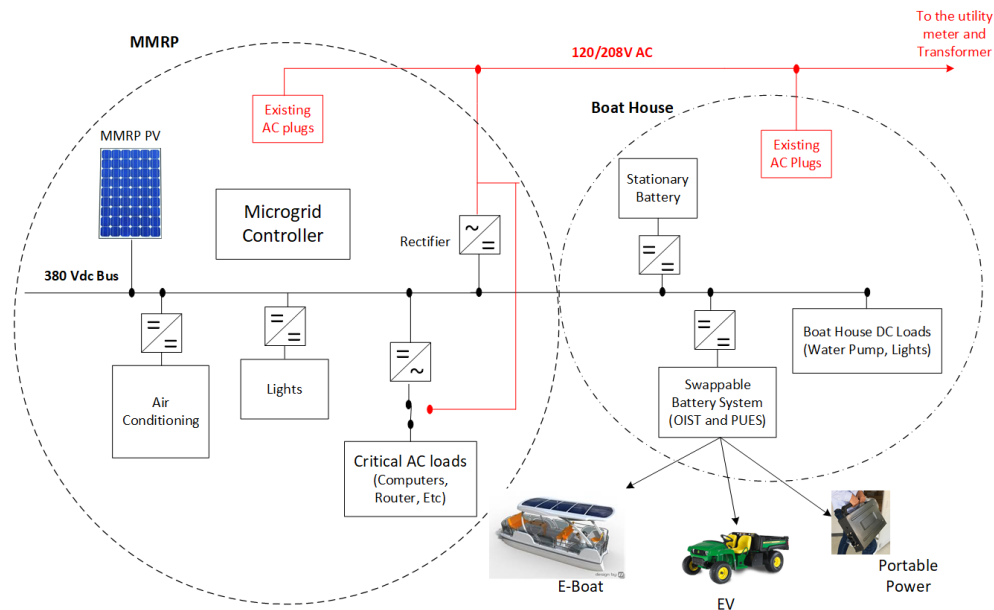


Figure 6.2.23: DC Microgrid Conceptual Single Line.

By implementation of this project, HNEI is targeting the following goals:

- Reduce electricity costs on the island via additional renewable resources and energy efficiency
- Support development and implementation of renewable energy technologies and their interconnection to the grid and integration within a microgrid
- Demonstrate the use and value of DC distribution systems with renewable energy resources
- Demonstrate the use and value of a microgrid controller to manage the microgrid's energy resources and loads
- Develop and demonstrate continued service to select critical loads in the event of loss of grid power
- Swappable battery system will be used to power electrical vehicles (EVs) (an E-Car and an E-Boat) utilizing renewable energy from the DC microgrid making them fully green transportation.
- Assess salt laden coastal environment impacts on microgrid equipment.

The swappable battery system was developed by the Okinawa Institute of Science and Technology (OIST) and the PUES Corporation in Okinawa ("PUES"), who are partners on this project and part of the Hawaii-Okinawa Clean Energy Partnership between the U.S. Department of Energy and the Ministry of Economy, Trade and Industry of Japan

Electrical Vehicles (EV) Development

As a part of this sustainable microgrid project and to represent green transportation for coastal islands, HNEI purchased two vehicles using APRISES 13 funding: A gas powered pontoon boat and an electric powered John Deere Gator modified to utilize the swappable batteries.

Using APRISES 13 funding and with the support of OIST and PUES, HNEI started the process of converting the boat from gas powered to electrical power utilizing the swappable batteries as its power source. HNEI installed PV panels on a new canopy designed for that purpose to enable the batteries to be charged directly from panels. HNEI also designed and tested a system to provide power to on-board auxiliary loads using the canopy mounted PV system. Utilizing other funding awards, PUES will install, test, and commission the power train for the E-Boat and the swappable battery charging station in the Boat House on Coconut Island.

The E-Boat modification is divided into parts: the power train modification and the on-board auxiliary loads power source development. The power train modification will replace the gas engine of the boat with a torquedo electric motor. Eight swappable batteries will be used to power this electrical motor. The goal is to prove reliability, efficiency and safety of the electric boat. Figure 6.2.24 presents wiring and schematic of E-Boat power train. The components of the power train for the E-Boat were purchased using APRISES 13 funding and the installation, testing and commissioning will be done using other funding awards. The development of the on-board auxiliary loads power source was completed using APRISES 13 funds and was the subject of four project based classes for Electrical Engineering undergraduate students (E296 & E396) administered by HNEI faculty members. This system includes two solar panels, a canopy frame, a battery, a battery management system, a solar charge controller, and an inverter. Students were responsible for design and implementation of this system with supervision by HNEI faculty. Figure 6.2.25 shows a schematic of their final design with wiring. This step of project has been completed and students' project reports are available on the HNEI website.

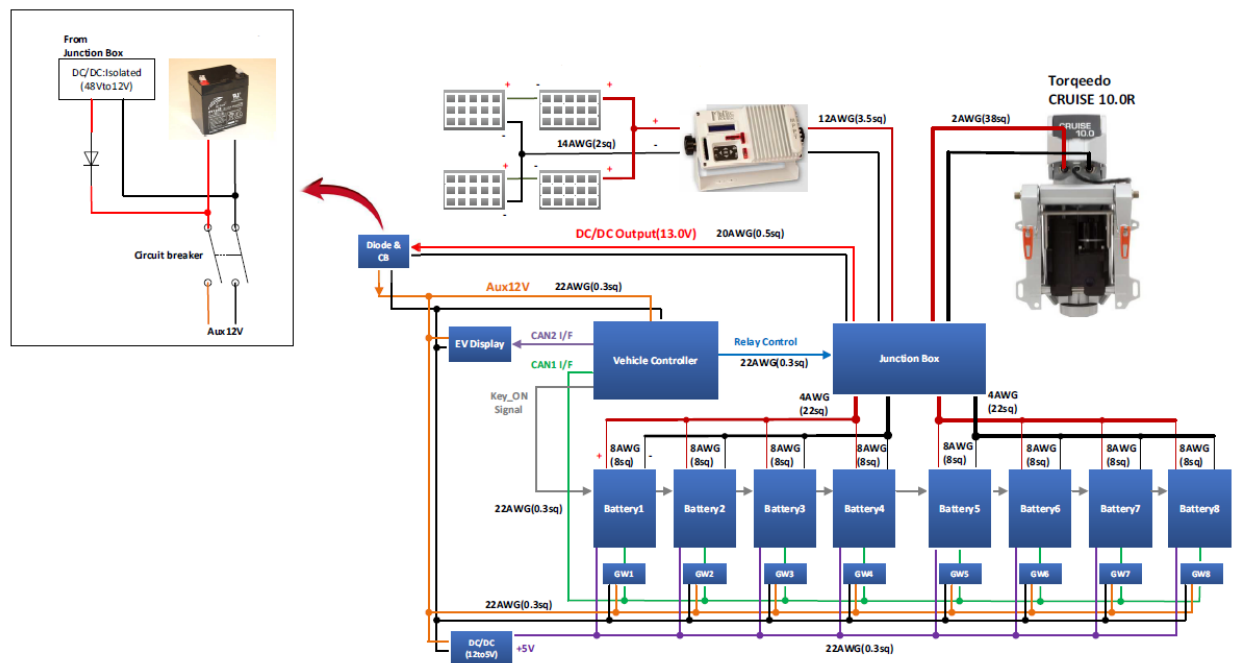


Figure 6.2.24: E-Boat power train.

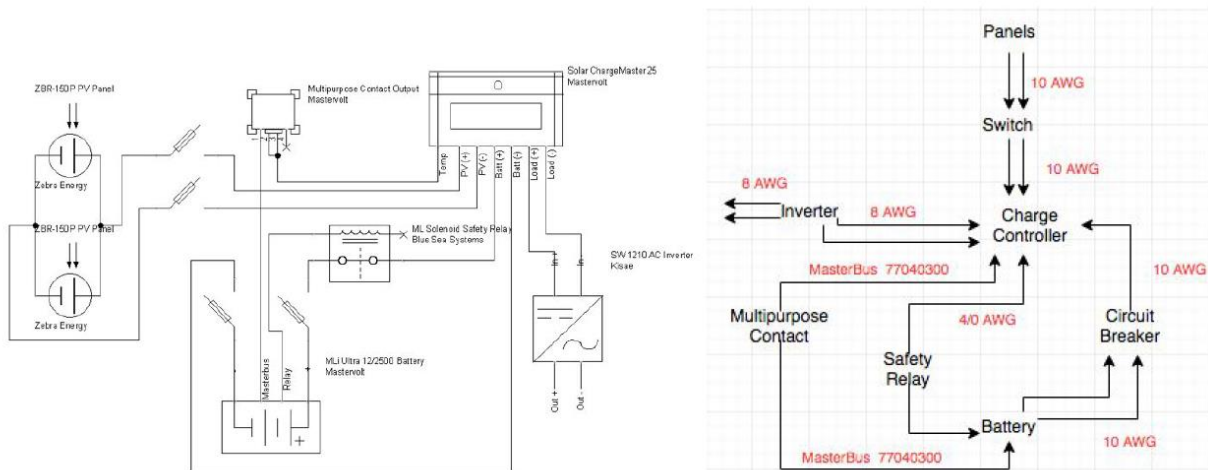


Figure 6.2.25: E-Boat auxiliary load's systems design and schematic.

PUES Swappable Battery System purchase

HNEI worked closely with PUES and OIST to modify their existing swappable battery station to make it compatible with the defined DC microgrid project and its energy needs. These components were procured, fabricated and shipped to the University of Hawaii utilizing APRISES 13 funding. HNEI is working with PUES engineers to assemble these components in the project site (Coconut Island) and to commission the charging station utilizing other funding awards.

Follow on procurement of the PV, Stationary Battery and Integrator:

HNEI engaged with a local consultant to assess the permitting requirements for the project and have determined that there are no State and County discretionary permits required to implement the project. As such, utilizing other funding awards, HNEI is moving forward with the procurement process to acquire the PV system, stationary battery, and system integration services that includes the design and implementation of the overall DC Microgrid system.

Solar Forecasting Project

Under this subtask, HNEI continued to develop new solar forecasting methods and systems, employ those systems in an operational framework, and calibrate and validate the predictions generated using ground observations.

The key accomplishments for this subtask are; fabrication of an operational solar forecasting system; development of a new methodology to significantly reduce the latency of the solar resource nowcast and forecast generation and PV power prediction; development of software to control and manage the Affordable High Resolution Irradiance Prediction System (AHRIPS).

The island electric grids in Hawaii are isolated and relatively small, with limited resources for grid stabilization. In addition, the high penetration of distributed, behind-the-meter, photovoltaic (PV) systems creates operational and power quality issues due to random, short-timescale changes in power output. Under previous funding, HNEI developed statistical techniques to characterize solar resource variability, and initiated work to build an advanced solar forecasting system intended to generate operational solar irradiance and PV power predictions. This system combines three separate components, each of which generate forecasts that focus on different time and space scales:

- 1) A regional numerical weather prediction (NWP) model is used to generate hours to days ahead forecasts, providing information useful for planning unit commitment.
- 2) Satellite imagery is used to generate minutes to hours ahead forecasts, providing information used for load following.
- 3) Ground-based sky imagers are used to generate solar irradiance nowcasts and seconds to minutes ahead forecasts, providing information useful for grid stabilization.

In the following, we discuss the continued work done on the solar forecasting system under APRISES13, including: (i) building and maintaining an operational forecasting system using the NWP and satellite components, (ii) performing an extensive evaluation and redesign of the operational satellite component; (ii) adding automated calibration and validation functions that use realtime irradiance and PV data from three test locations; (iii) utilizing these calibration and validation functions to perform a two month evaluation of the redesigned satellite component; and (iv) developing, building, and testing a new ground-based forecasting component.

Operational Solar Forecasting

Under this subtask, HNEI has built an operational solar forecasting system that generates: (i) regional, two-day ahead solar resource forecasts each night using Weather Research and Forecasting (WRF) model, and (ii) regional, five-hour ahead solar resource and PV power production forecasts every 15-minutes (during daylight hours) using data from the Geostationary Operational Environmental Satellite (GOES).

WRF is a widely used mesoscale NWP model developed at the National Center for Atmospheric Research. We employ a version of WRF tailored for cloud prediction and solar forecasting. The WRF forecasts cover the entire island chain at a 10 km resolution and the islands of Maui, Oahu and Hawaii at a 2 km resolution. WRF output is also essential for the satellite-based component. To ensure access to this information, WRF output from the Storm Evolution and Energetics Research Group at the University of Hawaii is also pulled into the data stream.

The GOES satellite is operated by the National Environmental Satellite, Data, and Information Service division at the National Oceanic and Atmospheric Administration, and data is made available by the Marshall Space Flight Center (MSFC) Science Research Office. The forecasting system utilizes both visible and infrared (IR) channel images to generate forecasts with a spatial resolution of 1km and a temporal resolution of 15 minutes.

Redesign of the satellite-based forecasting component

The main goal of the solar forecasting system's three component design is to cover a wide range of time and space scales, but it also allows for each component to pass information to, support operations of, and increase the capabilities of the other components. For example, the NWP-based component provides WRF temperature profiles that are used by the satellite system to determine cloud height. Under other funding, the ground-based sky imager component is set for its first operational deployment later this year. During which, it will use data from the satellite-based component for boundary conditions and to fill in portions of the sky that are not in view. Under this task, work was done to evaluate the reliability, latency, and accuracy of the satellite-based component and address those issues. This evaluation found:

- a) Incomplete data made available by MSFC;
- b) Hardware limitations that increased computation time, especially in handling GOES full disk images, which are released every 3 hours;
- c) Satellite navigation errors, with pixel locations off by as much as 2-3 km; and
- d) Issues in the software that caused the component to fail or lag.

To address this, data evaluations and new functionality were put in place to allow the system to quickly remove incomplete data and reset the satellite-based component; the component was moved to a dedicated high-performance linux rack-mount server to decrease computation time; a navigation correction algorithm has been added to processing; and the forecasting methodology was updated with the flow of data and sequence of processing steps redesigned for better

computational efficiency, and additionally sections of software with high failure rates or computation times were rewritten.

The following briefly introduces the main processing steps of the updated forecasting methodology:

- 1) Raw image processing: (i) conversion and calibration of raw GOES Variable Format data to scene radiance ($\text{mW}/[\text{m}^2\text{-sr-cm}^{-1}]$), from which reflectance from visible channel images and brightness temperature from IR is found, (ii) navigation of image pixels indexed as line and element number to latitude and longitude, (iii) extraction of data around the Hawaiian Island region and further refinement of the image navigation.
- 2) Solar resource nowcasts: the generation of direct and diffuse irradiance maps using solar geometry and clear sky irradiance models, and an augmented version of the Heliostat method (Hammer, 2003).
- 3) Cloud heights and shadows: the estimation of cloud-top-height (CTH) using the infrared window technique (Nieman et al., 1993), cloud brightness temperatures from IR imagery and WRF output; CTH data, along with a solar geometry model, then allows for parallax displacement correction and cloud shadow location estimation.
- 4) Cloud motion vectors: the estimation of cloud velocities using the Maximum Cross-Correlation technique applied sequential visible images, with a time separation of 30 minutes or less.
- 5) Solar resource forecasts: the prediction of upcoming cloud conditions using a rapid fluid dynamics solver driven by cloud motion estimates; updating solar geometry and clear sky conditions to the forecasting time, and the generation of direct and diffuse irradiance maps using Heliostat method.
- 6) Plane-of-array (POA) irradiance and power predictions: for a PV panel of a specified position, rating and orientation, the estimation of irradiance transmitted to the solar cell and PV power output from the panel, sun-position geometry, an empirical model of module cover and the PVWatts Version 5 model (Dobos, 2014).

This new methodology has significantly reduced the latency of the solar resource nowcast and forecast generation and PV power prediction. Nowcasts are now available within 10-15 minutes of realtime, 5-hour ahead forecasts are available within 20-25 minutes, and 5-hour ahead PV power predictions within 30 minutes.

With this methodology, the component makes all computations that are not a function of the orientation of the PV panel, then sets up forecasted data output; and, using new algorithms, quickly estimates power production for a large number of PV panels anywhere in the state, at any orientation.

Automated performance metrics

Under this subtask, the satellite-based component has been set to automatically generate calibration and validation statistics using ground data from three test sites. We have added functionality to the system that, for each test site, automatically generates irradiance and PV power nowcasts and forecasts, then gathers and compares against measured irradiance and PV power, generating and displaying performance metrics.

To evaluate the accuracy and precision of the operational forecasting system, plane-of-array irradiance and power production estimates and predictions are quantitatively compared against ground-based observations and measurements using four statistical performance metrics:

- 1) Root Mean Square (RMS) difference - gives a measure of the imperfection of the fit of the estimator to the data in the units of the estimate.
- 2) Mean Absolute Bias (MAD) - gives the statistical dispersion or mean difference in units of the estimate.
- 3) Correlation Coefficient (CC) - gives the strength and the direction of the linear relationship.
- 4) Mean Absolute Percent Error (MAPE) - measures the prediction accuracy, given as a percentage.

Validation data

The operational system has been setup to automatically gather PV power output and irradiance data from two HNEI PV test beds. The first was built under the Green Holmes Hall Initiative (GHHI) on the University of Hawaii at Manoa campus, on the island of Oahu. The second was built at the Maui Economic Development Board (MEDB) in the city of Kihei, on the island of Maui. The system also has been setup to gather PV power data from residential volunteers in the Maui Meadows neighborhood in the city of Wailea, on the island of Maui. PV inverters at these residences are being monitored and controlled as part of the Maui Advanced Solar Initiative project.

The location, rating, and orientation information required by the solar forecasting system is known at the HNEI test beds, and the location and rating of the PV panels at the volunteer residences in Maui Meadows is known. However, the orientation(s) of the panels is unknown. Furthermore, many installations have panels in multiple orientations, as residents used the available roof space.

Under APRISES13, we have developed (we believe to be) novel methodology to address the unknown orientation problem. The method estimates the (average) PV panel orientation from time-series of generation data, and is briefly described in the following: First, power observations are identified where the path between the Sun and panel was unobstructed and the sky was clear using a multiple step statistical approach. Next, power data is synthesized using a PV power production model and a clear sky irradiation model run with varying PV tilt and azimuth orientations. Finally, the orientation of the panel is estimated using least square difference

approach, determining the tilt and azimuth that best fit the clear sky power generation observations. Although the errors in this method have not yet been adequately quantitatively evaluated, preliminary evaluations suggested the orientation estimations are qualitatively accurate. These estimations are used to generate power production forecasts used for calibration and validation.

Operational and long-term validation and calibration

Under this subtask, functionality has been added to the operational system that allows for, nowcasts to be compared immediately after generation to recent observations from the three test sites, and forecasts to be compared as the observations are made available. Prior to comparison, raw 1-second ground-data are first averaged to the satellite time, using the nearest 60 seconds. An example of the automated calibration and validation statistics that are now generated throughout the day is shown in Figure 6.2.26. These results are from near the end of daylight, on February 23, 2018, using observations from the GHHI test site. Forecast performance metrics displayed in the Figure 1 are calculated from one-hour ahead forecasts. Each 5-hour forecast is shown, with the color and square point indicating the start time of the forecasts.

An additional automated evaluation of the forecasting system compares predicted GOES images created during the forecasting procedure against actual GOES image as they are made available. These comparison statistics are then compared against metrics derived from a persistence model, to further illustrate the performance of the forecasting system. Figure 6.2.27 gives an example of this output on the same day as above.

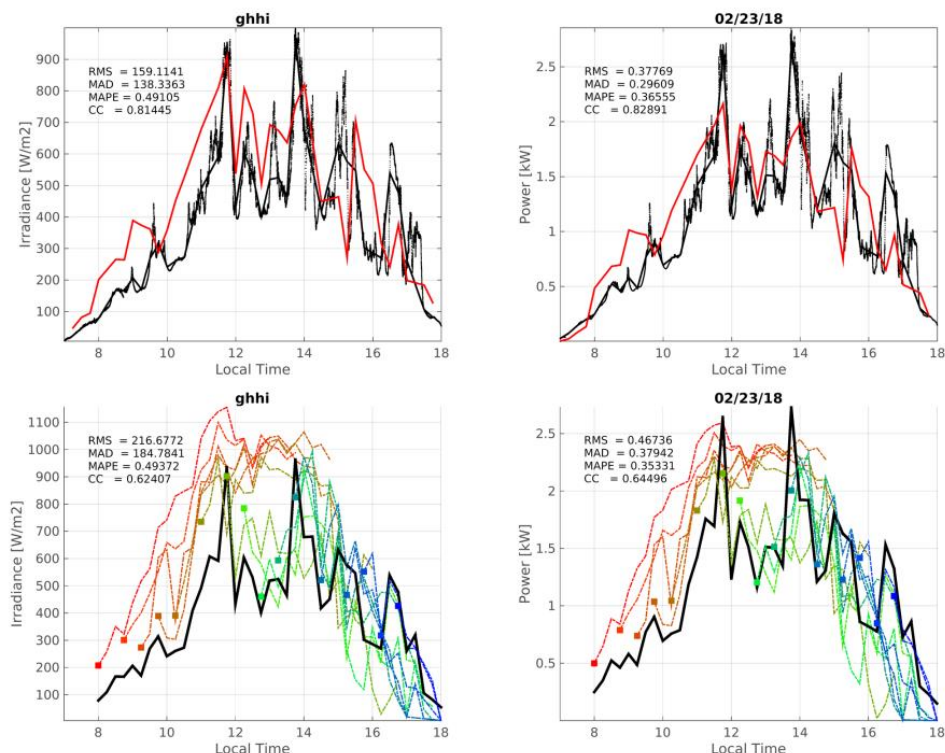


Figure 6.2.27: An example of the automated output from the operational forecasting system, which compares nowcasts and forecasts of irradiance and power generation against observations.

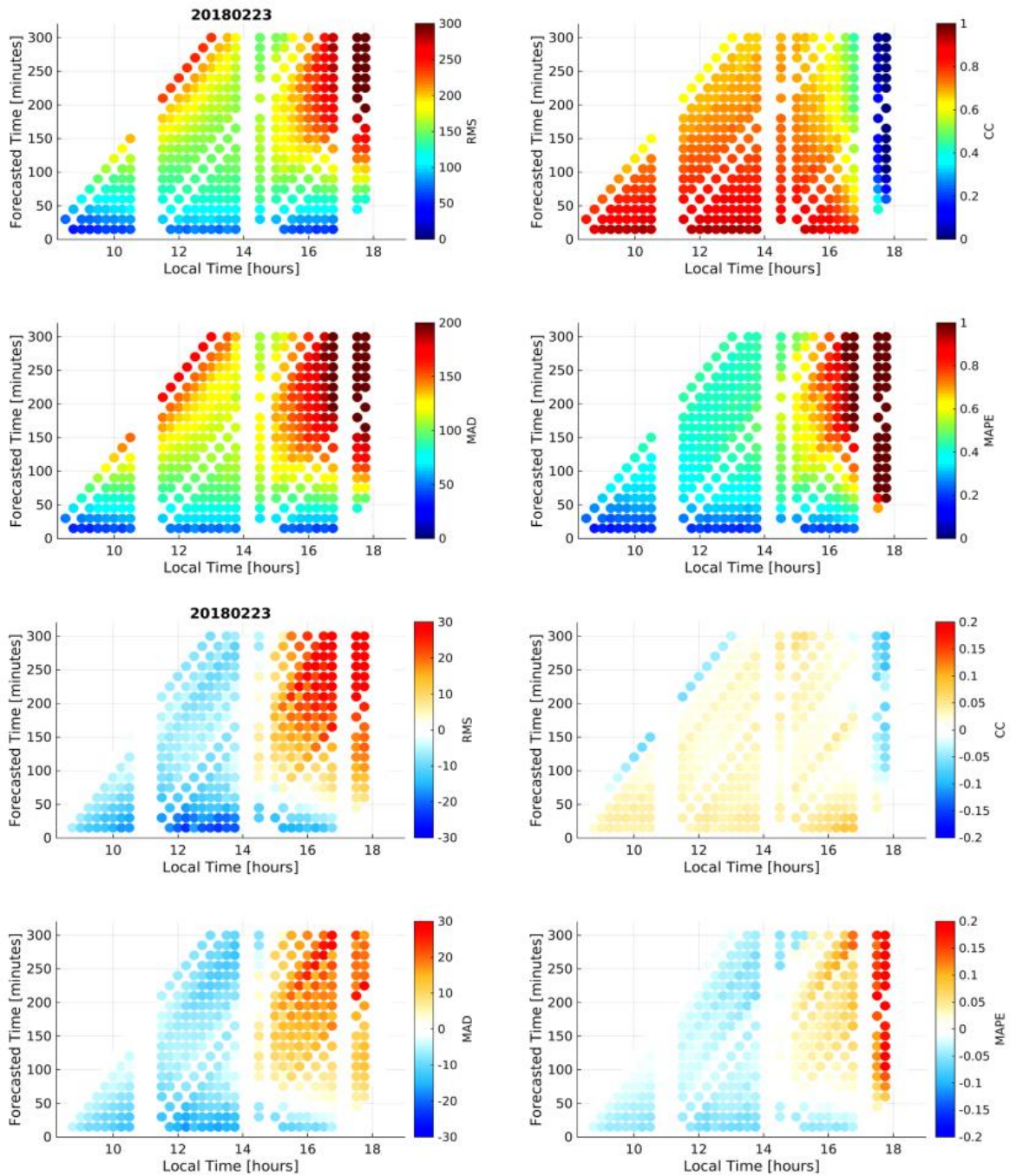


Figure 6.2.27: An example of the automated output from the operational forecasting system, which compares predicted GOES images against the actual, then compares those performance metrics against those from a persistence model.

Preliminary Performance Metrics of the Updated System

Using the above system, it is now relatively simple to compile longer time series statistics. In the following, we present results from two months of output from the updated system against ground observations. Irradiance and power production obviously vary diurnally, however, atmospheric features revealed in the GOES images also vary with sun position. To understand the how the quality of the satellite-based estimates in response, performance metrics are computed from data binned per hour of day, shown in Figure 6.2.28. RMS and MAD vary with irradiance, over the

day ranging from 50 to 200 W/m² and 50 to 150 W/m², respectively. The bias demonstrated in

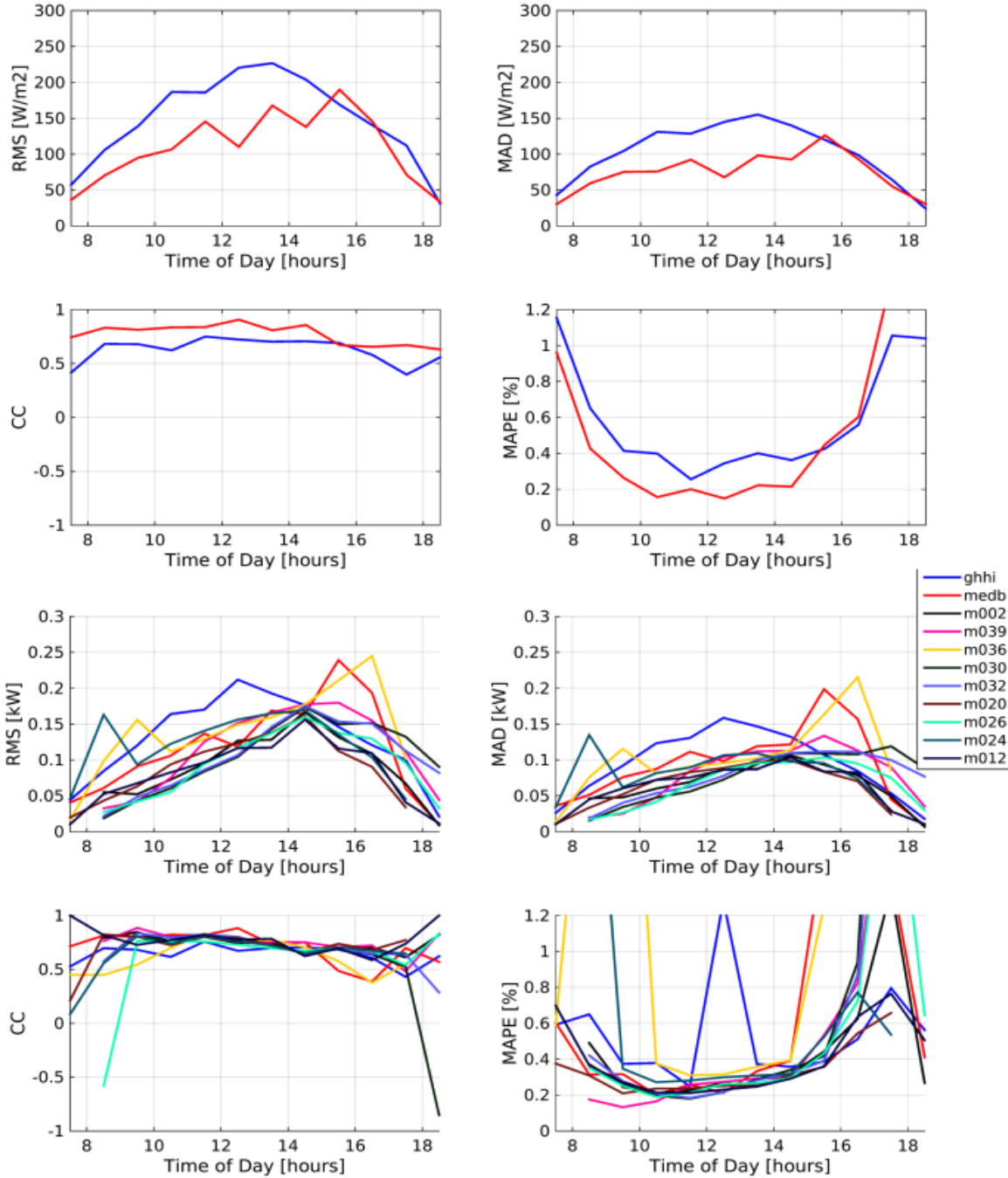


Figure 6.2.28: Results from a two month comparison of satellite nowcasts and forecasts to ground based observations.

the MAD metric accounts for much of the RMS error at both sites. A calibration in the Heliosat coefficients should be able to reduce much of this error. The patterns found in both the MAPE and CC metrics are also promising. During peak irradiance hours, when the RMS and MAD is highest, MAPE is at a minimum, with prediction errors of 20-40% and correlations show little

diurnal variability, remaining high (between 0.6 and 0.9) throughout the day. If bias is accounted for nowcasts error may drop significantly. Also, results may suggest some problems in the GHHI observations, as errors from that data set are significantly higher.

The power forecasts and observations are first normalized by the size of the system before power performance metrics are calculated to allow for better comparison between sites. Diurnal patterns in the performance metrics are similar to those found from irradiance data. During mid-day hours, normalized power RMS ranges from 0.1 to 0.2, with MAD levels ranging from 0.8 to 0.1,

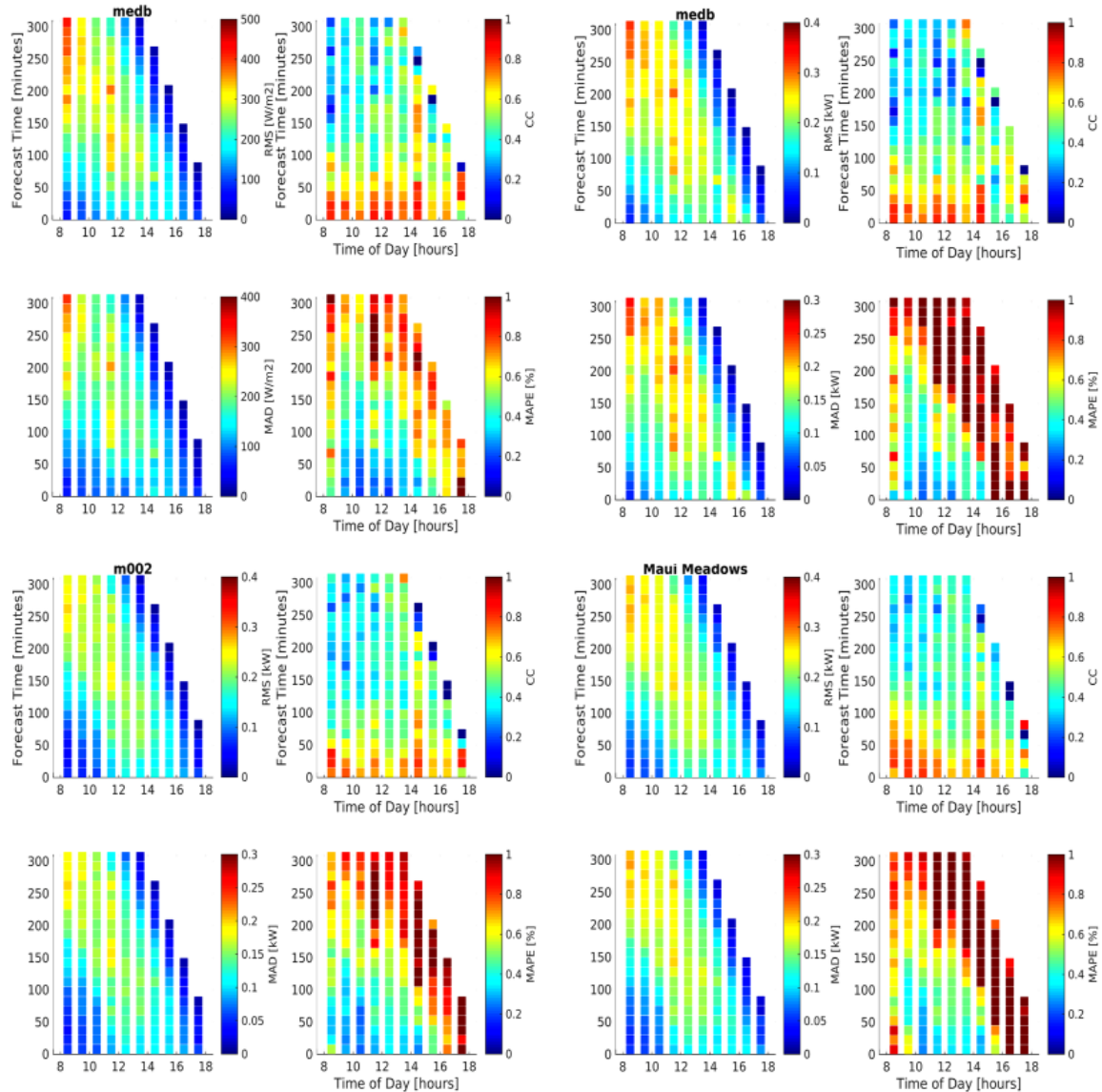


Figure 6.2.29: Results from a two-month comparison of satellite derived forecasts against ground observations.

excluding GHHI data and 2 Maui Meadows sites, which show decreased agreement in the afternoon, possibly due to panel shading. Correlation levels range from 0.7 to 0.8 and MAPE

ranges from 20 to 30%. The highest errors are again found from GHHI data, which is interesting, considering the Maui Meadows forecasts utilize PV orientations from unvalidated methodologies.

A similar comparison between irradiance and power production forecasts to ground data is shown in Figure 4. However, here data is binned per hour of day and forecasting time (at the resolution of the forecasts, 15 minutes). Performance metrics for irradiance and power are shown for the MEDB test beds, along with data from a single residence and data from all residences in Maui Meadows. Initial analysis of these results suggest the forecasting system is producing accurate results for at least 2-3 hours ahead, and may be capturing much of the variability until the late afternoon hours.

In future work, this preliminary evaluation will be expanded to a multi-year analysis. A comprehensive evaluation of the system will be conducted, using data generated by the operational system and forecasts from reprocessed, archived GOES imagery going back to 2012 compared against a variety of ground-based irradiance and power observations from around the island chain.

Development of the New Sky Imager Solar Forecasting Component

Under this subtask, HNEI has continued to design, build and test hardware for a new ground-based sky imager and solar forecasting instrument, the Affordable High Resolution Irradiance Prediction System (AHRIPS). During this time, software to control and manage the instrument operations, without human intervention, and to generate high-resolution, local solar forecasts was developed.

The hardware design focused on: (i) minimizing final production cost, using off-the-shelf, DIY, and open-source technologies, in order to facilitate the widespread deployment required to forecast distributed solar, (ii) being self powered and fully wireless, allowing for flexibility in where the instrument can be installed, and (iii) allowing for multiple instruments to work together in an edge computing framework, as well as to geolocate cloud formations and increase forecasting horizons.

In late 2016, under previous funding, two prototype AHRIPS instruments were designed and fabricated. Under APRISES13, the first generation of instruments were deployed and tested on the University of Hawaii (UH) at Manoa campus and a second generation of instruments was designed, built and tested. The second generation of AHRIPS devices (shown in Figure 5) include: a micro-controller able to monitor power levels and control the single-board computer, controllable power switches allowing power cycling for each main component, additional internal temperature and humidity sensors and fans to respond to excess heat or humidity, and a pyranometer, used for calibration and validation. Under this task, five, second generation instruments were built in mid-2017, then deployed and tested on the University of Hawaii (UH) at Manoa campus. This design significantly increased the robustness of the instrument. In testing, instruments functioned for several weeks completely without human intervention.

Under other funding, a third generation of instruments is currently being designed and built. This generation of instruments is planned for deployment on the island of Molokai. They will be tasked to generate PV production forecasts for Line 105a. Through an agreement with the Maui Electric Company, the instruments will be installed at the tops of secondary utility poles, providing excellent viewing conditions but limited access. Because of the remote deployment and limited

access, the design of this generation of instruments focuses less on minimizing production costs and more on overall system robustness. All internal electrical components have been upgraded to more reliable options and DIY technologies have been removed. The 2nd and 3rd generations are planned for concurrent deployments, during which the overall reliability of the instruments, and the quality of the forecasts will be compared and evaluated.



Figure 5: An AHRIPS 2nd generation instrument deployed on the roof of the Hawaii Institute of Geophysics building.

Journal Publications Resulting from these Efforts

Williamson, S., Bussinger, S., and Matthews, D., Development of a solar irradiance dataset for Oahu, Hawaii, submitted to Renewable Energy February 12, 2018.

References

Dobos, A.; PVWatts Version 5 Technical Reference, NREL/TP-6A20-60272. 2014.

Hammer, A., Heinemann, D., Hoyera, C., Kuhlemanna, R., Lorenza, E., Mullera, R., Beyer. H.G., Solar energy assessment using remote sensing technologies Remote Sensing of Environment 86 : 423–432, 2003.

Nieman, S.J., Schmetz, J., and Menzel, W.P., A Comparison of Several Techniques to Assign Heights to Cloud Tracers, Bulletin of the American Meteorological Society, 32, 15S9- 1568, 1993.

Grid Scale Energy Storage Project

Under previous awards (HEET 09, HEET 10 and APRISES 11) three Battery Energy Storage Systems (BESS) were procured, installed, and commissioned in the Hawaiian Islands. The initial system, deployed on the Hawaii Electric Light Company (HELCO) grid on the Island of Hawaii, continues to be operated by HELCO. HNEI has continued to collect data under APRISES 13 and other funding awards, but experiments have ceased. The Oahu BESS, deployed at the Campbell Industrial Park (CIP) substation, was commissioned in August 2016. Under the current effort (APRISES 13), a series of hardware and software problems, identified during the startup, were analyzed and addressed. Testing was then initiated. Results are described below. Under APRISES 12, the team also modified the hardware and software of the Molokai BESS resulting in significantly faster response to events. Under APRISES 13, the algorithms for the Molokai BESS have been further modified to improve responses to grid conditions. This work is described in detail below.

Oahu BESS

The Oahu BESS was fully commissioned for real-time control under HEET 09 and HEET 10. Testing continued under APRISES 13 included:

- Resolved hardware problems causing overheating of the inverter and communication outages with meters.
- Supported maintenance and safety meetings with several utility groups.
- Collected initial performance data under various algorithm settings.
- Identified an inverter design flaw that had led to an emergency shut-down and caused the release of a fire-suppressant.

Two algorithms were developed for the Oahu BESS under HEET 10 (Reference [1]): a frequency response algorithm and a power smoothing algorithm. Both algorithms were also designed to provide voltage regulation by sourcing or sinking reactive power. The frequency response algorithm was of interest to and funded by HECO. HNEI's primary interest was in the development and demonstration of the power smoothing algorithm. The testing of these algorithms is on-going under other funding. Hardware and software problems analyzed and addressed under APRISES13, along with initial testing results are described below.

A series of "Isolation Faults" occurred repeatedly after commissioning. This is an indication of low resistance between the BESS and ground. It was thought that the low resistance could be related to heat. This was tested, and the results are shown in Figure 6.2.31, which confirms the relationship between temperature and resistance. It took about 3 hours and 40 minutes to approach the low resistance threshold of 100kOhm when the reactive power was a sustained $\pm 1000\text{kVAR}$. Follow-on experiments showed that the 100kOhm limit would not be reached if the BESS was limited to $\pm 900\text{kVAR}$.

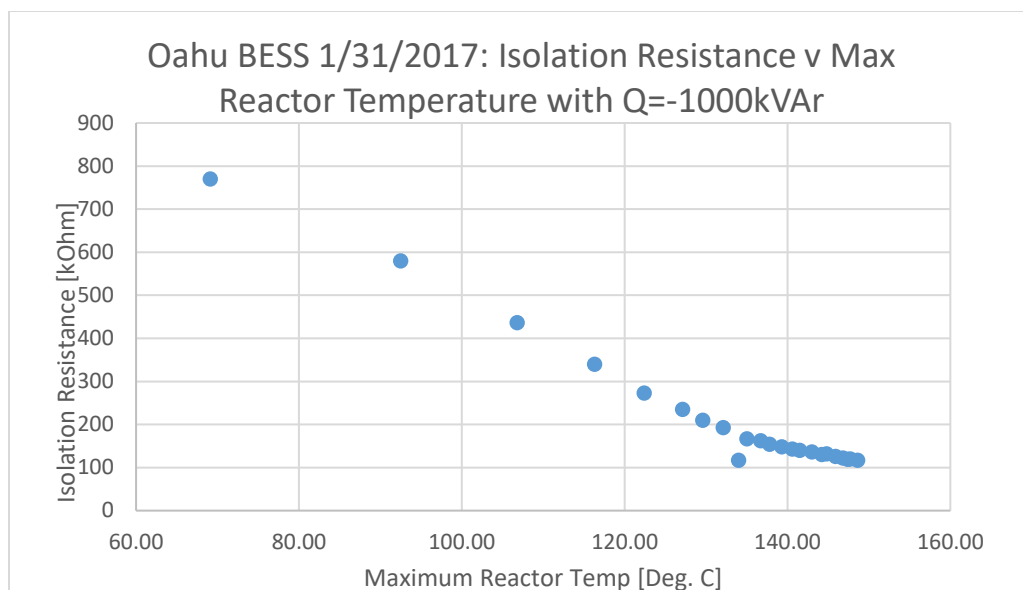


Figure 6.2.31: Isolation resistance versus highest temperature in reactors. It took 3 hours and 40 minutes to approach 100kOhm (the fault threshold).

During initial testing, it was observed that voltage regulation caused the inverter to run hot, even when the maximum reactive power was reduced to $\pm 900\text{kVAr}$. It was found that the algorithm was calling for the maximum amount of reactive power for sustained periods of time. An example of this is shown in the middle plot of Figure 6.2.3 0-16.2.32. Here, the real power was limited to $\pm 1000\text{kW}$ (the full capability of the inverter) while the reactive power was limited to $\pm 900\text{kVAr}$. Note that the real power (top plot) swings as needed between positive and negative values, while the reactive power is sustained at its limits for several hours at-a-time, leading to excessive heating. According to the inverter manufacturer, the temperatures observed over extended periods of time were within specification. However, the practical problem was that the inverter could not be operated at full specified reactive power because of isolation faults. Because of this, HECO funded Northern Plains Power Technologies (NPPT) to replace the voltage regulation algorithm with a voltage smoothing algorithm. This effort is on-going under other funding, including simulation work to determine if voltage smoothing will adversely interact with the sub-station's load tap changer.

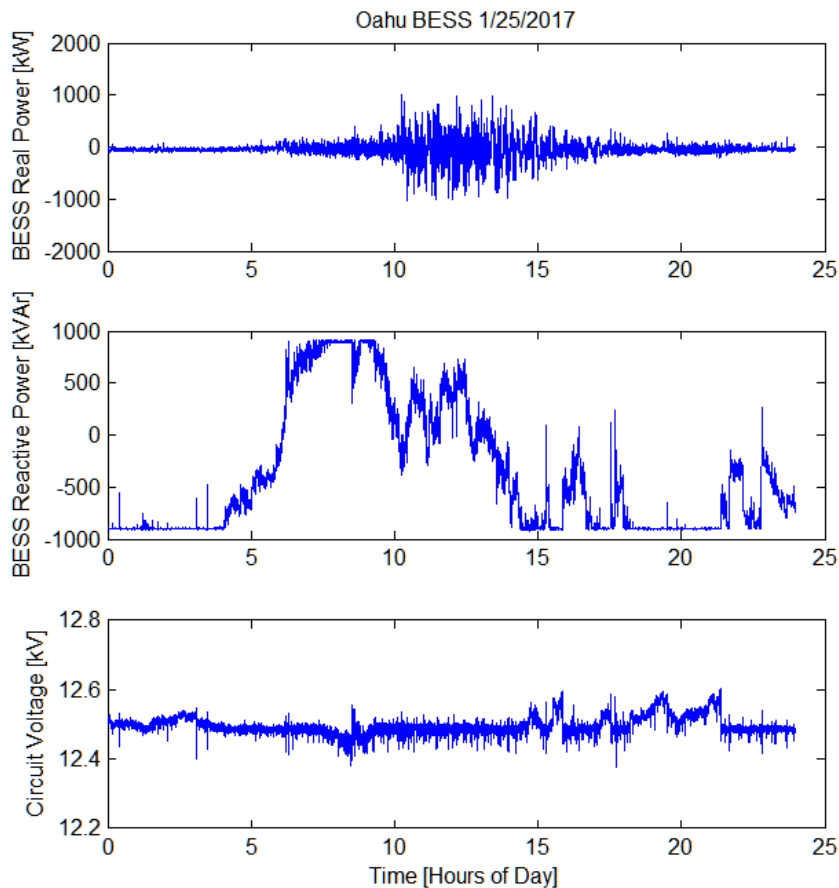


Figure 6.2.3 0-1: (Top) Battery Energy Storage System (BESS) Real Power (Middle) BESS Reactive Power (Bottom) Voltage.

An intermittent but highly frequent loss of communications between the Site Dispatch Controller (SDC), which is the center of all real-time processing, and one or more meters arose shortly after commissioning. The problems caused by the communications timeouts were two-fold: (1) they generate a vast number of trouble-code emails to operators, and (2) they cause the BESS to suddenly stop power commands. The later can be disruptive to the circuit when the BESS suddenly goes from sourcing or sinking significant power to zero.

The root-cause of the intermittent communications appears to have been a failing Uninterruptable Power Supply (UPS) power module and I/O relay. Some on-site diagnostics were conducted to determine the source of repeated “Fire System Failure” alarms. The diagnostics determined that the UPS I/O relay (which was also connected to the fire system) had failed. That failed device also obscured the warning that a battery in the UPS (which supplies power to the SDC) had also failed. The communications problems ceased after the UPS power module and relay were replaced.

Data collection and analysis was initiated after solving the problems discussed above. Performance data has been collected with the BESS providing:

- Real power only for power smoothing
- Reactive power only for voltage regulation
- Both real and reactive power for both power smoothing and voltage regulation

The first set of results is shown in Figure 6.2.30-2. The blue trace shows the voltage profile for a representative day with the BESS offline. The green trace shows the impact of the real-power-only case. These first two cases are highly comparable, with (arguably) slightly less voltage “noise” in the green trace. The red trace shows an exemplar case when only reactive power is used to provide voltage regulation. Note that the voltage regulation had reduced the excursive steps in voltage because the Load Tap Changer (LTC) is infrequently required to move positions to regulate voltage. The cyan trace shows that voltage excursion and variability appear to be reduced when both real and reactive power are used.

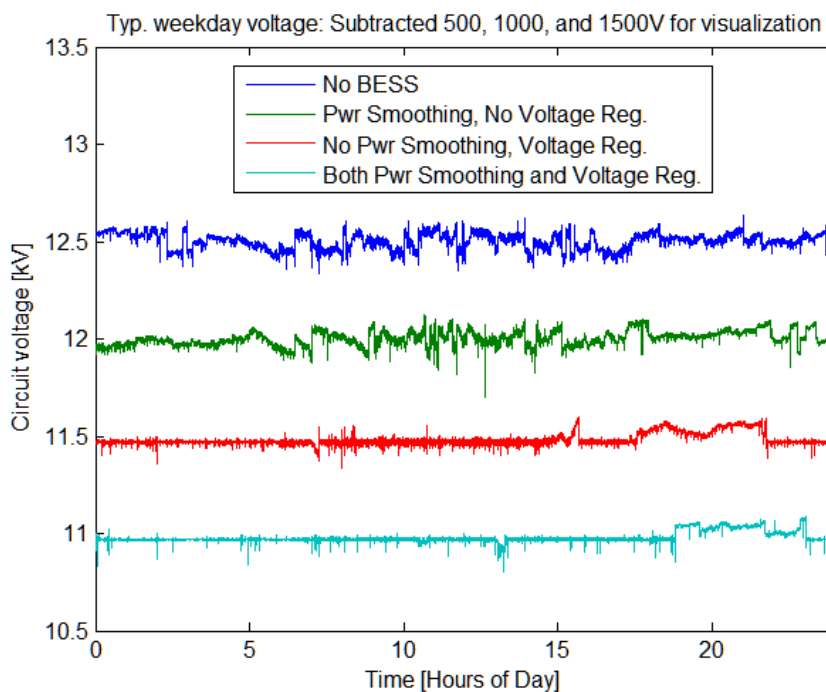


Figure 6.2.30-2: Voltage profiles for typical weekdays with a variety of BESS settings. Note: only the BESS-off case is presented at the correct voltage levels. Increments of 500kV were subtracted from the other three cases to prevent overlap, hindering visualization.

Histograms of the same data are shown in Figure 6.2.30-3. The same color schemes are used in this figure. Note that the most significant reduction in variability is achieved when both real and reactive power are used.

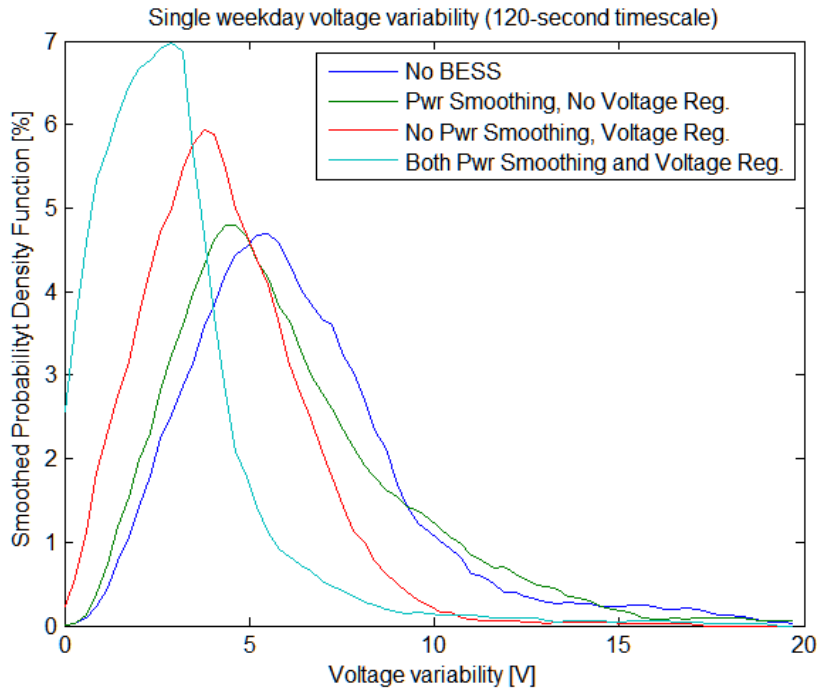


Figure 6.2.30-3: Smoothed density functions for data presented in Figure 6.2.30-2. Smoothing was applied to aid with visualization.

An additional initial result from the case when both real and reactive power are used is that the LTC changes are reduced by about 60%.

On September 4th, 2017, a short-circuit caused a smoke event that shut the BESS down. The short circuit activated the inverter's fire suppression protocol and the FM-200 fire suppressant was released. This event triggered a root-cause investigation led by HECO and supported by HNEI. The investigation revealed that two bus bars had short circuited. Under its own funding, HECO hired the inverter manufacturer, (Parker-Hannifin) to fabricate new the bus bars and will install them with spacers to avoid recurrence. Currently, HECO is working to re-start the Oahu BESS. It is expected to be operational in March 2018. This event is documented in [2]. Performance testing is expected to resume in March 2018 under other funding.

Molokai BESS

The Molokai BESS, installed and commissioned under prior funding, is rated at 2MW with an energy capacity of 397kW-Hr. The intention of this installation was to provide support during contingency events for a 4.5MW grid hosting more than 2MW of PV.

As an example, the type of contingency event we sought to resolve is typified by a loss of generation event on October 2nd, 2017. At the time of the event, there were 3 diesel generators operating:

- Generator 1 was providing droop response near its full rated power of 1.1MW.

- Generator 7 was operating at about 1.6MW (full rating is 2.2MW) in isochronous mode.
- Generator 9 was operating at around 750kW (full rating is 2.2MW) in isochronous mode.

Generator 1 suddenly tripped offline. Although Generators 7 and 9 responded by adding power, the frequency dropped below 59.3Hz, the low frequency threshold for disconnection for legacy distributed PV systems. When those systems tripped, an additional loss of generation was realized. Because of the additional loss of generation, the newer PV systems (57Hz threshold) tripped offline as well. Soon after that, load shedding occurred. This event is summarized in Figure 6.2.30-4, which shows high rate data for Generator 9. Unfortunately, high rate data are not available for Generators 1 or 7. The low rate data collected during this event showed that Generator 7 did output at least an additional 500kW. However, because this was only 2-second data, a higher value may have been missed. Molokai provides a case study of a low inertia system typical of small island systems where a 1MW loss of generation, for example, causes a frequency event that occurs too quickly for the conventional diesel generation to respond.

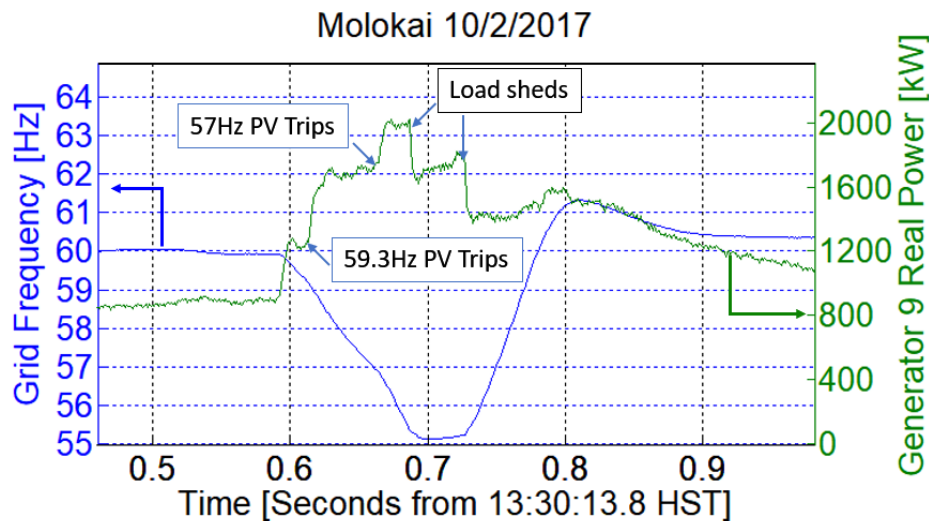


Figure 6.2.30-4: Molokai loss of generation event on 10/2/2017. The blue trace is the grid frequency and is associated with the left axis. The green trace is the real power from Generator 9 (a 2.2MW diesel) and is associated with the right axis. There were two PV trips, and two load sheds.

As previously stated, under previous awards, significant changes to the hardware and software were made to reduce the response time. The results of the initial tests are briefly reviewed here. These tests confirmed the following:

- The BESS would have destabilized the Molokai grid if the hardware and software modifications to reduce the BESS response time were not made.
- The BESS response with the speedup, reduced frequency deviations that were caused by known disturbances.

As previously reported, the tests involved the BESS producing either -400kW steps or -400kW pulses. The step responses are reviewed here for three cases:

- Grid frequency response with no BESS response (Figure 6.2.30-5, top). The blue trace, which is grid frequency, follows the blue axis on the left. The green trace, which is the step disturbance caused by the BESS, follows the green axis to the right. Notice that a -400kW disturbance results in a 400mHz frequency deviation.
- Grid frequency response when allowing the BESS to respond with no more than 100kW with the speedup architecture turned off (Figure 6.2.30-5, middle). Here, the colors and axes are the same, but the BESS algorithmic response is summed with the step. Note that the frequency response to the up-step is a damped oscillation. The oscillation is synced with the BESS power, meaning, even with a 100kW authority, the BESS had made the grid marginally stable. The grid could have become unstable if more than 100kW of authority was provided.
- Grid frequency response when allowing the BESS to respond with no more than 100kW with the speedup architecture turned on (Figure 6.2.30-5, bottom). This plot shows that when the speedup is enabled, the grid remains stable when the BESS response is added to the disturbance. Even with only 100kW of authority, the frequency deviation is slightly muted.

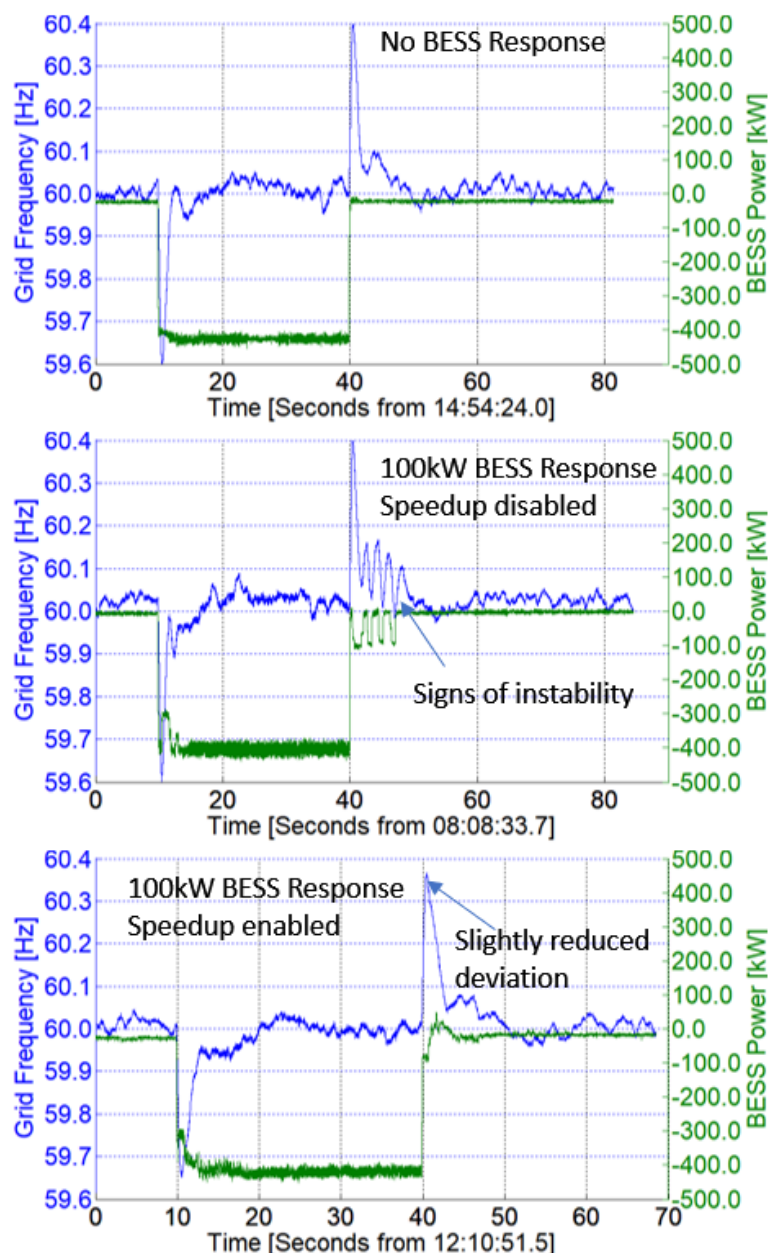


Figure 6.2.30-5: (Top) Grid response with the BESS not algorithmically responding; (Middle) grid response with BESS responding with 100kW of authority and speedup disabled; (Bottom) same with speedup enabled.

Under this award, as a result of analysis of high rate synchrophasor data, additional control issues were identified and additional upgrades to the algorithm were made. These results are described below.

An example early-version algorithm response is shown in Figure 6.2.30-6. Note that during all of the testing under APRISES 13, the BESS was limited to source or sink no more than 500kW.

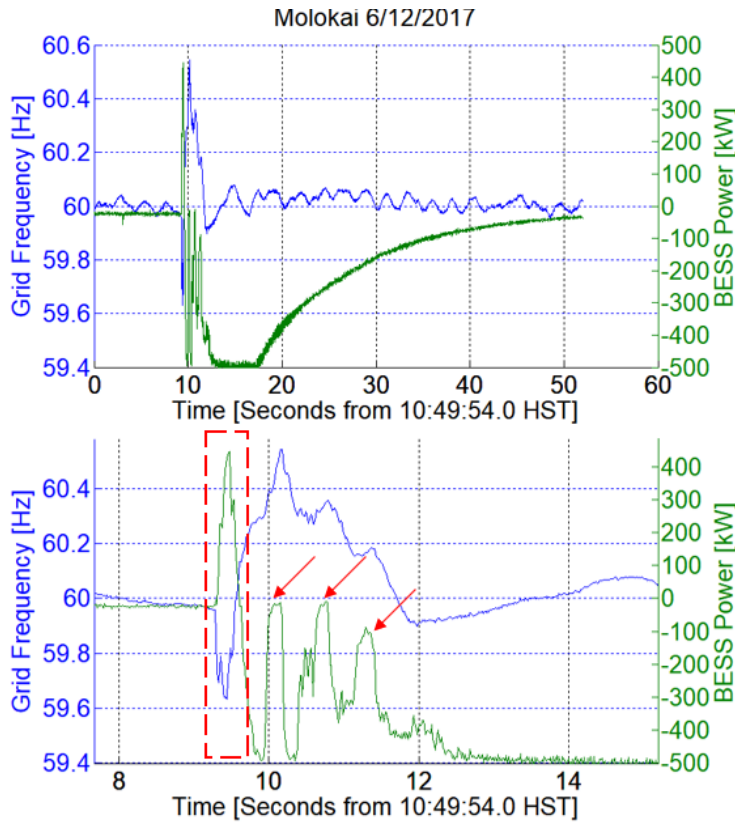


Figure 6.2.30-6: (Top) Fault response using algorithm Version v1.15.04. (Bottom) Expansion showing three points when BESS stopped responding (red arrows).

In Figure 6.2.30-6 (bottom), the algorithm responds properly to the initial under-frequency event (i.e., the blue and green traces look like reflections inside the red dashed rectangle). Also, the green and blue lines intersect when frequency is close to 60Hz, which is desirable. Next, the frequency overshoots when the diesel generators respond aggressively to the fault current. At that point, the BESS absorbs power at the full -500kW limit to mitigate the generator over-response. At about 10 seconds, the BESS suddenly drops to 0kW. This recurred two more times. The source of the problem was identified and resolved.

Modifications to the algorithm have yielded an improved response to large events. One example is shown in Figure 6.2.30-7. There are no signs of BESS drop-outs as seen in Figure 6.2.30-6 (bottom, red arrows).

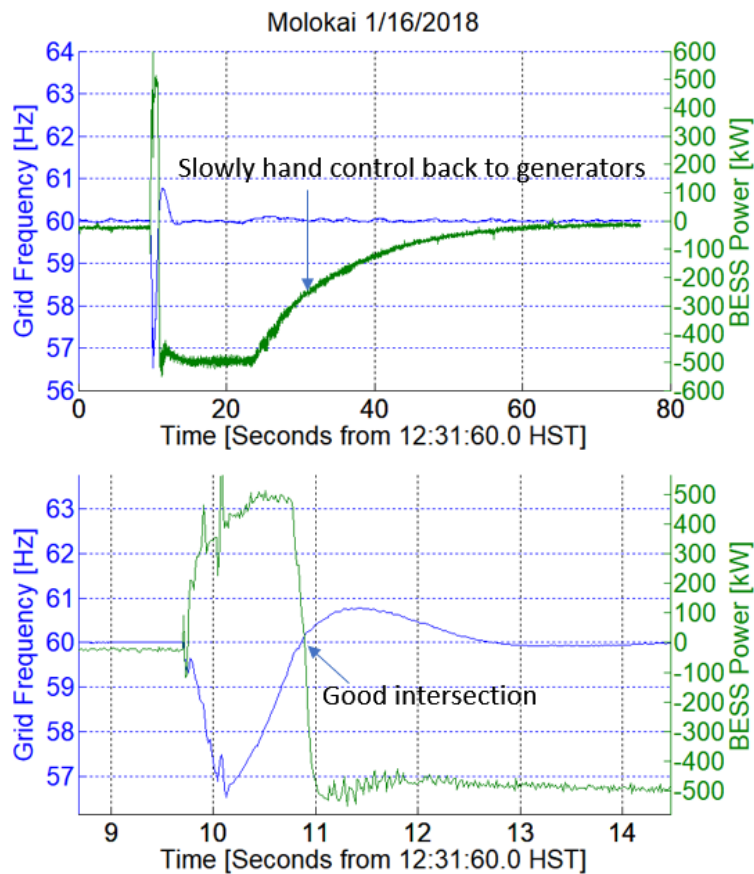


Figure 6.2.30-7: (Top) BESS response to a significant event after algorithm modifications (Version v1.15.06). (Bottom) An expansion near fault.

This fault shown in Figure 6.2.30-7 did not result in under-frequency load shedding. However, all PV on the island tripped resulting in a 1.3MW increase in load. After the fault cleared (~330ms), a 570kW circuit tripped. This appears to be about the time when the BESS reactive power absorbed about 800kVAr during the over-voltage period. This is shown in Figure 6.2.30-8. Note that the algorithm was not allowed to source or sink any reactive power. The inverter manufacturer has hypothesized that this was related to the behavior of the step-up transformer that connects the BESS to the circuit. This requires more investigation as future work.

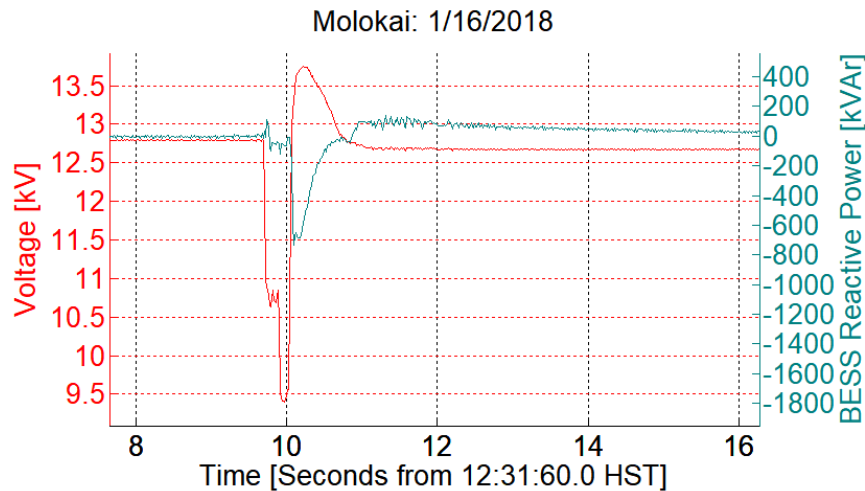


Figure 6.2.30-8: Unanticipated reactive power response following fault conditions.

An oscillation in grid frequency led to another lesson learned and required an upgrade to the algorithm. The source of the oscillation (shown in Figure 6.2.40) is not known. It occurs once every few months. It is possible this is attributable to a voltage control resource. In the left plot of the figure, the blue trace is grid frequency (associated with the left axis). The green trace is the BESS real power. Zooming in (right plot) shows that the grid frequency is oscillating at around 22 times per second with an amplitude of about 300mHz. The inverse of the cycle time is faster than the response time of the BESS. Therefore, responses from the BESS can exacerbate the problem. In the case shown, the BESS was turned off by grid system operators after around 90 seconds. At that point, the amplitude of the oscillations dropped by 33%.

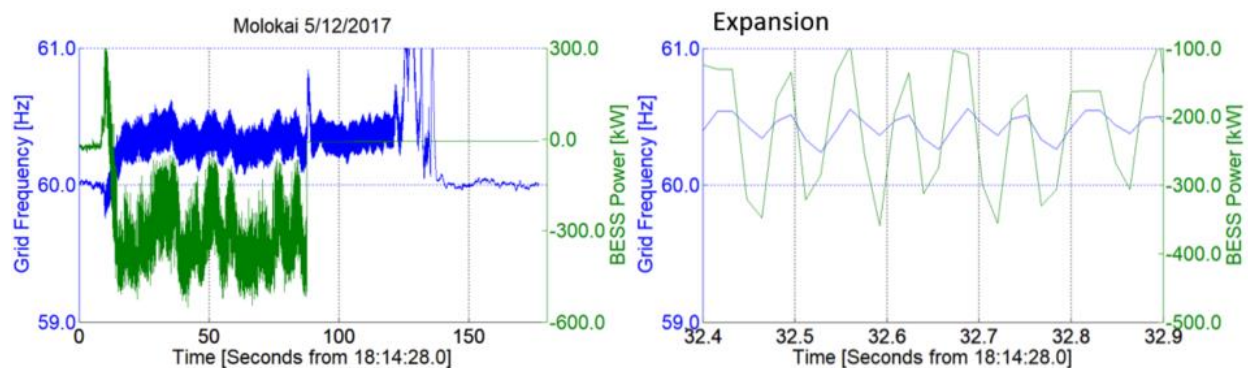


Figure 6.2.40: (Left) Full view of anomalous grid frequency oscillation. (Right) Expansion shows BESS exacerbating situation because oscillation frequency is close to the inverse of BESS response time.

The optimal solution to the frequency oscillation problem would be to determine the source of the problem. In lieu of that determination, an algorithm was devised to detect the condition and

suppress the BESS until the condition had abated. This detection algorithm has been tested in-lab and deployed.

Conclusions

Although some initial data has been collected with the Oahu BESS, more testing is required to determine its impact on the circuit using different algorithm settings. This will be done under other funding after repairs are made in the inverter.

The next step for the Molokai BESS will be to slowly increase the authority, ultimately to the 2MW specification. This will require continued analysis of naturally occurring grid contingencies (under other funding). Modeling is also planned as a future endeavor. Specifically, the modeling effort will integrate an existing grid model with a model of the BESS algorithm.

References

- [1] M. Ropp, S. Perlenfein, M. Tun, “Control Algorithm Requirements and Functional Specifications (Report 3 version 24 final)”, Northern Plains Power Technologies and Hawaii Natural Energy Institute, December 11, 2013.
- [2] HECO Report: “CIP BESS Bus Bar Short”, January 8th, 2018.

TASK 7: ENERGY EFFICIENCY

Under Task 7, three projects relating to energy efficiency in buildings were completed in collaboration with MKThink and other consultants and contractors: A) the final construction phase of the two Flexible Response to Ongoing Growth (FROG) net zero energy platforms at the University of Hawaii at Manoa (UH) with the installation of two 8 kW photovoltaic arrays, a weather station and a dedicated monitoring system; B) the scope of the comfort study was expanded to include other comfort variables, including temperature and humidity. In conjunction with these comfort variables, energy utilization of the buildings was broken down by time of day, and day of week to isolate the effect of individual classroom preferences by instructor or classroom users, and; C) a desiccant dehumidification pilot project was designed for implementation at a location in Hawaii and the applicability of ceiling fans to low energy, thermal comfort was explored.

A. Photovoltaic Installation and Research Platform Performance

Photovoltaic Systems

The energy neutral research platforms on UH Manoa campus were completed in 2017 with the installation of two 8 kW photovoltaic systems, one system for each of the two roofs. A Request for Proposals was issued in late 2016, with Haleakala Solar winning the award (one of the oldest and most experienced solar companies in Hawaii). Building plans and documents were developed between the January 2017 award and the county permit submittal in May 2017. Prior to County submittal, Haleakala Solar submitted plans and specs for review and received approval to connect to the grid from the local utility, the Hawaiian Electric Company. The permitting process took approximately six months with the building permit issued in early December 2017 in time for substantial completion of the installation the same year.

With the assistance of Haleakala Solar, HNEI and its collaborative partner, the UH School of Architecture's Environmental Research and Design Laboratory (ERDL) completed the installation of a Gill Metpak Professional weather station on the roof of FROG 1, allowing the direct monitoring of the microclimate of the UH Manoa FROGS. The schematic in Figure 7.1 was designed and prepared by Haleakala solar, illustrating the components of each of the two systems.

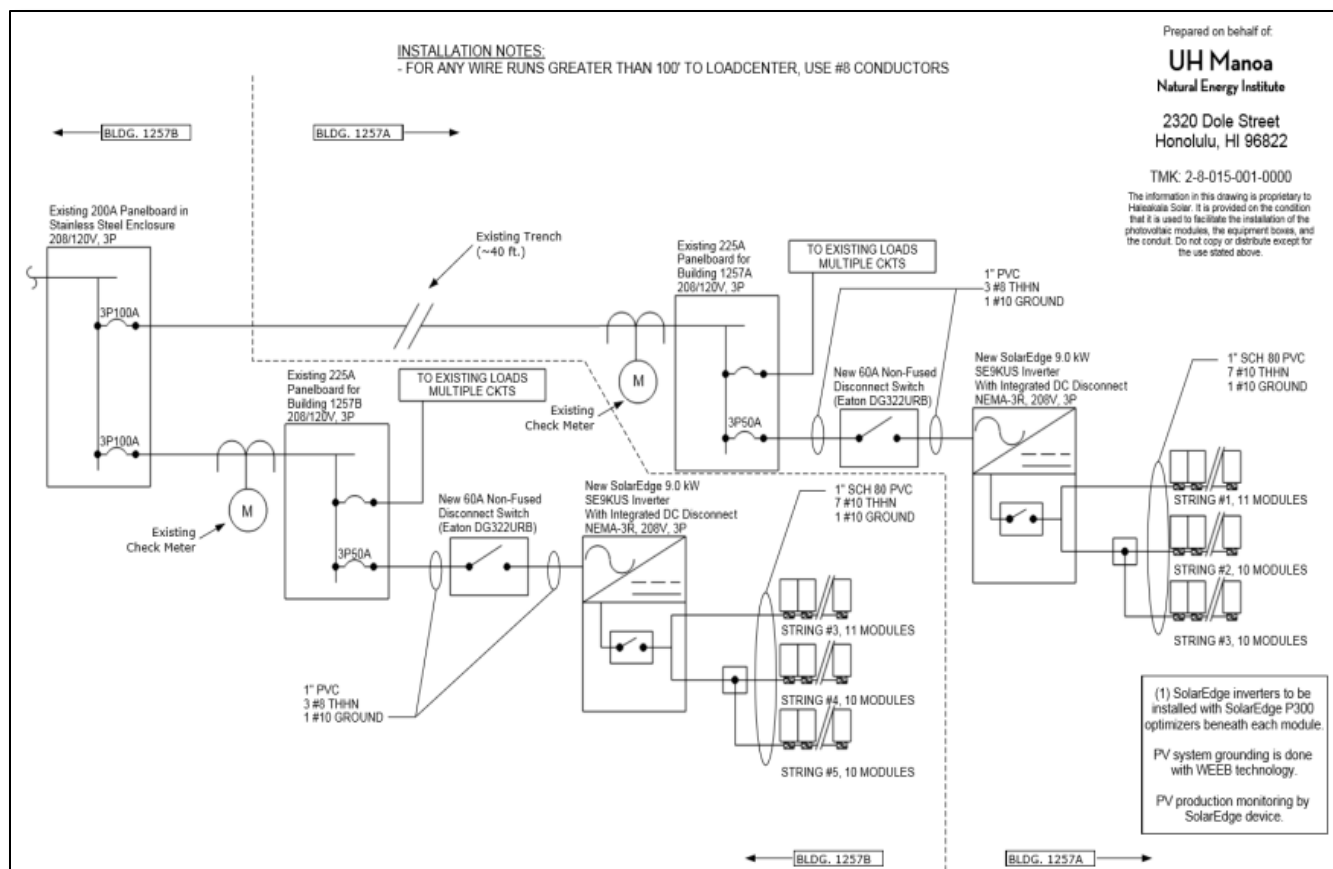



Figure 7.1. Schematic of UH Manoa Project FROG photovoltaic systems.

Components:

Inverters; Solar Edge SE9KUS three phase inverter (Fig. 7.2a)

Panels; 31 Hyundai model HiS-260RG photovoltaic panels. (Fig. 7.2b)

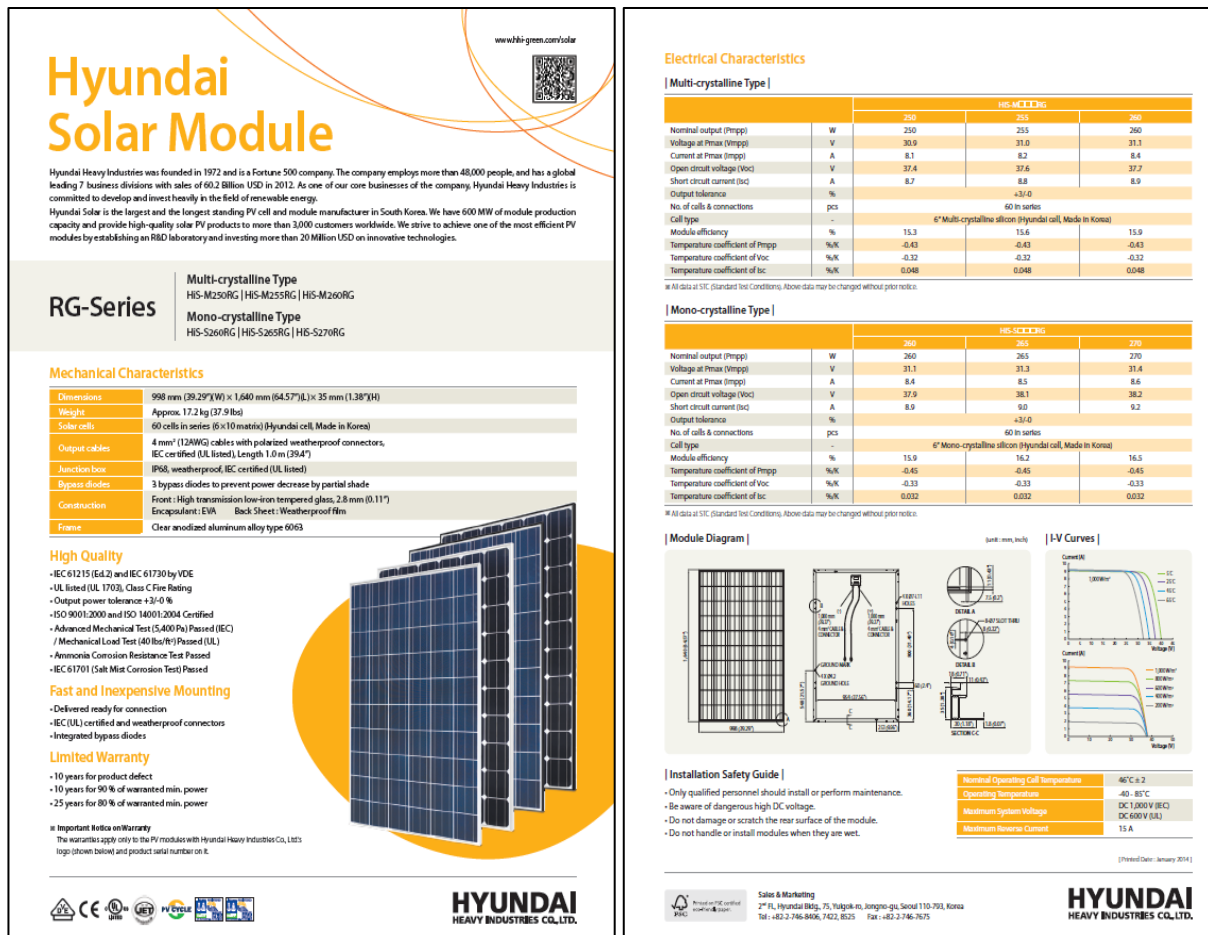
solar edge		Three Phase Inverters for the 208V Grid ⁽¹⁾ for North America	
		SE9KUS	SE14.4KUS
OUTPUT			
Rated AC Power Output	9000	14400	VA
Maximum AC Power Output	9000	14400	VA
AC Output Line Connections	4-wire WYE (L1-L2-L3-N) plus PE or 3 wire Delta		
AC Output Voltage Minimum-Nominal-Maximum ⁽²⁾ (L-N)	105-120-132.5		Vac
AC Output Voltage Minimum-Nominal-Maximum ⁽²⁾ (L-L)	183-208-229		Vac
AC Frequency Min-Nom-Max ⁽³⁾	59.3 - 60 - 60.5		Hz
Max. Continuous Output Current (per Phase)	25	40	A
GFDI Threshold	1		A
Utility Monitoring, Islanding Protection, Country Configurable Set Points	Yes		
INPUT			
Maximum DC Power (Module STC)	12150	19400	W
Transformer-less, Ungrounded	Yes		
Maximum Input Voltage DC to Gnd	250	300	Vdc
Maximum Input Voltage DC+ to DC-	500	600	Vdc
Nominal Input Voltage DC to Gnd	200		Vdc
Nominal Input Voltage DC+ to DC-	400		Vdc
Maximum Input Current	26.5	38	Adc
Maximum Input Short Circuit Current	45		Adc
Reverse-Polarity Protection	Yes		
Ground-Fault Isolation Detection	1MΩ Sensitivity	350KΩ Sensitivity ⁽⁴⁾	
CEC Weighted Efficiency	96.5	97	%
Night-time Power Consumption	< 3	< 4	W
ADDITIONAL FEATURES			
Supported Communication Interfaces	RS485, Ethernet, ZigBee (optional)		
Rapid Shutdown – NEC 2014 and 2017 690.12	Automatic Rapid Shutdown upon AC Grid Disconnect ⁽⁵⁾		
RS485 Surge Protection	Supplied with the inverter		
STANDARD COMPLIANCE			
Safety	UL1741, UL1741 SA, UL1699B, CSA C22.2, Canadian APCI according to T.L.L. M-07		
Grid Connection Standards	IEEE1547, Rule 21, Rule 14 (HI)		
Emissions	FCC part15 class B		
INSTALLATION SPECIFICATIONS			
AC output conduit size / AWG range	3/4" minimum / 12-6 AWG	3/4" minimum / 8-4 AWG	
DC input conduit size / AWG range	3/4" minimum / 12-6 AWG		
Number of DC inputs	2 pairs	3 pairs ⁽⁶⁾	
Dimensions (H x W x D)	21 x 12.5 x 10.5 / 540 x 315 x 260		in / mm
Dimensions with Safety Switch (H x W x D)	30.5 x 12.5 x 10.5 / 775 x 315 x 260		in / mm
Weight	73.2 / 33.2	99.5 / 45	lb / kg
Weight with Safety Switch	79.7 / 36.2	106 / 48	lb / kg
Cooling	Fans (user replaceable)		
Noise	< 50	< 55	dBA
Operating Temperature Range	-40 to +140 / -40 to +60 ⁽⁷⁾		°F / °C
Protection Rating	NEMA 3R		
<small>⁽¹⁾ For 277/480V Inverters refer to: http://www.solar-edge.com/files/2017/03/277-480V-Three-Phase-Inverter-Data-Sheet.pdf ⁽²⁾ For other regional settings please contact SolarEdge support ⁽³⁾ If not permitted by local regulations ⁽⁴⁾ IEC 62109-2:2011 has Manual Rapid Shutdown for NEC 2014 compliance (NEC 2017 compliance with outdoor installation) ⁽⁵⁾ Field replacement kit for 1 pair of inputs P/N: DCD-2PH-170K; Field replacement kit for 3 pairs of fuses and holders P/N: DCD-3PH-2PH-51 ⁽⁶⁾ For power derating information refer to: https://www.solar-edge.com/files/2017/03/temperature-derating-note-na.pdf</small>			



RoHS

© SolarEdge Technologies, Inc. All rights reserved. SOLAREGE, the SolarEdge logo, OPTIMIZED BY SOLAREGE are trademarks or registered trademarks of SolarEdge Technologies, Inc. All other trademarks mentioned herein are trademarks of their respective owners. Date: 11/2017/01/ENG. N/A. Subject to change without notice.

Figure 7.2a Specification sheets for Solar Edge three phase inverter.



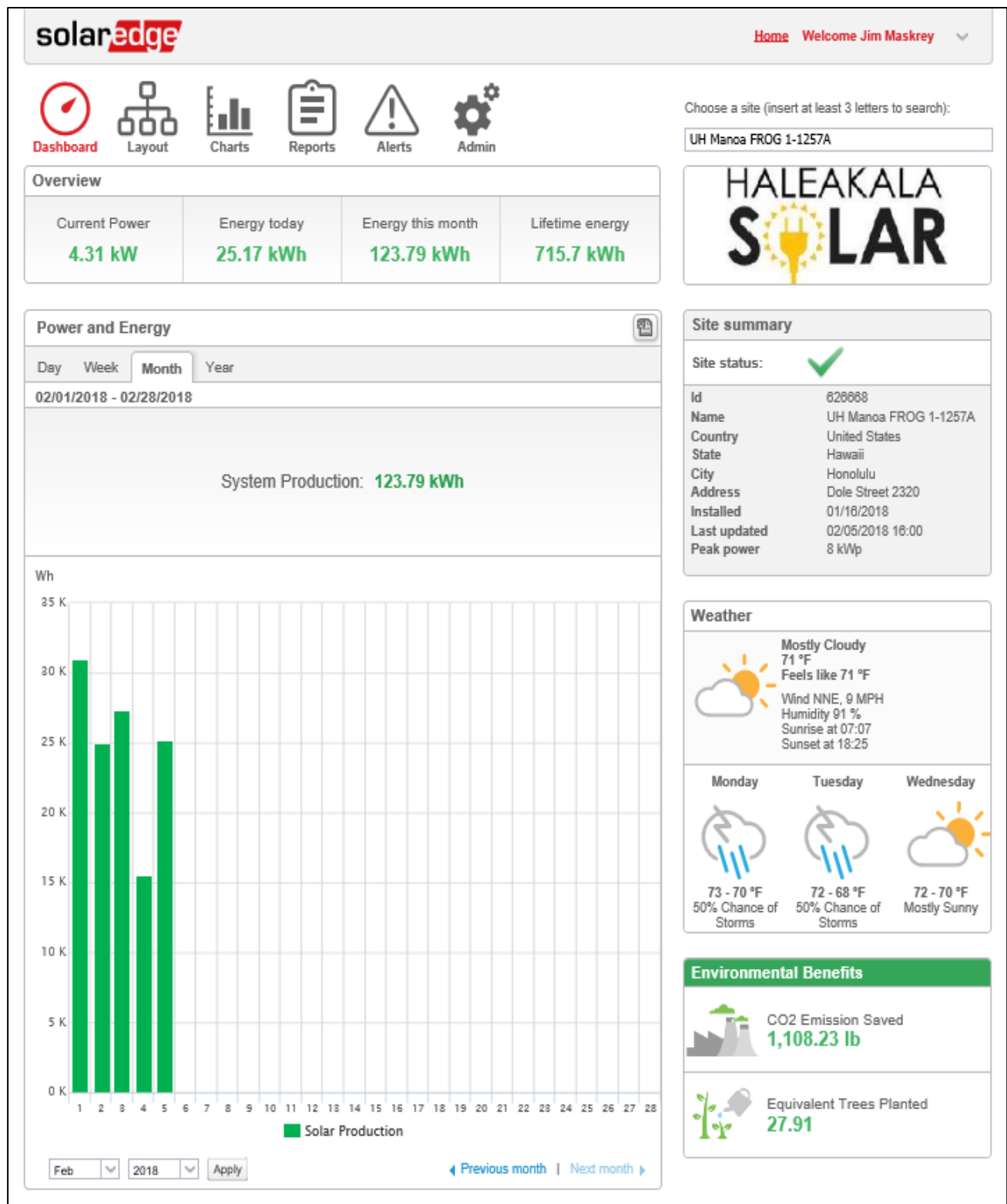


Figure 7.3. Home page Solar Edge cloud based monitoring system.

The monitoring system capabilities include:

- Tracks technical and financial performance of one or more SolarEdge photovoltaic systems
- A display of all installations on a map
- Enables logical and physical photovoltaic site visualization with real-time performance data for each individual module and for the whole system
- Presents historical and aggregated data, comparative analysis diagnostics and a guided root-cause fault analysis. All data is logged and can be securely reviewed and analyzed at any time from any location
- Enables the creation of the physical layout (see tutorials below)
- Enables generation of comprehensive reports on site's energy production, revenues and technical status
- Enables immediate fault detection and troubleshooting, efficient maintenance management, and site profitability analysis
- Configurable rule engine automatically detects problems, issues status reports and sends alerts via e-mail
- Remote service capabilities
- Interactive charts and site layout make it easy for installers to ensure a system is functioning properly after installation
- The Playback feature visualizes the harvested power of a site during a selected time fragment
- Kiosk display – enables to showcase the photovoltaic site performance on a display in public spaces (like building lobbies)
- High resolution data and visualization of past 12 months at 10 minute resolution

The dashboard provides power and energy information on a day, week, month or year screens down to 15 minute intervals, as shown in Figures 7.4 a-d.

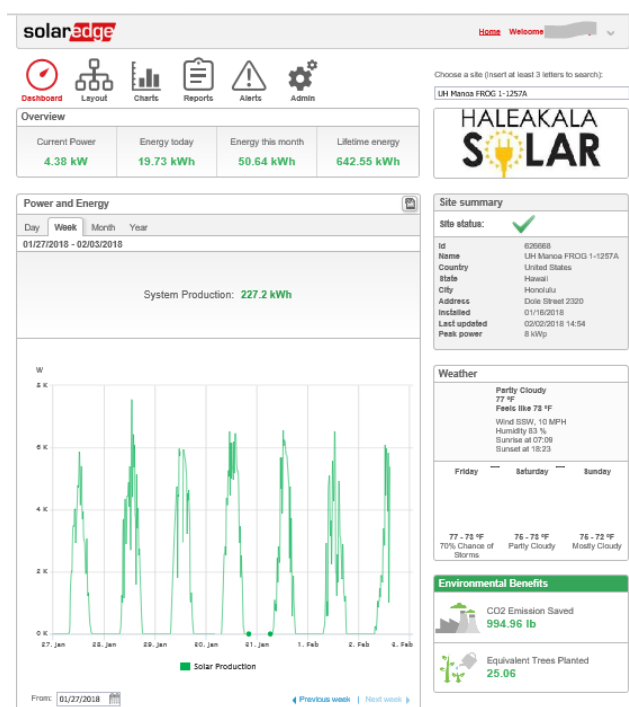
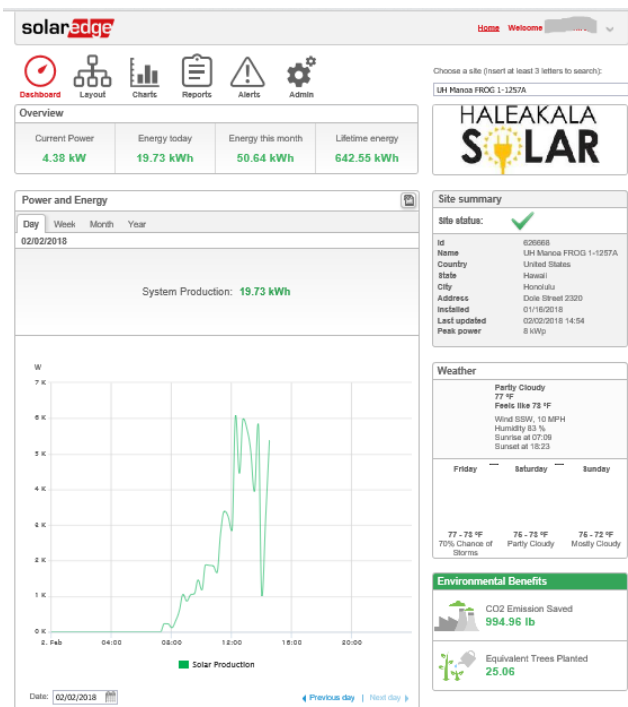


Figure 7.4 a-b: Screenshots of day and week generation profiles

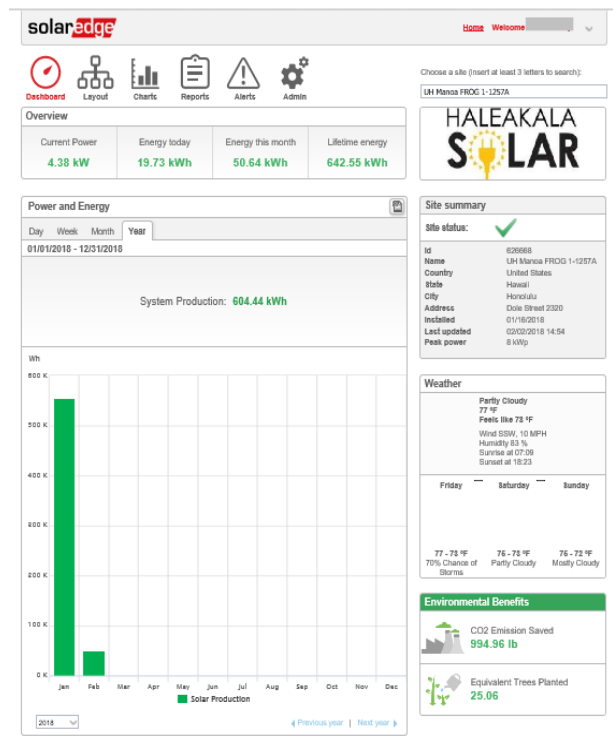
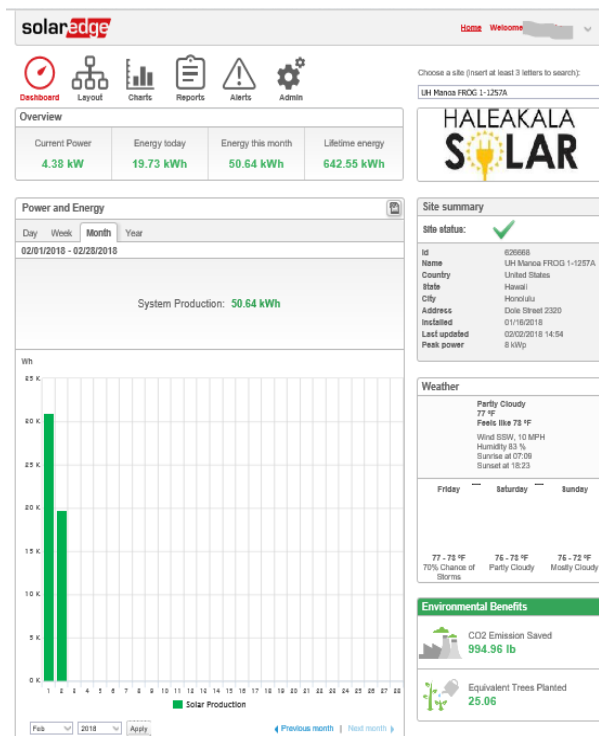


Figure 7.4 c-d: Screenshots of month and year generation profiles

The dashboard's reporting capabilities allows this 15-min interval data to be downloaded for energy and power consumption, as well as providing detailed information on site status, and data for site commissioning and module mismatch. These reports aid in commissioning the system at

the beginning of a project while helping to identify performance issues during ongoing routine operation. Report screens are illustrated in Figure 7.5.

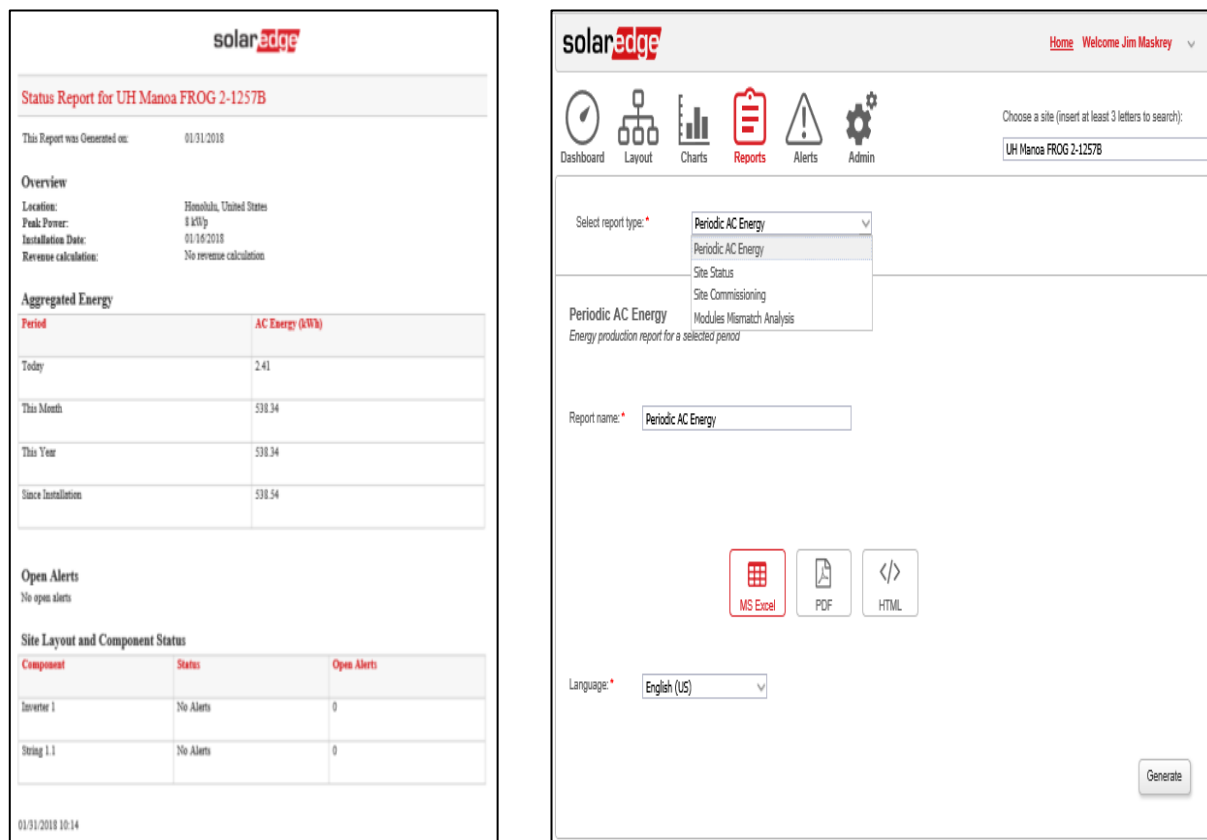


Figure 7.5. Solar Edge report generating capabilities

Conclusion

The installation of the solar photovoltaic systems, each including inverter, optimizers, monitoring instrumentation, and cloud based dashboard, conclude construction for the UH Manoa FROG platforms. Each 8 kW array generates enough electricity to offset the consumption by building users. The dedicated solar monitoring system is readily accessible through a single URL, allowing building managers to validate performance in real time and identify problems that might arise in the system. The reporting capabilities allow performance data to be downloaded for detailed analytics.

B. Environmental Research Support for Energy Neutral Research Platforms

In past APRISES awards, HNEI and its subawardee, MKThink, conducted a comparative analysis of test platforms and conventional classrooms in Hawaii. These were instrumented to monitor energy use, indoor environmental quality, and system operation sensors to compare their respective performance, as well as to compare their performance to predictive models, and to establish guidelines for building performance.

With APRISES 13, HNEI continued the ongoing monitoring of two 1,440-square-foot FROG platforms, tracking energy use and comfort performance. During this award period, HNEI contracted Sara Cerri to support data analysis of the two FROGs, evaluating and comparing energy use patterns during both occupied and unoccupied periods.

The two net-zero energy platforms, named UH Manoa FROG 1 and FROG 2 (Figure 7.6), were designed and constructed by Project FROG in 2016 (under previous ONR HEET10 funding, and summarized in the report available online, “Project FROG Test Platform Study at Kawaikini NCPS”). The classrooms are “mixed-mode” structures, using both natural ventilation and air conditioning. In addition to being used as classrooms for high school and university students, HNEI is using the structures as research platforms to 1) test efficient building technologies such as energy storage, advanced occupancy sensing, advanced fan control and to, 2) gather data on actual interior conditions and perceived indoor comfort.

CLASSROOM TYPE	Modular Portable FROG
PERFORMANCE	High Performance NZE
DESIGNER	Project FROG
SIZE	1,440 NSF
YEAR BUILT	2016
ENCLOSURE TYPE	Wood frame panels with fiber glass insulation (R-22 equivalent)
ROOF TYPE	Singly ply white membrane & insulation (R-22/ R-30)
CLIMATE	Tropical microclimate: Warm (<75°F avg.); Humid (>70% RH avg.); Sunny (>260 W/m ² /mo.)
ORIENTATION	North-south
USE TYPE	High School Classroom University Classroom




Figure 7.6: Details of the UHM FROG classroom (FROG 1, FROG2)

The UH Manoa FROG platforms are considered a second generation design and are expected to consume less energy than the first three classrooms installed in Hawaii (at Ilima Intermediate School in Ewa Beach, on Oahu, and two at Kawaikini New Century Charter School in Lihue, on Kauai). These structures will help to achieve the UH goal of becoming net zero energy by the year 2035. As research platforms, the UH Manoa classrooms incorporate a real-time dashboard that displays current and past operating conditions, including indoor comfort indicators, as well as the energy used by different components.

These second generation platforms feature high efficiency programmable LED lighting with adjustable modes and sensors that respond to the amount of natural daylight in the room to control lighting usage. The walls and ceiling are highly insulated, and the operable windows (on the north and south side) feature high-performance glazing that allows visible light through minimizing the infrared spectrum responsible for solar heat gain in a building. Both platforms have ceiling fans that improve the perceived comfort by moving air across the skin. and air conditioning systems specifically designed for mixed-mode buildings. They have been setup for a 1 hour on-demand timer/thermostat cycle off between classes and not run unless manually activated by users.

Energy Efficiency and Comfort Literature Database

In order to support defining the research questions related to the second generation FROG building project and the follow up monitoring of the first generation FROG building project, an energy efficiency and comfort literature database was created under APRISES13.

The database is a collection of hundreds of journal and conference papers, as well as reports of the last 15 years until October 2017. It is a literature research of papers (reverse chronological order) dealing with energy efficiency, comfort (thermal, visual, acoustic), and indoor air quality.

The database is organized in 9 columns:

- Date (year-month)
- Paper citation and link
- Abstract
- Paper type
- Keywords
- Paper highlights
- Paper outline
- Organizations involved in the research
- Download – is the paper available in download format? Y/N

The database is available both in Excel and pdf format on the HNEI website. The last format (Figure 7.7) shows some text highlighted with the aim to help researchers immediately find the paper results.

Papers are organized in paper type depending on the type of research presented:

- Literature review
- Field study
- Laboratory study

- Statistical study
- Modeling study
- Simulation/Parametric/Control study
- Informational
- Tool/Technology development

Keywords instead contain several indications about:

- building type/sector (school, university, university campus, residential, commercial)
- room type (office, laboratory)
- building mode of operation (natural ventilated, air conditioned, mixed-mode, ceiling fans, free running conditioned)
- climate type (tropical, warm and humid, cold)
- seasonal variations (spring, summer, fall, winter, rainy season, dry season)
- other factors (age factor, gender difference, individual control, adaptation/acclimatization, occupant behavior, post-evaluation survey, etc.)

#	Year	Title	Abstract	Paper type	Keywords	Highlights	Outline	Organization	Link	Downloaded?
71	201703	X. Deng, G. Kokogiannakis, Z. Ma, P. Cooper, "Thermal Comfort Evaluation of a Mixed-mode Ventilated Office Building with Advanced Natural Ventilation and Underfloor air Distribution System", Energy Procedia, Vol. 111, March 2017, pp. 520-523, http://www.sciencedirect.com/science/article/pii/S1876610217302448	This study uses field monitoring and post occupancy evaluation (POE) surveys to investigate the indoor thermal comfort of an office building that is located in subtropical zone. The building is special as it combines advanced natural ventilation (ANV) strategies and underfloor air distribution (UFAD) systems. A comparison between a static thermal comfort model and a dynamic thermal comfort model is also conducted. The results show that the thermal comfort conditions in the case study building are satisfactory in summer while in winter there is evidence of thermal discomfort. For the case study building, the static thermal comfort model gives outputs that matched well with the responses of the occupants during the POE survey in winter while the dynamic model is more representative of the sensation of the occupants in summer.	Field study	Mixed-mode ventilation; Thermal comfort; Post-occupancy evaluation (POE); Office building; Subtropical zone; Seasonal variation (winter, summer).	<ul style="list-style-type: none"> • This study uses field monitoring and post occupancy evaluation (POE) surveys to investigate the indoor thermal comfort of an office building that is located in subtropical zone. The building is special as it combines advanced natural ventilation (ANV) strategies and underfloor air distribution (UFAD) systems. • A comparison between a static thermal comfort model and a dynamic thermal comfort model is also conducted. The results show that the thermal comfort conditions in the case study building are satisfactory in summer while in winter there is evidence of thermal discomfort. 	<ol style="list-style-type: none"> 1. Introduction 2. Methods (case study building and location; field investigation) 3. Results analysis 3.1 Indoor thermal environment results: natural ventilation control over the whole year; temperature stratification measurements; POE analysis 3.2 Thermal comfort models comparison 4. Discussion 4.1 Indoor thermal environment results 4.2 Suitability of thermal comfort models to mixed-mode ventilated buildings 5. Conclusions References 	Sustainable Buildings Research Centre, University of Wollongong, Wollongong 2522, NSW, Australia	http://www.sciencedirect.com/science/article/pii/S1876610217302448	YES
72	201702	K. Sun, T. Hong, "A simulation approach to estimate energy savings potential of occupant behavior measures", Energy and Buildings, Vol. 136, 1 February 2017, pp. 43-62, http://www.sciencedirect.com/science/article/pii/S0378778816317716	Occupant behavior in buildings is a leading factor influencing energy use in buildings. Low-cost behavioral solutions have demonstrated significant potential energy savings. Estimating the behavioral savings potential is important for a more effective design of behavior change interventions, which in turn will support more effective energy-efficiency policies. This study introduces a simulation approach to estimate the energy savings potential of occupant behavior measures. First it defines five typical occupant behavior measures in office buildings, then simulates and analyses their individual and integrated impact on energy use in buildings. The energy performance of the five behavior measures was evaluated using EnergyPlus simulation for a real office building across four typical U.S. climates and two vintage. The Occupancy Simulator was used to simulate the occupant movement in each zone with inputs from the site survey of the case building. Based on the simulation results, the occupant behavior measures can achieve overall site energy savings as high as 22.9% for individual measures and up to 41.0% for integrated measures. Although energy savings of behavior measures would vary depending upon many factors, the presented simulation approach is robust and can be adopted for other studies aiming to quantify occupant behavior impact on building performance.	Simulation/parametric study	Occupant behavior; Behavior measure; Building performance simulation; Office building; Energy savings; Behavior modeling; EnergyPlus.	<ul style="list-style-type: none"> • Occupant behavior has significant impacts on energy use in buildings. • A simulation approach is proposed to estimate energy savings of behavior measures. • Five measures on lighting, plug-loads, HVAC, windows, and thermostat are studied. • Behavior measures can achieve up to 41.0% savings based on the simulation results. • Occupancy schedule significantly affects the energy savings of behavior measures. 	<ol style="list-style-type: none"> 1. Introduction 2. Methodology 2.1 Overview 2.2 Field investigation 2.3 The baseline model: generation of stochastic occupancy schedule; efficiency of the building based on ASHRAE standard 90.1; the variable refrigerant flow system; fixed HVAC equipment sizing 2.4 Simulation of the occupant behavior measures: lighting control; plug load control; thermal comfort criteria; HVAC control; window control 2.5 The occupant behavior model of turning on/off the lights and HVAC 2.6 The lighting usage in multi-occupant offices 3. Results (lighting control; plug load control; 	Building Technology and Urban Systems Division, Lawrence Berkeley National Laboratory, One Cyclotron Road, Berkeley, CA, USA	http://www.sciencedirect.com/science/article/pii/S0378778816317716	YES

Figure 7.7: Screenshot of the energy efficiency literature database.

UH Flexible Response to Ongoing Growth (FROG) Data Analysis

The UH FROG buildings started to be monitored at the end of September 2016, and when instrumentation and classroom scheduling stabilized, data was used for the following detailed analyses (covering the Fall 2017 semester from August 20 to December 16; weeks 34 to 50 of 2017):

- School days: 81 days
- Non-school days (weekends + holidays*): 38 days
- Total number of analyzed days: 119 days
- Beginning of data collection: first week of Fall 2017 semester, August 20 to 26, 2017, which corresponds to week 34 of 2017

*Holidays: September 4, 2017 (Monday) – Labor Day; November 10, 2017 (Friday) – Veterans’ Day; November 23, 2017 (Thursday) – Thanksgiving Day; November 24, 2017 (Friday) – Non-instructional day

It was attempted to monitor both interior and exterior conditions during the same period of time. The weather station installed at Hokenani Elementary School (<http://hnei.hidoe-thermal-comfort.4dapt.com/>) by the State of Hawaii Department of Education provided public access to temperature, relative humidity, solar radiation, wind speed, wind direction, and rain values. Due to intermittent periods of questionable data resulting from sensor problems, these measurements were discarded by the HNEI team. For future data analysis, the outdoor weather data from the weather station installed at the UH Manoa FROG buildings will be used. Figure 8 presents the sensor type used to collect the indoor environmental conditions and energy data.

The energy consumption of the building was evaluated using data collected at two sampling rates:

- 1 min average data with eGauge instrumentation. Only whole building data available at the following websites (<http://egauge791.egaug.es/57A4C/>, <http://egauge793.egaug.es/57A4C/>)
- 5 min average data with WebCNTRL instrumentation: disaggregated loads available (refers to Figure 7.8 for individual sensors).

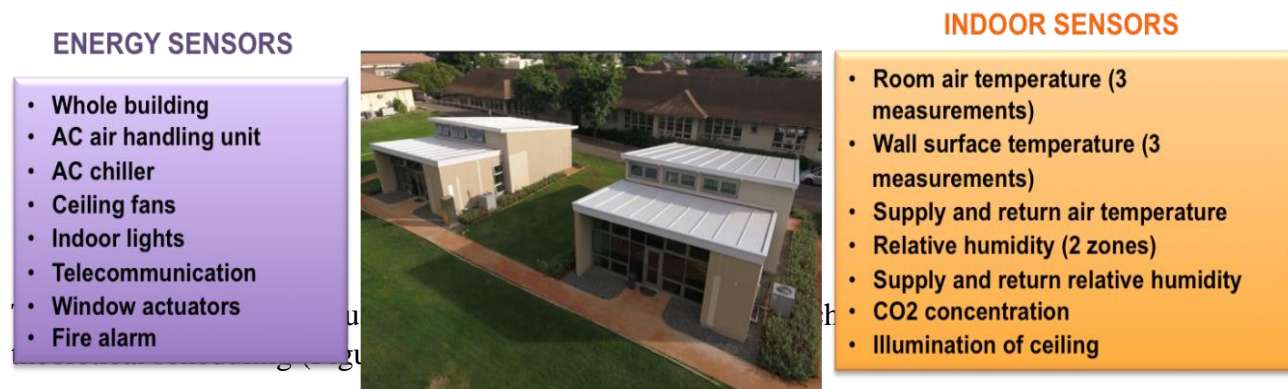


Figure 7.8: List of the energy and indoor sensors used in both buildings.

FROG 1	Sunday	Monday	Tuesday	Wednesday	Thursday	Friday	Saturday
7:30 - 12:30 AM							
1:45 - 4:15 PM							
4:30 - 7:00 PM							

FROG 2	Sunday	Monday	Tuesday	Wednesday	Thursday	Friday	Saturday
7:30 - 12:30 AM							
1:45 - 4:15 PM							
4:30 - 7:00 PM							

Figure 7.9: Theoretical Fall 2017 semester scheduling.

Figure 7.10 shows the weekly energy consumption of both UH FROG buildings. FROG 1 has a higher weekly energy use than FROG 2 due to the higher scheduled usage shown in Figure 9. This shows a declining energy consumption trend in both FROGs.

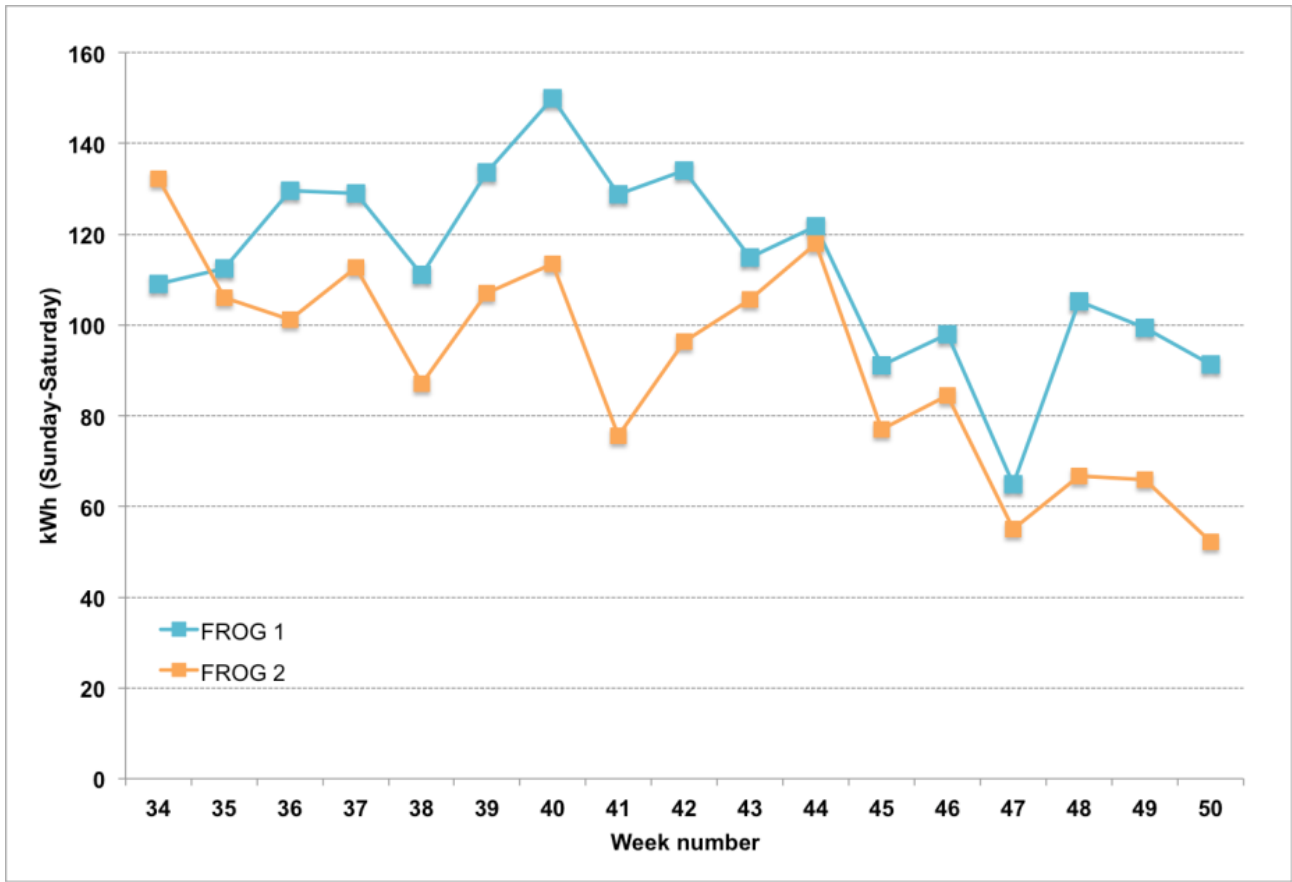


Figure 7.10: UHM FROGs weekly energy evaluated over a 24 hour period (weekdays) (eGauge data).

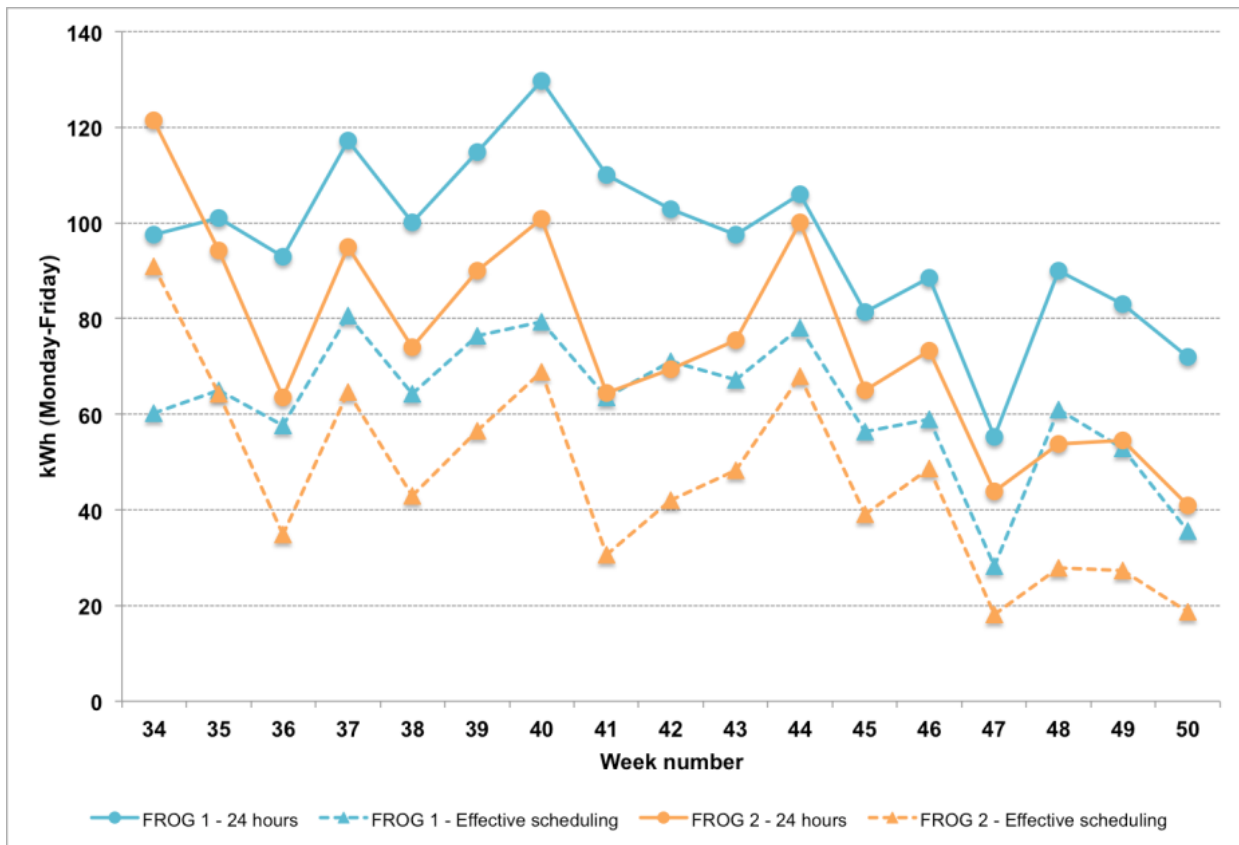


Figure 7.11: UH FROGs weekdays energy (Monday-Friday) - 24 hours versus effective scheduling building use (eGauge data).

Figure 7.11 shows both the weekday energy used over a 24 hour period and the effective scheduled building use. Both the energy used during the effective occupancy time and the 24 hour energy decreased over time. This is because users reduced air conditioning usage as will be shown in the weekly disaggregated load charts.

An Energy Use Intensity (EUI) comparison between the first generation FROGs (Kawaikini East, Kawaikini West, Ilima) and second generation FROGs (Manoa FROG 1 and FROG 2) shows that on average the second generation uses approximately 47% of the energy per square foot compared with the first generation, (Table 7.1, excluding solar generation).

Table 7.1 Actual source Energy Use Intensity (EUI).

	Kawaikini East	Kawaikini West	Ilima	*UH FROG 1	*UH FROG 2
Total annual energy (kWh/yr)	7,183	4,840	9,881	4,325	3,518
Actual EUI (kWh/sf/yr and kBTU/sf/yr)	5.6 /19.1	3.8 /13.0	7.7 / 6.3	3.0/10.2	2.4/11.7

*Total annual energy and actual EUI values were evaluated using eGauge data for the entire 2017 year (January 1, 2017-December 31, 2017)

End-use disaggregation (see Figure 7.11) indicates that less energy is used by both lighting and air conditioning systems in the second generation than in the first. Ceiling fans make up a larger proportion of the energy consumed in the second generation by virtue of the smaller lighting and cooling loads.

By considering the disaggregated loads collected by the WebCNTRL instrumentation, it is possible to evaluate the energy used by appliances for the entire Fall 2017 semester (Table 7.2).

Table 7.2 Energy summary (disaggregated loads)– August 20-December 16, 2017.

Fall semester 2017	Air conditioning (kWh)	Ceiling fans (kWh)	Indoor lights (kWh)	Other loads* (kWh)	Whole building (kWh)
FROG 1	866	282	212	576	1,936
FROG 2	573	228	194	528	1,523

*Other loads = Plug loads + Telecommunication + Window actuators + Fire alarm

If we want to compare how the users were using the buildings during the different teaching sessions and what their average energy consumption was, we need to normalize the data over the effective number of hours of the building occupancy. This was done using the average utilization demand (Avg. UD) parameter (in kWh/h).

The Avg. UD parameter was evaluated only for weekdays (Monday-Friday) on a 24 hour period, as well as for the different sessions of the day (Avg. UD morning session; Avg. UD afternoon 1 session; Avg. UD afternoon 2 session). Then, the parameter was also evaluated considering the total effective day occupancy (Avg. UD occupancy) and outside the effective building occupancy time (Avg. UD outside occupancy). With these last two parameters it is possible to compare both buildings' energy consumption.

The following Figure 7.12 shows a weekly summary (only weekdays have been considered) of the Avg. UD for both buildings. By considering the average weekly 24 hour values, there are no differences between the two buildings; but if one considers the normalized parameter at the session level, FROG 1, on average, uses more energy during the morning and afternoon sessions. Even when there is a decreasing trend in the energy consumption during the morning and afternoon 1 sessions, the Avg. UD values of the afternoon 2 sessions for both buildings stays quite constant. Thus, building occupants are using the appliances differently, even though the twin buildings are experiencing the same outdoor weather conditions.

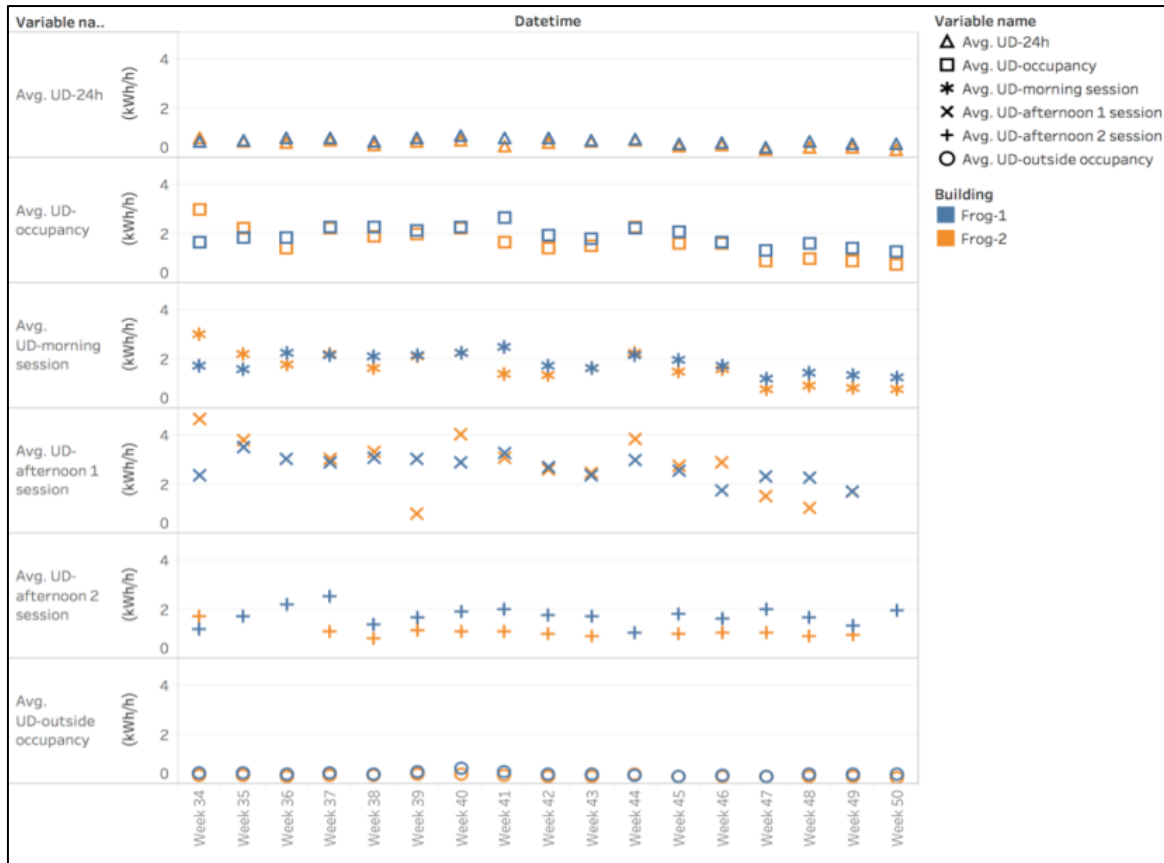


Figure 7.12: UHM FROGs weekdays Avg. UD parameters (kWh/h) (eGauge data).

This Avg. UD parameter shows another interesting result, which is related to occupant habits and behavior (Figure 7.13).

On week 40, FROG 1 shows an increase in the energy consumption (130 kWh, Figure 7.12). This increase did not happen during the effective occupancy time of the building (Avg. UD occupancy), but outside it (Avg. UD-24h, Avg. UD-outside occupancy) because people left the ceiling fans running at night (Figures 7.13-14) from about 6.00pm on October 2, 2017 to 6.00am on October 3, 2017. This also explains the increase in the energy value shown in Figure 7.13.

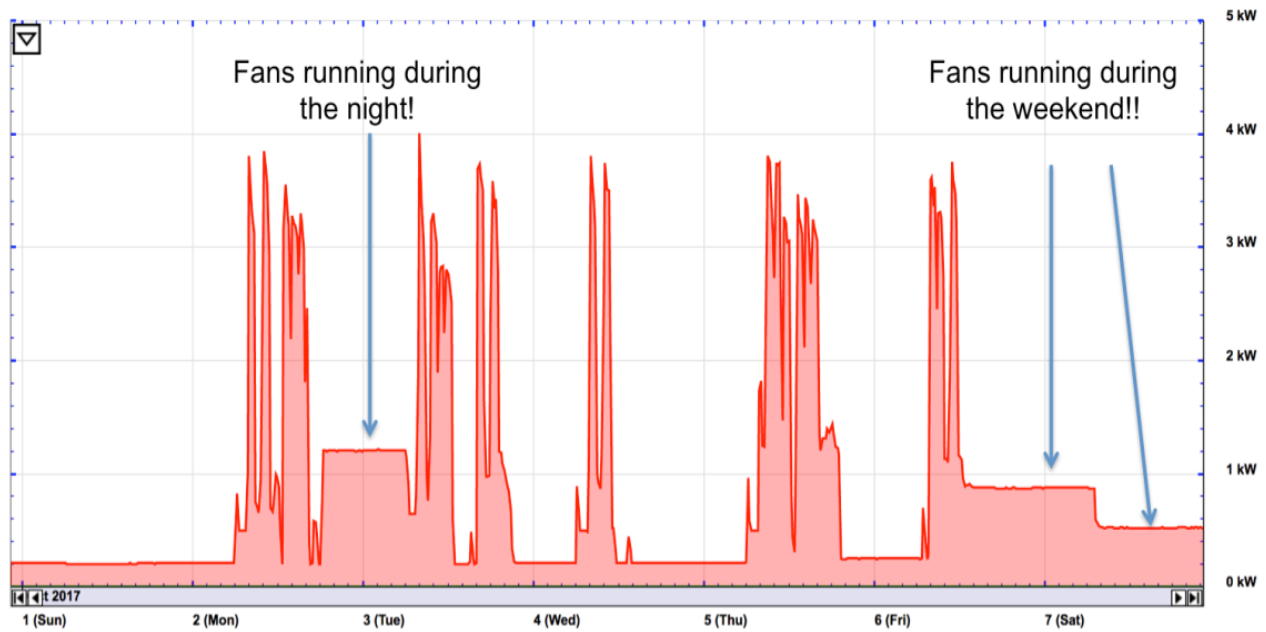


Figure 7.13: UHM FROG 1 – Week 40 whole building power usage (eGauge data).

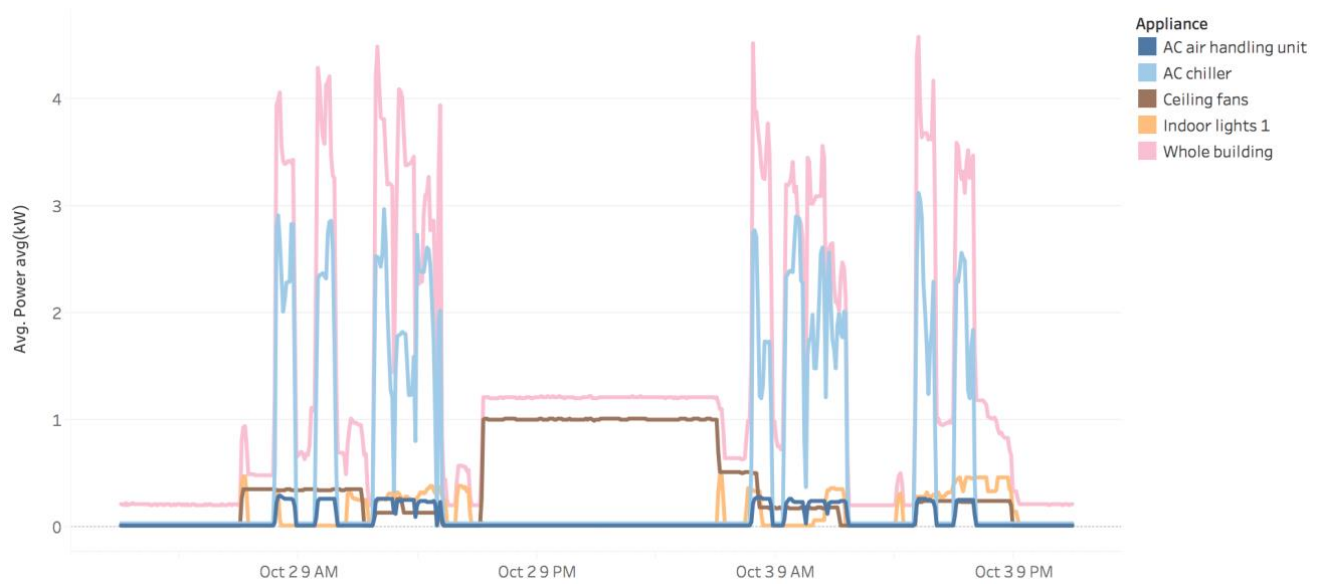
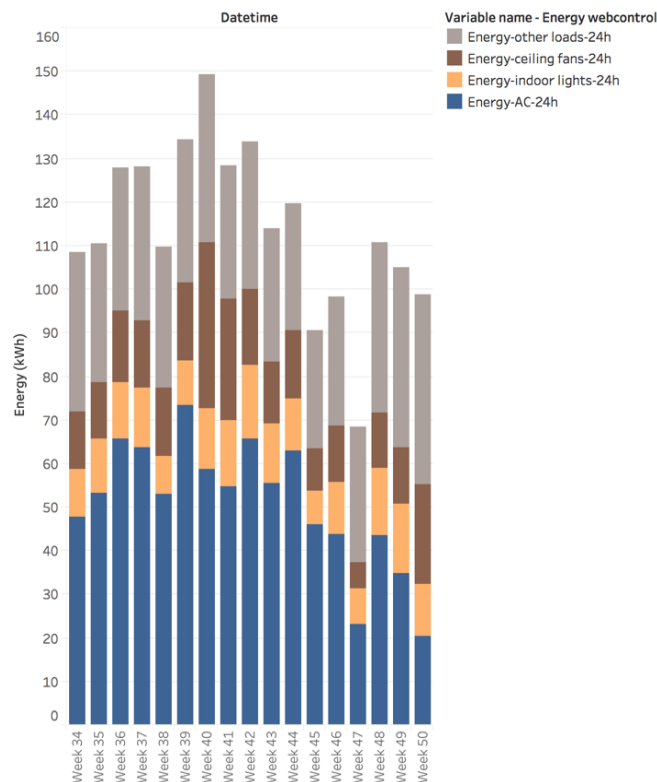


Figure 7.14: UH FROG 1 – Disaggregated load Week 40, Oct 2-3, 2017 (WebCNTRL data).

FROG 1



FROG 2

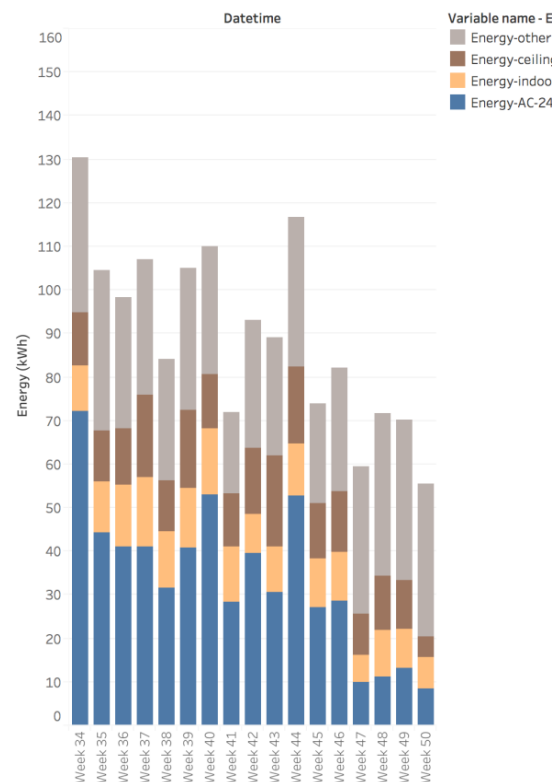


Figure 7.15: UH FROGs - weekly disaggregated load of the Fall semester (WebCNTRL data).

Figure 7.15 graphically represents the average weekly disaggregated loads, organized by week number, across end-uses. These values represent the entire weekly energy data. Both buildings show a decreasing trend in the energy consumption particularly in the use of the air conditioning system.

Comfortmeter questionnaire

Another activity funded in APRISES13 within the “Environmental Research Support for Energy Neutral Research Platforms” was starting a research collaboration with the Belgian company called Factor4 (<http://factor4.eu/>) which is part of a European Horizon2020 project called Quantum. In June 2016, a poster called “Strategies that influence performance of mixed-mode NZE buildings in Hawaii” (A.J. Maskrey, S. Cerri, E. Peppard) was presented at the 4th Sustainable Places 2016 conference in Anglet (France) and during the conference one of the authors met people from the Quantum project and started discussions about using the tool for buildings in a tropical environment, and tailoring it for university buildings and students.

After being reviewed by HNEI personnel, the Comfortmeter questionnaire was sent in October 2017 to the Office of Research Compliance at University of Hawaii to obtain Institutional Research Board (IRB) approval to start delivery in the coming Spring 2018 semester.

As TheComfortmeter online survey has been specifically adapted for use in the FROG buildings where students use the buildings for short periods of time (one semester) and for a few hours during the week. The survey covers all comfort-related topics, over 50 questions, relating to room air temperature, air quality, noise, odor, etc. After completing the survey, a user-anonymized, statistical evaluation regarding the performance of factors affecting user comfort is provided. The evaluation contains detailed analysis and practical advice to create a healthier environment for the users.

The survey does not require an on-site visit or any program installation on users' computers. The Comfortmeter analysis is completed via a standard web-browser. The Comfortmeter questionnaire will be issued to building users in March 2018.

Conclusions

- Fall 2017 semester: WebCNTRL instrument commissioning was substantially completed in the fall.
- An Energy Use Intensity (EUI comparison between the first (Kawaikini East, Kawaikini West, Ilima) and second generation UH Manoa FROGs (FROG 1, FROG 2) shows that on average the second generation uses approximately 47% of the energy per square foot compared with the first generation, (excluding solar generation).
- Monitoring the eGauge and WebCNTRL data helps determine typical daily energy usage and shapes the training methodology.
- Real time diagnosis helps find operational issues (e.g. leaving fans running over the weekend, night) and unusual appliance use.
- UH Institutional Research Board (IRB) approved starting the delivery of the Comfortmeter questionnaire in the coming Spring 2018 semester.

C. Emerging Technologies

Technology 1: Desiccant Dehumidification for Mechanical HVAC Systems in Tropical Environments

Humidity related problems have long been recognized as risks to occupants and building structures. Standard Heating Ventilation and Air Conditioning (HVAC) systems are challenged to deal effectively with elevated indoor humidity levels because sensible and latent cooling cannot be effectively separated.

With the objective to avoid indoor humidity problems sensible and latent cooling is decoupled. This can be done with the addition of conventional cooling-based dehumidification systems. However, desiccant systems are more effective since cooling the moist supply air to below-dewpoint temperatures is not required. The report “Phase I: Design Study and Project Site Selection” evaluates liquid desiccant dehumidification systems, and as part of the deliverable proposes a pilot design, identifying a potential site for a future Phase II implementation of the pilot under future funding.

The goal was to develop the concept and final design of a proposed hybrid liquid desiccant system, which provides innovative space conditioning technology to fit the Hawaii climate. This design is intended to be used under other funding for a pilot installation.

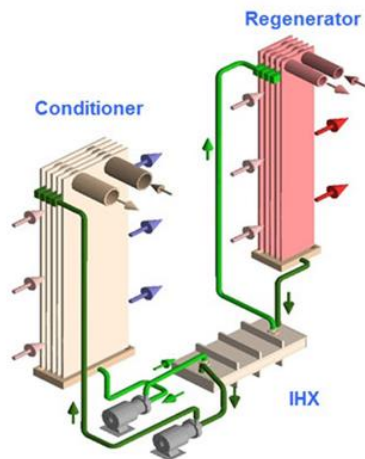
Work completed under APRISE13 includes:

- Investigated the commercially available desiccant technologies, and selected appropriate technology vendors
- Identified applications for desiccant dehumidification that separate sensible heat removal from latent in Hawaii
- Assessed design and implementation issues to integrate the dehumidification technology with HVAC systems
- Recommended system configuration and provided detailed project design; identified a site for implementation of Phase II pilot.

Low-Flow Liquid Desiccant Technology

Conventional liquid desiccant (LD) dehumidification systems have higher maintenance and operational challenges compared to standard HVAC technology. This has been a barrier to their wider use in general HVAC applications. A new liquid desiccant dehumidification technology, the so-called “low flow” desiccant process was selected in order to avoid these problems in the pilot design. The new low flow liquid desiccant technology has internally heated and cooled process vessels, and a significantly lower desiccant flow rate. This avoids desiccant droplet carryover to the conditioned spaces and smaller process vessels. The new liquid desiccant technology also requires less maintenance and is more energy efficient.

Figure 7.16 shows the low-flow liquid desiccant technology developed by AIL Research Inc. (AILR) selected for this project after evaluating six liquid desiccant vendors. The figure shows a schematic rendering and a photo of an internally cooled absorber. Unlike the packed columns type process vessels of conventional systems, the new low-flow technology uses evaporative matrix in the absorber and regenerator. Desiccant solution slowly flows downwards through the evaporative matrix while being in contact with air passing through it. Copper tubes integrated into the matrix, which contains a flow of cooling or heating water, provide the internal heat sink and source for the absorber and regenerator heat, respectively.



AILR low flow" LD dehumidifier with three main components: the conditioner, the regenerator and the interchange heat exchanger (IHX)



The AILR patented absorber and regenerators design. Cooling tube are imbedded into an evaporative medium

Figure 7.16a and b: The AILR “low flow” liquid desiccant technology components.

Figure 7.17 a,b and c shows example commercial and demonstration HVAC projects by others that use AILR liquid desiccant technology products. The figure shows (a) packaged Liquid Desiccant Air Conditioning (LDAC) systems containing absorber and regenerator, (b) and (c) LDAC units with solar thermal systems that provide heat to the regenerator. Presently, AILR’s LDAC technology is not widely used, since low-flow liquid desiccant dehumidification in building HVAC is an evolving and emerging technology.



(a) LDAC type installed at supermarkets in Seal Beach and Tustin, California.



(b) (above) a AILR LD unit was installed at a supermarket in Hawaii. The process heat for desiccant regeneration was supplied by solar thermal system.



(c) (left) An AILR LD unit was installed Tyndall AFB. Hot water is provided by a 1,350-square foot array of evacuated-tube solar collectors.

Figures 7.17 a, b and c: Selected commercial and institutional projects with AILR liquid desiccant technology products.

System Integration of Liquid Desiccant (LD) Technology with Sensible Cooling Technologies

The LD system dehumidifies the supply air to such an extent that the indoor latent load, e.g. the water vapor introduced to the conditioned space, can be safely absorbed by the dry air and expelled with the discharge air. The LD system does not, however, remove sensible heat, and therefore separate sensible cooling technologies were integrated into the design to reduce the temperature in the conditioned space. In this technology comparison it was assumed that the indoor air has been sufficiently dehumidified, e.g. the dew point has been sufficiently lowered, that the chilled water supply to the sensible cooling units remains below dew point and therefore condensation does not occur.

During the project several chilled-water cooling technologies were considered, with the passive chilled beam (PCB) technology selected for the pilot. Passive chilled beams do not use primary supply air to induce indoor air flow over the cooling elements inside the chilled beam. The PCB technology relies solely on density-induced air flow over the cooling elements inside the chilled beam. The PCB has no internal fan nor a connection to the primary air duct. Newer designs of PCB designs have significantly increased both the convective as well as the radiant heat transfer rates. Using PCBs allows complete decoupling of sensible and latent cooling load removal.

Figure 7.18 shows the PCB technology selected for the project, the Barcol's "Radiant Wave" product. Radiant Wave panels will be suspended below the ceiling. Placing the panel at a prescribed distance from the ceiling increases the convective heat transfer rates and also provides a significant portion of the cooling capacity as radiant heat transfer.

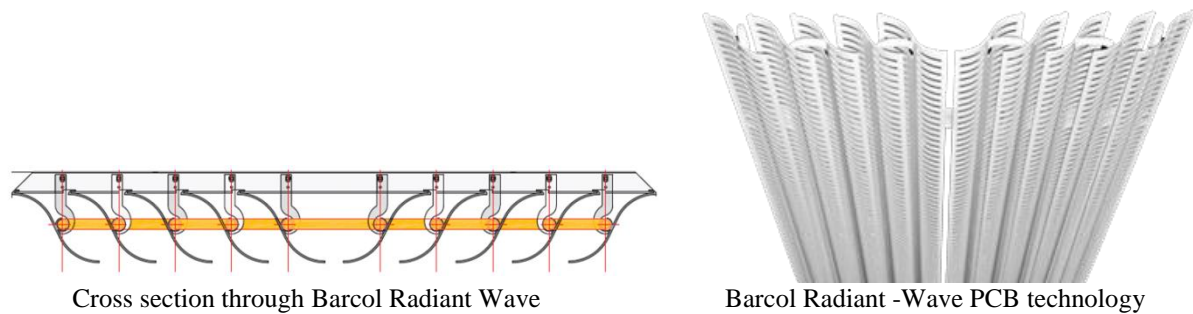


Figure 7.18: Passive Chilled Beam (PCB) technology selected for the project, Barcol Radiant Wave.

A schematic of the preferred configuration of the proposed LDAC system with liquid desiccant dehumidification and sensible cooling using passive chilled beams (PCBs) is shown in Figure 7.19. A water-to-air heat exchanger is added downstream of the LD unit to allow a controlled removal of sensible heat from the dried air stream coming out of the desiccant absorber unit. A ceiling fan was integrated into the design as a cost-effective convective means to cool the occupants.

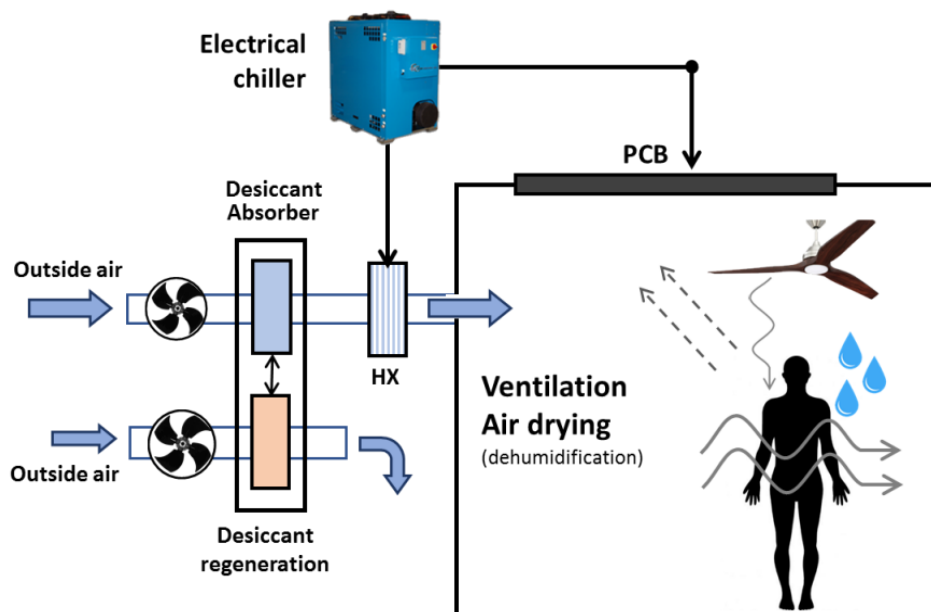


Figure 7.19: Configuration of the LDAC system with desiccant dehumidification and sensible cooling using passive chilled beams (PCBs).

The LDAC system provides significant electrical energy savings over standard HVAC systems. The results of the energy analysis suggest that the proposed LDAC would save approximately 30% of electric energy compared to the baseline of a standard HAC system. These predicted energy savings are similar to energy savings reported by a 2014 NREL study for several installations of AILR liquid desiccant systems.

The following are the primary factors for improved energy efficient operation:

- The LD dehumidification system uses only a limited amount of electricity for fans and pumps. The system uses thermal heat for desiccant regeneration and evaporative cooling for the heat sink of absorption heat of the absorber. The LD system does not use a vapor compression cycle. The heat for desiccant regeneration would preferably come from a solar thermal system or provided by waste heat.
- The passive chilled beams do not use electric energy directly.
- The sensible cooling units require heat sinks which can be supplied by either conventional vapor compression (VC) chillers or be thermally driven chillers, such as adsorption chillers. Using adsorption chillers requires installation of solar thermal systems with a thermal buffer storage tank. A prudent system design using adsorption chillers would implement some form of stand-by heat source to provide for heating water supply interruption due to intermittent availability of solar heat.

As a system sizing example, the project evaluated the energy performance of the proposed LDAC system serving a sample 8,000-sqft office space, and compared the energy use with a standard HVAC system. The LDAC used a ventilation flow rate that was twice that of a standard HVAC based on minimum ASHRAE ventilation rates. Even with additional ventilation cooling loads, using energy saving features, the predicted energy savings of the proposed LDAC results in \$9,000 energy cost saving per year, using energy prices typical for Hawaii. Figure 7.20 shows the results and the comparison of annual energy costs between a standard HVAC and the proposed LDAC system.

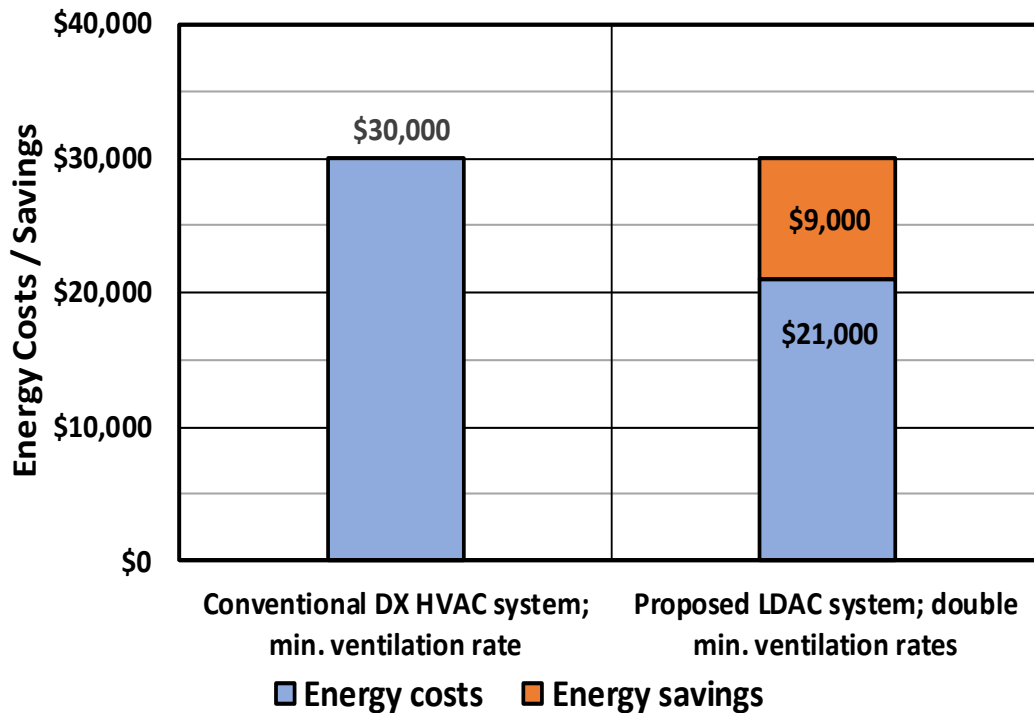


Figure 7.20: Comparison of annual energy costs between a standard HVAC and the proposed LDAC system in a sample 8,000 sqft office.

A detailed report, Desiccant Dehumidification is available on the HNEI website.

Reports Resulting from these Efforts

Sustainable Design & Consulting LLC and Hawaii Natural Energy Institute, *Desiccant Dehumidification Studies*, (November 2017)

Sustainable Design & Consulting LLC and Hawaii Natural Energy Institute, *“Technology Review and Availability of Liquid Desiccant Systems”*, (June 2017)

Sustainable Design & Consulting LLC and Hawaii Natural Energy Institute, *“Identify Application Potential of Liquid Desiccant Installations in Hawaii”*, (July 2017)

Sustainable Design & Consulting LLC and Hawaii Natural Energy Institute, *“Assessment of Liquid Desiccant Dehumidification Systems and Supporting Thermal Technologies and Concept Designs with Emphasis on Application Potential in Hawaii”*, (November 2017)

Sustainable Design & Consulting LLC and Hawaii Natural Energy Institute, *“Design Study Of A Packaged Liquid Desiccant (LD) System In A Test Facility To Carry Out A Test Program Under Lab Conditions And Subsequent On-Site Test Operation Of The LD System,”* (November 2017)

Sustainable Design & Consulting LLC and Hawaii Natural Energy Institute, “*Project Summary Report And Presentation: The Growing Indoor Humidity Challenges Of Buildings, And Strategies To Solve Them*”, (November 2017)

Technology 2: Advanced Design, Control and Application of Ceiling Fans; Ceiling Fan Gap Evaluation

Organizations in Hawaii and in other tropical areas continue to seek innovative applications of technologies to improve thermal comfort. While ceiling fans have been used for centuries, there are few tools that allow designers and planners to make deliberate, conscious fan selection based on research, constraints of the space and the physical characteristics of the fans. In addition, newer algorithms have been identified that modulate and vary fan speed to create "random" cycles of air movement that interrupt a continuous, repetitive flow of air across the skin, thereby increasing the perception of comfort. In this project, HNEI contracted MKThink to evaluate fan typologies, control options, and operational characteristics and provides research-based design guidelines to assist in space planning, design and product selection. The contractor also identified gaps between existing industry and market conditions and the current knowledge base, resulting in recommendations for areas of academic study to benefit the marketplace. This APRISES13 task completes work begun under APRISES11 (MKThink, September 2017).

Process

The four key elements of the “Phase 1” of the project include a detailed literature review, market research, and technical research under APRISES 11 that results in a gap analysis funded by APRISES 13, as outlined in Figure 7.21. Phase 2 would be part of future work funded under a different grant.

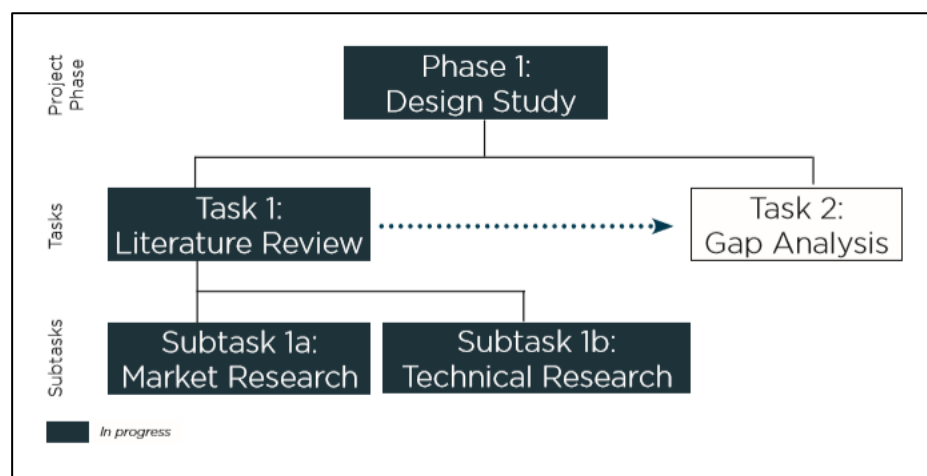


Figure 7.21: Four Key elements of this ceiling fan project.

Task 2, specific to APRISES 13 concludes the ceiling fan literature review and market report funded begun under APRISE11 in order to build on existing research to identify gaps for further study. This literature review included coverage of academic journals, industry journals, white papers, conference presentations and manufacturer information in order to develop a high-level understanding of:

- Available and emerging technology (including motor, blade shape, smart sensing, etc.)
- Applications
- Space type
- HVAC type - mixed mode, natural ventilation
- Control strategies
- Energy use
- Cost-benefit analysis
- Industry specific metrics including EPA Energy Star ceiling fan criteria

Results

A total of 33 gaps in the ceiling fan knowledge-base were identified during this research. The gaps include information that is not typically available for ceiling fan technology, as well as information that is not available for a subset of applications or performance metrics.

The gaps are organized using a 3x2 matrix to separate the *characteristics* of the ceiling fan systems from the *performance metrics* used to evaluate the system, Figure 7.22. The rows represent the characteristic categories as used in the Literature Review and Market Report: Operations, Size &

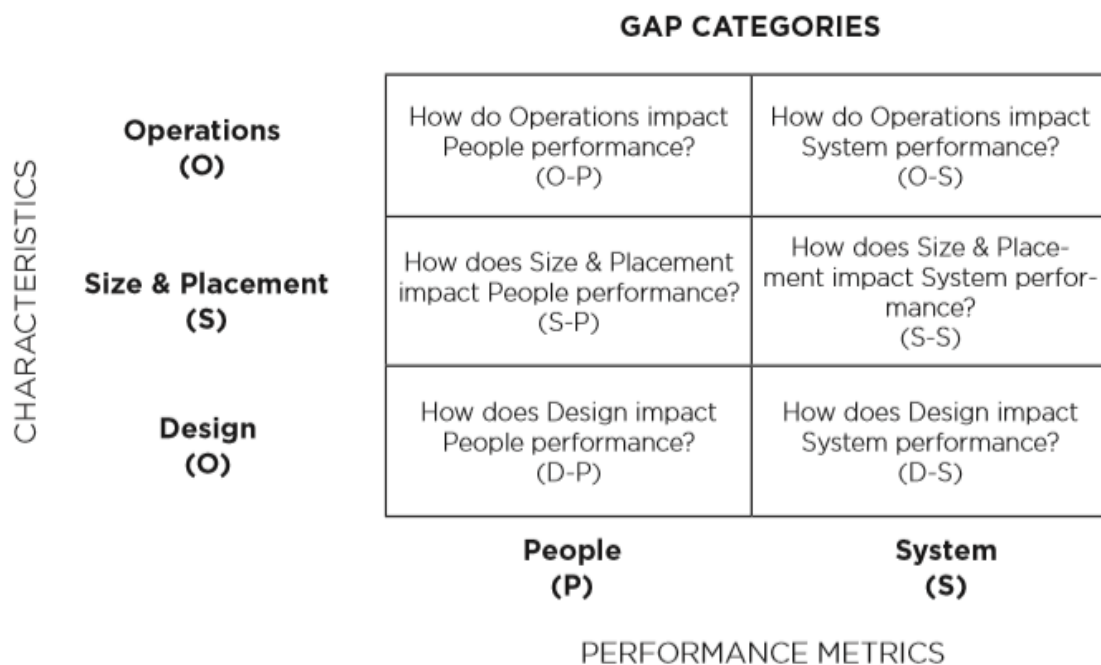


Figure 7.22: Classification of gap categories.

Placement, and Design. The columns represent the two performance metric categories: People (effectiveness) and System (efficiency). The report organizes and prioritizes the gaps using this matrix.

Gap Prioritization Methodology

The gaps are prioritized using the following criteria:

- Practitioner & User Focused - Studies were prioritized that leverage existing technologies (i.e. focus on improving Operations and Size/Placement because they can be immediately implemented). To assign priorities to the categories in the matrix below, points are first distributed from 1-3 by row. Points are allocated in the following way:
 - 3 points: Operations.
 - 2 points: Size & Placement..
 - 1 point: Design.
- Focus on People (Effectiveness) before System (Efficiency) - Studies were prioritized that link Design, Size/Place, and Operations to effectiveness (thermal comfort, etc.) before efficiency (CFM/W, etc.) To assign priorities to the categories in the matrix below, points are then distributed from 1-2 by column. Points are allocated in the following way:
 - 2 points: People.
 - 1 point: System.

Each category was assigned points based on the above criteria and then ranked from the lowest number of points to the highest to form the prioritization schedule (Figure 7.23). Gap categories that ended up in a tie were prioritized by those in People and Operations/Size-Placement, for the reasons stated in the prioritization criteria. The 33 projects were screened and ranked according to the prioritization schedule, resulting in the distribution matrix shown in Figure 7.24.

PRIORITIZATION SCHEDULE
(1 = High, 6 = Low)

Operations	1	4
Size & Placement	2	5
Design	3	6
	People	System

NUMBER OF GAPS

Operations	13	4	
Size & Placement	2	6	
Design	3	5	
	People	System	
	PERFORMANCE METRICS		

= Total
33

Figure 7.23: Ranking of priority criteria.

Figure 7.24: Number of gaps identified for each matrix cell.

Ceiling Fan Gap Analysis Results

The following list includes the gaps identified by the study in order of priority.

Priority One Topics:

Fan Speed: How does thermal comfort change with different fan speed settings?

Fan/Ventilation Interactions: How do ceiling fans impact thermal comfort when used in buildings with natural, mixed-mode and HVAC ventilation systems?

Cognitive Abilities: How does the use of ceiling fans impact cognitive abilities, learning ability and productivity in different settings?

Behavior Impacts: How is occupant behavior impacted by the use of ceiling fans?

Fan Type/Size: How is thermal comfort impacted by fan type, size and quantity?

Controls: How do usage patterns and user preferences vary across the different control technologies?

Multi-Fan Controls: How do user patterns change across the different multi-fan control devices?

Fan Use: How do usage patterns and preferences of ceiling fans differ by age?

School Codes & Standards: Can installation and operational codes and standards be developed for fan use in educational settings? What would these codes and standards look like?

Intermittent Speeds: How do modulating fan speed settings contribute to occupant comfort?

Personal Control: How is thermal comfort impacted by the different control technologies?

Lighting Obstructions: How does dimming the lights to reduce the strobe effect or maintaining the strobe effect impact occupants? What level of strobe is acceptable for human comfort?

Fan Comparisons: How do ceiling fans compare with other fan alternatives on thermal comfort (i.e. desk fans, standing fans)?

Priority Two Topics:

Alliesthesia: How might the placement of fans with variable speed modes create positive alliesthesia?

Air Movement with More than Two Fans: How do air movement profiles change with multiple ceiling fans?

Priority Three Topics:

Alliesthesia: How might the design of fans with variable fan speeds create positive alliesthesia?

Blade Quantity & Pitch: How does blade quantity, size, width and pitch impact thermal comfort in commercial and industrial applications?

Multi-Fan Controls: What are typical and proposed usage patterns with multi-fan controls? What design changes can impact usage patterns?

Priority Four Topics:

CFD Modeling: What is the accuracy of (e.g. +/- 20%) CFD at predicting air velocity and temperature distribution in a room?

Fan Use: When and how do occupants use ceiling fans in different room types in different applications (i.e. schools, offices)?

Fan/Ventilation Use: How are ceiling fans used when other ventilation systems are in use?

Fan/Ventilation Interactions: How does the use ceiling fans impact air movement when used in buildings with natural, mixed-mode & HVAC ventilation systems

Priority Five Topics:

Multiple Fan Placement: What are placement guidelines of multiple flat and airfoil blade ceiling fans for different room sizes and configurations?

Sizing & Placement Guidelines: What are sizing and placement guidelines for classrooms, cafeterias, and other school room types?

Strobe Effect: How can spatial orientation guidelines help minimize the strobe effect for all fan types? How might distance change by light source (i.e. fluorescent, LED) and light display type (i.e. panel, hanging light recessed lighting)?

Irregular Placement: How do placement guidelines for single and multiple ceiling fans change with irregular room and ceiling configurations where the fans cannot be placed equidistantly apart?

Multiple Fan Air Movement: What is the effect of occupants in a space on the air movement of multiple ceiling fans and how are pressure zones affected?

Air Profiles by Application: How do air movement and speed profiles vary for different room types in residential, commercial and industrial settings?

Priority Six Topics:

Air Speed Profiles: How do average air speed profiles change by fan type, blade type (i.e. flat, foil, HVLS), by size, and by manufacturer?

Blade Quantity & Pitch: How does blade quantity, size, width and pitch impact system performance in commercial and industrial applications?

Standardized Air Movement & Speed Profiles: How do flat and airfoil blade shapes impact standardized air movement and speed profiles?

Area of Influence: How does furniture or other obstructions affect ceiling fan areas of influence?

Retrofit Opportunities: How can existing fans be retrofitted to increase air flow efficiency (CFM/W)?

Conclusions

The Ceiling Fan Gap Analysis was concluded in January 2018 and identified and prioritized 33 gaps between the available literature and the knowledge base that would benefit designers and the industry. To address these 33 gaps, specific recommendations are made for future research to advance ceiling fan operation and application.

The detailed reports “Ceiling Fans: Literature Review and Market Report”; “Final Gap Analysis” are available on the HNEI website.

Reports Resulting from these Efforts

MKThink, *Ceiling Fans: DRAFT Literature and Market Report*, (June 2017)

MKThink, *Ceiling Fans: FINAL Literature and Market Report*, (September 2017)

MKThink, *Ceiling Fans: FINAL Gap Analysis*, (December 2017)